TU/e technische universiteit eindhoven

J. M. Burgerscentrum
Research School for Fluid Mechanics
TUD, TUE, UT, RUG, KUN

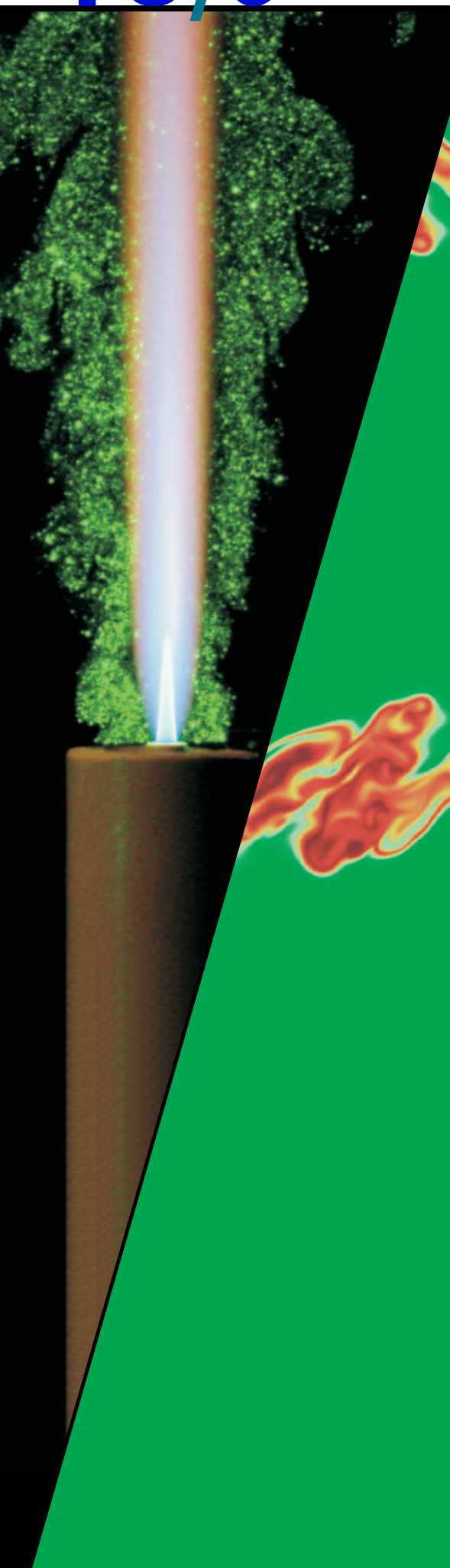

J. M. Burgerscentrum

Course on

Combustion

Organized by:

L. P. H. de Goey
D. Roekaerts

Lecture Notes

Edited by:

K. R. A. M. Schreel

Lecture notes of the

J. M. Burgerscentrum

Course on Combustion

1–4 April 2003
Eindhoven University of Technology
Department of Mechanical Engineering

Organised by:

prof. dr. L. P. H. de Goey
Eindhoven University of Technology

prof. dr. ir. D. J. E. M. Roekaerts
Delft University of Technology

Edited by:

dr. K. R. A. M. Schreel
Eindhoven University of Technology

ISBN 90-386-2885-4

Typeset with LaTeX in Y&Y MathTime Plus.

The cover shows DNS calculations on a compressible turbulent diffusion flame (courtesy of R. J. M. Bastiaans), and a photograph of the application of PIV in a high speed laminar methane/oxygen flame with co-flow (courtesy of K. R. A. M. Schreel).

Contents

List of Authors

Dr. N. J. Dam (Nico) . . . . . University of Nijmegen
Applied Physics
P. O. Box 9010
6500 GL Nijmegen
+31-24-3653016
nicod@sci.kun.nl

Prof. dr. L. P. H. de Goey (Philip) . . . . . Eindhoven University of Technology
Department of Mechanical Engineering
Section Combustion Technology
P. O. Box 513
5600 MB Eindhoven
+31-40-2472938
l.p.h.d.goey@tue.nl

Dr. ir. J. B. W. Kok (Jim) . . . . . Twente University
Department of Mechanical Engineering
P.O. Box 217
7500 AE Enschede
+31-53-4892582
j.b.w.kok@wb.utwente.nl

Prof. dr. H. B. Levinsky (Howard) . . . . . Groningen University
Department of Chemical Engineering
Nijenborgh 4
9747 AG Groningen
+31-50-5212677
h.levinsky@gasunie.nl

Prof. dr. ir. Th. M. van der Meer (Theo) . . . . . Twente University
Department of Mechanical Engineering
P.O. Box 217
7500 AE Enschede
+31-53-4892530
t.h.vandermeer@wb.utwente.nl

Prof. dr. J. J. ter Meulen (Hans) . . . . . University of Nijmegen
Applied Physics
P. O. Box 9010
6500 GL Nijmegen
+31-24-3653016
htmeulen@sci.kun.nl

Ir. J. A. van Oijen (Jeroen) . . . . . Eindhoven University of Technology
Department of Mechanical Engineering
Section Combustion Technology
P. O. Box 513
5600 MB Eindhoven
+31-40-2473286
j.a.v.oijen@tue.nl

Prof. dr. ir. D. J. E. M. Roekaerts (Dirk) . . . . . Delft University of Technology
Department of Multi-Scale Physics
Section Thermal and Fluid Sciences
P.O. Box 5046
2600 GA Delft
+31-15-2781448
dirkr@ws.tn.tudelft.nl

Dr. K. R. A. M. Schreel (Koen) . . . . . Eindhoven University of Technology
Department of Mechanical Engineering
Section Combustion Technology
P. O. Box 513
5600 MB Eindhoven
+31-40-2472117
k.r.a.m.schreel@tue.nl

Dr. L. M. T. Somers (Bart) . . . . . Eindhoven University of Technology
Department of Mechanical Engineering
Section CombustionTechnology
P. O. Box 513
5600 MB Eindhoven
+31-40-2472107
l.m.t.somers@tue.nl

Prof. dr. H. Spliethoff (Hartmut) . . . . . Delft University of Technology
Faculty of Design, Engineering and Production
Section Thermal Power Engineering
Mekelweg 2
2628 CD Delft
+31-15-2786071
H.Spliethoff@wbmt.tudelft.nl

Dr. ir. J. H. M. ten Thije Boonkkamp (Jan) . . . . . Eindhoven University of Technology
Department of Mathematics and Computer Science
P. O. Box 513
5600 MB Eindhoven
+31-40-2474123
j.h.m.tenthijeboonkkamp@tue.nl

Part 1

Introduction

Chapter 1

Introduction to Combustion

L. P. H. de Goey

1 Introduction

Combustion may take place in many different forms and circumstances. Depending on the flow type and the type of premixing, it is possible to distinguish different kinds of flame structures, each with its own characteristic features. The principle description of all gaseous combustion processes, however, is based on the same equations: the conservation equations for mass, species mass fractions, energy and momentum. There are two main categories of gaseous flames, which are categorised according to the type of mixing: premixed and non-premixed flames.

Premixed flames will be considered in section 2. The Borghi diagram for visualising the different combustion regimes in premixed turbulent combustion will be explained in section 2.1. Main focus will be on the different laminar flamelet regimes, where the flame time/length scales are so small that the flames bahave as laminar flames, i.e. as thin boundary layers embedded in the flow. The flame front structure of the premixed flames in the laminar flamelet regime can be considered as distorted 1D flame structures. The structure and burning velocity of idealised 1D flame fronts is studied in section 2.2. A similar procedure is followed for non-premixed flames in section 3.

2 Analysis of Premixed Flames

2.1 Regime diagram for premixed combustion

The nature of a combustion process heavily depends on the length and time scales in the flame front and the (turbulent) flow field. To classify the different combustion regimes in premixed flames one frequently uses the Borghi diagram, which has been modified by Peters [3] recently (see figure 1.1). In this diagram, combustion regimes are defined in terms of the ratio of velocity scales v'/s_L and length scales ℓ_t/ℓ_F. If the fluctuations in the flow field v' are small compared to the adiabatic burning velocity s_L and if the lenght scales of the largest flow structures ℓ_t are small compared to the flame thickness ℓ_F, the combustion takes place in the laminar flames region. The wrinkled flamelet region is entered if $v'/s_L < 1$ and $\ell_t/\ell_F > 1$: a laminar flame front is more or less undisturbed and wrinkled by the turbulent flow field. Distortions are damped by the propagation of the flame. However, if $v'/s_L > 1$ the burning velocity is not large enough to smoothen the fluctuations and we enter the corrugated flamelet regime. If v'/s_L increases further we enter the thin reaction zones regime, where the smallest flow distortions become smaller than the flame thickness. The boundary between the last two regimes is given by the relation $\ell_F = \eta$, where η is the length scale of the Kolomogorov eddies, the smallest eddies in the flow. A laminar premixed flame front has a flame thickness given by $\ell_F = D/s_L$ [4],

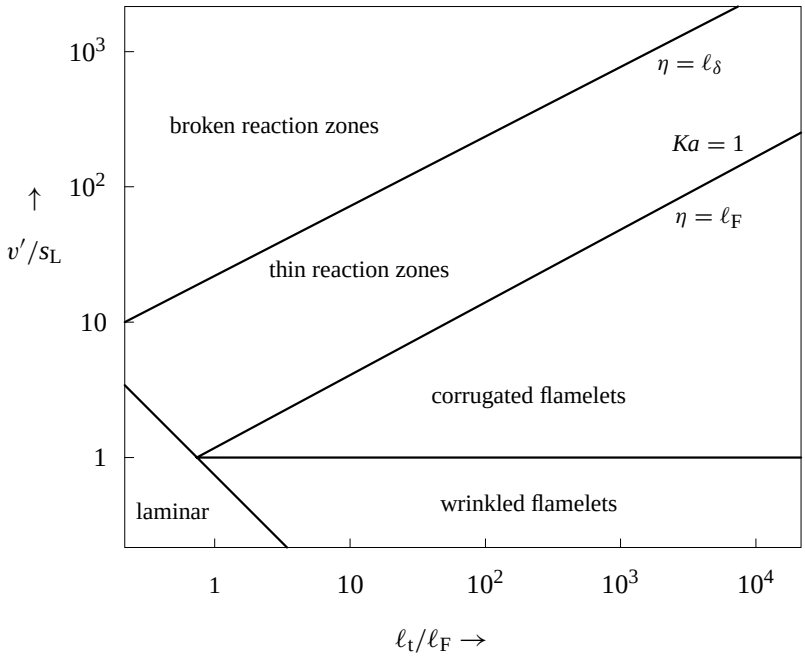

Figure 1.1: The modified Borghi-diagram for premixed turbulent combustion.

i.e. it is dictated by diffusive processes in the structure, D being a typical diffusion constant. The reaction layer, where the combustion actually takes place, has a thickness ℓ_δ which is an order of magnitude smaller than ℓ_F. As long as the smallest flow structures are larger, they cannot penetrate the reaction layer and this remains more or less undisturbed (thin reaction zones regime). When these flow structures become even smaller, combustion takes place in broken reaction zones: the system is entensively disturbed, so that the reaction may take place in regions instead of in layers.

Most of the advances in our understanding of flame structure have been achieved in the wrinkled and corrugated flamelet regimes, in which the characteristic time and length scales of the external perturbations (such as turbulence) of the flame front are large compared to those governing the flame front itself. This is no wonder, because the high temperatures encountered ($\approx$ 2000 K) accelerate the chemical reactions, so that the flame fronts are very thin structures. This means that the internal structure of the flame fronts is only weakly distorted by the perturbations in the flamelet combustion regimes. Following these ideas, a number of theoretical and numerical models has been developed recently for combustion processes in this regime. However, as the levels of turbulence increase and the typical flame temperatures decrease, the perturbing flow structures become comparable to the flame thickness (and vice versa), and other combustion regimes can be entered (e.g. thin reaction-zones regime and distributed reaction zones regime). These regimes have been relatively unexplored to date. Not only the interaction of the flame and the external distortions on a microscopic scale (turbulent eddies, acoustic waves, etc.) behaves completely different, possibly leading to more frequent extinction and ignition phenomena, also the meso- and macroscopic description drastically alters. Recent experimental evidence has indicated that, under the right conditions, turbulence and mixing processes can be so intense that a flame front is no longer observed, implying homogeneous ignition/oxidation; phenomena of this kind have been reported in the literature as ‘flameless oxidation’ or homogeneous-charge compression ignition. These new types of combustion phenomena are of great potential practical benefit; these techniques seem to offer improved efficiency and noise characteristics coupled with

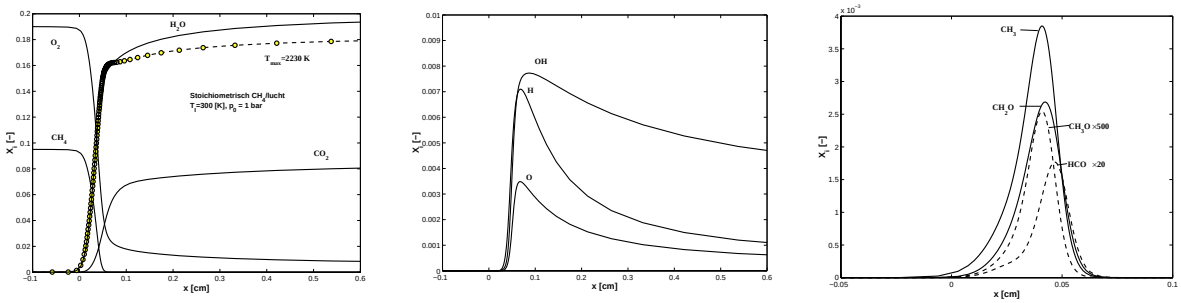

Figure 1.2: The internal structure of a 1D adiabatic stoichiometric premixed methane-air flame at ambient conditions; (a) temperature and major species mole fractions; (b) O, OH and H and (c) CH_3, CH_3O, CH_2O and CHO mole fractions

significantly lower pollutant emissions. We will not consider these regime here, but we will focus on the laminar flamelet regimes in which the flame fronts are thin and only weakly internally distorted by the flow.

2.2 Flame fronts and burning velocity

In the flamelet regimes, the local propagation velocity of the premixed flame in a fluid flow with local velocity $\vec{v}$ is given by $\vec{v}_\mathrm{f} = \mathrm{d}\vec{r}_\mathrm{f}/\mathrm{d}t = \vec{v} + s_\mathrm{L}\vec{n}$, where s_L is the local burning velocity and $\vec{n}$ the local unit vector normal to the flame front in the direction of the unburnt gases. The burning velocity s_L and the internal structure of such a flame is almost the same as the adiabatic burning velocity s_L^0 and internal structure of a perfectly flat (one-dimensional) flame. These adiabatic 1D flames are considered here. The internal structure of a flat stoichiometric methane-air flame at ambient conditions is presented in figure 1.2. The temperature profile and major species mole fractions are shown in figure 1.2a, the O, OH and H radical mole fractions in figure 1.2b and the intermediate species CH_3, CH_3O, CH_2O and CHO in figure 1.2c.

The adiabatic burning velocity is a function of the conditions of the unburnt mixture

$$s_\mathrm{L}^0 = s_\mathrm{L}^0(p_\mathrm{u}, T_\mathrm{u}, \phi),$$

p_u, T_u and ϕ being the pressure, temperature and equivalence ratio of the unburnt mixture, respectively. The physical background explaining the propagation velocity of a premixed flame depends on two major factors: first of all, the unburnt mixture just ahead of the flame front starts reacting only if the gas temperature has increased up to a value very close to the adiabatic burning velocity. This observation is related to the reaction time scale $t_R \approx (1/A\rho_\mathrm{u})\exp(E_\mathrm{a}/RT)$ (of a second-order global reaction) which is very large unless the temperature T almost equals T_b, due to the large activation energy E_a of the most important reactions. The exponential dependence of t_R is related to the Boltzmann translational energy distribution in the gas, indicating that only collisions with kinetic energy larger than E_a can undergo chemical reaction. The chemical reaction time scale is also inversely proportional to the frequency factor A of the reaction and the density of the mixture ρ_u. The second important factor which governs the propagation of a premixed flame is the rate of preheating of the cold layer in front of the reacting gas up to the temperature close to T_b. This layer ahead of the front is refered to as the preheating zone and is heated by molecular diffusion from the hot flame region, described by the diffusivity D. As the burning velocity depends on both parameters t_R and D, simple

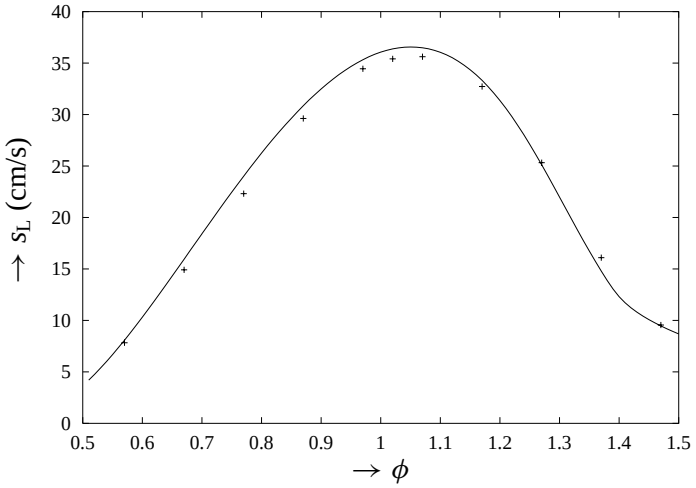

Figure 1.3: The adiabatic burning velocity s_L^0 of a methane-air flame as a function of fuel equivalence ratio at ambient conditions

scaling indicates that the following relation holds for s_L^0 [1]:

$$s_L^0 = \sqrt{\frac{D}{t_R}} = \sqrt{\rho_u A D \exp(-E_a/RT_b)}. \tag{1.1}$$

This equation is valid for second-order chemistry and its basic form can be derived also from first principles (i.e. by solving the 1D combustion equations). This formula indicates the importance of two major effects on s_L^0. First of all, s_L^0 is very sensitive to changes in the (adiabatic) burning velocity T_b, which can be influenced by changes in the unburnt gas temperature T_u of the mixture (it is found that $s_L^0 = 8 + 26.5(T_u/298)^{2.11}$ cm/s for a stoichiometric methane-air flame), but also by the heat loss from the flame (e.g. to a burner) and by changing the equivalence ratio. The adiabatic burning velocity of a methane/air flame at ambient conditions is presented as function of the equivalence ratio in figure 1.3. The burning velocity rapidly decreases if the equivalence ratio increases above 1.05 or decreases below 1.05, due to changes in T_b. A second important influence on s_L^0 follows from Eq.(1.1): the pressure dependence. Note that $\rho_u \propto p_u$ and $D \propto 1/p_u$, so that Eq.(1.1) indicates that s_L^0 is independent of p_u. This can be shown rigorously as well for a pure set of second-order reactions. In reality it is found, however, that s_L^0 decreases with p_u roughly as $s_L^0 \propto p_u^{-0.5}$ for methane-air. This decreasing burning velocity as the pressure increases is caused by the increasing importance of third-order (mainly chain-breaking) reactions which enhance the depletion of the radical pool and thus cause a slowing reaction process. Note that although s_L^0 decreases with p_u, the mass burning rate $m^0 = \rho_u s_L^0$ increases proportional with $p_u^{0.5}$.

3 Analysis of Non-Premixed Flames

3.1 Regime diagram for non-premixed combustion

Non-premixed flames are also sometimes refered to as diffusion flames, because diffusive mixing mostly is the rate-controling process, due to the high temperatures encountered in these flames. Again, as in the premixed laminar flamelet regime, this indicates that chemical reaction times are very short due to the high temperatures. However, it depends on the situation whether this is true: other regimes

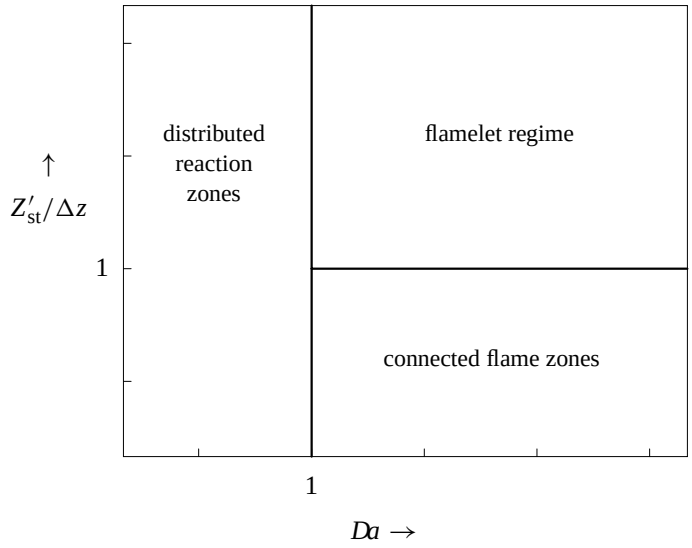

Figure 1.4: Regimes in non-premixed turbulent combustion.

are also possible, although the majority of combustion applications takes place in the flamelet regime. A regime diagram for combustion in non-premixed gases is introduced by Peters [2] and presented in figure 1.4. In premixed systems, the regime is constructed by considering the ratio of velocity scales and length scales of chemistry and turbulence. The regime diagram for non-premixed combustion is completely different than the one for premixed systems, because non-premixed flames do not have a characteristic velocity scale (i.e. burning velocity) and not a characteristic length scale, so that only time scales can be compared directly. As a measure for this, we introduce the Damköhler number $Da = t_\eta / t_R$, where t_η is the typical time scale of the smallest flow scales and t_R the chemical time scale. If the characteristic time of the smallest flow structures (e.g. Kolmogorov eddies) is larger than the chemical time scale, we have thin fronts embedded in the flow and we refer to this regime as the laminar flamelet regime. The characteristic chemistry time scale t_R is defined here as the point where the flow time scales are so small that the flame extinguishes. This automatically means that flame extinction occurs if $Da < 1$ and that $Da > 1$ refers to the flamelet regime. The thickness of the flamelet is directly related to the time scale and is not an independent variable. However, it is possible to consider a typical variation of the degree of mixing of fuel and oxidiser Z'_{st} at the flame front as an independent variable. If the local fluctuation in the degree of mixing is large compared to ΔZ (indicating the range in mixing where chemistry is important), the flame fronts are thin and remain separated when moved around by the turbulent structures. On the other hand, if this variation in mixing is small the gases become (almost) premixed, the front thickness is large and turbulent fluctuations lead to connecting flame fronts. The major characteristics of the thin non-premixed flamelet structures are treated in the next sub-section.

3.2 Structure of non-premixed flames

The position of a thin non-premixed flame in a flow depends on the mixing of the fuel and oxidiser gases. Let us first consider a pure mixing process of fuel and oxidiser without combustion and suppose that Y_F and Y_{ox} are the local mass fractions of fuel and oxidiser gases in the system. The pure mixing of fuel and oxidiser issuing from two separate streams 1 and 2 (see figure 1.5), then can be described

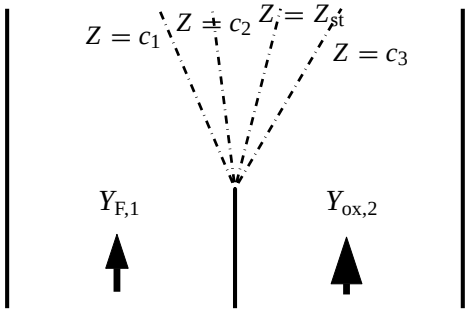

Figure 1.5: Mixing of two streams with fuel and oxidiser

by the so-called mixture fraction Z, defined as

$$Z = \frac{sY_F - Y_{ox} + Y_{ox,2}}{sY_{F,1} + Y_{ox,2}}, \tag{1.2}$$

with $Y_{F,1}$ the fuel mass fraction in stream 1 and $Y_{ox,2}$ the oxidiser mass fraction in stream 2. Furthermore, s is the so-called stoichiometric coefficient, indicating the ratio of oxidizer mass and fuel mass which would be necessary for complete combustion. Note that Z does not change due to chemical reaction, because if Y_F decreases by an amout x due to chemical reaction, Y_{ox} decreases by an amount sx, so that $sY_F - Y_{ox}$ and thus also Z remains constant. Z in Eq.(1.2) is normalised in such a way that Z is equal to 1 in stream 1 and 0 in stream 2.

The mixing of fuel and oxidiser can be predicted by solving the transport equation for Z, which describes pure mixing of the gases from the two streams without combustion. It is interesting to note that chemical reaction does not influence Z, so that the Z-field does not change if the mixing gases also react. The iso-plane $Z_{st} = Y_{ox,2}/(sY_{F,1} + Y_{ox,2})$, i.e. where $Y_F = sY_{ox}$, is an important iso-plane in the mixing flow because this is the plane where the fuel and oxidizer would burn optimally if the flow would be reacting, where the highest temperature would be found and where the chemical reaction time would be minimal. So this is the plane which the flame front finally tries to reach after ignition of the mixing flow.

In case of an infinitely fast reaction, the stoichiometric iso-plane Z_{st} of Z gives rise to a completely burnt mixture with $Y_{F,b} = Y_{ox,b} = 0$ after ignition. Away from this plane, $Y_{F,b}$ or $Y_{ox,b}$ becomes zero, so that the reaction layer becomes infinitely thin in this case. Eq.(1.2) indicates that there is a linear relation between the mass fractions $Y_{F,u}$ and $Y_{ox,u}$ of the non-reacting case on the one hand and Z on the other. This relation is presented in figure 1.6a. Furthermore, there also exists a linear relation between the species mass fraction $Y_{F,b}$, $Y_{ox,b}$, the temperature and the product species mass fractions for the reacting case on the one hand and Z on the other hand in case of an infinitely fast combustion reaction. This can be understood if one realises that $Y_{ox,b} = 0$ if $sY_{F,u} > Y_{ox,u}$ leading to $Z = \frac{sY_{F,b}+Y_{ox,2}}{sY_{F,1}+Y_{ox,2}}$, while $Y_{F,b} = 0$ if $sY_{F,u} < Y_{ox,u}$, giving $Z = \frac{-Y_{ox,b}+Y_{ox,2}}{sY_{F,1}+Y_{ox,2}}$. Similar relations can be derived for the product species mass fractions and the temperature as function of Z. Some of these relations are depicted in figure 1.6b. From this figure, it is possible to derive the mixture composition and temperature in the flame if the Z-field is given or known.

In case of a finite reaction time, the flame front around the stoichiometric iso-plane Z_{st} obtains a finite thickness, since $Y_{F,b}$ and $Y_{ox,b}$ are not completely zero at $Z = Z_{st}$. figure 1.7a shows the structure of the most important species in a non-premixed methane-air flame as a function of the position x in a stagnation flow. The burner used for this system consists of two opposed jets with air and methane generating a stagnation flow with a stagnation plane in the centre. The position $x = 0$ is chosen at the stagnation plane. Note that $Z_{st} = 0.055$ for this special case and the planar non-premixed flame

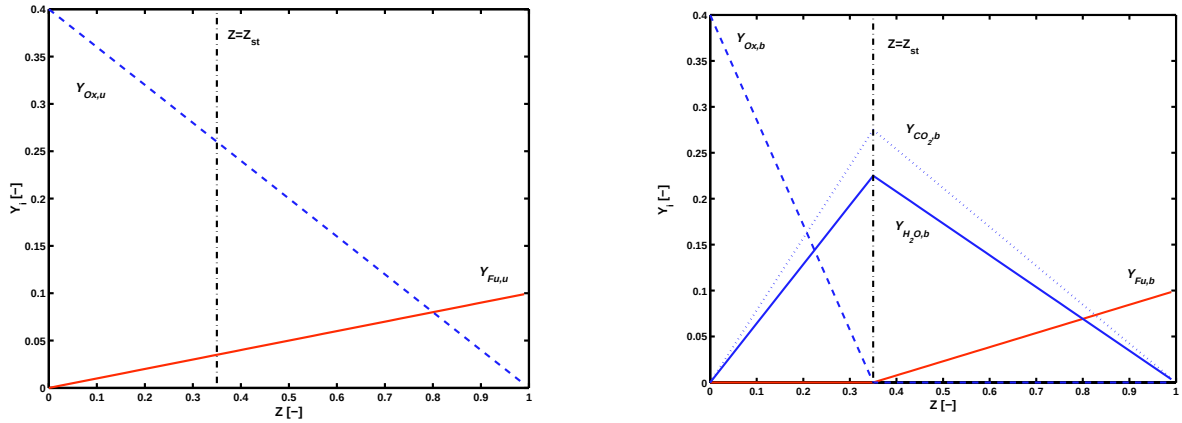

Figure 1.6: Fuel and oxidiser mass fractions as a function of the mixture fraction Z (a) for the pure mixing case ($Y_{\mathrm{F,u}}$ and $Y_{\mathrm{ox,u}}$) and (b) for the reacting case ($Y_{\mathrm{F,b}}$, $Y_{\mathrm{ox,b}}$, $Y_{\mathrm{H_2O,b}}$ and $Y_{\mathrm{CO_2,b}}$).

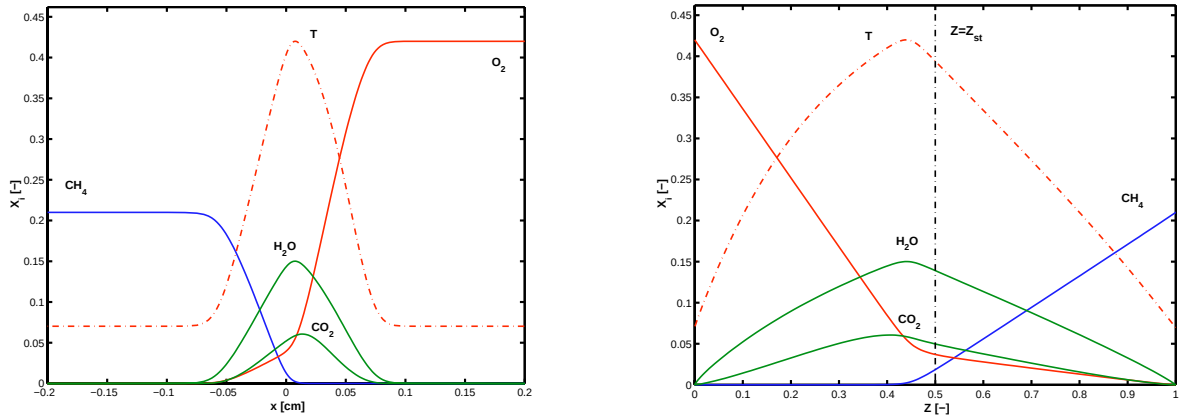

Figure 1.7: Internal structure of a methane-air diffusion flame in a stagnation flow (a) as a function of distance x and (b) as a function of mixture fraction Z.

then stabilises at the position where $Z = Z_{\mathrm{st}}$. Figure 1.7b shows the structure of the most important species in the flame as a function of Z. Note the striking correspondence with figure 1.6b.

References

[1] de Goey, L.P.H., Somers, L.M.T and Bongers, H., *Verbrandingtechnologie* TU/e course (2002).

[2] Peters, N., *ERCOFTAC summerschool on Laminar and Turbulent Combustion*, 1992.

[3] Peters, N., *Turbulent Combustion*, Cambridge University Press, Cambridge, 2000.

[4] Warnatz, Maas and Dibble, *Combustion*, Springer Verlag Berlin, 1996.

Part 2

Laminar Combustion

Chapter 2

Modelling Approaches to Chemical and Transport processes

L. M. T. Somers

1 Conservation Equations

Flames and other combustion processes fall in the area of chemically reacting flows, which are governed by a set of conservation equations describing the flow, the chemical species mass fractions and the enthalpy. The momentum and continuity equations are given by

$$\frac{\partial(\rho\mathbf{v})}{\partial t} + \nabla\cdot(\rho\mathbf{v}\mathbf{v}) + \nabla\cdot(\boldsymbol{\tau}) = -\nabla p, \tag{2.1}$$

$$\frac{\partial\rho}{\partial t} + \nabla\cdot(\rho\mathbf{v}) = 0, \tag{2.2}$$

ρ, p, and $\mathbf{v}$ being the mass density, pressure and the flow velocity and $\boldsymbol{\tau}$ being the stress tensor. The conservation equations for the N species mass fractions Y_i are

$$\frac{\partial(\rho Y_i)}{\partial t} + \nabla\cdot(\rho\mathbf{v}Y_i) + \nabla\cdot(\rho\mathbf{V}_i Y_i) = \dot{\rho}_i, \quad (i = 1, ..., N). \tag{2.3}$$

In this equation $\mathbf{V}_i$ is the diffusion velocity of species i, which generally is related to the local gradients of all species mass fractions Y_i, the temperature T and the pressure p described by the Stefan-Maxwell equations. Finally, $\dot{\rho}_i$ are the chemical source terms, with contributions from all reactions in the mixture. The set of conservation equations is closed by the balance equation for the specific enthalpy h, given by

$$\frac{\partial(\rho h)}{\partial t} + \nabla\cdot(\rho\mathbf{v}h) = -\nabla\cdot\mathbf{q} - \boldsymbol{\tau} : (\nabla\mathbf{v}) + \frac{\partial p}{\partial t} + \mathbf{v}\cdot\nabla p. \tag{2.4}$$

For a mixture the specific enthalpy h is defined as the sum over the specific enthalpy h_i of each species i:

$$h = \sum_{i=1}^{N} h_i(T)Y_i \tag{2.5}$$

with the normal definition of the specific heat of species i according to $dh_i = c_{p,i}dT$. Note that the chemical source terms $\dot{\rho}_i$ do not appear here! Equivalently, one could also use the conservation of specific **internal** energy $e = h - p/\rho$,

$$\frac{\partial(\rho e)}{\partial t} + \nabla\cdot(\rho\mathbf{v}e) = -\nabla\cdot\mathbf{q} - \boldsymbol{\tau} : (\nabla\mathbf{v}) + p\,(\nabla\cdot\mathbf{v}), \tag{2.6}$$

or for that matter the conservation of specific **total** energy, $\hat{e} = e + v^2/2$,

$$\frac{\partial(\rho\hat{e})}{\partial t} + \boldsymbol{\nabla}\cdot\left(\rho\mathbf{v}\hat{e}\right) = -\boldsymbol{\nabla}\cdot\mathbf{q} - \boldsymbol{\nabla}\cdot(\boldsymbol{\tau}\cdot\mathbf{v}) + \boldsymbol{\nabla}\cdot(p\mathbf{v}) + \rho\mathbf{v}\cdot\mathbf{g}, \tag{2.7}$$

to complete the set of conservation equations. The mixture specific internal energy e is defined as the sum over the specific internal energy e_i of each species i:

$$e = \sum_{i=1}^{N} e_i(T)Y_i \tag{2.8}$$

Now the specific heat $c_{V,i}$ of species i is defined according to $de_i = c_{V,i}dT$.

The equations (2.4,2.6,2.7) are equivalent and can be transformed into each other by using the relation between e and h and the conservation of momentum (eq. 2.1). It is merely a matter of taste. In some situations it is more 'natural' to use conservation of energy, for instance in constant volume systems. In most 'open' combustion systems however the conservation of enthalpy is to be preferred. In that case the pressure is approximately constant and the terms involving pressure in eq. 2.4 can be neglected. If also the effect of viscous forces is neglected this is referred to as the so-called ***'Combustion Approximation'***.

An often used quantity in theoretical analyses is the specific element mass fractions (eg. for stretched flames section 2.3 on page 38). An element mass fraction Z_j is defined by [24]

$$Z_j = W_j \sum_{i=1}^{N} \mu_{ji}\frac{Y_i}{M_i}, \quad (j = 1, \ldots, N_\mathrm{e}), \tag{2.9}$$

where the μ_{ji}-coefficients denote the species composition (i.e. the number of atoms of type j in species i) and where W_j is the molar mass of element j. N_e is the number of elements in the flame. The conservation equations for Z_j read

$$\frac{\partial(\rho Z_j)}{\partial t} + \boldsymbol{\nabla}\cdot(\rho\mathbf{v}Z_j) = -\sum_{i=1}^{N} w_{ji}\boldsymbol{\nabla}\cdot(\rho Y_i\boldsymbol{V_i}), \quad (j = 1, \ldots, N_\mathrm{e}), \tag{2.10}$$

stating that element mass fractions in a flame are only influenced by convection and diffusion and not by chemical reactions! In equation (2.10) we used the notation $w_{ji} = W_j\mu_{ji}/M_i$, denoting the mass fraction of element j in species i. These N_e conservation equations are, of course, *not* independent of the set (2.3).

The set of equations is not closed unless appropriate models for the heat-flux $\boldsymbol{q}$, the stress tensor $\boldsymbol{\tau}$, the diffusive velocities $\boldsymbol{V_i}$, an equation of state and a description of the chemical reactions as they appear in $\dot{\rho}_i$ are introduced. This will be done in the next sections of this lecture. Only then the equations above can be solved directly (Direct Numerical Simulation, DNS) if they are supplemented with sufficient boundary conditions and initial values. The flame fronts, however, are generally very thin and a very fine mesh and small time steps are required to resolve all the length and time scales in the flame front. This makes DNS of laminar flames very expensive. If the flow field is turbulent, additional time/length scales of the turbulent flow field should also be resolved, which is even more expensive if these are smaller than the flame scales. If the mesh is larger than the smallest flow scales, it is only possible to resolve the largest turbulent structures. Such Large-Eddy Simulations (LES) are less expensive, but one has to implement closure models for the dissipation of turbulent scales on the finest grid level. If the flame scales are also smaller than the mesh size, one has to implement models

for the combustion in these smallest scales as well. Accurate models for this are still lacking. For these reasons, most combustion models for turbulent flames are based on Reynolds Averaged Navier-Stokes (RANS) equations instead of the above equations, i.e. transport equations which are averaged to get rid of the small scale fluctuations. As a lot of unclosed terms for correlations between different fluctuations arise in these averaged equations, for which one has to implement closure models as well, the system is supplemented with additional equations for the transport of these fluctuations. These models will be studied in other lectures.

Depending on the boundary conditions, different flame structures arise. If the gaseous fuel is premixed with air one finds premixed flame fronts which propagate in the flow field. Diffusion flame structures do not propagate and are completely different in nature. They are found when the fuel gas is not mixed before the combustion chamber: the fuel mixes with air due to diffusive processes in the diffusion flame fronts and burns immediately afterwards. Premixed and non-premixed combustion systems will be discussed separately in the sections 2–3.

2 Constitutive Relations

Concentrations of all constituents appear in the expressions for the diffusive flux of heat ($\boldsymbol{q}$), species ($\boldsymbol{V}_i$) and momentum ($\boldsymbol{\tau}$). This observation is not specific for the reactive nature in combustion processes but also holds for non-reacting mixtures. The set of equations (2.1, 2.2, 2.3) and (2.26) on pages 13 and 18 is not closed. In the conservation equations for the four unknowns the density ρ, velocity vector $\boldsymbol{v}$, specific internal energy e and the mass fractions Y_i, new quantities have been introduced. For these, being the pressure p and the stress-tensor $\boldsymbol{\tau}$ in the Navier-Stokes and the energy equation, the heat-flux $\boldsymbol{q}$ in the energy equation and the diffusion velocity $\boldsymbol{V}_i$ in the convection-diffusion equation, relations have to be formulated such that the number of equations is equal to the total number of unknowns. This closure is obtained by posing so-called **constitutive relations**.

In most combustion problems each species can be considered to behave as a perfect gas. The 'partial' pressure is then given by

$$p_i = n_i RT (= nX_i RT)$$

with R the universal gasconstant (8.314 [J/mole/K]) and n_i the molar density [mole/m^3] (or concentration) of species i. For later use the concentration fraction (or mole-fraction) X_i is introduced, $X_i = n_i/n$. It is simply related to the mass fraction, $X_i = Y_i \bar{M}/M_i$, where $\bar{M}$ is the average molar mass and M_i the molar mass of species i. The n is the number density, or molar density of the mixture (moles per volume).

According to Dalton's law the static pressure is equal to the sum of the partial pressures thus leading to,

$$p = nRT, \tag{2.11}$$

where the equality $\sum_{i=1}^{N} X_i = 1$ is used. This provides a unique relation between pressure and temperature. This relation can be used to relate all remaining constitutive relations to the set (ρ, Y_i, T and $\boldsymbol{v}$), as is mostly done in combustion modelling.

The stress tensor $\boldsymbol{\tau}$ of the mixture is identical with the expression for a single-component Newtonian fluid, i.e.,

$$\boldsymbol{\tau} = -\eta[(\nabla \boldsymbol{v}) + (\nabla \boldsymbol{v})^T] + \tfrac{2}{3}\eta(\nabla \cdot \boldsymbol{v})\mathbf{I} \tag{2.12}$$

where η is the dynamic viscosity of the mixture. In fact, this expression is formally not correct since terms involving the gradients of the diffusion velocity, $\boldsymbol{V}_i$, are neglected with respect to those of the average velocity $\boldsymbol{v}$. Otherwise the assumption $\eta_i = Y_i \eta$ with η_i the dynamic viscosity of species i,

has to be posed, to derive equation (2.12) rigorously [1]. As shown by Hirschfelder et al. [2] this stress-tensor equation is the first Chapmann-Enskog approximation to the more complete expression.

The most accurate expression for the diffusion velocity, $\boldsymbol{V}_i$, appearing in the convection-diffusion equation yields [3],

$$\boldsymbol{V}_i = -\frac{D_i^T}{\rho Y_i T}\nabla T + \frac{n}{X_i \rho}\sum_{j=1;\, j\neq i}^{N} M_j D_{ij}\boldsymbol{d}_j, \qquad i = 1, \ldots, N \tag{2.13}$$

where the thermal diffusion coefficient D_i^T and the generalized diffusion coefficients D_{ij} are used. The first term denotes the effect on diffusion caused by temperature gradients (Soret-effect). The second term[1] involves the quantity $\boldsymbol{d}_j$ which takes the effect of concentration- and pressure gradients into account, i.e,

$$\begin{aligned} \boldsymbol{d}_j &= \nabla X_j + \left(X_j - Y_j\right)\frac{1}{p}\nabla p, \qquad j = 1, \ldots, N \\ &= \nabla X_j + X_j\left(1 - \frac{M_j}{\overline{M}}\right)\nabla \ln p, \qquad j = 1, \ldots, N \end{aligned} \tag{2.14}$$

This expression is only valid within the perfect gas assumption mentioned earlier. More general expressions can be found in [2, 4]. It should be noted that the pressure dependence disappears from (2.14) if all molar masses are equal.

Due to the multi-component nature of the medium, the expression for the heat flux $\boldsymbol{q}$ becomes fairly complex,

$$\boldsymbol{q} = -\lambda'\nabla T + \sum_{i=1}^{N} h_i \rho Y_i \boldsymbol{V}_i - RT\sum_{i=1}^{N}\frac{D_i^T}{X_i M_i}\boldsymbol{d}_i \ . \tag{2.15}$$

where h_i is the **specific** enthalpy of the i-th component, formally given by

$$h_i(T) = h_i^0 + \int_{T_0}^{T} c_{p,i}(T')dT' \tag{2.16}$$

with h_i^0 the enthalpy at the reference temperature T_0. The specific heat capacity, $c_{p,i}(T)$, of species i is assumed to be a function of temperature only. Pressure dependence is usually very small and will not be taken into account[2]. The first term in equation (2.15) is the *ordinary* single-component fluid heatflux. It should be noted that in a mixture the conductivity, λ', will **not** be the proportionality factor between heat conduction and the temperature gradient only. In fact, the second term, which incorporates the enthalpy transport due to the mass diffusion, also contains a term proportional to the temperature gradient, as can be seen in the expression for the diffusion velocity (2.13). The last term in (2.15) is the direct effect of concentration- (Dufour-effect) and pressure gradients on the heat flux. In fact the Dufour-effect in the heat flux is the counterpart of the Soret-effect in the diffusive flux[3].

In principle models for all constitutive relations are now determined and the problem is closed. Only the thermodynamical properties, e.g. h_i, e_i or $c_{p,i}$, and transport properties, e.g. λ',D_i^T or D_{ij}, are unknown at this point. Formal expressions for these quantities can only be derived rigorously from

[1] There appears to be some discussion lately on whether the $\sum_{j=1;\, j\neq i}^{N}$ should not read $\sum_{j=1}^{N}$ instead.

[2] Furthermore, there is very little accurate experimental data available to justify modelling it at all [5].

[3] Heatflux driven by concentration gradients vs. massflux driven by temperature gradients (Onsager).

molecular theory [2, 4, 5]. Typically, these properties involve the evaluation of so-called **collision integrals** which are very costly to compute and should therefore be avoided in numerical simulations of reactive flow phenomena. Excellent treatments on the principles can be found in the latter citations or in [3] where the expressions are extended to incorporate quantum-mechanical molecular states as well. However, most commonly data as tabulated in thermodynamical databases provided with the CHEMKIN-package [6, 7, 8] are used. These expressions will be treated in the section (2.2) of this lecture.

2.1 Simplified models for the diffusive flux

In the so-called 'Combustion Approximation' the term due to pressure gradients may be neglected. Furthermore, thermal diffusion is normally very small as well and will be neglected[4]. However, the diffusion velocity of a species still depends on the concentration gradients of every other. This is especially problematic in theoretical analysis of flames, in numerical modeling this is not a priori a problem. Within the earlier assumptions, it can be shown that the expression (2.13) can be rearranged to yield [9, 10, 3],

$$\nabla X_i = \sum_{j=1}^{N} \frac{X_i X_j}{\mathcal{D}_{ij}} (\boldsymbol{V}_j - \boldsymbol{V}_i) \tag{2.17}$$

which is commonly referred to as the **Stefan-Maxwell equation**. This expression is much simpler to evaluate since it involves the binary diffusion coefficients, $\mathcal{D}_{ij}$, which are virtually independent of the composition. For this reason only, the Stefan-Maxwell equation are to be preferred above the original expression for the diffusion velocity (2.13). The latter involves the generalized diffusion coefficients[5] which depend explicitly on the composition in a complicated and CPU-intensive manner[6].

For this reason in most laminar flame studies the diffusion flux is cast in a Fick-like expression,

$$\boldsymbol{V}_i = -\frac{D_{\mathrm{im}}}{X_i} \nabla X_i. \tag{2.18}$$

where the so-called mixture-averaged diffusion coefficient, D_{im}, describes the diffusivity of the species in the mixture. An exact derivation of this equation does not exist. In fact, it can be derived only from the Stefan-Maxwell equations if it is assumed that all $\boldsymbol{V}_j$ $(j \neq i)$ take a common value $\boldsymbol{V}$. Substituting this, and making use of the relation,

$$Y_i \boldsymbol{V}_i + (1 - Y_i)\boldsymbol{V} = 0$$

which is then true by definition, the Stefan-Maxwell equations (2.17) can be rearranged to yield,

$$D_{\mathrm{im}} = \frac{(1 - Y_i)}{\sum_{j \neq i}^{N} X_j / \mathcal{D}_{ij}} \tag{2.19}$$

[4] Only for very light species (H_2, H or He) this can have a considerable contribution to the total diffusive flux $\mathcal{O}(20\,\%)$.

[5] The relation between the two is known and relatively simple for a ternary mixture

$$D_{12} = \mathcal{D}_{12} \left\{ 1 + \frac{X_3[(M_3/M_2)\mathcal{D}_{13} - \mathcal{D}_{12}]}{X_1\mathcal{D}_{23} + X_2\mathcal{D}_{13} + X_3\mathcal{D}_{12}} \right\}$$

and similar relations for D_{21}, D_{23}, D_{32}, D_{13}, D_{31}.

[6] To first order the generalized diffusion coefficients involve a $(N \times N)$-matrix inversion for every species thus leading to $\mathcal{O}(N^3)$ operations per gridpoint [11].

where the coefficients $\mathcal{D}_{ij}$ are the earlier mentioned binary diffusion coefficients. Strictly, in a multi-component flow this expression only applies[7] for a trace species and is therefore often referred to as the **trace-species approximation**. In can be expected that this approximation applies quite well to modelling atmospheric fuel-air combustion processes since approximately 80% Nitrogen (N_2) is present under these circumstances. For certain applications the species balance equation is entirely written in terms of mass-fractions. To arrange that the expression (2.18) is rearranged according to,

$$Y_i \boldsymbol{V}_i = -\frac{M_i}{\bar{M}} D_{\mathrm{im}} \boldsymbol{\nabla} X_i \tag{2.20}$$

$$= -\frac{M_i}{\bar{M}} D_{\mathrm{im}} \boldsymbol{\nabla} (Y_i \frac{\bar{M}}{M_i}) \tag{2.21}$$

$$= -D_{\mathrm{im}} \left[\boldsymbol{\nabla} Y_i + Y_i \boldsymbol{\nabla} \ln(\bar{M}) \right] \tag{2.22}$$

where the identity $Y_i / X_i = M_i / \bar{M}$ has been used. The last term on the right-hand side is in CH_4 - air combustion negligible since the average molar mass is almost constant.

Substitution of the trace species diffusive flux in the balance equation thus gives an expression for the species mass-fraction which is very similar to the temperature equation (equation (2.26) on page 18),

$$\rho \frac{\partial Y_i}{\partial t} + \rho \boldsymbol{v} \cdot \boldsymbol{\nabla} Y_i - \boldsymbol{\nabla} \cdot (\rho D_{\mathrm{im}} \boldsymbol{\nabla} Y_i) = \dot{\rho}_i \ . \tag{2.23}$$

In many theoretical studies this feature is used explicitly to simplify the solution considerably. However, note that within these approximations the diffusive fluxes no longer sum to zero due to the assumptions made. Thus formally, the continuity equation no longer holds. Some authors correct this deficiency by calculating the mean overall diffusion velocity according to $\boldsymbol{V}_r = -\sum Y_i \boldsymbol{V}_i$ and substitute each $\boldsymbol{V}_i$ by $\boldsymbol{V}_i^c = \boldsymbol{V}_i + \boldsymbol{V}_r$. Others replace the balance equation, (2.23), for the species which is most abundant (N_2 in many cases) with $Y_{N_2} = 1 - \sum_{i=1}^{N-1} Y_i$. Thus mass conservation is used explicitly and the continuity equation is forced to hold.

Further simplification of the diffusive fluxes is possible if the so-called 'constant Lewis-number' approximation is applied. The Lewis number is defined as the ratio between enthalpy diffusivity (see eq. 2.4) λ / c_p and species diffusivity ρD_{im}

$$\mathrm{Le_i} = \frac{\lambda}{c_p \rho D_{im}} \tag{2.24}$$

In the late eighties and nineties this approximation was evaluated for methane-air mixtures[25, 26]. It appeared that a constant Lewis number applies very well for these flames and does not yield large errors in flame properties. Substituting the constant Lewis number approximation in the species conservation equation now yields a very often encountered version of this equation:

$$\rho \frac{\partial Y_i}{\partial t} + \rho \boldsymbol{v} \cdot \boldsymbol{\nabla} Y_i - \boldsymbol{\nabla} \cdot (\frac{\lambda}{c_p \mathrm{Le_i}} \boldsymbol{\nabla} Y_i) = \dot{\rho}_i \ . \tag{2.25}$$

Main application of this version of the species conservation equation is found in theoretical analyses. It can be used for instance to deduce a simpler version of the enthalpy conservation equation. As furthermore pressure and viscous effects are neglected, the equation for h can be simplified considerably, leading to

$$\frac{\partial (\rho h)}{\partial t} + \boldsymbol{\nabla} \cdot (\rho \mathbf{v} h) - \boldsymbol{\nabla} \cdot \left(\frac{\lambda}{c_p} \boldsymbol{\nabla} h \right) = \sum_{i=1}^{N} \left(\frac{1}{Le_i} - 1 \right) \boldsymbol{\nabla} \cdot \left(\frac{\lambda}{c_p} h_i \boldsymbol{\nabla} Y_i \right) . \tag{2.26}$$

[7] Or in a binary mixture, but that is trivial.

Furthermore, in the case of equal (e.g. unit) Lewis numbers ($Le_i = c$ or $D_{\mathrm{i}m} = D$), the conservation equation (eq. 2.10) for element mass fractions Z_j all behave the same. Even more, if the Z_j are all scaled between 0 and 1 they are described by a single transport equation for the so-called mixture fraction $Z = Z_j$:

$$\frac{\partial(\rho Z)}{\partial t} + \nabla \cdot (\rho \mathbf{v} Z) = \nabla \cdot (\rho D \nabla Z). \tag{2.27}$$

Normally, Z is scaled such that it is 0 in the oxidizer stream and 1 in the fuel stream.

2.2 Evaluating thermodynamic and transport properties

The evaluation of transport properties of any multi-component mixture is in general very complex, and normally very CPU-intensive [11, 3]. Especially the latter argument is of major importance in flame simulation. Therefore, many formulations exist with a different levels of approximation. In the early eighties some investigators have tested these formulations [12, 13]. The expressions presented below are a compilation of the (semi-empirical) formulae used by many authors. They are believed to yield accurate results for the respective fluxes, and do not use excessive CPU time.

For the mixture averaged viscosity, η, in most standard laminar flame packages (Sandia-codes), the semi-empirical formula of Wilke [14] is used,

$$\eta = \sum_{k=1}^{N} \frac{\eta_k}{1 + 1/X_k \sum_{j=1, j\neq k}^{N} X_j \Phi_{kj}} \tag{2.28}$$

where η_k are the single species gas viscosities. The quantity Φ_{kj} is given by,

$$\Phi_{kj} = \frac{1}{\sqrt{8}} \left\{ 1 + \left(\frac{M_k}{M_j} \right) \right\}^{-\frac{1}{2}} \left\{ 1 + \left(\frac{\eta_j}{\eta_k} \right)^{\frac{1}{2}} \left(\frac{M_j}{M_k} \right)^{\frac{1}{4}} \right\}^2$$

The mixture averaged conductivity, λ', can be put in a somewhat related form [15],

$$\lambda' = \sum_{k=1}^{N} \frac{\lambda_k}{1 + 1/X_k 1.065 \sum\limits_{j=1;\, j\neq k}^{N} (X_j \Phi_{kj})}$$

which, however, is not used frequently in numerical combustion studies. Now the Φ_{kj} is given by the expression,

$$\Phi_{kj} = \frac{1}{\sqrt{8}} \left\{ 1 + \left(\frac{M_k}{M_j} \right) \right\}^{-\frac{1}{2}} \left\{ 1 + \left(\frac{\lambda_j}{\lambda_k} \right)^{\frac{1}{2}} \left(\frac{M_j}{M_k} \right)^{\frac{1}{4}} \right\}^2 .$$

In most studies however, instead a semi-empirical formulation is applied [16],

$$\lambda' = \frac{1}{2} \left\{ \sum_{i=1}^{N} X_i \lambda_i + \left(\sum_{i=1}^{N} X_i / \lambda_i \right)^{-1} \right\} \tag{2.29}$$

which involves only the pure species conductivities. According to Coffee and Heimerl [12] this gives results with errors in the range of a few percent. In simulations where viscosity is not evaluated the latter expression is to be preferred because then the functions Φ_{kj} do not need to be evaluated. This is generally true for the simulation of premixed one-dimensional flames, in multi-dimensional

simulations there is no preference, since then the viscosity of the mixture will have to be evaluated anyway.

The properties, $D_{i\mathrm{m}}$ and c_p, are already introduced earlier in this lecture, and are presented for matters of completeness only,

$$D_{i\mathrm{m}} = \frac{(1-Y_i)}{\sum_{j\neq i}^{N} X_j/\mathcal{D}_{ij}} \qquad i = 1,\ldots,N \tag{2.30}$$

$$c_p = \sum_{i=1}^{N} Y_i c_{p_i} \tag{2.31}$$

and complete the mixture averaged thermodynamical and transport properties.

The pure species quantities, c_{p_i}, that arise in the averaged formula, (2.31), and, h_i, in the chemical source term of the energy equation (equation (2.26) on page 18) are well tabulated [8]. The properties are cast in a polynomial form presented below,

$$\begin{aligned} \frac{c_{p_i}}{R} &= \sum_{n=1}^{5} e_{n,i} T^{n-1} \qquad i = 1,\ldots,N \\ \frac{h_i}{RT} &= \sum_{n=1}^{5} \frac{e_{n,i}}{n} T^{n-1} + \frac{e_{6,i}}{T} \qquad i = 1,\ldots,N \end{aligned} \tag{2.32}$$

with R the universal gas constant.

The binary diffusion coefficients can not be tabulated because diffusivity is not an intrinsic property. They depend on the (Lennard-Jones) molecular potentials of the two species considered. Same holds for the viscosities and the conductivities as well, since these are expressed in terms of binary diffusion coefficients. Instead, the Lennard-Jones potential data for each species, necessary to evaluate these properties, are tabulated in the STANJAN-tables [6]. Then for a specific problem, appropriate fitting procedures, e.g. provided with the CHEMKIN-package [6], are used to put them in a similar polynomial form yielding,

$$\begin{aligned} \ln(\lambda_i) &= \sum_{n=1}^{P} a_{n,i} (\ln T)^{n-1} \qquad i = 1,\ldots,N \\ \ln(\eta_i) &= \sum_{n=1}^{P} b_{n,i} (\ln T)^{n-1} \qquad i = 1,\ldots,N \\ \ln(\mathcal{D}_{ij}) &= \sum_{n=1}^{P} d_{n,ij} (\ln T)^{n-1} \qquad i = 1,\ldots,N,\ \ j = 1,\ldots,N,\ \ j \neq i \end{aligned} \tag{2.33}$$

This procedure has to be performed once for every mixture, in contrast with the coefficients in (2.32) which can be evaluated for every species once and for all.

Now, the set of equations describing reacting flows are almost in a closed form. The only terms not specified yet, are the chemical source terms $\dot{\rho}_i$. Topics associated with this item are treated in the remaining part of this lecture.

3 Chemical Aspects in Combustion

In a previous part of this lecture general reactive flow equations are introduced, but the chemical source terms appearing in the species balance equations are not specified yet. In combustion of gas, these

involve so-called chain-reactions, which means that the oxidation of the fuel is composed of many elementary steps. These steps, or elementary reactions, have a physical relation with microscopic processes, in contrast with overall chemical reactions where the reaction equations merely state the overall conversion ratios.

For methane-air mixtures the elementary steps are known and tabulated. Complete CH_4 chemical models consist of approximately 36 species and 210 reactions [27]. Some general principles, present in these detailed chemical models, will be clarified in this section. These principles apply to all fields of reactive flows.

3.1 General elementary reactions

In general, any elementary reaction can be written in the form,

$$\nu'_1 A_1 + \nu'_2 A_2 + \ldots \nu'_N A_N \rightarrow \nu''_1 A_1 + \nu''_2 A_2 + \ldots \nu''_N A_N \tag{2.34}$$

where A_i represents one of the N species present in the model and $\nu'_i - \nu''_i$ the number of molecules A_i converted in the elementary reaction. Since neither nuclear fission, nor fusion processes will be considered, each reaction conserves the total number of elements (C, H, O and N in hydrocarbon air systems).

The formal reaction (2.34) implies that,

$$\frac{q_i}{(\nu'_i - \nu''_i)} = \frac{q_j}{(\nu'_j - \nu''_j)}$$

for any pair i, j of particles in the reaction. Here, q_i is defined as the net rate of increase of species i (in moles per volume[8] per second). It's now common practice to define **the reaction rate** q, as being equal to the q_i for a species when $(\nu'_i - \nu''_i)$ is equal to one. In return one then obtains,

$$q_j = (\nu'_j - \nu''_j)q. \tag{2.35}$$

The phenomenological **law of mass action** now states that a reaction rate is proportional to the product of the concentrations, n_i, which leads for the formal reaction (2.34) to the expression,

$$q = k \prod_{i=1}^{N} n_i^{\nu'_i} \tag{2.36}$$

where the proportionality parameter k, sometimes is referred to as the **specific reaction rate constant**. The reverse reaction of (2.34) often plays an important role as well,

$$\nu''_1 A_1 + \nu''_2 A_2 + \ldots \nu''_N A_N \rightarrow \nu'_1 A_1 + \nu'_2 A_2 + \ldots \nu'_N A_N .$$

Therefore, in flame modelling, it is convenient to rewrite the combination of both to,

$$\nu'_1 A_1 + \nu'_2 A_2 + \ldots \nu'_N A_N \rightleftharpoons \nu''_1 A_1 + \nu''_2 A_2 + \ldots \nu''_N A_N \tag{2.37}$$

where the symbol $\rightleftharpoons$ indicates the reversible nature. The net reaction rate of (2.37) is now given by,

$$q = k^{\mathrm{f}} \prod_{i=1}^{N} n_i^{\nu'_i} - k^{\mathrm{r}} \prod_{i=1}^{N} n_i^{\nu''_i} \tag{2.38}$$

[8]The volume is not specified but in chemical literature often cm^3 is used.

The k^{f} and k^{r} are now the specific reaction rate constants of the forward and reverse reactions, respectively.

In a practical gas-phase combustion system the reaction order, $\sum_{i=1}^{N} \nu_i'$, of the reactions involved in the chain mechanism will not exceed three. At low densities, or pressures < 100 bar, the probability of a collision between four or more molecules is so small, that these higher order reactions may be neglected. The remaining three reaction types, (first, second and third order), are treated in the following subsections.

3.2 Bimolecular reactions

The most common and least complicated type of reaction is the so-called **bimolecular** reaction e.g.

$$\mathrm{CH_4 + H \rightleftharpoons CH_3 + H_2}$$

where the methane molecule is attacked by an hydrogen radical to form a methyl radical and molecular hydrogen and reversely. The reaction rate is now given by,

$$q = k^{\mathrm{f}}[\mathrm{CH_4}][\mathrm{H}] - k^{\mathrm{r}}[\mathrm{CH_3}][\mathrm{H_2}]$$

where $[i]$ is an often used notation for the molar density n_i. Normally in reaction kinetics units[9] are given in [[moles/cm^3]]. The specific reaction rate constants are generally not constant. As argued by **Arrhenius** (1889) an appropriate representation is given by,

$$k = Be^{-E_{\mathrm{a}}/RT} \tag{2.39}$$

where the frequency factor B and the activation energy E_{a} do not depend on the temperature. However, some reactions show so-called **non-Arrhenius** behavior and extensive studies learn that the Arrhenius form cannot represent this behavior correctly [17]. Therefore, usually a slightly modified form of the reaction rate constants is chosen according to,

$$k = AT^n e^{-E_{\mathrm{a}}/RT} \tag{2.40}$$

which is normally used in literature. This extra T dependence is often attributed to effects of internal molecular orientation and internal molecular energy on the reaction probability.

3.3 Dissociation and Recombination Reactions

The two other important reaction types are the first-order and its 'counterpart' the third-order reaction. The first-order reaction[10] is often referred to as a **dissociation** reaction, e.g.,

$$\mathrm{H_2 + M \rightarrow H + H + M} \tag{2.41}$$

These uni-molecular reactions are believed to follow the mechanism as proposed by Lindemann. This mechanism, in itself a chain-reaction, proceeds via two paths, being an excitation reaction (I),

$$\mathrm{H_2 + M \rightleftharpoons H_2^* + M} \tag{I}$$

[9] These units are SI. Two differents sets defined within the SI regulations referred to as MKS-system (Meter-Kilogram-Second) and the in reaction kinetics more often used CGS-system (Centimeter-Gram-Second).

[10] Though not truly first order, like in particular dissociation reactions of a highly excited molecules $\mathrm{H_2^* \rightarrow H + H}$.

which in fact is bimolecular reaction of the hydrogen molecule with any other denoted by M, producing an intermediate, excited H_2 molecule. The specific reaction rates are k_0^{f} for the forward and k_0^{r} for the reverse reaction (de-excitation reaction). The excited hydrogen molecule then decomposes via a true uni-molecular reaction (II),

$$\mathrm{H}_2^* \rightarrow \mathrm{H} + \mathrm{H} \tag{II}$$

with specific reaction rate k_∞^{f}. Though the intermediate species (H_2^*) can have different, energetically excited states (quantum states), it is common practice to treat all with the same reaction rate [18]. The overall reaction rate for the dissociation reaction 2.41 is now composed of two steps,

$$q_{\mathrm{I}} = k_0^{\mathrm{f}}[\mathrm{H}_2][\mathrm{M}] - k_0^{\mathrm{r}}[\mathrm{H}_2^*][\mathrm{M}] \tag{2.42}$$

$$q_{\mathrm{II}} = k_\infty^{\mathrm{f}}[\mathrm{H}_2^*]. \tag{2.43}$$

The stoichiometric relations for both molecules now give,

$$q_{\mathrm{H}_2} = -q_{\mathrm{I}} \tag{2.44}$$

$$q_{\mathrm{H}_2^*} = q_{\mathrm{I}} - q_{\mathrm{II}}, \tag{2.45}$$

where it should be noted that q_{I} contains the H_2^* concentration explicitly. The application of a steady-state relation for the excited hydrogen molecule, $\mathrm{d}[\mathrm{H}_2^*]/\mathrm{d}t = 0$ eliminates the excited intermediate from the formal reaction rate. The dissociation rate for H_2 then yields,

$$q_{\mathrm{H}_2} = k^{\mathrm{f}}[\mathrm{H}_2] \tag{2.46}$$

with a formal specific reaction rate,

$$k^{\mathrm{f}} = k_0^{\mathrm{f}}[\mathrm{M}]\left(\frac{k_\infty^{\mathrm{f}}}{k_\infty^{\mathrm{f}} + k_0^{\mathrm{r}}[\mathrm{M}]}\right) \tag{2.47}$$

independent of the excited hydrogen molecule concentration.

A similar treatment for the **recombination** reaction,

$$\mathrm{H} + \mathrm{H} + \mathrm{M} \rightarrow \mathrm{H}_2 + \mathrm{M}$$

using the elementary steps (−I) and (−II),

$$\mathrm{H} + \mathrm{H} \rightleftharpoons \mathrm{H}_2^* \tag{−II}$$

$$\mathrm{H}_2^* + \mathrm{M} \rightarrow \mathrm{H}_2 + \mathrm{M} \tag{−I}$$

instead, yields for the recombination reaction,

$$q_{\mathrm{H}} = k^{\mathrm{r}}[\mathrm{H}][\mathrm{H}] \tag{2.48}$$

with the formal specific reaction rate now equal to,

$$k^{\mathrm{r}} = k_\infty^{\mathrm{r}}\left(\frac{k_0^{\mathrm{r}}[\mathrm{M}]}{k_\infty^{\mathrm{f}} + k_0^{\mathrm{r}}[\mathrm{M}]}\right). \tag{2.49}$$

The factors in brackets in both equations (2.47) and (2.49) indicate the probability that the reactions are completed after initiation[11]. An advantage of this formulation is that this definition of k^{f} and k^{r} follows the definition of chemical equilibrium,

$$K = \frac{[\mathrm{H}][\mathrm{H}]}{[\mathrm{H}_2]} = \frac{k^{\mathrm{f}}}{k^{\mathrm{r}}} = \frac{k_\infty^{\mathrm{f}} k_0^{\mathrm{f}}}{k_\infty^{\mathrm{r}} k_0^{\mathrm{r}}}.$$

[11] Being that $\mathrm{H}_2 + \mathrm{M} \rightarrow \mathrm{H}_2^* + \mathrm{M}$ is the initiation for dissociation and $\mathrm{H} + \mathrm{H} + \mathrm{M} \rightarrow \mathrm{H}_2^* + \mathrm{M}$ for recombination

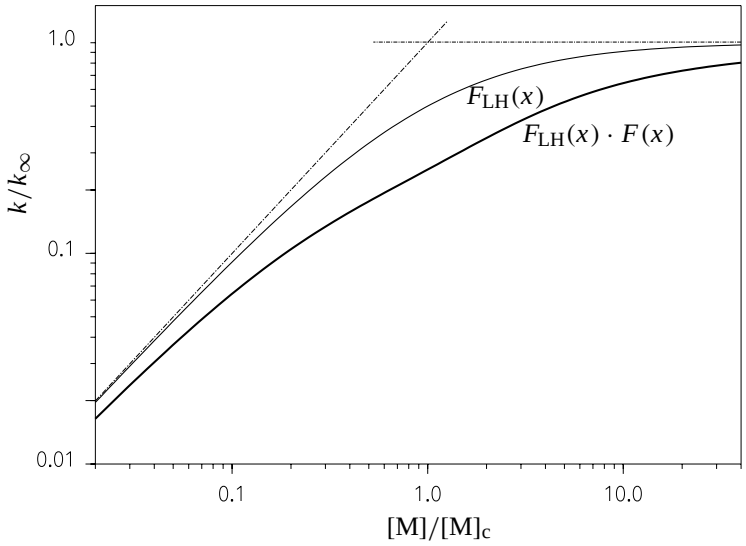

Figure 2.1: Fall-off curves represented in the reduced coordinate. The dotted lines indicate the high, (k_∞) and low pressure, ($k_0[\mathrm{M}]$) limiting cases. The solid line indicated with F_{LH} is the Lindemann-Hinshelwood expression. The extended expression (equation (2.53)) is shown with the second solid line indicated with $F_{\mathrm{LH}}(x) \cdot F(x)$. A value of ($\log F_\mathrm{c} = 0.3$) (equation (2.54)) is used.

High and low pressure limit

The [M]-dependence of the specific reaction rates k^f and k^r of these types of reactions is commonly referred to as the pressure dependence of dissociation and recombination reactions[12]. Two limiting cases can be recognized [18], one low pressure branch, $[\mathrm{M}] \to 0$, yielding,

$$\begin{aligned} k^\mathrm{f} &= k_0^\mathrm{f}[\mathrm{M}] \\ k^\mathrm{r} &= \frac{k_\infty^\mathrm{r}}{k_\infty^\mathrm{f}} k_0^\mathrm{r}[\mathrm{M}] \end{aligned} \tag{2.50}$$

where the excitation reaction is thought to be rate-controlling. At high pressures, $[\mathrm{M}] \to \infty$, the other limit is encountered,

$$\begin{aligned} k^\mathrm{f} &= \frac{k_0^\mathrm{f}}{k_0^\mathrm{r}} k_\infty^\mathrm{f} \\ k^\mathrm{r} &= k_\infty^\mathrm{r} \end{aligned} \tag{2.51}$$

as can be verified easily. Then the collisions between the 'third' particle and H_2 or H_2^* are so frequent that the uni-molecular decomposition I and the reversible process for the recombination case become rate-controlling. It's worth mentioning that the dissociation reaction switches from a uni-molecular to a bi-molecular behavior going from high to low pressures, whilst the recombination switches from tri-molecular to bi-molecular going from low to high pressures instead. Both limiting branches (2.50) and (2.51) are plotted in figure (2.1) with the dotted lines. The relations (2.47) and (2.49) are indicated by the top solid line.

[12]Though concentration or molar density dependence would be better.

Fall-off curve

Generally the real behavior of the specific reaction rate, solid line in figure 2.1, is not equal to the earlier derived expressions. To incorporate this experimental observed behavior a compact representation of the **fall-off curve**, as it is often referred to, is mostly of practical importance. Therefore, usually the so-called 'center', $[\mathrm{M}]_\mathrm{c}$, of the fall-off curve located at the intersection of both limiting branches of k is introduced. The reduced coordinate $x = [\mathrm{M}]/[\mathrm{M}]_\mathrm{c} = k_0/k_\infty$[13] offers a possibility to generate a compact expression for the reaction rate constant,

$$\frac{k}{k_\infty} = \frac{x}{1+x} \tag{2.52}$$

where the latter is often abbreviated by $F_\mathrm{LH}(x)$ after Lindemann and Hinshelwood who first introduced this function. In fact F_LH is no more than a switching function between two limiting branches of the reaction rates indicated by a dashed curve in Fig (2.1) and equals the expression (2.47) and (2.49) as can be verified easily.

The fall-off curve is often broader than F_LH and theoretical analysis shows that this effect can be accounted for reasonably by adding a factor $F(x)$, yielding,

$$\frac{k}{k_\infty} = F_\mathrm{LH}(x)F(x) \tag{2.53}$$

The function, $F(x)$, is in good approximation determined by,

$$\log(F(x)) = \left(\frac{1}{1+(\log x)^2}\right)\log(F_\mathrm{c}) \tag{2.54}$$

where $\log(F_\mathrm{c})$ is the depression from the real fall-off curve at the center of the Lindemann-Hinshelwood expression. It should be noted that more complex expressions are available that perform better in comparison with the observed behavior. They normally offer only minor modifications and do not have a large effect on the flame structure. An excellent survey can be found in [18, 19].

The third party

So far no attention has been paid to the concentration of the inert species M, or so-called 'bath-gas'. It does not take part in the reaction $(\nu_i' - \nu_i'' = 0)$ but is absolutely crucial as otherwise momentum and energy could not be conserved simultaneously. It can, however, be any particle present in the mixture. The concentration of the 'inert' particle will therefore, in the simplest case be given by p/RT. However, in most uni- and tri-molecular reactions the rate coefficient is different for every third body. Stated explicitly, for instance,

$$\mathrm{H_2} + \mathrm{H_2} \rightarrow \mathrm{H} + \mathrm{H} + \mathrm{H_2}$$

will have a higher rate than,

$$\mathrm{H_2} + \mathrm{O_2} \rightarrow \mathrm{H} + \mathrm{H} + \mathrm{O_2}.$$

On a molecular level this means that the collision probability of $\mathrm{H_2}$-$\mathrm{H_2}$ to form an excited hydrogen molecule ($\mathrm{H_2^*}$) is larger than of $\mathrm{H_2}$-$\mathrm{O_2}$ for this particular reaction. Instead of introducing a specific reaction rate for every collision partner, this effect is in most flame modelling studies incorporated

[13] Bear in mind that $[\mathrm{M}]_\mathrm{c} = k_\infty/k_0$ per definition

by introducing so-called 'enhanced efficiencies' σ_i, which can have values ranging from 1.0 to 10.0 approximately . The 'concentration' of the third particle M is than given by,

$$[\mathrm{M}] = \sum_{i=1}^{N} \sigma_i X_i \;\; p/RT \tag{2.55}$$

which reduces to the appropriate value p/RT when all σ_i are equal to one. To illustrate the principles presented here, in the next section 4 a specific mechanism is treated in some detail.

4 An example: methane mechanism, skeletal

Most hydrocarbons, in spite of the fact that the reaction paths are very different, show remarkable similarity in their combustion characteristics (with respect to major species profiles and burning velocity). The main reason for this is the claimed [20] dominance of the reactions,

$$\mathrm{H} + \mathrm{O_2} \rightleftharpoons \mathrm{OH} + \mathrm{O} \tag{2.56}$$

$$\mathrm{CO} + \mathrm{OH} \rightleftharpoons \mathrm{CO_2} + \mathrm{H} \tag{2.57}$$

which occur in the combustion of any hydrocarbon[14]. For the computation of the detailed structure of a hydrocarbon flame a reaction mechanism covering the details of the reaction path of the alkane to carbon-monoxide is inevitable. Also for the prediction of soot-formation and NO_x, accurate profiles of the intermediates are indispensable. E.g. for the case of natural gas combustion the reaction data of at least methane and to a lesser extent of ethane would have to be used.

In this section focus is on pure methane-air combustion for which the reaction data are relatively well known. A set of reactions is presented that will be used also lateron in section 6. The main aspects of this specific mechanism are treated.

For cases where the initial concentration of the fuel is not too high the path given in figure 2.2 describes the essential chain of reactions of the methane oxidation. Only under very fuel rich conditions the path to the C_3 and C_4 hydrocarbons becomes more and more important[15]. A good compilation of all the reaction rate data available to date is given in [22] and in [23]. The latter authors claim to find good agreement for the burning velocities of most C_1 and C_2 fuels with a reaction scheme consisting of 36 species and 210 reversible reactions. The most comprehensive and tested data-set for lower hydro-carbon combustion nowadays can be found on the website of the GRI initiative [27].

Fortunately, in fuel-lean to stoichiometric conditions good agreement with experimental data can be found if one considers the C_1-path only [25]. This leads to a large reduction in the number of species and reactions involved which is the main reason that we consider lean methane-air flames first. In table 2.1, page 30, this mechanism is presented. It is sometimes referred to as a skeletal mechanism since it represents only a minimal subset of the complete set. However, it is claimed in literature that it predicts the most important flame-features well, e.g. burning velocities, species profiles, flame temperatures [25]. There are 25 reactions and 15 species present in this scheme, which provides a considerable reduction of the problem size.

[14] Warnatz claims that the global combustion phenomena (burning velocity, quenching rate etc...) of any alkane can be modelled within a factor of two, by using only the H_2-O_2-CO mechanism, a realistic reaction set covering Alkane + O, H, OH $\rightharpoonup$ Alkyl + OH, H_2, H_2O conversion followed by an infinitely fast Alkyl to CO reaction.

[15] A complication in higher hydrocarbon fuels ($> C_2$), is the existence of different isomers of the alkyl, formed after decomposition. Each of these isomers (*e.g.* $n - C_3H_7$ versus $i - C_3H_7$ in the case of propane decomposition) has its own formation rate.

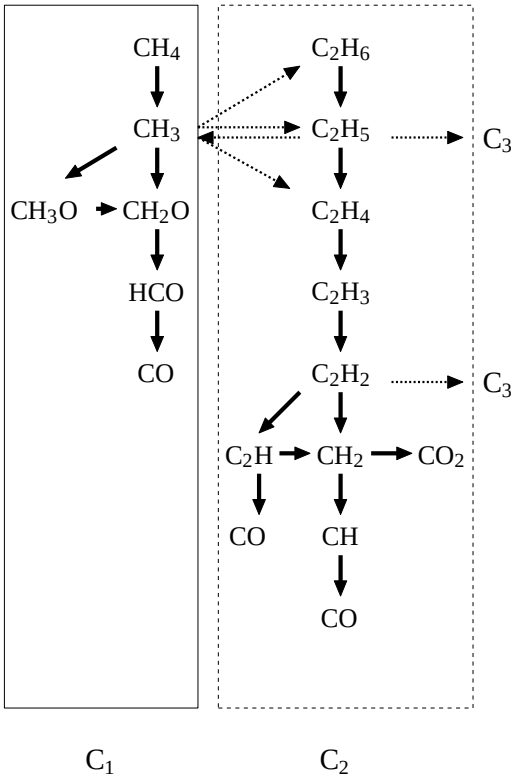

Figure 2.2: Main reaction path in methane combustion [21] for not too fuel-rich initial conditions. The dashed box describes what is usually referred to as the C_2-chain. The C_1 chain is shown in the box on the left.

The reaction set r_1–r_8 in table 2.1 is in fact the main reaction chain in the H_2-O_2 sub-system which is embedded in any hydrocarbon reaction mechanism. These reaction rates are very well known because of extensive studies in the early eighties on hydrogen flames. The reaction parameters of the chain CH_4 to CO and CO to CO_2 became well known in the late eighties when more computing power and sophisticated algorithms were developed and the research focussed on more complex fuels than hydrogen. In the following the role of several reactions in the hydrocarbon combustion process is discussed. The terminology used can be found in most literature on combustion [22, 25].

First of the so-called **initiation reactions** are treated. These are the reactions that account for the ignition of the reaction chain. The only initiation reaction[16] in the skeletal mechanism is a thermal-decomposition reaction (r_{10}) which is considered to be the most important,

$$CH_4\ (+\,M) \rightleftharpoons CH_3 + H + (M). \qquad (r_{10})$$

Sensitivity analysis shows that this initiation reaction is of minor importance for concentration profiles, burning velocity and flame temperature in a steady flame. For studies where ignition is important (e.g. engines, engine knock, shock-tubes) it is essential and other initiation reactions have to be provided as well [22, 25].

[16] Another initiation reaction in CH_4-air flames, but not tabulated here, is the $CH_4 + O_2 \rightharpoonup CH_3 + HO_2$ reaction.

Once initiated the fuel breakup to carbon-monoxide proceeds via a chain of reactions (r_{11} to r_{20}).

$$\mathrm{CH_4 + H \rightharpoonup CH_3 + H_2} \quad (r_{11})$$
$$\mathrm{CH_4 + OH \rightharpoonup CH_3 + H_2O} \quad (r_{12})$$
$$\mathrm{CH_3 + O_2 \rightharpoonup CH_3O + O} \quad (r_{18})$$
$$\mathrm{CH_3O + H \rightharpoonup CH_2O + H_2} \quad (r_{19})$$
$$\mathrm{CH_3O + M \rightharpoonup CH_2O + H + M} \quad (r_{20})$$
$$\mathrm{CH_3 + O \rightharpoonup CH_2O + H} \quad (r_{13})$$
$$\mathrm{CH_2O + H \rightharpoonup HCO + H_2} \quad (r_{14})$$
$$\mathrm{CH_2O + OH \rightharpoonup HCO + H_2O} \quad (r_{15})$$
$$\mathrm{HCO + H \rightharpoonup CO + H_2} \quad (r_{16})$$
$$\mathrm{HCO + M \rightharpoonup CO + H + M} \quad (r_{17})$$

This cascade of reactions is claimed to be very fast, which means that every intermediate product (i.e. CH_3, CH_3O, CH_2O and HCO) is rapidly consumed even at very low concentrations. The relatively slower oxidation step of CO to CO_2 proceeds via reaction r_9.

The total fuel-breakup chain in CH_4 flames consumes radicals. To keep the oxidation going, the so-called **chain-branching reactions** are important. These account for a fast increase of the concentration of the radicals O, OH and H, often referred to as the 'radical pool'. The most important chain-branching reaction in methane-air combustion is r_1,

$$\mathrm{H + O_2 \rightleftharpoons OH + O} \quad (r_1)$$

which is essential in the analysis of methane-air combustion. It is called branching because out of an initially present stable species (e.g. O_2) and a H-radical it produces two new radicals and thereby gives rise to an increase of the radical pool.

A third type of reactions are the **shuffle-** or **chain-propagating reactions**, reactions r_2–r_4 in table 2.1,

$$\mathrm{O + H_2 \rightleftharpoons OH + H} \quad (r_2)$$
$$\mathrm{OH + H_2 \rightleftharpoons H_2O + H} \quad (r_3)$$
$$\mathrm{OH + OH \rightleftharpoons H_2O + O} \quad (r_4)$$

The overall effect of these latter three reactions does not lead to an increase in the radical pool but is merely a conversion of radicals into another. Thereby stable products (e.g. H_2O) are created.

Finally, the reaction chain terminates because of the so-called **chain breaking reactions**. In the skeletal mechanism these are given by,

$$\mathrm{H + O_2 + M \rightharpoonup HO_2 + M} \quad (r_5)$$
$$\mathrm{OH + H + M \rightharpoonup H_2O + M} \quad (r_{24})$$
$$\mathrm{H + H + M \rightharpoonup H_2 + M} \quad (r_{25})$$

The net effect of this reaction set reduces the radical pool because it converts the radicals into stable products and is responsible for the formation of the final products. Note that although reaction (r_5)

in principle is radical conserving it still is considered as chain-breaking since the created peroxide-radical is less reactive than H and the rapid chain (r_6–r_8),

$$\mathrm{H} + \mathrm{HO_2} \rightharpoonup \mathrm{OH} + \mathrm{OH} \qquad (r_6)$$

$$\mathrm{H} + \mathrm{HO_2} \rightharpoonup \mathrm{H_2} + \mathrm{O_2} \qquad (r_7)$$

$$\mathrm{OH} + \mathrm{HO_2} \rightharpoonup \mathrm{H_2O} + \mathrm{O_2} \qquad (r_8)$$

has an overall effect of a conversion of HO_2 into stable products. The latter 6 reactions (r_5, r_6, r_7, r_8, r_{24}, and r_{25}) convert radicals into stable species either directly (r_7, r_8, r_{24} and r_{25}) or indirectly (r_5, r_6) by creating radicals that open a fast chain towards stable species.

The skeletal mechanism is used in section 6 to illustrate the classical reduction technique. However, it should always be kept in mind that because of the absence of the C_2-chain, the skeletal mechanism is not considered to be adequate for rich flames. In rich flames a path to the C_2-chain through reactions like $CH_3 + CH_3 \rightleftharpoons C_2H_6$ becomes more and more important, primarily due to the relatively high CH_3 concentration. An illustration of the importance of these effects of incorporating the C_2-chain in pre-mixed flame computations is presented in chapter 2 of [26].

References

[1] J.D. Buckmaster, G.S.S. Ludford, *Theory of Laminar Flames*, Cambridge University Press, London New York 1982

[2] Hirschfelder, J.O. Curtiss, C.F. and Bird, R.B., *Molecular Theory of Gases and Liquids* , JOHN WILEY and SONS, London New York 1954

[3] G. Dixon-Lewis, *Flame structure and flame reaction kinetics, II. Transport phenomena in multicomponent systems*, Proc. Roy. Soc A **307**, p. 111, 1968

[4] S. Chappman, T.G. Cowling, *The Mathematical Theory of Non-Uniform Gases*, Cambridge University Press, London New York 1970

[5] Williams, F.A., *Combustion Theory*, Second Edition, Addison-Wesley Publishing Company, Redwood City 1985

[6] Kee, R.J. Dixon-Lewis, G., Warnatz, J., Coltrin, M.E. and Miller, J.A., *A Fortran Computer Code Package for the Evaluation of Gas-Phase Multicomponent Transport Properties*, SANDIA REPORT SAND86-8246, Sandia National Laboratories, Albuquerque, New Mexico 87185 and Livermore, California 94551

[7] Kee, R.J., Rupley, F.M. and Miller, J.A., *Chemkin II: A Fortran Chemical Package for the Analysis of Gas-Phase Chemical Kinetics*, SANDIA REPORT SAND89-8009, Sandia National Laboratories, Albuquerque, New Mexico 87185 and Livermore, California 94551

[8] Kee, R.J., Rupley, F.M. and Miller, J.A., *The Chemkin Thermodynamic Data Base*, SANDIA REPORT SAND87-8215, Sandia National Laboratories, Albuquerque, New Mexico 87185 and Livermore, California 94551

[9] Muckenfuss, C, and Curtiss, C.F. , *Thermal Conductivity of Multicomponent Mixtures*, Journal of Chemical Physics **29**, p. 1273, 1958

Number	Reaction	A	n	E_a
1	$H + O_2 \rightleftharpoons OH + O$	$2.000 \cdot 10^{14}$	0.0	16800.0
		$1.575 \cdot 10^{13}$	0.0	690.0
2	$O + H_2 \rightleftharpoons OH + H$	$1.800 \cdot 10^{10}$	1.0	8826.0
		$8.00 \cdot 10^{9}$	1.0	6760.0
3	$H_2 + OH \rightleftharpoons H_2O + H$	$1.170 \cdot 10^{9}$	1.3	3626.0
		$5.090 \cdot 10^{9}$	1.3	18588.0
4	$OH + OH \rightleftharpoons O + H_2O$	$6.000 \cdot 10^{8}$	1.3	0.0
		$5.900 \cdot 10^{9}$	1.3	17029.0
5[a]	$H + O_2 + M \rightharpoonup HO_2 + M$	$2.300 \cdot 10^{18}$	−0.8	0.0
6	$H + HO_2 \rightharpoonup OH + OH$	$1.500 \cdot 10^{14}$	0.0	1004.0
7	$H + HO_2 \rightharpoonup H_2 + O_2$	$2.500 \cdot 10^{13}$	0.0	700.0
8	$OH + HO_2 \rightharpoonup H_2O + O_2$	$2.000 \cdot 10^{13}$	0.0	1000.0
9	$CO + OH \rightleftharpoons CO_2 + H$	$1.510 \cdot 10^{7}$	1.3	−758.0
		$1.570 \cdot 10^{9}$	1.3	22337.0
10[b]	$CH_4 + M \rightleftharpoons CH_3 + H + M$	$6.300 \cdot 10^{14}$	0.0	104000.0
		$5.200 \cdot 10^{12}$	0.0	−1310.0
11	$CH_4 + H \rightleftharpoons CH_3 + H_2$	$2.200 \cdot 10^{4}$	3.0	8750.0
		$9.570 \cdot 10^{2}$	3.0	8750.0
12	$CH_4 + OH \rightleftharpoons CH_3 + H_2O$	$1.600 \cdot 10^{6}$	2.1	2460.0
		$3.020 \cdot 10^{5}$	2.1	17422.0
13	$CH_3 + O \rightharpoonup CH_2O + H$	$6.800 \cdot 10^{13}$	0.0	0.0
14	$CH_2O + H \rightharpoonup HCO + H_2$	$2.500 \cdot 10^{8}$	0.0	3991.0
15	$CH_2O + OH \rightharpoonup HCO + H_2O$	$3.000 \cdot 10^{9}$	0.0	1195.0
16	$HCO + H \rightharpoonup CO + H_2$	$4.000 \cdot 10^{13}$	0.0	0.0
17	$HCO + M \rightharpoonup CO + H + M$	$1.600 \cdot 10^{14}$	0.0	14700.0
18	$CH_3 + O_2 \rightharpoonup CH_3O + O$	$7.000 \cdot 10^{12}$	0.0	25652.0
19	$CH_3O + H \rightharpoonup CH_2O + H_2$	$2.000 \cdot 10^{13}$	0.0	0.0
20	$CH_3O + M \rightharpoonup CH_2O + H + M$	$2.400 \cdot 10^{13}$	0.0	28812.0
21	$HO_2 + HO_2 \rightharpoonup H_2O_2 + O_2$	$2.000 \cdot 10^{12}$	0.0	0.0
22	$H_2O_2 + M \rightleftharpoons OH + OH + M$	$1.300 \cdot 10^{17}$	0.0	45500.0
		$9.860 \cdot 10^{14}$	0.0	−5070.0
23	$H_2O_2 + OH \rightleftharpoons H_2O + HO_2$	$1.000 \cdot 10^{13}$	0.0	1800.0
		$2.860 \cdot 10^{13}$	0.0	32790.0
24	$OH + H + M \rightharpoonup H_2O + M$	$2.200 \cdot 10^{22}$	−2.0	0.0
25	$H + H + M \rightharpoonup H_2 + M$	$1.800 \cdot 10^{18}$	−1.0	0.0

[a] High-pressure limit: switching function $F([M]) = \frac{1}{[M]_c/[M]+1}$ with $[M]_c = 0.0063e^{-18000.0/RT}$.

[b] Enhanced third body efficiencies σ_i: $CH_4 = 6.5$, $H_2O = 6.5$, $CO_2 = 1.5$, $CO = 0.75$, $O_2 = 0.4$, $N_2 = 0.4$. Others $= 1.0$.

Table 2.1: Skeletal Mechanism for CH_4-air combustion. The coefficients of the Arrhenius term $k = AT^n \exp(-E_a/RT)$ are given in the three columns on the right (see section 3.2). All units are cm, s, K and calories according to conventions used in standard literature on combustion.

[10] Monchik, L, Munn, R.J., and Mason, E.A. , *Thermal Diffusion in Polyatomic Gases: A Generalized Stefan-Maxwell Equation*, Journal of Chemical Physics **45**, p. 3051, 1966

[11] Dixon-Lewis, G., In *Combustion Chemistry* (ed. W.C. Gardiner) Springer-Verlag, New York, p. 21, 1984

[12] T.P. Coffee and J.M. Heimerl, *Flame structure and flame reaction kinetics, II. Transport phenomena in multicomponent systems*, Combustion and Flame **43**, p. 273, 1981

[13] Oran, E.S. and Boris, J.P., *Detailed Modelling of Combustion Systems*, Progress in Energy and Combustion Science **7**, p. 1, 1981

[14] Wilke, C.R., *A Viscosity Equation for Gas Mixtures*, Journal of Chemical Physics **18**, p. 517, 1950

[15] Mason,E.A. and Saxena, S.C., *Approximate Formula for the Thermal Conductivity of Gas Mixtures*, Phys. Fluids **1**, p. 361, 1958

[16] Mathur, S., Tondon, P.K. and Saxena, S.C., *Thermal Conductivity of Binary, Ternary and Quaternary Mixtures of Rare gases.* Mol. Phys. **12**, p. 569, 1967

[17] Zellner, R., *Non-Arrhenius Behavior in Bimolecular Reactions of the OH radical*
The Journal of Physical Chemistry **83**, p. 18, 1979

[18] Gardiner, W.C. and Troe, J., In *Combustion Chemistry* (ed. W.C. Gardiner, Springer-Verlag, New York, p. 173, 1984

[19] Troe, J., *Theory of Thermal Unimolecular Reactions in the Fall-off Range*, Ber. Bunsenges. Phys. Chem. **87**, p. 161, 1983

[20] Warnatz, J., *The Structure of Laminar Alkane-, Alkene-, and Acethylene Flames*, Eighteenth Symposium (International) on Combustion, The Combustion Institute, Pittsburgh, p. 369, 1981

[21] Warnatz, J., *The Mechanism of High Temperature Combustion of Propane and Butane*, Combustion Science and Technology, **34**, p. 177, 1983

[22] Warnatz, J., In *Combustion Chemistry* (ed. W.C. Gardiner, Springer-Verlag, New York, p. 197, 1984

[23] Egolfopoulos, F.N., Zhu, D.L. and Law, C.K., *Experimental and Numerical Determination of Laminar Flame Speeds: Mixtures of C_2-Hydrocarbons with Oxygen and Nitrogen*, Twenty-Third Symposium (International) on Combustion, The Combustion Institute, Pittsburgh, p. 471, 1990

[24] Mauss, F.,Peters, N., in *Reduced Kinetic Mechanisms for Applications in Combustion Systems* (Peters,N., Rogg,B., Eds), Lecture Notes in Physics m15, Springer-Verlag, Berlin, p. 58, 1993.

[25] Smooke, M.D. ed., *Reduced Kinetic Mechanisms and Asymptotic Approximations for Methane-Air Flames*, Lecture Notes in Physics, Springer-Verlag, Berlin Heidelberg, 1991

[26] Somers, L.M.T., *The Simulation of Flat Flames with Detailed and Reduced Chemical Models*, Ph.D. Thesis, Eindhoven University of Technology, 1994

[27] Bowman,G., Frenklach,M., Gardiner, B., Smith,G. and Serauskas,B, *GRI-Mech*, Gas Research Institute, Chicago, Illinois, USA, http://www.me.berkeley.edu/gri-mech/index.html

Chapter 3

Premixed and Non-Premixed Combustion

L. P. H. de Goey

1 Introduction

In the first lecture we introduced the different combustion regimes for both premixed and non-premixed flames, with the main focus on the so-called laminar flamelet regimes. For both flame types, the laminar flamelet combustion regime is the regime in which the flame fronts are thin compared to the length scale of all external influences in the (turbulent) flow. These regimes are also studied in this lecture. In the first lecture, a start was also made with the analysis of 1D undistorted premixed and non-premixed flame structures which govern the combustion behavior in the flamelet regime. However, it is well known that the internal structure and propagation characteristics of 1D flames are influenced by external flow distortions also present in the (turbulent) flow. This influence often leads to instabilities and other interesting phenomena. The analysis of the influence of external distortions on 1D flame behavior and the related effect on flame dynamics is the main focus of this lecture. In the next section, premixed flames will be considered first, while non-premixed flames will be studied in the last section.

2 Analysis of Premixed Flames

The flamelet description for premixed flames is treated in the next subsection. On the basis of a flame adapted coordinate system, the conservation equations are split in three parts: (1) a kinematic equation (similar to the G-equation) for the flame motion with the burning velocity included, (2) a flamelet system which describes the internal flame structure and the burning velocity and (3) a flame stretch K and curvature part R which couples (1) and (2). The influence of K and R on the burning velocity will be analysed using flame stretch theory in sections 2.2–2.4. It will be shown that the Lewis numbers play an important role in the behaviour of the burning velocity. On the basis of these results, flame dynamics will be studied in section 2.5. The Landau-Darrieus instability will be explained and the influence of the flame stretch and curvature in terms of the thermo-diffusive model will be presented. A flame stability diagram will be introduced. The appearance of cellular flames, flame pulsations and other phenomena will be explained on the basis of these theoretical ideas.

2.1 Combustion in the laminar flamelet regime

In this subsection we concentrate on laminar flames and turbulent frames in the laminar flamelet regimes, where the premixed flame fronts propagate through the flow and the internal structure is only weakly distorted by the external flow field. To analyse such structures we therefore zoom into the flame structure, study how it looks like and behaves when it is undistorted and (weakly) distorted.

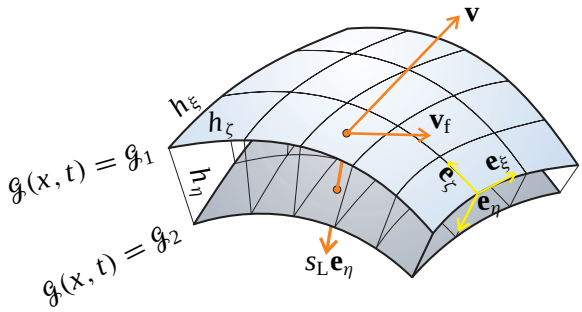

Figure 3.1: Flame-adapted coordinate system with isoplanes of $\mathcal{G}$.

This behavior is used in the so-called laminar flamelet models which have been proposed by different researchers to model combustion processes in these regimes. The system of transport equations of the previous lecture will be decomposed into three parts. The first part consists of the mass, momentum, enthalpy and element conservation equations and the gas law, which together describe the flow and mixing processes in the flame. Note that neither of these equations contains chemical source terms. The equations describing the propagation (similar to the G-equation) and internal structure (1D flamelets) of the flame are described by two separate systems of equations. These parts are derived by studying the mass, species and enthalpy equation in a flame-adapted coordinate system. This will be elaborated further in the remainder of this subsection.

We define the premixed flame as the region in space, where a scalar variable $\mathcal{G}$ has a value between 0 in the unburnt gases and 1 in the burnt gases. A 'flame surface' is defined as an iso-plane of $\mathcal{G}$, i.e. a surface where $\mathcal{G}(\mathbf{x}, t) =$ constant. The motion of such a surface is described by the kinematic equation [5]

$$\frac{\mathrm{d}\mathcal{G}}{\mathrm{d}t} := \frac{\partial \mathcal{G}}{\partial t} + (\mathbf{v}_\mathrm{f} \cdot \nabla)\mathcal{G} = 0, \tag{3.1}$$

stating that a point on a flame surface stays on this surface for all t. Here, $\mathbf{v}_\mathrm{f}$ is the local velocity of a flame surface. A local orthogonal coordinate system $\boldsymbol{\eta} = (\xi, \zeta, \eta)$ (see figure 3.1) is defined in terms of these flame surfaces. The factors $h_\xi = |\frac{\partial \mathbf{x}}{\partial \xi}|$, $h_\zeta = |\frac{\partial \mathbf{x}}{\partial \zeta}|$ and $h_\eta = |\frac{\partial \mathbf{x}}{\partial \eta}|$ are scale factors, defining the arc-lengths in the $\boldsymbol{\eta}$-coordinate system. Note that the unit normal vector $\mathbf{e}_\eta$ on a flame surface can be written as $\mathbf{e}_\eta = -\nabla\mathcal{G}/|\nabla\mathcal{G}|$.

The tangential component $\mathbf{v}_{\mathrm{f,t}}$ of the flame surface velocity is equal to the tangential component $\mathbf{v}_\mathrm{t}$ of the fluid velocity and the difference $\rho(\mathbf{v} - \mathbf{v}_\mathrm{f})$ is equal to the amount of mass, effectively consumed by the flame, so that we may write

$$\mathbf{v}_\mathrm{f} = \mathbf{v} + s_\mathrm{L}\mathbf{e}_\eta, \tag{3.2}$$

s_L being the local burning velocity. When equation (3.2) is substituted in equation (3.1) we find an equation which looks identical to the well-known G-equation [8]:

$$\frac{\partial \mathcal{G}}{\partial t} + (\mathbf{v} \cdot \nabla)\mathcal{G} = s_\mathrm{L}\,|\nabla\mathcal{G}|. \tag{3.3}$$

An important difference between Eq.(3.3) and the usual G-equation is that the description here is valid for any iso-surface in the flame front while the original G-equation is formulated in terms of an interface with zero thickness. This means that $\mathbf{v}$ and s_L are functions of the iso-plane in the formulation here. In [3], the stretch rate K is defined as the relative rate of change of the mass

$$M(t) = \int_{V(t)} \rho \,\mathrm{d}V \tag{3.4}$$

in a small part of the flame, enclosed by the volume $V(t)$, moving with velocity $\mathbf{v}_\mathrm{f}$:

$$K = \frac{1}{M}\,\frac{\mathrm{d}M}{\mathrm{d}t}. \tag{3.5}$$

Applying the transport theorem to $M(t)$ in equation (3.4) then leads to the following equation for the scalar field quantity K:

$$\rho K = \frac{\partial \rho}{\partial t} + \boldsymbol{\nabla}\cdot(\rho \mathbf{v}_\mathrm{f}). \tag{3.6}$$

Using equations (3.2) and (3.6) in equation (2.2) on page 13 gives

$$\boldsymbol{\nabla}\cdot(\rho s_\mathrm{L}\mathbf{e}_\eta) = \rho K \tag{3.7}$$

for the continuity equation. Note that all distortions from local 1D flame behavior are combined in the right-hand side term ρK. Apart from the usual terms related with flame curvature and flow straining, this definition of K incorporates additional contributions, for instance due to flame thickness variations.

The conservation equation for the scalar variable $\mathcal{G}$

$$\frac{\partial(\rho\mathcal{G})}{\partial t} + \boldsymbol{\nabla}\cdot(\rho\mathbf{v}\mathcal{G}) - \boldsymbol{\nabla}\cdot(\rho D_\mathcal{G}\boldsymbol{\nabla}\mathcal{G}) - \dot{\rho}_\mathcal{G} = 0, \tag{3.8}$$

with $D_\mathcal{G}$ and $\dot{\rho}_\mathcal{G}$ generally depending on the other field variables in the flame, is now reformulated in the $\boldsymbol{\eta}$-coordinate system. Using equations (3.1), equations (3.6) and (3.2), the following quasi-1D form for $\mathcal{G}$ is found rigorously:

$$\boldsymbol{\nabla}\cdot(\rho s_\mathrm{L}\mathcal{G}\mathbf{e}_\eta) - \boldsymbol{\nabla}\cdot(\rho D_\mathcal{G}\frac{1}{h_\eta}\frac{\partial\mathcal{G}}{\partial\eta}\mathbf{e}_\eta) - \dot{\rho}_\mathcal{G} = \rho K\mathcal{G}, \tag{3.9}$$

with all transport terms along the flame surfaces gathered in the right-hand side term $\rho K\mathcal{G}$. We used here that the diffusive flux is already directed in the $\mathbf{e}_\eta$-direction. It is important to note here that equation (3.9) is found from the full instationary conservation equation (3.8), using the stretch rate (3.6) and the kinematic equation (3.3). Alternatively, this means that the full conservation equation (3.8) for $\mathcal{G}$ would be solved exactly, when a method would be available in which the kinematic equation and the flamelet equation (3.9) are solved in a combined way, using the coupling with the scalar stretch field K of equation (3.6).

The same procedure can be applied to the other scalar variables Y_i, H and Z_j. The terms, which describe transport in the flame surfaces are neglected assuming that length scales of the flame stretch distortions of the flame along the flame surfaces are larger than the flame thickness as combustion takes place in the flamelet regime of the Borghi diagram. Introducing the mass burning rate $m = \rho s_\mathrm{L}$, the arc-length perpendicular to the flame $ds = h_\eta d\eta$ and the variable $\sigma = h_\xi h_\zeta = |\frac{\partial\mathbf{x}}{\partial\xi}\times\frac{\partial\mathbf{x}}{\partial\zeta}|$, which is a measure for the area on the flame surfaces through which transport takes place, the quasi-1D conservation equations can be expressed in the $\boldsymbol{\eta}$-coordinate system. These equations, which we refer

to as the 'flamelet' equations, then read:

$$\begin{aligned}
\frac{\partial}{\partial s}(\sigma m) &= -\sigma\ \rho K,\\
\frac{\partial}{\partial s}(\sigma m Y_i) - \frac{\partial}{\partial s}\left(\sigma\rho D_{i\mathrm{m}}\frac{\partial Y_i}{\partial s}\right) - \sigma\dot{\rho}_i &= -\sigma\ \rho K Y_i, \quad (i=1,\ldots,N),\\
\frac{\partial}{\partial s}(\sigma m H) - \frac{\partial}{\partial s}\left(\sigma\frac{\lambda}{c_p}\frac{\partial H}{\partial s}\right) - &\\
\sum_{i=1}^{N}\left(\frac{1}{Le_i}-1\right)\frac{\partial}{\partial s}\left(\sigma\frac{\lambda}{c_p}H_i^0\frac{\partial Y_i}{\partial s}\right) &= -\sigma\rho K H,\\
\frac{\partial}{\partial s}(\sigma m Z_j) - \frac{\partial}{\partial s}\left(\sigma\frac{\lambda}{c_p}\frac{\partial Z_j}{\partial s}\right) - &\\
\sum_{i=1}^{N} w_{ji}\left(\frac{1}{Le_i}-1\right)\frac{\partial}{\partial s}\left(\sigma\frac{\lambda}{c_p}\frac{\partial Y_i}{\partial s}\right) &= -\sigma\rho K Z_j, \quad (j=1,\ldots,N_{\mathrm{e}}).
\end{aligned} \tag{3.10}$$

Note that the derivative $\partial\sigma/\partial s$ is related to the curvature of the flame. These flamelet equations describe the internal flame structure (in terms of $Y_i(s)$, $\mathcal{G}(s)$, $H(s)$, $Z_j(s)$ or alternatively $Y_i(\mathcal{G})$, $H(\mathcal{G})$, $Z_j(\mathcal{G})$) and the eigenvalue for the mass burning rate $m(s)$ or $m(\mathcal{G})$ for a flamelet with a particular stretch field $K(\mathcal{G})$ and curvature field $\sigma(\mathcal{G})$.

2.2 Mass Burning Rate of Stretchless Flames

Let us first study the case of stretchless flames, i.e. $K = 0$. Note that flames may still be curved when $K = 0$. Integration of the conservation equations for mass, enthalpy and element mass fractions of the set (3.10) from the unburnt to the burnt gas mixture gives:

$$(\sigma m^0)_{\mathrm{b}} = (\sigma m^0)_{\mathrm{u}} \tag{3.11}$$

$$(\sigma m^0 H^0)_{\mathrm{b}} = (\sigma m^0 H)_{\mathrm{u}} \tag{3.12}$$

$$(\sigma m^0 Z_j^0)_{\mathrm{b}} = (\sigma m^0 Z_j)_{\mathrm{u}} \qquad (j=1,\ldots,N_{\mathrm{e}}), \tag{3.13}$$

where it has been used that the diffusive fluxes all vanish in the unburnt and burnt gases. The superscript '0' refers to the stretchless solution and the subscripts 'b' and 'u' denote the values of a variable in the burnt and unburnt gases, respectively. Equations (3.11), (3.12) and (3.13) simply indicate that the mass, enthalpy and element composition are constant in the flame area, i.e. $H_{\mathrm{b}}^0 = H_{\mathrm{u}}$ and $Z_{j,\mathrm{b}}^0 = Z_{j,\mathrm{u}}$, as expected.

Let us now turn to the mass burning rate m_{b}^0 of the stretchless flame, which can be computed from the quasi-1D equation for $\mathcal{G}$:

$$\mathcal{F}(s) - \frac{\partial}{\partial s}\mathcal{H}(s) = \mathcal{S}(s), \tag{3.14}$$

where we introduced the functions $\mathcal{F}$, $\mathcal{H}$ and $\mathcal{S}$:

$$\begin{aligned}
\mathcal{F}(s) &= \frac{\partial}{\partial s}(\sigma m\mathcal{G}),\\
\mathcal{H}(s) &= \sigma\rho D_{\mathcal{G}}\frac{\partial\mathcal{G}}{\partial s},\\
\mathcal{S}(s) &= \sigma\dot{\rho}_{\mathcal{G}}.
\end{aligned} \tag{3.15}$$

We multiply equation (3.14) with $\mathcal{H}(s)$ and subsequently integrate the resulting equation over s from s_u to s_b. The integral over the diffusion term $\frac{1}{2}\partial\mathcal{H}^2/\partial s$ then drops out, as the diffusion fluxes are zero in the (un)burnt mixture and we find

$$\int_{s_\mathrm{u}}^{s_\mathrm{b}} \mathcal{F}(s)\ \mathcal{H}(s)\ \mathrm{d}s = \int_{s_\mathrm{u}}^{s_\mathrm{b}} \mathcal{H}(s)\ \mathcal{S}(s)\ \mathrm{d}s. \tag{3.16}$$

The function $\mathcal{H}(s)$ in the left-hand side of this equation can be approximated very well by the (integrated) solution of equation (3.14) in the preheating zone, where $\mathcal{S} \ll \mathcal{F}$:

$$\mathcal{H}(s) = \int_{s_\mathrm{u}}^{s} (\mathcal{F}(\psi) - \mathcal{S}(\psi))\mathrm{d}\psi \approx \int_{s_\mathrm{u}}^{s} \mathcal{F}(\psi)\mathrm{d}\psi, \tag{3.17}$$

which, inserted in equation (3.16), leads to

$$\int_{s_\mathrm{u}}^{s_\mathrm{b}} \mathcal{F}(s)\ \left(\int_{s_\mathrm{u}}^{s} \mathcal{F}(\psi)\mathrm{d}\psi\right)\mathrm{d}s = \frac{1}{2}\left(\int_{s_\mathrm{u}}^{s_\mathrm{b}} \mathcal{F}(s)\ \mathrm{d}s\right)^2 \approx \int_{s_\mathrm{u}}^{s_\mathrm{b}} \mathcal{H}(s)\ \mathcal{S}(s)\ \mathrm{d}s. \tag{3.18}$$

The validity of the approximation in equation (3.17) is related to the fact that the reaction layer is much thinner than the preheating zone, so that the major contribution to the integral over $\mathcal{F}\mathcal{H}$ in equation (3.16) is found in the preheating zone. It should be noted that equation (3.18) is exact when the reaction sheet thickness goes to zero (e.g. for infinite activation energy). This approach is equivalent to the Large Activation Energy Asymptotics treatment [1, 7] to compute the mass burning rate.

The integrals in equation (3.18) can now be evaluated and substituted into equation (3.18), this gives the following expression for the mass burning rate:

$$m_\mathrm{b}^0(\mathcal{G}_\mathrm{u}, H_\mathrm{b}^0, Z_{1,\mathrm{b}}^0, \ldots, Z_{N_\mathrm{e},\mathrm{b}}^0) \approx \frac{1}{|\mathcal{G}_\mathrm{b}^0 - \mathcal{G}_\mathrm{u}|}\sqrt{2\int_{\mathcal{G}_\mathrm{u}}^{\mathcal{G}_\mathrm{b}^0}\left(\frac{\sigma}{\sigma_\mathrm{b}}\right)^2 \rho D_{\mathcal{G}}\ \dot{\rho}_{\mathcal{G}}\ \mathrm{d}\mathcal{G}}. \tag{3.19}$$

Note that the expression equation (3.19) for m_b^0 only depends on the initial state through $\mathcal{G}_\mathrm{u}$ in the 'friction' factor $1/|\mathcal{G}_\mathrm{b}^0 - \mathcal{G}_\mathrm{u}|$. Furthermore, we also explicity emphasized that the mass burning rate m_b^0 further explicitly depends on the enthalpy H_b^0 and element composition $Z_{j,\mathrm{b}}^0$ in the equilibrium state in equation (3.19). This follows from the following observation. The factor $\rho D_{\mathcal{Y}}\dot{\rho}_{\mathcal{G}}$ in equation (3.19) is a function of all flame variables Y_i ($i = 1, \ldots, N$) and T. However, the integral in equation (3.19) effectively runs only over the thin reaction layer, where $\dot{\rho}_{\mathcal{G}} \neq 0$ and where the system approaches the equilibrium state. Near the equilibrium point in composition space, all reaction paths are attracted to a one-dimensional subspace in most cases, independent of the intial composition. This means that for this case all flame variables can be written as function of $\mathcal{G}$ because $|\nabla\mathcal{G}| \neq 0$: $Y_i(\mathcal{G})$ and $T(\mathcal{G})$. Equation (3.19) then indicates that the integral over $\mathcal{G}$ is *independent* of the initial composition in this case and depends only on the equilibrium state. The local equilibrium state is described completely by the pressure (assumed to be constant), total enthalpy and element composition in the reaction layer, i.e. H_b^0 and $Z_{j,\mathrm{b}}^0$ for $j = 1, \ldots, N_\mathrm{e}$.

2.3 Mass Burning Rate of Stretched Flames

In this subsection we consider stretched flames. As in the previous section, we first study the conservation equations for mass, enthalpy and element mass fractions. Integration of the mass conservation equation in (3.10) through the flame gives

$$(\sigma m)_\mathrm{b} - (\sigma m)_\mathrm{u} = -\int_{s_\mathrm{u}}^{s_\mathrm{b}} \sigma\rho K \,\mathrm{d}s. \tag{3.20}$$

In the same way, integration of the enthalpy equation and element mass fraction equations in (3.10) through the flamelet and using (3.20) results in

$$H_\mathrm{b} - H_\mathrm{u} = \frac{-1}{(\sigma m)_\mathrm{b}} \int_{s_\mathrm{u}}^{s_\mathrm{b}} \sigma\rho K (H - H_\mathrm{u}) \,\mathrm{d}s \tag{3.21}$$

and

$$Z_{j,\mathrm{b}} - Z_{j,\mathrm{u}} = \frac{-1}{(\sigma m)_\mathrm{b}} \int_{s_\mathrm{u}}^{s_\mathrm{b}} \sigma\rho K (Z_j - Z_{j,\mathrm{u}}) \,\mathrm{d}s, \tag{3.22}$$

respectively. When the definition for H and H_u (equation (2.5) on page 13) and the definition for Z_j and $Z_{j,\mathrm{u}}$ (equation (2.9) on page 14) are inserted into the right-hand sides of (3.21–3.22) and when the Karlovitz integrals

$$Ka_i = \frac{Le_i}{(\sigma m^0)_\mathrm{b}} \int_{s_\mathrm{u}}^{s_\mathrm{b}} \sigma\rho K \tilde{Y}_i \,\mathrm{d}s, \tag{3.23}$$

$$Ka_T = \frac{1}{(\sigma m^0)_b} \int_{s_\mathrm{u}}^{s_\mathrm{b}} \sigma\rho K \tilde{H}_T \,\mathrm{d}s, \tag{3.24}$$

are introduced, $H_T = \int_{T_0}^{T} c_p(\xi) d\xi$ being the thermal enthalpy and $\tilde{f} = (f - f_\mathrm{u})/(f_\mathrm{b} - f_\mathrm{u})$ being normalised quantities, then gives the exact equations

$$H_\mathrm{b} - H_\mathrm{u} = \frac{-m_\mathrm{b}^0}{m_\mathrm{b} + Ka_T m_\mathrm{b}^0} \sum_{i=1}^{N} H_i^0 \left(\frac{Ka_i}{Le_i} - Ka_T \right) (Y_{i,\mathrm{b}} - Y_{i,\mathrm{u}}), \tag{3.25}$$

$$Z_{j,\mathrm{b}} - Z_{j,\mathrm{u}} = \frac{-m_\mathrm{b}^0}{m_\mathrm{b} + Ka_T m_\mathrm{b}^0} \sum_{i=1}^{N} w_{ji} \left(\frac{Ka_i}{Le_i} - Ka_T \right) (Y_{i,\mathrm{b}} - Y_{i,\mathrm{u}}). \tag{3.26}$$

Equations (3.25) and (3.26) describe the influence of preferential diffusion and flame stretch, incorporated in the Karlovitz integrals, on the local enthalpy and element composition of the burnt mixture even in the case of strong stretch. The quantities H_b and $Z_{j,\mathrm{b}}$ following from equations (3.25) and (3.26), have an important influence on the local mass burning rate m_b, because m_b is determined to a large extend by the mixture composition and enthalpy in the reaction layer, close to the burnt mixture (see also equation (3.19)). The precise description of this influence will be studied hereafter.

Let us now turn to the evaluation of the mass burning rate for stretched flames. The mass burning rate is again determined from equation (3.14), where $\mathcal{F}(s)$ is now given by

$$\mathcal{F}(s) = \frac{\partial}{\partial s}(\sigma m \mathcal{G}) + \sigma \rho K \mathcal{G}, \tag{3.27}$$

while $\mathcal{H}$ and $\mathcal{S}$ are still given in (3.15). The computation of the mass burning rate is analogous to the computation presented in the previous subsection, with $\mathcal{F}$ replaced by equation (3.27). We now find for the mass burning rate

$$m_\mathrm{b}(H_{T,\mathrm{u}}, H_\mathrm{b}, Z_\mathrm{b}) \approx m_\mathrm{b}^0(H_{T,\mathrm{u}}, H_\mathrm{b}, Z_\mathrm{b})(1 - Ka_T). \tag{3.28}$$

Note that the first term in the right-hand side is equal to the mass burning rate of a 'stretchless' flame m_b^0 with final enthalpy and composition given by H_b and $Z_{j,\mathrm{b}}$ instead of H_b^0 and $Z_{j,\mathrm{b}}^0$. If we finally use (3.28) in equation (3.25) and (3.26) we find the equations

$$\begin{aligned}
\Delta H_\mathrm{b} &= -\sum_{i=1}^{N} H_i^0 \left(\frac{Ka_i}{Le_i} - Ka_T \right) (Y_{i,\mathrm{b}} - Y_{i,\mathrm{u}}), \\
\Delta Z_{j,\mathrm{b}} &= -\sum_{i=1}^{N} w_{ji} \left(\frac{Ka_i}{Le_i} - Ka_T \right) (Y_{i,\mathrm{b}} - Y_{i,\mathrm{u}}), \\
m_\mathrm{b}(H_{T,\mathrm{u}}, H_\mathrm{b}, Z_\mathrm{b}) &\approx m_\mathrm{b}^0(H_{T,\mathrm{u}}, H_\mathrm{b}^0 + \Delta H_\mathrm{b}, Z_\mathrm{b}^0 + \Delta Z_\mathrm{b})\ (1 - Ka_T)\ ,
\end{aligned} \tag{3.29}$$

where $\Delta H_\mathrm{b} = H_\mathrm{b} - H_\mathrm{u} = H_\mathrm{b} - H_\mathrm{b}^0$ and $\Delta Z_{j,\mathrm{b}} = Z_{j,\mathrm{b}} - Z_{j,\mathrm{u}} = Z_{j,\mathrm{b}} - Z_{j,\mathrm{b}}^0$. The set of Equations (3.29) for H_b, $Z_{j,\mathrm{b}}$ and m_b describe the enthalpy, element composition and mass burning rate of stretched and curved premixed flamelets and forms the basis of the subsequent analysis of the flamelet system. This set is also valid in case of strong stretch rates: equations (3.25) and (3.26) follow rigorously from the flamelet equations and to derive equation (3.28) it only has been assumed that the reaction layer is thin. However, the system (3.29) is not closed because stretched flame solutions $\tilde{f}$ are needed in the Karlovitz integrals (3.23) and (3.24) to evaluate (3.29).

It is the aim of the analysis which follows to introduce smart approximations to close this set of equations in such a way that it may be used without solving the complete system (3.10) for each separate flamelet. The simplest method, which will be described in the next subsection, would be to restrict to weak stretch.

2.4 Weak Stretch Analysis

The simplest way to close the system (3.29) is to evaluate H_b, $Z_{j,\mathrm{b}}$ and m_b from stretchless-flame information only. Instead of the Karlovitz integrals (3.23) and (3.24) we then use the 'stretchless' Karlovitz integrals

$$Ka_i^0 = \frac{Le_i}{(\sigma m^0)_\mathrm{b}} \int_{s_\mathrm{u}}^{s_\mathrm{b}} \sigma \rho K \tilde{Y}_i^0 \, \mathrm{d}s \tag{3.30}$$

and

$$Ka_T^0 = \frac{1}{(\sigma m^0)_\mathrm{b}} \int_{s_\mathrm{u}}^{s_\mathrm{b}} \sigma \rho K \tilde{H}_T^0 \, \mathrm{d}s \tag{3.31}$$

in equation (3.29). For weak stretch it is possible to expand $m_b^0(\mathcal{G}_\mathrm{u}, H_\mathrm{b}, Z_\mathrm{b})$ around $m_\mathrm{b}^0(\mathcal{G}_\mathrm{u}, H_\mathrm{b}^0, Z_\mathrm{b}^0)$. We then find for m_b

$$\frac{m_\mathrm{b}}{m_\mathrm{b}^0} = 1 - Ka_T^0 \; + \; \Delta H_\mathrm{b} \, \frac{\partial}{\partial H_\mathrm{b}^0} \, (\ln m_\mathrm{b}^0) \; + \; \sum_{j=1}^{N_\mathrm{e}} \Delta Z_{j,\mathrm{b}} \, \frac{\partial}{\partial Z_{j,\mathrm{b}}^0} \, (\ln m_\mathrm{b}^0) + \text{h.o.t.}, \tag{3.32}$$

with h.o.t. containing higher-order terms in Ka_i^0.

Let us consider the physical significance of the different terms in equation (3.32). The term Ka_T is related to the fact that effective upstream transport of heat and mass from the reaction zone to the preheating zone is modified by flame stretch. The rate of upstream transport has an important influence on the propagation velocity of a premixed flame. The $\frac{\partial}{\partial H_\mathrm{b}^0}(\ln m_\mathrm{b}^0)$-term in the right-hand side is related to the effect of preferential diffusion on the local enthalpy, leading to a change in the mass burning rate on its turn. The last term, proportional to $\frac{\partial}{\partial Z_{j,\mathrm{b}}^0}(\ln m_\mathrm{b}^0)$, also arises from differential diffusion effects, which give rise to element composition and stoichiometry changes.

We now study the results for the special case of a flat flame ($\sigma = \sigma_\mathrm{b}$) with constant λ and c_p in a stagnation flow with $\rho K = \rho_\mathrm{b} K_\mathrm{b}$, so that $\sigma\rho K =$ constant in the flame region ($s_\mathrm{u} < s < s_\mathrm{b}$) (see e.g. [9]). We restrict the analysis to a one-step irreversible reaction $\mathcal{F} \rightarrow \mathcal{P}$ with a single Lewis number $Le_\mathcal{F} = Le_\mathcal{P} = Le$. For this special case, though, we find an identical expression for all Karlovitz integrals from equation (3.30) and (3.31):

$$\mathcal{K}a^0 = \frac{\lambda \rho_\mathrm{b} K_\mathrm{b}}{c_p (m_\mathrm{b}^0)^2}, \tag{3.33}$$

where we substituted the approximate stretchless 1D solution for $\tilde{Y}_i^0(s)$ and $\tilde{H}_T^0(s)$ in the preheating zone. Equation (3.29) now simplifies considerably:

$$\begin{aligned} \Delta H_\mathrm{b} &= \mathcal{K}a^0 \left(\frac{1}{Le} - 1 \right) c_p (T_\mathrm{b}^0 - T_\mathrm{u}); \qquad \Delta Z_{j,\mathrm{b}} = 0; \\ \frac{m_\mathrm{b}}{m_\mathrm{b}^0} &\approx 1 - \mathcal{K}a^0 \mathcal{M}_\mathrm{b}, \end{aligned} \tag{3.34}$$

where the Markstein number $\mathcal{M}_\mathrm{b}$ has been introduced

$$\mathcal{M}_\mathrm{b} = 1 - \left(\frac{1}{Le} - 1 \right) c_p (T_\mathrm{b}^0 - T_\mathrm{u}) \, \frac{\partial}{\partial H_\mathrm{b}^0} (\ln m_\mathrm{b}^0) = 1 + \frac{Le - 1}{Le} \frac{Ze^0}{2} \tag{3.35}$$

using $m_\mathrm{b}^0 \propto \exp(-E_\mathrm{a}/2RT_\mathrm{b}^0)$ with the Zeldovich number given by, as usual, $Ze^0 = E_\mathrm{a} \; (T_\mathrm{b}^0 - T_\mathrm{u})/R(T_\mathrm{b}^0)^2$, E_a being the activation energy. In 1979 Joulin and Clavin found $1 + (Le - 1)Ze^0/2$ for the Markstein number.

In 1985, Clavin extended the above theory to a constant stretch rate $K = K_\mathrm{b}$, but with variable density in the flame zone $\rho^0(s) = \rho_\mathrm{u} T_\mathrm{u}/T^0(s) = \rho_\mathrm{u}/(1 + \tau \exp(s/\delta))$, where the thermal expansion coefficient τ is defined by $\tau = (T_\mathrm{b}^0 - T_\mathrm{u})/T_\mathrm{u} = (\rho_\mathrm{u} - \rho_\mathrm{b}^0)/\rho_\mathrm{b}^0$. Now, substituting this expression for $\rho(s)$ in the Karlovitz integrals, we find the same results as Clavin for the Markstein number:

$$\mathcal{M}_\mathrm{b} = \left(\frac{\tau + 1}{\tau} \right) \ln(1 + \tau) + \frac{Ze^0}{2} (Le - 1)(1 + \tau) \int_0^\tau \frac{\ln(1 + x)}{x^2} \left(\frac{x}{\tau} \right)^{Le} \, dx. \tag{3.36}$$

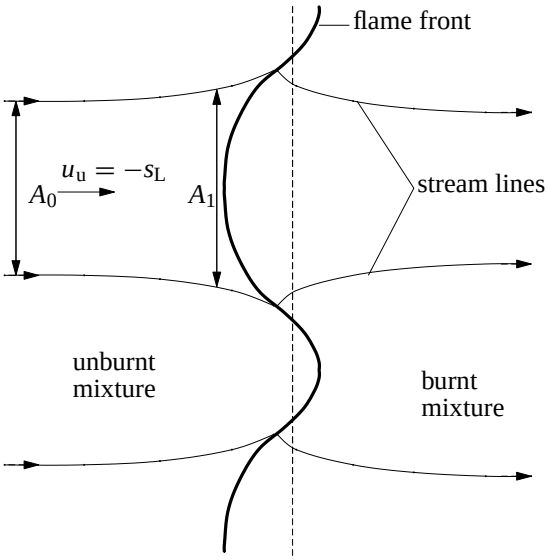

Figure 3.2: The Landau-Darrieus Instability.

2.5 Flame Stability

The flame stretch theory forms the basis for analysing the stability of premixed flames. Different kinds of instability might be observed and explained using this theory. The starting point of the analysis is formed by the observation of Darrieus and Landau that flames are inherently instable due to the thermal expansion in the flame, causing the so-called hydrodynamic instability. A flat flame which is distorted as shown in figure 3.2, induces flow field distortions. Due to the thermal expansion in the front, the flow velocity perpendicular to the front increases and the streamlines are bend towards the local normal vector on the front. They therefore must diverge in front of bulges in the front, leading to a decreasing local velocity ahead of the front. The result is that the burning velocity will be larger than the gas velocity and the distortion will grow: the flame is hydrodynamically instable. Mathematically, the instability is found by expanding the perturbation from the flat stationary structure in normal modes of the form $(\exp(\sigma t)\exp(ikx))$. Substitution in the balance equations leads to a dispersion relation $\sigma(k)$. Modes with wavenumbers k where $\sigma > 0$ are instable. The analysis of Landau and Darrieus gives a positive σ for all k.

In practice, however, it is possible to create stable laminar flames. The reason for this discrepancy is related to the influence of stretch and curvature on the burning velocity as described in the previous subsections. It depends on the Lewis number what happens. If $Le > 1$, positive stretch induces a decreasing flame temperature and a decrease in the mass burning rate (see equations (3.34), (3.36) and (3.35)). Thus, at the bulges, where $K > 0$, the velocity decreases due to the hydrodynamic instability, but the burning velocity decreases as well due to thermal-diffusive effects. The hydrodynamic instability may thus be damped, if the Markstein number is large enough, or if the Lewis number is sufficiently large $Le > Le_c$. On the other hand, the system is instable if $Le < Le_c$. Hydrogen flames have small Lewis numbers and display cellular structures. Heat loss of the flame (due to radiation or to a burner) may have a stabilizing influence on the flame instabilities if $Le < 1$. At the 'leading' positions on the cellular structure, where the temperature and propagation velocity is highest due to flame stretch the cooling is most important, leading to a damping effect of the stabilisation. This is seen in figure 3.3 from Joulin and Clavin [4] where the stability diagram of flames as a function of the scaled heat loss parameter $\ln(1/\mu^2)$ and the scaled Lewis number $Ze(Le-1)$ is plotted. This diagram is derived from an analysis, neglecting the hydrodynamic effect ($\tau = 0$). Note that the critical Lewis

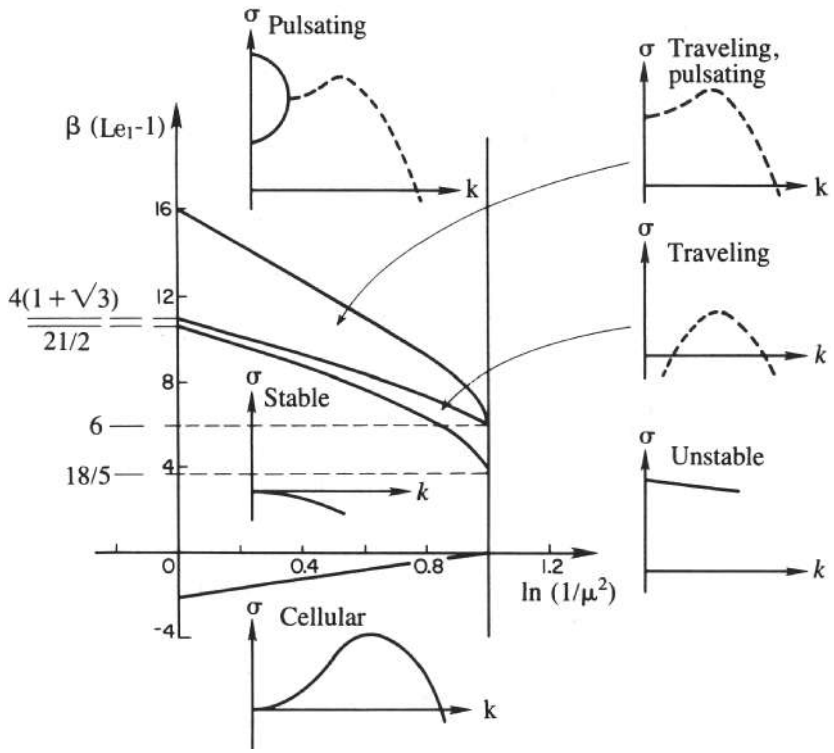

Figure 3.3: The stability diagram and corresponding dispersion relations for flat flames without thermal expansion (adapted from Joulin and Clavin [4]).

number is given by $Le_c = 1 - 2/Ze$ for zero heat loss, which is in accordance with $\mathcal{M}_b = 0$ following from the expression for the Markstein number of Joulin and Clavin. The flame displays a dispersion relation $\sigma(k)$ which corresponds to cellular structures for values for Le which are smaller than Le_c. At small values for the heat loss, this critical value is smaller than 1, but this critical value increases towards $Le_c = 1$ for increasing heat loss.

Note from figure 3.3 that other kinds of instability, such as pulsating flames, are detected for large Lewis numbers. These flames become less stable for increasing heat loss. Such pulsating flames are detected in practice near quenching at low burning velocities, when heat loss by radiation or to a burner becomes important. However, when the velocity is increased moving away from the flammability limits, these instabilities are not detected in case of hydrocarbon flames, because the Lewis numbers are not sufficiently large. The physical background of this kind of instability is hard to explain using the above theory. However, a simplified model can be used to explain the essential ingredients. This model is explained in the remainder of this subsection for a flame stabilised by cooling on top of a cooled burner with unit Lewis numbers $Le = 1$.

Consider a flat stationary burner-stabilised flame with flame temperature $\bar{T}_b$ and mass burning rate $\bar{m} = \bar{\phi}_u = \bar{\rho}_u \bar{u}_u$. If the flame is disturbed by a temporal distortion of some kind, a change in flame temperature T_b is assumed to lead to an instantaneous change in m, described by:

$$\frac{\partial m(\tau)}{\partial \tau} = \frac{Ze}{2} \frac{\bar{m}}{(\bar{T}_b - T_u)} \frac{\partial T_b}{\partial \tau} = \frac{Ze}{2} \frac{\bar{m}}{c_p(\bar{T}_b - T_u)} \frac{\partial J(\psi_f, \tau)}{\partial \tau} \tag{3.37}$$

where $dJ = \Delta H\, dY + c_p dT$ is the 'total enthalpy' in the system, Y being the fuel mass fraction and ΔH the enthalpy of combustion. This J depends not only on the time τ, but also on the (Von-Mises)

space variable ψ with $d\psi = \frac{\rho}{\rho_u} dx$. Fluctuations in J are transported in space with velocity $\bar{u}_u$, so that heat losses to the burner at $\psi = 0$ arrive at the flame front $\psi = \psi_f$ with a time lag. In the most general case, the shape of the enthalpy waves changes while they travel due to damping effects. Damping is neglected for simplicty, so that the shape of the enthalpy fluctuations remains the same. Then we may write:

$$\frac{\partial J(\psi_f, \tau)}{\partial \tau} = \frac{\partial J(0, \tau - \psi_f/\bar{u}_u)}{\partial \tau} = \Delta H \frac{\partial Y(0, \tau - \psi_f/\bar{u}_u)}{\partial \tau}, \tag{3.38}$$

where we used that T is constant at the burner outflow ($\psi = 0$) in the last step. Using the G-equation for the flame motion in terms of Y

$$\rho_u \frac{\partial Y}{\partial \tau}(\psi, \tau) = \Big(m(\tau) - \phi_u(\tau)\Big) \frac{\partial Y}{\partial \psi}(\psi, \tau) \tag{3.39}$$

we finally find a first-order differential equation for m:

$$\frac{\partial m(\tau)}{\partial \tau} + \frac{Z}{\tau_f} m(\tau') = \frac{Z}{\tau_f} \phi_u(\tau') \tag{3.40}$$

where we introduced the 'delayed time' $\tau' = \tau - \psi_f/\bar{u}_u$, the 'flame time' $\tau_f = \frac{\delta}{\bar{u}_u}$ and the 'feed-back' coefficient Z given by

$$Z = \frac{Ze}{2} \left(\frac{T_{ad} - \bar{T}_b}{\bar{T}_b - T_u} \right). \tag{3.41}$$

From the G-equation and its derivative, equation (3.40) can also be written as an equation of motion for the flame structure

$$\rho_u \frac{\partial^2 \psi}{\partial \tau^2}(\tau) + \rho_u \frac{Z}{\tau_f} \frac{\partial \psi}{\partial \tau}(\tau') = -\frac{\partial \phi_u(\tau)}{\partial \tau}. \tag{3.42}$$

This equation describes the motion of the flame structure $\psi(\tau)$, due to the external driving force $-\partial\phi_u(\tau)/\partial\tau$ (e.g. being an external acoustic field). The first term in the left hand side is the acceleration term and the second one the damping force, which acts on the flame with some time lag.

Let us study the solution of equation (3.40). When a harmonic 'driving term' $\phi_u(\tau) = \bar{\phi}_u + \hat{\phi}_u \exp(i\omega\tau)$ is applied, m behaves harmonically $m(\tau) = \bar{m} + \hat{m} \exp(i\omega\tau)$ (with $\bar{m} = \bar{\phi}_u$) as well. The total solution is then given by

$$m(\tau) = \bar{m} - \hat{m} \exp\left(\frac{\alpha \bar{u}_u \tau}{\psi_f}\right) \exp\left(\frac{i\beta \bar{u}_u \tau}{\psi_f}\right) + \hat{m} \exp(i\omega\tau) \tag{3.43}$$

where we used the initial value $m(t = 0) = \bar{m}$. Furthermore, α and β have to obey

$$\begin{aligned} \alpha &= -\hat{Z} \exp(-\alpha) \cos(\beta) \\ \beta &= +\hat{Z} \exp(-\alpha) \sin(\beta), \end{aligned} \tag{3.44}$$

where $\hat{Z} = \frac{\psi_f}{\delta} Z$.

The homogeneous part of the solution equation (3.43) for $m(\tau)$ indicates when solutions are stable or instable. Stable solutions are found when $\alpha < 0$, while the solution becomes instable if $\alpha > 0$, even if there is no external forcing ($\hat{\phi}_u = 0$). Combining equations (3.44) gives the following implicit relation for the dimensionless frequency β

$$\beta = \sin(\beta)\ \hat{Z} \exp\big(\beta \cot(\beta)\big) = f(\beta) \tag{3.45}$$

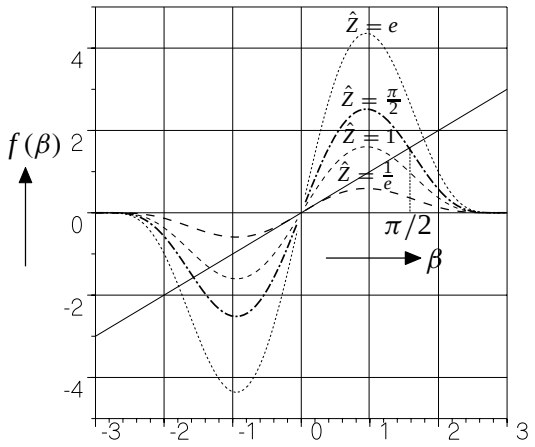

Figure 3.4: The implicit relation $f(\beta) = \beta$ for the dimensionless frequency β, predicting flame stability.

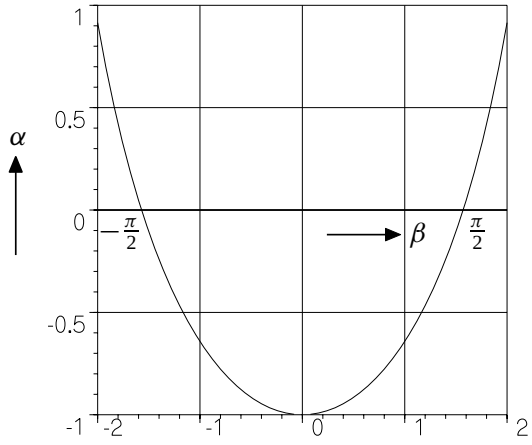

Figure 3.5: α as function of β for predicting flame stability.

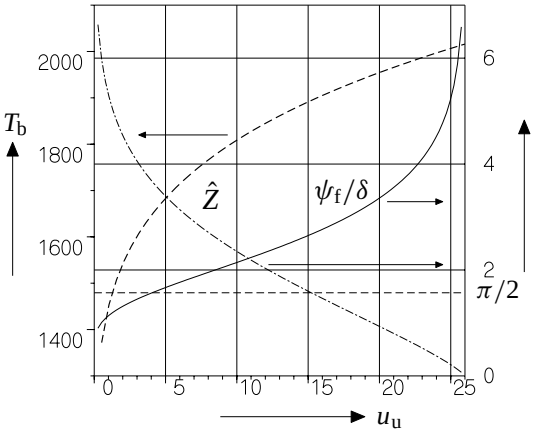

Figure 3.6: Feed-back coefficient $\hat{Z}$, stand-off distance and flame temperature T_b as function of the gas velocity for a methane/air flame with $\phi = 0.8$.

In figure 3.4, $f(\beta)$ is shown as function of β for several values of $\hat{Z}$. For the derivative of f in the origin we find $\mathrm{d}f(0)/\mathrm{d}\beta = \hat{Z}e$, which means that there exists no solution[1] of equation (3.45) for $\beta < \pi$ if $\hat{Z} < e^{-1}$. For $e^{-1} < \hat{Z} < \pi/2$ there exists a unique branching point (see figure 3.4) in the area with frequencies $\beta < \pi/2$, leading to stable solutions with $\alpha < 0$ (see figure 3.5). Instable solutions are found when $\alpha > 0$, $\pi/2 < \beta < \pi$, or for all flames with $\hat{Z} > \pi/2$.

In figure 3.6 some results are shown for a burner-stabilised methane/air flame with $\phi = 0.8$ as a function of the average flow velocity $\bar{u}_u$. Using $T_{ad} = 2016$ K, $T_u = 300$ K and $T_a = 34.566$ K and an adiabatic burning velocity of $s_{ad} = 26$ cm/s, $\bar{T}_b$ is shown as function of $\bar{u}_u$. Furthermore, $\psi_f/\delta = \ln((T_{ad} - T_u)/(T_{ad} - \bar{T}_b))$ and $\hat{Z}$ are plotted as function of $\bar{u}_u$. Note that $\hat{Z}$ becomes larger than $\pi/2$ for velocities lower than approximately 15 cm/s, indicating instability for lower velocities. In numerical (and experimental) observations, instability is found for a much lower velocity. This indicates that this theory is insufficiently accurate to predict instability. If damping of enthalpy waves is considered, a much lower value for the critical velocity if found, in accordance with experiments and other theoretical methods.

[1]Note that $f(\beta)$ decreases from infinity at $\beta = 2\pi$ to $f(5\pi/2) = \hat{Z}$ at $\beta = 5\pi/2$; thus for all $\hat{Z} < 5\pi/2$ there exists always a stable solution with $\alpha < 0$ in the area $2\pi < \beta < 5\pi/2$.

If the solution is stable ($\alpha < 0$), the homogeneous part of the solution damps out and after some time, the particular solution of equation (3.40) remains:

$$m_{\text{part}}(\tau) = \bar{m} + \hat{m} \exp(i\omega\tau) \tag{3.46}$$

where the amplitude $\hat{m}$ of the quasi-stationary solution is related to the amplitude of the acoustic forcing:

$$\hat{m} = \hat{\phi}_{\text{u}}\Big(1 + \frac{i\omega\tau_{\text{f}} \exp(i\phi)}{Z}\Big)^{-1}, \tag{3.47}$$

with the phase $\phi = \omega\psi_{\text{f}}/\bar{u}_{\text{u}}$. Equation (3.47) displays a resonance behavior also observed in other analysis of acoustic forcing of burner-stabilised flames.

3 Analysis of Non-premixed Flames

Diffusion flames burn in the areas in space where the fuel and oxidizer are mixing. These mixing processes are described by the transport equations for the element mass fractions (equation (2.10) on page 14). If we restrict the analysis to $Le_i = 1$ for simplicitly, the equations for Z_j are all the same and the Z_j behave similarly. For this reason we introduce the so-called mixture fraction $Z = (sY_F - Y_{\text{O}_2} + Y_{\text{O}_2,2})/(sY_{\text{F},1} + Y_{\text{O}_2,2})$ (see equation (2.27 on page 19)) to describe the mixing process. Here Y_{F} is the fuel mass fraction and the subscripts 1 and 2 indicate the boundary values in the fuel and oxidizer stream, respectively. Z has been scaled such that $Z = 1$ in the fuel stream and 0 in the oxidiser stream.

At the positions where fuel and oxidizer mix and burn in a flame, they are depleted very fast because chemical reactions are mostly very fast. The most simple model for a diffusion flame is the Burke-Schumann model which states the reaction is infinitely fast, indicating that fuel and oxigen deplete $Y_{\text{F}} = Y_{\text{O}_2} = 0$ at the flame front: if these species meet, they burn immediately giving an infinitely thin flame front at the position where the mixture fraction equals its so-called stoichiometric value $Z_{\text{st}} = Y_{\text{O}_2,2}/(sY_{\text{F},1} + Y_{\text{O}_2,2})$. The flame front can therefore be identified as the plane where $Z = Z_{\text{st}}$. This is very appealing because Z obeys the pure mixing equation (2.27) without chemical source term. Thus: the position of the flame front is purely determined by the mixing processes of the fuel and oxidizer stream. Furthermore, unlike premixed flames, where Z_j is more or less constant in the flame front, Z changes rapidly perpendicular to the flame front. This makes Z as a very suitable progress variabele in a non-premixed flame. So instead of $\mathcal{G}$ for premixed flames, we now use the mixture fraction as progress variabele to identify the position inside the flame structure.

As in case of a premixed flame, we consider the non-premixed flame in a coordinate system attached to the flame front. For the $\mathbf{e_1}$ axis we choose the coordinate in direction ∇Z. The other two axis $\mathbf{e_2}$ and $\mathbf{e_3}$ are chosen in the isoplane of Z. If we now transform the transport equations into the new coordinate system with Z as parameter in $\mathbf{e_1}$ direction we obtain the set of laminar flamelet equations for a diffusion flame, which can be approximated by

$$\begin{aligned} \rho\frac{\partial Y_i}{\partial t} + \rho\frac{\chi}{2}\frac{\partial^2 Y_i}{\partial Z^2} &= M_i \sum_{k=1}^{M} \nu_{ik}\omega_k + \dots \\ \rho c_p\frac{\partial T}{\partial t} + \rho c_p\frac{\chi}{2}\frac{\partial^2 T}{\partial Z^2} &= \sum_{k=1}^{M} Q_k\omega_k + \dots \end{aligned} \tag{3.48}$$

where $\chi = 2D(\nabla Z \cdot \nabla Z)$ is the so-called scalar dissipation rate. Notice that $1/\chi$ is a characteristic diffusion time scale. The dots in the right-hand side indicate small transport terms along the iso-planes of Z. The solution of this system describes the internal flamelet structure.

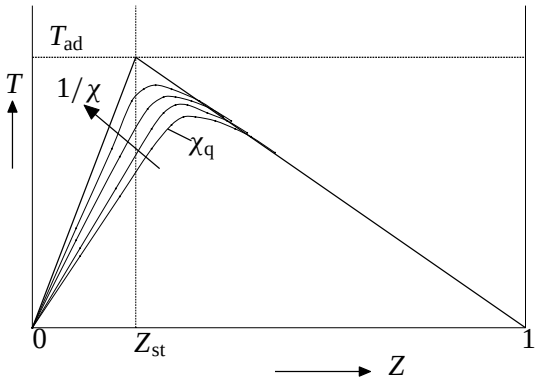

Figure 3.7: Solutions for $T(Z)$ at different values for χ; the Burke-Schumann limiting solution is indicated by $\chi \to \infty$.

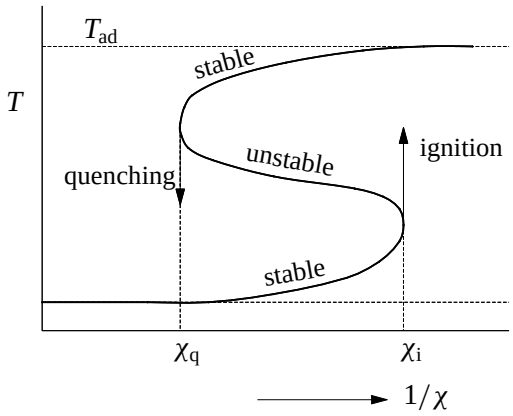

Figure 3.8: The S-curve for the flame temperature of a diffusion flame as function of the diffusive time scale $1/\chi$.

For stationary systems, the set of flamelet equations (3.48) does not depend on space $\mathbf{x} = (\mathbf{x}, \mathbf{y}, \mathbf{z})$ anymore but only on Z and χ. The solution of (3.48) can thus be written as $Y_i = Y_i(Z, \chi)$ and $T = T(Z, \chi)$. For given value of χ and boundary conditions for Y_i and T at the sides of the flamelet, the set (3.48) can be solved and stored as function of Z and χ in a flamelet data-base. $T(Z, \chi)$ is drawn schematically in figure 3.7. Notice that $T(Z)$ approaches the Burke-Schumann solution if $1/\chi \to \infty$. In that case, the charakteristic diffusion time scale goes to infinity and there is sufficient time for complete combustion, since the reaction time is small. The flame front is infinitely thin in this case and the scalar variables have discontinuous derivatives at the front position. For decreasing $1/\chi$, the diffusion time descreases and will become of the same order as the reaction time finally (see figure 3.8). Complete combustion can not be reached now and the flame temperature decreases. For a high value $\chi = \chi_q$ the flame even quenches. Notice that the S-curve indicates that there are two stable branches: a 'cold' branch, leading to ignition if $\chi = \chi_i$ and a 'hot' branch leading to quenching at $\chi = \chi_q$.

The question now remains how to use this flamelet model in CFD computations of non-premixed flames. This can be applied as follows. Flow and mixing above a burner in a non-premixed system can be computed using a CFD code solving the Navier-Stokes and mixture fraction equations, giving the solution for $\mathbf{v}$, ρ, p and Z. Chemistry does not play a role in this part. ¿From $Z(\mathbf{x})$ we can determine $\chi = 2D(\nabla Z \cdot \nabla Z)$ and $Y_i(Z, \chi)$ en $T(Z, \chi)$ can be evaluated subsequently from the flamelet database. From the temperature field it is possible to determine a new update of the density field $\rho(\mathbf{x})$, the viscosity and the transport coefficients, which influence the fluid flow on their turn. This problem can be solved iteratively.

In case of a gaseous diffusion flame, χ is very large near the burner, since the gradients in Z have very large values there and even go to infinity at the burner rim, where fuel and oxidizer meet. This means that the flame quenches near the burner, up to the point where $\chi = \chi_q$. Especially if the flow velocity is large, a large stand-off distance can be created in such a case. As fuel and oxidizer mix near the burner rim without burning, a premixed mixture is created above the burner rim. Thus at the stabilisation point we observe a premixed flame, propagating towards the burner rim. This premixed flame is stoichiometric near $Z = Z_{st}$, rich near the fuel feed and lean in the oxidizer feed. The stoichiometry thus changes along the premixed flame front, which quenches at the edges where the equivalence ratio approaches the flammability limits. The rich burnt gases near the fuel feed on

their turn mix with the lean burnt gases near the oxidizer feed, giving the diffusion flame near the stoichiometric mixture fraction plane $Z = Z_{st}$. We thus have a flame with a triple point at the ignition point, which is called a triple flame. Triple flames are frequently found also in turbulent flames, at points near quenching or ignition of the front.

References

[1] Bush, W. D. and Fendell, F. E.,*Combust. Sci. and Techn.* 1:421–428 (1970).

[2] Clavin, P., *Dynamic behavior of premixed flame fronts in laminar and turbulent flows*, Prog. Energy Combust. Sci. 11, pp. 1–59 (1985).

[3] Goey, L. P. H. de and Thije Boonkkamp, J. H. M. ten, A Mass-Based Definition of Flame Stretch for Flames with Finite Thickness, *Combust. Sci. and Techn.*, in press (1996).

[4] Joulin, G. and Clavin, P., *Combust. Flame*, 35, 139 (1979).

[5] Matalon, M., *Combust. Sci. and Techn.* 31:169–181 (1983).

[6] Peters, N., *ERCOFTAC summerschool on Laminar and Turbulent Combustion*, 1992.

[7] Williams, F. A., *Agard Conference Proceedings No. 164, p. II1.1–II1.15 (1975).*

[8] Williams, F. A., In *The Mathematics of Combustion*, (J. Buckmaster, Ed.), Society for Industrial and Applied Mathematics, Philidelphia, p. 97–131 (1985).

[9] Zeldovich, Y. B., Barenblatt, G. I., Librovich, V. I. and Makhviladze, G. M. *The Mathematical Theory of Combustion and Explosions*, Consultants Bureau, New York, 1985.

Chapter 4

Premixed Combustion Using Surface Radiant Burners

H. B. Levinsky

1 Introduction

Radiant surface burners are used in a wide variety of household and industrial combustion systems. Since they offer the possibility of enhancing radiative heat transfer and lowering NO_x emissions compared to conventional systems, these burners are finding utility in an ever- widening range of combustion situations. There are many incarnations of this type of burner, usually defined in terms of the characteristics of the burner material. Burners are made of porous ceramic foams, porous metal fiber, perforated ceramic tiles, and even perforated porous metal fiber. Whereas all these burners are superficially different, their principle mode of behavior is identical, and in this chapter we will focus on understanding the underlying physical processes responsible for this behavior.

2 Operating principle

The operating principle of radiant surface burners is simple. Recalling first the results from other lectures on flame structure, the solution of the governing equations under freely burning conditions is a combustion wave that propagates with the burning velocity s_L with respect to the unburned mixture. A balance between the velocity of flame propagation and the velocity of the fuel-air mixture leaving a given burner results in a flame that is stationary in the laboratory frame. If the exit velocity of the mixture is larger than burning velocity everywhere in the flow, the flame is pushed downstream from the burner exit and blows off (is no longer stabilized on the burner). If the burning velocity is larger than the exit velocity everywhere in the flow, then the flame will propagate upstream. If the openings in the burner, the burner 'ports', are larger than some minimum diameter (called the quenching distance, and is roughly equal to the thickness of the flame, see Lewis and von Elbe [1] for example), the flame will actually enter the burner. This phenomenon is known as flash back, and can cause damage to the burner, even leading to explosive situations. However, if the burner ports are very small, the flame cannot enter the burner, but rather will transfer heat upstream to the burner [2], lowering the flame temperature. Lowering the flame temperature in lean-premixed flames is responsible lowering the NO formation rate observed in practice. This description of the interaction between flame and burner is not confined to radiant burners; it was in fact originally conceived to explain the behavior of one-dimensional flames stabilized on a water-cooled sinter burner in the early 1950's [2]. In the original version, the heat transferred to the burner surface 'disappeared' into the cooling water; in a thermally insulated burner, the surface will heat up uniformly and radiate the heat to the surroundings. As we

shall see below, at a given exit velocity the heat transferred to the surface is independent of the surface temperature; thus, the flame structure will be the same, whether the burner is water cooled or hot and radiating. We point out here that this form of radiant surface combustion, relying on essentially one-dimensional 'upstream heat transfer', is distinct from *submerged* radiant combustion [3], in which the flame is located within an open porous structure; in that case, there is also substantial heat transfer to the burner *downstream* of the primary flame front. We will not consider this second type of radiant combustion here.

3 Simple expressions for heat-transfer properties [4]

If we assume that the behavior of the flame-burner system is essentially one dimensional, one could also assume that we could 'easily' model this system using the type of 1-D flame code discussed elsewhere in this course. We shall do so momentarily, but it is instructive to consider the heat transfer using more simple reasoning.

Let's first consider enthalpy conservation in the flame-burner system. Using subscripts 'u' and 'b' to denote the properties of the cold, fuel-air mixture and hot flame gases, respectively, and considering the radiation from the burner as the only heat-loss process, we can write

$$(\rho_0 u) H_\mathrm{u} = (\rho_0 u) H_\mathrm{b} + \epsilon \sigma T_\mathrm{surf}^4 \tag{4.1}$$

where $\rho_0 u$ the mass flow rate (ρ_0 the density and u the linear velocity of the cold mixture), H the specific enthalpy, ϵ the emissivity of the burner, σ the Stefan-Boltzmann constant and T_surf the temperature of the burner surface. Here we assume that the temperature of the surroundings is low enough to be neglected in equation (4.1), although its inclusion is straightforward. We rewrite equation (4.1) as

$$\epsilon \sigma T_\mathrm{surf}^4 = \rho_0 u (H_\mathrm{u} - H_\mathrm{b}) \tag{4.2}$$

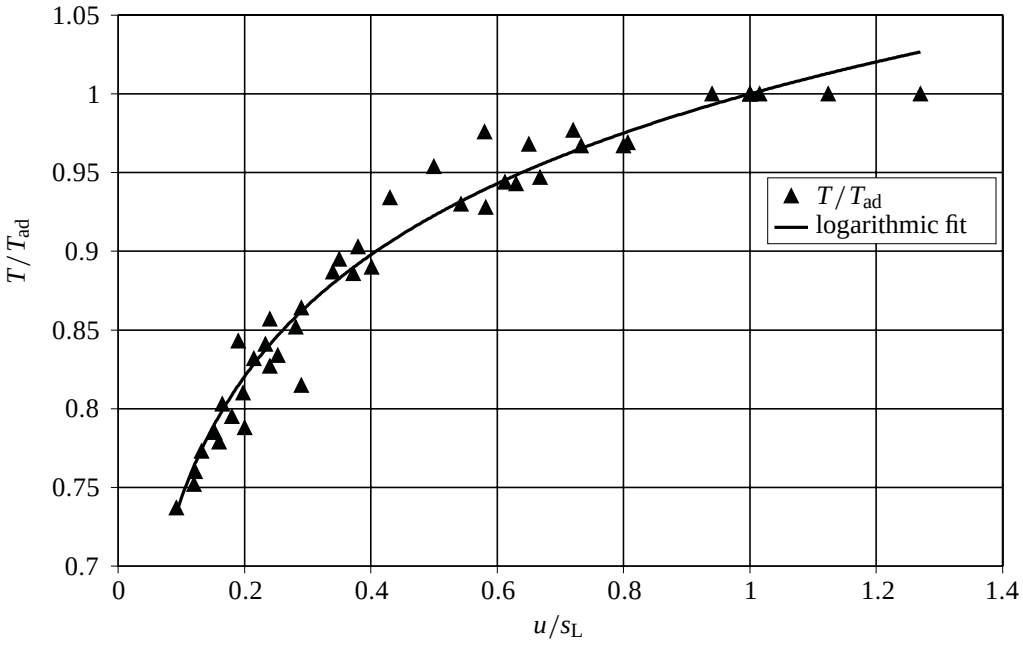

Figure 4.1: Relative temperature vs. relative velocity.

In other words, the burner radiates the heat lost from the flame. If we knew the relation between the enthalpy difference and exit velocity, we could predict the power radiated from the burner, $W_s = \epsilon\sigma T_{surf}^4$. Fortunately, from measurements of flame temperature versus exit velocity on a water-cooled sinter burner [5], we know a relationship between the exit velocity and the temperature of the hot gases. These data are replotted in figure 4.1, together with a logarithmic fit of the data, $T_b/T_{ad} = 1 + 0.1116\ln(u/s_L)$.

Making use of the average heat capacity, c_p, of the hot gases in the temperature region considered, $(H_u - H_b) = c_p(T_{ad} - T_b)$, equation (4.2) becomes

$$W_s = \epsilon\sigma T_{surf}^4 = \rho_0 u c_p (T_{ad} - T_b) \tag{4.3}$$

Note that the right-hand side of this equation only contains properties of the gases, and no properties of the burner; the radiated power is only a function of the exit velocity. Defining $X_u = u/s_L$, and substituting the expression for T_b/T_{ad}, we obtain

$$W_s = \epsilon\sigma T_{surf}^4 = -\rho_0 s_L c_p T_{ad} X_u 0.1116 \ln(X_u) \tag{4.4}$$

The radiated power and the radiant efficiency (dividing W_s by the calorific input of the fuel- air mixture) can now be easily calculated using readily available properties of the cold mixture; with the emissivity of the burner, we can also calculate the surface temperature. In figure 4.2 we compare the experimentally determined surface temperature of a ceramic foam burner [6] at equivalence ratio, $\phi = 0.9$ with that calculated through equation (4.4), using the reported emissivity [6]. The agreement in the region $u/s_L < 0.4$ is excellent (better than 20 K) and is within 50 K up to 0.6; the diverging results at higher u/s_L arise from the fact that flames tend to burn inhomogeneously on porous burners at high exit velocities, deviating from 1-D behavior. We point out here that this simple model with no adjustable parameters predicts the behavior of these burners as well as more sophisticated models [6, 7]. This lies in the accuracy of the fit used for the temperature correlation, which also

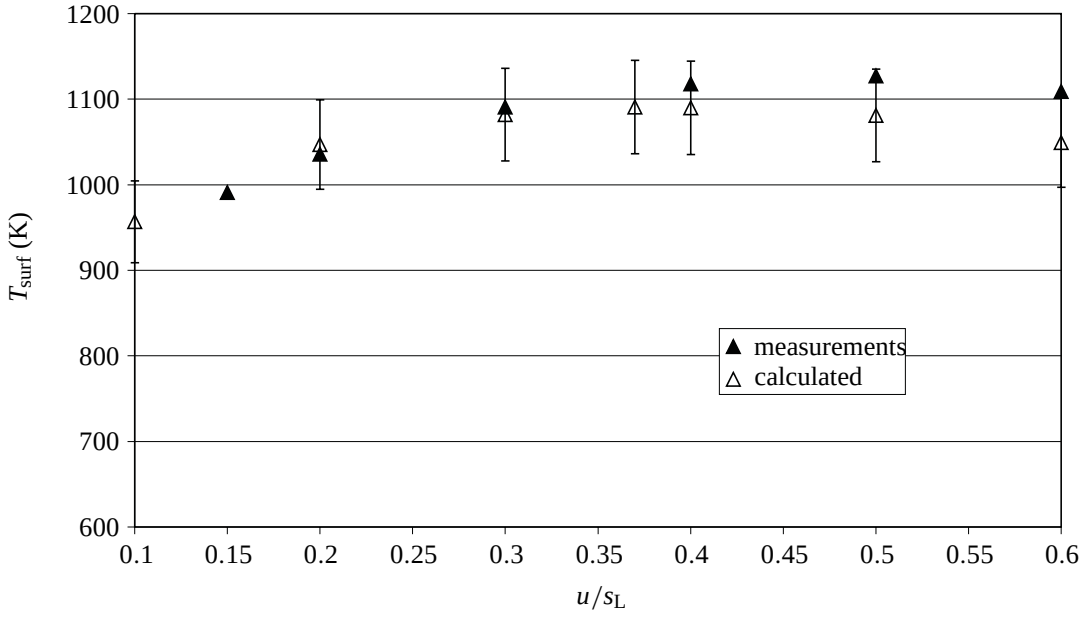

Figure 4.2: Comparison of calculated surface temperature with measurements; ceramic foam burner, $\phi = 0.9$, $\epsilon = 0.7$.

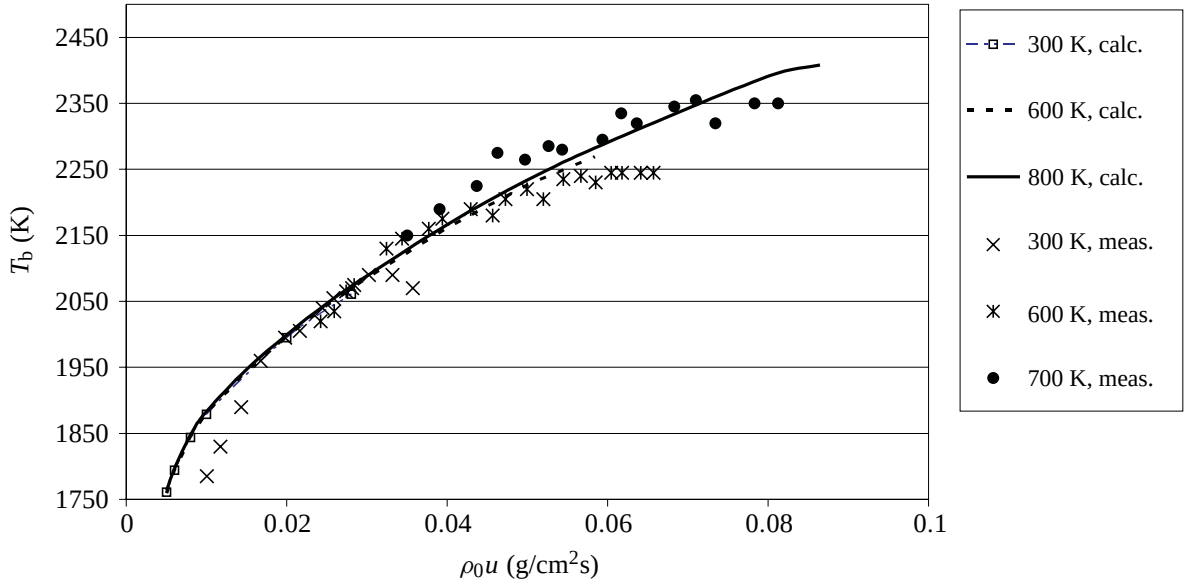

Figure 4.3: Temperature of methane/air flames as a function of mass flow rate, for different initial temperatures, $\phi = 1.3$.

determines the accuracy to which we can calculate the enthalpy transferred to the burner; the largest deviation in figure 4.1 is on the order of 5%. For practical design engineers, the use of equation (4.4) to derive the heat-transfer properties of a radiant burner is thus simple and accurate.

We remind the reader here that the data used for the calculated results are derived from a water-cooled burner. This result, taken together with the fact [8] that at identical equivalence ratios and exit velocities a water-cooled sinter burner and a radiating perforated ceramic tile yield identical temperatures, lends strong support to the simple 1-D description of the flame-burner interaction described above. The radiant efficiency of this type of burner, calculated using the heat of combustion for the calorific value of the fuel, is limited to roughly 30% [6, 7]. Since preheating is a way to increase the enthalpy of the fuel-air mixture, for example using process 'waste heat', it is interesting to see what effects preheating have on the behavior of the radiant burner.

4 Effects of preheating

The variation in measured flame temperature with exit velocity as a function of preheating is shown in figure 4.3 for $\phi = 1.3$; for reasons which shall become apparent, the exit velocity is expressed as mass flow rate. We first note that when plotted in figure 4.1, the scaled data are in excellent agreement with the correlation obtained for room-temperature reactants (with the exception of the lowest velocities, see below). For practical use, this means that equation (4.4) can also be used to derive all the heat-transfer characteristics of radiant burners.

Doing so, we calculate the radiative power using equation (4.4) for different degrees of preheating (none, 350 K and 730 K) for a stoichiometric flame in figure 4.4. Here we see a significant increase in radiative power. The effect on radiant efficiency is readily calculated, and we see that preheating to 730 K can nearly double the radiant efficiency. Of course, we must consider the material properties of the burner when thinking about preheating; even for a reasonably high emissivity, at 730 K preheating the burner surface can reach temperatures above 1800 K, too high for most materials.

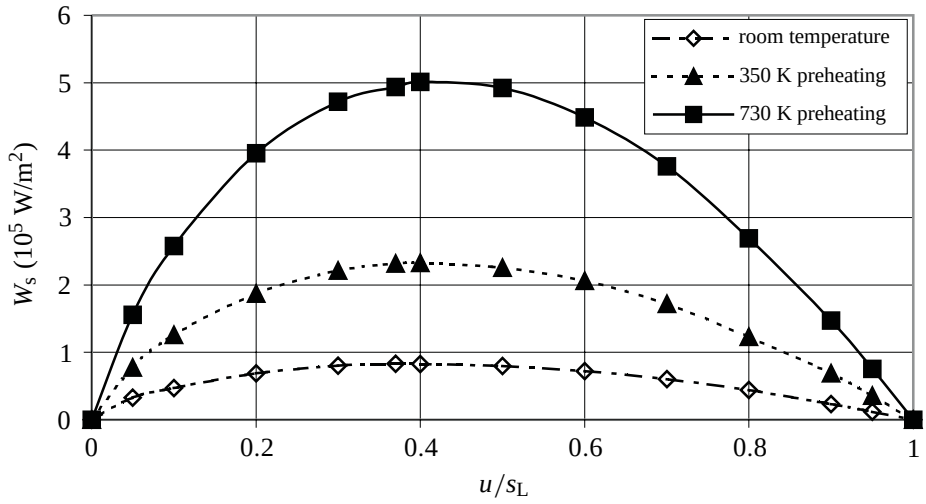

Figure 4.4: Maximun radiative power vs. v/s_L, preheating, $\phi = 1$.

That the relation between exit velocity and flame temperature is also relevant for preheating is satisfying, but is rather overshadowed by the observation that within experimental error all the curves in figure 4.3 coincide (in this figure, we present only three of the 20 experimental curves obtained, so as not to clutter the figure). It appears that at constant mass flow rate the flame temperature is independent of the degree of preheating: when $u < s_L$, any additional enthalpy from preheating is transferred to the burner. The deviation of each individual curve from the rest at higher flow rate is due to the fact that the flames become adiabatic when $u = s_L$; above this value, the flames are no longer one dimensional, but still adiabatic. With an eye towards further analysis, we have also included the simulated results using CHEMKIN and GRI-Mech 3.0 (see elsewhere in this course). Here too, we see excellent agreement with the measurements. The deviation at low flow rates is due to a small degree of mixing with the surrounding air, artificially lowering the local temperature in the flame on the ceramic burner (integrating a shroud ring similar to that used in the water-cooled sinter burner brings the results in perfect agreement with the calculations).

The question arises as to why a constant mass flow rate should result in identical temperatures. Consideration of the governing equations yields the following argument. The solution of these equations is completely determined by the initial conditions: mole fractions of the reactants, temperature of the 'cold' fuel-air mixture, and mass flow rate of the mixture. At a mixture temperature of T_0, at fixed ϕ, and $\rho_0 u$, the temperature profile is given by $T(x)$. Increasing the temperature to T_1, at the same conditions of ϕ and $\rho_0 u$, must result in the same temperature profile, but starting at T_1; in other words, increasing the temperature of the mixture only shifts $T(x)$ towards the origin, and must result in the same final temperature. This will be true as long as $T_1 < T_b$, the temperature at which significant chemical reaction can occur; interaction with the burner at $x = 0$ could then significantly alter the initial composition. Preheating of the mixture to 800 K does not achieve this, which in fact the constancy of the experimental data indicates. Thus, although somewhat counter-intuitive (or even fortuitous) when thinking in terms of the details of flame-burner interactions, the constancy of the flame temperature at constant ϕ and $\rho_0 u$ is 'simply' a necessary consequence of the governing equations.

Having concluded this, we remark further that when comparing flame temperatures at as a function of $\rho_0 u$, curves obtained at different equivalence ratios between 1.0 and 1.5 are also nearly identical (to within 50 K). When thinking qualitatively in terms of the effects of equivalence ratio and initial temperature on combustion properties, it is usually the burning velocity that varies most, whereas this

is the parameter being held constant in our discussion. Apparently, the changing the fuel concentration by a few percent is insufficient to bring about large changes in the temperature profile.

5 An important practical consideration

In the above, we have shown that simple one-dimensional considerations are more than adequate to describe most aspects of radiant burner behavior, even quantitatively. However, translation to practice requires a certain degree of care. A trivial aspect is that when the pressure drop across a burner surface is inhomogeneous (for example, due to inhomogeneities in porosity), the one-dimensional approximation will not be valid macroscopically. However, if one were to divide up the surface in homogeneous areas with known mass flux, the one- dimensional solutions can be used to average over the surface.

A more serious problem has to do with heat transfer through the burner. If the material is a good conductor of heat, it is possible that the upstream ('cold') side of the burner attains a temperature so high that the fuel-air mixture will ignite. This gives the same result as flash back. In ceramic burners, and particularly the foams, even when the material is a poor conductor of heat, if the 'pores' of the burner are too open, the flame can flash back. In this case the hot ceramic can transfer heat radiatively upstream through the burner. The hot ceramic can then preheat the fuel-air mixture, increasing the burning velocity and reducing the flame thickness. The net result of this process is that the flame will slowly creep through the burner, and ultimately flash back. More details of these processes can be found in refs. 6–8.

References

[1] B. Lewis and G. von Elbe, *Combustions, Flames and Explosions of Gases*, 3rd Edition, Academic Press, 1987.

[2] Botha, J.P. and Spaulding, D.B., Proc. R. Soc. London, Ser. A 225:71–96 (1954).

[3] Rumminger, M.D., Dibble, R.W., Heberle, N.H., and Crosley, D.R., Proc. Combust. Inst. 26:1755–1762 (1996).

[4] A. Sepman, G. Tiekstra, A.V. Mokhov and H.B. Levinsky, Proceedings of the Second Joint Meeting of the U.S. Sections of the Combustion Institute, The Combustion Institute, Pittsburgh, 2001, Paper 279.

[5] Mokhov, A.V. and Levinsky, H.B., Proc. Combust. Inst. 26:2147–2154 (1996).

[6] Bouma, P.H. and De Goey, L.P.H., Combust. Flame 119:133–143 (1999).

[7] Rumminger, M.D.,Hamlin, R.D., Dibble, R.W., Gas Research Institute report GRI-97/0182 (1997).

[8] B. Lammers, Ph.D. Thesis, Eindhoven University of Technology, 2001.

Chapter 5

Numerical Modelling of Laminar Flames: a Concise Introduction

J. H. M. ten Thije Boonkkamp

1 A Mathematical Model for Laminar Flames

In this section we present a mathematical model for laminar flames. We give a summary of available numerical methods and briefly address the difficulties associated with the numerical simulation of laminar flames.

The governing equations of a laminar flame are the conservation equations of mass, momentum and energy of the gas mixture and the balance equations of mass for the N_s species involved. These equations read [24]:

$$\begin{aligned} \frac{\partial \rho}{\partial t} + \nabla \cdot (\rho \mathbf{v}) &= 0, \\ \frac{\partial}{\partial t}(\rho \mathbf{v}) + \nabla \cdot (\rho \mathbf{v}\mathbf{v}) &= -\nabla p + \nabla \cdot \boldsymbol{\mathcal{T}} + \rho \mathbf{g}, \\ \frac{\partial}{\partial t}(\rho h) + \nabla \cdot (\rho \mathbf{v} h) &= -\nabla \cdot \mathbf{q}, \\ \frac{\partial}{\partial t}(\rho Y_i) + \nabla \cdot (\rho \mathbf{v} Y_i) + \nabla \cdot (\rho Y_i \mathbf{V}_i) &= w_i, \quad (i = 1, 2, \ldots, N_s - 1). \end{aligned} \tag{5.1}$$

The dependent variables in these equations are the density ρ, flow velocity $\mathbf{v}$, pressure p, specific enthalpy h, temperature T and species mass fractions Y_i. Other variables in (5.1) are the viscous stress tensor $\boldsymbol{\mathcal{T}}$, gravitational acceleration $\mathbf{g}$, heat flux vector $\mathbf{q}$, diffusion velocities $\mathbf{V}_i$ and reaction rates w_i. The first two equations in (5.1) are referred to as the flow equations and the latter two as combustion equations. Appropriate initial and boundary conditions for (5.1) have to be specified. Moreover, the conservation equations (5.1) have to be completed with the caloric equation of state

$$h = \sum_{i=1}^{N_s} Y_i h_i, \quad h_i := h_i^0 + \int_{T_0}^{T} c_{p,i}(\vartheta)\, \mathrm{d}\vartheta, \tag{5.2}$$

which defines h as a function of the temperature T and the species mass fractions Y_i, and the thermal equation of state

$$p_0 = \frac{\rho R T}{M}, \quad \frac{1}{M} := \sum_{i=1}^{N_s} \frac{Y_i}{M_i}. \tag{5.3}$$

In equation (5.2), h_i, h_i^0 and $c_{p,i}$ are the specific enthalpy, specific enthalpy of formation at reference temperature T_0 and specific heat at constant pressure of species i, respectively. In (5.3), R is the

universal gas constant, M the average molar mass of the gas mixture and M_i the molar mass of species i. The pressure p is set to a constant value p_0 in (5.3), which is a valid approximation for low Mach number flow [7].

Models for $\boldsymbol{\mathcal{T}}$, $\mathbf{q}$, $\mathbf{V}_i$ and w_i are required. The gas mixture in a laminar flame behaves like a Newtonian fluid and therefore the viscous stress tensor $\boldsymbol{\mathcal{T}} = (\tau_{k,l})$ is given by

$$\tau_{k,l} = \mu \left(\frac{\partial v_k}{\partial x_l} + \frac{\partial v_l}{\partial x_k} - \tfrac{2}{3}(\nabla \cdot \mathbf{v})\delta_{k,l} \right), \tag{5.4}$$

where μ is the viscosity coefficient of the mixture. An often employed model for the diffusion velocities $\mathbf{V}_i$ is the so-called generalized law of Fick [17], i.e.

$$Y_i \mathbf{V}_i = -D_{i,m} \nabla Y_i, \quad (i = 1, 2, \ldots, N_s - 1), \tag{5.5}$$

where $D_{i,m}$ is the mixture-averaged diffusion coefficient, describing the diffusivity of species i in the mixture. Relation (5.5) holds for trace species. Moreover, the diffusion velocity of the abundant species, numbered N_s, follows from the constraint

$$\sum_{i=1}^{N_s} Y_i \mathbf{V}_i = \mathbf{0}. \tag{5.6}$$

For the heat flux we use the common expression [24]

$$\mathbf{q} = -\lambda \nabla T + \rho \sum_{i=1}^{N_s} h_i Y_i \mathbf{V}_i, \tag{5.7}$$

where λ is the thermal conductivity. This expression for $\mathbf{q}$ only takes into account enthalpy transport through conduction and mass diffusion. Models for the reaction rates w_i are reported in literature; see e.g. [23].

Using (5.3), we can express the density ρ as a function of the combustion variables T and Y_i. Inserting this function into the continuity equation and combining the resulting equation with the combustion equations, we find the constraint

$$\nabla \cdot \mathbf{v} = S, \tag{5.8}$$

where S describes expansion of the gas mixture due to conduction, diffusion and heat production. Equation (5.8) is called the expansion equation and is used in Section 4 to derive a method for the pressure computation.

The numerical simulation of the above mathematical model generally involves the following steps:

1. space discretization
2. time integration
3. solution of algebraic systems
4. post processing.

In the space discretization step, we cover the domain with a grid and approximate all spatial derivatives on this grid somehow. There are various classes of methods available, the most important of which are the finite element methods (FEM), finite difference methods (FDM) and finite volume methods

(FVM). All these methods are frequently used in combustion theory and each method has its merits and drawbacks. We will not consider FEM; for an introductory text see e.g. [3]. For time dependent problems, we get after space discretization a set of ordinary differential equations, referred to as discrete conservation laws. The next step is then to integrate these equations. The main issue here is stability of the time integration technique. Next we have to solve the resulting nonlinear system. The most frequently used method for this is Newton iteration with all its variants. Furthermore, Newton iteration requires the solution of large linear systems. There is a host of methods available for the numerical solution of linear systems. Which method should be used depends on the properties of the linear system involved. The last step in the numerical simulation procedure is post processing of all data to make plots or movies of a flame. We will not discuss this topic.

Special attention should be given to the computation of the pressure. Unlike all other variables, the pressure p does not satisfy a convection-diffusion-reaction equation, it only occurs as a source term in the momentum equations. Moreover, it can not be computed from an equation of state, as is the case for compressible flows. This makes that the pressure only occurs implicitly in the discrete system. A class of methods to compute the pressure are the so-called pressure correction methods (PCM). In a PCM, the pressure computation is decoupled from the velocity computation in a predictor-corrector fashion. For incompressible flows, these methods are well established; see e.g. [9]. However, for combustion problems these methods are more difficult to apply and a lot of problems still have to be solved.

The above mathematical model for laminar flames has the following characteristics which makes it difficult to solve numerically. First, the conservation laws (5.1) are nonlinear partial differential equations of convection-diffusion-reaction type. Complex flows are possible and the chemical source terms are often extremely nonlinear. Consequently, Newton iteration has to be modified in order to converge at all. Second, the number of species and chemical reactions is often large, which make numerical simulation prohibitively expensive. To circumvent this problem, reduction techniques are often applied; see e.g. [16]. Third, a laminar flame has quite different time and length scales. As an example, figure 5.1 shows the mass fractions of some species and the temperature of a flat methane/air flame. In this figure, we can distinguish the burnt and unburnt gases, where the solution is virtually constant, and a very narrow region, the so-called flame front, where the actual combustion occurs and where all variables rapidly change. It is intuitively clear that inside the flame front much more grid points are required than in the (un)burnt gases, to get an accurate representation of the solution.

We have organized the remainder of this paper as follows. In Section 2 we discuss FVM and FDM for space discretization of the conservation equations (5.1). Time integration of the resulting discrete conservation equations is the topic of Section 3. In Section 4, we briefly address a PCM for the computation of the pressure. Finally, in Section 5, we discuss solution methods for (non)linear algebraic systems.

2 Space Discretization

We discuss in this section FVM and FDM for space discretisation of the conservation laws (5.1) and the expansion equation (5.8). Special attention should be given to the momentum equations.

All conservation laws in (5.1) can be written in the generic form

$$\frac{\partial}{\partial t}(\rho\phi) + \nabla \cdot \mathbf{f} = s, \quad \mathbf{f} := \rho\mathbf{v}\phi - \Gamma\nabla\phi, \tag{5.9}$$

for some variable ϕ, where $\mathbf{f}$ is the flux and s a source term. Finite volume methods are based on the

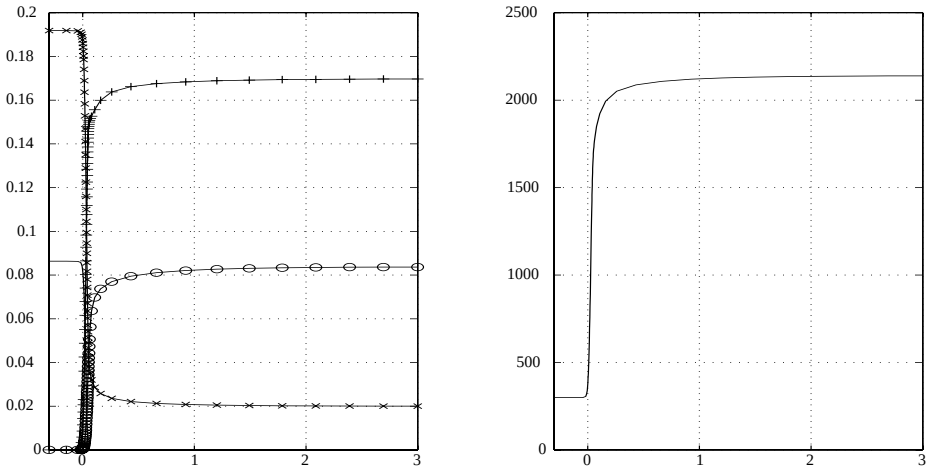

Figure 5.1: Mass fractions of major species (left) and temperature (right) of a one-dimensional methane/air flame.

integral form of the conservation law in (5.9), i.e.

$$\frac{\mathrm{d}}{\mathrm{d}t}\int_V \rho\phi \,\mathrm{d}\tau + \oint_{\partial V} \mathbf{f}\cdot\mathbf{n}\,\mathrm{d}\sigma = \int_V s\,\mathrm{d}\tau, \tag{5.10}$$

which holds for an arbitrary subvolume V with boundary ∂V and unit outer normal $\mathbf{n}$. In fact, equation (5.10) is the most fundamental conservation law, which reduces to the partial differential equation in (5.9), provided the variable ϕ is smooth enough.

In finite volume methods, the whole domain is covered with a grid consisting of a finite number of control volumes and the integral form (5.10) is applied to each of these control volumes. For the sake of simplicity, we restrict ourselves to a two-dimensional, rectangular and uniform grid. A patch of such a grid is shown in figure 5.2. We see that the grid nodes are located at the centres of the control volumes. Applying the integral form (5.10) to the control volume V_C corresponding to the central point C and approximating all integrals involved by the midpoint rule [6], we find the discrete conservation law

$$\frac{\mathrm{d}}{\mathrm{d}t}(\rho\phi)_\mathrm{C} + \frac{1}{\Delta x}\left(F_\mathrm{e} - F_\mathrm{w}\right) + \frac{1}{\Delta y}\left(G_\mathrm{n} - G_\mathrm{s}\right) = s_\mathrm{C}. \tag{5.11}$$

In (5.11), $(\rho\phi)_\mathrm{C}$ denotes the approximation of $\rho\phi$ at grid point C and F_e denotes the approximation of the x-component $f = \rho u\phi - \Gamma\frac{\partial\phi}{\partial x}$ of the flux at the centre of the eastern cell face e, etc. The finite volume method has to be completed with the computation of the numerical fluxes F_e, G_n, etc.

A numerical flux should satisfy the following three requirements. First, it should be second order accurate for both diffusion dominated as well as convection dominated problems, since the corresponding discrete conservation law (5.11) is also second order accurate in Δx and Δy. Second, the resulting scheme may not cause unphysical oscillations in the numerical solution and, third, the scheme may only have a three-point coupling in each spatial direction.

Numerical fluxes are usually computed with a FDM. Consider the computation of the numerical flux F_e. There are several possibilities for its computation. A first obvious possibility is the central difference approximation, given by

$$F_\mathrm{e} = \tfrac{1}{2}(\rho u)_\mathrm{e}\left(\phi_\mathrm{C} + \phi_\mathrm{E}\right) - \frac{\Gamma_\mathrm{e}}{\Delta x}\left(\phi_\mathrm{E} - \phi_\mathrm{C}\right). \tag{5.12}$$

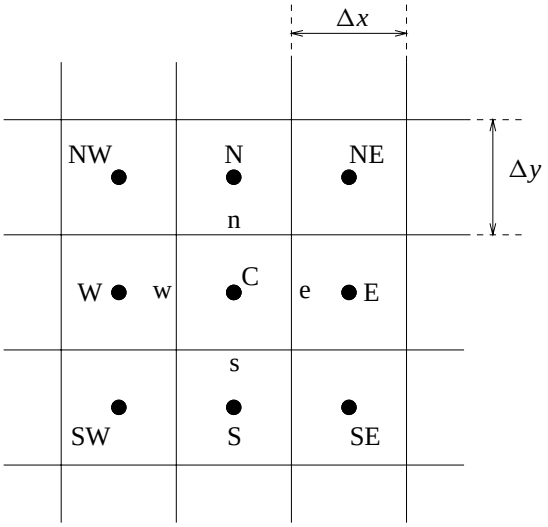

Figure 5.2: Patch of a finite volume grid with position names.

This approximation is second order accurate, however, it produces unphysical oscillations when convection is dominant; see e.g. [8]. A remedy to this shortcoming is the upwind numerical flux

$$F_\mathrm{e} = \rho_\mathrm{e}\left(\max(u_\mathrm{e},0)\phi_\mathrm{C} + \min(u_\mathrm{e},0)\phi_\mathrm{E}\right) - \frac{\Gamma_\mathrm{e}}{\Delta x}\left(\phi_\mathrm{E} - \phi_\mathrm{C}\right). \tag{5.13}$$

This flux is based on a one-sided difference approximation of the convective term and consequently, it is only first order accurate. There exist higher order upwind approximations of the flux, see e.g. [14, 15], however the resulting schemes have more than a three-point coupling in each spatial dimension. Another possibility is the exponential flux approximation due to Patankar [18]. In this case, the numerical flux is computed from a local, one-dimensional conservation law without source term. This way we find

$$F_\mathrm{e} = \mathcal{F}\left(\frac{\Gamma_\mathrm{e}}{\Delta x}, P_\mathrm{e}; \phi_\mathrm{C}, \phi_\mathrm{E}\right) := -\frac{\Gamma_\mathrm{e}}{\Delta x}\left(B(P_\mathrm{e})\phi_\mathrm{E} - B(-P_\mathrm{e})\phi_\mathrm{C}\right), \tag{5.14}$$

where $B(z) := z/(\mathrm{e}^z - 1)$ is the Bernoulli function and $P_\mathrm{e} := (\rho u)_\mathrm{e}\Delta x/\,\Gamma_\mathrm{e}$ the local Peclet number. In fact, the resulting exponential scheme is a combination of the central difference and the upwind schemes. For $P_\mathrm{e} = 0$ it is identical with the central difference scheme and for $|P_\mathrm{e}| \to \infty$ it reduces to the first order upwind scheme. A nice generalization of the exponential flux approximation is by van 't Hof et al. [11]. In this case the numerical flux is computed from a local one-dimensional conservation law including the source term. The result is

$$F_\mathrm{e} = \mathcal{F}\left(\frac{P_{\lambda,\mathrm{e}}}{P_\mathrm{e}}\frac{\Gamma_{\lambda,\mathrm{e}}}{\Delta x}, P_\mathrm{e}; \phi_\mathrm{C}, \phi_\mathrm{E}\right) + \left(\tfrac{1}{2} - W(P_\mathrm{e})\right)\Delta x s_\mathrm{C}, \tag{5.15}$$

where $W(z) := (\mathrm{e}^z - 1 - z)/(z(\mathrm{e}^z - 1))$ is a weight function and $v_{\lambda,\mathrm{e}} := W(-P_\mathrm{e})v_\mathrm{C} + W(P_\mathrm{e})v_\mathrm{E}$ ($v = P, \Gamma$) a weighted average of the variable v. A further advancement, taking into account the cross flux term $\frac{1}{\Delta y}(G_\mathrm{n} - G_\mathrm{s})$, is also possible; for more details see [11]. The resulting scheme is second order accurate, even for convection dominated flows, and does not generate unphysical oscillations.

Special attention should be given to the momentum equations. Consider e.g. the momentum equation for the velocity component u in x-direction, for which $s = -\frac{\partial p}{\partial x}$, i.e. the pressure gradient is a source term driving the flow. Omitting for simplicity the viscous terms, the discrete conservation law (5.11) changes to

$$\frac{\mathrm{d}}{\mathrm{d}t}(\rho u)_\mathrm{C} + \frac{1}{\Delta x}\left(\left(\rho u^2\right)_\mathrm{e} - \left(\rho u^2\right)_\mathrm{w}\right) + \frac{1}{\Delta y}\left((\rho uv)_\mathrm{n} - (\rho uv)_\mathrm{s}\right) = -\frac{1}{\Delta x}\left(p_\mathrm{e} - p_\mathrm{w}\right). \tag{5.16}$$

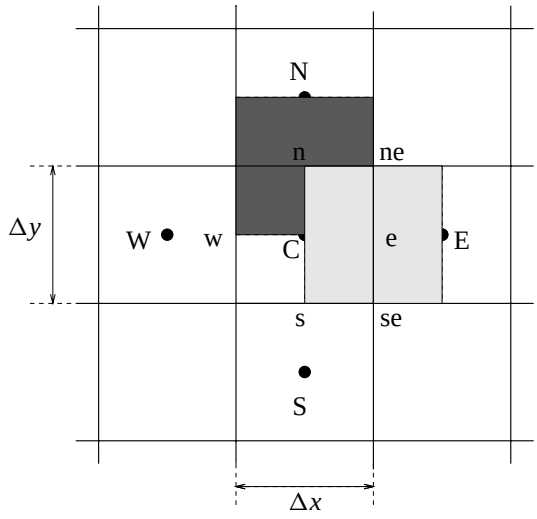

Figure 5.3: Patch of a staggered grid with control volumes for u_{e} and v_{n}.

Assume that the left hand side of this equation is known. Since the pressure p_{e} at the eastern cell boundary is unknown, we have to interpolate it from adjacent grid values, i.e. $p_{\mathrm{e}} = \frac{1}{2}(p_{\mathrm{C}} + p_{\mathrm{E}})$; and likewise $p_{\mathrm{w}} = \frac{1}{2}(p_{\mathrm{W}} + p_{\mathrm{C}})$. Substituting these relations into the right-hand side of (5.16), we obtain

$$-\frac{1}{\Delta x}\,(p_{\mathrm{e}} - p_{\mathrm{w}}) = -\frac{1}{2\Delta x}\,(p_{\mathrm{E}} - p_{\mathrm{W}})\,. \tag{5.17}$$

We see that there is no direct connection between neighbouring values of p and the consequence of this is a decoupling of the pressure field. To be more precise, if $p_{i,j}(t)$ denotes the numerical approximation of the pressure in gridpoint $\mathbf{x}_{\mathrm{C}} = (x_i, y_j)$ at time t, then it is clear that also $\widetilde{p}_{i,j}(t) := p_{i,j}(t) + P(t)(-1)^i$, for an arbitrary function $P(t)$, satisfies relation (5.17). Ignoring any boundary conditions, also $\widetilde{p}_{i,j}(t)$ is a solution of the discrete x-momentum equation (5.16) and we say that the grid function $(-1)^i$ is a spurious mode of the numerical pressure. Also taking into account the y-momentum equation, we conclude that the numerical pressure has the follwing three spurious modes: $(-1)^i$, $(-1)^j$ and $(-1)^{i+j}$. These modes are of course not physical and should be avoided.

A way to avoid spurious pressure modes is to use a staggered grid. In a staggered grid, the control volumes for u and v are displaced as shown in figure 5.3. Consider again the x-momentum equation. If the viscosity coefficient μ is constant, it can be written in the standard form (5.9), with the flux $\mathbf{f}$ and source term s given by

$$\begin{aligned} &\mathbf{f} = \rho\mathbf{v}u - \mu\nabla u, \\ &s = -\frac{\partial q}{\partial x}, \quad q := p - \tfrac{1}{3}\mu\nabla\cdot\mathbf{v}. \end{aligned} \tag{5.18}$$

Taking into account that $\frac{\partial q}{\partial x} = \nabla\cdot(q\mathbf{e}_x)$, we find the corresponding integral conservation law

$$\frac{\mathrm{d}}{\mathrm{d}t}\int_V \rho u\,\mathrm{d}\tau + \oint_{\partial V}\mathbf{f}\cdot\mathbf{n}\,\mathrm{d}\sigma = -\oint_{\partial V} q n_x\,\mathrm{d}\sigma, \tag{5.19}$$

with $n_x = \mathbf{n}\cdot\mathbf{e}_x$ the x-component of the unit outer normal on ∂V. Applying this integral form to the control volume V_{e} corresponding to u_{e} and approximating all integrals involved by the midpoint rule,

we find

$$\frac{\mathrm{d}}{\mathrm{d}t}(\rho u)_{\mathrm{e}} + \frac{1}{\Delta x}\,(F_{\mathrm{E}} - F_{\mathrm{C}}) + \frac{1}{\Delta y}\,(G_{\mathrm{ne}} - G_{\mathrm{se}}) = \\ - \frac{1}{\Delta x}\,(p_{\mathrm{E}} - p_{\mathrm{C}}) + \frac{\mu}{3\Delta x}\big((\nabla\cdot\mathbf{v})_{\mathrm{E}} - (\nabla\cdot\mathbf{v})_{\mathrm{C}}\big), \quad (5.20)$$

where F_{E} denotes the approximation of the x-component of the flux $f = \rho u^2 - \mu\frac{\partial u}{\partial x}$ at the eastern cell face E, etc.; see figure 5.3. Note that equation (5.20) contains the pressure values p_{C} and p_{E} at adjacent grid points, thus excluding spurious modes in the numerical pressure. Furthermore, in the staggered grid, the arrangement of grid points is such that locations for all fluxes are located precisely halfway between grid points for the corresponding variables. Consequently, we can apply all previously mentioned flux approximations, without using any interpolations.

The discretisation of the expansion equation (5.8) is based on the integral form

$$\oint_{\partial V} \mathbf{v}\cdot\mathbf{n}\,\mathrm{d}\sigma = \int_V S\,\mathrm{d}\tau, \quad (5.21)$$

applied to the control volume V_{C}; see figure 5.2. Approximating the integrals in (5.21) by the midpoint rule, we find

$$\frac{1}{\Delta x}(u_{\mathrm{e}} - u_{\mathrm{w}}) + \frac{1}{\Delta y}(v_{\mathrm{n}} - v_{\mathrm{s}}) = S_{\mathrm{C}}, \quad (5.22)$$

where $S_{\mathrm{C}} = S(\mathbf{x}_{\mathrm{C}})$, u_{e} is the numerical approximation of the velocity component u at the eastern cell face, etc. Note that u_{e} can be interpreted as a flux with $\rho\phi = 1$ and $\Gamma = 0$.

The space discretization procedure has to be completed with the implementation of the boundary conditions. Usually, ϕ satisfies either a Dirichlet boundary condition

$$\phi = \psi, \quad (5.23)$$

or a Neumann boundary condition

$$\frac{\partial\phi}{\partial n} = \psi. \quad (5.24)$$

As an example, we consider the control volume V_{C} adjacent to the boundary, as shown in figure 5.4. Since there is no grid point on the boundary, we introduce a virtual grid point as indicated in the figure. Using linear interpolation, we can easily show that the Dirichlet boundary condition (5.23) gives

$$\tfrac{1}{2}\,(\phi_{\mathrm{C}} + \phi_V) = \psi(\mathbf{x}_{\mathrm{e}}). \quad (5.25)$$

Likewise, the Neumann boundary condition (5.24) is approximated by

$$\frac{1}{\Delta x}\,(\phi_V - \phi_{\mathrm{C}}) = \psi(\mathbf{x}_{\mathrm{e}}). \quad (5.26)$$

These relations can then be used to elimate ϕ_V from the discrete conservation laws.

All codes for the numerical simulation of laminar flames have the possibility to adaptively refine the grid in the vicinity of the flame front. The general approach is to subequidistribute some weight function W, which is a measure for the smoothness of the solution, on the grid, i.e.

$$\int_C W\,\mathrm{d}\tau \le eps, \quad (5.27)$$

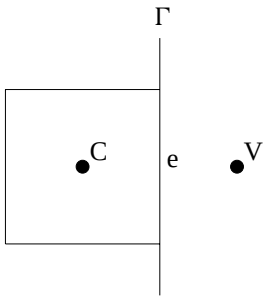

Figure 5.4: Control volume adjacent to a boundary.

where C are appropriately chosen grid cells and *eps* is a user specified constant. Based on such a subequidistribution, grid cells are refined. There are several refining techniques, resulting in truly unstructed grids or locally uniform grids. An example of the first refinement strategy is the Local Rectangular Refinement method by Bennett and Smooke [4, 5] and an example of the latter is the Local Defect Correction method by Anthonissen [1]. For more details, the reader is referred to these publications

3 Time Integration

After space discretization of the conservation laws in (5.1), we obtain a set of ordinary differential equations, which has to be integrated in time. For a comprehensive survey on integration methods for ordinary differential equations, see e.g. [10]. Key issue in the choice of a time integrator is stability of the method. For this reason, we have to restrict ourselves to implicit time integration methods.

Time scales in a laminar flame range typically from 10^{-9} s, for the very fast processes, to 10^2 s, for the slowest processes, which makes the system of differential equations very stiff [16]. If we want to simulate all the temporal details, we have to choose a time step compatible with the fastest time scales and we might then use an explicit method. This would require an extremely large number of time steps making numerical simulation not feasible. In practical flame simulation, we typically want to resolve time scales $\Delta\tau$ of approximately 1 ms, resulting in a few thousand time steps at most. In such a simulation we can resolve all processes (flow, transport etc.) except the fastest reactions.

To demonstrate that we have to use implict time integration methods, we consider the following standard equation

$$\frac{\partial \phi}{\partial t} = \Gamma \frac{\partial^2 \phi}{\partial x^2}, \tag{5.28}$$

modelling conduction and diffusion in a flame. If we discretize this equation, using the central difference approximation for the second derivative and the explicit Euler method for time integration, we obtain the scheme

$$\frac{1}{\Delta t}\left(\phi_j^{n+1} - \phi_j^n\right) = \frac{\Gamma}{\Delta x^2}\left(\phi_{j+1}^n - 2\phi_j^n + \phi_{j-1}^n\right), \tag{5.29}$$

with Δx the grid size, Δt the time step and ϕ_j^n the numerical approximation of $\phi(x_j, t_n)$. To investigate stability of this scheme, we substitute the Fourier mode

$$\phi_j^n = \lambda^n \mathrm{e}^{\mathrm{i}kx_j}, \tag{5.30}$$

with λ the amplification factor and k the wave number. Ignoring initial and boundary conditions, the Fourier mode (5.30) is a solution of (5.29), if λ is given by

$$\lambda = 1 - 4d \sin^2\left(\tfrac{1}{2}\xi\right), \quad \xi := k\Delta x, \tag{5.31}$$

with $d := \Gamma \Delta t / \Delta x^2$. Stability of scheme (5.29) means that (rounding) errors remain bounded during time integration, and a necessary condition for this is that $|\lambda| \leq 1$ for $0 \leq \xi < \pi$. This stability condition leads to the time step restriction

$$\Delta t \leq \frac{\Delta x^2}{2\Gamma}. \tag{5.32}$$

In practice, time step restriction (5.32) is often also a sufficient condition for stability. For a typical gas flame, we need a minimum grid size $\Delta x = 10^{-6}$ m to resolve the reaction layer and we have $\Gamma = 3$ m^2/s for hydrogen radicals. Combining these data with the time step restriction in (5.32), we find a maximum time step

$$\Delta t_{\max} \approx 10^{-13}\text{s} = 10^{-10}\Delta\tau. \tag{5.33}$$

Consequently, we have to choose our time step Δt very much smaller than the desired time scale $\Delta\tau$, because of stability. On the other hand, if we apply the implicit Euler method for time integration, we obtain the scheme

$$\frac{1}{\Delta t}\left(\phi_j^{n+1} - \phi_j^n\right) = \frac{\Gamma}{\Delta x^2}\left(\phi_{j+1}^{n+1} - 2\phi_j^{n+1} + \phi_{j-1}^{n+1}\right), \tag{5.34}$$

which has the amplification factor

$$\lambda = \left(1 + 4d\sin^2\left(\tfrac{1}{2}\xi\right)\right)^{-1}. \tag{5.35}$$

Obviously, $|\lambda| < 1$ and therefore the implicit Euler scheme is unconditionally stable. This means that we have no time step restriction and that we can choose our time step according to the desired resolution in time.

Basically, every implicit time integration method is unconditionally stable and can therefore be used in numerical flame simulations. A drawback of the implicit Euler method is that it is only first order accurate in the time step Δt. Therefore, the method is suitable to compute steady state solutions, where time accuracy is not of importance, but for transient problems, such as oscillating flames, higher accuracy is desirable. A nice alternative in this case could be diagonally implicit Runge-Kutta methods [10]. Both the implicit Euler method and the Runge-Kutta methods are so-called one-step methods, since they include only two time levels. Alternatively, there exist implicit multi-step methods, which are highly accurate. However, these schemes have more than two time levels, which makes them very expensive in terms of memory requirements.

4 A Pressure Correction Method

In this section we give an outline of a PCM to decouple the pressure computation from the computation of the flow velocity and the combustion variables. For a more detailed discussion, the reader is referred to [12].

Applying a finite volume space discretization method to the momentum equations, the combustion equations and the expansion equation, we find a system of differential algebraic equations (DAEs), which can be symbolically written as

$$\begin{aligned} \frac{\mathrm{d}\mathbf{v}}{\mathrm{d}t} &= \mathbf{C}(\boldsymbol{\varphi}, \mathbf{v})\mathbf{v} - \mathbf{G}(\boldsymbol{\varphi})\mathbf{p}, \\ \frac{\mathrm{d}\boldsymbol{\varphi}}{\mathrm{d}t} &= \mathbf{A}(\boldsymbol{\varphi}) + \mathbf{B}(\boldsymbol{\varphi})\mathbf{v}, \\ \mathbf{D}\mathbf{v} &= \mathbf{S}(\boldsymbol{\varphi}), \end{aligned} \tag{5.36}$$

where the vectors $\mathbf{v}$, $\mathbf{p}$ and $\boldsymbol{\varphi}$ contain approximations of the flow velocity, pressure and combustion variables, respectively. The terms $\mathbf{G}(\boldsymbol{\varphi})\mathbf{p}$ and $\mathbf{D}\mathbf{v}$ represent approximations of $\frac{1}{\rho}\nabla p$ and $\nabla\cdot\mathbf{v}$, respectively. The pressure vector $\mathbf{p}$ is a source term in the discretized momentum equations, and it has to be determined such that the discrete expansion equation is satisfied at all time levels.

We can derive an explicit equation for $\mathbf{p}$ in the following way. Differentiating the discrete expansion equation with respect to t and combining the result with the first differential equation in (5.36), we obtain

$$\mathbf{L}(\boldsymbol{\varphi})\mathbf{p} = \mathbf{D}\mathbf{C}(\boldsymbol{\varphi},\mathbf{v})\mathbf{v} - \frac{\mathrm{d}}{\mathrm{d}t}\mathbf{S}(\boldsymbol{\varphi}), \quad \mathbf{L}(\boldsymbol{\varphi}) := \mathbf{D}\mathbf{G}(\boldsymbol{\varphi}). \tag{5.37}$$

Note, that the term $\mathbf{L}(\boldsymbol{\varphi})\mathbf{p}$ represents an approximation of $\nabla\cdot\left(\frac{1}{\rho}\nabla p\right)$. The pressure equation (5.37) is sometimes referred to as the hidden constraint, to contrast it with the expansion equation which is a distinct constraint.

Based on the discussion in Section 3, we choose the implicit Euler time integration method. This way, we find the following discrete system

$$\begin{aligned}
\mathbf{v}^{n+1} - \Delta t\left(\mathbf{C}(\boldsymbol{\varphi}^{n+1},\mathbf{v}^{n+1})\mathbf{v}^{n+1} - \mathbf{G}(\boldsymbol{\varphi}^{n+1})\mathbf{p}^{n+1}\right) &= \mathbf{v}^{n},\\
\boldsymbol{\varphi}^{n+1} - \Delta t\left(\mathbf{A}(\boldsymbol{\varphi}^{n+1}) + \mathbf{B}(\boldsymbol{\varphi}^{n+1})\mathbf{v}^{n+1}\right) &= \boldsymbol{\varphi}^{n},\\
\mathbf{D}\mathbf{v}^{n+1} &= \mathbf{S}(\boldsymbol{\varphi}^{n+1}),
\end{aligned} \tag{5.38}$$

where $\mathbf{v}^{n+1}$ is an approximation of $\mathbf{v}(t_{n+1})$, etc. System (5.38) is generally difficult to solve for $\mathbf{v}^{n+1}$, $\mathbf{p}^{n+1}$ and $\boldsymbol{\varphi}^{n+1}$ simultaneously, due to the hidden constraint for the pressure. To circumvent the solution of (5.38), we introduce a two-stage PCM.

In the two-stage PCM , system (5.38) is solved in a predictor-corrector fashion. In the predictor step, the pressure vector $\mathbf{p}^{n+1}$ is replaced by the pressure vector $\mathbf{p}^{n}$ at the previous time level. This way, we find the following system

$$\begin{aligned}
\widetilde{\mathbf{v}} - \Delta t\left(\mathbf{C}(\boldsymbol{\varphi}^{n+1},\widetilde{\mathbf{v}})\widetilde{\mathbf{v}} - \mathbf{G}(\boldsymbol{\varphi}^{n+1})\mathbf{p}^{n}\right) &= \mathbf{v}^{n},\\
\boldsymbol{\varphi}^{n+1} - \Delta t\left(\mathbf{A}(\boldsymbol{\varphi}^{n+1}) + \mathbf{B}(\boldsymbol{\varphi}^{n+1})\widetilde{\mathbf{v}}\right) &= \boldsymbol{\varphi}^{n},
\end{aligned} \tag{5.39}$$

for the predicted velocity vector $\widetilde{\mathbf{v}}$ and the vector of combustion variables $\boldsymbol{\varphi}^{n+1}$. Note that the predicted velocity $\widetilde{\mathbf{v}}$ does *not* satisfy the discrete expansion equation. In the corrector step, the velocity vector $\mathbf{v}^{n+1}$ in the term $\mathbf{C}(\boldsymbol{\varphi}^{n+1},\mathbf{v}^{n+1})\mathbf{v}^{n+1}$ in (5.38) is replaced by the predictor value $\widetilde{\mathbf{v}}$, i.e.

$$\mathbf{v}^{n+1} - \Delta t\left(\mathbf{C}(\boldsymbol{\varphi}^{n+1},\widetilde{\mathbf{v}})\widetilde{\mathbf{v}} - \mathbf{G}(\boldsymbol{\varphi}^{n+1})\mathbf{p}^{n+1}\right) = \mathbf{v}^{n}. \tag{5.40}$$

Subtracting the first equation in (5.39) from (5.40) we obtain the relation

$$\mathbf{v}^{n+1} - \widetilde{\mathbf{v}} = -\Delta t\,\mathbf{G}(\boldsymbol{\varphi}^{n+1})\delta\mathbf{p}^{n}, \tag{5.41}$$

for the pressure difference $\delta\mathbf{p}^{n} := \mathbf{p}^{n+1} - \mathbf{p}^{n}$. Next, applying the discrete divergence operator $\mathbf{D}$ to (5.41) and imposing the expansion equation, we find the following system for $\mathbf{p}^{n+1}$:

$$\begin{aligned}
\mathbf{L}(\boldsymbol{\varphi}^{n+1})\delta\mathbf{p}^{n} &= \frac{1}{\Delta t}\left(\mathbf{D}\widetilde{\mathbf{v}} - \mathbf{S}(\boldsymbol{\varphi}^{n+1})\right),\\
\mathbf{p}^{n+1} &= \mathbf{p}^{n} + \delta\mathbf{p}^{n}.
\end{aligned} \tag{5.42}$$

After we have computed $\boldsymbol{\delta}\mathbf{p}^n$ from the first equation in (5.42), we can compute $\mathbf{v}^{n+1}$ from the simple relation

$$\mathbf{v}^{n+1} = \widetilde{\mathbf{v}} - \Delta t \mathbf{G}(\boldsymbol{\varphi}^{n+1})\boldsymbol{\delta}\mathbf{p}^n, \tag{5.43}$$

which follows readily from (5.41). Summarizing, we first compute $\widetilde{\mathbf{v}}$ and $\boldsymbol{\varphi}^{n+1}$ from the coupled system (5.39). Next, we compute the pressure $\mathbf{p}^{n+1}$ from (5.42) and finally we compute the new velocity $\mathbf{v}^{n+1}$ from (5.43). This PCM can be modified by applying a few corrector steps, however, one corrector step is usually sufficient.

5 Solution Methods for Algebraic Systems

After space discretization, and if necessary time integration, we obtain a large nonlinear system of algebraic equations. This system has to be solved iteratively and involves the solution of linear systems at each iteration step. In this section, we will outline numerical methods to solve nonlinear and linear systems occuring in numerical flame simulation.

Consider the nonlinear system (5.39), which we have to solve in the predictor step of the pressure correction method. This system can be symbolically written as

$$\mathbf{F}(\mathbf{y}) = \mathbf{0}, \tag{5.44}$$

where the vector of unknowns $\mathbf{y}$ contains the predicted velocity $\widetilde{\mathbf{v}}$ and the combustion variables $\boldsymbol{\varphi}^{n+1}$; see Section 4. However, system (5.44) might equally well represent some other subproblem in our mathematical model; think e.g. of the discretization of one of the combustion equations. Virtually all solution methods for (5.44) are based on Newton's method. It is defined by

$$\begin{aligned} &\mathbf{y}^{(0)} \quad \text{given,} \\ &\mathbf{y}^{(k+1)} = \mathbf{y}^{(k)} - \mathbf{J}^{-1}\left(\mathbf{y}^{(k)}\right)\mathbf{F}\left(\mathbf{y}^{(k)}\right), \quad k = 0, 1, 2, \ldots, \end{aligned} \tag{5.45}$$

where $\mathbf{y}^{(k)}$ denotes the k^{th} iterand and $\mathbf{J}(\mathbf{y}) := \mathbf{F}'(\mathbf{y})$ is the Jacobi matrix of $\mathbf{F}(\mathbf{y})$. The iteration (5.45) is repeated until $||\mathbf{F}\left(\mathbf{y}^{(k)}\right)|| < tol||\mathbf{F}\left(\mathbf{y}^{(0)}\right)||$ for some user specified tolerance tol. For combustion problems, iteration (5.45) will almost never converge, unless the initial guess $\mathbf{y}^{(0)}$ is very close to the solution of (5.44). Therefore, we have to modify the Newton iteration (5.45), to improve the initial guess $\mathbf{y}^{(0)}$ and/or the convergence behaviour.

For time dependent problems, an obvious choice for the initial guess $\mathbf{y}^{(0)}$ is the solution at the previous time level. When the time step Δt is sufficiently small, Newton iteration should converge. A way to improve the initial guess is by continuation. Assume that the nonlinear system (5.44) depends on a certain parameter, lets say the equivalence ratio ϕ. Suppose, we have the solution for a value ϕ_0 and we want to compute a new solution for a value ϕ_1. We can do this by solving a sequence of problems where ϕ is successively increased from ϕ_0 to ϕ_1; for more details see e.g. [2].

To improve the convergence behaviour of iteration (5.45), we can multiply the update vector $\boldsymbol{\delta}\mathbf{y}^{(k)} := \mathbf{J}^{-1}\left(\mathbf{y}^{(k)}\right)\mathbf{F}\left(\mathbf{y}^{(k)}\right)$ by a damping factor λ_k, with $0 < \lambda_k \leq 1$. This way we obtain the damped Newton iteration

$$\begin{aligned} &\mathbf{y}^{(0)} \quad \text{given,} \\ &\mathbf{y}^{(k+1)} = \mathbf{y}^{(k)} - \lambda_k \mathbf{J}^{-1}\left(\mathbf{y}^{(k)}\right)\mathbf{F}\left(\mathbf{y}^{(k)}\right), \quad k = 0, 1, 2, \ldots. \end{aligned} \tag{5.46}$$

A suitable choice for the damping factor is e.g. $\lambda_k = \left(1 + ||\mathbf{F}\left(\mathbf{y}^{(k)}\right)||\right)^{-1}$. This means that when (5.46) is converging, it reduces for $k \to \infty$ to the standard Newton method.

Also damped Newton iteration is often not convergent for combustion problems. A way to overcome this problem is to combine Newton iteration with time-stepping. Therefore, consider the system

$$\frac{\mathrm{d}\mathbf{y}}{\mathrm{d}t} = \mathbf{F}(\mathbf{y}), \tag{5.47}$$

instead of (5.44). In this formulation, $\mathbf{F}(\mathbf{y})$ represents the discretization of all terms in the conservation laws, except the accumulation terms. We now apply the implicit Euler time integration method to (5.47) and solve the resulting nonlinear system for $\mathbf{z} := \mathbf{y}^{n+1}$ by Newton iteration. This way we get the iteration

$$\begin{aligned} \mathbf{z}^{(0)} &= \mathbf{y}^n, \\ \mathbf{z}^{(k+1)} &= \mathbf{z}^{(k)} - \left(\mathbf{J}\left(\mathbf{z}^{(k)}\right) - \frac{1}{\Delta t}\mathbf{I}\right)^{-1}\left(\mathbf{F}\left(\mathbf{z}^{(k)}\right) - \frac{1}{\Delta t}\left(\mathbf{z}^k - \mathbf{y}^n\right)\right) \quad k = 0, 1, 2, \ldots. \end{aligned} \tag{5.48}$$

Note that for $\Delta t \to \infty$ iteration (5.48) changes to standard Newton iteration. The time step Δt should be chosen such that the matrix $\mathbf{J}\left(\mathbf{z}^{(k)}\right) - \frac{1}{\Delta t}\mathbf{I}$ is not singular and not even nearly singular. For stationary problems, we have to apply several time steps until we reach the steady state solution of (5.47). In this case we speak of the method of false transient.

Another way to speed up convergence of (5.45) is based on the embedding of (5.44) in the following time-dependent problem

$$\begin{aligned} \frac{\mathrm{d}\mathbf{y}}{\mathrm{d}\tau} &= -\mathbf{J}^{-1}(\mathbf{y})\mathbf{F}(\mathbf{y}), \quad (\tau > 0) \\ \mathbf{y}(0) &= \mathbf{y}^{(0)}, \end{aligned} \tag{5.49}$$

where τ is an artificial time. The differential equation in (5.49) is called the Davidenko equation and its steady state solution is the solution of (5.44). The damped Newton iteration (5.46) can be considered as the explicit Euler method applied to (5.49) with time step $\Delta\tau = \lambda_k$. Improving convergence of (5.46) is now equivalent with improving stability of the explicit Euler method for (5.49). A way to achieve this is to apply the mixed Euler method to (5.49), i.e. take $\mathbf{J}^{-1}(\mathbf{y})$ at level $\tau = \tau_k$ and $\mathbf{F}(\mathbf{y})$ at level $\tau = \tau_{k+1}$. This way we obtain

$$\mathbf{y}^{(k+1)} = \mathbf{y}^{(k)} - \lambda_k \mathbf{J}^{-1}\left(\mathbf{y}^{(k)}\right)\mathbf{F}\left(\mathbf{y}^{(k+1)}\right), \quad k = 0, 1, 2, \ldots. \tag{5.50}$$

Note that the implicit Euler method would require the inverse Jacobi matrix $\mathbf{J}^{-1}(\mathbf{y})$ at the new level $\tau = \tau_{k+1}$, making the method unfeasible. Equation (5.50) is a nonlinear system for $\mathbf{z} := \mathbf{y}^{(k+1)}$ and can be symbolically written as

$$\mathbf{G}(\mathbf{z}) := \mathbf{z} + \lambda_k \mathbf{J}^{-1}\left(\mathbf{y}^{(k)}\right)\mathbf{F}(\mathbf{z}) - \mathbf{y}^k = \mathbf{0}. \tag{5.51}$$

This system in its turn has to be solved by Newton iteration, and this way we obtain the iteration

$$\mathbf{z}^{(l+1)} = \mathbf{z}^{(l)} - \left(\mathbf{I} + \lambda_k \mathbf{J}^{-1}\left(\mathbf{y}^{(k)}\right)\mathbf{J}\left(\mathbf{z}^{(l)}\right)\right)^{-1}\mathbf{G}\left(\mathbf{z}^l\right), \quad l = 0, 1, 2, \ldots. \tag{5.52}$$

To reduce the computational costs of (5.52), we set $\mathbf{J}\left(\mathbf{z}^{(l)}\right) = \mathbf{J}\left(\mathbf{y}^{(k)}\right)$ during the iteration and we then obtain

$$\mathbf{z}^{(l+1)} = \frac{\lambda_k}{1+\lambda_k}\left(\mathbf{z}^{(l)} - \mathbf{J}^{-1}\left(\mathbf{y}^{(k)}\right)\mathbf{F}\left(\mathbf{z}^{(l)}\right)\right) + \frac{1}{1+\lambda_k}\mathbf{y}^{(k)}, \quad l = 0, 1, 2, \ldots. \tag{5.53}$$

The complete iteration consists of the outer loop (5.50) and the inner loop (5.53) and has usually a much better convergence behaviour than standard Newton iteration.

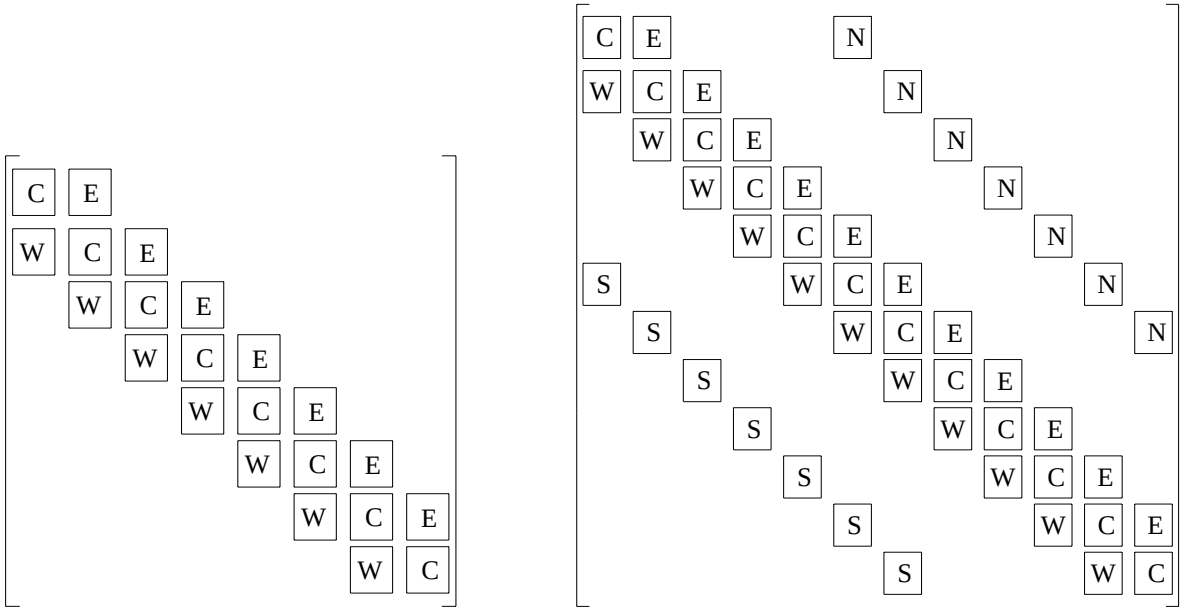

Figure 5.5: Sparsity pattern of the Jacobi matrix for a one-dimensional (left) and two-dimensional (right) flame simulation. In the right matrix some of the W and E blocks are zero blocks corresponding with control volumes adjacent to the boundary.

In combustion problems, the Jacobi matrix $\mathbf{J}(\mathbf{y})$ is often very difficult to compute analytically, because of complicated reaction rates and/or complicated transport models for conduction and diffusion. For that reason, the Jacobi matrix is usually computed numerically. The entry $J_{i,j}$ can be e.g. computed by one-sided differences as follows

$$J_{i,j} := \frac{\partial F_i}{\partial y_j} \approx \frac{1}{\delta}\left(F_i(\mathbf{y}+\delta\mathbf{e}_j) - F_i(\mathbf{y})\right), \tag{5.54}$$

where $\mathbf{e}_j$ is the jth unit vector and δ a small positive number; see e.g. [21]. This Jacobi matrix can be used in any of the iterative methods above.

A major drawback of Newton iteration and all its variants is that the computation of the Jacobi matrix, either analytically or numerically, is very expensive. Therefore, the Jacobi matrix is often kept constant during a few or all iterations. Another way is to build up a cheap approximation $\mathbf{B}(\mathbf{y})$ of $\mathbf{J}^{-1}(\mathbf{y})$ during iteration using so-called rank-1 updates. The resulting method is called the Broyden method; see e.g. [13]. All these methods are referred to as quasi-Newton methods.

To compute the pressure update $\boldsymbol{\delta}\mathbf{p}^n$ from (5.42) but also at each step of Newton iteration or one of its variants, we have to solve a linear system, which can be symbolically written as

$$\mathbf{A}\mathbf{y} = \mathbf{b}. \tag{5.55}$$

The efficiency of a numerical model highly depends on reliable and efficient solvers for (5.55). We first note that the coefficient matrix $\mathbf{A}$ is sparse, which means that each row in the matrix has only a few nonzero entries. The precise form of $\mathbf{A}$ depends on the numbering of the unknowns and equations.

We first consider a one-dimensional flat flame. Suppose, we collect all physical variables per control volume, such as e.g.

$$u_\mathrm{e},\, T_\mathrm{C},\, Y_{1,\mathrm{C}},\, \ldots,\, Y_{N_\mathrm{s}-1,\mathrm{C}},\, p_\mathrm{C}, \tag{5.56}$$

and subsequently number the control volumes. If we number the corresponding equations in the same way, the matrix **A** has a sparsity pattern as shown in figure 5. In fact, **A** is a block-tridiagonal matrix corresponding with the three-point coupling in the spatial direction. Each nonzero block in this matrix represents the coupling between all variables in a control volume. System (5.55) can be very efficiently solved using block-LU factorization, i.e. the matrix **A** is is factorized as $\mathbf{A} = \mathbf{LU}$, where **L** and **U** are a lower and an upper block triangular matrix, respectively. In fact, **L** has only one block-subdiagonal and **U** only one block-superdiagonal. Using this factorization of **A**, the solution method for (5.55) reads

$$\begin{aligned} \text{solve by forward substitution} \quad & \mathbf{Lz} = \mathbf{b}, \\ \text{solve by backward substitution} \quad & \mathbf{Uy} = \mathbf{z}. \end{aligned} \tag{5.57}$$

This method is very efficient because **L** and **U** together have the same number of nonzero entries as the original matrix **A**. Note that the computation of the LU-factorization only has to be done when a new Jacobi matrix is computed.

The situation is different for a two-dimensional flame. Suppose, we want to compute a flame on a rectangular domain. If we group all physical variables per control volume, number the control volumes along grid lines parallel to the x-axis and number the corresponding equations in the same way, we obtain for **A** a sparity pattern as shown in figure 5. The sparity pattern corresponds with the five-point coupling S-W-C-E-N between the variables as, indicated in figure 5.2. Alternatively, the nine-point coupling SW-S-SE-W-C-E-NW-N-NE would lead to a matrix with nine block-diagonals. The coefficient matrix **A** in figure 5 is a block-pentadiagonal matrix, however, not all block-diagonals are adjacent. LU-factorization of **A** would give matrices **L** and **U** which have their bands completely filled. For this reason LU-factorization is expensive in terms of CPU-time and memory requirements. Consequently, we have to use iterative methods in combination with preconditioning, to solve (5.55). There are many iterative methods available for linear systems; for an excellent survey see e.g. [19]. Reliable methods, suitable for nonsymmetric linear systems, are GMRES [20] and Bi-CGSTAB [22], and these are most frequently used in flame simulations.

References

[1] Anthonissen, M.J.H., *Local Defect Correction Techniques: Analysis and Application to Combustion*, Ph. D. Thesis, Eindhoven Univeristy of Technology, 2001.

[2] Ascher, U.M., Mattheij, R.M.M. and Russel, R.D., *Numerical Solution of Boundary Value Problems for Ordinary Differential Equations*, Prentice Hall, Englewood Cliffs, 1988.

[3] Axelsson, O. and Barker, V.A., *Finite Element Solution of Boundary Value Problems: Theory and Computation*, Academic Press, London, 1984.

[4] Bennett, B.A. and Smooke, M.D., Local rectangular refinement with application to axisymmetric laminar flames, *Combust. Theory Model.*, 2: 221–258, 1998.

[5] Bennett, B.A. and Smooke, M.D., Local rectangular refinement with application to nonreacting and reacting fluid flow problems, *J. Comput. Phys.*, 151: 684–727, 1999.

[6] Burden, R.L. and Faires, J.D., *Numerical Analysis*, Brooks/Cole Publishing Company, Pacific Grove, 1997.

[7] Buckmaster, J.D., An introduction to combustion theory, in: *The Mathematics of Combustion*, SIAM, Philadelphia, 1985, pp. 3–46.

[8] Feistauer, M., *Mathematical Methods in Fluid Dynamics*, Longman Scientific & Technical, Harlow, 1993.

[9] Gresho, P.M. and Sani, R.L., *Incompressible Flow and the Finite Element Method*, John Wiley, Chichester, 1998.

[10] Hairer, E. and Wanner, G., *Solving Ordinary Differential Equations II: Stiff and Differential-Algebraic Problems*, Springer, Berlin, 1996.

[11] Van 't Hof, B., Ten Thije Boonkkamp, J.H.M. and Mattheij, R.M.M., Discretization of the stationary convection-diffusion-reaction equation, *Numer. Methods Partial Differential Eq.* 14: 607–625, 1998.

[12] Van 't Hof, B., Ten Thije Boonkkamp, J.H.M. and Mattheij, R.M.M., Pressure correction for laminar combustion simulation, *Combust. Sci. and Tech.* 149: 201–233, 1999.

[13] Van 't Hof, B., *Numerical Aspects of Laminar Flame Simulation*, Ph.D. Thesis, Eindhoven University of Technology, 1998.

[14] Van Leer, B., Towards the ultimate conservative difference scheme. V. A second order sequel to Godunov's method, *J. Comp. Phys.* 32: 101–136, 1979.

[15] Leonard, B.P., A stable and accurate convective modelling procedure based on quadratic upstream interpolation, *Comp. Meths. Appl. Mech. Eng.* 19: 59–98, 1979.

[16] Maas, U. and Pope, S.B., Simplifying chemical kinetics: intrinsic low-dimensional manifolds in composition space, *Combust. Flame* 88: 239–264, 1992.

[17] Majda, A. and Lamb, K.G., Simplified equations for low Mach number combustion with strong heat release, in: *Dynamical Issues in Combustion Theory*, Eds. Fife, P.C., Linan, A. and Williams, F.A., Springer-Verlag, New-York, 1991, pp. 167–211.

[18] Patankar, S.V., *Numerical Heat Transfer and Fluid Flow*, McGraw-Hill, New York, 1980.

[19] Saad, Y., *Iterative Methods for Sparse Linear Systems*, PWS Publishing Company, Boston, 1996.

[20] Saad, Y. and Schultz, M.H., GMRES: a generalized minimum residual algorithm for solving nonsymmetric linear systems, *SIAM J. Sci. Stat. Comput.*, 7, 856–869, 1986.

[21] Somers, L.M.T., *The Simulation of Flat Flames with Detailed and Reduced Chemical Models*, Ph.D. Thesis, Eindhoven University of Technology, 1994.

[22] Van der Vorst, H.A., Bi-CGSTAB: a fast and smoothly converging variant of Bi-CG for the solution of nonsymmetric linear systems, *SIAM J. Stat. Comput.*, 12, 631–644, 1992

[23] Warnatz, J., Maas, U. and Dibble, R.W., *Combustion*, Springer Verlag, Berlin, 1996.

[24] Williams, Forman A., *Combustion Theory*, Addison-Wesley, Redwood City, 1985.

Chapter 6

Reduced chemical models

L. M. T. Somers

1 Introduction

In a previous lecture detailed chemical models are discussed. Such a chemical model has in principle the virtue to be independent of the flame-type which is studied. Formally, the same chemical model can be used for any type of reacting flow, e.g. diffusion and premixed flames either in pseudo one-dimensional configurations (flat flame, counter-flowing jets) or multi-dimensional flows. However, carrying out calculations is hampered by an important drawback. Due to the stiffness present in the governing equations, implicit techniques have to be used. This leads to large sparse matrix equations to be solved, with the leading dimension proportional to $N \times K$, where N is the number of species and K the number of mesh-points. It can readily be seen that for modelling of multi-dimensional reacting flows the memory requirements are large. Furthermore, the Newton-type iteration which is normally applied invokes a Jacobian matrix which, mostly, is evaluated numerically. This is a very costly process and is in fact the most important drawback of the detailed chemical models. Only due to the fast increase in computing power, the simulation of multi-dimensional reactive flows with detailed chemical models comes within our grasp. However, for the development of engineering tools for designing concepts as well as for computations of large scale reacting flow configurations, the application of detailed models is still (and will remain in the near future) impractical[1]. Reduction of the problem size and removing the stiffness in the equations is the best way to proceed.

2 Global Reaction Models

In the early years of computational reactive fluid dynamics when even simulations with detailed chemistry on the simplest geometries (1D laminar) where impossible due to lack of adequate computer capacity, so-called global reaction models were used frequently. These models replace the complex chain reactions with an overall reaction of the type,

$$\text{Fuel} + \text{Oxygen} \rightharpoonup \text{Products}.$$

Generally the parameters A, b, E_a in the Arrhenius-like reaction rate relation

$$\dot{\rho}_{fu} = -A[\text{Fu}]^{\alpha}[\text{Ox}]^{\beta} T^{\alpha+\beta} e^{-E_\text{a}/RT}$$

[1]Mid nineties with a contemporary supercomputer the computing time is of the order of two hours for a co-flowing axi-symmetrical laminar diffusion flame (computational domain 2.5 cm $\times$ 30 cm, 15 species reaction model) [1].

were fitted to reproduce data, like the adiabatic burning velocity (s_L) and temperature T_{ad} and occasionally the non-adiabatic flame temperature[2] obtained by experiments, e.g. [2, 3]. Later detailed chemistry simulations, e.g. [4], on 1D flames were used as well. The main advantage of this simplified chemical model is the reduced stiffness of the system of equations. Explicit techniques can now be used which do not require much storage [2].

The ultimate goal in the **systematic reduction techniques** in one way or another is reducing the stiffness and degrees of freedom required for application of detailed chemical models yet keeping the predictive quality with respect to the required physical phenomena. In the subsequent part of this lecture we will describe the approach, introduced some years ago by Peters et al. [5], referred to as 'convential systematically reduced chemical models'. It is used in many applications nowadays, see e.g. [6, 7, 12, 13]. In the final section a representant of what's called the 'mathematical systematic reduction technique' is shortly described.

The strategy of the 'conventional' approach is to use the detailed chemical model as basis and to apply steady-state and partial equilibrium assumptions to eliminate a number of the species in the model and to replace the corresponding (partial, ordinary) differential equations by algebraic relations. This leads to a reduction of the dimension of the matrix equations, which is desirable from a computational point of view. In general a systematically reduced chemical scheme is not very specific for the type of flame considered, e.g. for the one-dimensional premixed and diffusion flames the same model can be used [6, 7]. However, as for the global mechanism, each reduced scheme is to a certain extent deduced for the mixture which is to be considered and the properties which have to be predicted accurately. For example, the same basic detailed chemical[3] describes the combustion of most simple hydrocarbons in diffusion as well as pre-mixed flame types. However, each flame type yield a different systematically reduced scheme [7].

In remaining part of this lecture we will deal with is adequately referred to as systematical reduction techniques. A deduction of a reduced chemical model is not straightforward, and can be based on knowledge and experience of the author or on 'rigourous' mathematics. The former will be addressed as 'Conventional' and the latter as 'Mathematical'.

3 'Convential' Systematic Reduction Technique: mechanism for lean Methane-Air Flames

Systematically reduced chemical mechanisms are, contrary to earlier mentioned global mechanisms, obtained by a careful analysis of a detailed reaction model describing the oxidation of a specific fuel. Effectively, the objective of such an analysis will be to replace the (partial) differential equations for some species by algebraic expressions which, in principle, reduces the computational effort. The reduction strategy is based on two distinctive tasks. First, there is the actual **reduction** of the number of differential equations which have to be solved, i.e. the identification of the species that to adequate accuracy can be assumed to be in steady-state. Secondly, there is the so-called **truncation** of the expressions for the species which are to be considered in steady-state. Both the reduction of the problem size as well as the truncation of the resulting expressions will be treated in this lecture. However, first some general concepts will be introduced which can be applied to any detailed reaction mechanism. These principles will be applied to the skeletal mechanism used for lean methane-air flames as already presented in lecture 2, section 4 on page 26.

[2] Burner-stabilized flames.

[3] E.g. the GRI mechanism [8] can be used for the combustion of several small hydrocarbon molecules (methane,ethane, propane).

3.1 General Principles in Systematic Reduction

Two important features in the systematical reduction of the detailed chemical models are the so-called **steady-state approximation** and the **partial-equilibrium approximation**.

Steady-state approximation

The most important assumption is the steady-state approximation. It simply states that for a species the chemical source term is zero, i.e. for the i-th species

$$\dot{\rho}_i = M_i \sum_{j=1}^{M} \nu_{ij} q_j = 0, \tag{6.1}$$

with M_i the molar mass. Equation (6.1) gives an algebraic equation for each species considered to be in steady-state (involving many reactions in general). Obviously, the nomenclature stems from the description of homogeneous reacting systems, where this equation implies that the time-derivative of the concentration is zero. In a flame, the assumption implies that the time scales of the reactions consuming and producing a 'steady-state' species are much shorter than the time scales associated with diffusion and convection. Generally, if no further simplifications are made, the assumption (6.1) for each of the species taken in steady-state form a set of non-linear coupled algebraic equations. To reduce the complexity of this set and even more to obtain an explicit[4] expression, often the partial-equilibrium assumption is applied.

Partial Equilibrium approximation

In contrast to the steady-state assumption this is an approximation applied to a specific reaction. If applied to a certain reaction j symbolically denoted by $A_1 + A_2 \rightleftharpoons B_1 + B_2$ the partial-equilibrium assumption yields,

$$q_j = 0 \tag{6.2}$$

and the species involved in such a reaction relate to each other through,

$$\frac{[B_1][B_2]}{[A_1][A_2]} = K = \frac{k^{\mathrm{f}}}{k^{\mathrm{r}}}. \tag{6.3}$$

It is worth mentioning that in the special case that the reaction rate of a steady-state species involves only one reaction, it effectively is a partial equilibrium approximation for that specific reaction.

The next subsection discusses which species can be considered in a steady-state. The first part will deal with the arguments leading to the decisions as they are applied by most authors. The partial-equilibrium assumption will be used in the last subsection 3.4 where the derivation of an explicit expression from the set of algebraic equations is derived.

3.2 Deduction of a reduced mechanism

The success of reducing a detailed chemical model is strongly related to the ability of applying the steady-state assumptions to the proper set of species. Classically, this is done by simply comparing the contributions of the different parts (convection-, diffusion- and reaction- part) in the balance equation

[4]By explicit is meant; the equation that determines a variable is expressed in known quantities only, e.g. $X_l = f(X_i)$ with all X_i known at the point where X_l is evaluated.

for a specific species and a detailed investigation of the chemical source term. In order to make a direct comparison between the magnitude of the different components in these balance equations and the reaction rates of the individual reactions q_j in the chemical source terms, the balance equations are often expressed in terms of the 'specific molenumber'[5] of species i,

$$\Gamma_i = Y_i/M_i = X_i/\bar{M} \, .$$

The reason for this is best illustrated if we consider the conservation equation, e.g equation (2.23). For convenience we define the operator L as

$$L\{Y_i\} = \rho \boldsymbol{v} \cdot \nabla Y_i - \nabla \cdot (\rho D_{im} \nabla Y_i). \tag{6.4}$$

Whenever the flame is stationary, the time derivative vanishes and the conservation equation (2.23) reduces to,

$$L\{Y_i\} = M_i \sum_{j=1}^{M} \nu_{ij} q_j \tag{6.5}$$

where the expression for $\dot{\rho}_i$ is written explicitly in terms of the elementary reactions. It is clear that the equation for Γ_i yields,

$$L\{\Gamma_i\} = \sum_{j=1}^{M} \nu_{ij} q_j \tag{6.6}$$

where M_i cancels in the right-hand side. This cancelation is the reason for the introduction of Γ_i. It is now possible to compare the magnitude of diffusive and convective fluxes expressed in Γ_i with the reaction rates q_j directly.

The idea behind the steady-state assumption is best illustrated by comparing the magnitude of the different contributions to the balance equation. These terms are evaluated from results of a complete reaction model specifically for two species e.g. H_2O (figure 6.1), generally a non-steady state species, and HCO (figure 6.2) an intermediate species that will be considered to be in a steady-state later on. To compare the importance of each term in the convection-diffusion equation (6.6) the different fluxes and the net chemical reaction source term are shown in the figure on the left as a function of x. On the right the contributions to the chemical source term in terms of the elementary reactions of the skeletal mechanism are given.

From Figs. (6.1) and (6.2) it is clear that for H_2O the contribution of the elementary reactions is comparable to the magnitude of the net reaction rate as well as the magnitude of the convective and diffusive parts. For HCO, on the other hand, the magnitude of the reaction term is almost negligible compared to that of the elementary reactions of which it is composed. Since the diffusive and convective fluxes are comparable in magnitude to the net reaction rate in the flame zone their magnitude is thus negligible compared to that of the elementary rates. One could say that the concentration of HCO is determined mainly by the balance of formation and consumption reactions, thus implying the steady-state assumption, equation (6.1). The time scales associated with the consumption and production of HCO are much smaller than the ones associated with diffusive and convective processes.

We will now derive a 4-step mechanism for lean premixed methane-air flames. The number of steady-state assumptions that has to be employed can be obtained by a simple count of the free parameters in the flame problem. The skeletal mechanism can be considered as a 15 parameter (species) model, since there are 15 independent variables, i.e. the species. In order to obtain a 4 parameter model out of a set of 15, one has to pose 11 relations. Since conservation of elements is valid as

[5] Some authors refer to it as the 'specific abundance' of a species i.

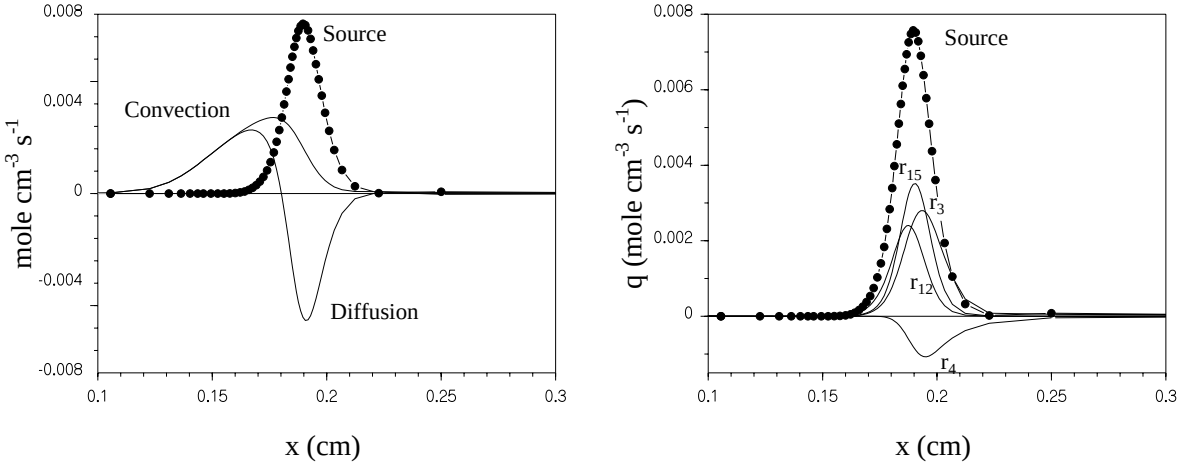

Figure 6.1: The diffusion and convection fluxes in terms of Γ and the net reaction rate for H_2O (left). The different parts of the source term (right), solid lines indicate the elementary reactions and the dotted line the net reaction rate. The listed numbers correspond to the ones in table 2.1 on page 30 of lecture 2.

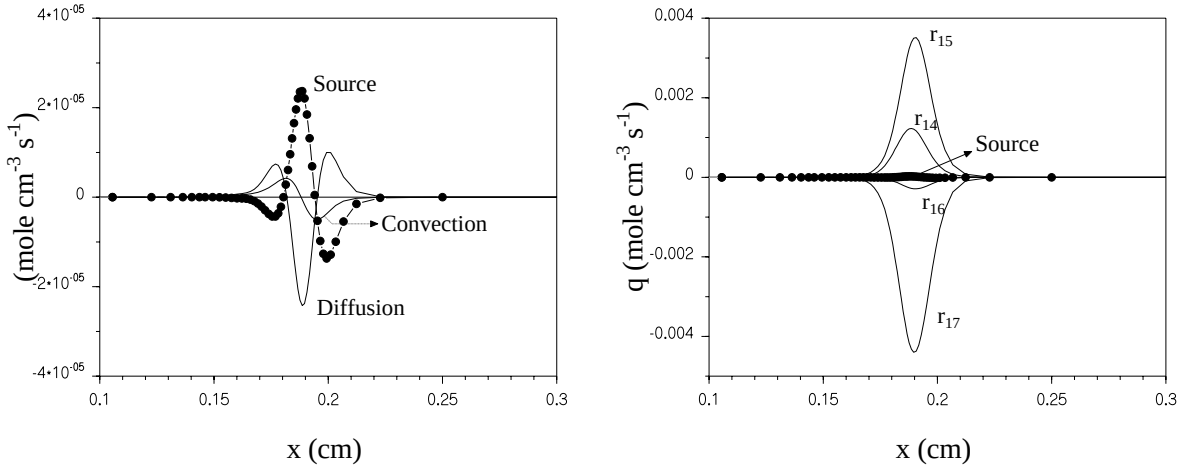

Figure 6.2: The diffusion and convection fluxes in terms of Γ and the net reaction rate for HCO are given (left). The different parts of the source term (right), solid lines indicate the elementary reactions and the dotted line the net reaction rate. The listed numbers correspond to the ones in table 2.1 on page 30 of lecture 2.

	CH_3	CH_3O	CH_2O	HCO	CO	H_2
Original	0.36330	0.00078	0.26770	0.00852	4.75700	1.89400
Weighted	0.43496	0.00077	0.26322	0.00845	4.75742	5.18866
	H	O	OH	HO_2	H_2O_2	
Original	0.71120	0.33250	0.74700	0.01613	0.00602	
Weighted	2.70910	0.38998	0.85958	0.01551	0.00575	

Table 6.1: Original and weighted maximum mole-fractions times 100 for an atmospheric adiabatic methane-air flame $\varphi = 0.80$.

long as nuclear reactions do not take place, there are 3 conservation equations, one for each of the elements C, H and[6] O. This means that 8 relations have to be introduced artificially (the steady state assumptions). For which species these assumptions apply best will be discussed in the following subsection.

Selection of the Steady-State species

Which species are most suitable for the steady-state assumption can be obtained either by plotting figures like figure 6.2 or looking at the maximum mole-fraction of each species in the flame for which the reduced mechanism is to be used. In our case we consider a lean adiabatic premixed flame and compute the maximum mole numbers of the intermediate species in table 6.1.

The set of intermediates can now be subdivided in two groups, one with a maximum mole fraction well below 1% and one well above. It is then common practice to consider the first group to be in steady-state since, due to fast reactions involving these species, every reaction creating a particle in this group is effectively balanced with a reaction consuming it. Therefore, the maximum mole fraction remains small and the net reaction rate can considered to be zero. In table 6.1 weighted mole fractions are given as well. These are equal to the original mole fraction weighted by the quantity $\sqrt{M_{\mathrm{N}_2}/M_{i,\mathrm{N}_2}}$, where

$$M_{i,\mathrm{N}_2} = \frac{2M_i M_{\mathrm{N}_2}}{M_i + M_{\mathrm{N}_2}} \tag{6.7}$$

which is roughly proportional to the binary diffusion coefficients of each species with respect to Nitrogen (which is abundant). It is known from asymptotic analysis that in the reactive layer, diffusive transport is dominant over convective transport [5]). Therefore, the weighted mole fractions are considered to be more significant and it is better to use the weighted maximum mole numbers. This is illustrated by the observation that in most treatments [H] is not taken in steady state whilst [O] and [OH] are. This would not have been concluded if the original maximum mole numbers would have been considered.

3.3 Actual reduction of the chemical set

In equation (6.8) the differential equations are given and each individual reaction is specified explicitly. This only done so for illustrative purposes and numbering is according to the reaction mechanism

[6]Without N_2 chemistry the N conservation can be left out since N_2 itself acts as a conserved scalar.

presented in 4 on page 30. For all species present in the skeletal mechanism this yields,

$$
\begin{aligned}
L\{\Gamma_{CH_4}\} &= -q_{10} - q_{11} - q_{12} \\
0 = L\{\Gamma_{CH_3}\} &= q_{10} + q_{11} + q_{12} + q_{13} - q_{18} \\
0 = L\{\Gamma_{CH_3O}\} &= q_{18} - q_{19} - q_{20} \\
0 = L\{\Gamma_{CH_2O}\} &= q_{13} - q_{14} - q_{15} + q_{19} + q_{20} \\
0 = L\{\Gamma_{HCO}\} &= q_{14} + q_{15} - q_{16} - q_{17} \\
L\{\Gamma_{CO}\} &= -q_9 + q_{16} + q_{17} \\
L\{\Gamma_{CO_2}\} &= q_9 \\
L\{\Gamma_{H_2}\} &= -q_2 - q_3 + q_7 + q_{11} + q_{14} + q_{16} + q_{19} + q_{25} \\
L\{\Gamma_{H}\} &= -q_1 + q_2 + q_3 - q_5 - q_6 - q_7 + q_9 + q_{10} - q_{11} + \\
&\quad q_{13} - q_{14} - q_{16} + q_{17} - q_{19} + q_{20} - q_{24} - 2q_{25} \\
L\{\Gamma_{O_2}\} &= -q_1 - q_5 + q_7 + q_8 - q_{18} + q_{21} \\
0 = L\{\Gamma_{O}\} &= q_1 - q_2 + q_4 - q_{13} + q_{18} \\
0 = L\{\Gamma_{OH}\} &= q_1 + q_2 - q_3 - 2q_4 + 2q_6 - q_8 - q_9 - q_{12} - q_{15} + 2q_{22} - q_{23} - q_{24} \\
0 = L\{\Gamma_{HO_2}\} &= q_5 - q_6 - q_7 - q_8 - 2q_{21} + q_{23} \\
L\{\Gamma_{H_2O}\} &= q_3 + q_4 + q_8 + q_{12} + q_{15} + q_{23} + q_{24} \\
0 = L\{\Gamma_{H_2O_2}\} &= q_{21} - q_{22} - q_{23} \\
L\{\Gamma_{N_2}\} &= 0
\end{aligned}
\tag{6.8}
$$

For the steady-state species the net reaction rate is taken equal to zero. The set is now reduced by eliminating precisely as much reaction rates as there are steady-state species. For instance if reaction 21 is to be eliminated, the steady-state assumption for H_2O_2 can be used to perform this task. Using $q_{21} - q_{22} - q_{23} = 0$, each occurrence of q_{21} can consequently be replaced by $q_{22} + q_{23}$, thereby eliminating q_{21} from all equations. Which reactions are to be eliminated is arbitrary[7] and does not affect the results of a computation *as long as the expressions for the steady-state species are not truncated*. The main idea is to eliminate the fastest reactions that destroy the steady-state species since the slowest are rate-determining. A kind of main chain by which the complete combustion takes place is then derived. Here, we choose to follow the approach of Peters and Seshadri or Peters and Williams [10, 11, 5]. From the H_2-O_2 subsystem they eliminate reactions q_2, q_3, q_7 and q_{22} being the fastest consumption rates for O, OH, HO_2 and H_2O_2, respectively. For the intermediates in the C_1-chain, CH_3, CH_3O, CH_2O and HCO, these 'fastest' reactions are q_{13}, q_{20}, q_{14} and q_{17}. The last four complete the minimum set of reactions that can be removed from the main reaction chain. Other reactions, which are linear combinations of the previously selected reactions, disappear as well from the main chain. For instance, reaction r_8 can be written as a linear combination of r_3 and r_7 i.e.,

$$
\begin{array}{rl}
H_2 + OH \rightleftharpoons H_2O + H & r_3 \\
H + HO_2 \rightleftharpoons H_2 + O_2 & r_7 \\
\hline
 & + \\
OH + HO_2 \rightleftharpoons H_2O + O_2 & r_8.
\end{array}
$$

Similar arguments apply for reactions r_4 $(= r_3 - r_2)$ and r_{15} $(= r_{14} + r_3)$, leading to the elimination of reaction rates q_4 and q_{15}.

[7] See for instance [5, 9] for typical differences in choices as applied by different authors.

The resulting work is to carry out the linear algebra with the set of balance equations. This is a rather tedious job, which can be automated as is done by Göttgens et al. (REDMECH [14]) or the algorithm presented in appendix B of [15]. Both the package developed by Göttgens et al. and the algorithm developed here, only need the basic detailed mechanism, the chosen steady-state species and for each of the latter a corresponding reaction to be removed from the main chain. The program then gives the global mechanism and the corresponding overall reaction rates. Here we will present the results only, yielding the following conservation equations for the **non** steady-state species,

$$L\{\Gamma_{CH_4}\} = -q_{\rm I} \tag{6.9}$$
$$L\{\Gamma_{CO}\} = -q_{\rm II} + q_{\rm I} \tag{6.10}$$
$$L\{\Gamma_{CO_2}\} = q_{\rm II} \tag{6.11}$$
$$L\{\Gamma_{H_2}\} = 4q_{\rm I} + q_{\rm II} + q_{\rm III} - q_{\rm IV} \tag{6.12}$$
$$L\{\Gamma_{H}\} = -2q_I - 2q_{\rm III} + 2q_{\rm IV} \tag{6.13}$$
$$L\{\Gamma_{O_2}\} = -q_{\rm IV} \tag{6.14}$$
$$L\{\Gamma_{H_2O}\} = -q_I - q_{\rm II} + 2q_{\rm IV} \tag{6.15}$$

Here, the global reaction rates of the 4-step model are introduced,

$$\begin{aligned} q_{\rm I} &= q_{11} + q_{10} + q_{12} \\ q_{\rm II} &= q_9 \\ q_{\rm III} &= q_5 - q_{10} + q_{16} - q_{18} + q_{19} - q_{21} + q_{23} + q_{24} + q_{25} \\ q_{\rm IV} &= q_1 + q_6 + q_{18} + q_{21} - q_{23}. \end{aligned} \tag{6.16}$$

The so-called **principal rate** of each overall reaction is the one appearing first after the equal-sign. The magnitudes of the overall reactions are determined by these reactions mainly. This can be determined by a sensitivity analysis. The global reactions are obtained from the stoichiometry in the set (6.9-6.15). The rate of reaction II, associated with $q_{\rm II}$, for instance, appears with -1 in the CO-balance equation (6.10), $+1$ in the CO_2-balance equation (6.11), -1 in the H_2-balance equation (6.12), $+1$ in the H_2O-balance equation (6.15) and is not present in all the others. When we gather all species with negative numbers on the left hand side and all those with positive numbers on the right hand side, we find global reaction II,

$$CO + H_2O \rightleftharpoons CO_2 + H_2 \qquad (r_{\rm II})$$

In a similar fashion all other overall reaction may be obtained and are presented below

$$CH_4 + 2H + H_2O \rightleftharpoons CO + 4H_2 \qquad (r_{\rm I})$$
$$CO + H_2O \rightleftharpoons CO_2 + H_2 \qquad (r_{\rm II})$$
$$H + H + M \rightleftharpoons H_2 + M \qquad (r_{\rm III})$$
$$O_2 + 3H_2 \rightleftharpoons 2H + 2H_2O. \qquad (r_{\rm IV})$$

where we included reaction $r_{\rm II}$ again. It should be noted that these overall reactions can be obtained by the same algorithm which performs the linear algebra mentioned earlier (Appendix B of [15]).

Some aspects of the overall reactions are worth mentioning. First, we see that fuel-breakup $r_{\rm I}$ itself is chain-breaking since it consumes radicals. It is for this reason that the H-radicals are not able to diffuse upstream, as is oberved in many applications. The H radical does not enter the fuel rich zone in pre-mixed flames. Furthermore, it is interesting to see that not O_2 but H_2O acts as the oxidizer in

the fuel breakup. Overall reaction r_{II} is the water-gas shift-reaction, which accounts for the CO to CO_2 conversion in the postflame zone. The recombination reaction r_{III} accounts for the chain-breaking in the post-flame zone. Its principal rate is given by reaction r_5 ($H+O_2+M \rightharpoonup HO_2+M$) and apparently not r_{25} ($H+H+M \rightharpoonup H_2+M$) as one might expect. Chain-branching is accounted for by the oxygen breakup reaction, r_{IV}, which effectively produces two radicals.

However, the set of equations is not complete yet. We may not expect that all steady-state species have disappeared from the rates $q_{\mathrm{I}} \ldots q_{\mathrm{IV}}$ of the overall reactions. This would have been pure coincidence and indeed is not the case as one can see easily. Even if one would truncate the overall rates to the principal rates (q_{11}, q_9, q_5 and q_1, respectively) which is the minimum set, we still need expressions for the concentration of HO_2, O and OH since these occur in reactions r_5, r_1 and r_9. The set (6.9–6.15) is not closed and we need expressions for most steady state species. These have to be solved from the steady-state subset of equations in (6.8) leading to a set of nonlinear algebraic equations, which is complicated to solve as it stands. In simulations this has to be done for each mesh point, which is in general very CPU time consuming in 1D and specifically in 2D and 3D. Therefore, one often tries to truncate the expression for the steady-state species in such a way that an easy-to-evaluate explicit set of equations evolves. The truncation procedure is again a sort of post-processing procedure since the strategy for the truncation procedure can be obtained only after carefully examining the separate parts in the expressions for the steady state species which follow from a simulation with the detailed chemical model. The procedure for lean methane-air flames [7] will be presented in the next subsection.

3.4 Truncation of the steady-state relations

Formally for the evaluation of the concentrations of the steady-state species we should solve the set:

$$\begin{aligned}
q_{10}+q_{11}+q_{12}+q_{13}-q_{18} &= 0 && \{\Gamma_{CH_3}\}\\
q_{18}-q_{19}-q_{20} &= 0 && \{\Gamma_{CH_3O}\}\\
q_{13}-q_{14}-q_{15}+q_{19}+q_{20} &= 0 && \{\Gamma_{CH_2O}\}\\
q_{14}+q_{15}-q_{16}-q_{17} &= 0 && \{\Gamma_{HCO}\}\\
q_1-q_2+q_4-q_{13}+q_{18} &= 0 && \{\Gamma_{O}\}\\
q_1+q_2-q_3-2q_4+2q_6-q_8-q_9-q_{12}-q_{15}+2q_{22}-q_{23}-q_{24} &= 0 && \{\Gamma_{OH}\}\\
q_5-q_6-q_7-q_8-2q_{21}+q_{23} &= 0 && \{\Gamma_{HO_2}\}\\
q_{21}-q_{22}-q_{23} &= 0 && \{\Gamma_{H_2O_2}\}.
\end{aligned} \tag{6.17}$$

for fixed non steady-state species and temperature, which is non-linear and coupled in the steady-state species concentrations. To reduce the amount of work, which is one of the main objectives of the reduction strategy, the complexity is to be reduced. Therefore truncation of this set has been given much attention in the nineties and can be considered to be the most important step in reducing the detailed chemical model from a numerical point of view. The approach which is used by Peters et al. to truncate the steady-state expressions is presented.

Truncation that's what it is.

First we determine the minimum set of expressions we have to deduce in order to perform a flame calculation with the reduced mechanism. Simple bookkeeping leads to the observation that in order to calculate the set (q_{I})–(q_{IV}) as presented earlier, we need expressions for all steady-state species. If

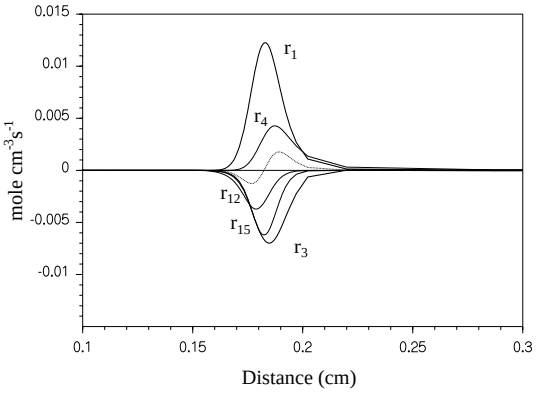

Figure 6.3: The net reaction rate of OH for an adiabatic $\varphi = 1.0$ flame as a function of place. The lines show the largest elementary reactions. Reactions r_1 and r_3 are the ones used in the truncated expression. The listed numbers correspond to the ones in table 2.1 on page 30 of lecture 2.

the overall rates would be restricted to the principal rates alone, this minimum set would be reduced to the species CH_3, O, OH and HO_2. Note that, since the steady-state relations for these species involve many reactions, there is no guarantee that the evaluation of the obtained expressions does not involve the other steady-state species as well.

We now continue with the deduction of expressions as proposed by Peters [5]. The way in which these expressions are obtained is by analyzing the source term of the different species. At first, a truncated expression for the concentration of OH is derived. For an estimate of the magnitudes of the contributions of the different elementary reactions consider figure (6.3). In the reaction zone the main contribution stems from reaction r_3 which leads to a leading order approximation[8] for OH:

$$[\mathrm{OH}]_* = \frac{k_3^{\mathrm{r}}[\mathrm{H_2O}][\mathrm{H}]}{k_3^{\mathrm{f}}[\mathrm{H_2}]} \ . \tag{6.18}$$

The next extension can be obtained if the forward rate, q_1^{f}, of reaction r_1 is included, since this rate has a non-negligible contribution in the reaction layer. However, if only q_1^{f} would be added this leads to an expression for [OH] which does not satisfy the correct equilibrium value downstream. Therefore, the backward rate of r_1 has to be added as well. The contribution of this backward rate is very small and can be viewed upon as a second-order correction to the expression for the OH concentration.

The expression for the OH concentration now follows from balancing q_1 and q_3:

$$[\mathrm{H_2}][\mathrm{OH}]k_3^{\mathrm{f}} - [\mathrm{H_2O}][\mathrm{H}]k_3^{\mathrm{r}} - [\mathrm{H}][\mathrm{O_2}]k_1^{\mathrm{f}} + [\mathrm{O}][\mathrm{OH}]k_1^{\mathrm{r}} = 0. \tag{6.19}$$

Since an *explicit* relation for [OH] is the principal goal, the yet unknown [O] in equation (6.19) should be replaced by an expression in terms of known quantities. Once more, it should be kept in mind that at this point the concentrations of the non steady-state species are assumed to be known and the only other unknown is the O-concentration. The elimination is performed by introducing an ad hoc approximation for the O-radical satisfying the partial equilibrium of reaction 4 leading to:

$$\begin{aligned} [\mathrm{O}] &= \frac{[\mathrm{OH}]_*^2 k_4^{\mathrm{f}}}{[\mathrm{H_2O}]k_4^{\mathrm{r}}} \\ &= \frac{[\mathrm{H_2O}][\mathrm{H}]^2 k_4^{\mathrm{f}}}{[\mathrm{H_2}]^2 k_4^{\mathrm{r}}} \left(\frac{k_3^{\mathrm{r}}}{k_3^{\mathrm{f}}}\right)^2 \ . \end{aligned} \tag{6.20}$$

Note that the leading-order approximation (6.18) for [OH] is substituted in the partial equilibrium

[8] In fact this leads to a partial equilibrium assumption of reaction 3.

expression. Substituting this downstream value[9] in the balance equation (6.19) leads to an explicit expression for [OH]:

$$[\mathrm{OH}] = \frac{[\mathrm{H_2O}][\mathrm{H}]k_3^{\mathrm{r}} + [\mathrm{H}][\mathrm{O_2}]k_1^{\mathrm{f}}}{[\mathrm{H_2}]k_3^{\mathrm{f}} + [\mathrm{H}]^2[\mathrm{H_2O}]k_1^{\mathrm{r}}k_4^{\mathrm{f}}k_3^{\mathrm{r}\,2} / \left([\mathrm{H_2}]^2 k_4^{\mathrm{r}} k_3^{\mathrm{f}\,2}\right)}. \tag{6.21}$$

This manipulation is expected not to be seriously in error, since the term involving the O radical (q_1^{r}) was only added to yield the correct equilibrium value for [OH] in the region downstream of the flame.

It should be stressed that the ad hoc expression (6.20) does not necessarily lead to a correct value for [O] itself. In fact it is not correct as we can see when proceeding with a more systematic approach to estimate the O-radical concentration. Following the same procedure for O as for OH the main contributions are determined. This leads to the balance equation:

$$[\mathrm{H}][\mathrm{O_2}]k_1^{\mathrm{f}} + [\mathrm{OH}][\mathrm{H}]k_2^{\mathrm{r}} + [\mathrm{OH}]^2 k_4^{\mathrm{f}} = [\mathrm{O}]\left(k_1^{\mathrm{r}}[\mathrm{OH}] + k_2^{\mathrm{f}}[\mathrm{H_2}] + k_4^{\mathrm{r}}[\mathrm{H_2O}] + k_{13}[\mathrm{CH_3}]\right) \tag{6.22}$$

Now a problem arises because a non-negligible contribution (i.e. r_{13}) necessitates the evaluation of an expression for [CH_3] which is not available yet. However, from the balance equation for CH_3,

$$\left([\mathrm{H}]k_{11}^{\mathrm{f}} + [\mathrm{OH}]k_{12}^{\mathrm{f}}\right)[\mathrm{CH_4}] = [\mathrm{CH_3}]\left(k_{10}^{\mathrm{r}}[\mathrm{H}][\mathrm{M}] + k_{11}^{\mathrm{r}}[\mathrm{H_2}] + k_{12}^{\mathrm{r}}[\mathrm{H_2O}] + k_{13}[\mathrm{O}]\right) \tag{6.23}$$

it can be observed that reaction 13 links both equations. But, except OH, which is known at this point, no other steady-state variables are involved. Therefore and due to the simple coupling between equation (6.22) and equation (6.23), this set can be solved in closed form leading to a quadratic expression for [O] yielding,

$$[\mathrm{O}] = \frac{-b + \sqrt{b^2 - 4ac}}{2a} \tag{6.24}$$

where

$$a = k_{13}B, \qquad b = BD + k_{13}(C - A), \qquad c = -AD \tag{6.25}$$

and,

$$\begin{aligned} A &= [\mathrm{H}][\mathrm{O_2}]k_1^{\mathrm{f}} + [\mathrm{OH}][\mathrm{H}]k_2^{\mathrm{r}} + [\mathrm{OH}]^2 k_4^{\mathrm{f}} \\ B &= [\mathrm{OH}]k_1^{\mathrm{r}} + [\mathrm{H_2}]k_2^{\mathrm{f}} + [\mathrm{H_2O}]k_4^{\mathrm{r}} \\ C &= \left([\mathrm{H}]k_{11}^{\mathrm{f}} + [\mathrm{OH}]k_{12}^{\mathrm{f}}\right)[\mathrm{CH_4}] \\ D &= [\mathrm{H}][\mathrm{M}]k_{10}^{\mathrm{r}} + [\mathrm{H_2}]k_{11}^{\mathrm{r}} + [\mathrm{H_2O}]k_{12}^{\mathrm{r}}. \end{aligned} \tag{6.26}$$

Using the expression for the *O*-radical gives,

$$[\mathrm{CH_3}] = \frac{C}{D + k_{13}[\mathrm{O}]} \tag{6.27}$$

which is the last species needed for the principal rates. Note that already an evaluation order for the steady-state relations appears, first OH and then O and CH_3 have to be calculated.

Expressions for the other species can be derived as well. Once the expressions for OH, O, and CH_3 are known, the truncated values for the other steady state species are easy to obtain. Below the

[9]Note that this expression may only be expected to be a correct estimate for [O] downstream, where the mixture approaches equilibrium.

results for the remaining intermediates CH_3O, CH_2O and HCO in the main chain are listed,

$$[CH_3O] = \frac{[CH_3][O_2]k_{18}}{[H]k_{19} + [M]k_{20}} \tag{6.28}$$

$$[CH_2O] = \frac{[CH_3][O]k_{13} + [CH_3O]\,([H]k_{19} + [M]k_{20})}{[H]k_{14} + [OH]k_{15}} \tag{6.29}$$

$$[HCO] = \frac{([H]k_{14} + [OH]k_{15})\,[CH_2O]}{[H]k_{16} + [M]k_{17}} \tag{6.30}$$

The expressions for ($[HO_2]$) and hydrogen-peroxide ($[H_2O_2]$) can be obtained from their main rates in the H_2-O_2 subsystem (r_5 - r_8). This leads to the following expressions,

$$[HO_2] = \frac{[H][O_2][M]k_5}{[H](\,k_6 + k_7\,) + [OH]k_8} \tag{6.31}$$

$$[H_2O_2] = \frac{[HO_2]^2k_{21} + [OH]^2[M]k^{\mathrm{r}}_{22} + [H_2O][HO_2]k^{\mathrm{r}}_{23}}{[M]k^{\mathrm{f}}_{22} + [OH]k^{\mathrm{f}}_{23}} \tag{6.32}$$

It should be stressed that the above set of equations form explicit expressions if they are evaluated in the order (6.21)–(6.32). The steady-state expressions together with the differential equations for the non steady-state species and the chemical source terms given in section (3.3) define the complete system.

4 Mathematical Systematic Reduction Technique

The major drawback of the 'conventional' approach towards the systematic reduction is the need for experience and deep insight into reaction mechanisms. Furthermore, once the mechanism is selected it will be used throughout the whole domain of the composition space where the particular application resides. It might well be true that the used mechanism is excellent in a certain temperature/composition range but completely wrong for the rest. The mathematical reduction techniques try to circumvent these drawbacks by applying rigourous mathematical methods which decide locally what appropriate 'steady-state' candidates are. Here the mathematical framework will be sketched. However details on implementation can be found in e.g. [16, 17].

For the analysis it is sufficient to consider the balance equations for species (equation 6.6). To study the chemical dynamics the convective and diffusive fluxes are negelected, yielding

$$\frac{\partial \Gamma_i}{\partial t} = w_i \tag{6.33}$$

where $w_i = \sum \nu_{ij} q_j$. To be able to determine mathimatically the fast and slow processes around a certain point in composition space $\boldsymbol{\Gamma}^0 = (\Gamma^0_1, \ldots, \Gamma^0_N)^T$, the source term $\boldsymbol{w} = (w_1, \ldots, w_N)^T$ is linearized around this reference:

$$\boldsymbol{w} \approx \boldsymbol{w}(\boldsymbol{\Gamma}^0) + \boldsymbol{J}(\boldsymbol{\Gamma} - \boldsymbol{\Gamma}^0) \tag{6.34}$$

the $\boldsymbol{J} = \left(\frac{\partial \boldsymbol{w}}{\partial \boldsymbol{\Gamma}}\right)_{\boldsymbol{\Gamma}^0}$, denotes the Jacobian matrix. Substitution of equation 6.33 gives the starting point of the analyis:

$$\frac{\partial \boldsymbol{\Gamma}}{\partial t} \approx \boldsymbol{w}(\boldsymbol{\Gamma}^0) + \boldsymbol{J}(\boldsymbol{\Gamma} - \boldsymbol{\Gamma}^0). \tag{6.35}$$

The local characteristics of the system can be examined by transforming these equations into the basis of the eigenvectors of the Jacobian matrix. The eigenvectors are $\boldsymbol{s}_i$ are defined by:

$$\boldsymbol{J}\boldsymbol{s}_i = \lambda_i \boldsymbol{s}_i$$

with λ_i the eigenvalue of the Jacobian matrix. If the transformation matrix is defined according to, $\boldsymbol{S} = (\boldsymbol{s}_1, \ldots, \boldsymbol{s}_N)$, the former equation writes,

$$\boldsymbol{J}\boldsymbol{S} = \boldsymbol{S}\boldsymbol{\Lambda} \tag{6.36}$$

where[10] $\boldsymbol{\Lambda} = diag(\lambda_1, \ldots, \lambda_N)$ is a matrix with only non-zero elements on its diagonal. Multiplication of equation 6.36 on the left by $\boldsymbol{S}^{-1}$ yields:

$$\boldsymbol{\Lambda} = \boldsymbol{S}^{-1}\boldsymbol{J}\boldsymbol{S}. \tag{6.37}$$

It should be noted the the eigenvalues and eigenvectors may be complex at this point. We will not go into details but in a practical implementation of this method this should be tackled. Differences in implementation found in literature depend on how a new basis is formed from the eigenvectors. Some construct an orthogonal basis (Schur-basis [16]), others use the eigenvectors as is (e.g. [17]).

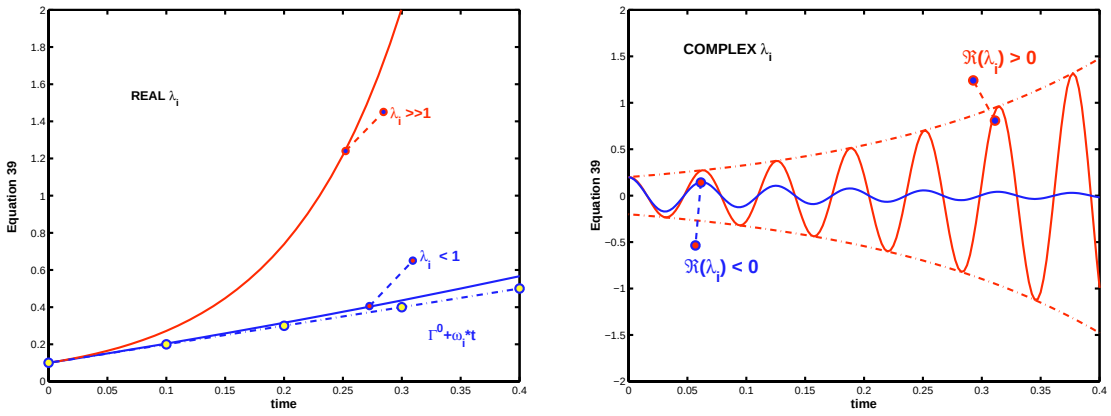

Figure 6.4: On the left: Equation 6.39 for $\lambda_i >> 1$ and $\lambda < 1$. The asymptotic solution $\hat{\Gamma}_i = \hat{\Gamma}_i^0 + \hat{w}_i t$ is given with the dotted line with circles. On the right: Equation 6.39 for $|\lambda_i| >> 1$ with $\Re(\lambda_i) > 0$ and $\Re(\lambda_i) < 0$ respectively.

Now we can use the eigenvector basis to transform equation 6.35 according to $\boldsymbol{\Gamma} = \boldsymbol{S}\hat{\boldsymbol{\Gamma}}$ thus yielding:

$$\frac{\partial \hat{\boldsymbol{\Gamma}}}{\partial t} \approx \hat{\boldsymbol{w}}(\hat{\boldsymbol{\Gamma}}^0) + \boldsymbol{\Lambda}(\hat{\boldsymbol{\Gamma}} - \hat{\boldsymbol{\Gamma}}^0). \tag{6.38}$$

What's the whole point of this exercition? The orginal differential equations in equation 6.35 are now transformed such that the individual equations

$$\frac{\partial \hat{\Gamma}_i}{\partial t} \approx \hat{w}_i(\hat{\Gamma}_i^0) + \lambda_i(\hat{\Gamma}_i - \hat{\Gamma}_i^0)$$

are independent from each other, they are decoupled. For each one the general solution is given by:

$$\hat{\Gamma}_i = \hat{\Gamma}_i^0 + \frac{\hat{w}_i(\hat{\Gamma}_i^0)}{\lambda_i}\left(e^{\lambda_i t} - 1\right) \tag{6.39}$$

[10] And NOT $\boldsymbol{J}\boldsymbol{S} = \boldsymbol{\Lambda}\boldsymbol{S}$!

This equation gives now the basis for a timescale analysis of different chemical processes. These processes, in general, can not be associated with a single species or reaction, but inevitably consider reaction groups. From equation 6.39 typical timescales can be distinguished. If the absolute value obeys $|\lambda_i| \ll 1$ equation 6.39 becomes[11]

$$\hat{\Gamma}_i = \hat{\Gamma}_i^0 + \hat{w}_i t$$

indicating that typical timescales are

$$\tau_i = 1/\hat{w}_i \quad \forall \quad |\lambda_i| \ll 1. \tag{6.40}$$

If the absolute value of the real part of an eigenvalue $|\Re(\lambda_i)| \gg 1$, the typical timescale is found from the exponent:

$$\tau_i = 1/|\Re(\lambda_i)| \quad \forall \quad |\Re(\lambda_i)| \gg 1. \tag{6.41}$$

Several observations follow from the value of λ_i. If its magnitude is large, movements in the direction of the associated eigenvector will proceed fast. The larger the eigenvalue the faster the process will be. Different ways of behaviour are determined by the sign of the real part and the magnitude of the imaginary part. A process with a negative real part of the eigenvalue will extinguish and reach a steady-state. If the imaginary part is large as well this relaxation will be oscillatory. If the real part of the eigenvalue is positive the associated process will not relax to a steady-state. This is illustrated in figure 6.4. Some eigenvalues will be zero. One can show rigourously that the fact that chemical reactions conserve elements can be used to construct eigenvectors that have eigenvalues equal to zero. In fact all eigenvectors with zero eigenvalue are associated with so-called conserved scalars.

Similar to the 'conventional' approach now the 'mathematical' method will introduce steady-state relations, albeit generally not coupled to specific species. The best candidates are selected from the ordering of the eigenvalues. The fastest timescales pose the best candidates. The number of candidates to be selected is determined by the dimension[12] of the so-called 'Low Dimensional Manifold' to be created. In order to be successful it is essential that many eigenvalues have negative real parts while their magnitude is large. That this is the case has been shown by e.g. Maas and Pope [16] for carbonmonoxide/hydrogen-air combustion systems, and in the PhD Thesis of Eggels [17] for hydrogen-air en methane-air systems.

The number of steady-state relations, or equally, the number of 'fast' reaction-groups, n_s to be selected is given by the required dimension, say n_m, of the manifold together with the number of conserved scalars (viz. elements) n_c. The so-called elemental composition vectors $\boldsymbol{\mu}_i$, with elements μ_{ij} the number of elements i in species j are left eigenvectors of the Jacobian with eigenvalue 0. Therefore, the number of steady-state assumptions n_s within the the set of $\hat{\Gamma}_i$ obeying a 'steady-state equation',

$$\frac{\partial \hat{\Gamma}_i}{\partial t} = 0 \quad \forall \quad i = n_m + n_c + 1, \cdots, n \tag{6.42}$$

only equals $n_s = n - (n_m + n_c + 1)$. Here n is the total number of species present in the model or equivalently the dimension of the composition space.

[11] Use $\lim_{x \to 0} e^x = 1 + x$

[12] The dimension is determined by the degrees of freedom in composition space, being the number of species n. The realizable compositions will be restricted by imposing steady-state relations generating a hyper-surface in composition space. This surface is mostly referred to as the 'Low-dimensional Manifold'

References

[1] Smooke, M.D., Xu, Y., Zurn, R.M., Lin, P., Frank, J.H. and Long, M.B., *Computational and Experimental Study of OH and CH Radicals in Axisymmetric Laminar Diffusion Flames* in Twenty-Fourth symposium on Combustion The Combustion Institute, Pittsburgh, p.813, 1992

[2] H.C. de Lange, *Modeling of premixed flames*, Ph.D. Thesis, University of Technology, Eindhoven 1992.

[3] van Maaren, A., *One-step chemical reaction parameters for premixed laminar flames*, Ph.D. Thesis, Eindhoven University of Technology, 1994.

[4] C.K. Westbrook and F.L. Dryer, *Simplified Reaction Mechanisms for the Oxidation of Hydrocarbon Fuels in Flames.*, Combustion Science and Technology **27**, p. 31, 1981

[5] Peters, N., in *Reduced Kinetic Mechanisms for Asymptotic Approximations for Methane-Air Flames* (Smooke, M.D., Ed.), Lecture Notes in Physics 384, Springer-Verlag, Berlin, p. 48, 1991

[6] Smooke, M.D. ed., *Reduced Kinetic Mechanisms and Asymptotic Approximations for Methane-Air Flames*, Lecture Notes in Physics, Springer-Verlag, Berlin Heidelberg, 1991

[7] Mauss, F.,Peters, N., in *Reduced Kinetic Mechanisms for Applications in Combustion Systems* (Peters,N., Rogg,B., Eds), Lecture Notes in Physics m15, Springer-Verlag, Berlin, p. 58, 1993

[8] Bowman,G., Frenklach,M., Gardiner, B., Smith,G. and Serauskas,B, *GRI-Mech*, Gas Research Institute, Chicago, Illinois, USA, http://www.me.berkeley.edu/gri-mech/index.html

[9] Bilger,R.W. Stårner, S.H. and Kee,R.J., *On reduced mechanisms for Methane-Air Combustion in Nonpremixed Flames*, Combustion and Flame **80**, p. 135, (1990)

[10] Seshadri, K. and Peters, N., *The inner structure of Methane-air flames.*, Combustion and Flame **81**, p. 96, 1990

[11] Peters, N. and Williams, F.A., *The asymptotic structure of Stoichiometric Methane-air flames.*, Combustion and Flame **68**, p. 185, 1987

[12] Paczko G., Lefdal, P.M. and Peters, N., *Reduced reaction schemes for methane, methanol amd propane flames*, Twenty-first Symposium (International) on Combustion, The Combustion Institute, Pittsburgh, p. 739, 1986

[13] Boersma, John , *Modelling of NO_x emission from natural gas fired turbine combustors*, Ph.D. Thesis, University of Technology, Twente 1993.

[14] Göttgens,J., Terhoeven, P., in *Reduced Kinetic Mechanisms for Applications in Combustion Systems* (Peters,N., Rogg,B., Eds), Springer-Verlag, Berlin, p. 343, 1993

[15] Somers, L.M.T., *The Simulation of Flat Flames with Detailed and Reduced Chemical Models*, Ph.D. Thesis, Eindhoven University of Technology, 1994

[16] Maas, U and Pope, S.B., *Simplifying Chemical Kinetics: Intrinsic Low-Dimensianal Manifolds in Composition Space*, Combustion and Flame **88**, p. 239, 1992

[17] Eggels, R.L.G.M., *Modelling of Combustion Processes and NO formation with Reduced Reaction Mechanisms*, Ph.D. Thesis, Eindhoven University of Technology, 1996

Chapter 7

Application of Flamelet-Generated Manifolds

J. A. van Oijen

1 Introduction

Although the speed and storage capacity of modern computers increases continuously, it is still impossible to employ models that use detailed chemistry for the simulation of combustion in practical furnaces. Especially the models for turbulent flames are tremendously complicated due to the large range of time and length scales involved. The modelling of laminar flames is easier because the flow is relatively simple. Nowadays, numerical simulations of one-dimensional laminar flames with detailed chemistry and transport models are often used in combustion research. Nevertheless, the computation time for multi-dimensional laminar flame models prohibits the simulation of flames in complex geometries or an investigation of the influence of different parameters.

The use of complex reaction mechanisms is, apart from some simple cases, impossible, because for each species a partial differential equation has to be solved, and a typical reaction mechanism for hydrocarbon combustion considers more than 100 species [27]. Furthermore, the chemical kinetics cause the system of differential equations to be very stiff, which makes the use of expensive implicit solvers inevitable. Therefore, much research is spent on the development of reduction methods, which create reduced chemical models based on the complex reaction mechanism. These simplified chemistry models reduce the computational effort considerably without losing too much accuracy.

The first and probably the most well-known systematic reduction method is introduced by Peters *et al.* [17, 18]. This method (referred to as conventional reduction technique) is based on the observation that due to very fast chemical processes in combustion problems many chemical species and reactions are in quasi-steady state or partial equilibrium. When a species is assumed to be in steady state, the corresponding differential equation can be replaced by an algebraic relation, which reduces the computational cost. The main disadvantage of the method is that a vast knowledge of the chemical kinetics is required, because the researcher has to decide which species can be assumed to be in steady state. This problem is solved in the reduction methods introduced by Lam and Goussis [10] and Maas and Pope [11]. In these reduction techniques a more mathematical approach is used, which makes it possible to perform the reduction procedure automatically without insight of the user in the chemical kinetics. In both methods the fast chemical processes are identified by a mathematical analysis of the chemical system. Linear combinations of species corresponding to the fast chemical processes are assumed to be in steady state. In the method of Maas and Pope the fast and slow chemical processes are separated by using an eigenvalue analysis of the Jacobian of the chemical sourceterm, while Lam and Goussis propose a computational singular perturbation method.

The methods based on steady-state assumptions are, however, less efficient in 'low'-temperature regions. At high temperatures many chemical processes are fast and can be assumed to be in partial

equilibrium. At lower temperatures the number of slow chemical processes increases and less species can be assumed to be in quasi-steady state. At these lower temperatures, convection and diffusion become important and the local mixture composition is determined by a balance between convection, diffusion and reaction.

In this lecture a reduction method is discussed, that is not only based on 'chemical' assumptions like existing reduction methods, but that also takes the main parts of convection and diffusion into account. It shares the idea with so-called flamelet approaches [9, 15] that a multi-dimensional flame can be considered as a set of one-dimensional (1D) flames: *flamelets*. This implies that the path followed in composition space in case of multi-dimensional flames will be close to the path found in 1D flames. Therefore, the chemical compositions in flamelets are used to construct a low-dimensional manifold in this method. The resulting manifold is referred to as a *Flamelet-Generated Manifold* (FGM).

In the following section a set of flamelet equations is derived, starting from the full set of transport equations. Then it is demonstrated how the solutions of the set of flamelet equations can be used to construct a manifold. The application of FGM in combustion simulations is discussed as well. Finally, some test results for 1D and 2D burner-stabilized methane/air flames are presented.

2 Flamelet equations

The FGM method shares its basic assumption with flamelet methods, that a multi-dimensional flame can be considered as a set of 1D flamelets. Therefore, the compositions in 1D flames will be representative for the compositions in more general flames as well. In this section a set of 1D flamelet equations is derived following the basic ideas of De Goey and Ten Thije Boonkkamp [8, 9]. Although this derivation has been presented in a previous lecture, it will be repeated here for the sake of completeness. In the following sections it is explained how the set of flamelet equations can be used to construct a FGM.

A premixed flame is defined as the region in space, where a scalar variable $\mathcal{Y}$ assumes values between $\mathcal{Y}_\mathrm{u} = 0$ in the unburnt gases and $\mathcal{Y}_\mathrm{b} = 1$ in the burnt gases. The subscripts u and b denote variables associated with the unburnt and burnt mixture, respectively. The variable $\mathcal{Y}$ can be any linear combination of species mass fractions, which obeys $\nabla\mathcal{Y} \neq 0$. A 'flame surface' is defined as an iso-surface of $\mathcal{Y}$, i.e. a surface at which $\mathcal{Y}(\boldsymbol{x}, t) = const$. The motion of such a surface is described by the kinematic equation

$$\frac{\mathrm{d}\mathcal{Y}}{\mathrm{d}t} := \frac{\partial\mathcal{Y}}{\partial t} + \boldsymbol{u}_f \cdot \nabla\mathcal{Y} = 0, \tag{7.1}$$

stating that a point on a flame surface stays on this surface for all t. The local velocity of a flame surface $\boldsymbol{u}_f$ is determined by a balance between the local fluid velocity $\boldsymbol{u}$ and the local burning velocity s_L:

$$\boldsymbol{u}_f = \boldsymbol{u} + s_\mathrm{L}\boldsymbol{n}. \tag{7.2}$$

The burning velocity is defined as the velocity at which the flame surface propagates normal to itself and relative to the flow in the unburnt mixture. The local normal vector $\boldsymbol{n}$ can be determined from the scalar field $\mathcal{Y}$,

$$\boldsymbol{n} = -\frac{\nabla\mathcal{Y}}{|\nabla\mathcal{Y}|}, \tag{7.3}$$

directed to the unburnt gas mixture. As figure 7.1 shows, the tangential component of the flame surface velocity is equal to the tangential component of the fluid velocity and the difference $\rho(\boldsymbol{u} - \boldsymbol{u}_f)$ normal

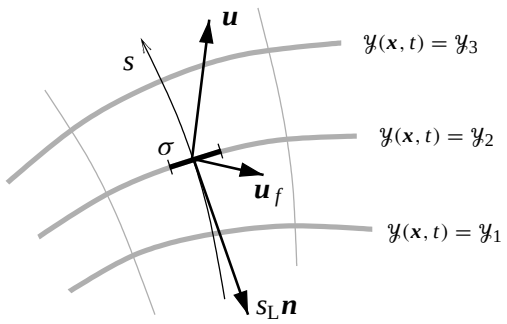

Figure 7.1: Flamelet system adapted to iso-surfaces of $\mathcal{Y}$.

to the flame surface is equal to the amount of mass effectively consumed by the flame. Substitution of (7.2) in (7.1) leads to the kinematic equation

$$\frac{\partial \mathcal{Y}}{\partial t} + \boldsymbol{u} \cdot \nabla \mathcal{Y} = s_\mathrm{L} |\nabla \mathcal{Y}|. \tag{7.4}$$

This equation is very similar to the well-known kinematic G-equation first introduced by Williams [29], which describes the motion of a single flame sheet ($\mathcal{Y} = \mathcal{Y}^0$). However, important differences are that (7.4) describes the motion of all flame surfaces with $\mathcal{Y}_\mathrm{u} < \mathcal{Y} < \mathcal{Y}_\mathrm{b}$, and that s_L is a field quantity in (7.4), while in the G-equation it is defined at the flame sheet only.

In [8], De Goey and Ten Thije Boonkkamp proposed the stretch rate K as the relative rate of change of the mass $M(t)$, defined as

$$M(t) = \int_{V(t)} \rho \, dV, \tag{7.5}$$

contained in an infinitesimal volume $V(t)$ in the flame, moving with velocity $\boldsymbol{u}_f$:

$$K = \frac{1}{M} \frac{\mathrm{d}M}{\mathrm{d}t}. \tag{7.6}$$

Applying Reynolds' transport theorem to $M(t)$ in (7.5) gives the following expression for the scalar field quantity K:

$$\rho K = \frac{\partial \rho}{\partial t} + \nabla \cdot (\rho \boldsymbol{u}_f). \tag{7.7}$$

Together with (7.2) this expression can be used to rewrite the continuity equation:

$$\nabla \cdot (\rho s_\mathrm{L} \boldsymbol{n}) = \rho K, \tag{7.8}$$

where all distortions from local 1D flame behaviour are combined in the right-hand side term ρK. Apart from the usual terms related to flame curvature and flow straining, this definition of K incorporates additional contributions, for instance due to flame thickness variations. A physical interpretation of the different contributions to flame stretch is presented in [8].

The conservation equation for the scalar variable $\mathcal{Y}$ reads

$$\frac{\partial (\rho \mathcal{Y})}{\partial t} + \nabla \cdot (\rho \boldsymbol{u} \mathcal{Y}) - \nabla \cdot \left(\frac{\lambda}{Le_\mathcal{Y} c_p} \nabla \mathcal{Y} \right) - \dot{\omega}_\mathcal{Y} = 0, \tag{7.9}$$

with $Le_{\mathcal{Y}}$ and $\dot{\omega}_{\mathcal{Y}}$ generally depending on the other field variables in the flame. Using the kinematic equation (7.4) and equations (7.7) and (7.2), the following equation for $\mathcal{Y}$ is found rigorously

$$-\nabla\cdot(\rho s_{\mathrm{L}}\boldsymbol{n}\mathcal{Y}) - \nabla\cdot\left(\frac{\lambda}{Le_{\mathcal{Y}}c_p}\nabla\mathcal{Y}\right) - \dot{\omega}_{\mathcal{Y}} = -\rho K\mathcal{Y}, \tag{7.10}$$

with all transport terms along the flame surfaces gathered in the right-hand-side term $-\rho K\mathcal{Y}$. Introducing the mass burning rate $m = \rho s_{\mathrm{L}}$, the arc-length perpendicular to the flame surfaces s and the variable σ, which is a measure for the flame surface through which transport takes place (cf. figure 7.1), equation (7.10) can be written in quasi-1D form normal to the flame surfaces:

$$\frac{\partial}{\partial s}(\sigma m\mathcal{Y}) - \frac{\partial}{\partial s}\left(\sigma\frac{\lambda}{Le_{\mathcal{Y}}c_p}\frac{\partial\mathcal{Y}}{\partial s}\right) - \sigma\dot{\omega}_{\mathcal{Y}} = -\sigma\rho K\mathcal{Y}. \tag{7.11}$$

The derivative of σ is related to the curvature κ of the flame surface via

$$\kappa = \nabla\cdot\boldsymbol{n} = -\frac{1}{\sigma}\frac{\partial\sigma}{\partial s}. \tag{7.12}$$

Using this expression for κ, (7.11) becomes

$$\frac{\partial}{\partial s}(m\mathcal{Y}) - \frac{\partial}{\partial s}\left(\frac{\lambda}{Le_{\mathcal{Y}}c_p}\frac{\partial\mathcal{Y}}{\partial s}\right) - \dot{\omega}_{\mathcal{Y}} = -\rho K\mathcal{Y} + \kappa F_{\mathcal{Y}}, \tag{7.13}$$

where all perturbations from 1D flat flame behaviour are gathered at the right-hand side. In (7.13) we introduced $F_{\mathcal{Y}}$ as a short-hand notation for the convective and diffusive flux of $\mathcal{Y}$. Using similar notations for the fluxes of the species mass fractions and the enthalpy, i.e.

$$F_i = mY_i - \frac{\lambda}{Le_i c_p}\frac{\partial Y_i}{\partial s}, \tag{7.14}$$

and

$$F_h = mh - \frac{\lambda}{c_p}\frac{\partial h}{\partial s} - \frac{\lambda}{c_p}\sum_{i=1}^{N_{\mathrm{s}}}\left(\frac{1}{Le_i} - 1\right)h_i\frac{\partial Y_i}{\partial s}, \tag{7.15}$$

the full set of conservation equations can be cast in a quasi-1D form, which we refer to as the flamelet equations:

$$\frac{\partial m}{\partial s} = -\rho K + \kappa m, \tag{7.16}$$

$$\frac{\partial F_i}{\partial s} - \dot{\omega}_i = -\rho K Y_i + \kappa F_i + Q_i, \tag{7.17}$$

$$\frac{\partial F_h}{\partial s} = -\rho K h + \kappa F_h + Q_h. \tag{7.18}$$

This set of equations describes the internal structure of the flame front in terms of $Y_i(s)$, $h_i(s)$ and the mass burning rate $m(s)$ for a flamelet with a particular stretch field $K(s)$ and curvature field $\kappa(s)$. When the set (7.16)–(7.18) is solved in combination with the kinematic equation (7.1) for all flame surfaces, the full set of conservation equations for species and enthalpy is solved. The terms Q_i and Q_h describe transport along the flame surfaces, which arises because the local iso-surfaces of the variables Y_i and h generally do not coincide with iso-surfaces of $\mathcal{Y}$. The terms Q_i and Q_h are given by

$$Q_i = \rho(\boldsymbol{u}_{fi} - \boldsymbol{u}_f)\cdot\nabla Y_i + \nabla\cdot\left(\frac{\lambda}{Le_i c_p}\nabla_{||}Y_i\right), \tag{7.19}$$

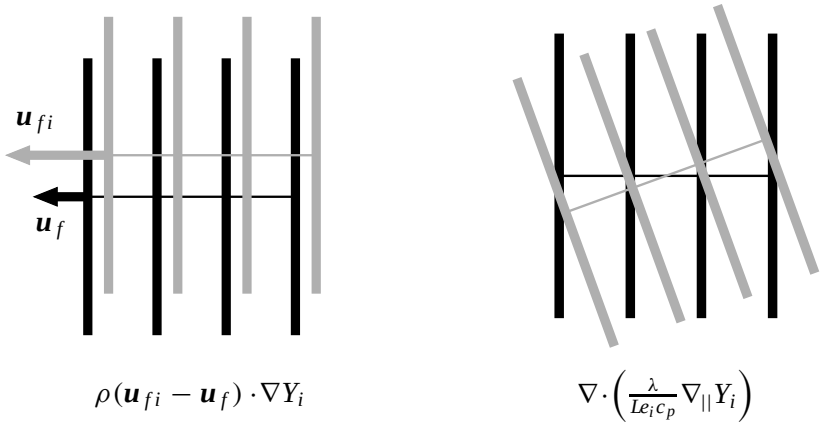

Figure 7.2: Schematic representation of the different contributions in Q_i. The black and gray lines denote iso-surfaces of $\mathcal{Y}$ and Y_i, respectively.

and

$$Q_h = \rho(\boldsymbol{u}_{fh} - \boldsymbol{u}_f) \cdot \nabla h + \nabla \cdot \left(\frac{\lambda}{c_p} \nabla_{||} h + \frac{\lambda}{c_p} \sum_{i=1}^{N_s} \left(\frac{1}{Le_i} - 1 \right) h_i \nabla_{||} Y_i \right), \tag{7.20}$$

with $\boldsymbol{u}_{fi}$ and $\boldsymbol{u}_{fh}$ the local velocities of the iso-surfaces of Y_i and h, respectively. In (7.19) and (7.20), $\nabla_{||}$ denotes the nabla operator in tangential direction only. As shown in figure 7.2, the first term on the right-hand side of (7.19) represents the relative movement of the iso-surfaces of Y_i with respect to the iso-surfaces of $\mathcal{Y}$. The second term denotes the diffusive transport of Y_i along the iso-surfaces of $\mathcal{Y}$.

So far, no approximations have been made. The set of flamelet equations (7.16)–(7.18) are found rigorously from the full set of conservation equations by using the stretch rate equation (7.7) and the kinematic equation (7.4). All perturbations from local 1D flat flame behavior are gathered in the right-hand sides of the flamelet equations. It is expected that in most situations in premixed laminar flames these perturbations are small compared to the other terms in the flamelet equations, although this might not be justified under extreme circumstances, such as near local flame quenching. The stretch terms in (7.16)–(7.18) can be neglected when the Karlovitz number is small:

$$Ka = \frac{K \delta_\mathrm{f}}{s_\mathrm{L}} \ll 1, \tag{7.21}$$

with δ_f the flame thickness. Curvature effects are negligible when the curvature radius κ^{-1} of the flame surfaces is much larger than the flame thickness:

$$|\kappa^{-1}| \gg \delta_\mathrm{f}. \tag{7.22}$$

If the transient time scales are longer than the flame time scale $\delta_\mathrm{f}/s_\mathrm{L}$, the first term in Q can be neglected as well. The second term in Q was computed numerically for the tip of a 2D Bunsen flame in [7] and it appeared to be very small. The approximation that this term is negligible, is related to the assumption that the length scales of the distortions along the flame surfaces are much larger than the flame thickness.

If all perturbations from 1D flat-flame behaviour are neglected, the following set of 1D equations remains:

$$\frac{\partial m}{\partial s} = 0, \tag{7.23}$$

$$\frac{\partial (mY_i)}{\partial s} - \frac{\partial}{\partial s}\left(\frac{\lambda}{Le_i c_p}\frac{\partial Y_i}{\partial s}\right) = \dot{\omega}_i, \qquad i = 1, \ldots, N_\mathrm{s}, \tag{7.24}$$

$$\frac{\partial (mh)}{\partial s} - \frac{\partial}{\partial s}\left(\frac{\lambda}{c_p}\frac{\partial h}{\partial s}\right) = \frac{\partial}{\partial s}\left(\frac{\lambda}{c_p}\sum_{i=1}^{N_\mathrm{s}}\left(\frac{1}{Le_i} - 1\right) h_i \frac{\partial Y_i}{\partial s}\right). \tag{7.25}$$

The balance equation (7.24) between convection, diffusion and reaction can be considered as a steady-state relation. Note that in the steady-state relations of conventional reduction techniques not only the multi-dimensional perturbations are neglected, but also the left-hand side of (7.24) describing the major parts of convection and diffusion.

The set of 1D equations (7.23)–(7.25) can be solved relatively easily with specialized 1D flame codes like CHEM1D [1]. A solution of this set of equations is called a flamelet and forms a curve in composition space, which can be regarded as a one-dimensional manifold.

3 Manifold construction

In this section it is described how the set of 1D equations (7.23)–(7.25) is used to create a manifold. As in the ILDM method a distinction is made between variables that are changed by chemical reactions (the species mass fractions Y_i) and variables that are conserved by chemical reactions (Z_j, p and h). The composition of the chemical equilibrium mixture is completely determined by the values of the conserved variables, while the combustion process from the unburnt to burnt state is described by the reactive controlling variables, which are referred to as progress variables. Following Maas and Pope [11], we first consider the case of constant conserved variables. In section 3.3 it is discussed how variations in the conserved variables should be treated.

3.1 One-dimensional manifold

In order to construct a FGM, the set of 1D flamelet equations (7.23)–(7.25) is solved treating the system as an adiabatic, freely-propagating, premixed, flat flame. This implies that the boundary conditions at the unburnt side are of Dirichlet type

$$Y_i(s \to -\infty) = Y_{i,-\infty}, \qquad h(s \to -\infty) = h_{-\infty}, \tag{7.26}$$

and at the burnt side of Neumann type

$$\frac{\mathrm{d}Y_i}{\mathrm{d}s}(s \to \infty) = 0, \qquad \frac{\mathrm{d}h}{\mathrm{d}s}(s \to \infty) = 0, \tag{7.27}$$

and that the mass burning rate m is an eigenvalue of the problem. The solution of this system is a 1D curve in composition space and is determined by its starting point $(Y_{i,-\infty}, h_{-\infty})$. The one-dimensional FGM in composition space is simply the flamelet starting at the point that represents the unburnt mixture for which the manifold is created. In this way the manifold connects the two most distinguished points in composition space: the point corresponding to the unburnt mixture $(Y_{i,-\infty}, h_{-\infty}) = (Y_{i,\mathrm{u}}, h_\mathrm{u})$ and the equilibrium point $(Y_{i,\infty}, h_\infty) = (Y_{i,\mathrm{eq}}, h_\mathrm{eq})$.

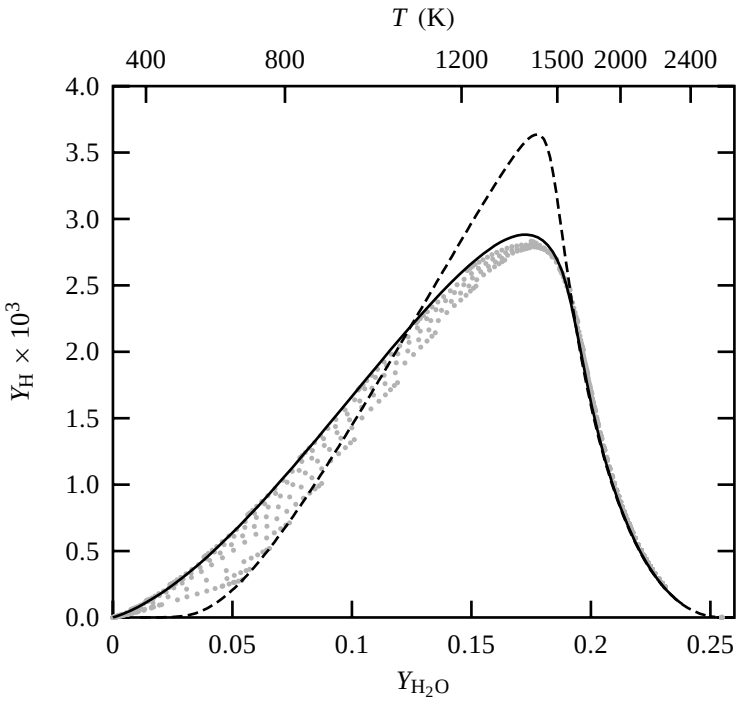

Figure 7.3: Projection of the 1D FGM (full line) and ILDM (dashed line) onto the H_2O–H plane for a stoichiometric hydrogen/air mixture. The gray dots represent the chemical state at different positions in a 2D premixed hydrogen/air flame computed with detailed chemistry. The temperatures indicated at the top axis correspond to the FGM.

As an example the one-dimensional FGM and ILDM for a stoichiometric hydrogen/air mixture are shown in figure 7.3 together with a scatter plot of the chemical state at different positions in a 2D stationary premixed Bunsen flame computed with detailed chemical kinetics. The detailed reaction mechanism is a subset of the reaction mechanism developed by Smooke [23] and includes 7 species and 7 reversible reactions. The mass fraction of atomic hydrogen Y_H is plotted as function of the mass fraction of water Y_{H_2O}, which is a suitable progress variable in this case, because it is continuously increasing in the flame from $Y_{H_2O,u} = 0$ in the unburnt mixture to the chemical equilibrium value $Y_{H_2O,eq} = 0.24$. If Y_H had been used as controlling variable, it would not have led to a unique mapping.

Generally, Lewis-number (or differential diffusion) effects cause local enthalpy and element mass fraction variations in flames and thus also in the FGM database. In the ILDM method, however, the element composition and the enthalpy of the mixture are constant throughout the manifold and variations in the conserved variables can only be accounted for by using additional controlling variables. Therefore, to make a fair comparison of the methods in figure 7.3, Lewis numbers equal to 1 have been used in the computation of both the FGM and the 2D flame so that differential diffusion effects are absent in all three cases. An example of a FGM computed with Lewis numbers unequal to 1, is presented in section 3.3.

Because the composition is determined by chemical processes in the high temperature range ($Y_{H_2O} > 0.19$, $T > 1600\,\mathrm{K}$), the ILDM and FGM are there equivalent. However, in the 'colder' zone ($Y_{H_2O} < 0.19$) diffusion processes disturb the balance between chemical production and consumption. Since the major parts of convection and diffusion are included in FGM, the FGM lies much

closer to the data of the detailed chemistry computation than the ILDM. In order to get accurate results in this region, the ILDM should be extended with additional progress variables, which decreases the numerical efficiency of the method. For this simple hydrogen reaction mechanism two progress variable will probably be enough. For more complex fuels and mechanisms many more controlling variables are needed to create an accurate ILDM. The addition of extra dimensions to the ILDM in order to satisfy accuracy requirements is described by Schmidt *et al.* [21].

The 2D Bunsen flame plotted in figure 7.3 is stabilized on a cold burner rim and is therefore locally cooled. This results in lower H radical concentrations than for the adiabatic FGM. In section 3.3 it is explained how these non-adiabatic effects can be accounted for in FGM.

3.2 Multi-dimensional manifolds

Like in the ILDM method, the accuracy of the FGM method can be enhanced by increasing the dimension of the manifold. With each additional dimension an extra progress variable, as well as the corresponding differential equation, is introduced. In this way an extra degree of freedom is added to the reduced system, which results in a more accurate description of the full system. When the dimension of the manifold is increased, a larger part of the composition space is covered. The addition of dimensions can be continued until the manifold spans the complete composition space. In that case the full system is recovered.

A 2D FGM can be constructed from a set of flamelets starting at different points on a 1D curve in composition space with constant conserved variables. This set of 1D flamelets forms a 2D surface in composition space: the 2D FGM, which can be parametrized by $N_{\mathrm{pv}} = 2$ progress variables. This method to generate multi-dimensional manifolds has been introduced by Pope and Maas [20]. A unique choice of the starting curve — manifold generator in [20] — cannot be given, although it should include the unburnt mixture and must be chosen in such a way that the resulting manifold covers an as large as possible range of the progress variables. Following these arguments Pope and Maas proposed a specification of the starting curve based on the extreme values of major species [20]. For a methane/air system a sensible choice of the major species is: CH_4, O_2, CO, H_2, CO_2, H_2O and N_2. A mixture of these major species is stable and does not react at room temperature ($\dot{\omega}_i = 0$). The other (or minor) species are taken zero at the starting curve.

The exact choice of the starting curve determines the resulting manifold, but it may not be crucial. If we assume that two controlling variables are sufficient to represent the chemical composition in a premixed flame satisfactorily, then the flamelets will rapidly relax towards a 2D attracting manifold. Therefore, however the starting points are chosen, the resulting manifold will be close to the underlying manifold except near the starting curve itself, where chemistry is negligible anyhow. This method to generate multi-dimensional manifolds can be extended to the general case of N_{pv} dimensions by choosing a $(N_{\mathrm{pv}} - 1)$-dimensional starting 'plane'.

As an example a 2D FGM is computed for a stoichiometric methane/air mixture. The projection of this manifold on the CO_2–CO plane is shown in figure 7.4. The origin of the plot corresponds to the unburnt mixture, which consists of CH_4, O_2 and N_2 only, and it is connected with the equilibrium point by the 1D manifold. The projection of the starting curve coincides with the horizontal and vertical axis in figure 7.4. Along the horizontal axis CO_2 and H_2O are added to the initial mixture, while along the vertical axis CO and H_2 are added. Along the whole starting curve the enthalpy and the element mass fractions are kept constant by changing the values of $Y_{\mathrm{CH_4}}$, $Y_{\mathrm{O_2}}$ and T, which causes all flamelets to end up in the same chemical equilibrium. The different flamelets rapidly converge to a 1D manifold, which indicates that, apart from the conserved variables, one progress variable might be enough to describe the chemical state in that region.

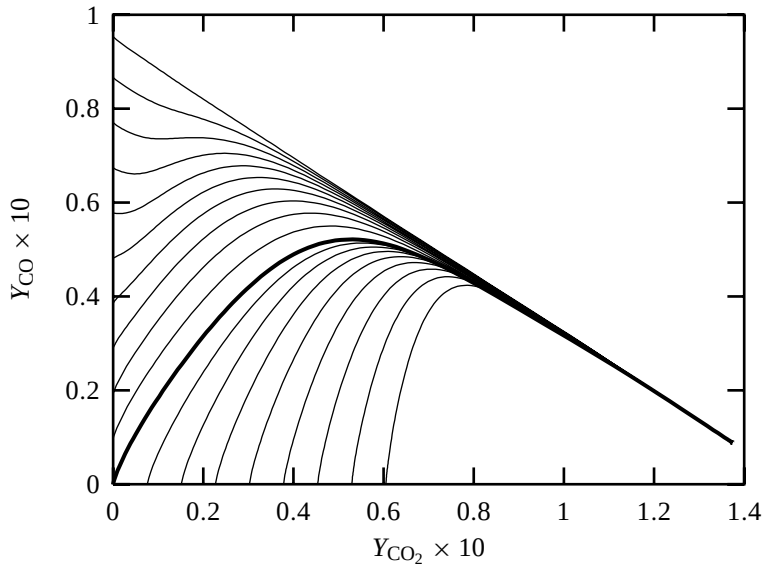

Figure 7.4: Projection of a two-dimensional FGM onto the CO_2–CO plane for a stoichiometric methane/air mixture. The bold line denotes the one-dimensional manifold.

For application in flame simulation codes, a manifold is parametrized by controlling variables. The species mass fractions or linear combinations of them can be used as controlling variables. In ILDM and FGM the selection of the controlling (or progress) variables is not related to fast or slow chemical processes as in the conventional reduction method. In fact any combination of species can be used as long as the parametrization of the manifold leads to a unique description of the mixture composition by the controlling variables. For the 1D manifold shown in figure 7.4 with a bold line, Y_{CO_2} is an appropriate controlling variable, while Y_{CO} would result in a non-unique mapping. On the other hand is Y_{CO} a suitable second controlling variable for the 2D manifold.

3.3 Conserved variables

In general, one or more of the conserved quantities p, h and Z_j might vary in space or time due to other processes than chemical reaction, e.g. mixing and cooling/heating. If variations in a conserved variable are expected to be important in the application, then this variable should be added to the manifold as an additional controlling variable. In burner-stabilized flames, e.g., the enthalpy changes due to non-adiabatic effects resulting from flame stabilization. Furthermore, cooling due to radiation or walls may cause the enthalpy to decrease. To account for these enthalpy changes, the FGM is extended with h being an additional parameter. The manifold is extended by solving the 1D flamelet equations (7.23)–(7.25) for different values of $h_{-\infty}$. Corresponding to the N_{pv}-dimensional manifold, we then obtain a $(N_{pv}+1)$-dimensional manifold parametrized by N_{pv} progress variables and one additional controlling variable h.

Changes in the other conserved variables can be treated similarly, yielding a N_{cv}-dimensional manifold with $N_{cv} = N_{pv} + N_{av}$ the total number of controlling variables and N_{av} the number of additional controlling variables. N_{av} has a maximum value of $N_e + 1$, i.e. the number of independent conserved variables. However, only a small number of additional controlling variables is needed for most applications, because in many cases several conserved variables can be assumed constant. In open systems, for instance, the pressure is constant and does not have to be used as an additional

controlling variable.

In the remaining part of this chapter we discuss the application of FGM to laminar premixed burner-stabilized flames. Since these flames are purely premixed, the element mass fractions are constant apart from local changes due to differential diffusion effects, which are included in the manifold. Because the pressure is also constant in these flames, the enthalpy is the only conserved variable in which significant changes are expected ($N_{\mathrm{av}} = 1$). Since no large multi-dimensional perturbations are expected as well, one progress variable is used ($N_{\mathrm{pv}} = 1$), resulting in a 2D manifold. As explained in section 3.2 more progress variables can be used to increase the accuracy of the method. Since this implies that more differential equations have to be solved and the look-up procedure in the database becomes more complicated, the gain in computation time will decrease. Therefore, a small number of controlling variables is preferred.

4 Application of FGM

The application of FGM in flame simulations can be divided in two parts. The first part is the pre-processing step: the generation and storage of the flamelet data. This is explained in section 4.1. The second part, described in section 4.2, considers the equations to be solved during the flame computation itself.

4.1 Storage and retrieval

The implementation of FGM in a reacting-flow code is similar to the implementation of ILDM. The low-dimensional manifold is found by solving steady-state equations in a pre-processing step and the manifold is stored in a look-up table. In the FGM method a manifold is constructed by using solutions of the 1D flamelet equations (7.23)–(7.25).

To construct a 2D manifold with enthalpy variations, a series of flamelets is computed for different values of $h_{-\infty}$ as mentioned in section 3.3. The first flamelet is solved for an initial mixture with a relatively high temperature, say $T_{-\infty,\max} = 390$ K. For the following flamelets the enthalpy is decreased by lowering the temperature of the initial mixture in steps of approximately 30 K. The 1D flamelet equations are solved by using a modified Newton method, in which the previous flamelet is used as the initial guess of the new solution. Since the difference between two succeeding flamelet solutions is small, a few iterations are sufficient to reach a converged solution. When an initial temperature of about $T_{-\infty,\min} = 240$ K is reached, another method to lower $h_{-\infty}$ is applied, because lower temperatures are not realistic. From hereon the enthalpy is decreased by converting a fraction of the initial fuel with oxygen into the products CO_2 and H_2O, keeping the element composition constant and the initial temperature at $T_{-\infty,\min}$. This process is continued until the flame temperature T_{b} becomes too low and the flame extinguishes.

This method to lower $h_{-\infty}$ is not unique and the initial mixtures could be chosen otherwise. However, as argued in section 3.2, the exact choice of the starting points is not crucial.

The resulting data set is shown in figure 7.5 for a stoichiometric methane/air mixture, where $Y_{\mathrm{O_2}}$ and h have been appointed as controlling variables. The mass fraction of oxygen is chosen as progress variable, because it is continuously decreasing in these flamelets. The progress variable is scaled using the initial and equilibrium value $Y_{\mathrm{O_2},-\infty}$ and $Y_{\mathrm{O_2,eq}}$ of the 1D manifold ($T_{-\infty} = 300$ K):

$$\mathcal{Y} = \frac{Y_{\mathrm{O_2}} - Y_{\mathrm{O_2},-\infty}}{Y_{\mathrm{O_2,eq}} - Y_{\mathrm{O_2},-\infty}}. \tag{7.28}$$

Since at low enthalpy the mass fraction of O_2 can be smaller than $Y_{\mathrm{O_2,eq}}$ at $h = h_{\mathrm{u}}$, the value of $\mathcal{Y}$ can

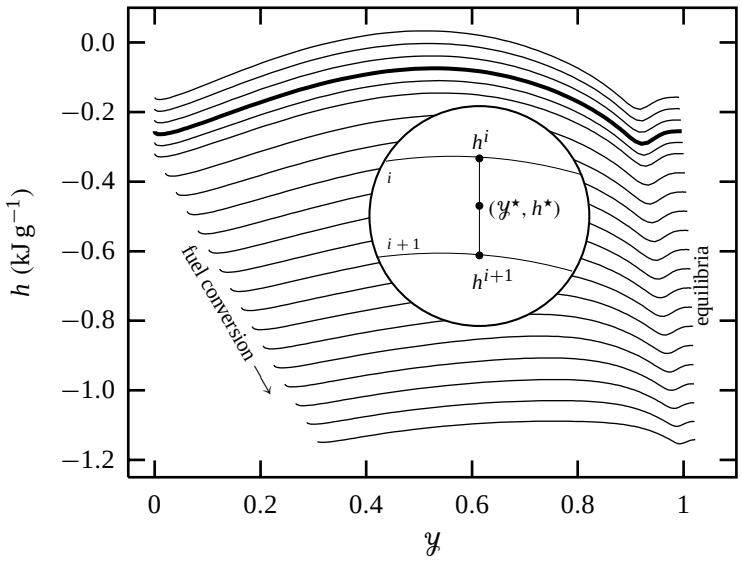

Figure 7.5: Projection of the two-dimensional FGM data set onto the $\tilde{y}$–h plane for a stoichiometric methane/air mixture. The bold curve indicates the 1D manifold. In the circle a detail of the underlying flamelets is magnified.

be larger than 1 (see figure 7.5). Because enthalpy is conserved in the flamelet equations, the initial and equilibrium value of h are the same in each flamelet. However, due to differential diffusion effects the enthalpy changes locally in the flamelets. This also holds for the element mass fractions, which are governed by a similar equation as the enthalpy. Since these local variations are included in the manifold, additional controlling variables are not needed to model differential diffusion effects, while in ILDM these changes can only be accounted for by using additional controlling variables.

In literature several techniques to store manifold data have been proposed, ranging from artificial neural networks [2] and *in situ* adaptive tabulation [19] to orthogonal polynomials [26]. The most important criteria for judging these storage techniques are the memory required for the storage of the table, the CPU time required to retrieve a value, and the accuracy of the retrieved value. In the following a method is explained which exploits the characteristics of the data set, resulting in a fast, accurate, and stable look-up procedure.

For each separate flamelet all dependent variables φ, that are needed in combustion simulations, and the enthalpy are stored as a function of the progress variable. To realize this, the $\tilde{y}$ range is divided into equal-sized regions, and a cubic polynomial is fitted to the data points in each region (see figure 7.6). The resulting fit, consisting of the separate cubic polynomials, and its first derivative are forced to be continuous at the region boundaries. In order to predict the inlet and equilibrium composition accurately, the fit matches the data set exactly at both compositions. The accuracy of the fit can be improved by increasing the number of regions or the order of the polynomials.

To retrieve data from the manifold for given values of the controlling variables the following procedure is followed. First it is determined where the entry $(\tilde{y}^\star,\ h^\star)$ is located. Therefore, the enthalpy is evaluated in two succeeding flamelets at $\tilde{y} = \tilde{y}^\star$, yielding h^i and h^{i+1} for flamelets i and $i+1$ such that $h^{i+1} < h^\star < h^i$ (cf. figure 7.5). In the next step, intermediate values for the dependent variables are evaluated in both flamelets: φ^i and φ^{i+1}. The final value $\varphi^\star$ is obtained using a linear

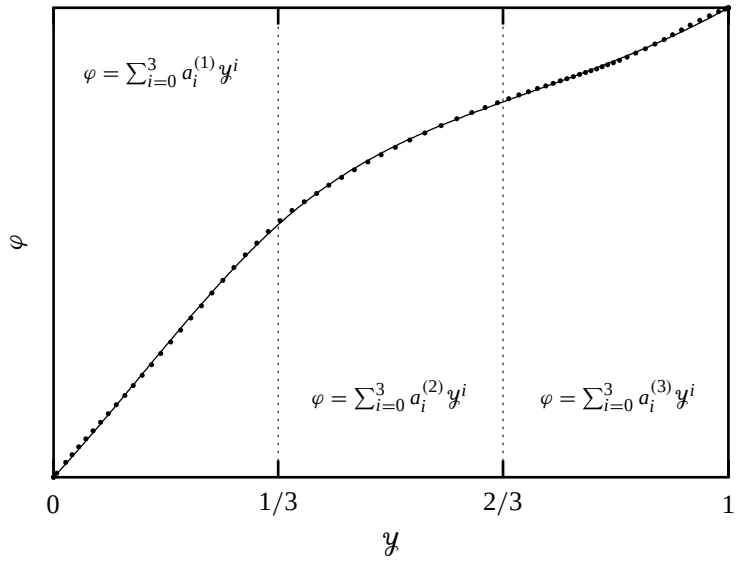

Figure 7.6: Piece-wise polynomial fit (line) to the data points (dots). In this example the $\mathcal{Y}$ range is divided in 3 regions and in each region the data is fitted with a cubic polynomial.

interpolation between these values:

$$\varphi^\star = \frac{h^\star - h^{i+1}}{h^i - h^{i+1}}\,\varphi^i + \frac{h^i - h^\star}{h^i - h^{i+1}}\,\varphi^{i+1}. \tag{7.29}$$

Due to this linear interpolation as a function of h, the first derivative of φ with respect to h is discontinuous at the flamelets, which may be a problem in gradient-based solvers. This problem can be solved by using a higher-order interpolation. However, since the dependent variables change very smoothly in the direction of h, this imperfection has no consequences in our case.

One of the main advantages of this storage technique is that the boundaries of the tabulated domain are known very accurately. Therefore, effective measures can be taken if an entry is outside this domain, resulting in a robust look-up method. Such a measure is needed, for instance, when burnt gases are cooled intensively, e.g. due to a local heat sink. The enthalpy of the mixture then drops below that of the 'coldest' flamelet, and the composition enters the so-called low-enthalpy region, shown in figure 7.7. Since no flamelet data is available there, the manifold must be continued into this region. A similar problem occurs in ILDM: at low temperatures the steady-state equations do not yield a solution and the manifold is continued into the cold region by linear extrapolation [12]. Recently, Gicquel *et al.* [5] proposed a method very similar to FGM called flame prolongation of ILDM (FPI) to tackle this problem. They prolongated the ILDM into the cold region by using the compositions in a 1D flame. Effectively, the 1D ILDM becomes exactly the same as the 1D FGM by using this prolongation technique. Application of FPI to multi-dimensional manifolds with two or more progress variables is not discussed in [5].

In FGM the manifold is prolongated into the low-enthalpy region as follows. First the low-enthalpy region is mapped onto the unit square $(\eta, \zeta) = [0, 1] \times [0, 1]$ by using

$$\eta = \frac{\mathcal{Y} - \mathcal{Y}_{-\infty}}{\mathcal{Y}_{\mathrm{eq}} - \mathcal{Y}_{-\infty}} \quad \text{and} \quad \zeta = \frac{h - h_{\min}}{h^L - h_{\min}}, \tag{7.30}$$

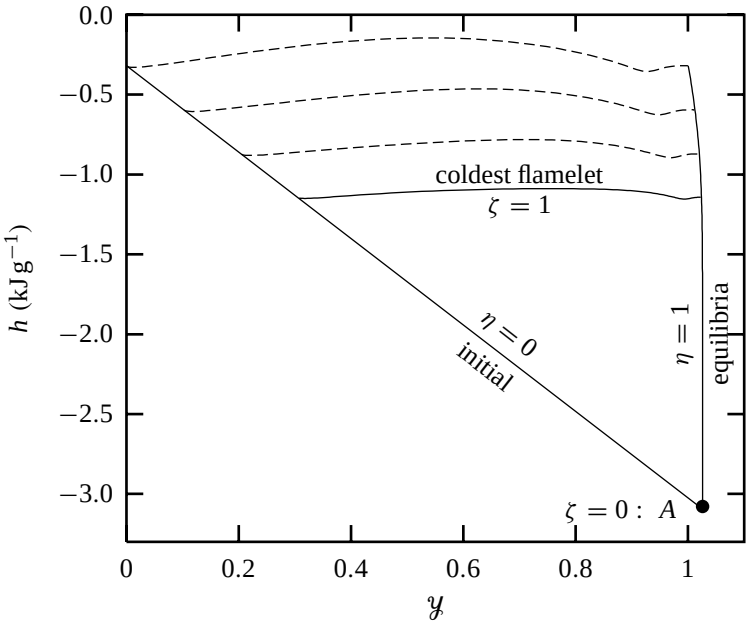

Figure 7.7: Interpolation in the low-enthalpy region.

where $h^L(\eta)$ is the enthalpy at the coldest flamelet and $h_{\min}$ the enthalpy of the chemical equilibrium with $T = T_{\min}$ (point A in figure 7.7). The profiles of the dependent variables along the coldest flamelet $\varphi(\eta, 1)$, the initial mixtures $\varphi(0, \zeta)$ and the chemical equilibria $\varphi(1, \zeta)$ are known. The values in the low-enthalpy region are approximated by interpolation using these profiles:

$$\varphi(\eta, \zeta) = \varphi(\eta, 0) + [\varphi(\eta, 1) - \varphi(\eta, 0)]\,[\eta f(\zeta) + (1 - \eta) g(\zeta)]\,, \tag{7.31}$$

with

$$f(\zeta) = \frac{\varphi(1, \zeta) - \varphi(1, 0)}{\varphi(1, 1) - \varphi(1, 0)} \quad \text{and} \quad g(\zeta) = \frac{\varphi(0, \zeta) - \varphi(0, 0)}{\varphi(0, 1) - \varphi(0, 0)}. \tag{7.32}$$

When $\varphi(1, 1) = \varphi(1, 0)$ or $\varphi(0, 1) = \varphi(0, 0)$, linear relations are used instead of (7.32), i.e. $f(\zeta) = \zeta$ and $g(\zeta) = \zeta$. Since in most practical cases extensive cooling takes place in the burnt gases after the flame front, most entries in the low-enthalpy region are very close to chemical equilibria ($\eta = 1$), where almost no interpolation error is made. Although this procedure to continue the manifold in the low-enthalpy region is rather 'ad-hoc' and might need some more attention, it appears to work quite well.

4.2 Reduced set of equations

After the FGM is stored in a database, it can be linked to a standard CFD code. This means that together with the momentum and continuity equations, the CFD code has to solve differential equations for the controlling variables. In ILDM these conservation equations for the controlling variables are derived by a projection of the full system onto the manifold. The different terms in the governing equations are projected using the left eigenvectors $\boldsymbol{s}^L_{\text{fast}}$ corresponding to the fast chemical processes [12]. Due to the definition of the ILDM, the convection and the chemical source terms remain unchanged and only the diffusion term is affected by the projection. The projection of the diffusion term in ILDM is schematically shown in figure 7.8 (*a*), where it can be seen that the diffusion term

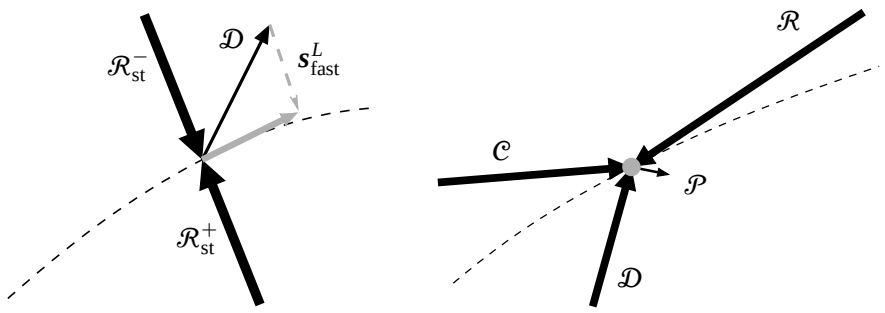

(*a*) $\mathcal{R}_{\rm st}^+ + \mathcal{R}_{\rm st}^- = 0$ (*b*) $\mathcal{C} + \mathcal{D} + \mathcal{R} = 0$

Figure 7.8: Projection of the different terms onto the manifold (dashed line) in the ILDM (*a*) and FGM (*b*) method. The different terms and their projections are represented by black and gray arrows, respectively.

$\mathcal{D}$ is restricted to the manifold due to the balance between the large chemical production $\mathcal{R}_{\rm st}^+$ and consumption $\mathcal{R}_{\rm st}^-$ terms in the steady-state relation. Since the burning velocity of premixed laminar flames is determined by a balance between reaction and diffusion, an accurate projection of the diffusion terms is important. Although the eigenvector projection is mathematically the only correct one, other (simplified) projection techniques have been used successfully [3, 4, 6].

As shown in figure 7.8 (*b*), the steady-state relations in the FGM method are given by a balance between 1D convection $\mathcal{C}$, diffusion $\mathcal{D}$ and reaction $\mathcal{R}$: $\mathcal{C} + \mathcal{D} + \mathcal{R} = 0$. The vector $\mathcal{P}$ represents the multi-dimensional perturbations in (7.17), which are projected onto the manifold by the large terms $\mathcal{C}$, $\mathcal{D}$ and $\mathcal{R}$. The main difference with ILDM is that in FGM the steady-state relations (7.24) hold for all species, effectively 'freezing' the mixture composition. Therefore, the multi-dimensional perturbations are not only projected *onto* the manifold, but *in* the manifold as well. This results in $\mathcal{P} = 0$, which is of course related to the assumption that the multi-dimensional perturbations are neglected. If a flame is extremely stretched or curved locally, the perturbations cannot be neglected and the dimension of the manifold should be increased, reducing the component of $\mathcal{P}$ perpendicular to the manifold.

Since in the FGM method all species are assumed to be in a '1D steady state', a projection of the full set of equations onto the manifold does not result in differential equations for the controlling variables like in ILDM. Therefore, ordinary conservation equations for the controlling variables $\mathcal{Y}$ and h are used in FGM. The differential equation for $\mathcal{Y}$ reads

$$\frac{\partial(\rho\mathcal{Y})}{\partial t} + \nabla\cdot(\rho\boldsymbol{u}\mathcal{Y}) - \nabla\cdot\left(\frac{\lambda}{Le_{\mathcal{Y}}c_p}\nabla\mathcal{Y}\right) = \dot{\omega}_{\mathcal{Y}}, \tag{7.33}$$

which does include the multi-dimensional perturbation for the progress variable $\mathcal{P}_{\mathcal{Y}}$. Because the multi-dimensional perturbations depend on the choice of progress variable, the final result also depends on this choice. This is not the case in ILDM if the eigenvector projection is applied. However, if the multi-dimensional perturbations are small, the differences between results computed with different progress variables will be negligible.

The conservation equation for the enthalpy is given by

$$\frac{\partial(\rho h)}{\partial t} + \nabla\cdot(\rho\boldsymbol{u}h) - \nabla\cdot\left(\frac{\lambda}{c_p}\nabla h\right) = \nabla\cdot\mathcal{H}, \tag{7.34}$$

where $\mathcal{H}$ represents the enthalpy flux due to differential diffusion:

$$\mathcal{H} = \frac{\lambda}{c_p} \sum_{i=1}^{N_s} \left(\frac{1}{Le_i} - 1 \right) h_i \nabla Y_i, \tag{7.35}$$

being a function of the species mass fraction gradients. Application of the chain rule yields

$$\mathcal{H} = \frac{\lambda}{c_p} \sum_{i=1}^{N_s} \left(\frac{1}{Le_i} - 1 \right) h_i \left(\frac{\partial Y_i}{\partial \mathcal{Y}} \nabla \mathcal{Y} + \frac{\partial Y_i}{\partial h} \nabla h \right), \tag{7.36}$$

stating that $\mathcal{H}$ depends on the gradients of $\mathcal{Y}$ and h. This may lead to unrealistic energy fluxes through inert walls, where $\frac{\partial Y_i}{\partial n} = 0$ but $\frac{\partial h}{\partial n} \neq 0$. This problem is caused by the introduction of a manifold and is thus present in all manifold techniques. In FGM this problem can be circumvented by assuming that locally the enthalpy is given by the flamelet relation $h = h^{1D}(\mathcal{Y})$, which is a function of $\mathcal{Y}$ only. This approximation is related to the assumption that locally no heat losses occur. Using this relation between h and $\mathcal{Y}$, the enthalpy flux $\mathcal{H}$ can be written as a function of the gradient of $\mathcal{Y}$ only:

$$\mathcal{H} = c \nabla \mathcal{Y}, \quad \text{with} \quad c = \frac{\lambda}{c_p} \sum_{i=1}^{N_s} \left(\frac{1}{Le_i} - 1 \right) h_i \left(\frac{\partial Y_i}{\partial \mathcal{Y}} + \frac{\partial Y_i}{\partial h} \frac{\partial h^{1D}}{\partial \mathcal{Y}} \right). \tag{7.37}$$

The coefficient c is stored in the FGM database together with the variables needed to solve the conservation equations, i.e. ρ, λ, c_p, T and $\omega_{\mathcal{Y}}$. This is obviously much more efficient and accurate than storing the species mass fractions and computing these variables at run-time.

5 Test results

To demonstrate the performance of the FGM method, two test cases of premixed laminar methane/air flames have been simulated by using a 2D manifold as presented in the previous section. Results are shown for one and two-dimensional burner-stabilized flames, and they are compared with results obtained with the reaction mechanism from Smooke [23], which consists of 16 species and 25 reversible reactions.

5.1 One-dimensional validation

Apart from numerical inaccuracies, the most elementary premixed flame – the freely propagating flat flame – should be reproduced exactly by FGM. Burner-stabilized 1D flames, however, are subjected to non-adiabatic effects due to heat losses to the burner and are therefore more challenging. The burner outflow is positioned at $x = 0$ and the burner area $x < 0$ is kept at a constant temperature of $T_{\text{burner}} = 300$ K. Stationary solutions are computed for different values of the mass burning rate m ranging from 0.05 to 0.40 $\text{kg m}^{-2}\,\text{s}^{-1}$. The adiabatic mass burning rate of this stoichiometric methane/air flame is $m = 0.421\ \text{kg m}^{-2}\,\text{s}^{-1}$, which corresponds to a laminar burning velocity of $s_L = 0.375\ \text{m s}^{-1}$. The flames are computed with the 1D flame solver CHEM1D [1] developed at the Eindhoven University of Technology. This code uses an exponential finite-volume discretization in space and the resulting system is solved using a fully implicit, modified Newton technique [24]. Adaptive gridding is implemented to increase the resolution around the flame front.

For $m = 0.30\ \text{kg m}^{-2}\,\text{s}^{-1}$ the profiles of the controlling variables Y_{O_2} and h are shown in figure 7.9. It can be seen that the results of the FGM method are in excellent agreement with those of the detailed reaction mechanism. Although the enthalpy is conserved in the flamelets that are used to construct the

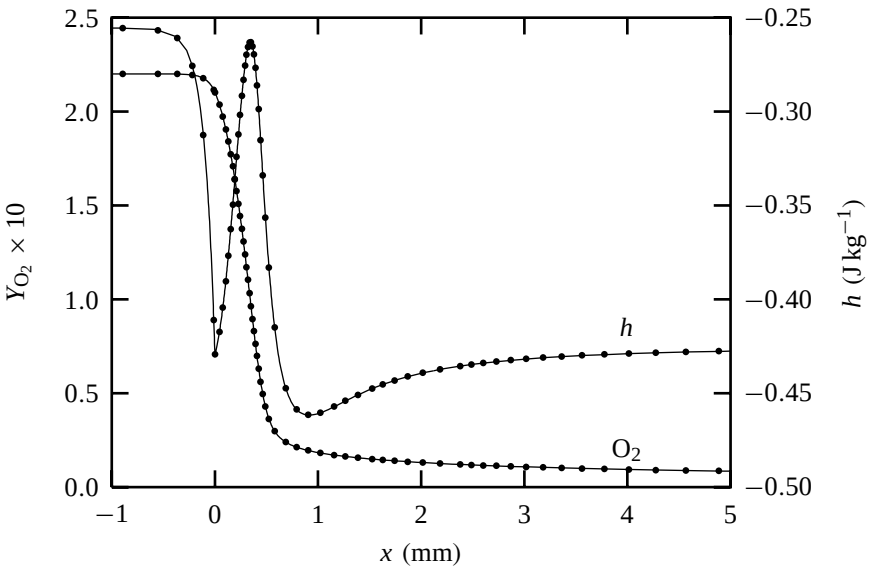

Figure 7.9: Profiles of the controlling variables Y_{O_2} and h in a one-dimensional burner-stabilized flame with $m = 0.30\ \mathrm{kg\,m^{-2}\,s^{-1}}$. Line: detailed chemistry; symbols: FGM. The symbols do not represent the computational grid; a much finer grid has been used in the calculations.

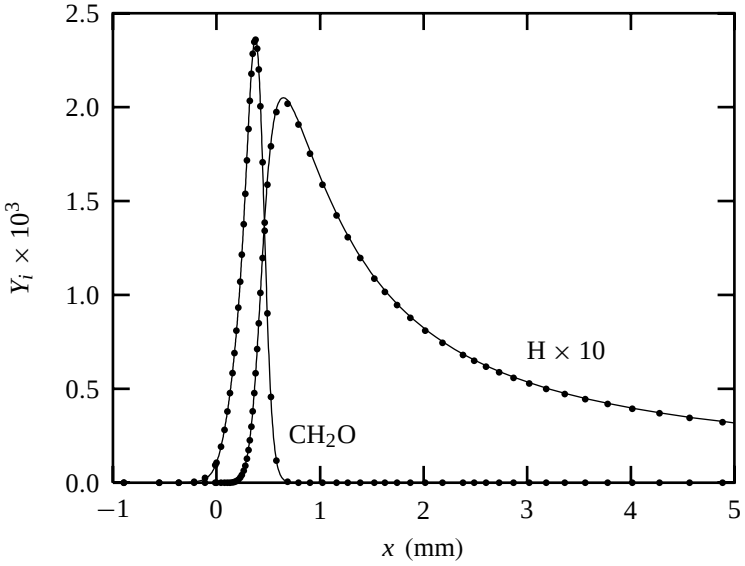

Figure 7.10: Profiles of the radicals Y_{CH_2O} and Y_H in a one-dimensional burner-stabilized flame with $m = 0.30\ \mathrm{kg\,m^{-2}\,s^{-1}}$. Line: detailed chemistry; symbols: FGM. The symbols do not represent the computational grid; a much finer grid is used in the calculations.

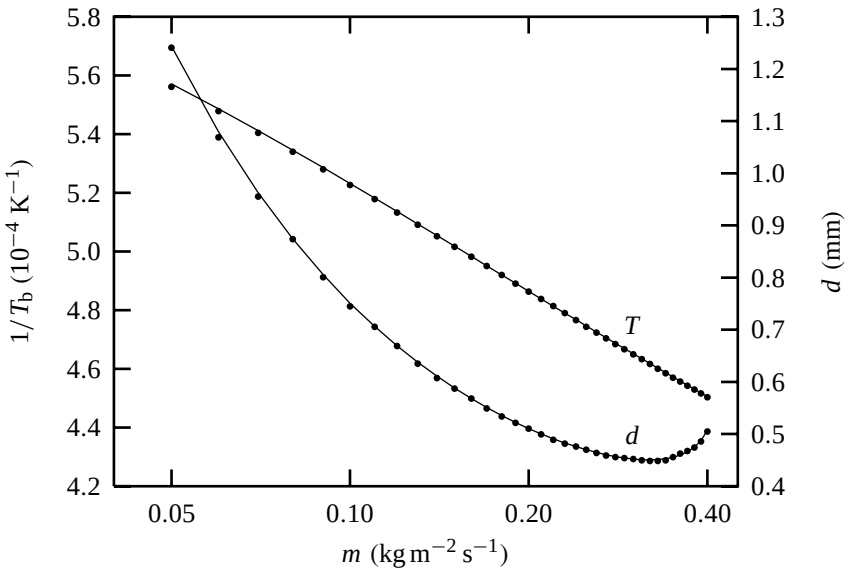

Figure 7.11: Arrhenius plot for the flame temperature T_b and the stand-off distance d as function of the mass burning rate m (log scale). Line: detailed chemistry; symbols: FGM.

manifold, the enthalpy drop due to heat losses in the burner is modelled correctly with FGM. Beside these non-adiabatic effects in the burner, the large gradients in h in the flame front due to Lewis-number effects ($0 < x < 1$ mm) are reproduced very well. The mass fractions of CH_2O and H are displayed as function of x in figure 7.10. Even for these radicals, which are very difficult to reproduce accurately using ILDM, the resemblance between the FGM and detailed results is striking.

In figure 7.11 two global observables of 1D burner-stabilized flames are presented as function of the mass burning rate. These global observables are the non-adiabatic flame temperature T_b and the stand-off distance d, here defined as the position where the absolute value of the chemical source term $|\dot{\omega}_{O_2}|$ reaches its maximum. The flame temperature is measured in the burnt mixture at $x = 10$ cm, and is presented in the form of an Arrhenius plot. The differences in the flame temperature are smaller than 5 K and, therefore, almost invisible in the figure. Although the results for the stand-off distance are somewhat poorer, the deviation is within 1 percent of the flame thickness and therefore, also hardly visible in figure 7.11. Because at low mass burning rates the deviation from an adiabatic flamelet increases, the difference between the FGM and detailed computations increases as well.

5.2 Two-dimensional validation

The potential of the FGM method is demonstrated by a calculation of a 2D burner-stabilized laminar premixed flame. In this test case almost all the features found in premixed laminar flames — such as flame cooling, differential diffusion, stretch and curvature — are present. We have simulated a methane/air flame with an equivalence ratio of $\phi = 0.9$ which stabilizes on a 2D slot burner in a box. The computational domain of the burner configuration is shown in figure 7.12. The burner slot is 6 mm wide, while the box is 24 mm wide. The burner and box walls are kept at a constant temperature of $T_{wall} = 300$ K. The velocity profile at the inlet is parabolic with a maximum velocity of $v_{max} = 1.0$ m s^{-1}.

Isocontours of T and the mass fractions of O_2, CO, H, CH_2O and O are shown in figure 7.13 on a portion of the computational domain for both the detailed and reduced chemistry computations. It can

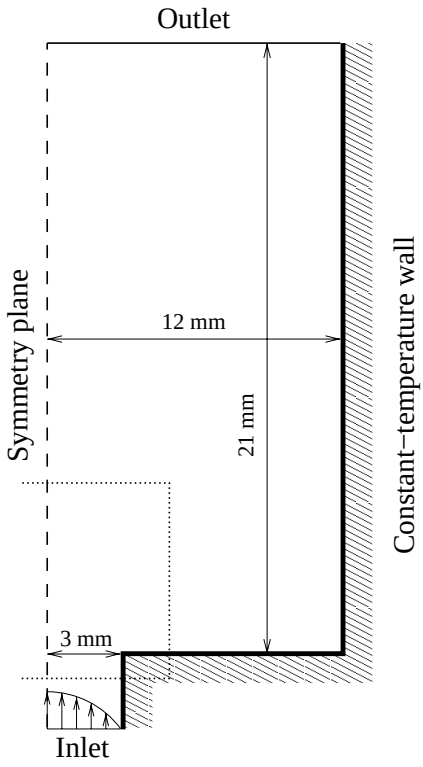

Figure 7.12: Numerical configuration used for the 2D computation. Results are shown for the region enclosed by the dotted line.

be seen that the results obtained with the FGM method are in excellent agreement with the detailed chemistry computations: not only the position of the flame front is predicted very well, but the absolute values of the mass fractions are reproduced as well. Flame cooling governing the stabilization of the flame on the burner is captured very well by FGM, although one can hardly speak of flamelets in this cold region. Also in the flame tip, where stretch and curvature are very important, the reduced chemistry computations appear to coincide with the detailed chemistry calculations. Close to the burner wall there are some differences in the Y_{CO} contours: the contours do not attach to the wall in the FGM case. Since Y_{CO} follows directly from the manifold database, which does not include diffusion along the flame front, the CO concentration is under-predicted by FGM in this diffusion-dominated area. To take this into account the manifold should be extended with a second progress variable.

The main difference between the detailed and reduced chemistry computations is the computation time. The computation with detailed chemistry took approximately two weeks to converge, while the FGM results were obtained within a few hours. These figures are only a rough indication of the gain in computation time, because different numerical solvers, grids and initial fields have been used. In the next section a more accurate study of the numerical efficiency of FGM is discussed.

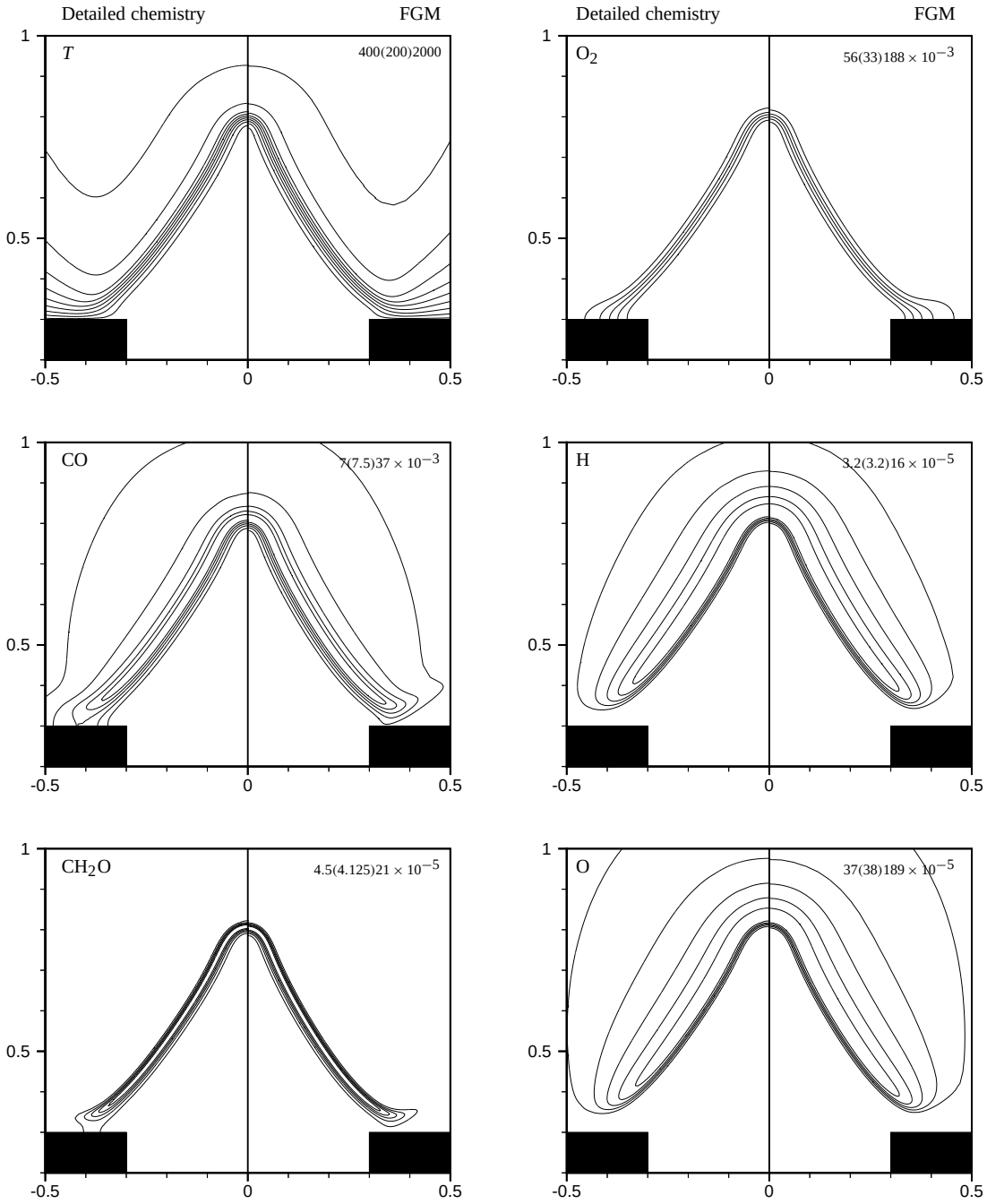

Figure 7.13: Isocontours of T, Y_{O_2}, Y_{CO}, Y_H, Y_{CH_2O} and Y_O computed using detailed chemistry (left) and FGM (right). The contours are drawn at equal intervals covering the entire range of each variable (indicated in the upper right corner of each graph). The same isolevels are used for detailed and FGM computations. The space coordinates are given in cm.

Mixture	Chemistry model		t_{step} (ms)	t_{total} (s)	Error (%)
H_2/air	Detailed	$N_s = 7$, $N_r = 7$	226	481	0
	ILDM	$N_{pv} = 1$, $N_{av} = 1$	110	63	8.63
	FGM	$N_{pv} = 1$, $N_{av} = 1$	112	62	0.08
CH_4/air	Detailed	$N_s = 16$, $N_r = 25$	657	998	0
	ILDM	$N_{pv} = 1$, $N_{av} = 1$	-	-	-
	FGM	$N_{pv} = 1$, $N_{av} = 1$	110	46	0.05
	FGM explicit	$N_{pv} = 1$, $N_{av} = 1$	9	21	0.05

Table 7.1: Results of time-dependent 1D flame simulations using different reaction models. The computation time per time step, t_{step}, the total simulation time, t_{total}, and the error (7.38) are shown.

5.3 Computational efficiency

Besides the accuracy, the efficiency is another important aspect of reduction methods. In order to give a further indication of the efficiency of FGM, the computation times of detailed and reduced chemistry simulations with ILDM and FGM are compared. For all models we determined the time needed to perform a time-dependent flame simulation at the same conditions. 1D burner-stabilized flames have been modelled for a period of 10^{-3} s. At $t = 0$ the mass flow rate has been reduced from 90% to 85% of the adiabatic mass burning rate. To solve the equations we have used the fully implicit solver CHEM1D [1] with adaptive time stepping. The FGM method has also been used with an explicit time stepper using constant time steps.

Two different mixtures are considered: a stoichiometric hydrogen/air and methane/air mixture. The hydrogen reaction mechanism contains 7 species and is a subset of the methane reaction mechanism from [23]. The manifolds used are 2D with one progress variable and the enthalpy as additional controlling variable. The same look-up procedure is used for both manifold methods. Lewis numbers equal to 1 are used in order to prevent variations in the element mass fractions. The computations are performed on a Silicon Graphics R10000 workstation and the results are shown in table 5.3.

For the hydrogen/air mixture the CPU time per time step t_{step} reduces a factor 2 when a manifold is applied. This speed up is caused by the reduction of the number of differential equations to be solved. For the detailed chemistry simulation of the methane/air mixture, t_{step} is 3 times larger than for the hydrogen/air mixture, because approximately 3 times as much differential equations and reaction rates have to be computed. For the reduced chemistry computations, however, t_{step} is independent of the number of species and reactions in the detailed reaction model. Therefore, the speed up is almost a factor 6 for the methane/air mixture. In this case the speed up is not only caused by a smaller number of equations to be solved, but by a faster evaluation of the chemical source terms as well. For the simple hydrogen mechanism with only 7 reactions, the direct computation of the chemical source term is as fast as the retrieval from the manifold database.

Another advantage of using reduced models is that larger time steps can be taken, because the smallest time scales have been eliminated. Therefore, the total CPU time t_{total} of the hydrogen/air computations using reduced chemistry is 8 times less than the detailed chemistry simulation. For the methane/air flame, the total speed up becomes a factor 20. An even higher efficiency is reached if an explicit time-integration scheme is used for the reduced chemistry computations. In that case the CPU time is reduced by almost a factor of 50 compared to the methane/air simulation using detailed chemistry. For more complex reaction mechanisms (GRI-mech: $N_s = 49$, $N_r = 279$ [22]) and multi-dimensional systems the speed up will be even larger.

Since the same storage and retrieval method is used for the ILDM and FGM computations, the

CPU times are almost the same. The results computed with the 2D FGM are, however, more accurate than the results computed with the 2D ILDM. To have an indication of the accuracy, the time evolution of the enthalpy $h(0,t)$ at the burner edge is compared with results obtained with detailed chemistry. The error is defined as the absolute difference with the enthalpy h^{det} computed with detailed chemistry averaged over the total simulation period Δt, viz.

$$\text{Error} = \frac{1}{\Delta t \, \Delta h} \int_0^{\Delta t} |h(0,t) - h^{\mathrm{det}}(0,t)| \, \mathrm{d}t. \tag{7.38}$$

The error is scaled with the total variation in the enthalpy $\Delta h = h^{\mathrm{det}}(0,0) - h^{\mathrm{det}}(0,\Delta t)$. For the hydrogen/air mixture the error in the ILDM computation is almost 9%. This error is mainly caused by the error in the adiabatic burning velocity, which is 8% too low in the ILDM case. The error of the FGM computations is smaller than 0.1% for both gas mixtures. For the methane/air mixture it is not possible to perform an ILDM computation, because an applicable 2D ILDM cannot be generated. Only in a small region around chemical equilibrium, enough chemical processes can be assumed in steady state. A 3D ILDM with two progress variables can be found for temperatures higher than 1200 K, but the accuracy is still too low and the mass burning rate is overestimated by a factor 2 [3]. Three progress variables and the enthalpy would result in a 4D manifold. Besides that these high-dimensional manifolds require a large amount of memory and are less efficient than low-dimensional manifolds.

The computation of the 2D FGM databases used in these simulations involved approximately 30 minutes, which is quite long compared to the CPU times listed in table 5.3. Obviously, it is not efficient to construct a FGM for a single 1D flame simulation. However, the computation time that can be gained by using FGM in a series of multi-dimensional flame simulations is orders of magnitude larger than the time needed to construct the database.

Another important numerical aspect of flame simulations is the computational grid. Related to the wide range of time scales, there is also a large difference in length scales in premixed laminar flames. In order to resolve the thin reaction layer, where peaks in the different radical concentrations occur (cf. figure 7.10), many grid points with fine spacing are required to get an accurate representation of the solution. When FGM is applied, these small scales do not have to be resolved, because the flame is described by the relatively slowly varying progress variable. To demonstrate this, adiabatic 1D flames have been computed on grids with a different number of grid points. In figure 7.14 the relative error in the mass burning rate is plotted as function of the number of grid points N_{p} in the flame front. The relative error is defined as $(m_{N_{\mathrm{p}}} - m)/m$, where $m_{N_{\mathrm{p}}}$ is the mass burning rate computed with N_{p} grid points in the flame front. The value of m is found by Richardson extrapolation.

The detailed chemistry and FGM results show the same behaviour: for large N_{p} the error decreases quadratically with the number of grid points, indicating that the space discretization is second order. At lower values of N_{p} the behaviour is only first order, which is typical for the discretization scheme of Thiart [25] used in the code. Because the smallest scales do not have to be resolved, the error of the FGM computations is approximately 50% smaller than detailed chemistry computations with the same number of grid points. In other words, when FGM is applied, 25 percent less grid points are required to reach the same accuracy as in the detailed chemistry computations.

6 Conclusions

In this chapter the FGM method has been introduced and it has been used to compute burner-stabilized premixed laminar flames. Since a manifold is generated by using flamelets in FGM, it can be con-

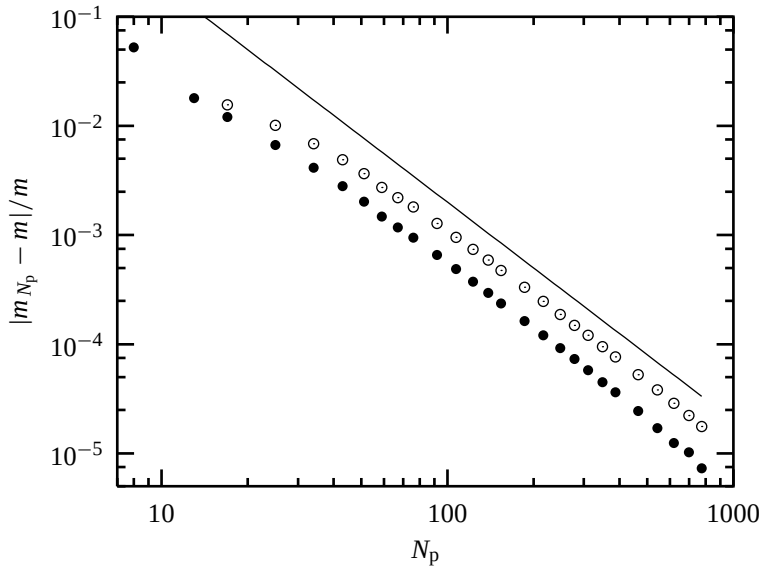

Figure 7.14: Relative error in the mass burning rate $(m_{N_p} - m)/m$ as function of the number of grid points N_p in the flame front. Open symbols: detailed chemistry; filled symbols: FGM. The line indicates a slope of -2.

sidered as a combination of a manifold and a flamelet approach. It combines the advantages of both approaches. FGM shares the basic idea with flamelet methods that a multi-dimensional flame can be regarded as a set of 1D flames. It is assumed that the structure of the flame front is similar in both types of flames and that the mixture composition is governed by a balance between 1D convection, diffusion and reaction. Since the main parts of convection and diffusion are included in the flamelet equations, the FGM is more accurate in regions where reaction is balanced by convection and diffusion than methods based on local chemical equilibria. In high-temperature regions, where chemistry is dominant, the flamelets are attracted by the ILDM and the ILDM and FGM are identical. Because FGM is more accurate in 'low'-temperature regions, less controlling variables are needed, which makes it an efficient reduction method. Test results of burner-stabilized methane/air flames show that only one progress variable apart from the enthalpy is sufficient to reproduce detailed chemistry simulations very well. A comparison with results obtained using a similar 2D ILDM is not possible, because for methane/air mixtures an ILDM with one progress variable can only be found in a small region around chemical equilibrium. This makes the application of this ILDM in flame simulations practically impossible. When two progress variables are used, a usable ILDM can be constructed. However, it overestimates the mass burning rate by a factor of two [3], which would probably result in flash-back for the 2D flame considered in this chapter, while the FGM with one progress variable predicts the correct position of the flame front.

The implementation of FGM in a flame simulation is typical for a manifold method. The reaction rates and other essential variables are stored in a database, which is used to solve the differential equations for the controlling variables. Because ordinary conservation equations are solved, the implementation in CFD codes is relatively easy compared with flamelet methods. In existing flamelet methods a kinematic equation for the scalar G is solved [16, 28]. In this so-called G-equation the burning velocity enters explicitly and the influence of flame stretch and curvature have to be modelled. Moreover, while the conservation equations for the controlling variables are valid throughout the complete domain, the G-equation is only valid at one value $G = G^0$, which denotes the position

of the flame sheet. Everywhere else G is simply defined as the distance to the flame sheet ($|\nabla G| = 1$), resulting in a flame of constant thickness. In FGM the flame thickness is in general not constant and, as the burning velocity, it follows from the conservation equations for the controlling variables. A disadvantage of solving conservation equations for the controlling variables, however, is that the flame front needs to be resolved. This requires a large number of grid points compared to flamelet methods which do not have to resolve the internal structure of the flame front.

An advantage of FGM is that the number of progress variables is not limited to one as in existing flamelet approaches. Although the test results show that one progress variable and the enthalpy are sufficient to reproduce detailed chemistry simulations very well, more progress variables can be added to increase the accuracy of the method. Addition of progress variables might cause problems in the look-up procedure as described in section 4.1, because the different flamelets converge to form a lower-dimensional manifold (cf. figure 7.4). However, this problem can be solved by using a modified look-up technique. When the difference between the flamelets is too small (and the dimension of the manifold has actually decreases locally), the values are retrieved from the flamelet(s) in the lower-dimensional manifold.

A disadvantage of FGM compared to ILDM is that a general procedure to create multi-dimensional manifolds cannot be derived. Since the researcher has to determine the starting points of the flamelets, the construction of a FGM cannot be automated to the same degree as that of an ILDM, where only the dimension of the manifold has to be prescribed by the researcher.

The test results presented in this lecture demonstrate the enormous potential of FGM. Results of computations with detailed chemistry have been reproduced very accurately within a fraction of the computation time. Since a FGM with one progress variable reaches the same accuracy for a methane/air flame as an ILDM with at least 3 dimensions, the dimension of the look-up database can be low. This not only reduces the computation time, but it also makes the numerical implementation relatively easy. The implementation of FGM in CFX-4 made it possible to simulate the combustion process in a realistic furnace [14] including radiation.

A detailed investigation of the effects of the multi-dimensional perturbations on the accuracy of FGM is given by Van Oijen [13]. The influence of flame stretch and the deviations from purely premixed behaviour are studied systematically in [13].

References

[1] CHEM1D, A one-dimensional laminar flame code, Eindhoven University of Technology `http://www.combustion.tue.nl/chem1d`

[2] Christo F.C., Masri A.R. and Nebot E.M., Artificial neural network implementation of chemistry with pdf simulation of H_2/CO_2 flames, *Combust. Flame* 106:406–427 (1996)

[3] Eggels R.L.G.M., *Modelling of Combustion Processes and NO Formation with Reduced Reaction Mechanisms*, Ph.D. thesis, Eindhoven University of Technology (1996)

[4] Eggels R.L.G.M. and de Goey L.P.H., Mathematically reduced reaction mechanisms applied to adiabatic flat hydrogen/air flames, *Combust. Flame* 100:559–570 (1995)

[5] Gicquel O., Darabiha N. and Thévenin D., Laminar premixed hydrogen/air counterflow flame simulations using flame prolongation of ILDM with differential diffusion, *Proc. Combust. Inst.* 28:1901–1908 (2000)

[6] Gicquel O., Thévenin D., Hilka M. and Darabiha N., Direct numerical simulations of turbulent premixed flames using intrinsic low-dimensional manifolds, *Combust. Theory Modelling* 3:479–502 (1999)

[7] de Goey L.P.H., Mallens R.M.M. and ten Thije Boonkkamp J.H.M., An evaluation of different contributions to flame stretch for stationary premixed flames, *Combust. Flame* 110:54–66 (1997)

[8] de Goey L.P.H. and ten Thije Boonkkamp J.H.M., A mass-based definition of flame stretch with finite thickness, *Combust. Sci. Technol.* 122:399–405 (1997)

[9] de Goey L.P.H. and ten Thije Boonkkamp J.H.M., A flamelet description of premixed laminar flames and the relation with flame stretch, *Combust. Flame* 119:253–271 (1999)

[10] Lam S.H. and Goussis D.A., Conventional asymptotics and computational singular perturbation for simplified kinetics modeling, in *Reduced kinetic mechanisms and asymptotic approximations for methane-air flames*, edited by M.D. Smooke, pp. 227–242, Springer Verlag, Berlin (1991)

[11] Maas U. and Pope S.B., Simplifying chemical kinetics: Intrinsic low-dimensional manifolds in composition space, *Combust. Flame* 88:239–264 (1992)

[12] Maas U. and Pope S.B., Laminar flame calculations using simplified chemical kinetics based on intrinsic low-dimensional manifolds, *Proc. Combust. Inst.* 25:1349–1356 (1994)

[13] van Oijen J.A., *Flamelet-Generated Manifolds: Development and Application to Premixed Laminar Flames*, Ph.D. thesis, Eindhoven University of Technology (2002)

[14] van Oijen J.A., Lammers F.A. and de Goey L.P.H., Modelling of complex premixed burner systems using flamelet-generated manifolds, *Combust. Flame* 127:2124–2134 (2001)

[15] Peters N., Laminar flamelet concepts in turbulent combustion, *Proc. Combust. Inst.* 21:1231–1250 (1986)

[16] Peters N., *Turbulent Combustion*, Cambridge University Press, Cambridge (2000)

[17] Peters N. and Rogg B. (editors), *Reduced kinetic mechanisms for applications in combustion systems*, Springer Verlag, Berlin (1993)

[18] Peters N. and Williams F.A., Asymptotic structure of stoichiometric methane-air flames, *Combust. Flame* 68:185–207 (1987)

[19] Pope S.B., Computationally efficient implementation of combustion chemistry using *in situ* adaptive tabulation, *Combust. Theory Modelling* 1:41–63 (1997)

[20] Pope S.B. and Maas U., *Simplifying Chemical Kinetics: Trajectory-Generated Low-Dimensional Manifolds*, Technical Report FDA 93-11, Cornell University (1993)

[21] Schmidt D., Blasenbrey T. and Maas U., Intrinsic low-dimensional manifolds of strained and unstrained flames, *Combust. Theory Modelling* 2:135–152 (1999)

[22] Smith G.P., Golden D.M., Frenklach M., Moriarty N.W., Eiteneer B., Goldenberg M., Bowman C.T., Hanson R.K., Song S., Gardiner Jr. W.C., Lissianski V.V. and Qin Z. `http://www.me.berkeley.edu/gri_mech/`

[23] Smooke M.D. and Giovangigli V., Formulation of the premixed and nonpremixed test problems, in *Reduced kinetic mechanisms and asymptotic approximations for methane-air flames*, edited by M.D. Smooke, pp. 1–28, Springer Verlag, Berlin (1991)

[24] Somers L.M.T., *The Simulation of Flat Flames with Detailed and Reduced Chemical Models*, Ph.D. thesis, Eindhoven University of Technology (1994)

[25] Thiart G.D., Finite difference scheme for the numerical solution of fluid flow and heat transfer problems on nonstaggerd grids, *Num. Heat Transfer, Part B* 17:41–62 (1990)

[26] Turanyi T., Parameterization of reaction mechanisms using orthogonal polynomials, *Comp. Chem.* 18:45–54 (1994)

[27] Warnatz J., Resolution of gas phase and surface combustion chemistry into elementary reactions, *Proc. Combust. Inst.* 24:553–579 (1992)

[28] Williams F.A., *Combustion Theory*, Addison-Wesley Publishing Company, Redwood city (1985)

[29] Williams F.A., Turbulent combustion, in *The Mathematics of Combustion*, edited by J. Buckmaster, pp. 97–131, Society for Industrial and Applied Mathematics, Philadelphia (1985)

Part 3

Turbulent Non-Premixed Combustion

Chapter 8

Introduction to turbulent combustion

D. Roekaerts

1 Overview

1.1 Practical importance

Turbulent combustion is of interest both because of its practical importance and because the fundamental scientific questions it raises. Some practical systems in which turbulent combustion takes place are furnaces, gas turbines, internal combustion engines and flares. The interest of society in an economic, clean and safe operation of these devices is an important driving force for the development of experimental techniques and models to acquire good understanding of turbulent combustion. Such understanding is needed in the design of systems producing minimal environmentally harmful emissions. For example, the strong dependence of nitric oxide (NO_x) formation on temperature has made it necessary to gain a better understanding of temperature fluctuations and their influence on mean chemical reaction rates. Apart from this, the global environmental effect by combustion products (CO_2) provides a drive towards more efficient and integrated combustion processes using fuels with a low C/H ratio.

On the other hand, description and prediction of phenomena in a turbulent reacting flow is also challenging from academic point of view. The combination of non-linear fluid dynamics with non-linear kinetics, causes very complex phenomena. Combustion in laminar flames is already complex due to the combination of complex diffusion properties and complex kinetics with a wide range of chemical time and length scales. But turbulence adds to this the complexity of a wide range of time and length scales in flow phenomena and makes the need for effective simplified models even stronger. Here 'simplified' in the first place refers to the fact that an incomplete and approximate picture of the phenomena is given. The model itself may in fact have a quite complex appearance. Different models are developed for different types of flames, e.g. turbulent premixed gaseous flames, turbulent non-premixed gaseous flames (also called turbulent diffusion flames) and spray flames. These notes only address gaseous combustion, with most emphasis on non-premixed flames.

1.2 Computational methods

The physical and chemical phenomena in turbulent flames are described by the transport equations for momentum, energy and mass fractions of all species, thermodynamic equations of state and expressions for kinetic rates and physical properties (viscosity, diffusivity). Solving this system of equations, resolving all details of the flow is called direct numerical simulation (DNS). This does not necessarily imply that all features of combustion are resolved. DNS studies often use simplified physical properties and kinetic rates, or neglect density changes by heat release.

The physical and chemical complexity of a turbulent reacting flow is most compactly characterised by the Reynolds number Re and the Damköhler number Da. The Reynolds number characterises the extent of the turbulent energy cascade. The ratio of sizes of large and small eddies scales as $Re^{0.75}$, the ratio of the time scale of large and small eddies scales as $Re^{0.5}$. The Damköhler number is the quotient of a characteristic time scale of turbulence (in combustion studies most often taken as the large scale) and a characteristic time scale of chemical reaction. Small Da corresponds to slow reactions and large Da to fast reactions. The complexity of the flow increases with Re and Da and only flows with sufficiently low Re and Da can be calculated using DNS. (The special case of sufficiently low Re and infinitely high Da can also be handled). Nevertheless DNS is a useful tool to come to fundamental understanding and also to produce data sets that can be used for the validation of models.

When considering models for turbulent flows one can distinguish between traditional turbulence models calculating a set of mean values (Reynolds Averaged Navier-Stokes model, RANS) and a more detailed approach calculating all structures in the flow larger than a certain limiting scale (Large-eddy simulation model, LES). RANS modelling is a well-established approach, implemented in many commercially available Computational Fluid Dynamics (CFD) codes. Because LES uses more generally valid assumptions and becomes more and more feasible with the increase in available computer power, it is expected that LES will also be more and more used in practical applications.

In RANS studies one considers the turbulent flow from a statistical point of view and then restricts the description to a subset of all statistical properties, e.g. in the simplest case only the mean value and variance of velocity and concentrations. The mean values that are considered can be time-averages or ensemble-averages depending on the situation. When not only average and standard deviation but the complete set of statistical properties at a point in space is considered the method is called Probability Density Function (PDF) method. In LES the evolution in time and space of a turbulent flow is calculated in such a way that all flow details which are larger in space than a certain given (filter) size are resolved. All smaller scales are only implicitly taken into account. In both classes some properties are not explicitly calculated, in the first class these are statistical properties such as correlations between variables at different position in space, in the second class this concerns small-scale or subgrid motions. Therefore, in both classes some assumptions are needed before a closed set of model equations is obtained: this situation is known as the turbulence closure problem.

In the case of RANS of turbulent reacting flow, chemical reaction terms represent a severe closure problem, because the mean chemical reaction rate cannot be expressed as a function of mean temperature and mean concentrations. The role of turbulent fluctuations can not be neglected. Different solutions to this problem have been proposed in the literature [3, 4, 5].

A very general method is that in which the joint probability density function (PDF) of scalars quantities (mass fractions and enthalpy, or a suitable subset based on reasonable approximations) is computed with the help of Lagrangian methods. Lagrangian methods solve evolution equations for properties of fluid elements (position, velocity, temperature, chemical composition, etc.) in contrast to Eulerian methods which solve transport equations for mass, momentum, energy and species. Many of these evolution equations are stochastic ordinary differential equations, for which special solution techniques have been developed. The essential advantage of Lagrangian methods compared to Eulerian methods, is that they do not have a turbulence closure problem related to chemical reaction. This follows from the fact that chemical reaction is a local process and the fluid elements used in the Lagrangian simulation each contain a complete description of a the local conditions [6, 7, 3, 4].

Also in LES, the chemical reaction term gives a closure problem. The resolved reaction rate, appearing in the Eulerian transport equation for the resolved concentrations, cannot be expressed in terms of the resolved concentration and temperature fields. The analogue in LES of the observation made in RANS that fluctuations influence the mean reaction rate, is that in this case subgrid scale

fluctuations influence the mean reaction rate. The analogue of the PDF approach in the context of LES then is a probability density function representing the relative occurrence of values of physical quantities on the sub grid scale. Such a density is called filtered density function (FDF), referring to the LES approach of calculating only phenomena at scales larger than a given filter scale [8]). In the combination of LES and FDF, phenomena on scales larger than the filter scale are explicitly calculated and the phenomena on smaller scales are represented in a statistical sense using the filtered density function. The FDF can be obtained by Lagrangian simulation in a similar way as the PDF.

Because combustion involves a lot of chemical species and reactions, successful modelling depends on the ability to select the most relevant thermo-chemical variables as independent scalars, for which full transport equations have to be solved, and keeping the other variables as dependent scalars. For non-premixed flames the primary variable is the *mixture fraction*, which characterises the mixing of fuel and oxidiser. For premixed flames it is the *progress variable*, which characterises the evolution from cold reactants to hot products. Selecting them as independent scalars, in both cases the profiles of dependent variables versus independent scalar are obtained from assumptions. E.g. in flamelet modeling they are obtained from the calculation of a laminar flame. We shall return to this in section 5.

In the following, first an introduction will be given to the statistical description of turbulence. To start, instantaneous conservation equations are considered because they provide the basis for the averaged equations and also for the transport equation satisfied by the probability density function. Next some basic concepts from statistics are considered. Finally the mean conservation equations are introduced and a discussion of the main closure problems and their possible solution in terms of second moment equations, PDF's, and fast chemistry models are given. Further information can be found in the literature [1, 2, 6, 9, 3, 4, 5].

2 Instantaneous conservation equations

Conservation of mass is expressed by the continuity equation:

$$\frac{\partial \rho}{\partial t} + \frac{\partial \rho U_i}{\partial x_i} = 0 \tag{8.1}$$

conservation of momentum (here in the absence of external forces) by the Navier-Stokes equation:

$$\frac{\partial}{\partial t}\rho U_i + \frac{\partial}{\partial x_j}\rho U_j U_i = -\frac{\partial p}{\partial x_i} - \frac{\partial}{\partial x_j} T_{ij} \tag{8.2}$$

in which p is pressure and T_{ij} the viscous stress tensor. For a Newtonian fluid the viscous stress tensor contains only simple shear effects and can be written as:

$$T_{ij} = -\mu\left(\frac{\partial U_i}{\partial x_j} + \frac{\partial U_j}{\partial x_i}\right) + \tfrac{2}{3}\mu\frac{\partial U_k}{\partial x_k}\delta_{ij} \tag{8.3}$$

in which μ is the dynamic viscosity.

The conservation equations for species mass fractions, denoted here by the scalar vector $\boldsymbol{\phi}$, read:

$$\frac{\partial}{\partial t}\rho\phi_\alpha + \frac{\partial}{\partial x_j}\rho U_j\phi_\alpha = -\frac{\partial}{\partial x_j} J_j^\alpha + \rho S_\alpha(\boldsymbol{\phi}) \tag{8.4}$$

where J_j^α is the diffusion flux and S_α is a chemical reaction source term. Neglecting effects of thermal diffusion and external body forces and assuming Fickian diffusion, the flux reads:

$$J_j^\alpha = -\rho\mathbb{D}\frac{\partial \phi_\alpha}{\partial x_j} \tag{8.5}$$

in which $\mathbb{D}$ is the mass diffusion coefficient which here for simplicity is assumed to be equal for all species. The enthalpy conservation equation which in general is also needed, is also of the form 8.4 with the enthalpy source term in particular containing effects of radiative heat transfer. The description is completed with the thermodynamic equation of state and the caloric equation of state (relating enthalpy and composition to temperature).

3 Basic definitions from statistics

3.1 One-point statistics

Consider the variable ϕ which is a function of space $\boldsymbol{x}$ and time t (denoted by $\phi(\boldsymbol{x}, t)$). The distribution function F of ϕ is defined as:

$$F_\phi(\psi; \boldsymbol{x}, t) \equiv \boldsymbol{P}\{\phi(\boldsymbol{x}, t) < \psi\} \tag{8.6}$$

in which ψ is the sample space variable of ϕ which takes all possible values of ϕ and $\boldsymbol{P}\{...\}$ stands for the probability that the field value ϕ at $(\boldsymbol{x}, t)$ is smaller than ψ. The *probability density function* (PDF) is defined as:

$$f_\phi(\psi; \boldsymbol{x}, t) = \frac{\partial}{\partial \psi} F_\phi(\psi; \boldsymbol{x}, t) \tag{8.7}$$

The probability that a realization of $\phi(\boldsymbol{x}, t)$ lies between ψ_1 and ψ_2 is given by:

$$\boldsymbol{P}\{\psi_1 < \phi(\boldsymbol{x}, t) < \psi_2\} = \int_{\psi_1}^{\psi_2} f_\phi(\psi; \boldsymbol{x}, t)\mathrm{d}t = F_\phi(\psi_2; \boldsymbol{x}, t) - F_\phi(\psi_1; \boldsymbol{x}, t) \tag{8.8}$$

The end values of F are appropriately defined as $F(-\infty) = 0$ and $F(+\infty) = 1$. Field values and probability functions in general are considered to be functions of space and time but to simplify the notation the variables $\boldsymbol{x}$ and t are often omitted without further notification.

The *average* or *expectation* of ϕ is denoted by $\boldsymbol{E}\{\phi\}$, $\langle\phi\rangle$, or by $\overline{\phi}$ and can be expressed in terms of the PDF by:

$$\langle\phi\rangle = \int_{-\infty}^{+\infty} \psi f_\phi(\psi)\mathrm{d}\psi \tag{8.9}$$

In the same way, the expectation of any function Q of ϕ can be defined by:

$$\langle Q\rangle = \int_{-\infty}^{+\infty} Q(\psi) f_\phi(\psi)\mathrm{d}\psi \tag{8.10}$$

With the definition of the *ensemble average* or *Reynolds average* the variable ϕ can be decomposed into its mean $\langle\phi\rangle$ and fluctuation ϕ' according to:

$$\phi = \langle\phi\rangle + \phi' \tag{8.11}$$

To clarify the notion of one-point statistics further, an example of two-point statistics is given. Consider the two-point one-time statistics of the field variable $\phi(\boldsymbol{x}, t)$ defined by $F_\phi(\psi_1, \psi_2; \boldsymbol{x}, \boldsymbol{x} + \boldsymbol{r}, t)$ which describes the probability that $\phi(\boldsymbol{x}, t) < \psi_1$, *and* $\phi(\boldsymbol{x}+\boldsymbol{r}, t) < \psi_2$. This function cannot be expressed in terms of the one-point statistics of ϕ. In the limit of $|\boldsymbol{r}| \to 0$ this description reduces to the combined statistics of ϕ and its gradients. This means that gradient statistics cannot be described in terms of the one-point statistics of a variable and that such terms are unclosed in any one-point closure.

3.2 Joint probabilities

We now consider combined statistics of several variables (e.g. velocities and species concentrations). This provides information about correlations between variables.

Consider the n stochastic variables $\boldsymbol{\phi} = \phi_1, \phi_2, ... \phi_n$ which have a *joint* probability function defined by:

$$F_{\boldsymbol{\phi}}(\boldsymbol{\psi}) \equiv \boldsymbol{P}\{\phi_1 < \psi_1, \phi_2 < \psi_2, ... \phi_n < \psi_n\} \tag{8.12}$$

The joint PDF is defined by:

$$f_{\boldsymbol{\phi}}(\boldsymbol{\psi}) = \frac{\partial^n}{\partial\psi_1\partial\psi_2 ... \partial\psi_n} F_{\boldsymbol{\phi}}(\boldsymbol{\psi}) \tag{8.13}$$

From the joint PDF of $\boldsymbol{\phi}$ the statistics of one variable ϕ_α can be obtained by integration over the other $n-1$ directions of the $\boldsymbol{\psi}$ space:

$$f_{\phi_\alpha}(\psi_\alpha) = \int_{-\infty}^{+\infty} ... \int_{-\infty}^{+\infty} f_{\boldsymbol{\phi}}(\boldsymbol{\psi})\, \mathrm{d}\psi_1 ... \mathrm{d}\psi_{\alpha-1}\mathrm{d}\psi_{\alpha+1} ... \mathrm{d}\psi_n \tag{8.14}$$

This one-variable PDF is also called the *marginal* PDF of ϕ_α. As in the univariate case (see equation (8.10)) the expectation of any function of the variables ϕ_i can be expressed as an integral over the phase space of this function times the joint PDF.

3.3 Conditional probability

The conditional probability $\boldsymbol{P}\{\boldsymbol{A}|\boldsymbol{B}\}$ is defined as the probability that $\boldsymbol{A}$ occurs given that $\boldsymbol{B}$ occurs, and is given by:

$$\boldsymbol{P}\{\boldsymbol{A}|\boldsymbol{B}\} = \frac{\boldsymbol{P}\{\boldsymbol{A}, \boldsymbol{B}\}}{\boldsymbol{P}\{\boldsymbol{B}\}} \tag{8.15}$$

In the same manner the conditional PDF of $\phi_1|\phi_2$ can be defined as:

$$f_{\phi_1|\phi_2}(\psi_1|\psi_2) = \frac{f_{\phi_1,\phi_2}(\psi_1, \psi_2)}{f_{\phi_2}(\psi_2)} \tag{8.16}$$

The expression $f_{\phi_1|\phi_2}(\psi_1|\psi_2)\mathrm{d}\psi_2$ now defines the PDF of ϕ_1 given the fact that $\psi_2 < \phi_2 < \psi_2 + \mathrm{d}\psi_2$.

Conditional statistics are an important concept in PDF modeling. It turns out that all unclosed terms in the PDF equations can be written in terms of conditional averages (e.g. of the fluctuating velocity given a value of the scalar). In other words, these terms can in general not be expressed as a pure function of the describing variables. These *conditional averages* $\langle Q(\phi_1, \phi_2)|\phi_2 = \psi_2\rangle$ can be written in terms of the conditional PDF $f_{\phi_1|\phi_2}$ by:

$$\langle Q(\phi_1, \phi_2)|\phi_2 = \psi_2\rangle = \int_{-\infty}^{+\infty} Q(\psi_1, \psi_2)\, f_{\phi_1|\phi_2}(\psi_1|\psi_2)\mathrm{d}\psi_1 \tag{8.17}$$

3.4 Favre averaging

In turbulent flames, density can vary by a factor of five or more and density fluctuations can have large effects on the turbulent flow field. To simplify the equations describing variable density flow it is common to use density-weighted (Favre) averaging.

Let the density be denoted as ρ, and let the vector $\boldsymbol{\phi}$ denote the thermo-chemical scalar variables (e.g. species concentrations, temperature). In the low Mach-number limit, where it is assumed that pressure variation does not affect the density, the density is a pure function of the scalar vector $\boldsymbol{\phi}$.

Favre averages are defined by:

$$\widetilde{Q} = \frac{\langle \rho Q \rangle}{\langle \rho \rangle} \tag{8.18}$$

and Favre-decomposition into mean and fluctuation is defined as:

$$Q = \widetilde{Q} + Q'' \tag{8.19}$$

in which Q'' denotes the Favre-fluctuation. Note that with the definition of Favre- and Reynolds averages and fluctuations:

$$\widetilde{Q''} = 0 \qquad\qquad \overline{Q'} = 0$$

and in general:

$$\widetilde{Q'} \neq 0 \qquad\qquad \overline{Q''} \neq 0$$

It is also useful to define the Favre-probability density function by:

$$\widetilde{f}_{\boldsymbol{\phi}}(\boldsymbol{\psi}) = f_{\boldsymbol{\phi}}(\boldsymbol{\psi}) \frac{\langle \rho | \boldsymbol{\phi} = \boldsymbol{\psi} \rangle}{\langle \rho \rangle} = f_{\boldsymbol{\phi}}(\boldsymbol{\psi}) \frac{\rho(\boldsymbol{\psi})}{\langle \rho \rangle} \tag{8.20}$$

Because the density is a pure function of the scalar space variables, the conditional average reduces to a function in $\boldsymbol{\psi}$ and the second equality holds. Favre-averages can be expressed in terms of the Favre-PDF according to:

$$\widetilde{Q}(\boldsymbol{\phi}) = \int_{-\infty}^{+\infty} Q(\boldsymbol{\psi})\, \widetilde{f}_{\boldsymbol{\phi}}(\boldsymbol{\psi}) \mathrm{d}\boldsymbol{\psi} \tag{8.21}$$

The Favre-PDF has the same properties as a standard probability density function and all properties discussed in the previous sections (multivariate statistics, conditional statistics) can be applied in a straightforward manner.

4 Averaged equations

By averaging the flow equations a set of equations describing the mean flow properties is obtained. Defining:

$$\frac{\mathrm{D}}{\mathrm{D}t} = \frac{\partial}{\partial t} + \widetilde{U}_i \frac{\partial}{\partial x_i} \tag{8.22}$$

and Favre-averaging the momentum and species equations (8.2) and (8.4) gives:

$$\langle \rho \rangle \frac{\mathrm{D}}{\mathrm{D}t} \widetilde{U}_i = -\frac{\partial \langle p \rangle}{\partial x_i} - \frac{\partial}{\partial x_j} \langle T_{ij} \rangle - \frac{\partial}{\partial x_j} \langle \rho \rangle \widetilde{u_j'' u_i''} \tag{8.23}$$

$$\langle \rho \rangle \frac{\mathrm{D}}{\mathrm{D}t} \widetilde{\phi}_\alpha = -\frac{\partial}{\partial x_j} \langle J_j^\alpha \rangle + \langle \rho \rangle \widetilde{S}_\alpha - \frac{\partial}{\partial x_j} \langle \rho \rangle \widetilde{u_j'' \phi_\alpha''} \tag{8.24}$$

in which the last terms of the RHS's of the equations represent the Reynolds stress and the Reynolds flux which occur in unclosed form. These terms contain second moments of the velocity distribution and joint velocity-scalar distribution respectively, and cannot be expressed in terms of the first moments or means. Another unclosed term in the equations is the averaged reaction term. Reaction rates are in general highly non-linear functions of composition and temperature and the averaged reaction rate cannot be expressed as a function of mean concentrations.

As a framework for statistical turbulence modelling we now consider second moment closure [10, 11]. The simpler linear eddy viscosity (k-ϵ) models are still widely used for reacting flow computations and they perform reasonably well for simple jet flows. However, in recent years also the use of

nonlinear eddy-viscosity models and of RSM for reacting flow computations [12] has become more tractable. Using a hybrid Monte Carlo method to compute the joint velocity-scalar PDF (see below), it is preferable to use RSM from a theoretical point of view.

The conservation equations for the Reynolds stresses and Reynolds fluxes can be derived by standard methods from equations (8.2) and (8.23). A common approach to modeling of variable-density flows is to apply the constant-density second-moment closure models to variable-density flows simply by recasting the Reynolds-averaged terms into Favre averages. However, the variable-density second-moment equations contain additional terms, containing $\partial\widetilde{U}_k/\partial x_k$, $\overline{u_i''}$ or $\overline{\phi_\alpha}''$, which are zero in constant-density flows. The full second-moment equations for variable density flows and modeling of the unclosed terms are reported by Jones [13, 12] and references therein.

4.1 Reynolds-stress equations

Assuming high Reynolds number, viscous terms are neglected except for the viscous dissipation term ϵ_{ij}. The Reynolds stress equations for variable density flows then read:

$$\overline{\rho}\frac{\mathrm{D}}{\mathrm{D}t}\widetilde{u_i''u_j''} = -\overline{\rho}\widetilde{u_i''u_k''}\frac{\partial\widetilde{U}_j}{\partial x_k} - \overline{\rho}\widetilde{u_j''u_k''}\frac{\partial\widetilde{U}_i}{\partial x_k} \tag{8.25a}$$

$$-\left[\overline{u_i''\frac{\partial p'}{\partial x_j}} + \overline{u_j''\frac{\partial p'}{\partial x_i}} - \tfrac{2}{3}\delta_{ij}\overline{u_k''\frac{\partial p'}{\partial x_k}}\right] \tag{8.25b}$$

$$-\overline{\rho}\epsilon_{ij} \tag{8.25c}$$

$$-\frac{\partial}{\partial x_k}\left[\overline{\rho}\widetilde{u_i''u_j''u_k''} + \tfrac{2}{3}\delta_{ij}\overline{u_k''p'}\right] \tag{8.25d}$$

$$-\overline{u_i''}\frac{\partial\overline{p}}{\partial x_j} - \overline{u_j''}\frac{\partial\overline{p}}{\partial x_i} \tag{8.25e}$$

$$+\tfrac{2}{3}\delta_{ij}\overline{p'\frac{\partial u_k''}{\partial x_k}} \tag{8.25f}$$

Here the Reynolds average is denoted by an overbar and the combined use of an overbar and tilde, as in $\widetilde{\overline{x}}$, is used to denote the Favre average of a long expression. The terms on the RHS are: (8.25a) the production by mean shear P_{ij}, (8.25b) the pressure-strain correlation Π_{ij}, (8.25c) the viscous dissipation ϵ_{ij}, (8.25d) the turbulent flux $\mathcal{T}_{ij}$, and two terms which are zero in constant density flows containing (8.25e) a mean pressure gradient, and (8.25f) the trace of the fluctuating strain tensor. The production terms are in closed form whereas the fluctuating pressure, dissipation, turbulent flux, and fluctuating density terms have to be modeled.

The viscous dissipation ϵ_{ij} is modeled by assuming local isotropy at the smallest scales where viscous dissipation takes place. The dissipation model then reads:

$$\epsilon_{ij} = \tfrac{2}{3}\epsilon\delta_{ij} \tag{8.26}$$

For the dissipation of turbulent kinetic energy ϵ a standard modeled equation is solved. The triple correlation terms $\widetilde{\overline{u_i''u_j''u_k''}}$ present in the flux terms can be modelled by a generalized gradient diffusion model that reads:

$$\widetilde{\overline{u_i''u_j''u_k''}} = -C_s\frac{k}{\epsilon}\widetilde{u_k''u_l''}\frac{\partial\widetilde{u_i''u_j''}}{\partial x_l} \tag{8.27}$$

where the constant C_s has a value around 0.25. Modeling of the fluctuating density terms can be found in the papers by Jones [13, 12]. The final unclosed term is the pressure-strain redistribution

term. This term does not produce or destroy turbulent kinetic energy but only redistributes energy over the components of the stress tensor. Several closure models proposed for this term are reviewed in [5].

4.2 Reynolds-flux and scalar-variance equations

Assuming only one scalar variable, the equations for the turbulent scalar flux or Reynolds flux $\widetilde{u_i''\phi''}$ and for scalar variance $\widetilde{\phi''\phi''}$ respectively read:

$$\overline{\rho}\frac{\mathrm{D}}{\mathrm{D}t}\widetilde{u_i''\phi''} = -\overline{\rho}\widetilde{u_j''\phi''}\frac{\partial\widetilde{U}_i}{\partial x_j} - \overline{\rho}\widetilde{u_i''u_j''}\frac{\partial\widetilde{\phi}}{\partial x_j} \tag{8.28a}$$

$$-\overline{\phi''\frac{\partial p'}{\partial x_i}} \tag{8.28b}$$

$$-\frac{\partial}{\partial x_j}\widetilde{\overline{\rho}u_j''u_i''\phi''} \tag{8.28c}$$

$$-\overline{\phi''}\frac{\partial\overline{p}}{\partial x_i} \tag{8.28d}$$

$$+\widetilde{\overline{\rho}u_i''S(\phi)} \tag{8.28e}$$

and,

$$\overline{\rho}\frac{\mathrm{D}}{\mathrm{D}t}\widetilde{\phi''\phi''} = -2\overline{\rho}\widetilde{u_j''\phi''}\frac{\partial\widetilde{\phi}}{\partial x_j} \tag{8.29a}$$

$$-\overline{\rho}\epsilon_\phi \tag{8.29b}$$

$$-\frac{\partial}{\partial x_j}\widetilde{\overline{\rho}u_j''\phi''\phi''} \tag{8.29c}$$

$$+2\widetilde{\overline{\rho}\phi''S(\phi)} \tag{8.29d}$$

The terms on the right hand sides of these equations are, in analogy with the Reynolds-stress equations, the production terms (8.28a and 8.29a), the pressure scrambling term Π_i^ϕ (8.28b), the viscous dissipation of scalar variance ϵ_ϕ (8.29b), the turbulent fluxes (8.28c and 8.29c) and an additional mean pressure-gradient term which is zero in constant density flows (8.28d). Furthermore, for a reacting scalar, unclosed reaction source terms (8.28e and 8.29d) appear in the equations.

The dissipation rate of scalar variance $g = \widetilde{\phi''\phi''}$ is Closed by linking it to the dissipation rate of mechanical energy:

$$\omega_\phi \equiv \frac{\epsilon_\phi}{g} = C_\phi\omega \equiv C_\phi\frac{\epsilon}{k} \tag{8.30}$$

The empirical constant C_ϕ has the standard value 2. Although the constant may vary throughout the flow it is reasonably constant in diffusion flames where the fluctuations in velocity and scalars are induced by the same process; namely the different velocities and concentrations of fuel and oxidizer streams.

5 Closure of the chemical source term

As mentioned in the introduction, solving the moment conservation equations for turbulent reacting flows (8.24, 8.28a−e and 8.29a−d) the averaged reaction rate term poses a serious problem. Because

of the highly non-linear behavior of this term, the average value cannot be expressed accurately as a function of scalar mean and variances but the joint PDF of at least some of the scalars is important.

The simplest model for the mean chemical source term is to disregard the influence of turbulent fluctuations and to evaluate the chemical source term at mean conditions. However this is a bad model in the case of fast reactions as prevailing in combustion. Alternatively, simple models have been constructed in which the mean reaction rate is proportional to a turbulent mixing frequency (Eddy-Break-Up model). This is meant for the situation that turbulent mixing is rate controlling. It contains empirical constants, which have to be estimated for each application.

The development of better models for closing the mean chemical reaction rate has proceeded along different lines for the cases with premixed reactants and with non-premixed reactants. In the case of fast reactions in a premixed situation the flame front separates regions with reactants from regions with products. In the case of fast reactants in a non-premixed situation the flame fronts arise where in the zones where the reactants meet after turbulent mixing. The physical mechanisms active in premixed and non-premixed flames are essentially the same, but their relative importance is different. In premixed flames flame propagation is essential and to describe it, a model for chemical conversion at the flame front is needed, or at least a correlation for the flame speed. In non-premixed combustion mixing is essential and to describe it a non- reacting scalar (mixture fraction) is sufficient. In both cases the influence of turbulent fluctuations is enormous and has to be taken into account. Here we give a brief overview of different models found in the literature. Many interesting relations between different models exist, but it is not the purpose to indicate them here. More details can be found e.g. in [1].

5.1 Premixed reactants

Turbulence increases the area of the flame front (wrinkling) and also modifies the flame front (stretch, curvature). This modifies the overall conversion rate compared to that of laminar flame propagation. Correlations have been developed for the relation between turbulence intensity and conversion enhancement factor. This also depends on the ratio of length scale of turbulent eddies and flame front thickness and the ratio of standard deviation of turbulent velocity and laminar flame speed. The different cases are summarized in the *regime diagram*. Different models have been developed for different regions of the regime diagram, from flamelet models (fast reactions) to well-stirred reactor (slow reactions). In general it is possible to estimate the applicable region of the regime diagram from information on turbulent length and time scales (depending on size of vessel and nozzle, injection speed etc) on the one hand and chemical length and time scales on the other hand.

The available models can be divided in two subgroups: flamelet models and PDF models. The flamelet models rely on the presence of a clearly defined and relatively thin flame front. At first the substructure of the flame front is disregarded. But in a refinement step, details of the substructure of the flame front, if required can be obtained from a separate laminar flame calculation. The PDF methods do not make the assumption of thin flame front and have the ambition to calculate the mean flame front structure directly. Since the chemical source term is a function of the scalar variables, its mean value can be calculated by integration once the scalar PDF is known.

Flamelet models

1. The Bray-Moss-Libby model assumes infinitely fast chemical reaction and correspondingly a infinitely thin flame front. The model predicts the mean and standard deviation of the location of the flame front. Extensions of this model give the mean chemical reaction rate expressed in

terms of mean crossing frequency of flame fronts.

2. In flame surface density models the mean chemical reaction rate is expressed as product of reaction rate at the flame surface times mean surface density. The flame surface density is obtained from an additional modeled transport equation.

3. In the G-equation approach (level set method): an equation is solved for mean and variance of a function G, which is the distance to the nearest flame front.

PDF models

1. In presumed Probability Density Function (PDF) models the mean source term is written exactly as function of the PDF of concentrations. A form of the PDF is assumed and is quantitatively given as function of lower moments (mean, variance, co-variance). This method has been successfully applied for the case of a low number of species, provided sufficient information is available to have a good presumed shape of the PDF.

2. In the full PDF approach a balance equation for the PDF is solved. The success of this model depends on the availability of a good micromixing model. Detailed kinetics can be included in exact form, but in practice leads to high computational cost.

5.2 Non-premixed reactants

The regime diagrams for non-premixed combustion are less well established than the regime diagrams for premixed combustion. But similarly as in premixed combustion, in the limit of fast reactions flamelet models apply. When the turbulence level gets too high the reaction zone is disturbed and even quenched and the limit of applicability of the flamelet model is reached.

In turbulent non-premixed flames the basic variable of almost all approaches is the *mixture fraction*, which in words can be defined as ”the fraction of the mass present locally, which originally is coming from the fuel stream”. It takes values between 0 (oxidizer) and 1 (fuel) and is evolving by mixing processes only. Mathematically this can be defined as a normalised element mass fraction but other possibilities exist [14]. Several notations, e.g. Z, ξ and f, are used in the literature. The mixture fraction satisfies a transport equation without chemical source term. In the limit of fast reactions the mixture fraction together with a fast chemistry model completely defines the state of the system. A mean chemical source term does not have to be computed.

The relation between the physical scalar variables and mixture fraction is given by the specific conserved-scalar chemistry model used (e.g. mixed-is-burnt model, equilibrium model, constrained equilibrium model, flamelet model).

The *mixed-is-burnt model* assumes an infinitely-fast irreversible global reaction of fuel and oxidizer to products which results in piecewise linear relations between composition and mixture fraction. This model however does not include the formation of intermediate species like CO and H_2 or radical species like O, H, and OH.

The *chemical equilibrium model* does consider the intermediate species, but assumes that the reactions are always fast enough to reach full chemical equilibrium, only depending on the available atoms and energy. For the case of methane-air combustion this assumption is valid in the high temperature regions of the flame but in the low temperature regions on the rich side of the flame the slow burn-out of CO does not reach equilibrium and the CO concentration is underpredicted. This effect can be remedied by making some extra assumptions, leading to partial-equilibrium or constrained-equilibrium

models. In these models some variables are constrained to stay away from their equilibrium value. In the simplest case this constraint is fixed, in a more general case the constrained is an independent scalar variable (See Appendix). In the *laminar flamelet model* the local state of the mixture in the flame front is assumed to be the same as that in a laminar diffusion flame. Then by construction the balance between diffusion processes and finite rate of reaction, resulting in deviations from chemical equilibrium, is taken into account.

The thermo-chemical variables are non-linear functions of mixture fraction. Therefore to obtain their mean value (e.g. mean density, mean temperature) it is not sufficient to know the mean mixture fraction, and turbulent mixture fraction fluctuations, characterised by the PDF, have to be known.

In listing the models of turbulent non-premixed flames in the literature the notion PDF model is sometimes used as an alternative (or even an opponent) for flamelet model. This is based on a sharp distinction between considering the PDF of a non-reacting scalar (mixture fraction) and the PDF of reacting scalars. Using a model for the PDF of a mixture fraction is a well-established approach, which forms an essential ingredient of laminar flamelet modeling. On the other hand the joint PDF of reacting scalars, in the framework of flamelet modeling is fully determined by the flamelet assumption and does not have to be computed. Models to calculate the joint PDF of reacting scalars are needed when the laminar flamelet models fail. Making a similar subdivision as in the case of premixed systems, we subdivide in flamelet models (including mixture fraction PDF) and PDF models. Two recently developed models which cannot simply be put in any of these two classes and are of interest in both premixed and non-premixed combustion are added as separate types: conditional moment closure and linear eddy model.

Flamelet models, including mixture fraction PDF models

1. Fast chemistry models not using mixture fraction (eddy break up model)
2. Fast chemistry models using mixture fraction as the only independent scalar.
    - Mixed-is-burnt model (one step kinetics, infinitely fast, irreversible or reversible)
    - Equilibrium model (multi-component mixture in local equilibrium depending on mixture fraction)
3. Laminar flamelet model: Apart from mixture fraction a second variable, *scalar dissipation rate* or *strain rate* is used to quantify the strength of the disturbance of the flame front by the flow.
4. Fast chemistry models for the main conversion and one or more other reacting scalars for the slower ‘secondary processes’ (NOx, soot).
5. Enthalpy as extra variable to describe heat loss
6. Flame surface density model: by analogy to the premixed case a flame surface density model can be formulated for the non-premixed case. Here the flame surface is the surface of stoichiometric mixture fraction.

The basic version of the laminar flamelet model assumes that the balance between reaction and laminar diffusion in the flame structure is in steady state (steady flamelet model), the more general flamelet model does not make this assumption (unsteady flamelet model). Steady flamelets are computed and put in a flamelet library before the turbulent reacting flow calculation. An unsteady flamelet can only be calculated if the evolution of scalar dissipation rate in time is known, depends on information that

comes available in the turbulent reacting flow calculation. Whether or not an unsteady flamelet model is needed depends on the estimated turbulent time scale variation while moving with the flow.

Many studies in the literature use an assumed shape of the mixture fraction PDF in the form of a β-function. The β-function is selected because it can, as a function of its parameters, take various forms that resemble physically realistic scalar PDF's (e.g. single-delta function PDF's in fuel or oxidizer streams, or Gaussian-like PDF's in well mixed situations). The assumed shape of the mixture fraction PDF depends on the mean and the variance, which are computed from a modeled transport equation. In these equations closure of the Reynolds flux is needed, which can be done either by gradient diffusion assumption or by solving a modeled Reynolds flux equation, which can be expected to be more accurate. Some studies calculate the PDF of mixture fraction from a transport equation, which in principle is more general.

Multi-scalar PDF models

1. In multi-scalar assumed shape PDF models transport one solves equations for mean, variance and co-variance of a set of scalars (mass fractions, enthalpy). These models become more and more cumbersome when the number of scalars increases because the joint PDF of reacting scalars can take many forms and scalar correlations can have large influence on the mean reaction rates. It is recommended to select the additional independent scalars not only on chemical criteria, but to also take into account available knowledge on joint statistical properties. In reaction progress variable models this is done by working with normalised scalars, taking values in the interval [0,1], constructed to be nearly statistically independent.

2. In full PDF models one solves a transport equation for the joint PDF of reacting scalars. These models are very general, but for the closure of the PDF transport equation a *micromixing* model is needed. Standard micromixing models incorporate turbulent mixing time scales but do not incorporate the laminar diffusive mixing which becomes important in the flamelet regime. Full PDF mehods are rather computationally expensive and use special solution methods (stochastic simulation). The drawback of computational cost has become less severe with the advent of more computer power and special stochastic noise reducing numerical methods. Nevertheless appropriate reduced chemical reaction mechanisms have to be used. Presently, the largest chemical mechanisms used in the literature on full PDF models have about sixteen independent variables. In the lecture on LES, the scalar FDF method, closely related to the scalar PDF method will be explained.

3. In velocity-scalar PDF models one solves a transport equation for the joint PDF of velocity and scalars. Knowledge of the joint velocity-scalar PDF would at once imply a closure of all unknown terms in the mean transport equations: the Reynolds stress, the Reynolds flux and the mean chemical source term. This observation and the fact that a new class of elegant Lagrangian solution algorithms can be used make calculation of the velocity-scalar PDF an attractive alternative. The method has a clear advantage when the gradient diffusion assumption for the Reynolds flux is doubtful. The step from full scalar PDF to velocity-scalar PDF is analogous to the step from gradient diffusion model to full second moment closure. In a separate lecture the velocity-scalar PDF model will be explained in more detail.

5.3 Conditional moment closure

In conditional moment closure modeled transport equations are solved for the conditional moments of species mass fractions and temperature. This means that the average is taken conditional on a specific value of mixture fraction. It turns out to be easier to close the mean source term in the conditional moment equation than the mean source term in the standard moment equation. But the drawback is that the conditional moment depends on an extra independent coordinate, namely the value of mixture fraction held fixed by the condition. This adds an extra dimension to the problem. In a three-dimensional flow problem the conditional moment depends on four coordinates. A complete description can be found in Klimenko and Bilger [16]. Recently double- conditioning, not only on mixture fraction, but also on scalar dissipation rate has been considered [17].

5.4 Linear eddy model

The linear eddy model introduces the concept of a linear segment moving in the turbulent flow. The concentration along this linear segment evolves in time due to diffusion along the line and due to discontinuous re-arrangement events induced by a hypothetical three-dimensional eddy. The advantage of this model is that the re-arrangements can be described to reflect the complete Kolmogorov (or any other) spectrum of turbulent flow. The linear eddy model is rather computationally expensive, because the coordinate along the linear eddy also acts as an effective extra dimension of space (In each cell of the normal computational grid one or more lines are present).

6 Partially premixed reactants

Real systems often are neither perfectly premixed neither perfectly non- premixed. For example: when ignition takes place after a time too short before a homogenous state is reached (stratification in an IC engine), or in the region close to the nozzle of a non premixed system turbulence levels can be so high that ignition is suppressed and mixing proceeds without reaction until a region with lower turbulence level is reached (lifted flame). The partially premixed systems show some interesting new features. E.g. a triple flame structure can occur at the lower edge of lifted non-premixed flame, which creates a need for appropriate model extensions. In the literature combinations of models for premixed and non premixed situations are developed to cover the case of partially premixed reactants. For example: a combination of flamelet model and G-equation for the lifted flame.

7 Conclusion

While preparing model calculations of turbulent reacting flow it is always good to check all relevant Damköhler numbers to monitor the turbulence-chemistry interaction regime and to choose the most suitable model accordingly.

Flamelet models and PDF models are more appropriate respectively for situations with fast reactions and slow reactions compared to the flow. However, it cannot be expected that there is a sharp distinction between flamelet and non-flamelet regimes. It can be expected that the predictions of the flamelet models will gradually deteriorate when the reactions get slower compared to the time scales of the flow and the flame-like substructures in the flow become less ideal. Similarly it can be expected that the full PDF models with the current generation of micromixing models will become more accurate in the non-flamelet regime because in that regime the assumptions that have been made in the micromixing models are more appropriate.

8 Appendix: Further explanation of constrained equilibrium model

In diffusion flames reaction occurs mainly in a thin reaction zone around stoichiometric mixture fraction and chemistry is frozen outside this zone. Partial-equilibrium models assume that slow three-body reactions, involving three reactants and two products or vice versa, do not reach equilibrium. Compared to full equilibrium, they lead to improved predictions in the low temperature region at the rich side of stoichiometric, but it involves an additional independent scalar specifying the state of nonequilibrium of the three body reactions (progress variable).

The constrained-equilibrium model of Bilger and Stårner [18] combines the partial-equilibrium assumptions with the explicit definition of a reaction zone around stoichiometric mixture fraction. The model assumes a fuel breakdown or pyrolysis sheet at $\xi = \xi_{\rm ig} > \xi_{\rm st}$. There all fuel reacts by a one-step irreversible infinitely fast reaction to some intermediate species. At the stoichiometric mixture fraction $\xi = \xi_{\rm st}$ all intermediate species are consumed. For methane combustion, Bilger and Stårner take C_2H_4 as the intermediate species and the pyrolysis sheet is located at $\xi_{\rm ig} = \xi_{\rm st} + 0.018$. The constraints then are that the intermediate increases linearly with mixture fraction between $\xi = 0$ and $\xi = \xi_{\rm st}$ and decreases linearly between $\xi = \xi_{\rm st}$ and $\xi = \xi_{\rm ig}$ and that the fuel species increases linearly with mixture fraction between $\xi = \xi_{\rm ig}$ and $\xi = 1$. To obtain the other species an equilibrium calculation is done. In an applications described in the lectures on PDF methods a simplified version of this constrained equilibrium model is used. The assumed profiles of fuel and intermediate are used, but given these constraints, the three body reactions are taken in equilibrium.

References

[1] Thierry Poinsot and Denis Veynante. Theoretical and numerical combustion. R.T. Edwards Inc, 2001.

[2] J. Warnatz, U. Maas, and R.W. Dibble. *Combustion*. Springer-Verlag, Berlin, 1996.

[3] R.O. Fox. Computational methods for turbulent reacting flows in the chemical process industry. *Revue de l'Institut Français du Pétrole*, 51(2):215–243, 1996.

[4] Norbert Peters. *Turbulent Combustion*. Cambridge University Press, Cambridge, 2000.

[5] Stephen B. Pope. *Turbulent Flows*. Cambridge University Press, 2000.

[6] S.B. Pope. PDF methods for turbulent reactive flows. *Progress in Energy and Combustion Science*, 11:119–192, 1985.

[7] S.B Pope. Lagrangian PDF methods for turbulent flows. *Annual Review Fluid Mechanics*, 26:23–63, 1994.

[8] S.B. Pope. Computations of turbulent combustion: progress and challenges. In *Proceedings of the Combustion Institute*, **23**, pages 591–612, 1990.

[9] C. Dopazo. Recent developments in PDF methods. In P.A. Libby and F.A. Williams, editors, *Turbulent reacting flows*, pages 375–474. Academic press, London, 1994.

[10] B.E. Launder, G.J. Reece, and W. Rodi. Progress in the development of a Reynolds-stress turbulence closure. *Journal of Fluid Mechanics*, 68:537–566, 1975.

[11] J.L. Lumley. Second-order modeling of turbulent flows. In W. Kollmann, editor, *Prediction Methods for Turbulent Flows*, pages 1–31. Hemisphere Publishing Company, 1980.

[12] W.P. Jones. Turbulence modelling and numerical solution methods for variable density and combusting flows. In P.A. Libby and F.A. Williams, editors, *Turbulent reacting flows*, pages 309–374. Academic press, London, 1994.

[13] W.P. Jones. Models for turbulent flows with variable density and combustion. In W. Kollmann, editor, *Prediction methods for turbulent flows*, pages 379–421. Hemisphere, Washington DC, 1980.

[14] F.A. Williams. *Combustion Theory*. Benjamin/Cummings Publishing Co., Menlo Park, CA, second edition, 1985.

[15] N. Peters. Laminar diffusion flamelet models in non-premixed turbulent combustion. *Progress in Energy and Combustion Science*, 10:319–339, 1984.

[16] A.Y. Klimenko and R.W. Bilger. Conditional moment closure for turbulent combustion. *Progress in Energy and Combustion Science*, 25:595–687, 1999.

[17] Chong M. Cha, George Kosály and Heinz Pitsch Modeling of extinction and reignition in turbulent nonpremixed combustion using a doubly-conditional moment closure approach *Phys. Fluids*, 13:3824-3835, 2001

[18] R.W. Bilger and S.H. Stårner. A simple model for carbon monoxide in laminar and turbulent hydrocarbon diffusion flames. *Combustion and Flame*, 51:155–176, 1983.

Chapter 9

Flamelet Modelling of Non-Premixed Turbulent Flames

L. M. T. Somers

1 Flamelets: introduction

As for pre-mixed combustion, the modelling of turbulent diffusion flames heavily relies on simplifying the chemical processes (and transport processes for that matter). Various approaches exist and depending on the simplifications different models emerge. A compact organization of such models according to Vervisch and Veynante [1] or Poinsot and Veynante [2] is given by

- Infinitely fast chemistry (mixed is burnt)
- Finite rate chemistry assuming a local diffusive-reactive structure similar to the one observed in laminar flames (flamelet assumption)
- Finite rate chemistry with a separated treatment of chemical reaction from molecular and heat transport (Conditional Moment Closure (CMC), pdf-method). Diffusion is then addressed using turbulent micro-mixing modelling, while chemical sources can be dealt with in a exact closed form (pdf).

For a definition of the different regimes in turbulent combustion modelling one may read the latest book by Peters 'Turbulent Combustion' [3]. Basic ingredients of the analysis is that the smallest eddy-length-scale (viz. Kolmogorov scale) is larger than the thickness of the flame. Furthermore the turn-over time of the smallest eddie should be longer than a typical reaction time. In a nutshell the flamelet treatment as covered in this lecture assumes that the flame is a thin interface between fuel and oxidizer. In a more or less geometrical analysis the contributions normal to this surface are separated from the ones along this surface. This leads to identification of the so-called flamelets, which can be associated with one-dimensional counterflow laminar diffusion flames (section 3).

2 Flamelet equations: derivation

Consider the previously introduced balance equations (2.1–2.3) and (2.26) of lecture 1 on pages 13 and 18. Assuming equal diffusivities for fuel and oxidizer ($Le_{\mathrm{fu}} = Le_{\mathrm{ox}}$) one can perform a series of manipulations with the balance equations for fuel and oxidizer to get rid off the chemical source term. This yields what is known as a Schvab-Zeldovich equation [1, 2, 4, 5] for the so-called mixture fraction Z:

$$\frac{\partial \rho Z}{\partial t} + \nabla \cdot (\rho \vec{v} Z) = \nabla \cdot \left(\frac{1}{Le} \frac{\lambda}{c_p} \nabla Z \right) \tag{9.1}$$

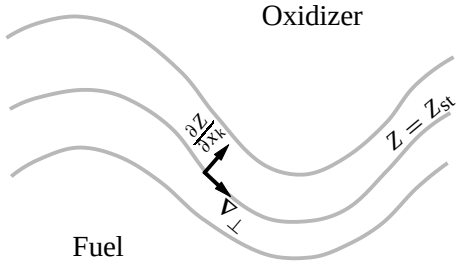

Figure 9.1: Definition of coordinate transformation.

The **mixture fraction** Z is defined according to

$$Z = \frac{\nu Y_{\text{fu}} - Y_{\text{ox}} + Y_{\text{ox},2}}{\nu Y_{\text{fu},1} + Y_{\text{ox},2}} \tag{9.2}$$

where $Y_{\text{ox},2}$ is the oxygen mass-fraction in the oxidizer stream and $Y_{\text{fu},1}$ the fuel mass fraction in the fuel stream (see figure (9.2)). The ν is defined by

$$\nu = \frac{\nu_{\text{ox}} M_{\text{ox}}}{\nu_{\text{fu}} M_{\text{fu}}}.$$

which is the stoichiometric oxygen-to-fuel mass-ratio according to the global reaction:

$$\nu_{\text{fu}}\text{Fu} + \nu_{\text{ox}}\text{Ox} \rightarrow \text{Products}.$$

This mixture fraction is used to perform a transformation of the mass-fraction and enhalpy equation in a new frame of reference where Z is one of the co-ordinates (see figure 9.1). A local orthogonal co-ordinate system attached to the surface of stoichiometry is introduced and the derivatives in this plane are denoted by the subscript '$\perp$',

$$\rho\frac{\partial Y_i}{\partial t} + \rho\vec{v}_\perp \cdot \boldsymbol{\nabla}_\perp(Y_i) = \rho\frac{\chi}{2}\frac{\partial^2 Y_i}{\partial Z^2} + \boldsymbol{\nabla} \cdot_\perp (\rho D \boldsymbol{\nabla}_\perp Y_i) - \rho D \boldsymbol{\nabla}_\perp (\ln(|\boldsymbol{\nabla} Z|)) \cdot \boldsymbol{\nabla}_\perp Y_i + \dot{\rho}_i \tag{9.3}$$

In equation 9.3 the scalar dissipation rate χ is introduced:

$$\chi = 2D\left(\frac{\partial Z}{\partial x_j}\right)^2 = 2D|\boldsymbol{\nabla} Z|^2 \tag{9.4}$$

which is the inverse of a characteristic diffusive time $\tau_\chi = \chi^{-1}$. As this time decreases mass and heat transfer through the stoichiometric plane are enhanced.

If the flamelet is thin, or equivalently if gradients perpendicular to the stoichiometric surface $Z = Z_{\text{st}}$ are large compared to the derivatives (viz. $\boldsymbol{\nabla}_\perp$-terms) along this surface, an order of magnitude analysis[1], shows that the balance equations to leading order are given by:

$$\rho\frac{\partial Y_i}{\partial t} = \rho\frac{\chi}{2}\frac{\partial^2 Y_i}{\partial Z^2} + \dot{\rho}_i \tag{9.5}$$

[1] Similar to that for boundary layer analysis

and a similar equation for the enthalpy balance. This results in the observation that if unsteady effects are neglected[2], the diffusion flame is fully determined by the mixture fraction Z and the scalar dissipation rate χ, yielding

$$Y_i = Y_i(Z, \chi); \quad T = T(Z, \chi)$$

From the 3D-simulation of fully compressible time-dependent simulation of a mixing layer (figure 9.2) it is seen that flame is a thin interface separating oxidizer (top) and fuel (bottom). Large gradients in Z exist perpendicular to the plane $Z = Z_{\text{st}}$ throughout the time-dependent simulation (figures 9.2c, d). Furthermore, a strong correlation is present between the chemical source term and the stoichiometric plane. This seems to be a good example for the flamelet regime.

In most implementations the flamelet approach is used in such a way that the 'flame equations' or chemistry can be solved separately from the hydrodynamics. The χ which is a function of Z is then replaced by its value at the stoichiometric plane $\chi_{\text{st}} = \chi(Z_{\text{st}})$. These 'flamelet'-equations are solved 'off-line', prior to the hydrodynamic simulation. As a function of the two parameters χ_{st} and mixture fraction Z a representative library is built (see figure 9.8 for an impression). During the hydrodynamic simulation the library is used. The 'stiffness' due to the chemistry is in this way separated from the flow computation. In the next section some general aspects of the flamelet structure are discussed.

3 Laminar Counterflow Diffusion Flame(lets)

The counterflow geometry (figure 9.3) is often used in experimental as well as numerical studies. This is mainly due to the fact that within certain approximations the problem description can be reduced to a set of one-dimensional pde's. However, originally the opposed-jet configuration was studied by Potter and Butler [7] to study fuels that were too reactive to be burned pre-mixed (e.g. rocket fuels).

Consider a two-dimensional counterflow configuration (figure 9.3). It can be shown that there exists a transformation in terms of a similarity coordinate that leads to a system of one-dimensional differential equations [8, 9]. This is a rather complicated procedure therefore here a simpler derivation is presented [3]. For that we need to introduce the *Ansatz*

$$u = Ux \quad \textit{Ansatz.}$$

Applying this *Ansatz* we get:

$$\text{Continuity} \quad \frac{\partial \rho v}{\partial y} + \rho U = 0 \tag{9.6}$$

$$\text{Momentum} \quad \rho v \frac{\partial U}{\partial y} = -\rho U^2 + P + \frac{\partial}{\partial y}\left(\mu \frac{\partial U}{\partial y}\right) \tag{9.7}$$

$$\text{Mixture fraction} \quad \rho v \frac{\partial Z}{\partial y} = \frac{\partial}{\partial y}\left(\rho D \frac{\partial Z}{\partial y}\right) \tag{9.8}$$

$$\text{Mass fraction} \quad \rho v \frac{\partial Y_i}{\partial y} = \frac{\partial}{\partial y}\left(\rho D_i \frac{\partial Y_i}{\partial y}\right) + \dot{\rho}_i \tag{9.9}$$

Here definitions are according to the co-ordinate system defined in figure 9.3. The parameter P is the axial pressure gradient and is related to the strain rate a

$$P = \rho_\infty a^2$$

[2]This is supposed to be true. Only near to extinction unsteady effects play a role.

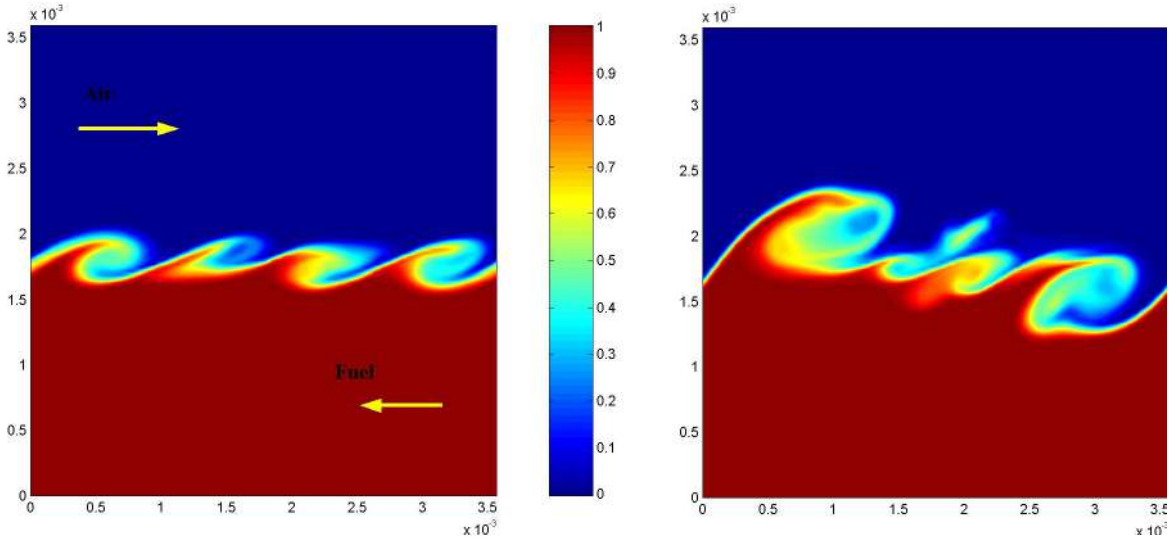

(a) Mixture-fraction. Time t_1.

(b) Mixture-fraction. Time t_2.

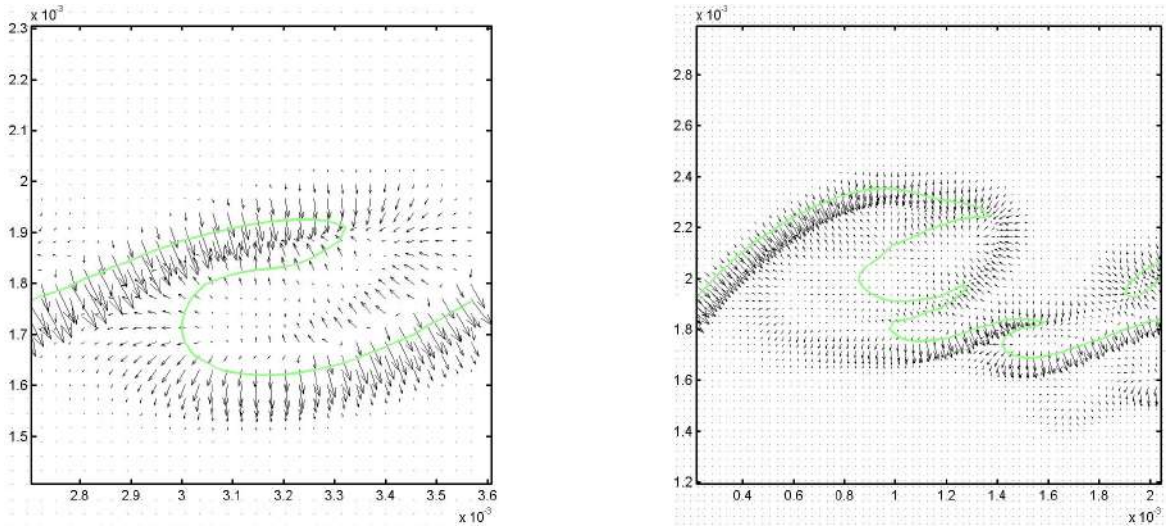

(c) Vectors ∇Z, solid line $Z = Z_{\text{st}}$ at t_1.

(d) Vectors ∇Z, solid line $Z = Z_{\text{st}}$ at t_2.

Figure 9.2: Results from a fully compressible time-dependent simulation [6] with a high-order dns-code. The simulation is a 3D simulation of a mixing layer including combustion which develops a Kelvin-Helmholtz instability at the interface. Pictures are at a certain early stage (a,c,e) of the simulation where vortex pairs are starting to develop and at a later stage (b,d,f) where structure becomes less regular.

continued on next page...

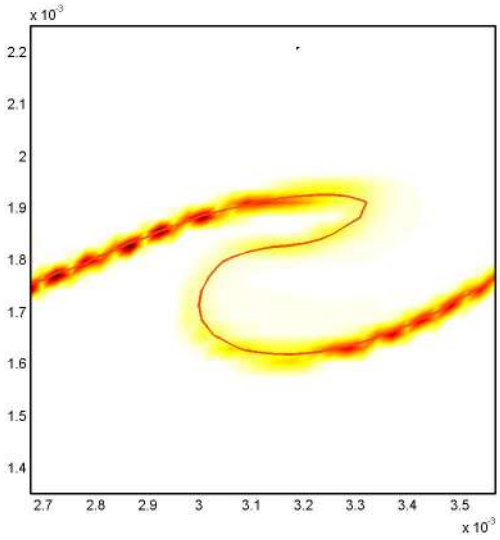

(e) Chemical source term, solid line $Z = Z_{\text{st}}$ at t_1.

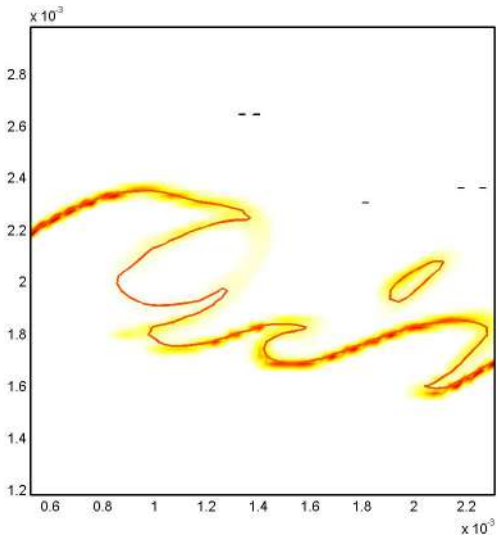

(f) Chemical source term, solid line $Z = Z_{\text{st}}$ at t_2.

Figure 9.2: Continued.

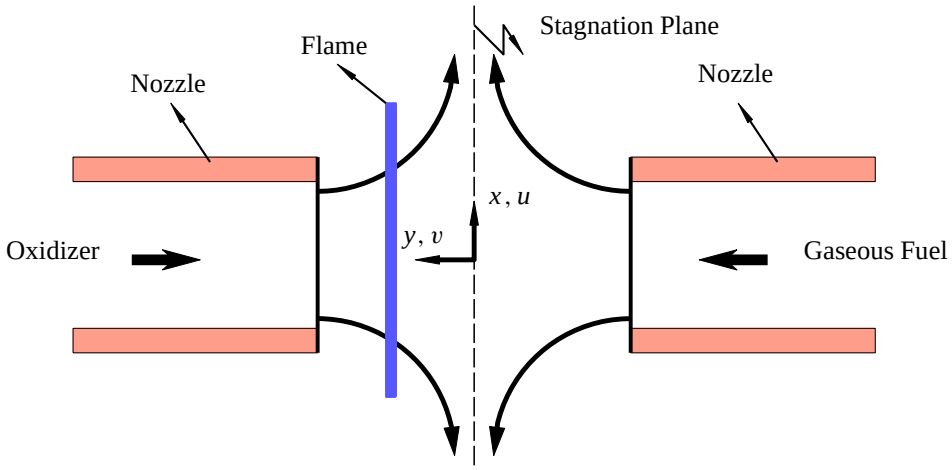

Figure 9.3: Counterflow diffusion flame. Schematic of a practical set-up. Dashed line shows the stagnation plane. The gray fat-line illustrates the flame.

The strain rate a is the applied velocity gradient at the boundary, μ is the viscosity.

Now two possible scenarios exist to get a well-defined system of equations. On one hand one can impose two potential flows coming from opposite directions $y = +\infty$ and $y = -\infty$. This is true only if the nozzles are far enough from the stagnation plane and the flame. On the other hand one could impose no-slip boundary conditions at the location of the nozzles. However, this leads to an ill-posed problem, having too much boundary conditions. For that scenario the strain-rate can no longer be imposed and has to be an eigenvalue of the system. Here the first scenario is considered. One can now show that these equations lead to the flamelet equations derived from the flame-normal analysis in section 2.

Let's apply the thansformation

$$\frac{\partial}{\partial y} = \frac{\partial Z}{\partial y}\frac{\partial}{\partial Z}$$

to the equation for the mass-fractions above. We then obtain:

$$\begin{aligned}
\rho v \frac{\partial Z}{\partial y}\frac{\partial Y_i}{\partial Z} &= \frac{\partial}{\partial y}\left(\rho D \frac{\partial Y_i}{\partial y}\right)\frac{\partial Y_i}{\partial Z} + \rho D\left(\frac{\partial Z}{\partial y}\right)^2 \frac{\partial^2 Y_i}{\partial Z^2} + \dot{\rho}_i \\
\left[\rho v \frac{\partial Z}{\partial y} - \frac{\partial}{\partial y}\left(\rho D \frac{\partial Y_i}{\partial y}\right)\right]\frac{\partial Y_i}{\partial Z} &= \rho D\left(\frac{\partial Z}{\partial y}\right)^2 \frac{\partial^2 Y_i}{\partial Z^2} + \dot{\rho}_i \\
0 &= \rho D\left(\frac{\partial Z}{\partial y}\right)^2 \frac{\partial^2 Y_i}{\partial Z^2} + \dot{\rho}_i
\end{aligned} \tag{9.10}$$

where it is now easily seen that this yield the flamelet equations (equation 9.5, on page 132) already introduced earlier.

For this one-dimensional system it can be shown [3] that within certain approximations one can derive an analytical expression for χ as a function of the strain rate a and the mixture fraction Z. Using separation of variables the solution to eq. 9.8 can be written as

$$Z = c_1 I(y) + c_2$$

where

$$I(y) = \int_0^y \frac{1}{\rho D}\left\{\exp \int_0^y \frac{v}{D}\,\mathrm{d}y\right\}\mathrm{d}y.$$

The constants $c_{1,2}$ follow from appropriate boundary conditions $Z = 1$ for $y \to \infty$ and $Z = 0$ for $y \to -\infty$. Of course this analysis does not help much per se since ρ, v and D in the former equation are not known at this point. However if a number of not to serious assumptions are made [3] the following expression can be derived:

$$Z = \tfrac{1}{2}\,\mathrm{erfc}\left(\eta/\sqrt{2}\right) \tag{9.11}$$

with the non-dimensional co-ordinate[3]:

$$\eta = \sqrt{\frac{a}{D_\infty}}\int_0^y \frac{\rho}{\rho_\infty}\,\mathrm{d}y' \tag{9.12}$$

Apply the definition of the scalar dissipation rate and the error-function[4]. Then invert eq. 9.11 to express η as a function of Z. This finally gives:

$$\chi(y) = \frac{a}{\pi}\exp\left(-2\left[\mathrm{erfc}^{-1}(2Z)\right]^2\right) \tag{9.13}$$

[3]The function erfc is the complementary error-function, $\mathrm{erfc}(x) = 1 - \mathrm{erf}(x)$ with erf the error-function.

[4]Note that $\mathrm{erf}(x) = \int_0^x \exp(-t^2)\,\mathrm{d}t$. Thus $\partial\,\mathrm{erf}(x)/\partial x \propto \exp(-x^2)$.

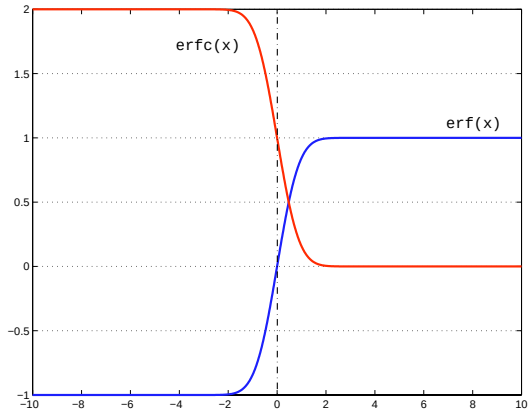

Figure 9.4: Error function erf and complementary error function erfc. Note the definition $\mathrm{erf}(x) = 2(\sqrt{\pi})^{-1} \int_0^x \exp(-t^2)\,\mathrm{d}t$.

thus connecting the flamelet equations to the counterflow diffusion flame equations with a given strain-rate a. The function $\mathrm{erfc}^{-1}(x)$ denotes the **inverse** of the $\mathrm{erfc}(x)$-function and not its reciprocal $1/\,\mathrm{erfc}(x)$. As an illustration in section 3.2 simulations of counterflow diffusion flames using the set of equations (9.6–9.9). First however we will discuss the Burke-Schuman limit or equivalently the infinite rate chemistry.

3.1 Burke-Schuman limit

A particular solution of the flamelet equations is named after Burke and Schumann. They applied the limit of infinite rate chemistry to the flamelet equations. It can be seen that then an infinitely thin reaction layer exists at $Z = Z_{\mathrm{st}}$ where all combustion takes place. Outside this layer the source term vanishes and the flamelet equation for the mass fractions and enthalpy reduces to a homogeneous one:

$$\rho D \left(\frac{\partial Z}{\partial y}\right)^2 \frac{\partial^2 Y_i}{\partial Z^2} = 0$$

with general solution $Y_i = c_1 Z + c_2$. This results in the following linear relations in composition space:

$$Y_{\mathrm{fu}} = Y_{\mathrm{fu},1} \frac{Z - Z_{\mathrm{st}}}{1 - Z_{\mathrm{st}}} \quad \text{and} \quad Y_{\mathrm{fu}} = 0 \quad \text{for} \quad Z \geq Z_{\mathrm{st}} \tag{9.14}$$

$$Y_{\mathrm{ox}} = Y_{\mathrm{ox},2} \left(1 - \frac{Z}{Z_{\mathrm{st}}}\right) \quad \text{and} \quad Y_{\mathrm{ox}} = 0 \quad \text{for} \quad Z \leq Z_{\mathrm{st}} \tag{9.15}$$

In figure 9.5 the solution is presented. Due to the assumption of infinite rate chemistry the Burke-Schuman solution is independent of the strain, therefore the solution is a function of Z alone.

3.2 Non-equilibrium chemistry

If the chemistry is not infinitely fast the complete system of equations must be solved. Since chemistry is 'stiff' special computer codes [10, 11] are needed to solve the discretized equations (see also lecture of Boonkkamp). The general package developed at the TU/e is tailored to model these kind of equations. However, in contrast to packages used in turbulence modelling, here the original equations (9.6-9.9) are solved whilst other authors (e.g. Peters) solve the flamelet-equations and assume assume $\chi(Z) = \chi(Z_{\mathrm{st}})$ as a constant having the value found at the stoichiometric plane. For the simulations presented here we've taken one specific, yet particular case. In all simulations the pressure is

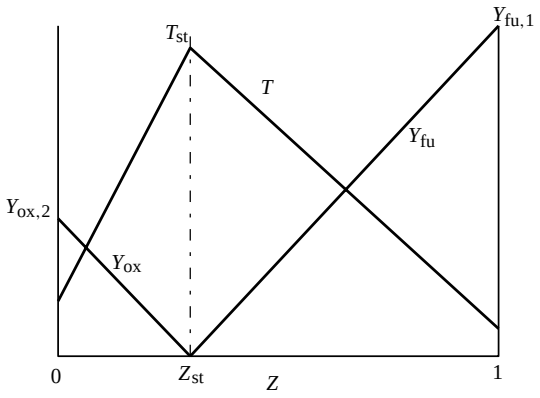

Figure 9.5: The Burke Schumann solution presented in mixture space

4 bar and the temperature at the nozzle is 1400 K and the equivalence ratio[5] φ is 1. The mechanism used is presented in section 4 of lecture 2 on page 30.

From figure 9.6(a) one can see already that combustion takes place in a narrow region of the simulation. To get optimal resolution yet keeping a reasonable amount of grid-points the computer codes adapts the mesh to the solution. Although from figure 9.6a it can be concluded that fuel and oxidizer only co-exist in a small region, in mixture fraction space figure 9.6b however the picture is quite different. Especially in the high strain limit the oxidizer extends well into the fuel side as does the fuel into the oxidizer side. For low strain limits only in a region around $Z = Z_{st}$ fuel and oxidizer co-exist. In figures 9.6c,d important radicals are presented. In c) intermediates from the C_1 reaction chain are given and in d) H and OH important members of the radical pool. The latter two species are responsible for the propagation of the reaction chain (see lecture 4). It can be seen that the intermediates like CH_3 do not extend far into the oxidizer side. They are rapidly consumed at the reaction layer. The radicals like OH on the other hand do not extend far into the fuel side. These are rapidly consumed as the methane is attacked and converted to CO.

Figures 9.7 also show that with increasing strain the reaction zone becomes narrower, leading to larger gradients in temperature accompanied by lower peak temperatures. Finally the heat-conduction (and radical diffusion) from the reaction zone is no longer balanced by the generation of heat by combustion and the flame will extinguish. It is interesting to notice that the mixture fraction offers a very nice co-ordinate transformation from a numerical point of view. All profiles, including the species, remain smooth nearly independent of the applied strain.

In an application of the flamelet approach several flames in a certain range of conditions are computed. The results are stored in a library as a function of the two controlling parameters Z and χ_{st}. Just to get an impression in the following picture the temperature and OH mole fraction is plotted as function of the strain-rate a and Z.

In the final section some aspects of the implementation in a simulation of turbulent combustion is treated.

4 Presumed pdf modelling

At some point in modelling turbulent combustion one gets into trouble. If you're not using dns, but apply some kind of 'averaging' [6], you run into problems with respect to 'unclosed' terms. In addition

[5] $\varphi = \frac{\nu Y_{fu,1}}{Y_{ox,2}}$

[6] Either RANS (time-averaging) or LES (space-averaging).

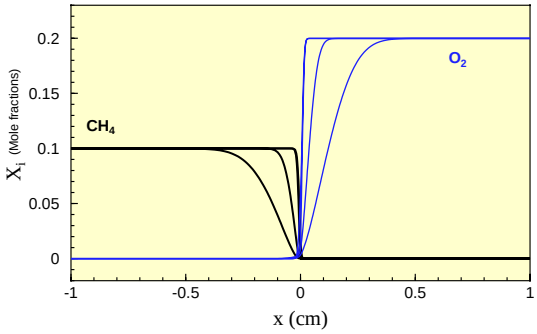

(a) Methane and Oxygen mass fractions vs. space. Complete domain.

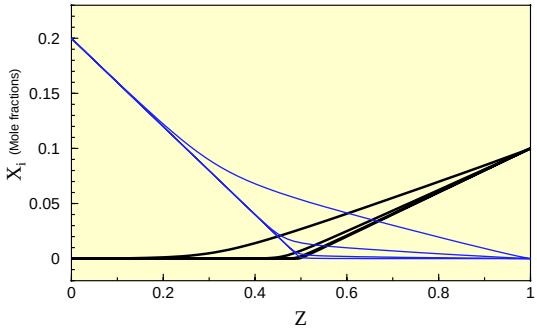

(b) Methane and Oxygen mass fractions vs. mixture fraction. Nb. fuel side corresponds to $Z > Z_{\mathrm{St}}$.

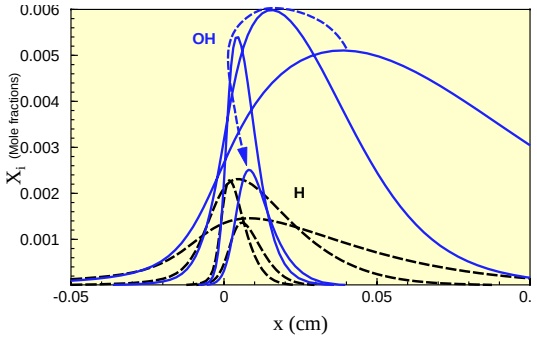

(c) H and OH radical. Domain $(-0.05, 0.1)$. The arrow indicates increasing strain.

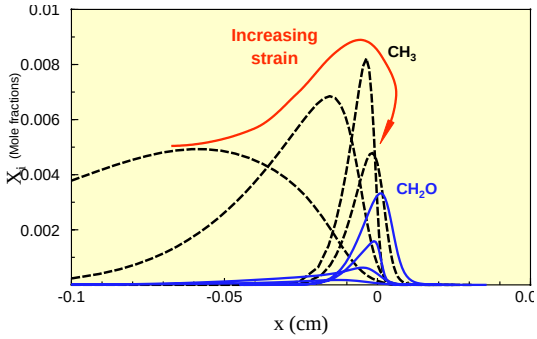

(d) Methyl and CH_2O. Domain $(-0.1, 0.05)$. The arrow indicates increasing strain.

Figure 9.6: The mole fraction of several species at 4 different strain rates ($a = 100, 1000, 10000, 20000$ 1/s) as a function of x. The $a = 20000$ 1/s is not converged and will extinguish. In figure (c) and (d) some characteristic radicals are plotted.

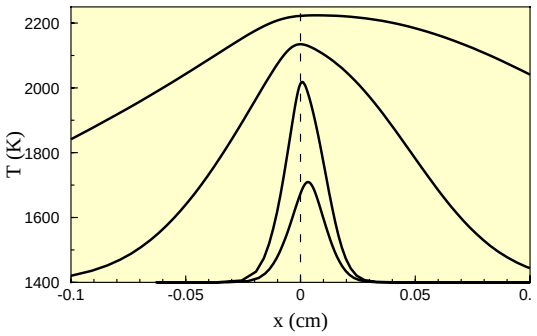

(a) Temperature vs. distance, zoomed: one tenth of the complete domain.

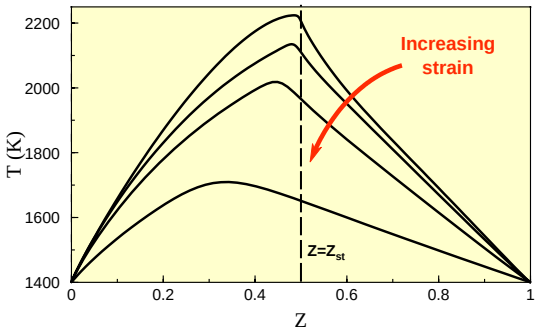

(b) Temperature vs. mixture fraction.

Figure 9.7: Temperatures for 4 different strain rates ($a = 100, 1000, 10000, 20000$ 1/s). The $a = 20000$ 1/s is not converged and will extinguish.

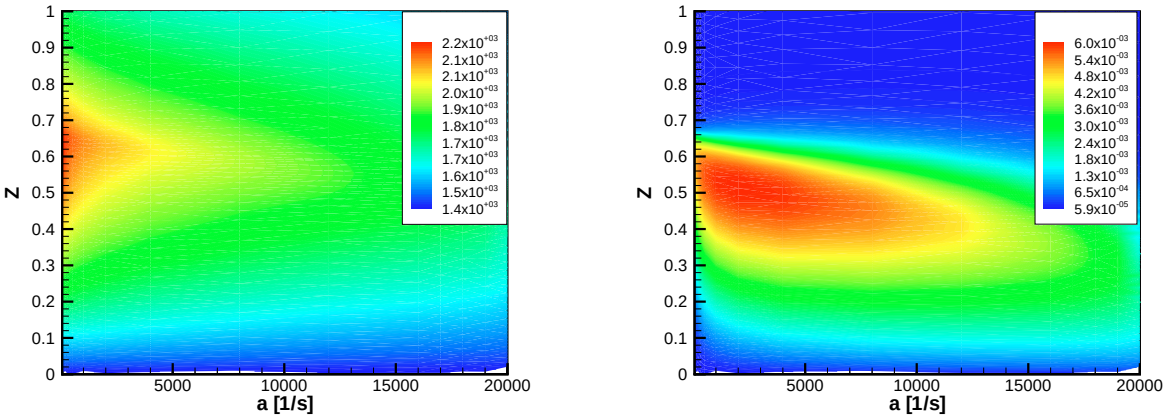

(a) Temperature

(b) OH radical

Figure 9.8: Illustration of two entries (T and OH) of a flamelet library.

to closures applied in non-reacting turbulence modelling, in combustion extra closures are needed. For instance the 'averaged' equation for a species mass balance reads:

$$\frac{\partial \bar{\rho}\widetilde{Y}_i}{\partial t} + \nabla \cdot (\bar{\rho}\widetilde{\boldsymbol{v}}\widetilde{Y}_i) + \nabla \cdot (\overline{\rho \vec{v} Y_i}) = \overline{\dot{\rho}_i} \tag{9.16}$$

where the contribution of molecular diffusivity has been neglected since it is believed to be much smaller than the turbulent diffusion, $\nabla \cdot (\overline{\rho \vec{v} Y_i})$. As is common in turbulence modelling the this term is modelled with the gradient flux approximation,

$$\nabla \cdot (\overline{\rho \vec{v} Y_i}) = -\bar{\rho} D_Y \nabla \widetilde{Y}_i \tag{9.17}$$

with $D_Y = \nu_T / Pr$ where ν_T is the eddy viscosity and Pr a Prandtl-number of order unity. Here we employed the usual Favre-averages definition (see Lecture Roekaerts). After this introduction of the closure for the scalar flux, which is similar to the closures used normally to describe the Reynold-stresses, the only remaining unclosed terms is the chemical source term $\overline{\dot{\rho}_i}$. Obviously, due to the non-linear dependence of the chemical kinetics to the concentration of species and especially the temperature $\overline{\dot{\rho}_i(Y_i, T)} \neq \dot{\rho}_i(\widetilde{Y}_i, \widetilde{T})$. At this point Probability Density Functions (pdf's) come into play.

In general the mixture fraction $\widetilde{Z}$ and its variance $\widetilde{Z''^2}$ are computed. The equation for the mixture fraction is given by [3, 9]

$$\frac{\partial \bar{\rho}\widetilde{Z}}{\partial t} + \nabla \cdot (\bar{\rho}\widetilde{\boldsymbol{v}}\widetilde{Z}) - \bar{\rho} D_Z \nabla \widetilde{Z} = 0. \tag{9.18}$$

Here as usual gradient transport is used to model the transport term. Additionally an equation for the variance is needed (see [3]),

$$\frac{\partial \bar{\rho}\widetilde{Z''^2}}{\partial t} + \nabla \cdot (\bar{\rho}\widetilde{\boldsymbol{v}}\widetilde{Z''^2}) - \bar{\rho} D_Z \nabla \widetilde{Z''^2} = 2\bar{\rho} D_Z \left(\nabla \widetilde{Z}\right)^2 - \bar{\rho}\widetilde{\chi}. \tag{9.19}$$

also using gradient transport. The scalar dissipation rate $\widetilde{\chi} = 2D\widetilde{|\nabla Z|^2}$ is modelled according to

$$\widetilde{\chi} = c_\chi \frac{\widetilde{\epsilon}}{\widetilde{k}} \widetilde{Z''^2}.$$

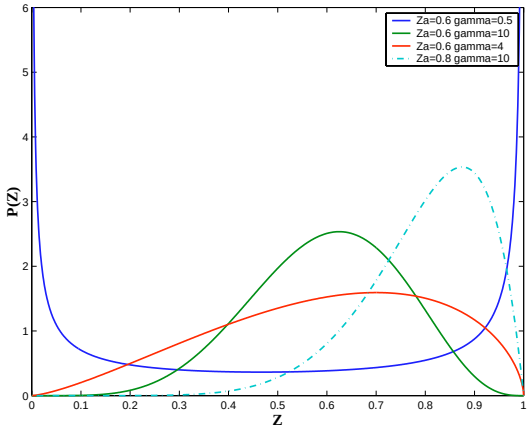

Figure 9.9: Illustration for different values of α, β and γ.

This relation is derived from an integral time for a scalar $\tau_Z = \widetilde{Z''^2}/\widetilde{\chi}$ and the assumption that it is proportional to a characteristic flow time $\tau = \widetilde{\epsilon}/\widetilde{k}$. Most of the discussion normally is on the value of the proportionality constant c_χ. Values of $2-3$ are encountered. However, some authors [12, 13] claim that a more elaborate model is needed for the average scalar dissipation rate $\widetilde{\chi}$ for which then a transport equation is formulated.

The expectation of a certain variable can now be computed using a probability density function and the computed flamelets. By definition we have

$$\widetilde{F}(\vec{x},t) = \int_0^1 \int_0^\infty F(Z,\chi) P(Z,\chi:\vec{x},t) dZ d\chi \tag{9.20}$$

whereas the **joint**-pdf $P(Z,\chi:\vec{x},t)$ is normally given as $P(Z:\vec{x},t)\cdot P(\chi:\vec{x},t)$ which assumes statistical independence. If the shape of the probability function is presumed and not computed through a pdf-transport equation the approach is called pre-sumed pdf modelling. The shape of the $P(Z)$ is by most authors given as a beta-function depending on $\widetilde{Z}$ and the variance $\widetilde{Z''^2}$,

$$P(Z:\vec{x},t) = \frac{Z^{\alpha-1}(1-Z)^{\beta-1}}{\Gamma(\alpha)\Gamma(\beta)}\Gamma(\alpha+\beta) \tag{9.21}$$

Γ is the gamma-function and the two parameters $\alpha = \widetilde{Z}\gamma$ and $\beta = (1-\widetilde{Z})\gamma$ with γ given by,

$$\gamma = \frac{\widetilde{Z}(1-\widetilde{Z})}{\widetilde{Z''^2}} - 1$$

are related to the mean $\widetilde{Z}(\vec{x},t)$ and variance $\widetilde{Z''^2}(\vec{x},t)$. The shape of the beta-function is chosen because it can mimic various functions. For instance if γ is large it approaches a gaussian distribution while for $\alpha < 0$ a singularity develops at $Z = 0$ and for $\beta < 0$ at $Z = 1$ (figure 9.9). Peters [3] argues that the beta-function does not always provide enough flexibility. For instance a distribution with a singularity at $Z = 0$ and an additional local maximum at an intermediate value of Z can not be represented. Peters [14] advocates a composite model for such shapes which appear in shear layers and jets. With respect to the pdf of the scalar dissipation rate a log-normal distribution is used [9]:

$$P(\chi:\vec{x},t) = \frac{1}{\chi\sigma(\vec{x},t)\sqrt{2\pi}} \exp\left(-\frac{1}{2\sigma^2(\vec{x},t)}\left(\ln(\chi)-\gamma(\vec{x},t)\right)^2\right) \tag{9.22}$$

The function $\sigma(\vec{x},t)$ and $\gamma(\vec{x},t)$ are given by the first and second moment of the scalar dissipation rate:

$$\widetilde{\chi} = \exp(\gamma + 0.5\sigma^2) \text{ and } \widetilde{\chi''^2} = \widetilde{\chi}^2\left(\exp(\sigma^2) - 1\right)$$

Normally a value of $\sigma^2 = 2$ is proposed. In that way $\widetilde{\chi''^2}$ does not need to be modelled.

Applying the pre-sumed pdf to the chemical source term we get

$$\widetilde{\dot{\rho}}_i(\vec{x},t) = \int_0^1 \int_0^\infty \dot{\rho}_i(Z,\chi) P(Z:\vec{x},t) P(\chi:\vec{x},t) dZ d\chi \tag{9.23}$$

which finalizes the closure-problem. Off course in literature a lot of discussion is about applicability of the flamelet concept. Currently time-dependent effects seem to be the center of attention as can be read in recent issues of Combustion and Flame and proceedings of latest symposia of the Combustion Institute. More details of the flamelet concept can be read in the excellent book 'Turbulent Combustion' of N. Peters [3], or 'Turbulent Reacting Flows' edited by Libby and Williams [15]. Also recommended for further reading are the Lecture notes of Vervisch and Veynante [1] and the book by Poinsot and Veynante [2] as they give some nice similarities between modelling approaches for pre-mixed and non pre-mixed turbulent combustion in general.

References

[1] L. Vervisch and D. Veynante, *Introduction to Turbulent Combustion Modelling*, Von Karman Lecture series, VKI LS 1999–04, 1999.

[2] T. Poinsot, L. Vervisch and D. Veynante, *Numerical Turbulent Combustion Modelling*, 2002.

[3] Peters, N., *Turbulent Combustion* Cambridge Monographs on Mechanics, Cambridge University Press, Cambridge UK, 2000.

[4] Williams, F.A. *Combustion Theory*, Second Edition, Addison-Wesley Publishing Company, Redwood City 1985.

[5] Peters, N. and Williams, F.A., *The asymptotic structure of Stoichiometric Methane-air flames*, Combustion and Flame **68**, p. 185, 1987.

[6] Bastiaans, R.L.G.M., Somers, L.M.T. and de Lange, H.C., *DNS of non-premixed combustion in a compressible mixing layer.*, In: Geurts, B.J. (ed), *Modern Simulation Strategies for Turbulent Flow*, To be published.

[7] Potter, E.A., Butler, J.N., *Title unknown*, ARS J. 29:54, (1959).

[8] Dixon-Lewis, G., David, T., Gaskell,P.H., Fukutani,S., Jinno,H., Miller, J.A., Kee, R.J., Smooke, M.D., Peters, N., Effelsberg, E., Warnatz, J., and Behrendt, F. *Calculation of the structure and extinction limit of a methane-air counterflow diffusion flame in the forward stagnation region of a porous cylinder*, Twentieth Symposium (International) on Combustion The Combustion Institute, Pittsburgh, p. 1893, 1985.

[9] Peters, N. and Kee, R.J., *The computation of stretched laminar methane-air diffusion flames using a reduced four-step mechanism*, Combustion and Flame **68**, p. 17, 1987.

[10] *The CHEMKIN-III Collection*, http://www.ca.sandia.gov/chemkin/,http://www.reactiondesign.com/.

[11] *CHEM1D: a computer code for solving one-dimensional flame equations* Eindhoven University of Technology, Eindhoven, The Netherlands. http://www.combustion.tue.nl/

[12] Pope, S.B., *Consistent modelling of scalars in turbulent flows* Phys. Fluids, **26**, p. 404, 1983.

[13] Jones, W. P., and Musonge, P., *Closure of the Reynolds stress and scalar flux equations* Phys. Fluids, **31**, p. 3589, 1988.

[14] Effelsberg, E. and Peters, N., *A composite model for the conserved scalar pdf*, Combust. Flame **50**, p. 351, 1983.

[15] Libby, P.A., Williams, F.A. (eds), *Turbulent Reacting Flows*, Combustion Treatise, Academic Press, London UK, 1993.

Chapter 10

Turbulent Non-Premixed Combustion: Progress Variable Methods

J. B. W. Kok

Abstract

A model is presented to predict non-adiabatic combustion of syngas under gas turbine conditions. Mixing, combustion and heat loss are described with four independent scalar variables. These are the mixture fraction, an enthalpy variable and two reaction progress variables for combustion of hydrogen and carbon monoxide. In the combustion model turbulence is taken into account by weighting with an assumed shape PDF. The model is used to calculate a 16 kW flame in an air cooled combustion chamber. The fuel consists of 40% CO, 40% H_2 and 20% N_2 resulting in a calorific value of 11.9 MJ/kg. The calculated CO, CO_2, O_2 and NO concentrations are compared with suction probe measurements at several locations in the combustion chamber. The non-adiabatic calculations and the measurements show good agreement. Adiabatic calculations show a significant overprediction of NO. It is concluded that the non-adiabatic model is necessary and suitable to calculate NO formation in flames with heat loss.

Nomenclature

a	Planck absorption coefficient
C	composed concentration
D	diffusion coefficient
f	mixture fraction
g	mixture fraction variance
h	static enthalpy
i	enthalpy variable
k	turbulent kinetic energy
M	molecular weight
p	pressure
P	probability density function
r	hydrogen reaction progress
s	CO reaction progress
S	source term species number
T	temperature
$\underline{u}$	velocity vector
U	weighting function for i

Greek symbols

α	rate of mixing
ε	dissipation rate
μ	viscosity
ρ	density
σ	Prandtl number, Boltzman's constant
χ	rate of scalar dissipation
λ	coefficient of conduction

Subscripts

i	co-ordinate component,

Superscripts

˜	Favre averaging

V	weighting function for s	$\overline{\ }$	PDF averaging
W	weighting function for r		
x	generalised co-ordinate		
X	mole number		
y	mass fraction		

1 Introduction

At the University of Twente research is performed on the combustion of natural gas and coal gas in combustion chambers with a high thermal power density like in a gas turbines. The emissions of CO, NO and noise are of great interest to designers and users of combustion chambers with regard to environmental legislation, safety and durability. The combustors are characterized by complex three-dimensional flow, flame stabilization by flow recirculation and fast, staged mixing of fuel and air.

Gas turbines can be fired on liquid fuel (kerosene or diesel oil), natural gas, propane gas or other gaseseous fuels. Most large gas turbines for stationary power generation are fired on natural gas. A fuel becoming increasingly important in view of CO_2 emission limitation is syngas derived from biomass or other resources. It will be clear that a full discussion of combustion in gas turbines for all fuels would be more than a full course and text book. A good reference for this is [1]. In order to demonstrate the type of modeling presently available for practical applications, here is chosen to discuss the combustion of synthesis gas. Specific is here, that it contains carbon monoxide and hydrogen, but no hydrocarbons. It allows a good explaination of the models and it suits the more advanced problems of gas turbine engineering in correlation with the use of biomass and other syngas resources.

In this paper the modeling of combustion and the emission of CO and NO in turbulent non-adiabatic CO/H_2 diffusion flames are discussed. The model needs to be efficient to limit the CPU time needed for a combustion calculation. On the other hand, to predict NO emission accurately, the model has to be sufficiently detailed. Physical phenomena that have to be described are turbulence, the mixing of fuel and air, chemical reaction and heat transfer. The effects of turbulence were predicted using the k-epsilon or Reynolds Stress closure model, which both are standard available in a commercial CFD code (here CFX is used). The latter three physical phenomena are described with a model developed at the University of Twente. This model code has been linked to the CFD code through user scalars and a thermochemical database.

In a gas turbine combustor fired with a mixture of CO and H_2, premixing usually is avoided with a view to auto-ignition. The fuel and air are mixed rapidly immediately downstream of the burner in the combustor. The ratio between the rates of mixing and combustion has a large effect on the flame behavior. A complication here is, that due to the interaction between turbulence and the fast chemical reactions, the mean chemical source terms can not be calculated directly [2]. In the simplest model the combustion is assumed to proceed infinitely fast to chemical equilibrium (e.g. the mixed=burnt model). This approach will give the global flame shape and the calculation of a mean chemical source term is avoided. For intermediate species concentrations, the result will however be inaccurate, as these species are not in chemical equilibrium near the combustion interface. These non-equilibrium concentrations are important for the calculation of nitric oxide production.

An advanced model is the laminar flamelet model, that can predict non-equilibrium intermediate species concentrations. In the flamelet model the chemical reaction rates are assumed to be finite but fast as compared to the rate of mixing. In that case reactions occur in a thin wrinkled flame sheet, and

the model assumes similarity between a laminar flame and the local turbulent flame behavior. The mean species concentrations are uniquely determined by two variables: the mixture fraction and the rate of scalar dissipation. It follows that the mean reaction source term can be written in the flamelet model as a function of the mixture fraction and the rate of scalar dissipation. Peters [3] has shown that under specific conditions the laminar flamelet model gives good accuracy at low computational costs. The model will decrease in accuracy in case the flame has both fast and slow reactions and/or a significant rate of heat loss.

A reaction progress variable model (denoted as 'FRS') developed for a turbulent adiabatic diffusion flame with detailed chemistry and both fast and slow reactions was presented by Kok and Louis [4]. The FRS model is now extended to a non-adiabatic model (named 'FIRS'). That model takes heat loss into account and is presented in this paper. The model, its four combustion scalars and the calculation of the mean chemical and radiation source terms, are explained in sections 2–5. The thermochemical database, which is derived for the model, is described in section 6. Experiments were performed to obtain data to verify the model. The experimental set-up that was used to perform measurements on a 16 kW syngas diffusion flame with heat loss is presented in section 7. Also shown in section 7 is the set-up of the numerical simulations of the investigated flame. The results of the measurements on, and the simulations of the syngas flame are discussed and compared in section 8. Subsequently adiabatic and non-adiabatic simulation results are compared in order to assess the effect of heat loss. Finally in section 9 conclusions are formulated.

2 The 'FIRS' non-adiabatic reaction progress variable model

In the FIRS reaction progress variable model, finite chemical reaction rates are taken into account by calculating the source terms of fast chemical reactions implicitly. To this end the detailed chemical reaction mechanism is reduced to a small number of variables, for example by assuming partial equilibrium or steady state of intermediate species. The slow reactions source terms are calculated explicitly. Initially, in the burner inlet, both the fuel flow and the air flow are assumed to be in chemical equilibrium. Subsequently, the chemical system is forced from global equilibrium by the mixing of fuel and air. The chemical system evolves back to global equilibrium as a result of the slow chemical reactions. In the model based on these phenomena, the mean chemical reaction rates are determined by the mixture fraction ('f'), the rate of mixing, the heat transfer ('i') and the reaction progress variables ('r' and 's'): hence the 'FIRS' model. The reaction progress variables r and s describe the H_2 and CO conversion respectively. When these variables are known, the local mass fractions can be calculated from algebraic equations, arising from the reduction of a detailed reaction mechanism [4, 5]. From the mass fractions the local source terms in the transport equations for the variables can be calculated. As the reaction progress variables describe the deviation from equilibrium, super-equilibrium radical concentrations are taken into account. With these radical concentrations thermal NO formation is calculated in a post-processing step.

3 Mixing of fuel and air

A diffusion flame is characterized by a separate inflow of one or more air streams and a fuel stream. Depending on the burner construction, chemistry and flow conditions, these streams mix in the flame. The mixing of fuel and air is described with two scalar transport equations: one for the mean mixture fraction f and one for its 2$^{\text{nd}}$ moment (the variance $g = \langle f''^2 \rangle$ [6]). The mixture fraction f equals 1

in the fuel stream and 0 in the air stream, and is defined as:

$$f = \frac{Y_{\text{fuel}} - Y_{\text{fuel},2}}{Y_{\text{fuel},1} - Y_{\text{fuel},2}} \tag{10.1}$$

with $Y_{\text{fuel},i}$ the mass fraction of fuel elements present in stream i, and Y_{fuel} the local mass fraction of fuel elements. The turbulent transport terms in the equations for the first two moments are closed with the gradient hypothesis. This results in the following turbulent transport equation for the mixture fraction:

$$\nabla(\rho\tilde{u}\,\tilde{f}) - \nabla(D\nabla\,\tilde{f}) = 0. \tag{10.2}$$

The diffusion coefficient D is the sum of molecular diffusion coefficient D_{m} and the turbulent diffusion coefficient D_{t}. The turbulent diffusion coefficient is defined as the ratio of the kinematic turbulent viscosity and the turbulent Schmidt number. For the variance of f: $g = \langle f''^2 \rangle$ the following turbulent transport equation can be derived:

$$\nabla(\overline{\rho}\underline{\tilde{u}}g) - \nabla(D\nabla g) = \tfrac{1}{2}c_{g_1}\overline{\rho}\chi - c_{g_2}\overline{\rho}\alpha \tag{10.3}$$

with rate of scalar dissipation $\chi = 2D_{\text{m}}(\partial f/\partial x_i)^2$ and mixing rate $\alpha = \tilde{\epsilon}g/k$. In equations (10.2) and (10.3), $\underline{\tilde{u}}$ is the Favre averaged velocity vector. In equation (10.3) it can be observed, that the rate of growth of g is determined by the balance between the rate of scalar dissipation and the mixing rate.

4 Heat Transfer

4.1 Enthalpy transport equation

The specific enthalpy h of an ideal gas mixture with temperature T and number of species σ, each species in the gas mixture having a mass fraction y_i, is given by [7]:

$$h(T, y_i) = \sum_{i=1}^{\sigma} h_i(T) y_i(x, t) \tag{10.4}$$

with

$$h_i(T) = h_i^0 + \int_{T=T_0}^{T(x,t)} c_{p,i}(T)\ \mathrm{d}T. \tag{10.5}$$

In the mixture of ideal gases a mixture specific heat coefficient can be defined as:

$$c_p(y_i, T) = \sum_{i=1}^{\sigma} y_i c_{p,i}(T). \tag{10.6}$$

Then the local instantaneous value of specific enthalpy is:

$$h(y_i, T) = \sum_{i=1}^{\sigma} y_i h_i^0 + \int_{T=T_0}^{T} c_p(T)\ \mathrm{d}T. \tag{10.7}$$

In an adiabatic combustion model the local instantaneous value of enthalpy is a linear function of mixture fraction, varying between the enthalpy value at the fuel inlet and the enthalpy value at the air inlet. When heat loss is taken into account, the local value of enthalpy depends not only on mixture fraction but also on the balance of the enthalpy transport. In that case an additional transport equation has to be solved for the enthalpy as an independent variable. The general enthalpy transport equation

is given in [7] (p. 74/eq. 72). In view of the scope of the present paper this equation will be simplified. Here it is assumed that all binary diffusion coefficients are equal. In that case the drift flux is reduced to a Fick diffusion equation. Further are neglected the Dufour heat flux, pressure diffusion and thermal diffusion. This leads to the following transport equation for the instantaneous value of the enthalpy:

$$\rho \frac{\mathrm{D}}{\mathrm{D}t}\left(h + \tfrac{1}{2}\underline{u}\cdot\underline{u}\right) = \frac{\partial p}{\partial t} + \rho \sum_{i=1}^{\sigma} \underline{f}_i \cdot \left(y_i \underline{u} - D_\mathrm{m} \nabla y_i\right) - \nabla \cdot \underline{q} - Q_\mathrm{R} \tag{10.8}$$

with:

$$\underline{q} = \lambda \nabla T - \rho \sum_{i=1}^{\sigma} h_i D_\mathrm{m} \nabla y_i. \tag{10.9}$$

At the end of this subsection the radiation sink term Q_R will be discussed. The temperature can be eliminated from equation (10.9) with equation (10.7), leading to the following expression for the heat flux vector:

$$q = -\frac{\lambda}{c_p}\nabla h - \left(\rho D_\mathrm{m} - \frac{\lambda}{c_p}\right) \sum_{i=1}^{\sigma} h_i \nabla y_i. \tag{10.10}$$

In most flames the velocities are only moderately high and $\underline{u}\cdot\underline{u}$ can be neglected compared to h. In line with the mixture fraction species transport equation the Lewis number will be assumed equal to unity:

$$Le = \frac{\lambda}{\rho c_p D_\mathrm{m}} = 1. \tag{10.11}$$

The transport equation for the instantaneous value of the enthalpy is then simplified to:

$$\rho \frac{\mathrm{D}}{\mathrm{D}t} h = \frac{\partial P}{\partial t} + \nabla \cdot \left(\frac{\lambda}{c_p}\nabla h\right) - Q_\mathrm{R}. \tag{10.12}$$

Based on equation (10.12), a transport equation will be formulated for the mean of the enthalpy in a turbulent flow with combustion and heat loss. In a non-adiabatic non-premixed flame the enthalpy variable h and the mixture fraction f are two independent variables. In their statistical behaviour they are correlated however. The enthalpy variable is now transformed to a new variable that is to a large extent statistically independent of the mixture fraction. The minimum value of the enthalpy is defined as the enthalpy of the mixture when instantly cooled to the temperature of the surroundings. Subsequently the enthalpy is normalised using the adiabatic and the minimum enthalpy:

$$i = \frac{h - h_\mathrm{min}}{h_\mathrm{ad} - h_\mathrm{min}} = \frac{\displaystyle\int_{T_0}^{T} c_p \,\mathrm{d}T - \int_{T_0}^{T_\mathrm{surr}} c_p \,\mathrm{d}T}{\displaystyle\int_{T_0}^{T_\mathrm{ad}} c_p \,\mathrm{d}T - \int_{T_0}^{T_\mathrm{surr}} c_p \,\mathrm{d}T} \tag{10.13}$$

or

$$i = \frac{h - h_\mathrm{min}}{U(f)} \tag{10.14}$$

In the fuel flow and airflow at the burner inlet, the enthalpy loss variable i equals unity by definition. In the adiabatic case, when enthalpy is conserved, the enthalpy loss variable remains unity. When heat loss is taken into account, i will be smaller than unity. In the flame $h - h_\mathrm{min}$ and the denominator U each have a similar statistical correlation with f, and their ratio 'i' is statistically independent of f.

Substituting the definition 14 of the enthalpy variable in equation (10.12) gives for a steady flame the following *instantaneous* equation for i:

$$\nabla(\rho \underline{u} i) - \nabla\left(\frac{\lambda}{C_p}\nabla i\right) = (\nabla f)^2(i-1)\frac{\lambda}{C_p}\frac{U_{ff}}{U} + 2\frac{\lambda}{C_p}\frac{U_f}{U}\nabla f \nabla i - S_i, \tag{10.15}$$

where U_{ff} denotes the second derivative of U to f and is the net radiation sink term Q_{R}, normalised with U. The term containing $\nabla f \nabla i$ in equation (10.15) can be neglected because f and i are independent and non-correlated variables. Favre decomposition and averaging yields for the *mean* i transport equation:

$$\nabla(\overline{\rho}\tilde{\underline{u}}\tilde{i}) - \nabla\left(\left(\frac{\lambda}{C_p} + D_{\mathrm{t}}\right)\nabla\tilde{i}\right) = \tfrac{1}{2}C_{g_2}\alpha g(\tilde{i}-1)\frac{\lambda}{C_p}\frac{\overline{U_{ff}}}{U} - \overline{S}_i. \tag{10.16}$$

The term containing the gradient of f squared is modelled as in the mixture fraction variance equation. As f and i are not correlated variables, the mean source terms in equation (10.16) can be calculated by weighting over an assumed shape Probability Density Function (see section 6). An equation for the variance of i is omitted because the variation of species concentrations and temperature with i is quite linear.

4.2 Radiation emission

The net radiation sink term S_i is the balance between emitted and absorbed radiation per unit volume (weighted with U). The energy emitted by an infinitesimal volume of gas, integrated over all wavelengths, is given by [8]:

$$S_{i,\mathrm{emitted}} = \frac{4\displaystyle\int_{\lambda=0}^{\infty} a_\lambda e_{\lambda b}(\lambda, T)\,\mathrm{d}\lambda}{U(f)} = \frac{4a_{\mathrm{P}}(T, p)\sigma T^4}{U(f)}. \tag{10.17}$$

Assuming the flame to be non-luminous, the mean Planck absorption coefficient a_{P} is given by the expression [9, 10]:

$$a_{\mathrm{P}}(T, p) = a_{\mathrm{P},\mathrm{CO}_2}p_{\mathrm{CO}_2} + a_{\mathrm{P},\mathrm{H}_2\mathrm{O}}p_{\mathrm{H}_2\mathrm{O}} + \ldots \tag{10.18}$$

The species specific absorption coefficient $a_{\mathrm{P},X}$ is a function of the temperature only [9]. Here for the $a_{\mathrm{P},X}$ a correlation is used as proposed by Chen *et al.* [11]; also data are used as provided by RADCAL [12, 13].

4.3 Radiation absorption

In a volume of gas, radiation is absorbed that is radiated from the surrounding gas and the walls. In general this is a complicated expression that is determined by the history of all incident rays in the entire volume. Here as a start the flame is assumed to be optically thin. In that case the absorbed energy is given by:

$$S_{i,\mathrm{absorbed}} = -\frac{4(a_{\mathrm{mP},\mathrm{CO}_2}p_{\mathrm{CO}_2} + a_{\mathrm{mP},\mathrm{H}_2\mathrm{O}}p_{\mathrm{H}_2\mathrm{O}})\sigma T^4}{U(f)} \tag{10.19}$$

Here $a_{\mathrm{mP},X}$ is the modified mean Planck absorption coefficient of species X. As an approximation in this paper the $a_{\mathrm{mP},X}$ is taken equal to $a_{\mathrm{P},X}$. This is discussed in more detail by for example Tien [9]. The net radiation sink term S_i is now given by the sum of equations (10.17) and (10.19). In case the flame becomes optically thick, the emission term remains unchanged and determined by local variables. A more eloborate expression would however be necessary for the absorption, which is determined by the over-all variable field. This situation would complicate the calculation of a mean radiation source term. The situation of optically thick flames is outside the scope of the present paper.

5 Progress of Chemical Reaction

The combustion process in the CO/H_2 flame is described by two reaction progress variables, indicating the conversion of hydrogen and carbon monoxide. Earlier by Janicka [14, 15] a one progress variable model was introduced for the adiabatic combustion of turbulent hydrogen diffusion flames with a 6 species and 8 chemical reactions mechanism. Later, Correa [16] used a two reaction progress variable model for the adiabatic combustion of CO/H_2 mixtures. This model was verified in an experiment with an almost adiabatic flame [17]. Recently a two reaction progress variable model for the adiabatic turbulent combustion of CO/H_2 mixtures with 10 species, 21 reactions was derived systematically by Kok and Louis [4]. In this section the latter model is generalised to the non-adiabatic situation.

A detailed chemical reaction system with 19 elementary hydrogen reactions (specified in Appendix I), is reduced to a system depending on one progress variable. For this variable a composed concentration is chosen, such that the highly non-linear source terms of the two-body reactions in the reaction mechanism, having high activation energies, cancel each other. This means that only the source terms of reactions without activation energy remain in the net source term of the combined mass fraction [4, 15]. This technique (used earlier by Dixon-Lewis *et al.* [18] to reduce the stiffness of laminar flame equations) is demonstrated below for the reduction of the hydrogen chemical reaction mechanism.

Consider a set of M elementary reactions involving N species and L elements. The chemical reactions with subscript k between the species with subscript i and with chemical symbol χ_i can be represented in a general form as [7] (p. 556):

$$\sum_{i=1}^{N} \nu'_{ik} \chi_i \rightleftharpoons \sum_{i=1}^{N} \nu''_{ik} \chi_i \quad k = 1, \ldots, M \tag{10.20}$$

The net rate of production of species i due to all M chemical reactions is then given by the i^{th} component of the species rate of production vector:

$$\frac{\mathrm{d}C_i}{\mathrm{d}t} = \omega_i = \sum_{k=1}^{M} \nu_{ik} \varpi_k \tag{10.21}$$

with components of the reaction tensor defined by $\nu_{ik} = \nu''_{ik} - \nu'_{ik}$.

The composed variable will be determined for the hydrogen mechanism (see Appendix I) as follows. The reactive species involved are H_2, OH, H, O, HO_2, H_2O_2 and H_2O, O_2(in order of numbering). The number of species is 8 and the number of elements is 2. Hence, the dimension of the reactive species space is 6. If this dimension is reduced to 1, in total 6 source terms can be eliminated from the composed variable source term. Choosing for the independent species H_2, OH, H, O, HO_2, H_2O_2 in the reactive subspace, the composed variable is given by the expression:

$$C = a_1 C_{\mathrm{H_2}} + a_2 C_{\mathrm{OH}} + a_3 C_{\mathrm{O}} + a_4 C_{\mathrm{H}} + a_5 C_{\mathrm{HO_2}} + a_6 C_{\mathrm{H_2O_2}}. \tag{10.22}$$

The chemical source term of C is then:

$$\frac{\mathrm{d}C}{\mathrm{d}t} = \omega_1(a_2 - a_3 + a_4) + \omega_2(-a_1 + a_2 + a_3 - a_4) + \omega_3(-a_1 - a_2 + a_3) + \ldots \tag{10.23}$$

In view of their large activation energies, the coefficients of the independent reactions H1, H2, H3, H17, and H18 are eliminated:

$$\begin{aligned} a_2 - a_3 + a_4 &= 0 \qquad -a_1 - a_2 + a_3 = 0 \qquad a_2 - a_4 + a_5 - a_6 = 0 \\ -a_1 + a_2 + a_3 - a_4 &= 0 \qquad a_2 - a_3 - a_6 = 0 \end{aligned} \tag{10.24}$$

Scaling C such that $a_1 = 1.00$, the solution of this system of equations for the remaining 5 independent linear equations with 5 unknowns is:

$$\begin{array}{lll} a_1 = 1.00 & a_3 = 1.00 & a_5 = -0.50 \\ a_2 = 0.50 & a_4 = 1.50 & a_6 = -1.00. \end{array} \tag{10.25}$$

The composed concentration becomes:

$$C = 1.00C_{\mathrm{H_2}} + 0.50C_{\mathrm{OH}} + 1.00C_{\mathrm{O}} + 1.50C_{\mathrm{H}} - 0.50C_{\mathrm{OH_2}} - 1.00C_{\mathrm{H_2O_2}} \tag{10.26}$$

And the instantaneous rate of change with time of C due to chemical reaction is:

$$\frac{\mathrm{d}C}{\mathrm{d}t} = \sum_{k=4}^{19}\sum_{j=1}^{6} a_j \nu_{jk} \varpi_k = -2(\varpi_5 + \varpi_6 + \varpi_7 + \varpi_8 + \varpi_{15}) \tag{10.27}$$

This chemical source term is incorporated in a turbulent transport equation for the mean of C. In equation (10.27) it can be observed, that not only the source terms with high activation energy are eliminated but also the source terms of the dependent reactions H4, H9–H14, H16 and H19. In Appendix II it is explained that this way a composed concentration is created with effectively a small Damkohler number. That enables probability density function averaging with assumed shape functions.

As described above the combined mass fraction now is defined as:

$$Y^*_{\mathrm{H_2}} = Y_{\mathrm{H_2}} + \frac{M_{\mathrm{H_2}}}{M_{\mathrm{O}}} Y_{\mathrm{O}} + \tfrac{3}{2}\frac{M_{\mathrm{H_2}}}{M_{\mathrm{H}}} Y_{\mathrm{H}} + \tfrac{1}{2}\frac{M_{\mathrm{H_2}}}{M_{\mathrm{OH}}} Y_{\mathrm{OH}} - \tfrac{1}{2}\frac{M_{\mathrm{H_2}}}{M_{\mathrm{HO_2}}} Y_{\mathrm{HO_2}} - \frac{M_{\mathrm{H_2}}}{M_{\mathrm{H_2O_2}}} Y_{\mathrm{H_2O_2}} \tag{10.28}$$

This composed concentration is an independent variable, but statistically correlated with the mixture fraction and the enthalpy. To reduce the statistical correlation with the scalars f and i, the combined mass fraction is normalized with the completely burnt and the unburnt situation to give the dimensionless progress variable r:

$$r = \frac{Y_{\mathrm{H_2^*}} - Y^{\mathrm{u}}_{\mathrm{H_2^*}}}{Y^{\mathrm{b}}_{\mathrm{H_2^*}} - Y^{\mathrm{u}}_{\mathrm{H_2^*}}} = \frac{Y_{\mathrm{H_2^*}} - Y^{\mathrm{u}}_{\mathrm{H_2^*}}}{W(f,i)} \tag{10.29}$$

The normalisation function W depends on heat loss as well as mixing. Substituting this definition in a conventional convection-diffusion equation for the combined mass fraction, with gradient closure for the turbulent flux term and applying Favre decomposition and averaging yields the following transport equation for the mean of r:

$$\nabla(\overline{\rho}\tilde{\underline{u}}\tilde{r} - (D\nabla\tilde{r})) = \left(\frac{\overline{W_{ff}}}{W} + (1-\tilde{i})\frac{\overline{U_{ff}}}{U}\frac{\overline{W_i}}{W}\right)\tfrac{1}{2}\tilde{r}C_{g_2}\overline{\rho}\tilde{\alpha}g + \tilde{r}\frac{\overline{W_i}}{W}\overline{S_i} + \overline{S_r}. \tag{10.30}$$

Initially the fuel flow and airflow are in chemical equilibrium at the burner inlet, with r equal to unity. Due to mixing of both flows a mixture is created that deviates from equilibrium. This process is described by the 1st rhs term in the r-equation, which is negative and causes r to decrease at the flame interface. This is restored by the positive 4th rhs term S_r, which is the normalized chemical reaction source term for the combined mass fraction. This term contains contributions from the slow three-body reactions only [4]. Additional terms due to heat transfer are the 2nd and the 3rd term. Like the 1st and 4th term they deviate and restore respectively the chemical reaction system from and to equilibrium, this time due to heat transfer.

The conversion of carbon monoxide is described similarly to the hydrogen conversion. The mass fraction of CO is normalized with the partially burnt mass fraction (CO reactions in equilibrium, while the H_2 reactions may deviate from equilibrium) and the unburnt situation to give the dimensionless variable s:

$$s = \frac{Y_{\mathrm{CO}} - Y_{\mathrm{CO}}^{\mathrm{pb}}}{Y_{\mathrm{CO}}^{\mathrm{u}} - Y_{\mathrm{CO}}^{\mathrm{pb}}} = \frac{Y_{\mathrm{CO}} - Y_{\mathrm{CO}}^{\mathrm{pb}}}{V(f,i,r)}. \tag{10.31}$$

The turbulent transport equation for the mean of s is:

$$\begin{aligned}\nabla(\overline{\rho}\tilde{u}\tilde{s} - (D\nabla\tilde{s})) = {} & \\ (\tilde{s}-1)\left(\overline{\frac{V_{ff}}{V}} - \overline{\frac{V_r}{V}}\,\overline{\frac{W_{ff}}{W}}\tilde{r} + (\tilde{i}-1)\left(\overline{\frac{V_f}{V}}\,\overline{\frac{U_{ff}}{U}}\,\overline{\frac{W_i}{W}}\tilde{r} - \overline{\frac{V_i}{V}}\,\overline{\frac{U_{ff}}{U}}\right)\right)\tfrac{1}{2}C_{g_2}\overline{\rho}\tilde{\alpha}g & \\ + (\tilde{s}-1)\left(\overline{\frac{V_i}{V}S_i} - \overline{\frac{V_r}{V}S_r} - \tilde{r}\,\overline{\frac{W_i}{W}}\,\overline{\frac{V_r}{V}S_i}\right) + \overline{S_S}. & \end{aligned} \tag{10.32}$$

In the case of adiabatic combustion, when i equals one and the radiation source term is zero, the equations for the reaction progress variables reduce to the adiabatic equations, discussed by Kok and Louis [4] and Correa [16].

6 Probability Density Function Averaging and the Thermochemical Database

In order to take turbulent fluctuations into account, the instantaneous concentrations and source terms are weighted over a Probability Density Function. The Favre averaged mean of the source terms, mass fractions and temperature is calculated by convolution with a joint probability density function P:

$$\tilde{\phi} = \frac{1}{\overline{\rho}}\int_0^1\int_0^1\int_0^1\int_0^1 \rho\phi P(f,i,r,s)\,\mathrm{d}f\,\mathrm{d}i\,\mathrm{d}r\,\mathrm{d}s. \tag{10.33}$$

As the independent variables are normalized, they can be assumed to be statistically independent and the joint PDF can be factorised in the individual PDF's:

$$P(f,i,r,s) = P(f)P(i)P(r)P(s). \tag{10.34}$$

The most important fluctuations are the mixture fraction fluctuations, because the mass fractions, temperature and NO production vary non-linearly with mixture fraction. These fluctuations are taken into account by using a beta function for P_f. The adiabatic enthalpy depends linearly on the mixture fraction, but due to the weighting the influence of the mixture fraction is eliminated from the dimensionless non-adiabatic scalar i. The mass fractions and temperature vary almost linearly with i. For that reason turbulent fluctuations in i have only a small effect and a single delta function can be chosen for P_i. Similarly a single delta function can be chosen for P_r and P_s. By formulating the combined variable for the hydrogen combustion, the influence of higher order moments (fluctuations) of r is negligible. The CO reactions are not very sensitive to fluctuations, as their activation energy is low [16].

The species mass fractions are determined at specified values of f, i, r, s by the definitions of these variables, the elemental balances and the conditions of partial equilibrium and steady state. The resulting set of non-linear algebraic equations is solved for the range of f, i, r, s [19] and the instantaneous source terms are calculated from the mass fractions. Partial equilibrium and steady state

conditions however can be assumed only at temperatures above 1200 K. At lower local temperatures, data in the database are found by interpolation to the inlet values and higher temperature tabulated data. In a flame stabilized by a hot recirculation area this is not a problem, as all relevant processes take place at elevated temperatures. To speed up flame calculations, the mass fractions and the source terms in the transport equations are calculated and PDF averaged in advance and stored in a thermo-chemical database as a function of the independent variables (f, g, i, r and s) and the mixture fraction variance g. The non-linear dependence of flame temperature and species concentrations on the mixture fraction near the stoichiometric mixture fraction calls for close mixture fraction spacing in the database to describe the mixing source terms accurately. For this reason 21 mixture fraction steps are used in the thermo-chemical database, with spacing of 0.01 near the stoichiometric value. The variance of mixture fraction space is divided in 13 intervals, starting with an interval of $5.0 \cdot 10^{-5}$. Each successive interval is twice the size of the previous one. For the reaction progress variables, r and s, 10 steps are used, refined to a spacing of 0.01 near the burnt conditions. The maximum deviation from equilibrium is expected to be less than 35 percent for both variables. Finally, 8 steps are used for the heat loss variable from the adiabatic condition to 50 percent heat loss.

Like the other source terms, the mean radiation source term is obtained in a pre-processing step by averaging over the independent variables using the PDF's discussed above. This is possible, thanks to the fact that absorption is taken into account only from uniform wall radiation. If optically thick cases were to be considered absorption from all sources would have to be calculated, and the averaging of the mean radiation term would have to be performed during the CFD calculation.

The formation of thermal NO is computed with the Zel'dovich mechanism in a post processing step ([4] and Appendix I). For convenience the NO source term is stored in the database with the other source terms. The local production of NO is shown in figure 10.1 as a function of f and i. The deviation from equilibrium is five percent for the reaction progress variables r and s. It is observed that the NO production is high at the stoichiometric value of f and at zero percent heat loss, hence in the hottest part of the flame. Also shown here, is that the database shows a dependence of NO production on the enthalpy variable which is much more linear than on the mixture fraction. This supports the assumption that a single delta function can be used for enthalpy averaging.

7 Set-up of experiments and numerical simulations

An experimental set-up was built at the Laboratory of Thermal Engineering of the University of Twente specifically for measurements on non-adiabatic flames with a power of 20–100 kW and with fuels composed of a mixture of $CO/H_2/N_2$. In the set-up the burner is mounted to an air cooled combustion chamber. In subsection 7.1 the burner and combustor construction, and the fuel supply are described. The measurements performed and the measurement accuracy are discussed in section 7.2. The set-up to simulate numerically the flame in this combustor is presented in subsection 7.3.

7.1 The Burner, the Combustor and the Fuel Supply

Fuel and air are supplied to a diffusion burner shown in figure 10.2. It consists of a central fuel tube, surrounded by a concentric air tube. The inner diameter D of the burner is 50 mm, which is half the diameter of the combustion chamber. A cylindrical flame holder is attached to the end of a rod extending axially through the burner. The rod is mounted in the axis of the burner by three ribs in the burner outlet tube. The axial position of the flame holder can be varied by adjusting the rod in its mounting on the left hand side of the burner. During the measurements the distance between the burner and the flame holder was chosen to be 10 mm. The inlet air tube has a bend with a 45 degrees

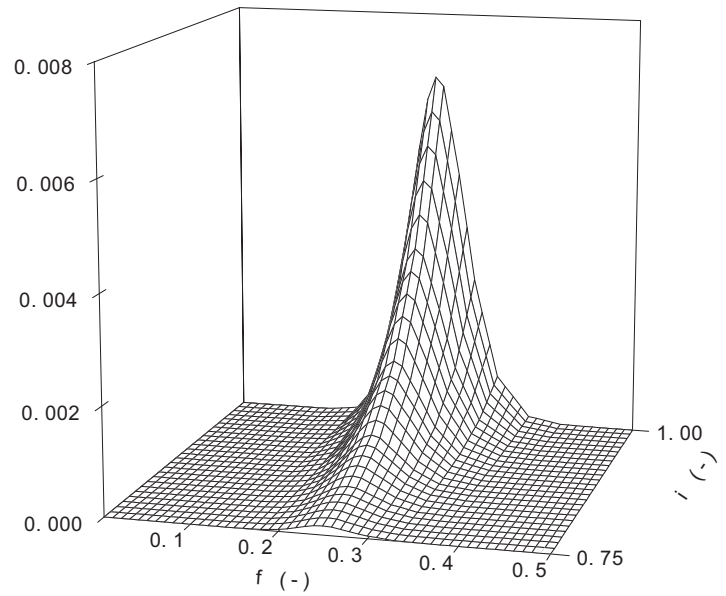

Figure 10.1: Local production of NO as a function of mixture fraction and enthalpy variable at a deviation from equilibrium of 5% for both reaction progress variables.

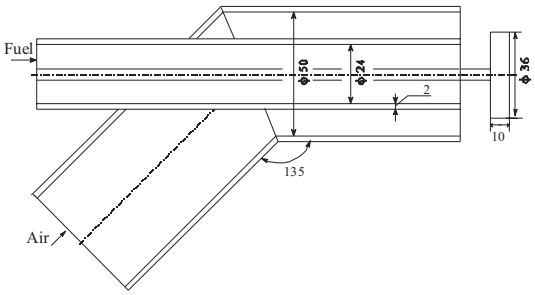

Figure 10.2: The non-premixed burner with variable flame holder.

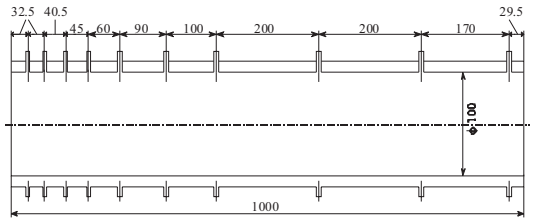

Figure 10.3: The cooled cylindrical combustion chamber.

angle, to separate the concentric fuel and air pipes upstream. To verify the axisymmetry of the air flow, which might have been perturbed by the air tube bend, hot wire measurements were performed at the burner outlet. These measurements did not show a significant deviation from axisymmetrical flow.

The combustor is depicted in figure 10.3, and is constructed of two concentric tubes. The burner is mounted to the inner tube of the combustor which has a diameter of 100 mm and a length of 1.0 m. Cooling air flows between the two tubes to cool the outside wall of the inner tube, similar to a gas turbine combustion chamber. At the exit of the combustion chamber the cooling air is mixed with the flue gas and escapes via a chimney. Two series of sample ports are located at regular axial distances along the combustor geometry. One set of ports can be used to insert a sample probe into the combustor. The combustor is positioned such that the ports have an angle of 45° with the vector of gravitational acceleration, so the profiles are measured diagonally from the top left to the bottom right. The other ports give access to the area between the two tubes and can be used to measure the temperature of the cooling air or the inner tube's outside wall temperature. Not shown in figure 10.3 are the retractable spark plug, which is used to ignite the mixture, and the UV detector. If the flame

Species	Analyser	Range	Calibration
CO	Beckman Industrial Model 870	0–31.4 vol%	29.7 vol%
CO_2	Maihak defor	0–25 vol%	14.76 vol%
O_2	Maihak oxygor 6n	0–25 vol%	5.1 vol%
NO_x	Beckman Industrial model 951A	0–100 ppm	46.6 ppm

Table 10.1: Analysers used to measure species concentrations.

blows off that is detected by the UV detector and the installation shuts down automatically.

The gases composing the fuel gas are obtained from compressed gas storage bottles and are mixed in a mixing device. For the measurements fuel consisting of 40% CO, 40% H_2 and 20% N_2 with a calorific value of 11.9 MJ/kg is used. The use of this fuel results in an adiabatic flame temperature of 2315 K at an inlet temperature of 303 K for both fuel and air and at the stoichiometric air/fuel ratio.

7.2 Measurements and accuracy

In the experiments radial profiles of CO, CO_2, O_2 and NO concentrations were measured at axial distances of 0.065, 0.15, 0.30, 0.40 and 0.60 m from the burner exit. A sample gas flow was extracted from the flue gas flow in the combustor with a water cooled stainless steel sampling probe with an outside diameter of 7 mm and an inner diameter of the gas tube of 1.5 mm. To prevent the condensation of water the cooling water has a temperature of 80°C, and the sample is transported with a heated hose to the analysis equipment. Before it is analysed the gas sample is cooled to 0°C to remove the water vapour. All measurements are therefore dry measurements and in comparisons the simulation results are post-processed accordingly. The gas analysis instrumentation equipment is stated in Table 10.1.

The accuracy of the measurements is influenced by several factors. The gas sample was cooled rapidly to a temperature where the reactions are frozen in time. The analysers were calibrated before and after the session. The differences between these calibrations were very small. Hence it can be assumed that the measured value is close to the actual concentration in the gas sample. Another source of errors is the local quenching of the flame by the cooled probe. This causes the reactions to be arrested by the probe, thus resulting in higher CO and O_2 concentrations and lower CO_2 concentration measured than present in the unperturbed flame. But as the speed of the flow is high (fuel and air inlet velocity of approximately 3 m/s) this effect will be small. The effect of quenching on the NO concentration will be very small. Another source of errors is the result of the positioning of the probe. The accuracy with which the probe is positioned in radial direction is 0.5 mm. When large gradients in radial direction are present, this together with the smoothing effect of the probe size, can be a source of errors.

7.3 The simulation set-up

The combustion model, described in the previous sections, was implemented in the commercial CFD package CFX 4.2 [20]. The flow solver and the k-epsilon turbulence model of this package are used to calculate the flow field. The combustion model computes the species concentrations, temperature and density and the scalar variable source terms from the values of f, i, r, s. The model is implemented by adding convection-diffusion user scalar transport equations. The scalar variable source terms and the density are returned to CFX by the FIRS model.

In the simulations the combustor volume is meshed with the three dimensional grid shown in

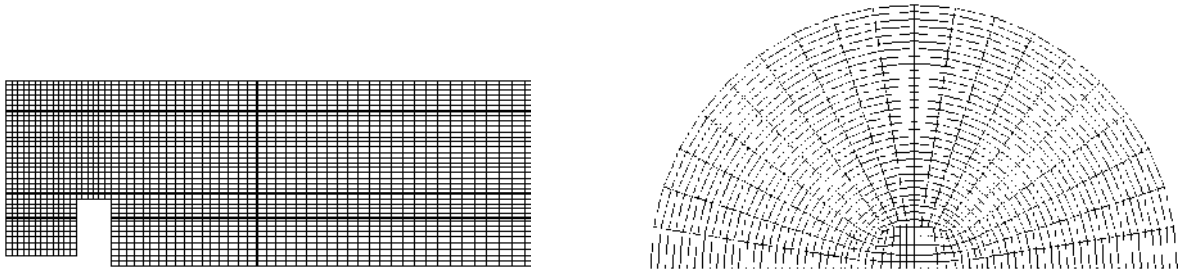

Figure 10.4: Three dimensional computational mesh of 92.460 cells. a: longitudinal cross-section; b: axial cross section.

figure 10.4. This grid contains 92.460 cells. Only half the combustion chamber is modelled in view of the vertical symmetry plane. Horizontal symmetry is not present due to buoyancy effects. The hot gas flow in the post-flame region is deflected upward. The rod on which the flame holder is mounted is modelled as a square bar using the inner eight cells of the rectangular region in figure 10.4b. The remainder of this rectangular region, together with the first three cells in radial direction composes the fuel inlet. The air inlet is described by the next six cells in radial direction. The combustion chamber is modelled up to a length of 0.65 m, which is just downstream the eighth sample port position.

The fuel and air inlet velocities are 4.13 and 2.88 m/s respectively. The Reynolds number in the inlet flows is 10,000. In the flame the flow remains turbulent, be it at the relatively low Reynolds number of 4,000. This all results in a thermal power of 16 kW (HHV) and an air factor of 1.3. For the calculation of the radiation source term, the wall temperature was set uniformly to 600 K, but the results are not sensitive to this value. Direct influence of the cooled wall on the mixture adjacent to this wall by conductive and convective heat transport was neglected. The inlet values for the turbulent kinetic energy k were taken from cold flow hot wire measurements in the burner inlet and equal to 0.15 m^2/s^2 (fuel) and 0.12 m^2/s^2 (air). The values of the rate of dissipation of turbulent kinetic energy at the inlet were determined from the measured k vales with the correlation $\epsilon_{\text{inl}} = k_{\text{inl}}^{1.5}/0.3D$ (D is the combustor diameter). All modeling constants were set to CFX defaults, shown in Table 10.2. The total CPU time needed to obtain a converged solution was 9 hours on a single R8000 processor of a SGI Power Challenge computer. The code that creates the thermo-chemical database for this fuel needs about 6 hours CPU time on this computer.

8 Results of simulation and experiment

8.1 The Predicted Flow Field

The simulated flow pattern near the flame holder is shown as a vector plot in figure 10.5. The bluff body flame holder is observed to deflect the fuel and airflow to larger radii, and increases the rate of

Turbulence model			Mixing model
$C_\mu = 0.09$	$C_{\epsilon_1} = 1.44$	$\sigma_k = 1.00$	$D_{\text{m}} = 2.57 \cdot 10^{-5}$
	$C_{\epsilon_2} = 1.92$	$\sigma_\epsilon = 1.22$	$D_{g_1} = 2.00$
	$C_{\epsilon_3} = 0.00$	$\sigma_{\text{pr}} = 0.90$	$D_{g_2} = 2.00$

Table 10.2: Modeling CFD turbulence constants used in CFX.

mixing of both flows. Downstream the flame holder at the combustor center, a recirculation zone is created, which ignites the fresh mixture at its circumference and thus stabilizes the flame.

The predicted values of mixture fraction, enthalpy loss and hydrogen reaction progress variable on the vertical symmetry plane of the combustor are shown in contour plots in figures 10.6 to 10.8 respectively. The mixture fraction contours in figure 10.6 show that the fuel and air flow are deflected to larger radii, afterwards they mix slowly, despite the turbulence generated by the flame holder. This results in a long flame, which extends over a large part of the combustion chamber. The deflection from axial flow, due to buoyancy effects, can be seen clearly. From the dimensionless enthalpy contours in figure 10.7 it is observed that the total heat loss in the combustion chamber is high, up to 50% at an axial distance of 0.65 m. This is due to the relatively low velocity and the high amount of radiating species. Because of this heat loss, the formation of NO is arrested after the first part of the flame. The contours in figure 10.8 show that the hydrogen reactions have a deviation from equilibrium in a large part of the combustion chamber, with a maximum deviation of 8% near the flame holder. This results in a reduction of temperature and an increase in radical concentrations (to super-equilibrium). The net result of these effects is found to be an increase in the predicted amount of thermal NO. The deviation from equilibrium of the CO reactions is much smaller in the entire combustion chamber (2% maximum).

The predicted mean temperature contour plots on the symmetry plane are presented in figure 10.9. The maximum temperature reached in the flame is 1890 K, while the adiabatic flame temperature is 2315 K. The low maximum temperature, as compared to the adiabatic flame temperature, is caused by mixture fraction fluctuations, deviation from equilibrium and enthalpy loss.

8.2 Radial Profiles of Species Concentrations

Radial profiles of species concentrations were measured at five axial distances. Representative radial profiles at two axial locations are presented in the next four figures. In figure 10.10 the predicted and measured radial profiles of CO at $x = 0.065$ m and $x = 0.3$ m are compared. The calculation with the FIRS model shows good agreement with the measurements. Initially the conversion of CO is slightly underpredicted compared to the measurements. This difference remains visible at larger axial distance. The prediction of the CO concentration could be improved ad hoc by reducing the dissipation of turbulence at the inlet, which has a large influence on the initial mixing of fuel and air. In spite of this observation, measured inlet values obtained by hot wire measurements were used, instead of fitted turbulence inlet values. At $x = 0.065$ m, the tip of the (simulated) recirculation zone, the CO profile is symmetrical. Downstream the profile shows a shift of CO to the upper part of the

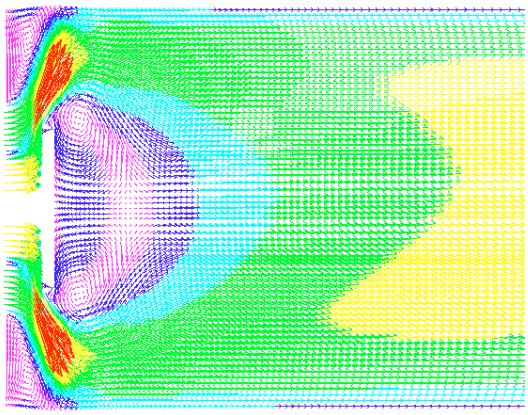

Figure 10.5: Vector plot of the flow near the flameholder.

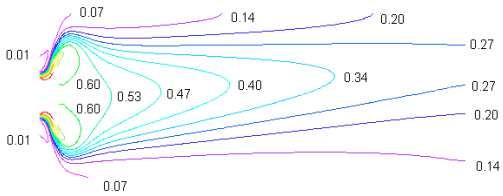

Figure 10.6: Contour plot of mean mixture fraction at the combustor symmetry plane.

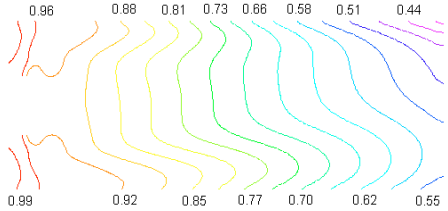

Figure 10.7: Contour plot of enthalpy loss variable at the combustor symmetry plane.

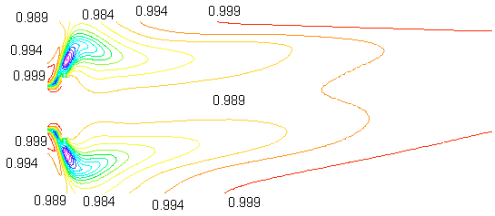

Figure 10.8: Contour plot of mean hydrogen reaction progress variable at the combustor symmetry plane.

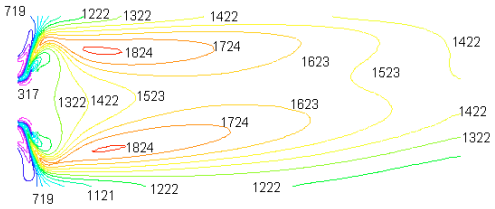

Figure 10.9: Contour plot of the mean temperature at the combustor symmetry plane

combustion chamber due to buoyancy effects. This is observed both in measurements and predictions.

In figure 10.11 the CO_2 profiles are shown. CO_2 is formed on the combustion interface and partly transported into the fuel core by recirculation. Two peaks can be seen in the plot, separated by the rich fuel core. The total amount of CO_2 increases along the combustion chamber. The predicted CO_2 profiles agree well with the measurements. In the fuel core the amount of CO_2 is underpredicted,

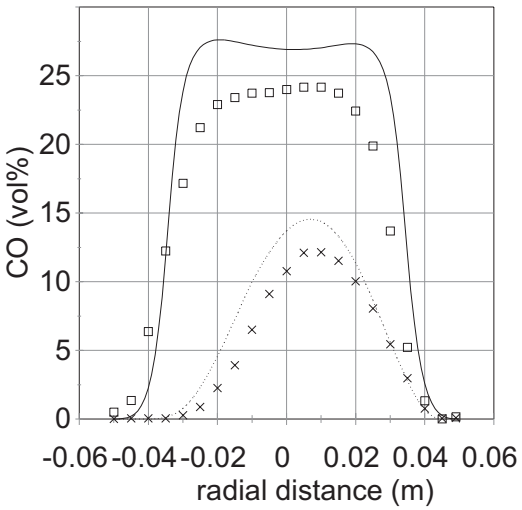

Figure 10.10: Comparison of predicted and measured CO concentration at $x = 0.065$ (solid line, squares) and $x = 0.3$ m (dashed line, crosses).

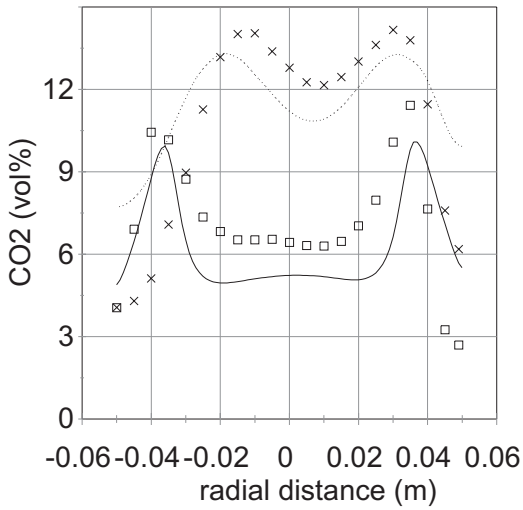

Figure 10.11: Comparison of predicted and measured CO2 concentration at $x = 0.065$ (solid line, squares) and $x = 0.3$ m (dashed line, crosses).

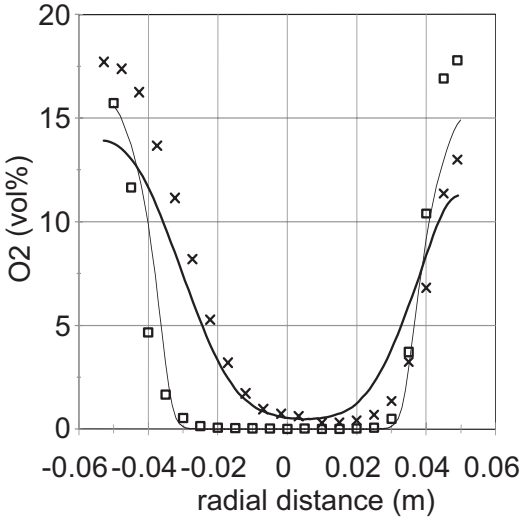

Figure 10.12: Comparison of predicted and measured O_2 concentration at $x = 0.065$ (solid line, squares) and $x = 0.3$ m (dashed line, crosses).

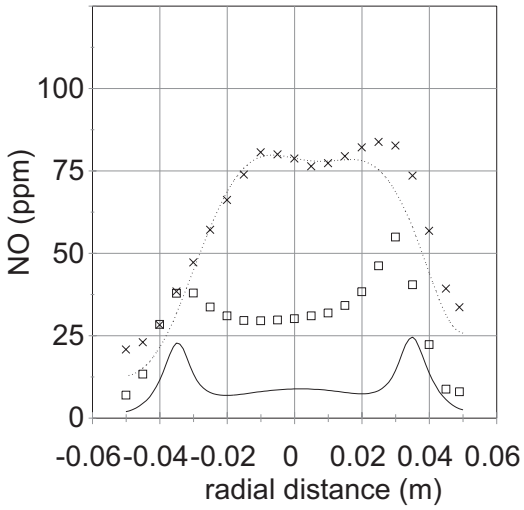

Figure 10.13: Comparison of predicted and measured NO_x concentration at $x = 0.065$ (solid line, squares) and $x = 0.3$ m (dashed line, crosses).

corresponding with the overprediction of CO. This indicates that the amount of air mixed into the fuel core is slightly underpredicted.

The oxygen profiles in figure 10.12 show the rich fuel core where all O_2 is converted to reaction products and the co-flow of air. The amount of O_2 near the combustor wall is less than the amount of O_2 in the air. Some fuel has already mixed in and was burned. The fuel core decays only slowly because the mixing of fuel and air is slow.

In figure 10.13 the calculated and measured NO concentrations are compared. At $x = 0.065$ m the NO concentration is underpredicted by a factor two in the peak regions. Possibly this is explained by the high production of NO this region, leading to high axial gradients in concentration. A small uncertainty in axial distance gives different results. Further downstream the predicted NO concentration compares well with measurements. After 0.3 m the production of NO is arrested because the temperature is reduced below the production threshold due to radiation heat loss. This point and the local NO concentration are predicted very well by the non-adiabatic FIRS model. At $x = 0.6$ m the NO profile is uniform and the measured NO concentration is 70 ppm.

8.3 Influence of Heat Loss

To assess the magnitude of the effect of heat loss, the simulation is repeated with the FRS model. This model is adiabatic ($i = 1$), but otherwise identical with the FIRS model. Initially, at $x = 0.065$ m, both models predict CO similar concentration profiles. This is depicted in figure 10.14. Further downstream the adiabatic FRS model predicts higher CO concentrations than the non-adiabatic model, as can be seen in figure 10.15, where the CO concentration at $x = 0.6$ m calculated with each model is compared with the measurements. This can be expained by the combination of higher temperature due to neglect of heat loss and the fact that the deviation from equilibrium for the CO system is always very small. This will lead to a shift of the CO system from CO_2 to CO and hence higher CO concentrations. In addition to that the CO concentration predicted by the FRS model can be increased by an overprediction of the buoyancy effect with the adiabatic model. This results in decreased mixing

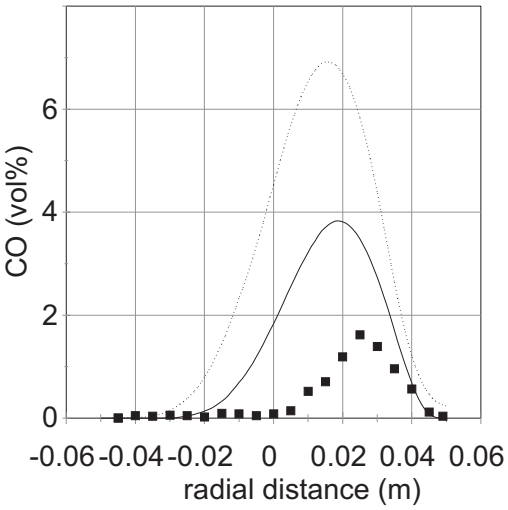

Figure 10.14: Comparison of predicted and measured CO concentration at $x = 0.6$ m. Squares: measurements; thick solid line: RPV model; dashed line: adiabatic RPV model.

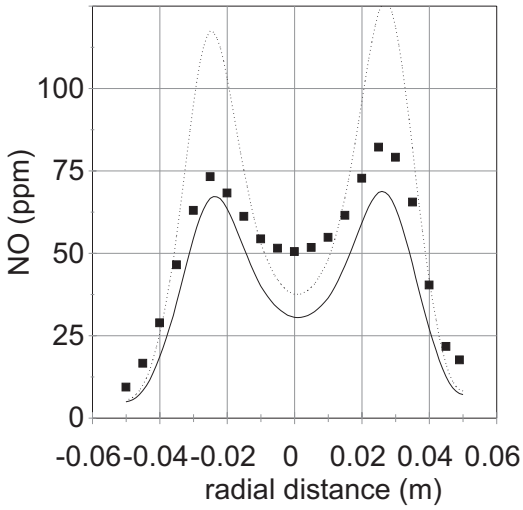

Figure 10.15: Comparison of predicted and measured NO fraction at $x = 0.15$ m. Squares: measurements; thick solid line: RPV model; dashed line: adiabatic RPV model.

rates of fuel and air.

In figure 10.15 the predicted and measured NO profiles at $x = 0.15$ m are compared. The non-adiabatic model agrees well with the measurements, while the adiabatic model overpredicts the NO concentration by 50% at the peak regions. Further downstream the overprediction of the adiabatic model is increased to concentrations as high as 500 ppm. The explanation is, that the formation of thermal NO is not arrested by a decrease in temperature with axial distance, in the absence of heat loss. The heat loss model incorporated in the FIRS model is therefore essential to predict NO formation correctly.

In the non-adiabatic transport equations for the reaction progress variables, r and s, additional source terms appear due to heat loss. In the H_2 equation this is a mixing source term (second term between brackets in equation (10.22) and a term caused by a change in equilibrium composition due to heat loss. These two extra terms have a similar effect as the adiabatic mixing term and the chemical source term in the r equation. In [19] it was shown however that these two terms can be neglected, compared to their adiabatic counterparts, when the heat loss is less than 10 percent. This also applies to the CO equation. Hence in case of modest heat loss its effect on chemistry can be taken into account solely via the database, in which the composition and temperature vary with the enthalpy loss variable i.

9 Conclusion

In this paper a model is introduced that can simulate the combustion of syngas in non-adiabatic turbulent combustors. By using a commercial CFD flow solver and its incorporated turbulence model, complex three dimensional geometries, like gas turbine combustion chambers, can be simulated. All chemistry data is contained in averaged form in a database, which is generated prior to the flame calculation. This makes the model fast and easy to use.

Simulation of non-adiabatic combustion is achieved by including an equation for heat loss. This

additional equation is normalized to reduce the statistical dependence on the mixture fraction. When heat loss is significant it influences the variables for the combustion of hydrogen and carbon monoxide via this normalization. Another effect on chemistry is the variation of mass fractions with enthalpy in the database. In case of modest heat loss, its main influence is via the change in composition due to the reduction in temperature.

The model is verified using probe measurements in an air cooled combustion chamber. Prediction of major species like CO, CO_2 and O_2 as well as the prediction of NO agree well with the measurements. Hence it can be concluded that the turbulent reduced chemistry model gives a good prediction of the mean chemical reaction rates. The transition point at which the temperature has decreased under the temperature threshold to form significant thermal NO is predicted correctly. Therefore it can be concluded that the heat loss is predicted correctly.

As a next step it can be considered to apply the model to the combustion of methane by adding a reaction progress variable ('t') for the conversion of methane to hydrogen and carbon monoxide. This is discussed by Kok *et al.* [21].

Acknowledgment

This research was made possible by the financial support from NOVEM, Sittard, which is financed by the Dutch ministry of Economic Affairs. The calculations of the flow field, turbulence and combustion scalar field were performed with the Computational Fluid Dynamics package CFX of AEA Technology. The support of Dr. I.P. Jones and his associates of AEA Technology is appreciated.

References

[1] Lefebvre, A., Gas Turbine Combustion, Taylor & Francis, Philadelphia, 2nd ed., 1998.

[2] Liñan, A., Williams, F.A., 1992, *Fundamental aspects of combustion,* Oxford University Press, Oxford.

[3] Peters, 1988, *Laminar flamelet concepts in turbulent combustion*, 21st Symp. (Int.) Comb., The Combustion Institute, Pittsburgh, 893.

[4] Kok, J.B.W., Louis, J.J.J., *Combust. Sci. and Tech.* 131: 225 (1998).

[5] Eggels, R.L.G.M., Louis, J.J.J., Kok, J.B.W., De Goey, L.P.H., *Combust. Sci. and Tech.* 123:347-362 (1997).

[6] Spalding, D.B., *Chemical engineering science* 26:95-107 (1971).

[7] Williams, F.A., *Combustion theory*, Addison-Wesley, Reading, 1985.

[8] Siegel, R., Howell, J.R., *Thermal radiation and heat transfer*, McGraw-Hill, Washington, 2nd edition, 1981.

[9] Tien, C.-L., 1968, *Thermal radiation properties of gases*, Advances in heat transfer vol 5, eds IrvineTh.F., & Hartnett J.P., pp 253-321, Academic Press, New York, 1968.

[10] Modest, M.F., *Radiative heat transfer*, McGraw-Hill, New York, 1993.

[11] Chen, Y., Lui, Rogg, B., *Lecture notes in physics* m15:196-223, Springer-Verlag, Berlin, 1993.

[12] Grosshandler, W.L., RADCAL: *A narrow band model for radiation calculations in a combustion environment*, NIST Technical Note 1402, NIST, Gaithersburgh, MD, 1993.

[13] Kok, *Radiation*, report WB ThW98/TMV002, University of Twente, 1997.

[14] Janicka, J., Ph.D. Thesis, Techn. Hochschule Aachen, 1979.

[15] Janicka, J., Kollmann, W., *Combust. Flame* 44:319-336 (1982).

[16] Correa, S.M., *Archivum Combustionis* 5, No. 3-4: 223-243 (1985).

[17] Correa, S.M., Gulati, A., *Combust. Flame* 89:195-213 (1992).

[18] Dixon-Lewis, , G., Goldsworthy, F.A., Greenberg, J.B., 1975, *Proc. R. Soc. London* A 346, 261-278.

[19] Louis, J.J.J., PhD thesis University of Twente, Enschede, The Netherlands, 1997.

[20] User guide CFX flow solver, AEA technology, Computational Fluid Dynamics Services, 1995.

[21] Kok, Jim B.W., Louis, Jurgen J.J., Yu, Jiang Hong, *The IRST model for turbulent premixed non-adiabatic methane flames*, Combust. Sci. and Tech., vol. 149, 225-247, 1999.

Appendix I: the chemical reaction mechanism

Reaction	*A* [cm,mole,s]	*b* [-]	*E* [kJ/mole]	Nr
The hydrogen chemical reaction mechanism				
$H + O_2 \rightleftharpoons OH + O$	2.00E+14	0.00	70.30	H1
$H_2 + O \rightleftharpoons OH + H$	5.06E+04	2.67	26.30	H2
$H_2 + OH \rightleftharpoons H_2O + H$	1.00E+08	1.60	13.80	H3
$OH + OH \rightleftharpoons H_2O + O$	1.50E+09	1.14	0.42	H4
$H + H + M \rightleftharpoons H_2 + M$	1.80E+18	-1.00	0.00	H5
$H + OH + M \rightleftharpoons H_2O + M$	2.20E+22	-2.00	0.00	H6
$O + O + M \rightleftharpoons O_2 + M$	2.90E+17	-1.00	0.00	H7
$H + O_2 + M \rightleftharpoons HO_2 + M$	2.30E+18	-0.80	0.00	H8
$HO_2 + H \rightleftharpoons OH + OH$	1.50E+14	0.00	4.20	H9
$HO_2 + H \rightleftharpoons H_2 + O_2$	2.50E+13	0.00	2.90	H10
$HO_2 + H \rightleftharpoons H_2O + O$	3.00E+13	0.00	7.20	H11
$HO_2 + O \rightleftharpoons OH + O_2$	1.80E+13	0.00	-1.70	H12
$HO_2 + OH \rightleftharpoons H_2O + O_2$	6.00E+13	0.00	0.00	H13
$HO_2 + HO_2 \rightleftharpoons H_2O_2 + O_2$	2.50E+11	0.00	-5.20	H14
$OH + OH + M \rightleftharpoons H_2O_2 + M$	3.23E+22	-2.00	0.00	H15
$H_2O_2 + H \rightleftharpoons H_2 + HO_2$	1.70E+12	0.00	15.70	H16
$H_2O_2 + H \rightleftharpoons H_2O + OH$	1.00E+13	0.00	15.00	H17
$H_2O_2 + O \rightleftharpoons OH + HO_2$	2.80E+13	0.00	26.80	H18
$H_2O_2 + OH \rightleftharpoons H_2O + HO_2$	5.40E+12	0.00	4.20	H19
The CO chemical reaction mechanism				
$CO + OH \rightleftharpoons CO_2 + H$	6.00E+06	1.50	-3.10	C1

$CO + O + M \rightleftharpoons CO_2 + M$	7.10E+13	0.00	-19.00	C2
The NO ('Zeldovich') chemical reaction mechanism				
$N_2 + O \rightleftharpoons NO + N$	1.80E+14	0.00	319.0	N1
$N + O_2 \rightleftharpoons NO + O$	6.40E+09	1.00	26.10	N2
$N + OH \rightleftharpoons NO + H$	3.00E+13	0.00	0.000	N3

Rate constants: $k_\mathrm{f} = AT^\mathrm{b} \exp(-E/RT)$;

Third body efficiencies: CO: 0.75; O_2: 0.4; CO_2: 1.5; H_2O: 6.5; N_2: 0.4

Appendix II: The reaction progress variable model

Consider a set of M elementary reactions involving N species and L elements. The chemical reactions with subscript k between the species with subscript i and with chemical symbol χ_i can be represented in a general form as ([7], p. 556):

$$\sum_{i=1}^{N} \nu'_{ik} \chi_i = \sum_{i=1}^{N} \nu''_{ik} \chi_i \quad k = 1, \ldots, M. \tag{A1}$$

The net rate of production of species i due to all M chemical reactions is then given by the i_th component of the species rate of production vector:

$$\frac{\mathrm{d}C_i}{\mathrm{d}t} = \omega_i = \sum_{k=1}^{M} \nu_{ik} \varpi_k, \tag{A2}$$

with components of the reaction tensor defined by $\nu_{ik} = \nu''_{ik} - \nu'_{ik}$. According to the law of mass action the rate of progress variable ϖ_k is given by:

$$\varpi_k = k_{\mathrm{f},k} \left(\prod_{l=1}^{N} C_l^{\nu'_{ik}} - \frac{1}{K_{\mathrm{c},k}} \prod_{l=1}^{N} C_l^{\nu''_{lk}} \right), \tag{A3}$$

with equilibrium constant $K_{\mathrm{c},k}$ defined by the ratio of forward and backward rate constants:

$$k_{\mathrm{r},k} = \frac{k_{\mathrm{f},k}}{K_{\mathrm{c},k}}. \tag{A4}$$

Assuming an Arrhenius temperature dependence, the forward rate constant can be expressed by:

$$k_{\mathrm{f},k} = A_k T^{\beta_k} \exp\left(-\frac{E_k}{RT} \right). \tag{A5}$$

Of concern in a turbulent reacting flow are those reactions that have a large activation energy E_k. For example the important reaction H1 in the hydrogen mechanism in Appendix I has a large activation energy of 70 kJ/mole. This reaction will be very sensitive to temperature fluctuations. Hence in a turbulent flow, the mean reaction rate can not be calculated accurately by weighting over an assumed shape PDF, because the answer would be very sensitive to the shape of the PDF ([2], p. 142). If the

rate constant in equation (A5) (taking for convenience) is developed in a Taylor series around a mean temperature and averaged subsequently, the mean rate constant becomes:

$$k_{\mathrm{f},k} = A_k \exp\left(-\frac{E_k}{RT}\right)\left[1 + \left(\frac{E_k}{2R\overline{T}} - 1\right)\frac{E_k}{R\overline{T}^3}\overline{\left(T - \overline{T}\right)^2} + \ldots\right]. \tag{A6}$$

This series is convergent, but at high activation energies it may take up to 15 terms (e.g. moments) before higher orders terms can be neglected. This property inhibits direct calculation of the source terms of these reactions with a moment method. However, often it can be observed that the contribution of that reaction is large and the chemical time scale small. A chemical relaxation time for reaction number k in *forward* direction and specie number i can be defined as the ratio of the concentration of C_i and the change of C_i with time:

$$\tau_{ik} = \frac{C_i}{\frac{\mathrm{d}C_i}{\mathrm{d}t}} = \frac{C_i}{\nu_{ik} k_{\mathrm{f},k} \prod_{l=1}^{N} C_l^{\nu'_{lk}}}. \tag{A7}$$

When this time is small as compared to the turbulent mixing length, the Damkohler number is large for this reaction. But then this reaction can be regarded as an equilibrium reaction. In that case the time scale of the *combined* forward and backward reaction :

$$\tau_k = \frac{C_i}{\frac{\mathrm{d}C_i}{\mathrm{d}t}} = \frac{C_i}{\omega_i} = \frac{C_i}{\nu_{ik}\varpi_k} \tag{A8}$$

is large as ϖ_k approaches zero for partial equilibrium and the Damkohler number of the combined reaction is small. Similarly for steady state of species number i, a time scale can be formulated of the combined reactions as: .

$$\tau_i = \frac{C_i}{\sum_{k=1}^{M} \omega_i} = \frac{C_i}{\sum_{k=1}^{M} \nu_{ik}\varpi_k} \tag{A9}$$

In steady state de denominator will approach zero, the chemical reaction time will be large with respect to the turbulent mixing time and the Damkohler number of the reaction of the species will be small. Hence when looked at the contribution of individual reactions the Damkohler number is large and in a turbulent reacting flow the individual mean source terms can not be calculated accurately by averaging over an assumed shape PDF. But the *combined* effect of the ensemble of reactions often takes place at a much larger time scale and at small Damkohler number.

This can be used to circumvent the problem of the calculation of the individual mean turbulent chemical reaction source term. Of crucial importance in this method is the fact that the dimension of the chemical space in a flame is much smaller than the number of independent species variables. This is due to the mentioned partial equilibria of reactions and steady state of species. Consider a set of M elementary reactions involving N species and L elements. The dimension of the reactive species space is $D = N - L$. The flame is in many cases confined to a subspace of the reactive species space with dimension 1–5. Here it is assumed that the reaction mechanism chosen is such that the subspace has the dimension of 1. In that case the evolution of all species variables can described by one new variable composed of D species. This variable is formulated such that source terms from D individual reactions cancel each other (this was first proposed by [18]). The molar concentration C of this variable is calculated from:

$$C = \sum_{j=1}^{D} a_j C_j. \tag{A10}$$

The weighting coefficients a_j are chosen such, that the source terms with high activation energy, for example of the equilibrium reactions, cancel each other in the combined source term. The reactions $k = 1, \ldots, M$ are renumbered in order of decreasing activation energy.

The total reaction source term of C is:

$$\omega = \sum_{j=1}^{D} a_j \omega_j = \sum_{j=1}^{D} a_j \sum_{k=1}^{M} \nu_{jk} \varpi_k. \tag{A11}$$

Subsequently the order of summation over j and k is interchanged in the source term:

$$\omega = \sum_{j=1}^{D} a_j \omega_j = \sum_{j=1}^{D} a_j \sum_{k=1}^{M} \nu_{jk} \varpi_k = \sum_{j=1}^{D} \sum_{k=1}^{M} a_j \nu_{jk} \varpi_k = \sum_{k=1}^{M} \sum_{j=1}^{D} a_j \nu_{jk} \varpi_k. \tag{A12}$$

The weighting coefficients $\mathrm{a_j}$ in C are now chosen such that:

$$\sum_{j=1}^{D} a_j \nu_{jk} \varpi_k = 0 \tag{A13}$$

for the reactions numbered $k = 1$ to D. The remaining source term for C becomes:

$$\omega = \sum_{k=D+1}^{M} \sum_{j=1}^{D} a_j \nu_{jk} \varpi_k. \tag{A14}$$

From this expression D, source terms with high activation energy have been eliminated. Hence, the source term of C only contains slow contributions, which are relatively insensitive to a variation in the temperature and in the shape of the Probability Density Function. For that reason, the mean of this source term can be calculated explicitly with the use of an assumed shape PDF. The time scale at which the combined species changes due to chemical reaction is:

$$\tau_c = \frac{\sum_{i=1}^{D} \alpha_i C_i}{\sum_{k=D+1}^{M} \sum_{i=1}^{D} \alpha_i \nu_{ik} \varpi_k}. \tag{A15}$$

In this expression for τ_c the denominator is small, because all the large source terms have been eliminated. Hence the time scale τ_c is large and the Damkohler number of the composed variable C is small. The mean turbulent source term $S_C(C,\ f, h)$ of C can now be averaged with sufficient accuracy over the assumed shape joint Probability Density Function:

$$\overline{S_C} = \iiint \frac{\rho}{\overline{\rho}} S_C P(C,\ f)\ \mathrm{d}C\ \mathrm{d}f. \tag{A16}$$

Chapter 11

Joint velocity-scalar PDF methods for turbulent combustion

D. Roekaerts

In this lecture the joint velocity-scalar PDF approach to turbulent combustion modeling is described. This approach was mainly developed by S.B. Pope and includes from the start the complete one-point joint statistics of velocity and scalars. This is conceptually appealing because it delivers in one framework closure models for Reynolds stresses, Reynolds fluxes and chemical source terms. In the final section results of test calculations are presented for a challenging test case, combining a complex flow pattern with effects of high mixing rates and chemical kinetics. For this bluff-body-stabilized diffusion flame, the relative importance of modeling of the velocity, mixing and chemistry terms is studied. The PhD thesis of H. A. Wouters [1], and a more extended version of these notes prepared in collaboration with H. A. Wouters and T. W. J. Peeters [2] can be consulted for further details and other applications.

1 PDF transport equation

From the conservation equations, the transport equation can be derived [3] for the joint velocity-scalar PDF $f_{\boldsymbol{U\phi}}(\boldsymbol{V},\boldsymbol{\psi};\boldsymbol{x},t)$. By integrating this quantity over a range of values of $\boldsymbol{V}$ and $\boldsymbol{\psi}$ the probability that $\boldsymbol{U}$ and $\boldsymbol{\phi}$ take values in these ranges is obtained. It is also useful to consider the joint velocity-scalar mass density function (MDF) defined as $\mathcal{F}_{\boldsymbol{U\phi}}(\boldsymbol{V},\boldsymbol{\psi},\boldsymbol{x};t) = \rho(\boldsymbol{\psi})\, f_{\boldsymbol{U\phi}}(\boldsymbol{V},\boldsymbol{\psi};\boldsymbol{x},t)$. The transport equation for the MDF reads:

$$\frac{\partial}{\partial t}\mathcal{F} + \frac{\partial}{\partial x_i}V_i\mathcal{F} = -\frac{\partial}{\partial V_i}\left[\frac{1}{\rho(\boldsymbol{\psi})}\left(-\frac{\partial\langle p\rangle}{\partial x_i} - \frac{\partial\langle T_{ij}\rangle}{\partial x_j}\right)\mathcal{F}\right] \tag{11.1a}$$

$$-\frac{\partial}{\partial V_i}\left[\frac{1}{\rho(\boldsymbol{\psi})}\left\langle -\frac{\partial p'}{\partial x_i} - \frac{\partial T'_{ij}}{\partial x_j}\,\middle|\, \boldsymbol{U}=\boldsymbol{V},\boldsymbol{\phi}=\boldsymbol{\psi}\right\rangle \mathcal{F}\right] \tag{11.1b}$$

$$-\frac{\partial}{\partial \psi_\alpha}\left[\left(-\frac{1}{\rho(\boldsymbol{\psi})}\frac{\partial\langle J_i^\alpha\rangle}{\partial x_i} + S_\alpha(\boldsymbol{\psi})\right)\mathcal{F}\right] \tag{11.1c}$$

$$-\frac{\partial}{\partial \psi_\alpha}\left[\frac{1}{\rho(\boldsymbol{\psi})}\left\langle -\frac{\partial J_i^{\alpha\prime}}{\partial x_i}\,\middle|\, \boldsymbol{U}=\boldsymbol{V},\boldsymbol{\phi}=\boldsymbol{\psi}\right\rangle \mathcal{F}\right] \tag{11.1d}$$

in which the first two terms (11.1a and 11.1b) on the right hand side describe the evolution in velocity space and the last two terms (11.1c and 11.1d) describe the evolution in scalar space. (The notation $\langle A|\, B\rangle$ denotes the conditional expectation value of A upon condition B). Terms 11.1a and 11.1c occur in closed form whereas

the unclosed terms 11.1b and 11.1d contain conditional averages. These effects cannot be expressed in terms of the one-point distribution of $\boldsymbol{U}$ and $\boldsymbol{\phi}$.

The terms that contain the mean pressure gradient and the mean viscous stress tensor can be expressed in terms of the mean velocity field and thus occur in closed form. Assuming high Reynolds number, effects of mean shear $\langle T_{ij} \rangle$ are usually neglected. The unclosed terms describe the mean effects of the fluctuating pressure gradient and the fluctuating viscous stress tensor, conditional on the values of velocity and scalars.

The terms that describe the evolution in scalar space contain the effects of the mean molecular diffusion flux and of reaction. The reaction rate can be expressed as a function of the scalar variables $\boldsymbol{\phi}$ and therefore it is contained in closed form. Although the Monte Carlo PDF method allows for an exact treatment of chemistry from the point of view of turbulence modeling, the use of a full reaction mechanism would require the integration of a stiff system of many coupled equations. In the Monte Carlo Method chemical reaction has to be followed in many thousands of particles and to make the calculation feasible judicious simplification is needed. Here we refer to the lecture on chemistry reduction methods for a description of some possibilities in this respect. The term containing the conditional mean effects of the fluctuating diffusion flux describes molecular mixing or micro-mixing and is unclosed. Since mixing by diffusion is an essential process bringing reactants and/or heat together the modelling of this term is important. It is directly related to the conditional scalar dissipation rate and connections with other approaches to turbulent combustion modeling can be formulated on the basis of this.

Starting from the transport equation for the joint velocity-scalar mass density function it is straightforward to derive the equation for the joint velocity-scalar Favre PDF $\widetilde{f}_{\boldsymbol{U}\boldsymbol{\phi}}$. Both formulations are equivalent. The Eulerian transport equations for the moments of $\widetilde{f}_{\boldsymbol{U}\boldsymbol{\phi}}$ can be derived by multiplying each term by a function of V_i and ψ_α (*e.g.*, $V_i V_j$, $V_i V_j V_k$, $\psi_\alpha \psi_\beta$, or $V_i \psi_\alpha$) and integrating over the phase space $(\boldsymbol{V}, \boldsymbol{\psi})$. In this way also a transport equation for the Reynolds stresses can be derived and it is a good question to ask which Eulerian second-moment closure model is implied by a choice of closure of the PDF transport equation, or the other way round, to ask whether a proposed second moment closure model has a Lagrangian counterpart. Such questions are discussed in detail by Pope [4] and Wouters [1].

2 Monte Carlo solution method

The PDF transport equation (equation 11.1a−d) is a partial differential equation in many dimensions. In the case of d spatial dimensions and n independent scalars, solving the stationary equation by means of a finite-difference technique would require a sufficiently accurate discretization in $2d + n$ dimensions. Alternatively, in a Monte Carlo solution method, the $2d + n$ dimensional mass density function is represented by a large ensemble of N notional fluid particles. Here the term 'notional fluid particles' is used to distinguish from real physical fluid elements. The particle properties evolve according to particle models such that the evolution of the statistics of the particle ensemble corresponds to the modeled PDF evolution. It is not required that single notional particle trajectories represent real fluid element trajectories. The Monte Carlo method is computationally more efficient already for the case $d = 2$, $n = 1$. Furthermore it offers additional opportunities for model development. The basics of the Monte Carlo method and several of the numerical algorithms involved are described in detail by Pope [3], Haworth and El Tahry [5], Correa and Pope [6], and Wouters [1]. This involves the method of fractional steps, the estimation of mean fields and mean field gradients, particle boundary conditions and the integration of particle evolution equations. Recent developments are summarised

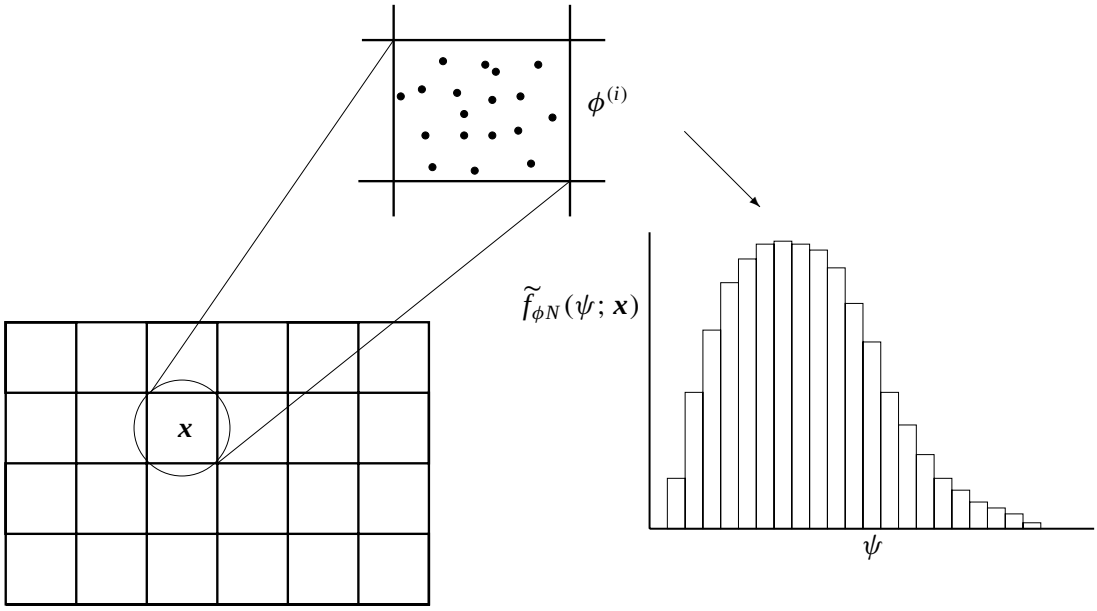

Figure 11.1: Illustration of the Eulerian PDF estimate $f_{\phi N}(\psi; \boldsymbol{x})$ from an ensemble of Lagrangian particles $\phi^{(i)}$ in a cell at position $\boldsymbol{x}$.

by Naud [8].

Here we consider systems whose one-point statistics depend on two spatial coordinates only ($d = 2$). All Eulerian quantities, like mean velocity and scalar fields and the mass density function, are defined on a two-dimensional grid. The Eulerian joint velocity-scalar mass density function is represented by a spatially equally distributed ensemble of Lagrangian notional 'fluid' particles with properties like position, velocity and composition.

Each of the particles represents an amount of mass Δm and the particles are distributed such that the distribution of mass in space corresponds to the actual density field. An estimate of the Eulerian Favre joint velocity-scalar PDF or, equivalently, the joint velocity-scalar mass density function in a cell is given by the velocities and scalar properties of the particles present in that cell. Note that the mass density function is defined on a grid but that the particles are not. The particles each have their own position and velocity and are not bounded to a grid. The estimation of the Eulerian PDF from the ensemble of Lagrangian particles is illustrated in figure 11.1.

The particle properties evolve according to a modeled Lagrangian system of the following general form:

$$\mathrm{d}x_i = U_i \mathrm{d}t \tag{11.2a}$$

$$\mathrm{d}U_i = -K_i^u \mathrm{d}t + b_i\, j \mathrm{d}W_j \tag{11.2b}$$

$$\mathrm{d}\phi_\alpha = -K_\alpha^\phi \mathrm{d}t + b_\alpha \beta \mathrm{d}W_\beta \tag{11.2c}$$

The drift vectors $\boldsymbol{K}^u$ and $\boldsymbol{K}^\phi$ for respectively the velocity and scalars describe a deterministic change, the terms containing the increment of the Wiener process $\mathrm{d}W$ describe a stochastic change, in the form of a diffusion process (see below). All Wiener increments in (2b) and (2c) are independent of each other. The specific expressions for the drift and diffusion terms for velocities and scalars define the model. Examples of particle velocity and scalar evolutions are given below.

The coefficients of the particle models contain basically two different kind of mean quantities. First there are the Eulerian mean quantities, like $\widetilde{U}_i$ and $\widetilde{\phi}_\alpha$. These can be estimated from the particle properties e.g. by the following expression:

$$\widetilde{\phi} = \frac{1}{N_c} \sum_{i=1}^{N_c} \phi^{(i)} \tag{11.3}$$

in which the summation is over all particles present in a cell. (In practice also smoothing algorithms are used) Second, the modeled terms contain a characteristic mean turbulent frequency that determines the rate at which the modeled processes take place. This frequency *cannot* be estimated from the particle properties in the joint velocity-scalar description and it has to be supplied externally. Another special term is the mean pressure gradient. The mean pressure field can be obtained from the velocity and density fields and, in principle, it is closed. Direct calculation of the mean pressure field would require a pressure solver that uses the particle velocity and mass distributions as input. Here a hybrid Monte Carlo method is employed in which both the pressure and turbulent frequency fields are solved by an external Eulerian finite-volume method according to the method of Correa and Pope [6].

3 Hybrid flow field model

The hybrid Monte Carlo method consists of a Eulerian finite-volume submodel and a Lagrangian Monte Carlo submodel.

The hybrid algorithm is illustrated in figure 11.2. The Eulerian model solves for the mean velocity, pressure, turbulent kinetic energy and turbulent dissipation. Given these mean fields, the Lagrangian Monte Carlo method solves for the joint velocity-scalar mass density function. Effects of thermo-chemistry are solved in the Lagrangian algorithm. Mean thermo-chemical properties that influence the flow field, like density and molecular viscosity fields, are then coupled back to the finite-volume method which solves for the new turbulent flow field. Subsequent submodel calculations are performed until a stable solution is reached.

In this algorithm, conventional modeling of the Eulerian flow field equations is needed also, and closer inspection is needed of the relation between closure in the Lagrangian and the Eulerian framework.

During the Monte Carlo calculations, by an overall shift and scaling of particle velocities in each cell, the Eulerian mean velocities and turbulent kinetic energy are imposed onto the Lagrangian fluid particles.

A basic requirement for the Monte Carlo algorithm is that the particle ensemble gives a physically correct estimate of the mass density function.

This is expressed mathematically by the requirement that the sum of particle masses divided by the cell volume, gives a correct representation of the density field. Using a two-dimensional rectilinear grid, large cells correspond to a large volume in three dimensions. Moreover, in axisymmetrical configurations, cells near the axis represent a small volume in three dimensions whereas cells far from the axis correspond to a larger three-dimensional volume. If all particles are to represent the same amount of mass Δm, the particle number in a cell must depend on the local density *and* on the three-dimensional cell volume. For example, in cells with a small volume or with low density the number of particles is lower and the statistical accuracy in these cells is lower. As a result, the statistical accuracy varies throughout the domain which is undesirable. To remedy this effect an ensemble with variable particle weights $w^{(i)}\Delta m$ is used allowing the use of a nearly constant number of particles per cell. Then the average in Equation 11.3 has to be replaced by a weighted average.

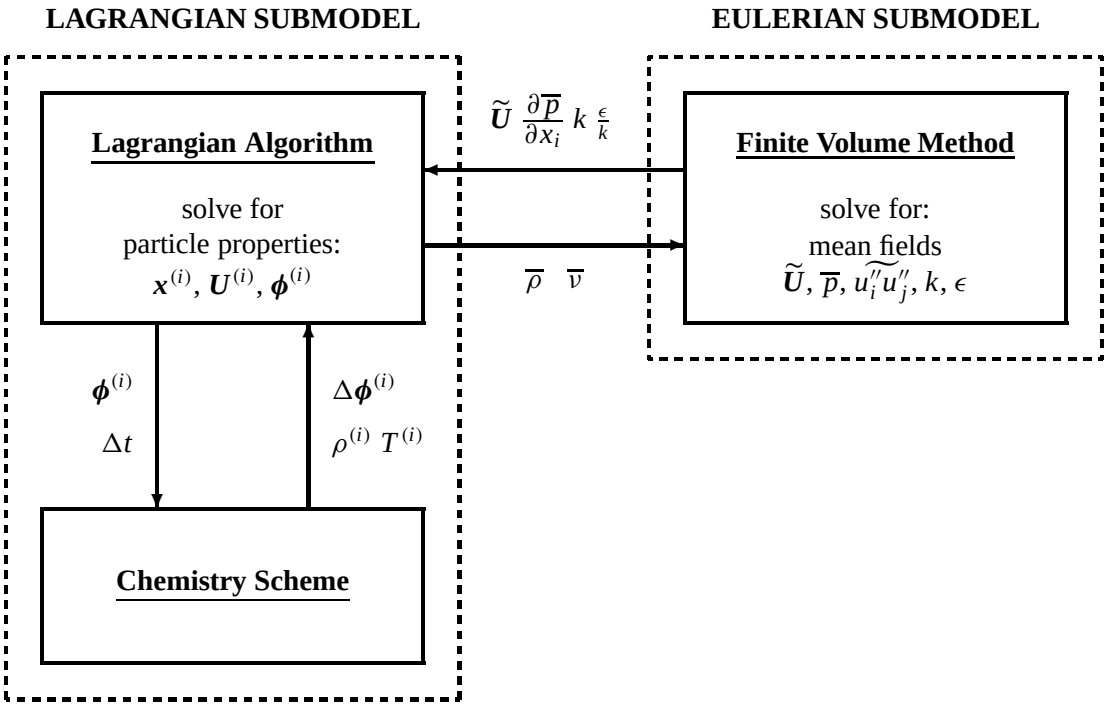

Figure 11.2: Sketch of the hybrid Monte Carlo method. Left side: Lagrangian submodel with chemistry solver. Right side: Eulerian submodel that solves for mean flow field.

4 Modeling of the velocity evolution

4.1 Langevin models

The unclosed terms in the joint velocity-scalar mass density function equation that describe the evolution in velocity space read:

$$-\frac{\partial}{\partial V_i}\left[\left\langle -\frac{\partial p'}{\partial x_i} - \frac{\partial T'_{ij}}{\partial x_j}\middle| \boldsymbol{U}=\boldsymbol{V}, \boldsymbol{\phi}=\boldsymbol{\psi}\right\rangle \widetilde{f}\right] \tag{11.4}$$

here written in terms of the Favre joint PDF instead of the mass density function. To illustrate the closure procedure, we first consider the Simplified Langevin Model (SLM) [7]. A Langevin model is a stochastic model for fluid particle velocities. The modeled particle velocity equation consists of a linear drift towards the local Favre mean and an added isotropic diffusion term, and reads:

$$\mathrm{d}U_i^* = -\left(\frac{1}{2}+\frac{3}{4}C_0\right)\omega(U_i^* - \widetilde{U}_i)\mathrm{d}t + (C_0\epsilon)^{1/2}\mathrm{d}W_i \tag{11.5}$$

in which $\omega = \epsilon/k$ is the mean turbulent frequency, U_i^* is a stochastic velocity realization, C_0 a constant with a physical meaning explained below , and $\mathrm{d}W_i$ a stochastic Wiener increment. The Wiener process is a stochastic process with zero mean and covariance:

$$\langle \mathrm{d}W_i \mathrm{d}W_j \rangle = \mathrm{d}t\,\delta_{ij} \tag{11.6}$$

The Wiener or diffusion process is continuous but not differentiable and has the properties of a Markov process. This means that the stochastic velocity increments only depend on the present state of the fluid element and not on its history. Using Ito calculus the Langevin model then corresponds to an evolution of the velocity PDF given by Risken [9], and Gardiner [10]):

$$\frac{\partial \widetilde{f}_{\boldsymbol{U}}}{\partial t} = \left(\frac{1}{2} + \frac{3}{4}C_0\right)\omega\frac{\partial}{\partial V_i}\left[(V_i - \widetilde{U}_i)\,\widetilde{f}_{\boldsymbol{U}}\right] + \frac{1}{2}C_0\epsilon\frac{\partial^2 \widetilde{f}_{\boldsymbol{U}}}{\partial V_i^2} \tag{11.7}$$

The basic properties of the SLM are that it yields the correct evolution of turbulent kinetic energy and that it yields isotropization of the velocity distribution. To describe complex flow fields an extended model is needed: the *Generalized Langevin model* (GLM) which is of the form

$$\begin{aligned} \mathrm{d}U_i^* = &\left(-\frac{1}{\rho}\frac{\partial\langle p\rangle}{\partial x_i} - \frac{\partial\langle T_{ij}\rangle}{\partial x_j}\right)\mathrm{d}t \\ &+ G_{ij}(U_j^* - \widetilde{U}_j)\mathrm{d}t + (C_0\epsilon)^{1/2}\mathrm{d}W_i \end{aligned} \tag{11.8}$$

in which C_0 is a positive constant, $\boldsymbol{W}(t)$ an isotropic Wiener process, ϵ the dissipation of turbulent kinetic energy and G_{ij} is a second-order tensor which is modeled as a function of local mean quantities. A 'general' form of G_{ij} in terms of the local mean velocity gradients, Reynolds stresses and dissipation was derived by Haworth and Pope [7].

The reason for using the Langevin model to model turbulent velocities is found in the consistency of the model with Kolmogorov's hypothesis of turbulence [11]. For high Reynolds number there is a separation between the large energy containing scales and the small scales at which viscous dissipation takes place. The cascade of energy from the large to the small scales occurs in the inertial subrange where the energy dissipation rate ϵ is the only relevant parameter. The effects modeled by the tensor G_{ij} are characterized by the time-scales of mean deformation $|\partial\langle U\rangle/\partial x|^{-1}$ and energy dissipation $T = k/\epsilon$. The Wiener process models effects that take place on a shorter time-scale. The specific form of the diffusion coefficient is determined by the modeled Lagrangian structure function which, for the Langevin model, reads:

$$\langle \Delta U_i \Delta U_j\rangle_L \equiv \langle (U_i(t+s) - U_i(t))(U_j(t+s) - U_j(t))\rangle_L = C_0\epsilon s\delta_{ij} \tag{11.9}$$

with ΔU_i the velocity increment of a Lagrangian fluid element. This is consistent with Kolmogorov's inertial range scaling with C_0 being a universal constant. A value $C_0 = 2.1$ was determined experimentally from diffusion measurements in grid turbulence by Anand and Pope [12]. For a detailed treatment of dynamical properties of the Langevin model and consistency with Kolmogorov's theory, see [7, 14, 13].

An important feature of the Lagrangian models is that these describe the evolution of individual fluid element velocities. This means that, for finite model coefficients, the Langevin model always describes physically realizable distribution of velocities (e.g. positive normal stresses and turbulent kinetic energy). Consequently, the Langevin model is always realizable by construction as are all moment equations derived from the Langevin model.

Because the Langevin model describes the evolution of the full joint velocity distribution it also provides a modeled evolution equation for the second moments of velocity. In particular, in the case of an isotropic dissipation tensor ($\epsilon_{ij} = \frac{2}{3}\epsilon\delta_{ij}$) the exact expression for the pressure strain correlation in the Reynolds stress equation

$$\Pi_{ij}^* = -\frac{1}{\rho}\left(\overline{u_i''\frac{\partial p'}{\partial x_j}} + \overline{u_j''\frac{\partial p'}{\partial x_i}}\right) \tag{11.10}$$

is represented by

$$\Pi^*_{ij} = G_{ik}\widetilde{u''_j u''_k} + G_{jk}\widetilde{u''_i u''_k} + \left(\tfrac{2}{3} + C_0\right)\epsilon\delta_{ij} \tag{11.11}$$

In the approach followed here, following the lines of Pope [4], the model parameters in the expression for G_{ij} are specified such that the modeled pressure-strain correlation equals that of several well-known second-moment closures.

A basic second-moment closure model for Π^*_{ij} is the combination of a Linear return-to-isotropy or Rotta term and a linear isotropization-of- production (IP) term. The model (with fixed model constants $C_1 = 1.8$ and $C_2 = 0.6$) is referred to as the *Isotropization-of-Production Model* (IPM) and the corresponding GLM is called the Lagrangian IP model (LIPM). The Simplified Langevin model (SLM) corresponds to the *Rotta* model (only linear return-to-isotropy $C_1 = 4.15$, $C_2 = 0$). For the (L)IPM and the SLM/Rotta model, hybrid Monte Carlo calculations were performed in a bluff-body stabilized diffusion flame using both the Eulerian second-moment model and the Lagrangian Langevin models [15]. Some results of these calculations are presented below.

Since the full joint probability of velocities and scalars is known the Lagrangian models also provide modeled evolution equations for the third-moments of velocity and the turbulent scalar fluxes. The third-moment equations are governed by the Langevin model for velocities whereas the combination of Langevin model and micro-mixing model provides a model for the scalar fluxes.

4.2 Consistency

When solving the modeled velocity PDF transport equation with the hybrid Monte Carlo method some caution is needed. In the hybrid method the turbulent flow field is represented in two ways: on the one hand by the Eulerian mean velocity and turbulent kinetic energy fields of the finite-volume submodel, and on the other hand by the velocity distribution of the Lagrangian Monte Carlo submodel. Although a unique definition of the turbulence model is not guaranteed, both submodels use the same solution for the mean velocity and turbulent kinetic energy fields. Turbulent transport of mean momentum and production of turbulent kinetic energy are governed by the Reynolds stresses and consistency between the two submodels on the level of mean velocities and kinetic energy inevitably requires a consistent treatment of the second moments.

Several studies, using the hybrid method, have used the k-ϵ model in combination with the SLM [16, 17]. In the Eulerian k-ϵ model, the Reynolds stresses are given by an algebraic relation and the second-moment equations are not modeled explicitly. No equivalent model in terms of a Langevin model exists. As a result, the k-ϵ model cannot be part of a consistent hybrid model. In the hybrid method employed here, a consistent hybrid turbulence model is obtained by using the same second-moment equation in both submodels with the Langevin model chosen equivalent to the finite-volume turbulence model for the pressure-strain correlation. The third-moments are still treated inconsistently in the two submodels. In the Lagrangian method the third-moments are exact whereas in the second moment closure models these are given by a generalized gradient diffusion model. Effects of this inconsistency on the level of the third moments are assumed to be small (See [8] for a confirmation of this assumption).

Recently new fully consistent hybrid algorithms have been developed, see Muradoglu *et al.* [18] and references therein. E.g. in these methods Reynolds stresses are calculated in the Monte Carlo submodel only.

5 Modeling of scalar micro-mixing

5.1 Introduction

The process of micro-mixing is a very important mechanism in turbulent reacting flows. On the largest scales mixing of species takes place by turbulent convection but only after species are mixed by molecular diffusion on the smallest scales, chemical reaction can occur. For Damköhler number around unity, turbulent mixing and reaction are strongly coupled whereas for high Damköhler number the overall reaction rate is limited by the mixing process. In both cases, for a prediction of the mean chemical source terms an accurate description of the scalar distribution is needed. Micro-mixing models are designed to mimic several physical properties of molecular scalar mixing. These properties stem either from the Navier-Stokes equations or are motivated by observations in measurements or DNS of inert scalar mixing. Below we start from exact equations for scalar mixing and list several basic properties of turbulent scalar mixing. Then the two most widely used micro-mixing models are reviewed: Interaction by Exchange with the Mean and Coalescence/Dispersion.

5.2 Turbulent scalar mixing

Exact equations

The evolution of the Favre joint velocity-scalar PDF under the influence of turbulent molecular scalar mixing is given by equation 11.1a. The unclosed term consists of the mean molecular diffusion flux conditional on the velocity and scalar values. The evolution of the PDF under the influence of micro-mixing is given by:

$$\frac{\partial}{\partial t}\widetilde{f}_{U\boldsymbol{\phi}} = -\frac{\partial}{\partial \psi_\alpha}\left[\frac{1}{\rho}\left\langle -\frac{\partial J_i^{\alpha\prime}}{\partial x_i}\middle| \boldsymbol{U}=\boldsymbol{V}, \boldsymbol{\phi}=\boldsymbol{\psi}\right\rangle \widetilde{f}_{U\boldsymbol{\phi}}\right] \tag{11.12}$$

Assuming Fickian diffusion and equal and constant diffusivities, the term on the RHS can be rewritten as:

$$-\mathbb{D}\frac{\partial^2}{\partial x_i^2}\widetilde{f}_{U\boldsymbol{\phi}} - \mathbb{D}\frac{\partial^2}{\partial \psi_\alpha \partial \psi_\beta}\left[\left\langle \frac{\partial \phi_\alpha{}''}{\partial x_i}\frac{\partial \phi_\beta''}{\partial x_i}\middle| \boldsymbol{U}=\boldsymbol{V}, \boldsymbol{\phi}=\boldsymbol{\psi}\right\rangle \widetilde{f}_{U\boldsymbol{\phi}}\right] \tag{11.13}$$

The first term describes the diffusion in physical space and is usually neglected assuming high Reynolds numbers. Using the same argument the effects of the mean diffusion flux $\langle J_j^\alpha \rangle$ are neglected also. This term (see equation 11.1c) contains only mean field gradients and is contained in closed form. The remaining unclosed term is the conditional scalar dissipation or cross-dissipation which is defined by:

$$\epsilon_{\phi,\alpha\beta} = \mathbb{D}\left\langle \frac{\partial \phi_\alpha{}''}{\partial x_i}\frac{\partial \phi_\beta''}{\partial x_i}\middle| \boldsymbol{U}=\boldsymbol{V}, \boldsymbol{\phi}=\boldsymbol{\psi}\right\rangle \tag{11.14}$$

The effects of this term on the scalar distribution can be summarized by a decay of scalar variance combined with a relaxation of the scalar PDF to a Gaussian-like shape. Whichever model is used to mimic these effects, all models require an additional time-scale that determines the scalar variance decay rate. The decay of scalar (co)-variance is given by the averaged, unconditional, scalar dissipation or cross-dissipation which is given by:

$$\frac{\mathrm{d}}{\mathrm{d}t}\widetilde{\phi_\alpha{}''\phi_\beta''} = -2\epsilon_{\phi,\alpha\beta} \tag{11.15}$$

The closure of the variance decay rate also arises in modeling of the second-moment equations. For single inert scalar mixing the scalar variance decay rate most often is modeled to be proportional to the decay rate of turbulent kinetic energy where the constant of proportionality C_ϕ takes a standard value of 2.0.

Properties of turbulent scalar mixing

The rationale behind the use of a particular model for micro-mixing lies in the ability to mimic relevant physical properties of the mixing process. Here several important properties of the mixing process are reviewed: (1) the scalar mean is conserved, (2) correct variance decay rate, (3) boundedness of scalars, (4) linearity and independence, (5) relaxation to a Gaussian for inert scalar mixing, and (6) localness in composition space.

CONSTANT SCALAR MEAN In the absence of a mean diffusion flux, molecular scalar mixing does not affect the mean scalar value. Conservation of the scalar mean is a strictly required property of mixing models. Models that do not satisfy this property may, for example, destroy or produce a conserved scalar like mixture fraction; violating mass and element balances.

SCALAR VARIANCE DECAY Under the assumptions of high Reynolds numbers, the scalar variance equation shows that the decay of scalar variances by molecular diffusion is given by the scalar dissipation ϵ_ϕ. The joint velocity-scalar PDF does not provide information on the decay rate and the decay rate must be supplied externally. All micro-mixing models are designed to reproduce the available information on the decay rate.

BOUNDEDNESS OF SCALAR VALUES An important property of scalar mixing is that mixing cannot cause scalar values to occur below the minimal or above the maximal values. For example: in a region with mixture fraction values between 0.5 and 1, molecular mixing cannot cause scalar values to occur below 0.5 or above 1. In more dimensions, consider a bounded region which contains all scalar values. During a mixing step, all scalar values must remain within the bounds of the previously spanned region. Boundedness must be satisfied to prevent unphysical scalar values like negative mass fractions or temperature.

LINEARITY AND INDEPENDENCE The scalar transport equations, for non-reacting scalars, are linear in the scalar values. This implies that, for equal diffusivities, any linear combination of non-reacting scalar variables evolves according to the same set of equations. A good micromixing model should respect this linearity principle. Related to this, the independence principle implies that, in mixing, the evolution of the statistics of one scalar are not influenced by the distribution of the other scalars [19]. The models reviewed here satisfy these two fundamental properties.

RELAXATION TO A GAUSSIAN IN HOMOGENEOUS TURBULENCE Turbulent scalar mixing does not only result in a decay of scalar variance but the PDF shape relaxes to a bell-shaped distribution. For mixing of temperature fluctuations in grid-generated turbulence [20] and in DNS simulations of inert mixing homogeneous isotropic turbulence [21] it has been observed that an initially binary distribution evolves to a Gaussian. In computations of mixing in inhomogeneous flows, like jet diffusion flames, it may not be so relevant whether or not a model reproduces the exact Gaussian shape for the homogeneous test case. But models that can reproduce the DNS data are favored.

A good measure of the evolution of the PDF shape is the evolution of the normalized central moments of a distribution:

$$\hat{\mu}_n = \frac{\mu_n}{(\mu_2)^{n/2}} \tag{11.16}$$

with $\mu_n = \langle \phi'^n \rangle$. For a binary distribution $\hat{\mu}_4 = \hat{\mu}_6 = 1$ and for a standard Gaussian distribution $\hat{\mu}_4 = 3$ and $\hat{\mu}_6 = 15$. The relaxation of the scalar PDF from a binary distribution is measured by the evolution of these moments in time and by the way in which the Gaussian values are approached.

LOCALNESS IN SCALAR SPACE The concept of localness in multidimensional scalar space was introduced by Subramaniam and Pope [22] (for a single scalar the concept already appears in Norris and Pope [23]). The additional requirement introduced is that mixing of scalar particles is governed by its close neighborhood in composition space. A motivation for it is that the mixing of fluid particles in a physical volume of fluid, where scalar fields are continuous, is also local in scalar space. However, it may not be necessary to satisfy this requirement in order to represent mixing of the scalar PDF correctly. The mixing models reviewed here do not satisfy the localness condition.

5.3 Modeling of micro-mixing

In this section two most widely used micro-mixing models are described: Interaction by Exchange with the Mean model and Coalescence/Dispersion or Curl's Models. For a discussion of other models (Mapping Closure models, Langevin models) we refer to Wouters [1].

Interaction by Exchange with the Mean model

The simplest micro-mixing model is the *Interaction by Exchange with the Mean* (IEM) or *Linear Mean Squares Estimate* (LMSE) model [24, 25]. The IEM model is widely used because of its simplicity and ability to mimic the most important effects of mixing. The model conserves the scalar mean and yields the correct variance decay rate.

The decay of scalar variance is modeled by a deterministic relaxation of all scalar values to the local mean.

$$\mathrm{d}\phi_\alpha{}^* = -\frac{1}{2}\omega_\phi(\phi_\alpha{}^* - \widetilde{\phi}_\alpha)\mathrm{d}t \tag{11.17}$$

in which ω_ϕ is the modeled scalar variance decay rate. The IEM model corresponds to an evolution of the scalar PDF given by:

$$\frac{\partial \widetilde{f}_{\boldsymbol{\phi}}}{\partial t} = \frac{1}{2}\omega_\phi \frac{\partial}{\partial \psi_\alpha}\left[(\psi_\alpha - \widetilde{\phi}_\alpha)\widetilde{f}_{\boldsymbol{\phi}}\right] \tag{11.18}$$

In the multi-scalar formulation given here, all scalars relax to the respective mean at the same decay rate ω_ϕ.

With respect to the physical properties of turbulent scalar mixing that were mentioned in the previous section, the IEM model only mimics the first four properties; conservation of the mean, a correct variance decay rate, boundedness of scalars, and linearity and independence. The model does not predict any relaxation of the shape of the scalar distribution. The predicted evolution of normalized moments is $\mathrm{d}\hat{\mu}_n/\mathrm{d}t = 0$ for all n.

Coalescence/Dispersion models

Coalescence/Dispersion (C/D) or particle-pair interaction models are most easily defined in terms of a particle model where mixing takes place in randomly selected particle pairs. The original model

was proposed by Curl [26]. Improvements of Curl's model were proposed by Janicka *et al.* [27], and Pope [28], the extension of the model to the case with variable particle weights is given in Nooren *et al.* [17], and Wouters [1]. Coalescence/Dispersion models are attractive because the models are relatively simple to use. Furthermore, C/D models are able to mimic the physics of mixing in a better way than the IEM model does and perform reasonable well for mixing of multiple reacting scalars.

The standard C/D model for scalar particles is defined as follows: consider an ensemble of N particles with equal weights $w^{(i)} = 1$ and scalar values $\phi^{(i)}$. For every mixing step, two randomly chosen particles (p, q) mix with a certain probability P_{mix}. The particle pair mixes towards the pair mean scalar value:

$$\phi_\alpha{}^{(p)}(t + \Delta t) = \phi_\alpha{}^{(q)}(t + \Delta t) = \phi^{(p,q)}_{\alpha,\text{mean}} = \frac{1}{2}\left[\phi_\alpha{}^{(p)}(t) + \phi_\alpha{}^{(q)}(t)\right] \tag{11.19}$$

while the other particles remain unchanged. For a selected particle pair, all scalars α take part in mixing. For this case of equally weighted particles the decay of variance in a mixing step Δt is given by:

$$\langle g\rangle(t + \Delta t) = \langle g\rangle(t)\left(1 - \frac{P_{\text{mix}}}{N}\right) \tag{11.20}$$

with $\langle g\rangle$ an arbitrary scalar variance. In the limit $\Delta t \to 0$ the correct decay of variance is obtained if P_{mix} is chosen:

$$P_{\text{mix}} = N[1 - \exp(-\omega_\phi \Delta t)] \approx \omega_\phi N \Delta t \tag{11.21}$$

The numerical implementation of this algorithm is straightforward.

The PDF shapes predicted by this model in case of mixing of a binary PDF are unrealistic. To remedy the latter effect, Janicka *et al.* [27] propose a modification of the model in which a particle pair only exchanges a fraction of the scalar values. This fraction is chosen randomly from a uniform distribution. The modified C/D model yields a relaxation of the PDF shape to a bell-shaped function but the normalized skewness and super-skewness do not approach the Gaussian values. To improve the asymptotic behavior of the C/D model, Pope [28] proposes an extension with an age-biased selection of particles. This results in a probability of selection of particles that is biased to particles with a larger age, where age is defined as the time a particle has not taken part in mixing. Improvements as proposed by Pope have been tested only for the test case of binary mixing. Although the modified C/D model with $A(a) = 1$ overpredicts the tails of the PDF, with infinite moments $\hat{\mu}_4$ and $\hat{\mu}_6$, the PDF is bell-shaped and the disagreement with a Gaussian PDF is noticeable only in the low tails of the distribution. In all calculations reported here, the modified C/D model by Janicka *et al.* [27], extended for particles with unequal weights [17], is used.

Summarising, with respect to the physical properties of turbulent scalar mixing, the C/D model conserves the scalar mean, yields the correct variance decay rate, and satisfies the requirements of boundedness, linearity and independence. For homogeneous inert mixing the PDF evolves to a bell-shaped function but does not approach an exact Gaussian.

6 Modeling of a bluff-body-stabilized diffusion flame

6.1 Introduction

To illustrate the theoretical developments described above, this section reports on the study of a bluff-body-stabilized methane-air diffusion flame using second-moment closures and multi-scalar chemistry. The bluff-body configuration serves as a model for industrial type low NO_x burners. Here

the bluff-body flame is chosen as a test case because the flow pattern exhibits complex phenomena, like recirculation regions and stagnation points, and because the coupling between turbulence and chemistry is strong. The flow is very sensitive to density fluctuations and the flame shows effects of finite-rate chemistry. The configurations studied here were subject of a 1994 ERCOFTAC-SIG workshop [29, 30]. It was shown that the k-ϵ model is insufficient to model the bluff-body flow characteristics. Here two second-moments closure models are used besides the standard k-ϵ model. Chemistry is modeled with the conserved-scalar constrained equilibrium model and with the three-scalar ILDM scheme. The objective was to make a comprehensive study of the relative importance of the model used for convection, for micro-mixing, and for chemical kinetics. Monte Carlo predictions are compared to available experimental data of mean velocities, turbulent kinetic energy and temperature. The Monte Carlo model was implemented in a computer code `PDF2DS` Provided by Prof. S.B. Pope. (The Delft version of this code is called PDFD). The finite-volume submodel calculations are performed with `BIGMIX` which is an in-house finite-volume code of TU Delft [31].

We mention that also other authors have reported their results for this flame in the literature (e.g. Fallot *et al.* [32], and Warnatz *et al.* [33]).

6.2 Test case specification

The configuration consists of a fuel jet 5.4 mm in diameter, surrounded by a 50 mm diameter bluff body. The coaxial air inlet has an outer diameter of 100 mm and a low-velocity coflow of air is present around the air inlet. The thickness of the coaxial air pipe is 1 mm. Figure 11.3 depicts the bluff-body configuration and sketches a typical flow pattern. In the experiment, the burner is unconfined but in the simulation, a solid wall is assumed at a radius of 200 mm to prevent numerical problems with outflow of particles in the Monte Carlo method. Test calculations have shown that the presence of this confinement does not influence the flow in the regions of interest.

The inlet velocities for the fuel, air and coflow are 21 m/s, 25 m/s and 1 m/s, respectively. The fuel inlet Reynolds number based on the fuel inlet diameter is $Re = 7000$ and for the air inlet, based on the bluff-body diameter, $Re = 80\,000$. Initially boundary conditions were the same as prescribed at the SIG workshop [29]. However, the original inlet conditions are modified to improve the predictions with respect to the length of the recirculation zone, and to obtain a stable convergence of the second-moment equations. Inlet profile calculations are set up to approximate the experimental configuration.

The finite-volume calculations are performed on a rectangular nonuniform mesh of 150×150 points. On this mesh grid independent solutions are obtained and differences with solutions on an 80×80 mesh are small. The Monte Carlo simulations are performed on a 80×80 mesh using 150 particles per cell. To reduce stochastic fluctuations, mean properties are averaged over 500 iterations. Additional Monte Carlo calculations with 150 particles per cell on a grid of 150×150 and with 400 particles per cell on a grid of 80×80, are performed to test the influence of grid dependence and the statistical accuracy. Monte Carlo simulations require about 200 Mb internal memory and 100 hours of CPU time on a HP–735 workstation or 10 hours on 8 PE's of a massively parallel CRAY–T3E supercomputer.

6.3 Choice of PDF model

This section summarizes the models used in this study and gives a motivation for the specific model choices.

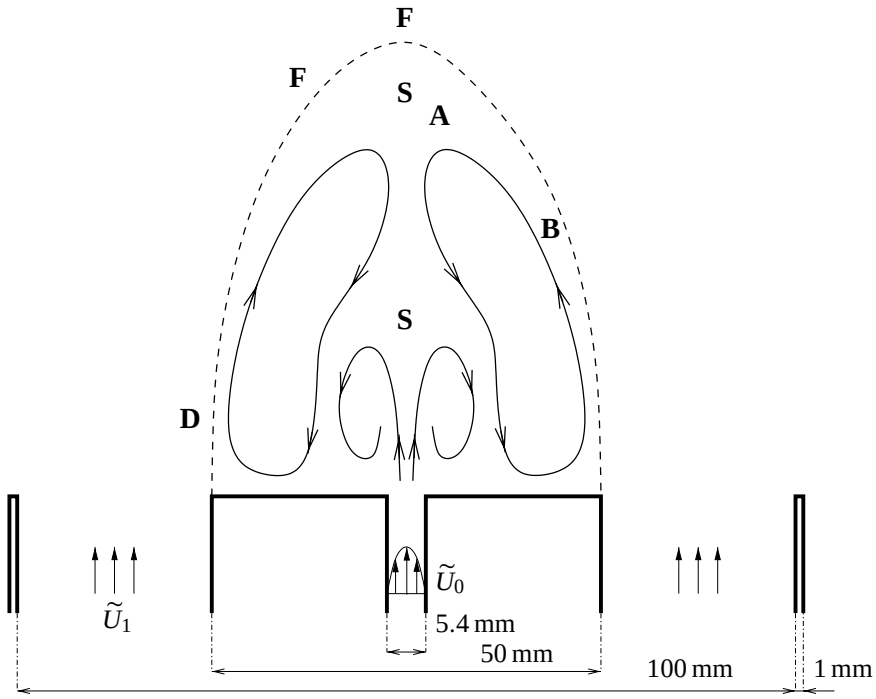

Figure 11.3: Bluff-body flow configuration and characteristic flow pattern. Mean fuel jet velocity $\widetilde{U}_0 = 25$ m/s, uniform air inlet velocity $\widetilde{U}_1 = 21$ m/s. Bold faced letters indicate: **S** stagnation regions, **D** 'diffusion flame' region, **F** main reaction or flame region, **A** and **B** scatterplot positions of figure 11.7.

Hybrid turbulence model

Three different hybrid turbulence models have been used. The hybrid SLM/k-ϵ model is used because it is a standard turbulence modeling approach using the hybrid Monte Carlo method [16, 17]. In this flow the inconsistency of this model with respect to the representation of the Reynolds stress tensor, is apparent [1].

Two consistent hybrid models used are the SLM/Rotta and the LIPM/IPM models. The SLM/Rotta model is used because it is seen as the simplest consistent hybrid turbulence model. The consistent LIPM/IPM model is used because this second-moment closure model is seen as a basic Reynolds-stress model and it is expected to perform reasonably well for the bluff-body configuration.

In the inert flow, several other second-moment models were evaluated, without reaching significant improvement of the predictions.

The approach of tuning the turbulence model to the experimental flow data separately for every chemistry and mixing model is not used here. Rather, the turbulence model constants are kept constant while investigating the relative performance of different micromixing and chemistry models. In the reacting case, flow and scalar fields are strongly coupled and changes in the scalar field model will directly affect the flow field. If the fitting procedure is employed, then changes in the turbulence model constants will be large, provided an acceptable choice for the constants even exists.

Chemistry modeling

Initially, chemical reaction is simplified using the conserved-scalar constrained-equilibrium (CE) model. It is assumed that the reaction is fast such that it is limited only by the mixing of fuel and oxidizer.

CE predictions however, show an overprediction of the mean temperature and, moreover, the flame length is overpredicted severely. Because of the strong recirculation, burned products flow back into the inlet region where the mixing rate of species is large. There, effects of partial premixing and finite-rate kinetics are important. To capture these effects, a three-scalar ILDM reduced kinetics scheme is used. The ILDM scheme can successfully describe finite-rate kinetics effects *and* correctly reduces to the equilibrium model in the fast chemistry limit.

Here, for the case of non-premixed methane-air combustion the detailed mechanism is simplified to a three-dimensional manifold, parameterized by mixture fraction and the H_2O and CO_2 mass fractions. The remaining thermo-chemical variables like the other mass fractions, temperature and density, and the reaction rates of H_2O and CO_2 are tabulated as a function of these three parameters. In order to avoid a CPU-intensive integration of the rate equations for H_2O and CO_2 mass fractions during the Monte Carlo simulations, the reaction rates are pre-integrated for the specific time-step of the simulation. For all simulations performed in this study, thermo-chemical variables are tabulated as a function of the describing variables in a locally refined table as described by Peeters [34, 31].

Scalar micro-mixing

Using the conserved-scalar CE chemistry model, modeling is required for micro-mixing of a single inert scalar. For this case, four mixing models are available: IEM, C/D, Mapping Closure Model (MCM) and Binomial Langevin (BL) models.

With ILDM chemistry, scalar mixing involves mixture fraction and two additional reacting scalars, Y_{CO_2} and Y_{H_2O}. The C/D model performs very well for inert single-scalar mixing in jet flows [35] and it has been shown to perform well in reacting jet diffusion flames with CE and with ILDM chemistry [17]. For these reasons, the C/D model is selected as a standard model for mixing of multiple reacting scalars. A second model that was selected for scalar mixing in combination with ILDM chemistry is the modified multi-scalar BL model which was described by Wouters [1].

6.4 Results for reacting flow

Results for the reacting flow are given in the following order: first a summary of flow field predictions is given, next results for thermo-chemical fields of the conserved-scalar constrained-equilibrium model are shown and the limitations of this model are discussed. Then, improvements using a three-scalar ILDM reduced kinetics scheme are presented. Finally results on the performance of micromixing models are given. A study of the inert flow, including consistency tests can be found in Wouters [1].

Flow field predictions

Experimentally, the flow exhibits *one* stagnation point, at $x = 70$ mm with a peak in turbulent kinetic energy of $k = 44$ m^2/s^2. All three hybrid models in combination with CE chemistry and C/D micromixing, predict a minimum in the axial velocity for $x \approx 70$ mm with the minimal value close to zero. The peak value of turbulent kinetic energy is underpredicted by all models. With the IPM, predictions are reasonable for $x < 70$ mm. Here, the initial decay of the axial velocity is predicted

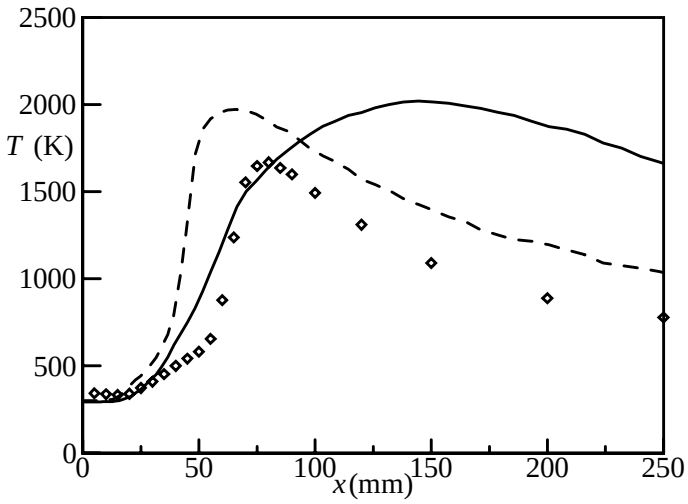

Figure 11.4: Axial profiles of temperature. Predictions use IPM turbulence model and C/D micro-mixing model. Symbols: —— CE chemistry model ($T_{\max} = 2020$ K), – – – ILDM chemistry model ($T_{\max} = 1980$ K), ◇ ◇ ◇ measurements ($T_{\max} = 1667$ K).

correctly. At higher axial distances, the performance of the model is unclear. In this region the mean temperature is overpredicted severely (see figure 11.4) which clearly has its effect on the flow field. Here, the limitations of the CE chemistry model play a role.

Constrained-Equilibrium results

Figure 11.4 depicts the axial profile of the mean temperature. Moving along the axis in the axial direction, the experimental data show a sharp rise in temperature, up to a peak temperature of 1667 K at $x = 80$ mm. After the peak temperature is reached, the temperature drops rapidly. CE predictions are in reasonable agreement with the experiments up to $x = 80$ mm but the predicted temperature rises further and reaches a maximum of 2020 K at $x = 145$ mm. Moreover, the high temperature zone extends over a much larger region.

Radial profiles of temperature, which are depicted in figure 11.5a, show that predictions are reasonable for $x \leq 50$ mm. At $x = 10$ and 30 mm the temperature is overpredicted by ≈ 250 K but the shape of the profiles is good. At $r = 25$ mm a peak indicates the presence of a reaction zone starting at the edge of the bluff-body. There the assumption of a diffusion flame, that can be described by a conserved-scalar model, seems to be reasonable. At $x = 50$ mm, the temperature maximum is overpredicted because the temperature at the centerline rises too early (see also figure 11.4).

At higher axial distances near the stagnation zone, mixing rates are high and a well-mixed composition of fuel and air exists above the recirculation zone. Here, reaction is not limited by mixing and effects of finite-rate kinetics are important. The conserved-scalar CE model is not able to capture these effects and therefore it overpredicts the temperature in this region.

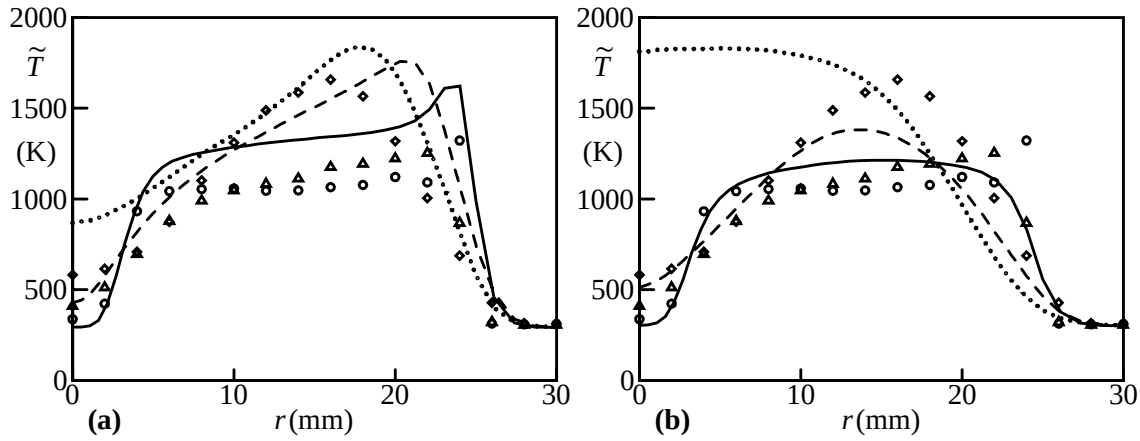

Figure 11.5: Radial profiles of mean temperature. Predictions with IPM turbulence model and C/D micro-mixing model. a) CE chemistry, b) ILDM chemistry. Lines: predictions, —— $x = 10$mm, – – – $x = 30$mm, · · · · · $x = 50$mm. Symbols: measurements, ○ ○ ○ $x = 10$mm, △△△ $x = 30$mm, ◇ ◇ ◇ $x = 50$mm.

ILDM results

Final results of the ERCOFTAC-SIG workshop [30] show that models that do not employ the fast-chemistry assumption perform much better downstream of the recirculation zone, even when using k-ϵ turbulence modeling. To satisfactorily describe the effects of partial premixing and finite-rate kinetics, a three-scalar ILDM reduced kinetics scheme is used.

In figure 11.4, the axial profile of mean temperature is depicted for CE and ILDM chemistry models and measurements, and the implications of the chemistry model are clearly seen. ILDM chemistry yields a faster axial decay of temperature after the peak temperature is reached. The CE model overpredicts the temperature in this region even though the mixture fraction fields in the CE and ILDM calculations are almost the same. At $x \approx 45$ mm, the ILDM prediction shows a sharp rise in temperature which is not seen in the measurements or in the CE predictions. The faster ignition is caused by differences in the flow field. Because of the strong coupling between chemistry and flow field, small differences in the mean density result in a much stronger recirculation with a minimal axial velocity on the axis of -3.9 m/s at $x = 50$ mm.

Grey-scale plots of the mean temperature for CE and ILDM predictions and the measurements are shown in figure 11.6. Looking at the overall picture, the ILDM flame is more compact and it is located closer to the bluff body than seen in the experiments. Compared to the CE predictions the flame length is much shorter and the predictions are in better agreement with the experiments. However, the temperature is still overpredicted by approximately 200 K in the flame region. The reason for the improvements obtained with the ILDM chemistry scheme over the CE model is that the fast-chemistry assumption, made in the CE model, is not valid in this flame.

To illustrate the differences between the two chemistry models, figure 11.7 shows scatter plots of mixture fraction and H_2O mass fraction at two positions in the flame. Scatter plot positions are sketched in figure 11.3. Figure 11.7a shows a scatter plot at $x = 37.5$ mm and $r = 7.86$ mm (position A) in the region where the mixture fraction variance and mixing rate reach a maximum. A scatter plot at $x = 38$ mm and $r = 15$ mm (position B) is shown in figure 11.7b. This position is located in the shear layer above the edge of the bluff body at an axial location where the source terms of Y_{CO_2}

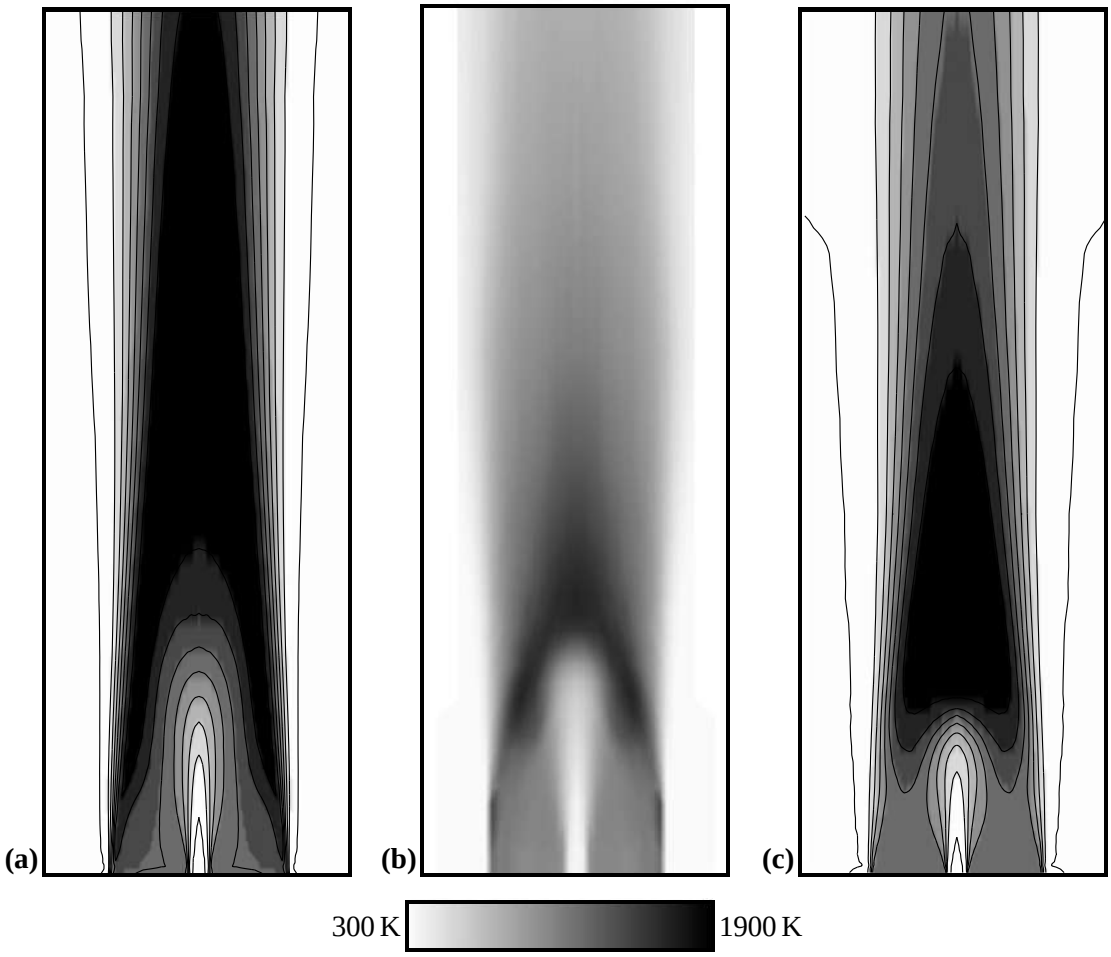

Figure 11.6: Greyscale plot of the mean temperature. a) CE chemistry predictions ($T_{\max} = 2020\,\mathrm{K}$), b) measurements ($T_{\max} = 1667\,\mathrm{K}$), c) ILDM chemistry predictions ($T_{\max} = 1980\,\mathrm{K}$). Contour values at 300, 500, . . . 1900 K. For the calculations only part of the domain is shown.

and Y_{H_2O} reach a local maximum. At position A, the mixture fraction variance is large and almost the entire mixture fraction space is occupied. For $\xi > 0.25$ points are scattered around the equilibrium line but for lower mixture fraction values, many points are found below the equilibrium limit. At this position, the ILDM model predicts a mean temperature below the equilibrium value. Position B is located in the shear layer above the edge of the bluff body where the CE results showed that the assumption of diffusion limited chemistry gives reasonable predictions of the mean temperature (see also figure 11.5a). The scatter plot shows that the ILDM results are far from equilibrium. The figure clearly shows that mixing rates are high which yields many points near stoichiometry but with low Y_{H_2O} values.

Radial profiles of the mean temperature, up to one bluff-body diameter downstream, are depicted in figure 11.5b. The profiles show no overprediction of temperature at the edge of the bluff body ($15 < r < 25$ mm) as seen in the CE results. The profile at $x = 50$ mm clearly shows the early rise of temperature which corresponds to a flame closer to the bluff body. The ILDM results fail to show a peak at $r = 25$ mm as is seen in the CE profiles. The scatter plot 11.7b indicates also that the

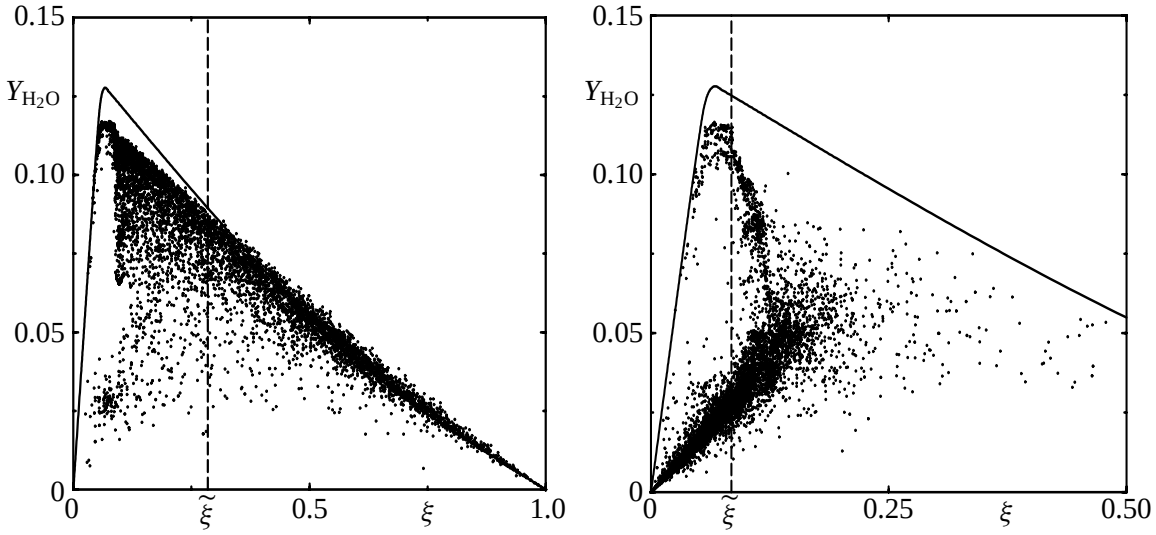

Figure 11.7: Scatterplot of H_2O mass fraction versus mixture fraction. ILDM chemistry with C/D micro-mixing. a) at $x = 37.5$ mm and $r = 7.86$ mm, $\widetilde{\xi} = 0.285$, b) at $x = 28$ mm and $r = 22$ mm, $\widetilde{\xi} = 0.084$. Typical scatterplot positions are indicated in figure 11.3. Solid line denotes the constrained-equilibrium limit. Dashed vertical line denotes the value of the mean mixture fraction.

equilibrium temperature is not reached in this region.

6.5 Conclusion

Summarizing, the three-scalar ILDM reduced chemistry scheme is able to describe the effects of partial premixing and finite-rate kinetics that occur in this flame. Mean temperature fields are in better agreement with the experiments than the CE predictions which show a large overprediction of the flame height. With the ILDM scheme, temperature is still overpredicted by approximately 200 K in the entire flame region.

Also the importance of modeling of the micro-mixing term in this flow has been investigated [1]. It was found that scalar micro-mixing and the coupling between micro-mixing and reaction are not crucial in this flow. The remaining deficiencies of the present PDF model are attributed to modeling of momentum and scalar transport. Apparently, macro-mixing by turbulent convection is the driving force in scalar mixing.

Finally, it should be remarked that the large underprediction of turbulent kinetic energy at the stagnation point positions and the low Reynolds numbers of the fuel and air jets indicate that this flow exhibits unstable phenomena which cannot be described by the *stationary* Favre-averaged PDF model used. Instationary PDF calculations or Large Eddy Simulation would be needed to overcome this limitation, but would require even more computer power.

References

[1] H.A. Wouters. *Lagrangian models for turbulent reacting flows.* PhD thesis, Delft University of Technology, 1998.

[2] H.A. Wouters, T.W.J. Peeters, and D. Roekaerts. Joint velocity-scalar PDF methods. In B.E. Launder and N.D. Sandham, editors, *Closure strategies for turbulent and transitional flows*. Cambridge University Press, 2001. in press.

[3] S.B. Pope. PDF methods for turbulent reactive flows. *Progress in Energy and Combustion Science*, 11:119–192, 1985.

[4] S.B Pope. On the relationship between stochastic Lagrangian models of turbulence and second-moment closures. *The Physics of Fluids*, 6(2):973–985, 1994.

[5] D.C. Haworth and S.H. El Tahry. Probability density function approach for multidimensional turbulent flow calculations with application to in-cylinder flows in reciprocating engines. *AIAA Journal*, 29(2):208–218, 1990.

[6] S.M. Correa and S.B. Pope. Comparison of a Monte Carlo PDF/finite-volume mean flow model with bluff-body Raman data. In *Proceedings of the Combustion Institute*, **24**, pages 279–285, 1992.

[7] D.C. Haworth and S.B. Pope. A generalized Langevin model for turbulent flows. *The Physics of Fluids*, 29:387–405, 1986.

[8] B. Naud *PDF modeling of turbulent sprays and flames using a particle stochastic approach*. PhD thesis, Delft University of Technology, 2003.

[9] H. Risken. *The Fokker-Planck equation*. Springer-Verlag, Berlin, 1984.

[10] C.W. Gardiner, *Handbook of stochastic methods*. Springer-Verlag, 2nd, Berlin, 1990.

[11] A.S. Monin and A.M. Yaglom. *Statistical Fluid Mechanics*. MIT Press, Cambridge, Massachusetts, 1971.

[12] M.S. Anand and S.B. Pope. Diffusion behind a line source in grid turbulence. In L.J.S. Bradbury *et al.*, editor, *Turbulent Shear Flows*, volume 4, pages 46–61. Springer-Verlag, New York, 1985.

[13] S.S. Girimaji and S.B. Pope. A diffusion model for velocity gradients in turbulence. *Physics of Fluids A*, 2(2):242–256, 1990.

[14] S.B Pope. Lagrangian PDF methods for turbulent flows. *Annual Review Fluid Mechanics*, 26:23–63, 1994.

[15] H.A. Wouters, P.A. Nooren, T.W.J. Peeters, and D. Roekaerts. Simulation of a bluff-body-stabilized diffusion flame using second-moment closure and Monte Carlo methods. In *Proceedings of the Combustion Institute*, **26**, pages 177–185, 1996.

[16] S.M. Correa, A. Gulati, and S.B. Pope. Raman measurements and joint PDF modeling of a nonpremixed bluff-body-stabilized methane flame. In *Proceedings of the Combustion Institute*, **25**, pages 1167–1173, 1994.

[17] P.A. Nooren, H.A. Wouters, T.W.J. Peeters, D. Roekaerts, U. Maas, and D. Schmidt. Monte Carlo PDF modelling of a turbulent natural-gas diffusion flame. *Combustion Theory and Modelling*, 1(1):79–96, 1997.

[18] M. Muradoglu, P. Jenny, S.B. Pope, and D.A. Caughey. A consistent hybrid finite-volume/particle method for the PDF equations of turbulent reactive flows. *Journal of Computational Physics*, 154:342–371, 1999.

[19] S.B. Pope. Consistent modeling of scalars in turbulent flows. *The Physics of Fluids*, 26:404–408, 1983.

[20] Jayesh and Z. Warhaft. Probability distribution, conditional dissipation, and transport of passive temperature fluctuations in grid-generated turbulence. *Physics of Fluids A*, 4(10):2292–2307, 1992.

[21] V. Eswaran and S.B. Pope. Direct numerical simulations of the turbulent mixing of a passive scalar. *The Physics of Fluids*, 31(3):506–520, 1988.

[22] S. Subramaniam and S.B. Pope. A mixing model for turbulent reactive flows based on Euclidian Minimum Spanning Trees. *Combustion and Flame*, 115:487–514, 1997.

[23] A.T. Norris and S.B. Pope. Turbulent mixing model based on ordered pairing. *Combustion and Flame*, 83:27–42, 1990.

[24] C. Dopazo. Relaxation of initial probability density functions in the turbulent convection of scalar fields. *The Physics of Fluids*, 22(1):20–30, 1979.

[25] C. Dopazo. Recent developments in PDF methods. In P.A. Libby and F.A. Williams, editors, *Turbulent reacting flows*, pages 375–474. Academic press, London, 1994.

[26] R.L. Curl. Dispersed phase mixing: I. Theory and effects in simple reactors. *Journal of the American Institute of Chemical Engineers*, 9(2):175–181, 1963.

[27] J. Janicka, W. Kolbe, and W. Kollmann. Closure of the transport equation for the probability density function of turbulent scalar fields. *Journal Non-Equilibrium Thermodynamics*, 4:47–66, 1979.

[28] S.B. Pope. An improved turbulent mixing model. *Combustion Science and Technology*, 28:131–145, 1982.

[29] First ASCF Workshop. Steady-state combustion chambers and furnaces. Test case specifications, ERCOFTAC-SIG, October 1994.

[30] First ASCF Workshop. Steady-state combustion chambers and furnaces. Final results, ERCOFTAC-SIG, October 1994.

[31] T.W.J. Peeters. *Numerical modeling of turbulent natural-gas diffusion flames*. PhD thesis, Delft University of Technology, 1995.

[32] L. Fallot, M. Gonzalez, R. Elamraoui, and M. Obounou. Modelling finite-rate chemistry effects in non-premixed turbulent combustion: test on the bluff-body stabilized flame. *Combustion and Flame*, 110:298–318, 1997.

[33] J. Warnatz, U. Maas, and R.W. Dibble. *Combustion*. Springer-Verlag, Berlin, 1996.

[34] T.W.J. Peeters, D. Roekaerts, and C.J. Hoogendoorn. Modelling of turbulent non-premixed flames. Part 4. Adaptive property tabulation. Technical Report BCWT.93.4, Technische Universiteit Delft, 1993.

[35] H.A. Wouters, P.A. Nooren, T.W.J. Peeters, and D. Roekaerts. Effects of micro-mixing in gas-phase turbulent jets. *International Journal of Heat and Fluid Flow*, 19:201–207, 1998.

Part 4

Turbulent Premixed Combustion

Chapter 12

Large eddy simulation of turbulent combustion

D. Roekaerts

1 Introduction

In large eddy simulation (LES) the larger three-dimensional unsteady turbulent motions are directly represented (resolved), whereas the effects of the smaller scale motions are modeled (filtered). A compact and precise introduction to LES models can be found in Ref. [1]. The development of LES methods for reacting flows has been attracting growing attention in the last years.

Developments have been made in different directions for different applications: atmospheric flows, premixed combustion, non-premixed combustion. In this lecture an elementary introduction to LES of reacting flow is given, followed by a short overview of some recent developments from the literature and a presentation in some detail of one specific approach, the filtered mass density function (FMDF) method.

It is useful to present first an estimate on the computational grid needed to perform a direct numerical simulation (DNS) of a turbulent premixed combustion system. Let the large eddies of the velocity field have characteristic length, rms-velocity and time scales ℓ, u and $\tau = \ell/u$. The ratio of the ℓ to the length scale of the smallest eddies η (Kolmogorov scale) is of order $Re^{0.75}$. Let the laminar flame have thickness e_L and speed v_L. To resolve all eddies the cell size must be of the order of the scale of the smallest eddies and the size of the computational domain must be larger than the scale of the large eddies. The ratio of these scales then determines N, the required number of cells per direction in space. Since it is proportional to $Re^{0.75}$, the number of cells in three dimensions scales as $Re^{2.25}$. Taking into account also the need to have an accurate solution in time one finds that the computational effort scales with Re^3 [1]. The requirement to resolve all flame fronts is an independent requirement. Assuming that the number of grid points needed to resolve a flame front is n (say 10), one has that the new requirement on N is:

$$\frac{\ell}{N} = \Delta x \leq \frac{e_L}{n} = \frac{\nu}{n v_L} = \frac{\ell u}{n v_L Re} \tag{12.1}$$

The variable ν denotes both viscosity and diffusivity (The Lewis number was set to one). This leads to

$$N \geq n \frac{v_L}{u} Re \tag{12.2}$$

Using the estimate $e_L v_L = \nu$ and introducing the Damkohler number

$$Da = \frac{\ell/u}{e_L/v_L} \tag{12.3}$$

one finds

$$N \geq n\sqrt{Re\,Da} \tag{12.4}$$

Depending on the value of Da this is a weaker or stronger requirement than the requirement from turbulence only. Introducing some representative values it can be seen that the computational effort needed for DNS of practical combustion systems is prohibitive.

The computational expense of LES is smaller but can still be too high. It will be of interest when the most important phenomena to be studied are present in the large scale motions and when the predictions are not sensitive to the model used to represent the unresolved motions. E.g. in the study of combustion systems LES methods can be very relevant in the study of large scale combustion instabilities. However, because chemical reaction is a local process and in combustion, flame fronts can be thin, the construction of a good filtering procedure is a complex problem. The resolved reaction rate, appearing in the Eulerian transport equation for the resolved concentrations, cannot be expressed in terms of the resolved concentration and temperature fields. The analogue in LES of the observation made in RANS that fluctuations influence the mean reaction rate, is that in this case subgrid scale fluctuations influence the resolved reaction rate [2]. It can be expected that the phenomena on the unresolved scale in LES will be less universal in reacting flow than in non-reacting flow. At least they will be Damköhler number dependent. The essential advantage of LES, compared to RANS, is that by grid refinement (more precisely decrease of the filter scale) more and more effects of the fluctuations are resolved and less is modeled. E.g. in the case of premixed combustion: more and more flame structures are computed and instantaneous zones of fresh and burnt gases, where turbulence characteristics are quite different, are clearly identified [3].

2 LES equations

2.1 Filtering procedure

For systems with periodic boundary conditions, the filtering can be done in the spectral space, i.e. on Fourier transformed fields, or in the physical space. In the study of combustion systems where periodic boundary conditions are often not suited and flame structures are to be modeled, filtering in physical space is most often used and we restrict to that case here.

The filtered and Favre-filtered values of the flow and thermochemical variables $Q(\boldsymbol{x}, t)$ are represented by $\langle Q(\boldsymbol{x}, t)\rangle_\ell$ and $\langle Q(\boldsymbol{x}, t)\rangle_{\mathrm{L}} = \langle \rho Q\rangle_\ell / \langle \rho\rangle_\ell$, respectively.

The filtered quantity Q is defined as:

$$\langle Q(\boldsymbol{x}, t)\rangle_\ell = \int Q(\boldsymbol{x}', t) G_\Delta(\boldsymbol{x}', \boldsymbol{x}) d\boldsymbol{x}' \tag{12.5}$$

where G_Δ is the LES filter. Δ refers to the filter width. The most popular filters are a box filter and a Gaussian filter. In the first case the filter corresponds to a spatial averaging of the quantity over a box of size Δ. In the second case the spatial averaging is with filter

$$G_\Delta(\boldsymbol{x}', \boldsymbol{x}) = \left(\frac{6}{\pi\Delta^2}\right)^{3/2} \exp\left(-\frac{6}{\Delta^2}|\boldsymbol{x}' - \boldsymbol{x}|^2\right). \tag{12.6}$$

These filters are normalised, positive, spatially and temporally invariant.

Any quantity Q may be split into a filtered component $\langle Q\rangle_\ell$ and an unresolved component Q', according to $Q = \langle Q\rangle_\ell + Q'$. Two differences between mathematical properties of the Reynolds averaging procedure and the filtering procedure have to be taken into account when deriving the equations: firstly, filtering the filtered field a second time may lead to a different result than the filtered field. Then $\langle Q'\rangle_\ell$ may be nonzero. Secondly, exchange of the order of filtering and derivation operators is valid only under some restrictive conditions, e.g. it requires that the filter size is independent of spatial location). The extra terms are often assumed to be handled as part of the subgrid scale models.

2.2 Filtered equations

By filtering the flow equations (without body forces) a set of equations describing the resolved flow properties is obtained. Defining:

$$\frac{\mathrm{D}}{\mathrm{D}t} = \frac{\partial}{\partial t} + \langle U_i \rangle_{\mathrm{L}} \frac{\partial}{\partial x_i} \tag{12.7}$$

and filtering the momentum and species equations gives:

$$\langle \rho \rangle_\ell \frac{\mathrm{D}}{\mathrm{D}t} \langle U_i \rangle_{\mathrm{L}} = -\frac{\partial \langle p \rangle_\ell}{\partial x_i} - \frac{\partial}{\partial x_j} \langle T_{ij} \rangle_\ell - \frac{\partial}{\partial x_j} \langle \rho \rangle_\ell (\langle U_j U_i \rangle_{\mathrm{L}} - \langle U_j \rangle_{\mathrm{L}} \langle U_i \rangle_{\mathrm{L}}) \tag{12.8}$$

$$\langle \rho \rangle \frac{\mathrm{D}}{\mathrm{D}t} \langle \phi_\alpha \rangle_{\mathrm{L}} = -\frac{\partial}{\partial x_j} \langle J_j^\alpha \rangle_\ell + \langle \rho \rangle_\ell \langle S_\alpha \rangle_{\mathrm{L}} - \frac{\partial}{\partial x_j} \langle \rho \rangle_\ell (\langle U_j \phi_\alpha \rangle_{\mathrm{L}} - \langle U_j \rangle_{\mathrm{L}} \langle \phi_\alpha \rangle_{\mathrm{L}}) \tag{12.9}$$

in which the last terms at the right hand side of the equations represent the unresolved Reynolds stress and the Reynolds flux which occur in unclosed form, as does the filtered chemical reaction rate. (filtered values of laminar diffusion fluxes also have to be modeled). An equation similar to (12.9) holds for enthalpy and assuming that there are $\sigma - 1$ scalars representing the chemical composition, the enthalpy can be added as last, i.e. σ-th component of ϕ. Closure of the filtered chemical reaction rate can be done along similar lines as used in RANS for closure of the mean reaction rate. Examples are given below.

2.3 Modeling of unresolved turbulent fluxes

The unresolved Reynolds stress can be closed by the following eddy viscosity assumption

$$\langle \rho \rangle_\ell (\langle \mathbf{UU} \rangle_{\mathrm{L}} - \langle \mathbf{U} \rangle_{\mathrm{L}} \langle \mathbf{U} \rangle_{\mathrm{L}}) = -2 \langle \rho \rangle_\ell \nu_{\mathrm{t}} \langle \mathbf{S} \rangle_{\mathrm{L}} \tag{12.10}$$

with $\langle \mathbf{S} \rangle_{\mathrm{L}}$ the resolved strain rate tensor

$$\langle \mathbf{S} \rangle_{\mathrm{L}} = \frac{1}{2} \left((\nabla \langle \mathbf{U} \rangle_{\mathrm{L}}) + (\nabla \langle \mathbf{U} \rangle_{\mathrm{L}})^T \right) \tag{12.11}$$

where ν_{t} is the sub-grid kinematic eddy viscosity given by the Smagorinsky model as

$$\nu_{\mathrm{t}} = (C_S \Delta)^2 |\mathbf{S}| \tag{12.12}$$

Here Δ is the filter width. The Smagorinsky constant C_S for homogeneous and isotropic turbulence has been estimated as $C_S \approx 0.2$, but it is not universal, and better models have been developed. E.g. the dynamic model provides a methodology for determining an appropriate local value of C_S [1].

The unresolved Reynolds flux can be closed using an eddy diffusivity assumption as:

$$\langle U_j \phi_\alpha \rangle_{\mathrm{L}} - \langle U_j \rangle_{\mathrm{L}} \langle \phi_\alpha \rangle_{\mathrm{L}} = -\frac{\nu_{\mathrm{t}}}{Sc_{\mathrm{t}}} \frac{\partial \langle \phi_\alpha \rangle_{\mathrm{L}}}{\partial x_j} \tag{12.13}$$

where Sc_{t} is a subgrid scale turbulent Schmidt number.

3 Review of recent literature

Several methods have been proposed to account for subgrid-scale mixing and chemical reaction in a LES. Because of the large formal similarity between modeling problems in RANS and in LES, not

surprisingly many closures for LES of reacting flows are direct analogues of closures in the context of RANS. An overview has been given by Vervisch and Veynante [3]. They conclude that extensions of simple procedures such as neglecting fluctuations of eddy break-up type of models were not successful. Next they separately review approaches developed for non-premixed combustion and for premixed combustion. Here we proceed similarly by refering to a selection of recent publications. Only a qualitative description is given.

3.1 Non-premixed combustion

The analogue of the probability density function (PDF) of fluctuations in RANS, in the context of LES is a probability density function representing the relative occurrence of values of physical quantities on the sub grid scale. Such a density in the literature has been called large-eddy PDF (LEPDF) or also *filtered density function* (FDF), referring to the LES approach of calculating only phenomena at scales larger than a given filter scale [2]. Here we shall use the name FDF. In the combination of LES and FDF, phenomena on scales larger than the filter scale are explicitly calculated and the phenomena on smaller scales are represented in a statistical sense using the filtered density function. The FDF can be obtained by assumed shape methods or by Monte Carlo methods in a similar way as the PDF.

Exploiting that combustion is a fast process, non-premixed combustion is described by solving the transport of a conserved scalar (mixture fraction) and obtaining the chemical composition and temperature from a fast chemistry model. Assumed FDF models relate the subgrid distribution of mixture fraction to its low order statistical moments. The mean is known from the resolved field, but the variance must be modeled. Different approaches for modelling the subgrid variance have been used, see Ref. [4] and references therein. Recent developments are reported in Refs. [5] and [6]. Branley and Jones [7] have applied the assumed FDF model in the calculation of a hydrogen diffusion flame.

A flame surface density based model for LES of turbulent nonpremixed combustion has been described by Zhou and Mahalingam [19]. The filtered flame surface density is modelled as the conditional filtered gradient of the mixture fraction and the FDF.

Pitsch [8] has used unsteady flamelet modeling to calculate a methane/air diffusion flame (Sandia Flame D). Unsteady flamelet modeling was developed earlier in the context of RANS, see [9] and

references therein. Subgrid scale quantities were determined using the dynamic procedure. The eddy-diffusivity has been computed using from the assumption of a constant subgrid turbulent Schmidt number 0.4, determined from independent simulations using a dynamic procedure. The chemical mechanism used is a reduced version of the GRI 2.11 mechanism, consisting of 29 global reactions. (GRI 2.11 includes reactions among 48 species).

Colucci et al. [10, 11, 12] have developed a Monte Carlo method for computation of the FDF, following Monte Carlo methodology for the computation of the PDF [13]. In [12] two-dimensional LES results are presented for a nonpremixed methane jet flame using 25 step chemical mechanism. This Monte Carlo FDF method is explained in detail below.

The models mentioned until now essentially contain only one subgridscale mixing frequency. In the *linear eddy model* (LEM) ([14, 15, 16] and references therein) phenomena at all relevant length and time scales are included, including multiple mixing frequencies, but in one dimension only. Turbulent mixing is modeled by a stochastic rearrangement of subsets of the one-dimensional profile of the scalar fields. One-dimensional laminar diffusion, and possibly reaction, is included explicitly. A collection of linear eddies represents the flow at the subgrid level. The linear eddies move according to both resolved and unresolved, hence modeled, flow field. The linear eddies also interact with each other at the subgrid scale.

Conditional moment closure (CMC) is applied to LES in Ref. [17]. Apart from the subgrid FDF of mixture fraction, also conditional expectation values of the other variables (conditional on values of mixture fraction) are computed.

In Ref. [18] the scalar field is described by clouds of tracer particles and the subgrid contribution of the tracer displacement is modelled by a kinematic model which obeys Kolmogorov's inertial-range scaling. The focus is on the PDF of the separation of particle pairs. The model predicts the scalar variance field.

3.2 Premixed combustion

LES of premixed combustion in general has to cope with the situation that the flame thickness δ_L of a premixed flame is smaller than the LES filter size. Therefore the flame front is not resolved in the calculation, and step changes over one grid cell occur in resolved variables. To overcome this difficulty specific approaches, sometimes closely related to each other, have been proposed ([20] and references therein)

ARTIFICIALLY THICKENED FLAME By rescaling the flame thickness with a factor $F > 1$ and simultaneously rescaling the reaction rate with a factor $1/F$, the premixed flame system is transformed into another system with the same laminar flame speed, but with a larger flame thickness [20], which can be described with less computational effort. However, since the Damköhler number of the artificially thickened flame is also smaller by a factor F than the original flame the turbulence-chemistry interaction is not invariant under the transformation. To accommodate this the *efficiency function* has been developed which describes the necessary correction of the reaction rate to accommodate for that effect. The input parameters in the efficiency parameter are related to the subgrid scale turbulence.

FLAME-FRONT TRACKING TECHNIQUE In the flame front tracking technique, the flame surface is viewed as an infinitesimally thin propagating surface. The key idea is to track the position of the flame front using a field variable G. The flame surface is associated to a given iso-level $G = G^*$. The G-field does not have to follow the gradients of the progress variable (e.g. temperature) and can be smoothed out to be resolved on a LES grid. The challenge is to propose a model for the subgrid scale turbulent flame speed, entering the filtered G-equation. According to Colin *et al.* [20] the G-equation approach is, up to now, the most advanced technique for LES of premixed combustion. There also further references can be found.

FILTERING OF THE EQUATION FOR PROGRESS VARIABLE Another approach, developed in Ref. [21] starts from the balance equation for the progress variable. The filtered equation is solved on a mesh, but the mesh size is chosen finer than the filter width. In this way the computational efficiency of LES can be combined with resolution of the gradients in the resolved progress variable. A flame surface density formulation is proposed to describe the subgrid contribution of molecular diffusive and reaction rate processes. The quality of this closure has been investigated by comparing with data from a DNS.

FLAME WRINKLING DENSITY FUNCTION The approach presented in Ref. [22] uses the laminar flamelet approach with conditional filtering. By conditioning the continuity equation on the unburned gas before filtering, a transport equation for the resolved part of the unburned gas mass fraction is obtained. From the transport equation for the subgrid flame area density and the resolved unburned

gas volume fraction, a transport equation for the subgrid flame wrinkling is derived. The subgrid flame wrinkling can be regarded as the turbulent to laminar flame speed ratio.

3.3 Partially-premixed combustion

Domingo, Vervisch and Bray [23] have developed LES models for partially premixed flames in non-premixed turbulent combustion. (I.e. when fuel and oxidizer have mixed before burning). Combustion in the premixed mode is assumed to occur in the thin flamelet burning regime. Subgrid closure schemes for fully premixed and non-premixed combustion are combined. A criterion using the resolved unsteady fuel and oxidiser fields is introduced to discriminate between the various degrees of partial premixing and to estimate the proportions of premixed and non-premixed combustion at subgrid level.

4 Algorithm to compute the filtered mass density function

4.1 Definition

Above the FDF has been introduced as the probability density function associated with the composition of the flow at the subgrid scale. For the development of a computational algorithm, it is convenient to define the filtered mass density (FMDF), $\mathcal{F}_{\mathrm{L}}$, rather than the FDF. It gives the mass density of *mass* with composition $\boldsymbol{\psi}$ in the subgrid region sampled by the filter function D_{Δ}. It is defined by

$$\mathcal{F}_{\mathrm{L}}(\boldsymbol{\psi};\boldsymbol{x},t) = \int \rho(\boldsymbol{\psi})\delta\left(\boldsymbol{\psi}-\boldsymbol{\phi}(\boldsymbol{x}',t)\right) G_{\Delta}(\boldsymbol{x}',\boldsymbol{x})\,\mathrm{d}\boldsymbol{x}' \tag{12.14}$$

Its important properties are:

$$\int \mathcal{F}_{\mathrm{L}}(\boldsymbol{\psi},\boldsymbol{x};t)\,\mathrm{d}\boldsymbol{\psi} = \langle\rho(\boldsymbol{x},t)\rangle_{\ell} \tag{12.15}$$

$$\int \frac{\mathcal{F}_{\mathrm{L}}(\boldsymbol{\psi},\boldsymbol{x};t)}{\rho(\boldsymbol{\psi})}\,\mathrm{d}\boldsymbol{\psi} = 1 \tag{12.16}$$

$$\int \mathcal{F}_{\mathrm{L}}(\boldsymbol{\psi},\boldsymbol{x};t)Q(\boldsymbol{\psi})\;textd\boldsymbol{\psi} = \langle\rho Q\rangle_{\ell} = \langle\rho\rangle_{\ell}\langle Q\rangle_{\mathrm{L}} \tag{12.17}$$

4.2 Representation by ensemble of notional particles

In order to solve the transport equation for the FMDF, in the case of multiple scalars, Monte Carlo methods are preferred compared to finite difference methods for the same reasons as in PDF methods. (Computational efficiency). A first step towards a Monte Carlo method to compute (an approximation to) the FMDF is its representation by a discrete FMDF. Consider the turbulent flow in a volume $\mathcal{V}$ of physical space, ($\boldsymbol{x}$-space). The filtered amount of mass in this volume is M given by

$$M = \int \langle\rho(\boldsymbol{x})\rangle_{\ell}\,\mathrm{d}\boldsymbol{x} \tag{12.18}$$

where $\int d\boldsymbol{x}$ represents the integral over $\mathcal{V}$.

In the volume $\mathcal{V}$ the FMDF now is represented by N notional particles, each representing an amount of mass Δm,

$$\Delta m \equiv \frac{M}{N} \tag{12.19}$$

The n-th particle has composition $\boldsymbol{\phi}^{(n)}$ and position $\boldsymbol{x}^{(n)}$. The $(\sigma+3)$-dimensional vector $(\boldsymbol{\phi}^{(n)}, \boldsymbol{x}^{(n)})$ defines the state of the particle and is called state vector. This state corresponds to the point $(\boldsymbol{\psi}, \boldsymbol{x}) = (\boldsymbol{\phi}^{(n)}, \boldsymbol{x}^{(n)})$ in the $(\sigma+3)$-dimensional state space, the $(\boldsymbol{\psi}, \boldsymbol{x})$-space.

The discrete filtered mass density function is defined by:

$$\mathcal{F}_{LN}(\boldsymbol{\psi}, \boldsymbol{x}) \equiv \Delta m \sum_{n=1}^{N} \delta(\boldsymbol{\psi} - \boldsymbol{\phi}^{(n)})\delta(\boldsymbol{x} - \boldsymbol{x}^{(n)}) \tag{12.20}$$

Each particle is an independent sample of the FMDF. Therefore the expected value of (12.20) can be written as

$$\begin{aligned} \langle \mathcal{F}_{LN}(\boldsymbol{\psi}, \boldsymbol{x})\rangle_\ell &= \Delta m \sum_{n=1}^{N} \langle \delta(\boldsymbol{\psi} - \boldsymbol{\phi}^{(n)})\delta(\boldsymbol{x} - \boldsymbol{x}^{(n)})\rangle_\ell \\ &= M\langle \delta(\boldsymbol{\psi} - \boldsymbol{\phi}^{(n')})\delta(\boldsymbol{x} - \boldsymbol{x}^{(n')})\rangle_\ell, \quad 1 \le n' \le N \end{aligned} \tag{12.21}$$

The discrete FMDF, through the composition and the position of the particles, has to satisfy

$$\langle \mathcal{F}_{LN}(\boldsymbol{\psi}, \boldsymbol{x})\rangle_\ell = \mathcal{F}_L(\boldsymbol{\psi}, \boldsymbol{x}) \tag{12.22}$$

From this it can be derived that the probability density function for the position of the particles is proportional to the filtered density and that the probability density function for the composition of the particles is proportional to the Favre filtered probability density function.

4.3 Computation of filtered quantities from the discrete FMDF

In the particle method the discrete representation is computed and used to approximate the moments of the FMDF of the system as follows.

Divide the volume $\mathcal{V}$ in k cells; let $\boldsymbol{x}_{(k)}$ and $\mathcal{V}_k$ be the coordinate of the centre and the volume of the k-th cell. These cells have to be sufficiently small in order that the composition of each cell is statistically homogeneous, and sufficiently large such that the number of particles in the k-th cell, N_k, is large.

The discrete representation of the FMDF in Cartesian coordinates is:

$$\mathcal{F}_{LN}(\boldsymbol{\psi}, \boldsymbol{x}; t) = \Delta m \sum_{n=1}^{N} \delta(\boldsymbol{\psi} - \boldsymbol{\phi}^{(n)})\delta(\boldsymbol{x} - \boldsymbol{x}^{(n)}) \tag{12.23}$$

By multiplying (12.23) with $Q(\boldsymbol{\psi})$ and integrating over $\boldsymbol{\psi}$-space we obtain:

$$\int Q(\boldsymbol{\psi})\mathcal{F}_{LN}(\boldsymbol{\psi}, \boldsymbol{x}; t)d\boldsymbol{\psi} = \Delta m \sum_{n=1}^{N} Q(\boldsymbol{\phi}^{(n)})\delta(\boldsymbol{x} - \boldsymbol{x}^{(n)}) \tag{12.24}$$

By taking the volume average over the subvolume $\mathcal{V}_k$ we obtain:

$$\frac{1}{\mathcal{V}_k}\int_{\mathcal{V}}\int Q(\boldsymbol{\psi})\mathcal{F}_{LN}(\boldsymbol{\psi}, \boldsymbol{x}; t)d\boldsymbol{\psi}\, d\boldsymbol{x} \;=\; \frac{\Delta m}{\mathcal{V}_k} \sum_{n|\boldsymbol{X}^{(n)}\in\mathcal{V}_k} Q(\boldsymbol{\phi}^{(n)}) \tag{12.25}$$

This is an exact relation between properties from the finite Monte Carlo ensemble. Assuming that the ensemble consists of samples of the continuous filtered mass density function, one has that the right hand side is an approximation of the expected value of the left hand side. If we replace at the left

hand side $\mathcal{F}_{LN}$ by $\mathcal{F}_L$ the equality becomes an approximation. The statistical error is of order $1/\sqrt{N_k}$. Assuming that the FMDF is uniform over the cell we find

$$\int Q(\boldsymbol{\psi})\mathcal{F}_L(\boldsymbol{\psi}, \boldsymbol{x}''_{(k)}; t)d\boldsymbol{\psi} \approx \frac{\Delta m}{\mathcal{V}} \sum_{n|\boldsymbol{X}^{(n)}\in\mathcal{V}_k} Q(\boldsymbol{\phi}^{(n)}) \tag{12.26}$$

with $\boldsymbol{x}''_{(k)}$ a point in the k-th cell. The right hand side by definition is equal to $\langle\rho(\boldsymbol{x}''_{(k)})Q(\boldsymbol{x}''_{(k)})\rangle_\ell$. By applying equation (12.26) in the case $Q \equiv 1$ we obtain an approximation of the filtered density (See equation (12.15)). Finally we obtain:

$$\begin{aligned}\langle Q(\boldsymbol{x}''_{(k)})\rangle_{\mathrm{L}} &\equiv \frac{\langle\rho(\boldsymbol{x}''_{(k)})Q(\boldsymbol{x}''_{(k)})\rangle_\ell}{\langle\rho(\boldsymbol{x}''_{(k)})\rangle_{\mathrm{L}}} \\ &\approx \frac{1}{N_k}\sum_{n|\boldsymbol{X}^{(n)}\in\mathcal{V}_k} Q(\boldsymbol{\phi}^{(n)})\end{aligned} \tag{12.27}$$

In words: the ensemble mean is an approximation of the Favre filtered value.

4.4 Algorithm for the computation of the discrete FMDF

The basic assumption in the particle method to solve the transport equation for the FMDF is that the time evolution of the FMDF can be directly translated into a time evolution of the particles representing the discrete FMDF. This goes beyond the mere representation of an individual FMDF by an ensemble. It promotes them to dynamical quantites which evolve in time. If the subgrid scale dynamics would be known the model for time evolution of particle properties could use that information. In the absence of that information, model equations have to be used.

The FMDF at time t is represented by $N(t)$ particles in the $\boldsymbol{\psi}$-$\boldsymbol{x}$-space, with every particle representing a fixed mass Δm. At time t the state of the n-th particle is:

$$\boldsymbol{\phi}^{(n)}(t), \boldsymbol{x}^{(n)}(t),\ n = 1, 2, \ldots, N(t) \tag{12.28}$$

To obtain equations of motion for the particle properties we use the assumption that a correspondence exists between model approximations in the equation for the FMDF and model approximations in the equations of motion of the notional particles. The exact transport equation for the FMDF can be derived but is unclosed. Transport by unresolved velocity fluctuations and by the unresolved fluctuations in diffusion flux appear as unclosed terms. Using eddy viscosity modeling, with turbulent dynamic viscosity μ_{t}, for the former, and IEM model for the latter the modelled transport equation for the FMDF is given by

$$\begin{aligned}\frac{\partial}{\partial t}\mathcal{F}_L(\boldsymbol{\psi}, \boldsymbol{x}; t) + \frac{\partial}{\partial x_i}\left(\langle U_i\rangle_{\mathrm{L}}\mathcal{F}_L(\boldsymbol{\psi}, \boldsymbol{x}; t)\right) =& \frac{\partial}{\partial x_i}\left[\frac{\mu_{\mathrm{t}}}{Sc_{\mathrm{t}}}\frac{\partial}{\partial x_i}\left(\frac{1}{\langle\rho\rangle_\ell}\mathcal{F}_L(\boldsymbol{\psi}, \boldsymbol{x}; t)\right)\right] \\ &+ \frac{\partial}{\partial\psi_\alpha}\left[\omega(\psi_\alpha - \langle\phi_\alpha\rangle_{\mathrm{L}})\mathcal{F}_L(\boldsymbol{\psi}, \boldsymbol{x}; t)\right] \\ &- \frac{\partial}{\partial\psi_\alpha}\left[S_\alpha(\boldsymbol{\psi})\mathcal{F}_L(\boldsymbol{\psi}, \boldsymbol{x}; t)\right]\end{aligned} \tag{12.29}$$

Here ω is the 'frequency of mixing withing the subgrid'. It is modeled by

$$\omega = C_\omega\frac{\nu + \frac{\nu_{\mathrm{t}}}{Sc_{\mathrm{t}}}}{\Delta^2} \tag{12.30}$$

with C_ω a model constant. (For more details we refer to Jaberi *et al.* [10]). Equation (12.29) can be written as

$$\frac{\partial}{\partial t}\mathcal{F}_L(\boldsymbol{\psi}, \boldsymbol{x}; t) = (P_1 + P_2)\mathcal{F}_L(\boldsymbol{\psi}, \boldsymbol{x}; t) \tag{12.31}$$

with P_1 and P_2 the operators:

$$\begin{aligned} P_1 &= -\frac{\partial}{\partial x_i}\langle U_i\rangle_{\mathrm{L}} + \frac{\partial}{\partial x_i}\left[\frac{\mu_{\mathrm{t}}}{Sc_{\mathrm{t}}}\frac{\partial}{\partial x_i}\frac{1}{\langle\rho\rangle_\ell}\right] \\ &= -\frac{\partial}{\partial x_i}\left[\langle U_i\rangle_{\mathrm{L}} + \frac{1}{\langle\rho\rangle_\ell Sc_{\mathrm{t}}}\left(\frac{\partial\mu_{\mathrm{t}}}{\partial x_i}\right)\right] + \frac{\partial}{\partial x_i}\left[\frac{\mu_{\mathrm{t}}}{Sc_{\mathrm{t}}\langle\rho\rangle_\ell}\right] \end{aligned} \tag{12.32}$$

and

$$P_2 = \frac{\partial}{\partial\psi_\alpha}\left[c\,\omega(\psi_\alpha - \langle\psi_\alpha\rangle_{\mathrm{L}})\right] - \frac{\partial}{\partial\psi_\alpha}S_\alpha(\boldsymbol{\psi}) \tag{12.33}$$

The operator P_1 describes the transport of the FMDF in the $\boldsymbol{x}$-space, the operator P_2 describes the transport of the FMDF in the $\boldsymbol{\psi}$-space. Both operators act simultaneously. However, to obtain the effect of this simultaneous action after a short time interval Δt, one can use the method of fractional steps, i.e. have only one operator act first and have the second operator act on the result of the first step. The numerical error then is of order $(\Delta t)^2$. Translated to operations on particles, the method of fractional steps means that we can first perform the operations corresponding to P_1 generating an intermediate ensemble and then have the operations corresponding to P_2 act on the intermediate ensemble.

P_1 is an example of a Fokker-Planck-operator. It describes the evolution of the probability density function of a continuous Markov proces. It is defined by the drift vector

$$K_i(\boldsymbol{x}, t) \equiv \langle U_i\rangle_{\mathrm{L}} + \frac{1}{\langle\rho\rangle_\ell Sc_{\mathrm{t}}}\left(\frac{\partial\mu_{\mathrm{t}}}{\partial x_i}\right), \quad i = 1, 2, 3 \tag{12.34}$$

and the diffusion matrix:

$$D_{ij} = 2\frac{\mu_{\mathrm{t}}}{Sc_{\mathrm{t}}}\frac{1}{\langle\rho\rangle_\ell}\delta_{ij}, \quad i, j = 1, 2, 3 \tag{12.35}$$

The Fokker-Planck-equation for the probability density function is equivalent to a class of stochastic differential equations for the stochastic process $\boldsymbol{x}(t)$. In discretised form, the Ito stochastic differential equation for a realisation $\boldsymbol{x}^{(n)}(t)$ of the stochastic process is given by:

$$x_i^{(n)}(t + \Delta t) = x_i^{(n)}(t) + K_i(\boldsymbol{x}^{(n)}(t), t)\ \Delta t + \sigma_{ij}(\boldsymbol{x}^{(n)}(t), t)\ \Delta W_j(t) \tag{12.36}$$

Here $W_j(t),\ \ j = 1, \ldots, 3$ are three independent Wiener-processes. At time step Δt the increment of the Wiener-process is a Gaussian-distributed variable with mean zero and standard deviation $\sqrt{\Delta t}$. The increments at different time steps are statistically independent. The matrix σ_{ij} has to satisfy

$$D_{ij} = \sum_{k=1}^{3}\sigma_{ik}\sigma_{jk} \tag{12.37}$$

It is seen that given the filtered velocity $\langle U_i\rangle_{\mathrm{L}}$ and the gradient diffusion model for turbulent transport the position of particles changes according to an Ito-equation with drift vector (12.34) and matrix σ_{ij} of the form:

$$\sigma_{ij} = \sqrt{\frac{2\mu_{\mathrm{t}}}{\langle\rho\rangle_\ell Sc_{\mathrm{t}}}}\delta_{ij} \tag{12.38}$$

The filtered velocity $\langle U_i \rangle_{\rm L}$ and the filtered turbulent diffusivity $\mu_{\rm t}$ depend on the position of the particle. An alternative to the Lagrangian algorithm described here would be an Eulerian algorithm where particles associated with an FDF are associated with the cells of a finite volume grid and which jump from cell to cell to represent convection and diffusion. The two methods have been compared in the context of PDF calculations of a supersonic hydrogen diffusion flame by Mobus *et al* [24]. They looked at numerical diffusion, spatial accuracy and numerical efficiency. Using the same grid, the Lagrangian algorithm has a larger accuracy, but a higher cost than the Eulerian algorithm. In large eddy simulations the quantities that are calculated in general show sharper gradients than in RANS and reaching the best spatial accuracy with the given grid is of importance. This explains why for LES, Lagrangian Monte Carlo methods are preferred.

The form of the operator P_2 is typical for the evolution of the probability density function when the underlying process is deterministic (only one derivative). For each n the time evolution over time Δt is given by:

$$\boldsymbol{\phi}^{(n)}(t+\Delta t) = \boldsymbol{\phi}^{(n)}(t) - c\,\omega(\boldsymbol{x}^{(n)}(t))(\boldsymbol{\phi}^{(n)}(t) - \langle\boldsymbol{\phi}\rangle_{\rm L})\Delta t + \underline{S}(\boldsymbol{\phi}^{(n)}(t))\Delta t \tag{12.39}$$

The mean $\langle\boldsymbol{\phi}\rangle_{\rm L}$ that appears can be calculated from the ensemble of particles present in the same subvolume $\mathcal{V}_k$ as the n-th particle. The resolved turbulence frequency ω can be evaluated at the position of the particle after application of (12.36).

4.5 LES-FMDF solution algorithm

Once the discrete FMDF is known an approximation for the filtered reaction rate in the filtered scalar transport equation is known, and the term is closed. However since the FMDF solution algorithm provides also the necessary information to calculate the resolved scalar field directly by ensemble averaging over properties of notional particles, it is not necessary to solve the resolved scalar equations. The model then consists of a LES model for the description of the velocity field and the FMDF model for the description of the scalar field. The resolved density appears in both sub models and provides the influence of chemical reactions and heat release on the flow field. Further refinements and results can be found in Jaberi *et al.*[10].

References

[1] Stephen B. Pope. *Turbulent Flows*. Cambridge University Press, 2000.

[2] S.B. Pope. Computations of turbulent combustion: progress and challenges. In *Proceedings of the Combustion Institute,* **23**, pages 591–612, 1990.

[3] Luc Vervisch and Denis Veynante. Turbulent combustion modeling. In *Lecture notes, Von Karman Institute*, 1999. 177 pages.

[4] Clifton Wall, Bendiks Jan Boersma, and Parviz Moin. An evaluation of the assumed beta probability density function subgrid-scale model for large eddy simulation of nonpremixed, turbulent combustion with heat release. *The Physics of Fluids*, 12:2522–2529, 2000.

[5] C. Pantano and S. Sarkar. A subgrid model for nonlinear functions of a scalar. *Phys. Fluids*, 13:3803-3819, 2001

[6] S.M. de Bruyn Kops and J.J. Riley. Mixing models for large-eddy simulation of nonpremixed turbulent combustion. *J. Fluids Eng*, 123:341-346, 2001

[7] N. Branley and W.P. Jones. Large eddy simulation of a turbulent nonpremixed flame. *Combustion and Flame*, 127:1913-1934, 2001.

[8] H.Pitsch and H. Steiner. Large-eddy simulation of a turbulent methane/air diffusion flame (Sandia flame D). *The Physics of Fluids*, 12:2541–2554, 2000.

[9] Heinz Pitsch. Unsteady flamelet modeling of differential diffusion in turbulent jet diffusion flames. *Combustion and Flame*, 123:358–374, 2000.

[10] F.A. Jaberi, P.J. Colucci, S. James, P. Givi, and S.B. Pope. Filtered mass density function for large-eddy simulation of turbulent reacting flows. *Journal of Fluid Mechanics*, 401:85–121, 1999.

[11] P.J. Colucci, F.A. Jaberi, P. Givi, and S.B. Pope. Filtered density function for large eddy simulation of turbulent reacting flows. *The Physics of Fluids*, 10:499–515, 1998.

[12] S. James and F.A. Jaberi. Large scale simulations of two-dimensional nonpremixed methane jet flames. *Combustion and Flame*, 123:465–487, 2000.

[13] S.B. Pope. PDF methods for turbulent reactive flows. *Progress in Energy and Combustion Science*, 11:119–192, 1985.

[14] William H. Calhoon Jr. and Suresh Menon. Linear-eddy subgrid model for reacting large-eddy simulations: heat release effects. In *35th Aerosciences meeting and exhibit*, 1997. AIAA 97-0368.

[15] Won-Wook Kim and Suresh Menon. Numerical modeling of turbulent premixed flames in the thin-reaction zones regime. *Combustion Science and Technology*, 2000.

[16] V.K. Chakravarthy and S. menon. Linear eddy simulations of Reynolds number and Schmidt number effects of turbulent scalar mixing. *The Physics of Fluids*, 13:488–499, 2001.

[17] W.Kendal Bushe and Helfried Steiner. Conditional moment closure for large eddy simulation of nonpremixed turbulent reacting flows. *The Physics of Fluids*, 11:1896–1906, 1999.

[18] P. Flohr and J.C. Vassilicos. A scalar subgrid model with flow structure for large-eddy simulations of scalar variances. *Journal of Fluid Mechanics*, 407:315–349, 2000.

[19] Xiangyang Zhou and shankar Mahalingam. A flame surface density based model for large eddy simulation of turbulent nonpremixed combustion. *Phys. Fluids*, 14, L77-L80, 2002

[20] O. Colin, F. Ducros, D. Veynante, and T. Poinsot. A thickened flame model for large eddy simulations of turbulent premixed combustion. *The Physics of Fluids*, 12:1843–1863, 2000.

[21] M. Boger, D. Veynante, H. Boughanem, and A. Trouvé. Direct numerical simulation analysis of flame surface density concept for large eddy simulation of turbulent premixed combustion. In *Twenty-Seventh Symposium (International) on Combustion*, 1998.

[22] H.G. Weller, G. Tabor, A.D. Gosman, and C. Fureby. Application of a flame-wrinkling LES combustion model to a turbulent mixing layer. In *Twenty-Seventh Symposium (International) on Combustion*, 1998.

[23] Pascale Domingo, Luc Vervisch and Ken Bray. Partially premixed flamelets in LES of non-premixed turbulent combustion. *Combust. Theory Modelling*, 6:519-551, 2002

[24] JH. Mobus, P. Gerlinger, and D. Bruggemann. Comparison of Eulerian and Lagrangian Monte Carlo PDF methods for turbulent diffusion flames. *Combustion and Flame*, 124:519–534, 2001.

Chapter 13

Flamelet Models for Premixed Turbulent Combustion

L. P. H. de Goey

Abstract

Existing models for simulating premixed turbulent combustion in the laminar flamelet regime will be reviewed. Basis of all the ideas is that the flame fronts are very thin. One class of models makes use of a progress variable, which describes the degree of burning of the local flamelets. To describe turbulent combustion using this method, an equation is derived for the average value of the progress variable. Unclosed terms for turbulent mixing and average chemical source term appear. Closure models for these terms have to be introduced. Frequently a simple gradient transport assumption is used to close the turbulent mixing term, but it is well known that counter-gradient diffusion often plays a role in premixed turbulent combustion. The physics behind these phenomena are analysed and models are reviewed. The averaged chemical source term is mostly modelled as being proportional to the flame surface density and the laminar burning velocity. In the Bray-Libby-Moss (BML) model it is effectively assumed that the flame front is infinitely thin, so that the mixture can only be in two states: an unburnt state and a burnt state. For this special case, a simple closure for the chemical source term can be derived, which is similar to that of the eddy-break-up model. A transport equation for the flame surface density can be derived as well, as is done in the Coherent Flame Model (CFM), first introduced by Marble and Broadwell. The closure of this equation is still under thorough investigation and is discussed in the lecture. Also very popular is the model making use of the averaged kinematic G-equation, used by Peters and coworkers [10]. Turbulent transport terms do not appear in this equation. However, a propagation term proportional to the turbulent burning velocity appears, which is proportional to the so-called flame surface area ratio. Simple and more complex models are available for modelling this term, which are closely related to models derived for the flame surface density.

1 Introduction

In the last decades, a lot of different models have been developed for turbulent premixed combustion. Some of them are based on the laminar flamelet concept, which uses the observation that a turbulent flame can be considered as a collection of thin laminar flames, convected, curved and rolled-up by the turbulent flow structures, see e.g. Peters [10]. This physical picture holds if all the flame scales are much smaller than the flow scales, so that the flame structure remains almost frozen when convected around. Application of flamelet models has proven to be very succesful to describe practical combustion situations. Examples of such models are the Bray-Moss-Libby (BML) model, the Coherent

Flame Model (CFM), and the G-equation flamelet model. Key issue of these and other models is the derivation of an equation for the averaged progress variable $\tilde{\mathcal{Y}}$ like

$$\frac{\partial}{\partial t}(\overline{\rho}\tilde{\mathcal{Y}}) + \nabla\cdot(\overline{\rho}\tilde{\mathbf{v}}\tilde{\mathcal{Y}}) + \nabla\cdot(\widetilde{\overline{\rho}\mathbf{v}''\mathcal{Y}''}) = \langle m\rangle_{\mathrm{f}}\bar{\Sigma}, \tag{13.1}$$

from the instantaneous progress variable $\mathcal{Y}$:

$$\frac{\partial(\rho\mathcal{Y})}{\partial t} + \nabla\cdot(\rho\mathbf{v}\mathcal{Y}) = \nabla\cdot(\rho D\nabla\mathcal{Y}) + \dot{\rho}_{\mathcal{Y}} = -m\mathbf{n}\cdot\nabla\mathcal{Y}, \tag{13.2}$$

where $m = \rho s_{\mathrm{L}}$ is the laminar mass burning rate. Equation (13.1) is found by averaging equation (13.2), using the definition of the Favre-average: $\tilde{f} = \overline{\rho f}/\overline{\rho}$.

The averaged convection term $\nabla\cdot(\overline{\rho}\tilde{\mathbf{v}}\tilde{\mathcal{Y}})$ and the turbulent diffusion term $\nabla\cdot(\widetilde{\overline{\rho}\mathbf{v}''\mathcal{Y}''})$ are found from averaging the instantaneous convection term in equation (13.2). The turbulent diffusion term is unclosed and is mostly modelled using the gradient diffusion assumption. The averaging of the chemical source term in equation (13.2) is very difficult. One way to close the source term is by using the laminar flamelet assumption, stating that reaction is concentrated in thin surfaces. The averaged chemical source is then given by $\langle m\rangle_{\mathrm{f}}\bar{\Sigma}$, with $\langle m\rangle_{\mathrm{f}}$ the averaged laminar mass consumption rate of the instantaneous flame front and $\bar{\Sigma} = -\overline{\mathbf{n}\cdot\nabla\mathcal{Y}}$ the flame surface density, indicating the amount of (laminar) flame surface per unit volume. These factors are still unclosed and must be modelled. The mentioned models differ in the way these terms are closed.

2 Bray-Libby-Moss Model

A very important implication of combustion in the flamelet regime is that reaction and diffusive mixing takes place in thin layers near the flame front and that these processes are strongly correlated. The simplest way to model the flame is as an infinitely thin layer, separating unburnt and burnt gases. This is the basic assumption used in the BML model, which was initiated by Bray and Moss (1977) and extended in a number of papers afterwards, to derive a simple closure for the chemical source term. In case of an infinitely thin flame, the probability density function $P(\mathcal{Y},\mathbf{x},t)$ for finding a value $\mathcal{Y}$ at position $\mathbf{x}$ and time t is a double-delta function

$$P(\mathcal{Y},\mathbf{x},t) = \beta\delta(1-\mathcal{Y}) + (1-\beta)\delta(\mathcal{Y}), \tag{13.3}$$

which has a single unknown parameter β. This β can be related to the averages $\tilde{\mathcal{Y}}$ and $\overline{\rho}$ by using

$$\overline{\rho\mathcal{Y}} = \overline{\rho}\tilde{\mathcal{Y}} = \int \rho\mathcal{Y}P(\mathcal{Y})d\mathcal{Y} = \beta\rho_{\mathrm{b}} \tag{13.4}$$

or $\beta = \overline{\rho}\tilde{\mathcal{Y}}/\rho_{\mathrm{b}}$. Furthermore, for the average density we have

$$\overline{\rho} = \int \rho P(\mathcal{Y})d\mathcal{Y} = (1-\beta)\rho_{\mathrm{u}} + \beta\rho_{\mathrm{b}} = \rho_{\mathrm{u}} - \tau\overline{\rho}\tilde{\mathcal{Y}} \tag{13.5}$$

leading to $\overline{\rho} = \rho_{\mathrm{u}}/(1+\tau\tilde{\mathcal{Y}}) = \rho_{\mathrm{b}}(1+\tau)/(1+\tau\tilde{\mathcal{Y}})$ which gives a unique expression for β in terms of $\tilde{\mathcal{Y}}$:

$$\beta = \frac{(1+\tau)\tilde{\mathcal{Y}}}{1+\tau\tilde{\mathcal{Y}}}. \tag{13.6}$$

This means that the PDF is completely determined by $\tilde{\mathcal{Y}}$ and the heat release coefficient $\tau = (T_b - T_u)/T_u = (\rho_u - \rho_b)/\rho_b$, which is fixed for given combustion reaction. For instance, the correlation $\widetilde{\mathcal{Y}''^2}$ is also simply related to $\tilde{\mathcal{Y}}$, since $\overline{\rho}\widetilde{\mathcal{Y}''^2} = \overline{\rho(\mathcal{Y} - \widetilde{\mathcal{Y}})^2} = \overline{\rho}(\widetilde{\mathcal{Y}^2} - (\tilde{\mathcal{Y}})^2) = \overline{\rho}\tilde{\mathcal{Y}}(1 - \tilde{\mathcal{Y}})$. Correlations between the progress variable and the velocity can be expressed in terms of $\tilde{\mathcal{Y}}$ and the conditional velocities

$$\langle \mathbf{v} \rangle_b = \frac{\int \rho \mathbf{v} \mathcal{Y} \, \mathrm{d}\mathcal{Y}}{\int \rho \mathcal{Y} \, \mathrm{d}\mathcal{Y}} \tag{13.7}$$

and

$$\langle \mathbf{v} \rangle_u = \frac{\int \rho \mathbf{v}(1 - \mathcal{Y}) \, \mathrm{d}\mathcal{Y}}{\int \rho (1 - \mathcal{Y}) \, \mathrm{d}\mathcal{Y}}, \tag{13.8}$$

being the average velocities in the burnt and unburnt mixture parts. With these conditional velocities we may derive an equation for the turbulent diffusion velocity, using

$$\overline{\rho \mathbf{v}} = \langle \mathbf{v} \rangle_b \overline{\rho \mathcal{Y}} + \langle \mathbf{v} \rangle_u \overline{\rho(1 - \mathcal{Y})} \tag{13.9}$$

which gives

$$\langle \mathbf{v} \rangle_b - \tilde{\mathbf{v}} = (1 - \tilde{\mathcal{Y}})(\langle \mathbf{v} \rangle_b - \langle \mathbf{v} \rangle_u) \tag{13.10}$$

or

$$\langle \mathbf{v} \rangle_b \tilde{\mathcal{Y}} - \tilde{\mathbf{v}} \tilde{\mathcal{Y}} = \tilde{\mathcal{Y}}(1 - \tilde{\mathcal{Y}})(\langle \mathbf{v} \rangle_b - \langle \mathbf{v} \rangle_u). \tag{13.11}$$

This effectively leads to the following expression for the Reynolds flux correlation term

$$\widetilde{\mathbf{v}'' \mathcal{Y}''} = \langle \mathbf{v} \rangle_b \tilde{\mathcal{Y}} - \tilde{\mathbf{v}} \tilde{\mathcal{Y}} = \tilde{\mathcal{Y}}(1 - \tilde{\mathcal{Y}})(\langle \mathbf{v} \rangle_b - \langle \mathbf{v} \rangle_u). \tag{13.12}$$

A relation between diffusive mixing and reaction in case of the BML model can be found as follows. Starting from the conservation equation (13.2) for the progress variable $\mathcal{Y}$, one can easily derive a similar equation for $\mathcal{Y}^n$ after multiplication with $n\mathcal{Y}^{n-1}$:

$$\frac{\partial(\rho \mathcal{Y}^n)}{\partial t} + \nabla \cdot (\rho \mathbf{v} \mathcal{Y}^n) - \nabla \cdot (\rho D \nabla \mathcal{Y}^n) + \tfrac{1}{2} n(n-1) \mathcal{Y}^{n-2} \rho \chi - n \mathcal{Y}^{n-1} \dot{\rho}_{\mathcal{Y}} = 0, \tag{13.13}$$

where $\chi = 2D \nabla \mathcal{Y} \cdot \nabla \mathcal{Y}$ is the scalar dissipation rate, describing mixing processes. For $Z_n = \mathcal{Y} - \mathcal{Y}^n$ we then have:

$$\frac{\partial(\rho Z_n)}{\partial t} + \nabla \cdot (\rho \mathbf{v} Z_n) - \nabla \cdot (\rho D \nabla Z_n) = \tfrac{1}{2} n(n-1) \mathcal{Y}^{n-2} \rho \chi - (n \mathcal{Y}^{n-1} - 1) \dot{\rho}_{\mathcal{Y}}. \tag{13.14}$$

The flame front is considered to be infinitely thin, so $\mathcal{Y}$ can be eighter 0 (unburnt gases) or 1 (burnt gases). This means that $\mathcal{Y}^n = \mathcal{Y}$, or $Z_n = 0$ which gives for the averaged source term using $n = 2$ in equation (13.14):

$$\overline{\dot{\rho}}_{\mathcal{Y}} = \frac{\overline{(2\mathcal{Y} - 1)\dot{\rho}_{\mathcal{Y}}}}{(2\mathcal{Y}_m - 1)} = \frac{\overline{\rho \chi}}{(2\mathcal{Y}_m - 1)} \tag{13.15}$$

with $\mathcal{Y}_m$ being the average value for $\mathcal{Y}$ in the reaction layer. Equation (13.15) indicates the close relation between chemistry and diffusive mixing processes in the laminar flamelet regime and is used in the BML model to derive a closure for $\overline{\dot{\rho}}_{\mathcal{Y}}$. Note that the scalar dissipation rate expresses the decay

of fluctuations in the progress variable by turbulence, or $\overline{\rho\chi} = \overline{\rho\mathcal{Y}''^2}/\tau_t$, where the turbulence time τ_t has been introduced. Using this in equation (13.15) gives for the source term:

$$\overline{\dot{\rho}}_{\mathcal{Y}} = \frac{\overline{\rho\mathcal{Y}''^2}}{\tau_t(2\mathcal{Y}_m - 1)} = \frac{\overline{\rho}\tilde{\mathcal{Y}}(1-\tilde{\mathcal{Y}})}{\tau_t(2\mathcal{Y}_m - 1)}. \tag{13.16}$$

The turbulence time τ_t is mostly equated to k/ϵ. Expression (13.16) for the source term is equivalent with the result for the Eddy-Break-Up (EBU) model, which is used frequently in the modelling of turbulent flames. A similar expression has also been derived by Bray, Moss and Libby. Note that this expression (13.16) gives us effectively a closure model for the flame surface density $\bar{\Sigma}$:

$$\bar{\Sigma} = \frac{\epsilon}{k}\frac{\tilde{\mathcal{Y}}(1-\tilde{\mathcal{Y}})}{s_L(2\mathcal{Y}_m - 1)}. \tag{13.17}$$

3 Coherent Flame Model (CFM)

In the CFM model, first introduced by Marble and Broadwell (1977) and extended later by for instance Pope (1988) and Candel and Poinsot (1990), a transport equation is used for the flame surface density to close the chemical source term $\overline{\dot{\rho}}_{\mathcal{Y}}$ in a more accurate way. The following exact equation can be derived for $\bar{\Sigma} = -\overline{\mathbf{n}\cdot\nabla\mathcal{Y}}$:

$$\frac{\partial}{\partial t}\overline{\Sigma} + \nabla\cdot\overline{(\mathbf{v}_f\Sigma)} = \langle K_A\rangle_f\overline{\Sigma}, \tag{13.18}$$

which states that the flame surface changes due to stretching of the flame surface

$$K_A = \frac{1}{A}\frac{dA}{dt} = \nabla\cdot\mathbf{v}_f - \mathbf{nn}:\nabla\mathbf{v}_f, \tag{13.19}$$

when traveling along with the flame which has a velocity equal to $\mathbf{v}_f = \mathbf{v} + s_L\mathbf{n}$. Here, K_A is the flame stretch rate, i.e. the relative rate of change of flame surface. Equation (13.18) is not yet closed: the average flame stretch due to turbulence must be modelled. A lot of research has been done to formulate accurate closure models for this interaction. Part of these studies use Direct Numerical Simulations to formulate quantitative models. A review of existing closures has been given recently by Duclos et al.(1993). The following description seems to be the most accurate closure available at the moment:

$$\begin{aligned}
&\frac{\partial}{\partial t}(\overline{\rho}\tilde{\mathcal{Y}}) + \nabla\cdot(\overline{\rho}\tilde{\mathbf{v}}\tilde{\mathcal{Y}}) + \nabla\cdot(\overline{\rho}\,\widetilde{\mathbf{v}''\mathcal{Y}''}) = \langle m\rangle_f\bar{\Sigma},\\
&\frac{\partial}{\partial t}(\overline{\rho}\bar{\Sigma}) + \nabla\cdot(\overline{\rho}\tilde{\mathbf{v}}\bar{\Sigma}) + \nabla\cdot(\overline{\rho}\langle\mathbf{v}''\rangle_f\bar{\Sigma}) = C_s\Gamma\,\frac{\varepsilon}{k}\,\overline{\rho}\bar{\Sigma} + m\nabla^2\overline{\mathcal{Y}} + C_c\overline{\rho}\frac{(1-2\tilde{\mathcal{Y}})}{\tilde{\mathcal{Y}}(1-\tilde{\mathcal{Y}})}(\bar{\Sigma})^2
\end{aligned} \tag{13.20}$$

where the three terms in the right-hand side of the equation for $\bar{\Sigma}$ denote the stretching of the flame due to straining effects of the turbulent structures, flame propagation and the change of flame surface due to curved propagating flames. The parameters $C_{s,c}$ are constants.

This averaged transport equation for $\bar{\Sigma}$ is derived as follows from equation (13.18). The flame velocity $\mathbf{v}_f$ in equation (13.18) can be separated in a fluid velocity $\mathbf{v}$ and a burning velocity $s_L\mathbf{n}$. The term, proportional to $\mathbf{v}$ then gives a convective term $\nabla\cdot(\overline{\rho}\tilde{\mathbf{v}}\bar{\Sigma})$ and a turbulent diffusion term $\nabla\cdot(\overline{\rho}\langle\mathbf{v}''\rangle_f\bar{\Sigma})$ in the averaged transport equation for $\bar{\Sigma}$, $\langle\mathbf{v}''\rangle_f$ being the velocity fluctuation on the flame surface. The part with the burning velocity $s_L\mathbf{n}$ leads to the propagation term. Furthermore, the flame stretch K_A can be split in a strain part S_A and a flame curvature part s_L/R. The fluctuating

strain contribution is governed by the time scale k/ϵ of the largest eddies, so that $\overline{\rho S_A'' \Sigma} \propto \frac{\epsilon}{k}\overline{\rho}\tilde{\Sigma}$. The function $\Gamma = \Gamma(\frac{u'}{s_L}, \frac{l}{\delta_f})$, refered to as the ITNFS model, has been introduced by Meneveau and Poinsot (1991) as an additional efficiency function to include the influence of the smaller structures as well. Here, u' is the velocity fluctuation, l the integral turbulence length scale and δ_f the laminar flame thickness. For the curvature part we may write

$$\overline{\rho s_L \Sigma / R} \propto \overline{\rho}\frac{(1-2\tilde{\mathcal{Y}})}{\tilde{\mathcal{Y}}(1-\tilde{\mathcal{Y}})}(\tilde{\Sigma})^2. \tag{13.21}$$

The curvature term is positive near the unburnt flame boundary, where the curved flame structures are predominantly convex towards the fresh mixture, creating flame surface. This term is negative near the burnt flame boundary, destructing flame surface.

The transport equation (13.18) for $\tilde{\Sigma}$ has a source term equal to $\langle K_A \rangle_f \overline{\Sigma}$. This means that first-order stretch effects arising from the finite flame thickness are included in the correlation between reaction and mixing, when the CFM model is used. So, instead of (13.15) for the BML model we now have:

$$\overline{\rho\chi} = (2\mathcal{Y}_m - 1)\overline{\rho}_{\mathcal{Y}}\,(1 + \mathcal{O}(\overline{Ka})) \tag{13.22}$$

with $\overline{Ka} = \langle K_A \rangle_f \delta_f / s_L$ the average Karlovitz number, being the dimensionless stretch rate. The absense of stretch effects in the BML model is related to the fact that the flame front thickness is assumed to be zero, so that $\overline{Ka} = \langle K_A \rangle_f \delta_f / s_L = 0$. Equation (13.22) describes the influence of turbulent fluctuations in the preheating zone on the relation between mixing and chemistry in the flame. This makes the CFM models more accurate for representing the averaged chemical source term. Mantel and Borghi (1991) use a transport equation for the scalar dissipation rate $\overline{\chi}$ instead of an equation for $\tilde{\Sigma}$. It can be shown that the scalar dissipation rate $\overline{\chi}$ is also proportional to $\tilde{\Sigma}$.

G-equation Model

In the G-equation model, derived by Peters in a number of papers and combined in his book [10], the strong correlation between mixing and reaction in the laminar flamelets is taken into account by replacing the combined terms $\nabla \cdot (\rho D \nabla \mathcal{Y}) + \dot{\rho}_{\mathcal{Y}}$ in equation (13.1) by the propagation term $-m\mathbf{n} \cdot \nabla \mathcal{Y}$, with m the laminar mass burning rate and $\mathbf{n} = -\nabla \mathcal{Y} / |\nabla \mathcal{Y}|$ the unit vector on the laminar flame front pointing towards the unburnt mixture. The arising equation is the kinematic equation for a reference plane in the flame front

$$\frac{\partial(\rho G)}{\partial t} + \nabla \cdot (\rho \mathbf{v} G) = -m\mathbf{n} \cdot \nabla G \tag{13.23}$$

and is refered to as the G-equation. The field $G(\mathbf{x}, t)$ is defined in such a way that it is equal to $\mathcal{Y}_0$ at $G = G_0$, representing an iso-plane of the instantaneous progress variable $\mathcal{Y}$ and is extended in some way for $G \neq G_0$ (normally, Peters uses $|\nabla G| = 1$, defining G as a distance function from G_0). An equation for the averaged G-field can be derived, leading to

$$\frac{\partial(\overline{\rho}\tilde{G})}{\partial t} + \nabla \cdot (\overline{\rho}\tilde{\mathbf{v}}\tilde{G}) = m\bar{\sigma} = \overline{\rho} s_T |\nabla \tilde{G}| \tag{13.24}$$

which, for $\tilde{G} = G_0 = \tilde{\mathcal{Y}}_0$, is the kinematic equation for a reference plane in the averaged turbulent flame front. Beyond $\tilde{G} = G_0$, the $\tilde{G}$-field is again extended as a distance function by solving $|\nabla \tilde{G}| = 1$ together with equation (13.24). The kinematic equation states that the flame front moves with turbulent burning velocity s_T with respect to the average turbulent gas velocity. The so-called

flame surface area ratio $\bar{\sigma} = \overline{|\nabla G|}$ is dimensionless and is related to the flame surface density $\bar{\Sigma}$. It is a parameter describing the local wrinking of the instantaneous flame, compared to the average tubulent flame front. A major difference with the BML and CFM models is that only $\tilde{G} = G_0$ has a physical meaning, so that the G-equation only predicts the position of the turbulent flame. The average progress variable $\tilde{\mathcal{Y}}$ in the BML/CFM models, on the other hand, resolves the structure of the turbulent flame. Furthermore, since the G-equation is a kinematic equation, a diffusion term does not appear in equation (13.24). This means that no model is needed for the closure of the covariance $\widetilde{\mathbf{v}''G}$ as in the case of the BML/CFM model, meaning that gradient and counter-gradient diffusive flux modelling is not necessary. However, to predict the thickness of the turbulent flame brush l_F, an additional kinematic equation has to be solved for $l_\mathrm{F}^2 = \widetilde{G''^2}$:

$$\overline{\rho}\frac{\partial \widetilde{G''^2}}{\partial t} + \overline{\rho}\tilde{\mathbf{v}}\cdot\boldsymbol{\nabla}\widetilde{G''^2} = \nabla_\parallel\cdot(\overline{\rho}D_\mathrm{t}\nabla_\parallel\widetilde{G''^2}) + 2\overline{\rho}D_\mathrm{t}(\nabla\tilde{G})^2 - c_\mathrm{s}\overline{\rho}\frac{\epsilon}{k}\widetilde{G''^2}. \tag{13.25}$$

Again, this equation only holds on the flame front interface $\tilde{G} = G_0$. The first term in the right-hand side is a diffusive term along the flame and can be considered as an effective curvature term. The second and third term in the right-hand side are turbulent production and dissipation terms. A transport equation for the flame surface area ratio $\bar{\sigma}$ completes the G-equation model, to predict the turbulent burning velocity. The derivation of the transport equation for $\bar{\sigma}$ is similar to that for $\bar{\Sigma}$ and finally reads:

$$\overline{\rho}\frac{\partial\bar{\sigma}}{\partial t} + \overline{\rho}\tilde{\mathbf{v}}\cdot\boldsymbol{\nabla}\bar{\sigma} = \nabla_\parallel\cdot(\overline{\rho}D_\mathrm{t}\nabla_\parallel\bar{\sigma}) + c_0\overline{\rho}\frac{(-\widetilde{\mathbf{v}''\mathbf{v}''}):\nabla\tilde{\mathbf{v}}}{k}\bar{\sigma} + c_1\overline{\rho}\frac{D_\mathrm{t}(\nabla\tilde{G})^2}{\widetilde{G''^2}}\bar{\sigma} - c_2\overline{\rho}\frac{s_\mathrm{L}}{\sqrt{\widetilde{G''^2}}}\bar{\sigma}^2. \tag{13.26}$$

This kinematic equation has a curvature term (first term in rhs), a production of flame surface due to mean velocity gradients (second term in rhs), turbulent production (third term) and kinematic restoration due to flame motion (fourth term). The G-equation model is an elegant and efficient combustion model which can be used to model turbulent flames in different situations, since it is not needed to resolve the complete flame structure.

4 Gradient and Counter-Gradient Diffusion

In turbulent flows, one usually models the covariance $\widetilde{\mathbf{v}''\mathcal{Y}''}$ using a gradient turbulent diffusion flux assumption: $\widetilde{\mathbf{v}''\mathcal{Y}''} = -\nu_\mathrm{t}\nabla\tilde{\mathcal{Y}}$, with $\nu_\mathrm{t} = u'L = k^2/\varepsilon$ the turbulent viscosity. However, experiments have shown that socalled counter-gradient diffusion plays an important role in premixed turbulent combustion. The appearance of counter-gradient diffusion is related to the phenomenon that burnt pockets of gas in the unburnt region move preferentially towards the burnt gas zone in the average pressure gradient $\nabla\overline{p}$ over the flame, because of their lower density compared to unburnt gas pockets. This phenomenon has been studied first by Libby and Bray (1980a) and Libby and Bray (1980b) for a planar turbulent flame and by many others after them. To describe the influence of the pressure gradient on the correlation $\widetilde{\mathbf{v}''\mathcal{Y}''}$, a second-order turbulence closure relation has to be used for the transport equation of the covariance $\widetilde{\mathbf{v}''\mathcal{Y}''}$. It appears that counter-gradient diffusion is important in the center part of the flame brush, but that the leading and trailing edge of the flame are essentially dominated by gradient diffusion[1]. Furthermore, the second-order closure equation for $\widetilde{\mathbf{v}''\mathcal{Y}''}$ does not

[1]This means that the turbulent burning velocity s_T, which is governed by the combustion behavior near the leading edge of the flame is **not** influenced by counter-gradient diffusion.

lead to a diffusive flux formulation as in case of gradient diffusion, which might lead to convergence problems when applied in numerical models. For these reasons, it would be nice if there would be a simple formulation, which combines a gradient diffusive-flux formulation (for the behavior near the flame edges) with a simple expression for the counter-gradient part (being large in the center of the flame brush). Such a simple model has been formulated on the basis of heuristic arguments by Veynante et al. (1997):

$$\widetilde{\mathbf{v}''\mathcal{Y}''} = -\tilde{\mathcal{Y}}(1-\tilde{\mathcal{Y}})\tau s_{\mathrm{L}}\tilde{\mathbf{n}} - \alpha\ \nu_{\mathrm{t}}\nabla\tilde{\mathcal{Y}} \tag{13.27}$$

where α is a coefficient derived from DNS computations. For small velocity fluctuations u', expansion dominates, leading to counter-gradient diffusion for low Reynolds numbers, while the second term describes gradient diffusion for large u'.

However, it appears that the counter-gradient diffusion part in (13.27), proportional to $\tilde{\mathcal{Y}}(1-\tilde{\mathcal{Y}})$, does not vanish fast enough near the unburnt flame edge $\tilde{\mathcal{Y}} \to 0$ and therefore has an unwanted unphysical effect on the turbulent burning velocity. An alternative model can be derived from the second-order closure of the covariance equation of $\widetilde{\mathbf{v}''\mathcal{Y}''}$, which has a more physical basis. Starting point will be the description of counter-gradient diffusion using the BML model. Following (Libby and Bray, 1980) the following transport equation for the covariance can be derived for a flat turbulent flame:

$$\frac{d}{dx}(\tilde{u}\overline{\rho u''\mathcal{Y}''} + \overline{\rho u''^2\mathcal{Y}''}) + \overline{\rho u''\mathcal{Y}''}\frac{d\tilde{u}}{dx} + \overline{\rho u''^2}\frac{d\tilde{\mathcal{Y}}}{dx} + \overline{\mathcal{Y}''}\frac{d\overline{p}}{dx} + \overline{\mathcal{Y}}\frac{d\overline{p'}}{dx} = \langle mu''\rangle_{\mathrm{f}}\bar{\Sigma} - \overline{\chi'} \tag{13.28}$$

where the dissipation term $\overline{\chi'}$ arises from the viscous term in the momentum equation. Using the profile of 1D flamelets it appears that $\nabla u = (\langle u\rangle_{\mathrm{b}} - \langle u\rangle_{\mathrm{u}})\nabla\mathcal{Y}$ and $\langle u''\rangle_{\mathrm{f}} = (\langle u\rangle_{\mathrm{b}} - \langle u\rangle_{\mathrm{u}})\langle\mathcal{Y}''\rangle_{\mathrm{f}}$, i.e. the gradients and fluctuations in the velocity are equal to the gradients and fluctuations in the local progress variable, multiplied with the jump in conditional velocity over the front. Using these $u-\mathcal{Y}$ correlations gives

$$\langle mu''\rangle_{\mathrm{f}}\Sigma - \overline{\chi'} = (\langle u\rangle_{\mathrm{b}} - \langle u\rangle_{\mathrm{u}})\langle m(\mathcal{Y} - \tilde{\mathcal{Y}} - k_1)\rangle_{\mathrm{f}}\Sigma, \tag{13.29}$$

after introducing the (Prandtl) number $k_1 = \mu c_p/\lambda$, for the right-hand side consumption terms in the covariance equation (13.28). The covariance equation is now rewritten in terms of the scaled variable

$$F = \frac{\overline{\rho u''\mathcal{Y}''}}{\rho_u u_{\mathrm{u}}} = \frac{u''\tilde{\mathcal{Y}}''}{u_{\mathrm{u}}(1+\tau\tilde{\mathcal{Y}})}. \tag{13.30}$$

Using the following additional relations for a 1D turbulent flame

$$\begin{aligned}
\overline{\rho} &= \rho_{\mathrm{u}}/(1+\tau\tilde{\mathcal{Y}}) \\
\tilde{u} &= u_{\mathrm{u}}(1+\tau\tilde{\mathcal{Y}}) \\
\langle m\rangle_{\mathrm{f}}\Sigma = \rho_{\mathrm{u}}u_{\mathrm{u}}(1+F')\frac{d\tilde{\mathcal{Y}}}{dx}\overline{\mathcal{Y}''} &= \overline{\mathcal{Y}} - \tilde{\mathcal{Y}} = \tau\frac{\tilde{\mathcal{Y}}(1-\tilde{\mathcal{Y}})}{1+\tau\tilde{\mathcal{Y}}} \\
\frac{d(\overline{p+p'})}{dx} = -\frac{d}{dx}(\overline{\rho}\tilde{u}^2 + \overline{\rho u'^2}) &= -\rho_{\mathrm{u}}u_{\mathrm{u}}^2(\tau+I')\frac{d\tilde{\mathcal{Y}}}{dx}
\end{aligned} \tag{13.31}$$

it then appears that all terms are proportional to the factor $d\tilde{\mathcal{Y}}/dx$ which drops out. The new equation thus only depends on $\tilde{\mathcal{Y}}$ as independent variable instead of x (phase space):

$$((1+\tau\tilde{\mathcal{Y}})F)' + K' + \tau F + I = \frac{\tau\tilde{\mathcal{Y}}(1-\tilde{\mathcal{Y}})}{(1+\tau\tilde{\mathcal{Y}})}(\tau+I') - (1+F')F\frac{(1+\tau\tilde{\mathcal{Y}})}{(1-\tilde{\mathcal{Y}})}\left(1 - \frac{\phi_n - k_1}{\tilde{\mathcal{Y}}}\right) \tag{13.32}$$

where $'$ denotes differentiation with respect to $\tilde{\mathcal{Y}}$, $I = \overline{\rho u''^2}/\rho_\mathrm{u} u_\mathrm{u}^2$ is the scaled kinetic energy of turbulent fluctuations perpendicular to the flame and $K = \overline{\rho u''^2 \mathcal{Y}''}/\rho_\mathrm{u} u_\mathrm{u}^2$. We also introduced the moment $\phi_n = \langle \mathcal{Y} \rangle_\mathrm{f}$, a number which is close to 1, because reaction takes place near $\mathcal{Y} = 1$. Libby and Bray report that this equation shows gradient diffusion transport, if the pressure-gradient term (first term in the right-hand side) is discarded, where K' and I are production terms, while the chemical source and dissipation term (proportional to $(1 + F')F$) are consumption terms. Counter-gradient diffusion is found by the authors if the pressure-gradient term is included.

It is possible to derive a simple decomposition in gradient and counter-gradient parts. Insert $F = F_\mathrm{g} + F_\mathrm{c}$ (with F_g and F_c denoting the gradient and counter-gradient parts) in the above equation, giving, after separating the corresponding contributions and after uncoupling the equations assuming that $(1 + F_\mathrm{g}' + F_\mathrm{c}')F_\mathrm{c} = (1 + F_\mathrm{c}')F_\mathrm{c}$ and $(1 + F_\mathrm{g}' + F_\mathrm{c}')F_\mathrm{g} = (1 + F_\mathrm{g}')F_\mathrm{g}$ (because turbulent fluctuations are normally smaller than $\rho_\mathrm{u} u_\mathrm{u}$)

$$((1 + \tau\tilde{\mathcal{Y}})F_\mathrm{g})' + K' + \tau F_g + I = -(1 + F_\mathrm{g}')F_\mathrm{g}\frac{(1 + \tau\tilde{\mathcal{Y}})}{(1 - \tilde{\mathcal{Y}})}\left(1 - \frac{\phi_n - k_1}{\tilde{\mathcal{Y}}}\right), \tag{13.33}$$

and

$$((1 + \tau\tilde{\mathcal{Y}})F_\mathrm{c})' + \tau F_\mathrm{c} = \frac{\tau\tilde{\mathcal{Y}}(1 - \tilde{\mathcal{Y}})}{(1 + \tau\tilde{\mathcal{Y}})}(\tau + I') - (1 + F_\mathrm{c}')F_\mathrm{c}\frac{(1 + \tau\tilde{\mathcal{Y}})}{(1 - \tilde{\mathcal{Y}})}\left(1 - \frac{\phi_n - k_1}{\tilde{\mathcal{Y}}}\right). \tag{13.34}$$

We now assume that $F_\mathrm{g} = -\nu_\mathrm{t}\frac{d\tilde{\mathcal{Y}}}{dx}$ and solve (13.34) to find an expression for F_c. To be able to solve this equation analytically, a few further assumptions have to be introduced. First of all $(1 + F_\mathrm{c}')$ is replaced by 1 for relatively small perturbations and $(\tau + I')$ is substituted by τ neglecting the influence of pressure fluctuations. Finally, we assume that $\phi_n = k_1$ in (13.34) based on the observation of Bray and Libby that $\phi_n = 0.833$ and $k_1 = 0.85$. Using all these approximations yields

$$F_\mathrm{c}' + \frac{2\tau}{(1 + \tau\tilde{\mathcal{Y}})}F_\mathrm{c} = \frac{\tau^2\tilde{\mathcal{Y}}(1 - \tilde{\mathcal{Y}})}{(1 + \tau\tilde{\mathcal{Y}})^2} - F_\mathrm{c}\frac{1}{(1 - \tilde{\mathcal{Y}})}, \tag{13.35}$$

where the first term on the right-hand side produces the counter-gradient diffusion flux by the average pressure gradient and the second term denotes its dissipation near the burnt flame boundary. This equation, combined with the boundary condition $F_\mathrm{c}(0) = 0$ can be solved exactly giving

$$F_\mathrm{c}(\tilde{\mathcal{Y}}) = \frac{\tau^2}{2}\tilde{\mathcal{Y}}^2(1 - \tilde{\mathcal{Y}})\frac{(1 + \frac{2}{3}\tau\tilde{\mathcal{Y}})}{(1 + \tau\tilde{\mathcal{Y}})^2}. \tag{13.36}$$

No unknown parameters enters F_c, the only parameter being the expansion factor τ. This behavior of F_c as a function of $\tilde{\mathcal{Y}}$ is presented in figure 13.1. Comparing figure 13.1 with figure 4b of Libby and Bray (1981), which shows $F = F_\mathrm{c} + F_\mathrm{g}$, indicates that the behavior is similar but that the maximum in figure 6 is larger. This might be partly related to the fact that (the negative) F_g should be added to figure 13.1 to make a direct comparison possible. Note that F_c has a maximum near $\tilde{\mathcal{Y}} = 0.5$ and that it increases almost linearly with τ as the results of Libby and Bray.

Combining the diffusive formulation of F_g with (13.36) for F_c gives, when generalized to a flame propagating in general direction $\tilde{\mathbf{n}}$ yields:

$$\overline{\rho}\mathbf{v}''\tilde{\mathcal{Y}}'' = -\frac{\tau^2\rho_\mathrm{u} s_\mathrm{T}}{2}\tilde{\mathcal{Y}}^2(1 - \tilde{\mathcal{Y}})\frac{(1 + \frac{2}{3}\tau\tilde{\mathcal{Y}})}{(1 + \tau\tilde{\mathcal{Y}})^2}\tilde{\mathbf{n}} - \mu_\mathrm{t}\nabla\tilde{\mathcal{Y}} = -m_\mathrm{T}F_\mathrm{c}(\tilde{\mathcal{Y}})\tilde{\mathbf{n}} - \mu_\mathrm{t}\nabla\tilde{\mathcal{Y}} \tag{13.37}$$

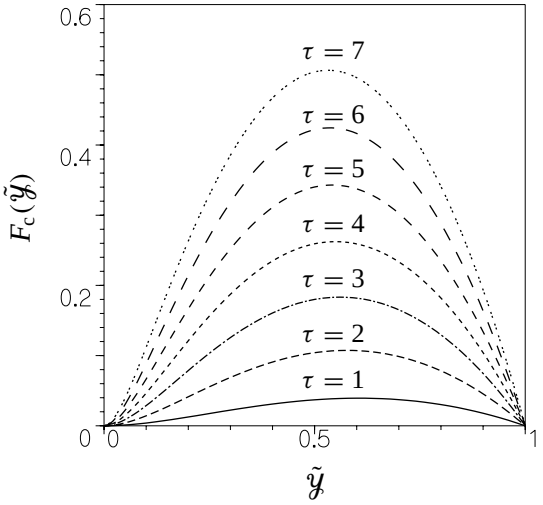

Figure 13.1: The behavior of the counter-gradient diffusion flux F_c as a function of $\tilde{y}$ using the simple model of equation (13.34).

where the minus sign is related to the orientation of the unit vector $\tilde{\mathbf{n}}$. Compared to the expression of Veynante, it appears that the most important differences in the counter-gradient diffusion part are the proportionallity to $(\tilde{y})^2$ instead of $\tilde{y}$ near the unburnt boundary and that the turbulent burning velocity s_T appears instead of the laminar burning velocity s_L. A similar simple decomposition of the flux in a gradient and counter-gradient part can be derived for the $\bar{\Sigma}$-equation:

$$\langle \mathbf{v} \rangle_f'' \overline{\Sigma} = -m_T G_c(\tilde{y}) \bar{\Sigma} \tilde{\mathbf{n}} - \mu_t \nabla \bar{\Sigma}. \tag{13.38}$$

with

$$G_c(\tilde{y}) = \frac{\tau^2}{2} \tilde{y}(1-\tilde{y}) \frac{(1+\frac{2}{3}\tau\tilde{y})}{(1+\tau\tilde{y})^2}. \tag{13.39}$$

References

[1] Bray, K.N.C. and Moss, J.B., *Acta Astronautica* 4, 291–320 (1977).

[2] Candel, S.M., and Poinsot, T.J., *Combust. Sci. and Techn.* 70: 1–15 (1990).

[3] Duclos, J.M., Veynante, D. and Poinsot, T., *Combust. Flame* 95:101–117 (1993).

[4] Libby, P.A. and Bray, K.N.C., *AIAA J.* AIAA-80-013 (1980).

[5] Libby, P.A. and Bray, K.N.C., *Combust. Flame* 39:33–41 (1981).

[6] Mantel, T. and Borghi, R., *13th ICDERS,* p. 167 (1991).

[7] Pope, S.B., *Int. J. Engng. Sci.* 265, 445–469, (1988).

[8] Marble, F. and Broadwell, J., *Technical report TRW-9-PU Project Squid,* Perdue University West Lafayette (1977).

[9] Meneveau, C., and Poinsot, T., *Combust. Flame* 86:311–1332 (1991).

[10] Peters, N., *Turbulent Combustion* Cambridge University Press, (2000).

[11] Veynante, D., Trouve, A., Bray, K. and Mantel, T., *J. Fluid Mech.* 332, 263–293, (1997).

Part 5

Laser Diagnostics

Chapter 14

Molecular Physics in a Nutshell

J. J. ter Meulen

1 Bohr's quantum model

According to the quantum model of Bohr for the hydrogen atom the electron is considered as a point charge $-e$ moving around the nucleus (charge $+e$) in circular orbits (see figure 14.1). Only orbitals with specific radii r are stable. This follows from the quantization of the orbital angular momentum $L = mvr$ with m and v the mass and velocity of the electron, respectively:

$$L = n\hbar, \quad \text{with } n = 1, 2, 3, \ldots \tag{14.1}$$

where $\hbar = h/2\pi$, with h the constant of Planck, equal to $6.626 \cdot 10^{-34}$ Js. Each orbital corresponds to a specific potential energy E. The electron can change its potential energy by jumping from one orbital to another. If it jumps from an orbital with an energy E_i to an orbital with a lower energy E_f the difference in energy is released in the form of radiation with frequency ν according to

$$E_\mathrm{i} - E_\mathrm{f} = h\nu \tag{14.2}$$

In the other way around, if the electron is in an orbital with energy E_i it can make a transition to an orbital with a higher energy E_f by absorbing radiation with frequency ν given by equation (14.2).

The potential energy of the electron is:

$$U = k_e \frac{e^2}{r} \tag{14.3}$$

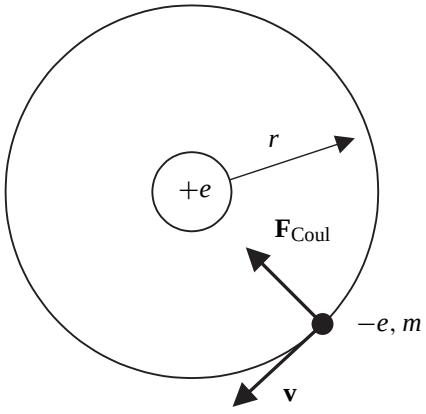

Figure 14.1: Bohr's model of the hydrogen atom.

and the total energy is given by:

$$E = \tfrac{1}{2}mv^2 - k_e\frac{e^2}{r} \tag{14.4}$$

It follows from the force balance that the Coulomb force is equal to the mass times the centripetal force:

$$\frac{k_e e^2}{r^2} = \frac{mv^2}{r} \tag{14.5}$$

Consequently, the energy is equal to:

$$E = -\frac{k_e e^2}{2r} \tag{14.6}$$

From equations (14.1) and (14.5) it follows that:

$$r = \frac{n^2\hbar^2}{mk_e e^2} \equiv r_n. \tag{14.7}$$

The smallest radius r_1 is called the Bohr radius a_0 and is equal to 0.0529 nm. When expressed in the Bohr radius, r_n is given by:

$$r_n = n^2 a_0. \tag{14.8}$$

The energy E_n of the n^{th} orbital is:

$$E_n = -\frac{k_e e^2}{2a_0 n^2} = -\frac{13.6}{n^2} \tag{14.9}$$

The energy levels are schematically depicted in an energy level diagram, as shown in figure 14.2, where also possible transitions between them can be indicated. The series of transitions from excited

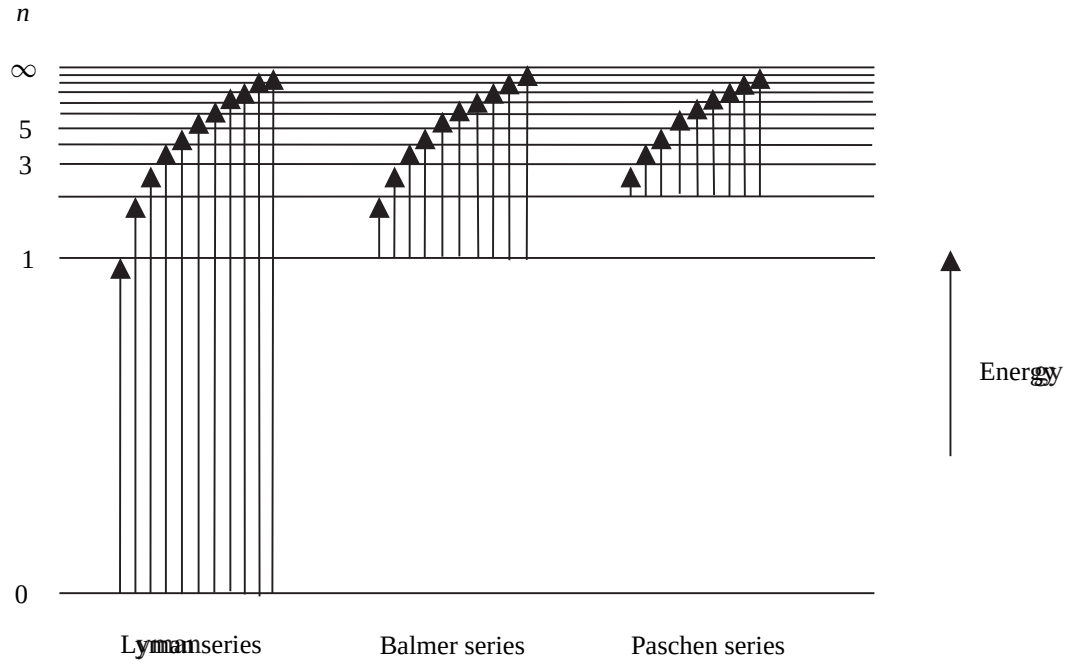

Figure 14.2: Energy level diagram of the hydrogen atom including the series of possible transitions between the energy levels.

energy states to the lowest state, the 'ground state', of the hydrogen atom is called the Lyman series, with frequencies of the emitted radiation:

$$\nu = \frac{k_e e^2}{2a_0 h}\left(1 - \frac{1}{n^2}\right) \tag{14.10}$$

The integer number n is called the principal quantum number.

2 Molecular energies

In an atom the energy levels represent different allowed electronic states, between which transitions are possible by absorption or emission of radiation. A molecule also can absorb or emit energy as a result of transitions between different electronic states. However, there are two other principle ways in which a molecule can change its energy, and which cannot occur in atoms. This is related to the two possible motions of the nuclei in the molecule: rotation and vibration, as illustrated in figure 14.3. A molecule can absorb (or emit) a quantum of energy and increase (or decrease) its vibrational energy. In the same way it can change its rotational energy. The quanta associated with these different types of energy changes—electronic, vibrational, rotational—are of very different energy. In the Born-Oppenheimer approximation the electronic and nuclear motions are treated independently. Since the nuclei are so much heavier than the electrons, and consequently move much slower, the electrons easily can follow their motion. The electron distribution can be considered as a smeared charge cloud that adapts its shape to the nuclear positions. As a result the electronic energy to a good approximation only depends on the nuclear coordinates. Although in an exact treatment the rotation and vibration motions of the nuclei cannot be decoupled, we can, as a good approximation, treat them independently. The total molecular energy E_{T} can then be considered as being made up of three contributions:

$$E_{\mathrm{T}} = E_{\mathrm{el}} + E_{\mathrm{vib}} + E_{\mathrm{rot}} \tag{14.11}$$

In general the order of magnitude of the electronic energies is 1–10 eV, of the vibrational energies 10^{-1} eV and of the rotational energies 10^{-4}–10^{-3} eV. In molecular spectroscopy usually energies are expressed as inversed wavelengths, $\lambda^{-1} = E/hc$, in cm^{-1} units. Sometimes also kcal/mole is used. The conversion factors are 1 eV = 8000 cm^{-1} = 23 kcal/mole. A schematic view of the energy levels of a diatomic molecule is given in figure 14.4. For a particular electronic state, indicated by E' or E'' where $'$ stands for an excited state and $''$ for the ground state, a series of vibrational states is possible, indicated by v' or v'', which is called the vibrational quantum number, with values $0, 1, 2, 3, \ldots$ For each vibrational state a series of rotational states is possible, indicated by K' or K'', the rotational

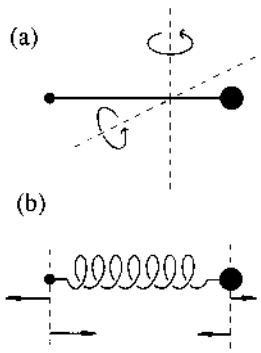

Figure 14.3: The two possible nuclear motions in a diatomic molecule: (a) rotation and (b) vibration.

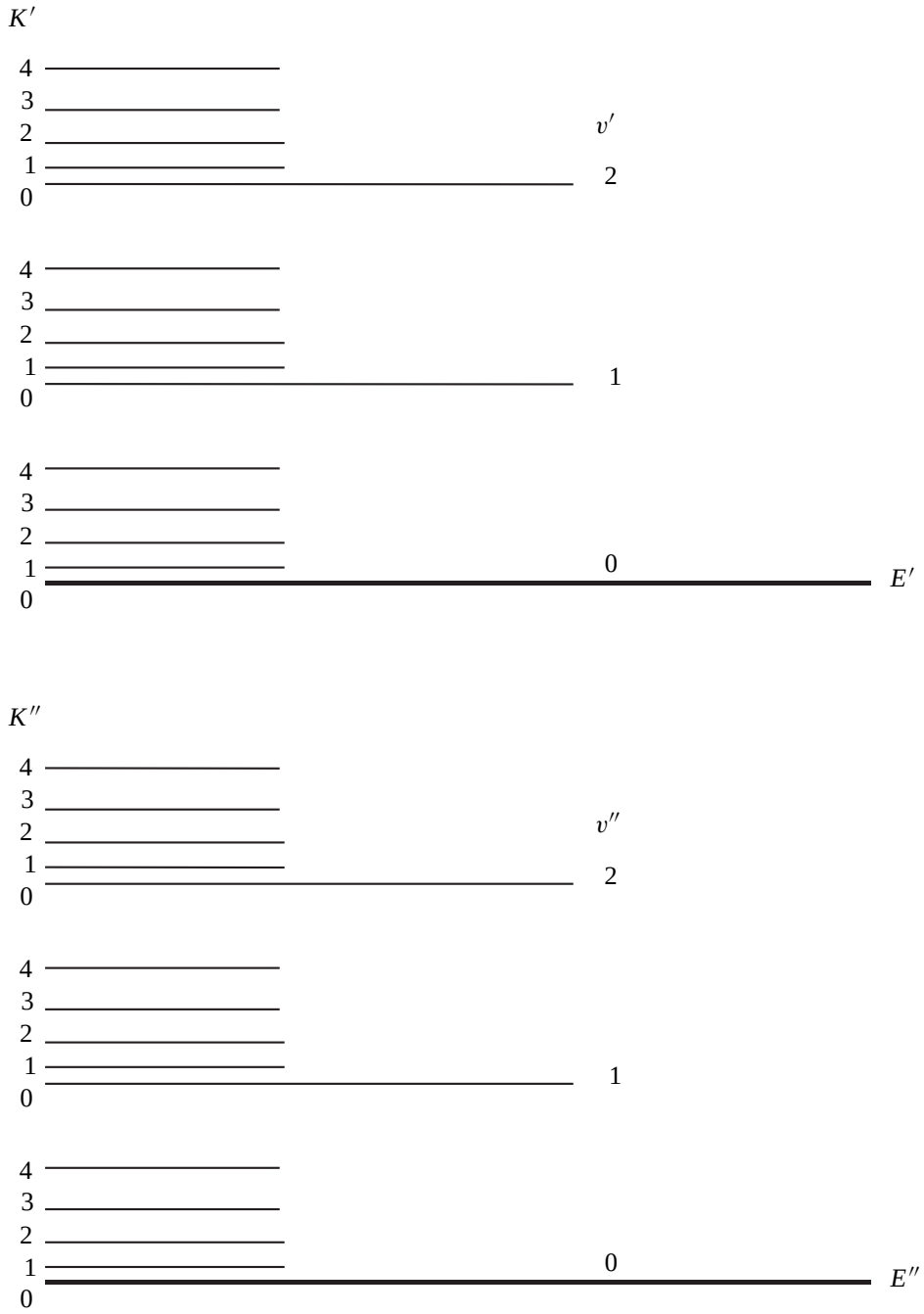

Figure 14.4: Energy level scheme of a diatomic molecule. The lower electronic energy level E'' has a number of vibrational and rotational states which are indicated by their quantum numbers v'' and K'', respectively. The excited electronic, vibrational and rotational states are indicated by E', v' and K', respectively.

quantum number. For most diatomic molecules the values for K are $0, 1, 2, 3, \ldots$ However, in some cases, as for open shell molecules K can take also half-integer values.

The probabilility that a molecule is in a particular vibrational and rotational state (v_i, K_i) is given by the Boltzmann distribution:

$$f(v_i, K_i) = N g_i \exp\left(-\frac{E_i}{kT}\right) \tag{14.12}$$

where E_i is the energy of the state, $g_i = (2K_i + 1)$ is the degeneracy of the state and N is a normalization factor. Since the average energy of a molecule at room temperature is about 1 kcal/mole it follows from the Boltzmann distribution that molecules in general will be in the lowest vibrational level of the ground electronic state, but will possess several quanta of rotational energy.

Transitions between different rotational levels of the same vibrational state give rise to spectra in the far-infrared or microwave region. These spectra are called rotational spectra. Transitions between different vibrational levels within the same electronic state give rise to spectra in the near-infrared and are called vibrational spectra. Since in a vibrational transition also the rotational quantum number can change one also speaks about rovibrational spectra. Transitions between electronic levels give rise to spectra in the visible or ultra-violet region. These spectra are called electronic spectra or sometimes rovibronic spectra since both the vibrational and rotational quantum number can change.

For a bound electronic state the potential energy has a minimum value at a given distance between the nuclei, as shown in figure 14.5 for a diatomic molecule. At short distances the two positively charged nuclei repel each other, whereas at large distances attraction occurs due to the electronic charges. The internuclear distance at the potential minimum R_e is called the equilibrium distance.

In figure 14.5 also the vibrational energy levels are depicted. One of the atoms is positioned at $R = 0$, the other one vibrates about the minimum of the potential curve, the internuclear distance changing according to the curve up to the minimum and maximum value given by the intersections of the curve with the vibrational level. The vibrational energy is quantized according to figure 14.4. For small movements of the atoms from their equilibrium position the restoring force is proportional to the displacement and the atoms vibrate with simple harmonic motion (see below). The lower part of the curve is, therefore, parabolic in shape. At higher energies the curve deviates from a from a parabola, and the vibration becomes anharmonic. At sufficiently high vibrational energies the molecule will dissociate. The energy at which this occurs is called the dissociation energy, D_0 or D_e, corresponding to

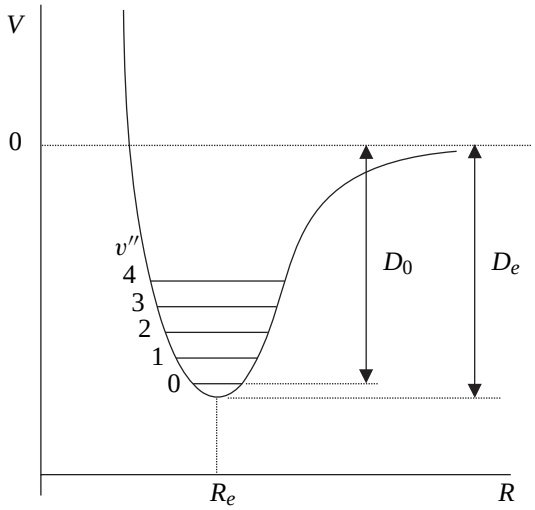

Figure 14.5: Potential energy curve of a diatomic molecule.

the energy above the ground vibrational state ($v'' = 0$) or above the potential minimum, respectively. The energy difference between D_0 and D_e is called the zero-point energy.

3 Rotation of diatomic molecules

Consider a diatomic molecule consisting of the atoms A and B with masses m_A and m_B, respectively, and at a fixed internuclear distance R ('rigid rotor approximation'). The moment of inertia I about an axis passing through the center of mass and perpendicular to the molecular axis is:

$$I = m_A r_A^2 + m_B r_B^2 \tag{14.13}$$

where r_A and r_B are the distances of atoms A and B from the center of mass, respectively. Since

$$m_a r_A = m_B r_B \tag{14.14}$$

it follows that the moment of inertia can be written as:

$$I = \left(\frac{m_A m_B}{m_A + m_B} \right) R^2 = \mu R^2 \tag{14.15}$$

with μ the reduced mass.

The angular momentum L of the molecule is

$$L = I\omega \tag{14.16}$$

where ω is the angular frequency. In quantum mechanics the motion of a particle is given by the Schrödinger equation, from which it is found that (as for the electron around a nucleus) the angular momentum is quantized according to:

$$L = \hbar\sqrt{K(K+1)} \tag{14.17}$$

where K is the rotational quantum number with values restricted to:

$$K = 0, 1, 2, 3, \ldots \tag{14.18}$$

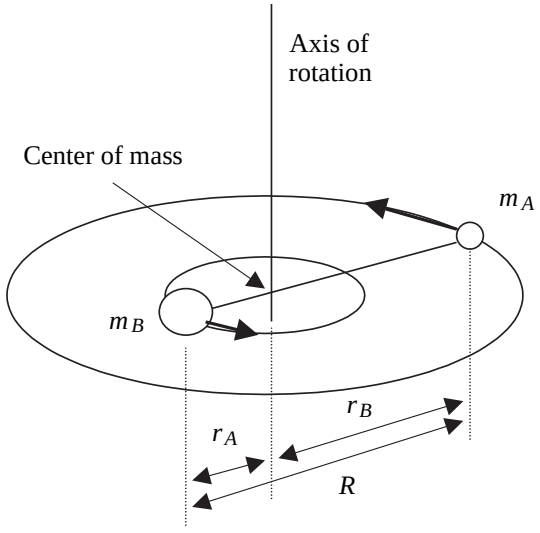

Figure 14.6: Rotation of a diatomic molecule.

The energy of the rotating molecule is given by:

$$E = \tfrac{1}{2} I\omega^2 = \frac{L^2}{2I} \tag{14.19}$$

It follows that also the rotational energy is quantized:

$$E_{\text{rot}} = \frac{\hbar^2}{2I} K(K+1) \tag{14.20}$$

Usually the rotational energy is expressed in cm^{-1} units:

$$F(K) = BK(K+1) \tag{14.21}$$

where $F(K) = E_{\text{rot}}/hc$ is called the rotational term value and B is the rotational constant in cm^{-1}:

$$B = \frac{h}{8\pi^2 cI} \tag{14.22}$$

A typical rotational energy level scheme is shown in figure 14.7, where also transitions between the levels are indicated. Only transitions involving a change in rotational quantum number K of ± 1 are allowed. In figure 14.7 the possible transitions with $\Delta K = +1$ are shown, corresponding to the absorption of energy. There are two restrictions in order to make transitions possible:

1. the molecule should have an electric dipole moment, such as for HCl, in order to interact with the electric field of the electromagnetic radiation field, and
2. the molecule should be heteronuclear; it follows from symmetry considerations that transitions with $\Delta K = \pm 1$ are forbidden for homonuclear molecules, such as H_2 or O_2.

A transition between a rotational state with quantum number K and a state with quantum number $K+1$ means an energy change of

$$\Delta F = F(K+1) - F(K) = 2B(K+1) \tag{14.23}$$

which is also called the transition frequency ν (in cm^{-1}).

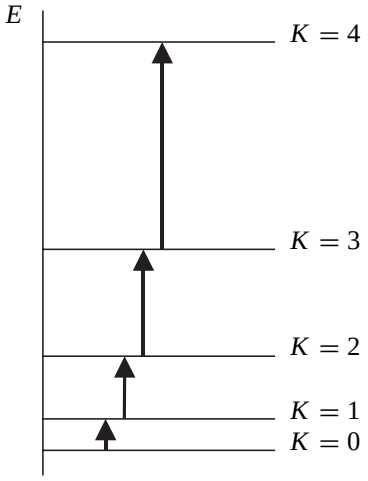

Figure 14.7: Lowest rotational energy levels of a diatomic molecule and possible transitions with $\Delta K = \pm 1$.

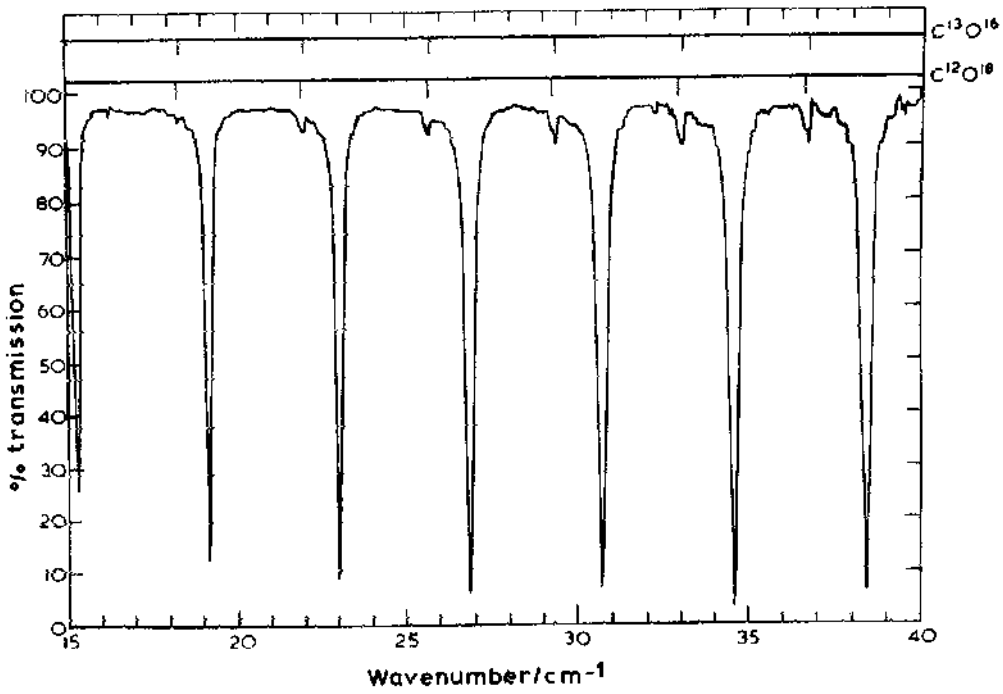

Figure 14.8: Far infrared spectrum of $C_{12}O_{16}$ showing rotational transitions with $K'' = 3$–9. Also lines of the isotope $C_{13}O_{16}$ can be seen. Adapted from Fleming and Chamberlain [1].

Usually B is given in cm^{-1} units. For instance for CO the value of B is 1.977 cm^{-1}. A typical absorption spectrum of CO is shown in figure 14.8. According to equation (14.23) the spectrum consists of equidistantial lines with a frequency separation of about 4 cm^{-1}. The intensity distribution is mainly determined by the Boltzmann population distribution. For high rotational states the centrifugal distortion has to be taken into account. As a result of the faster spinning of the molecule the bond is slightly stretched by a centrifugal force. Consequently the moment of inertia is increased and the rotational constant becomes smaller. It is found that this can be corrected for by an extra term in the expression for the rotational energy:

$$F_v(K) = B_v K(K+1) - D_v \left(K(K+1)\right)^2 . \tag{14.24}$$

The constant D is called the centrifugal distortion constant and is typically four orders of magnitude smaller than B. The subscript v stands for the vibrational quantum number and takes into account the vibrational dependence of the rotational constants B and D. The vibrational dependence follows from the fact that the equilibrium internuclear distance R_e increases with v as can be seen from figure 14.5. Consequently the moment of inertia will increase with v as well and the rotational constant becomes smaller. This is taken into account by a correction term in the expression for B:

$$B_v = B_e - \alpha_e \left(v + \tfrac{1}{2}\right) \tag{14.25}$$

where B_e is the hypothetical rotation constant in the equilibrium position and α_e the rotation-vibration interaction constant, which is typically two orders of magnitude smaller than B_e.

4 Vibration of diatomic molecules

In the neighbourhood of the minimum of the potential energy curve (see figure 14.5) the shape of the curve is very nearly a parabola:

$$V = V_0 + \tfrac{1}{2}k(R - R_e)^2. \tag{14.26}$$

The interatomic force that gives rise to this potential energy follows by differentiation:

$$F = -\frac{\mathrm{d}V}{\mathrm{d}R} = -k(R - R_e). \tag{14.27}$$

This force is the restoring force of a spring, and, like a spring, also a molecule undergoes a simple harmonic oscillation. Classically the frequency of a harmonic oscillation of a body with mass m and connected to a spring with force constant k is:

$$\nu = \frac{1}{2\pi}\sqrt{\frac{k}{m}}. \tag{14.28}$$

When the harmonic oscillator problem is solved quantum-mechanically it turns out that the vibrational motion is quantized as the rotational motion, and the frequencies are:

$$\nu = \left(v + \tfrac{1}{2}\right)\frac{1}{2\pi}\sqrt{\frac{k}{m}}, \tag{14.29}$$

where v is the vibrational quantum number with possible values:

$$v = 0, 1, 2, 3, \ldots \tag{14.30}$$

The vibrational energies corresponding to these frequencies are:

$$E_{\mathrm{vib}} = h\left(v + \tfrac{1}{2}\right)\frac{1}{2\pi}\sqrt{\frac{k}{m}}. \tag{14.31}$$

The lowest vibrational state ($v = 0$) has a non-zero energy $\frac{1}{2}h\nu_0$. The higher vibrational states do not obey equation (14.29) because the parabolic approximation to its potential energy curve becomes less and less valid with increasing energy. If the anharmonicity is taken into account the vibrational energy can be written as:

$$E_{\mathrm{vib}} = \left(v + \tfrac{1}{2}\right)h\nu_0 - \left(v + \tfrac{1}{2}\right)^2 xh\nu_0. \tag{14.32}$$

where x is the anharmonicity constant. As a result the spacing between the vibrational energy levels becomes smaller with increasing vibrational quantum number. Usually the vibrational energy is expressed in cm^{-1} units according to:

$$G(v) = \omega_e\left(v + \tfrac{1}{2}\right) - \omega_e x_e\left(v + \tfrac{1}{2}\right)^2, \tag{14.33}$$

where $G(v) = E_{\mathrm{vib}}/hc$ is called the vibrational term value and ω_e the vibrational wavenumber.

5 Vibration-rotation spectra

Including both vibrational and rotational energies the total term values S(v,K) are given by the sum of the rotation term values Fv(K), given in equation (14.24), and the vibrational term values G(v), given in equation (14.33):

$$S(v, K) = \omega_e \left(v + \tfrac{1}{2}\right) - \omega_e x_e \left(v + \tfrac{1}{2}\right)^2 + B_v K(K+1) - D_v \left(K(K+1)\right)^2, \tag{14.34}$$

when higher order terms are neglected.

For hetero-nuclear molecules transitions are possible between two rotational states belonging to two different vibrational states if the following selection rules are satisfied:

$$\Delta v = \pm 1 \tag{14.35a}$$

$$\Delta K = \pm 1 \tag{14.35b}$$

In figure 14.9 the possible transitions from a vibrational state $|v\rangle$ to a vibrational state $|v+1\rangle$ are illustrated, together with their spectroscopic notation. The $\Delta K = -1$ transitions are called the P branch and the $\Delta K = +1$ transitions are called the R branch. Each transition is labelled $P(K)$ or $R(K)$ where K represents the rotational quantum number of the lowest state. Transitions with $\Delta K = 0$ are forbidden except for open shell diatomic molecules with a non-zero electronic angular momentum, such as NO and OH. These transitions, which are called the Q branch, are nearly coincident because the rotational splittings in the two vibrational states are only slightly different. In figure 14.9 also a so called stick spectrum is depicted, showing the frequencies and relative intensities of the transitions. The frequencies follow from equation (14.34):

$$P\text{-branch:} \quad \nu_P(K'') = \nu_0 - (B' + B'')K'' + (B' - B'')K''^2 \tag{14.36a}$$

$$Q\text{-branch:} \quad \nu_Q(K) = \nu_0 + (B' - B'')K + (B' - B'')K^2 \tag{14.36b}$$

$$R\text{-branch:} \quad \nu_R(K') = \nu_0 - (B' + B'')K' + (B' - B'')K'^2 \tag{14.36c}$$

where

$$\nu_0 = \omega_e - 2\omega_e x_e \left(v + \tfrac{1}{2}\right) \tag{14.37}$$

is called the band origin of this vibrational transition.

The relative intensities are given by the product of the line strength of the transition and the population of the initial state, which depends on the term energy and the temperature according to the Boltzmann distribution, given in equation (14.12). The line strength follows from quantum mechanics and is a function of K' and K''.

6 Electronic spectra

The electronic energy states of a molecule are determined by the electronic configuration which is built up by all electrons in their individual orbitals. The properties of a particular electronic configuration are amongst others given by the total orbital angular momentum L and the total electronic spin S of the electrons. Similar to the angular momentum associated with the nuclear end-over-end rotation of a diatomic molecule also the total electronic spin and orbital angular momentum are quantized. The orbital angular momentum is strongly coupled to the internuclear axis, and it follows from quantum

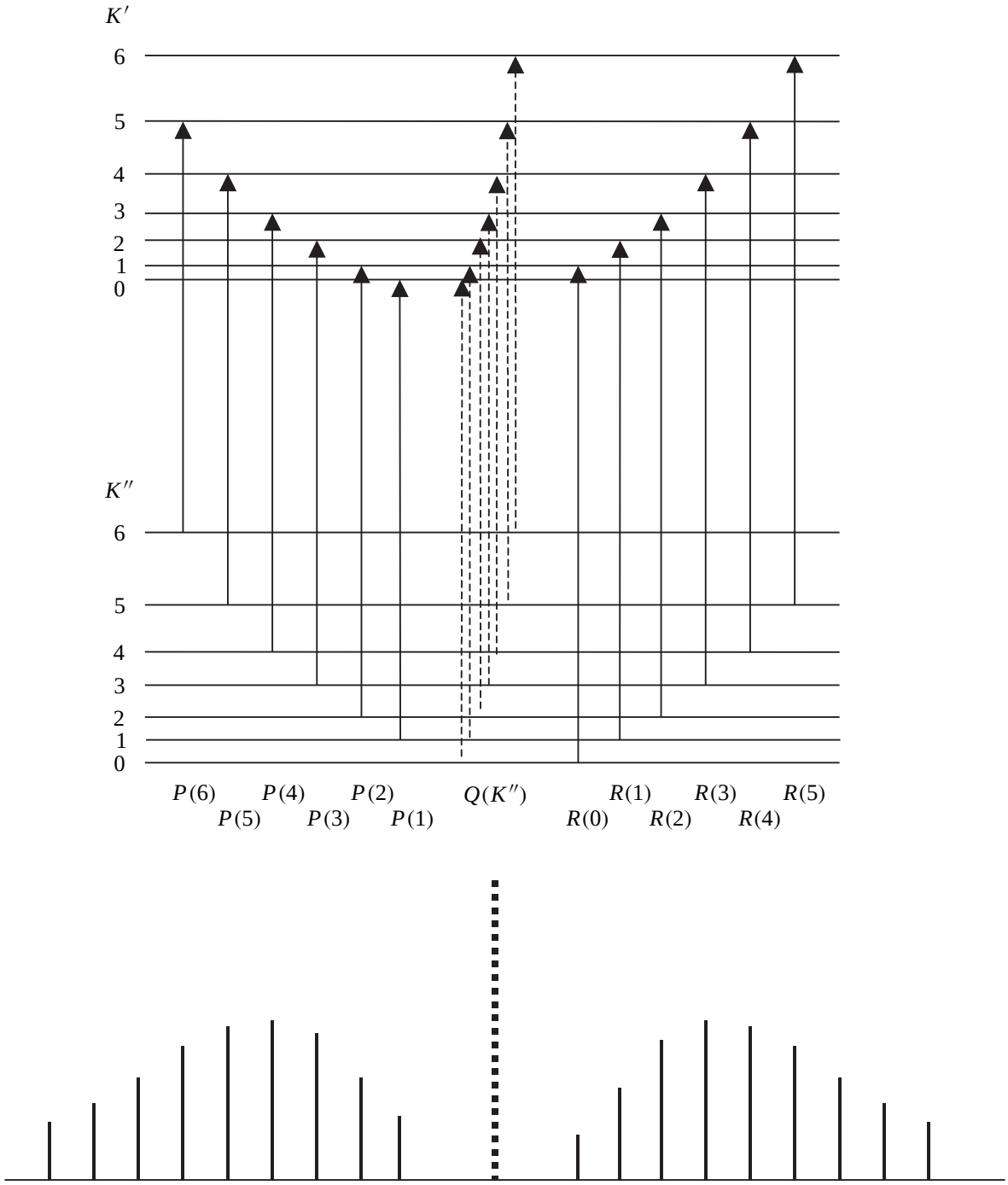

Figure 14.9: Rovibrational transitions of a hetero-nuclear diatomic molecule, their spectroscopic notation and a stick spectrum. The dashed transitions are allowed for open shell molecules with a non-zero electronic angular momentum.

mechanics that it is only the component of L along the internuclear axis which is important. This component which is denoted by Λ, can take the values

$$\Lambda = 0, 1, 2, 3, \ldots \tag{14.38}$$

The electronic states are designated by the notation $^{2S+1}\Lambda$ where $\Sigma, \Pi, \Delta, \Phi, \ldots$ is used for $\Lambda = 0, 1, 2, 3, \ldots$ and $2S + 1$ is called the multiplicity. This notation is preceded by a character, which is X for the ground electronic state and $A, B, C, \ldots$ for the excited states with the same multiplicity or $a, b, c, \ldots$ if the multiplicity is different from the one of the ground state. Transitions between states with different multiplicity are forbidden, which means that the lowest excited state with a multiplicity different from the one of the ground state, denoted with a, is a metastable state.

Each electronic state has a potential energy curve similar to the one shown in figure 14.5 for a diatomic molecule. In figure 14.10 the potential energy curves of C_2 are shown. The ground electronic state is $X^1\Sigma_g^+$, from which it can be seen that $S = 0$ and $\Lambda = 0$. The subscript g and superscript $+$ denote a symmetric behaviour of the electronic configuration with respect to two different symmetry operations. For large R the dissociation fragments are indicated. In table 14.1 observed transitions between the electronic states of C_2 are listed. As can be seen only transitions between states with same multiplicity have been observed. This and other selection rules (which also hold for the transitions in table 14.1) are:

$$\begin{aligned} &\Delta S = 0 \\ &\Delta\Lambda = 0, \pm 1 \\ &+ \leftrightarrow + \quad \text{and} \quad - \leftrightarrow - \\ &g \leftrightarrow u \end{aligned} \tag{14.39}$$

These selection rules follow from the interaction between electric dipole moment of the molecule and the electric field of the radiation field. This electric dipole moment consists of an electronic part and a nuclear part. It is the electronic part that determines the selection rules (14.39) for an electronic transition. The nuclear part is responsible for the selection rules between the rotational and vibrational states. Since in an electronic transition also the rotational and vibrational states changes

Transition	Name associated	Spectral region (nm)
$b^3\Sigma_g^- \rightarrow a^3\Pi_u$	Ballik-Ramsay	2700–1100
$A^1\Pi_g \leftrightarrow X^1\Sigma_g^+$	Phillips	1549–672
$d^3\Pi_g \leftrightarrow a^3\Pi_u$	Swan	785–340
$C^1\Pi_p \rightarrow A^1\Pi_u$	Deslandres-d'Azambuja	411–339
$e^3\Pi_g \leftrightarrow a^3\Pi_u$	Fox-Herzberg	329–237
$D^1\Sigma_u^+ \leftrightarrow X^1\Sigma_g^+$	Mulliken	242–231
$E^1\Sigma_g^+ \rightarrow A^1\Pi_u$	Freymark	222–207
$f^3\Sigma_g^- \leftarrow a^3\Pi_u$	—	143–137
$g^3\Delta_g \leftarrow a^3\Pi_u$	—	140–137
$F^1\Pi_u \leftarrow X^1\Sigma_g^+$	—	135–131

Table 14.1: Electronic transitions observed in C_2.

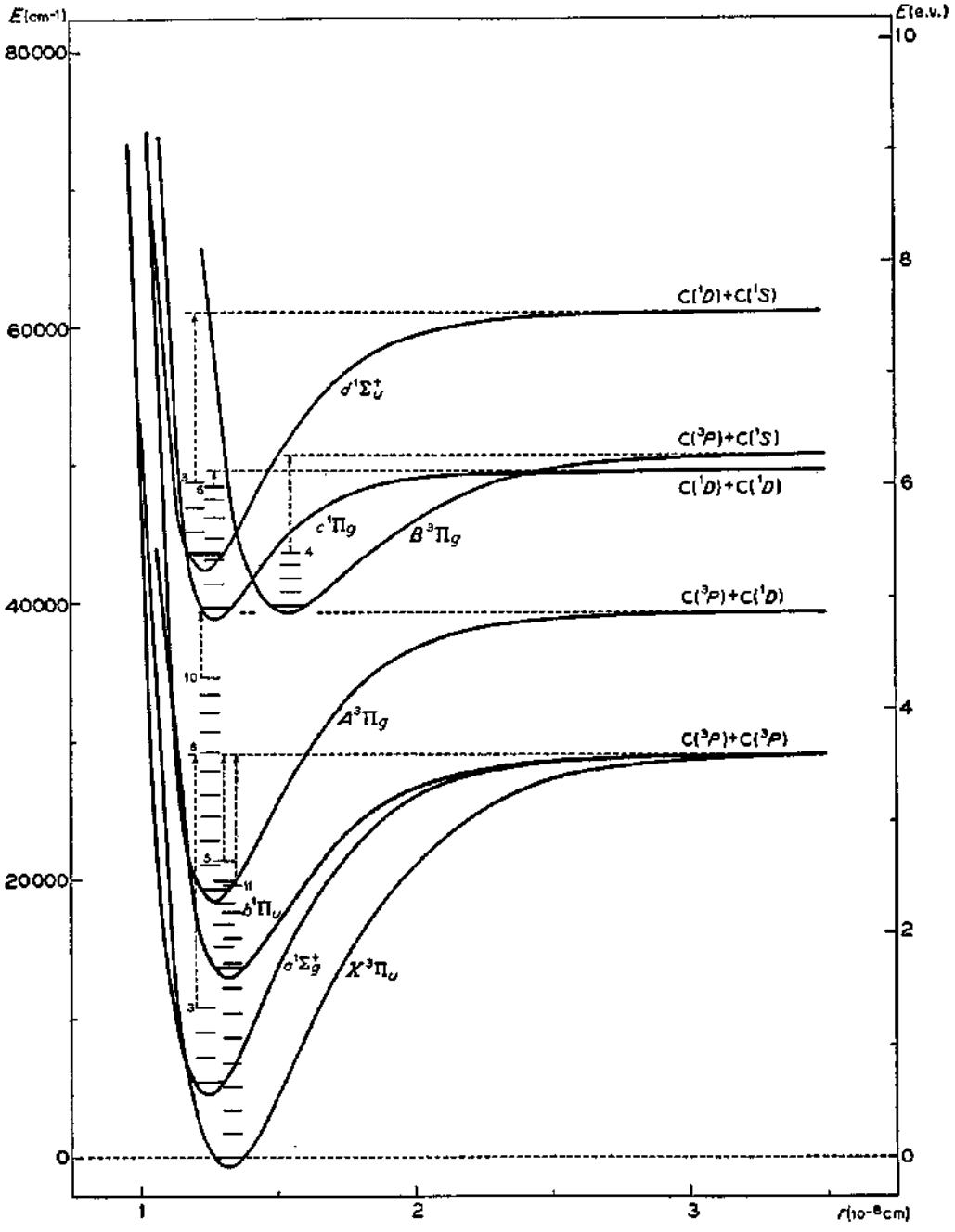

Figure 14.10: Potential energy curves of C_2.

also the selection rules for a rotational and vibrational transition have to be taken into account:

$$\begin{aligned} \Delta K &= 0, \pm 1 \\ \Delta v &= 0, \pm 1, \pm 2, \pm 3, \ldots \end{aligned} \tag{14.40}$$

In contrast to transitions between states of the same electronic state there is no particular selection rule for vibrational transitions between states belonging to different electronic states. Figure 14.11 shows sets of vibrational energy levels associated with two different electronic states between which an electronic transition is allowed. Two series of transitions can be distinguished. A series of transitions which start from the same vibrational state, either in the lower or in the upper state, is called a progression; here the frequency separation between the spectral lines is given by the vibrational spacings in the upper or lower electronic state. A series of transitions with the same Δv is called a sequence; in this case the distances between the spectral lines are much smaller since these are given by the difference of the vibrational spacings in lower and upper electronic state.

The relative intensities of the vibrational spectral lines is determined by the Franck-Condon principle, which follows from the quantummechanical treatment of the transition probability. In addition also the population distribution of the initial vibrational states has to be taken into account. Usually this is a Boltzmann distribution (equation (14.12)), but this is not necessarily the case for vibrational states, since their populations can deviate from thermal equilibrium (for instance as the result of a particular production process).

The total term value S for a molecule in a rovibrational state $|v, K\rangle$ in an electronic state with a term value T, corresponding to the energy of the potential energy minimum of the electronic state relative to the potential energy minimum of the ground electronic state, is given by:

$$S = T + G(v) + F(v, K) \tag{14.41}$$

where $G(v)$ and $F(v, K)$ are given by equations (14.33) and (14.24), respectively. Values for S can be calculated from the molecular constants involved in G and F. These constants are tabulated in

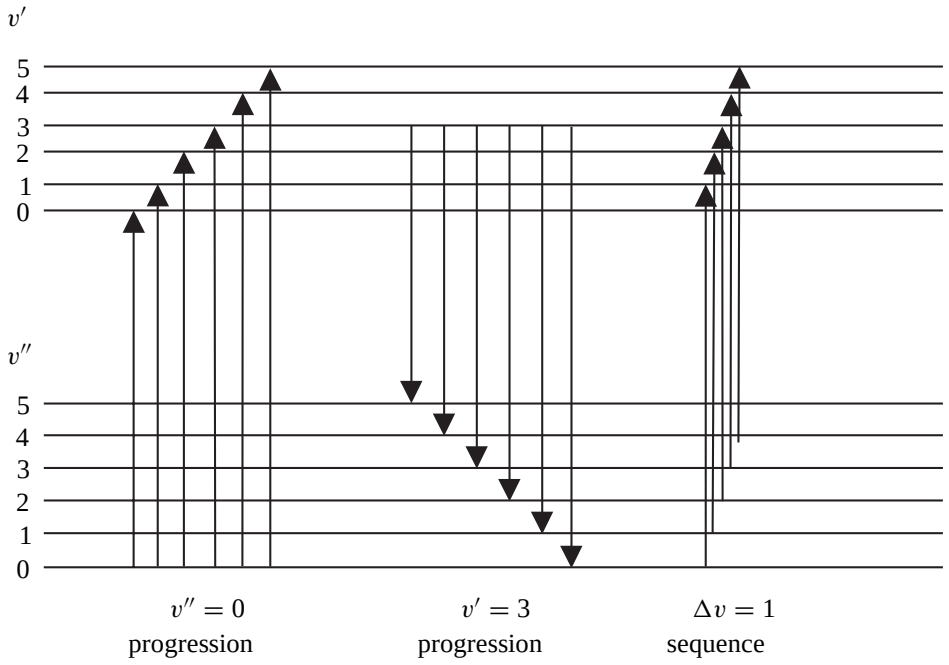

Figure 14.11: Series of vibrational transitions in the electronic spectrum of a diatomic molecule.

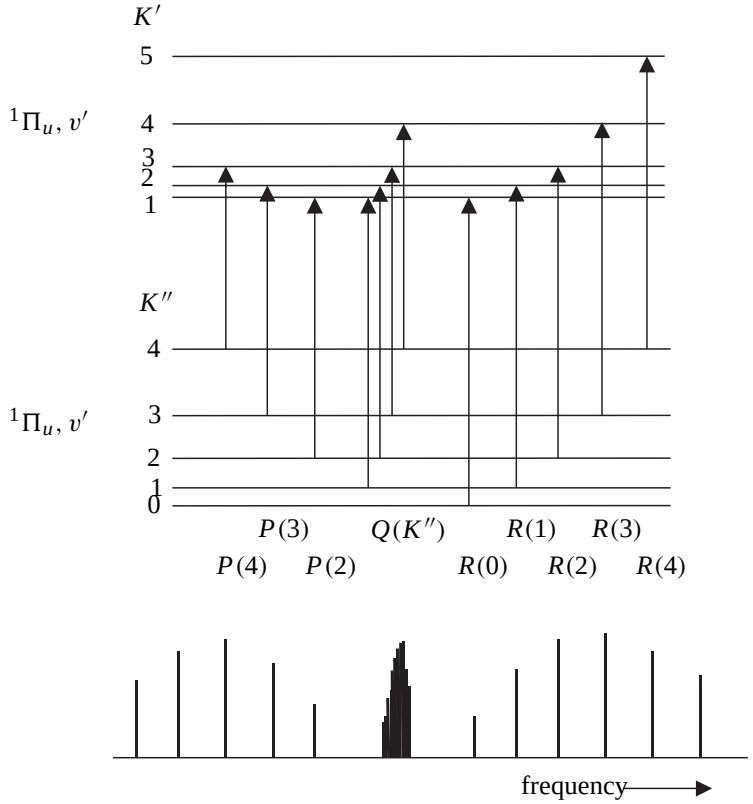

Figure 14.12: The rotational structure of a $^1\Pi_u$, $v' \leftarrow {}^1\Sigma_g$, v'' transition. Due to the electronic orbital angular momentum in the $^1\Pi_u$ state the structure is more complex than indicated. In fact each rotational level is split in a doublet (Λ-doublet). Also a total (nuclear + electronic) orbital angular momentum J should be used instead of K. This is also the reason that the lowest indicated value is 1 instead of 0.

handbooks, as for instance by Herzberg [2]. In table 14.2 the constants are given for some molecules which are major species in combustion processes. From the total term values the structure of the spectrum can be calculated. An example of a spectral structure is given in figure 14.12, where the lowest transitions of a $^1\Pi_u$, $v' \leftarrow {}^1\Sigma_g$, v'' transition are shown.

Usually the spectral structure is more complicated due to the presence of electronic spin and angular orbital momentum. Moreover the sequence of lines of a particular branch can reverse as a result of different molecular constants in the two electronic states involved in the transition. This is illustrated in figure 14.13, where the $A^1\Pi_u \leftarrow X^1\Sigma_g$ spectrum of AlH is presented. The position where the reversal takes place is called a bandhead.

7 Polyatomic molecules

Polyatomic molecules cover such a wide range of different types that it is not possible here to treat them here. Only a few general properties will be considered. The polyatomic molecules can be divided in tow groups: the linear and the non-linear molecules. For linear polyatomics the description of the spectral structure is similar to that of diatomic molecules, including the classification of energy states and the electronic and rotational selection rules. Due to the larger degree of freedom these molecules have more possibilities for vibrational motion. In addition to the stretching vibration of diatomics

Molecule	Electronic state	T_e [cm^{-1}]	ω_e [cm^{-1}]	$\omega_e x_e$ [cm^{-1}]	B_e [cm^{-1}]	α_e [cm^{-1}]	D_e [10^{-6} cm^{-1}]	r_e [Å]
N_2	$a'\,^1\Sigma_u^-$	68152.66	1530.25	12.0747	1.4799	0.01657	5.55	1.2755
	$A\,^3\Sigma_u$	50203.6	1460.64	13.87	1.4546	0.0180	6.1	1.2866
	$X\,^1\Sigma^+$	0	2358.57	14.324	1.99824	0.017318	5.76	1.09768
C_2	$B'\,^1\Pi_u$	8145	1608.2	12.1	1.62			
	$A'\,^1\Sigma_g$	6443	1470.4	11.2	1.49			
	$a\,^3\Pi_u$	716.2	1641.3	11.7	1.63			
	$X\,^1\Sigma_g^+$	0	1854.8	13.4	1.82			
CO	$A\,^1\Pi$	65075.7	1518.2	19.40	1.6115	0.0232	7.33	1.2353
	$a'\,^3\Sigma^+$	55825.4	1228.60	10.468	1.3446	0.0189	6.41	1.3523
	$a\,^3\Pi$	48686.70	1743.4	14.3	1.69124	0.01904	6.36	1.20574
	$X\,^1\Sigma^+$	0	2169.81358	13.28831	1.93128087	0.01750441	6.1214	1.128323
NO	$A\,^2\Sigma^+$	43965.7	1017	11	1.9965	0.01915	5.4	1.0634
	$X\,^2\Pi_{3/2}$	119.82	1904.04	14.100	1.72016	0.0182	10.2	1.15077
	$X\,^2\Pi_{1/2}$	0	1904.20	14.075	1.67195	0.0171	0.5	1.15077
OH	$B\,^2\Sigma^+$	69774	940.0	105	5.086		9.29	1.869
	$A\,^2\Sigma^+$	32684.1	3178.8	92.91	17.358	0.786	20.39	1.0121
	$X\,^2\Pi_{1/2}$	126.23	3737.76	84.881	18.910	0.7242	19.38	0.96966
	$X\,^2\Pi_{3/2}$	0	3737.76	84.881	18.910	0.7242	19.38	0.96966
H_2	$C\,^1\Pi_u$	100089.8	2443.77	69.524	31.362	1.664	2.23	1.0327
	$B\,^1\Sigma_u^+$	91700.0	1358.09	20.888	20.015	1.1845	1.625	1.2928
	$X\,^1\Sigma_g^+$	0	4401.21	121.33	60.853	3.062	4.71	0.74144

Table 14.2: Molecular constants of some molecules which are major species in combustion processes.

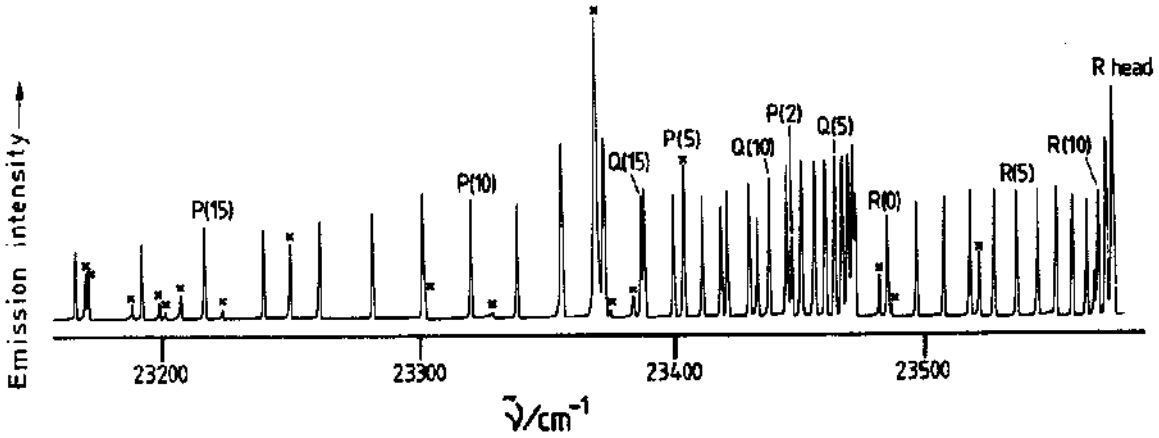

Figure 14.13: The $A^1\Pi_u \leftarrow X^1\Sigma_g$ electronic spectrum of AlH showing clearly a reversal of the lines of the R branch. The lines indicated by an x are originating from impurities.

they also show bending vibrations. Each vibrational mode (3 for a triatomic nolecule) is indicated by a quantum number: $\nu_1, \nu_2, \nu_3, \ldots$ Each vibrational state, which is designated by $(\nu_1, \nu_2, \nu_3, \ldots)$ has its own rotational ladder. Electronic transitions of linear polyatomic molecules show the same structure as transitions of diatomic molecules. However, it is possible that a polyatomic molecule which is linear in its electronic ground state may be non-linear in some excited electronic states, causing a more complicated structure of the spectrum.

For non-linear polyatomic molecules the use of symmetry arguments in discussing electronic state properties is essential. Such a treatment is far beyond the scope of this course. The interested reader is referred to handbooks about molecular structure, such as by Herzberg [3].

8 Absorption and emission of radiation

For the description of absorption and emission of radiation by an atom or a molecule we consider only two energy states between which an transition is possible. These states can be two different electronic, vibrational or rotational states When such a two-level system is subject to radiation of frequency ν, corresponding to the energy separation $\Delta E = h\nu$ of the levels two different processes may occur:

1. stimulated absorption, in which the atom or molecule in the lower energy state absorbs a quantum of radiation and is excited to the upper state, or

2. stimulated emission, in which the atom or molecule in the upper state emits a photon of the same frequency and decays to the lower energy state.

In addition a third process may occur, independent of the presence of the radiation field:

3. spontaneous emission, similar to process (2) but without the stimulating field.

These three processes are illustrated in figure 14.14. The population transfer between the two states can be expressed in terms of the so called Einstein coefficients. The rate of change of population N_2 of state 2 due to induced absorption is given by:

$$\frac{\mathrm{d}N_2}{\mathrm{d}t} = N_1 B_{12} \rho(\nu) \tag{14.42}$$

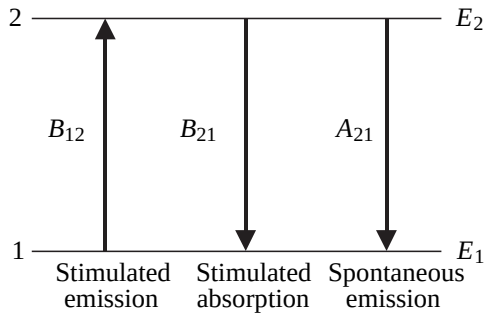

Figure 14.14: The three possible transition processes for a two-level system.

where B_{12} is the Einstein coefficient for stimulated absorption and $\rho(\nu)$ the radiation density, given by:

$$\rho(\nu) = \frac{8\pi h \left(\frac{\nu}{c}\right)^3}{\exp(h\nu/kT) - 1} \tag{14.43}$$

Similarly, induced emission changes the population N_2 by:

$$\frac{\mathrm{d}N_2}{\mathrm{d}t} = -N_2 B_{21} \rho(\nu) \tag{14.44}$$

where B_{21} is the Einstein coefficient for stimulated emission, related to B_{12} via:

$$B_{12} = \frac{g_2}{g_1} B_{21} \tag{14.45}$$

where g_1 and g_2 are equal to $2K'' + 1$ and $2K' + 1$, respectively.

For spontaneous emission:

$$\frac{\mathrm{d}N_2}{\mathrm{d}t} = -A_{21} N_2 \tag{14.46}$$

where A_{21} is the Einstein coefficient for spontaneous emission. The absence of a dependence on the radiation density $\rho(\nu)$ indicates a spontaneous process. This process determines the natural lifetime τ of the excited state. From equation (14.46) it follows directly that τ is related to A_{21} via:

$$\tau = A_{21}^{-1} \tag{14.47}$$

In general, more spontaneous transitions are possible from an excited state and the lifetime is the inverse of the sum over all spontaneous emission coefficients. Typical natural lifetimes of excited molecules are 10^{-7} s for electronic states, 10^{-4} s for vibrational states and 1 s for rotational states.

In the presence of a radiation field all three processes can take place simultaneously. Assuming no population loss:

$$\frac{\mathrm{d}N_1}{\mathrm{d}t} = -\frac{\mathrm{d}N_2}{\mathrm{d}t} \tag{14.48}$$

the following expression for the population transfer is obtained from equations (14.42), (14.44–14.46):

$$\frac{\mathrm{d}N_2}{\mathrm{d}t} = \left(N_1 - \frac{g_1}{g_2} N_2\right) B_{12} \rho(\nu) - N_2 A_{21}. \tag{14.49}$$

In thermal equilibrium the populations are related through the Boltzmann law (equation (14.12)):

$$\frac{N_2}{N_1} = \frac{g_2}{g_1} \exp\left(-\frac{E_2 - E_1}{kT}\right). \tag{14.50}$$

Substituting this relation and equation (14.43) in equation (14.49) gives the result:

$$A_{21} = \frac{8\pi h\nu^3}{c^3} B_{21}. \tag{14.51}$$

The Einstein B coefficient is determined by the quantum numbers of the two states involved and is independent of the frequency ν. It follows that the Einstein A coefficient is proportional to the frequency to the third power, which explains why the lifetime of excited electronic states is so much shorter than the typical lifetime of an excited vibrational or rotational state.

References

[1] J. W. Fleming and J. Chamberlain, *Infrared Phys.* **14** (1974) 277.

[2] G. Herzberg, *Molecular Spectra and Molecular Structure. I. Spectra of Diatomic Molecules*, Van Nostrand Reinhold Company, New York (1950) .

[3] G. Herzberg, *Molecular Spectra and Molecular Structure. II. Spectra of Polyatomic Molecules*, Van Nostrand Reinhold Company, New York (1950).

Chapter 15

Laser Diagnostics in Flames

Nico Dam

Introduction

Optical flow diagnostics is the art of characterising a flow (reactive or not) in space and time by means of light scattering. In its most straightforward implementation, one just looks at the light that is emitted spontaneously by the process of interest. More detailed information can usually be obtained if the flow is irradiated by an external light source, and individual spectral components of the scattered light are collected. More often than not a laser is used as light source, and in this case we speak of Laser Diagnostics, the subject of this chapter.

Numerous implementations of laser diagnostics have been developed over the past decades, and there is a vast amount of literature on the application of laser diagnostics to a whole zoo of combustion processes. Fortunately, there are two recent reviews of the subject, that I would recommend to anyone working in this field of research:

- *Applied Combustion Diagnostics*, by K. Kohse-Höinghaus and J.B. Jeffries (eds.) [1] (further referenced as ACD);

- *Laser Diagnostics for Combustion Temperature and Species*, by A.C. Eckbreth [2].

It is not my intention to review the working principles of lasers and detection equipment; for background info see e.g.

- *Laser Spectroscopy: Basic concepts and instrumentation*, by W. Demtröder [3] (further referenced as DLS).

- *Lasers*, by P.W. Milonni and J.H. Eberly [4].

This chapter is divided in two parts. The first part is mainly an introduction to non-resonant light scattering. (Resonant light scattering has been touched upon in the previous chapter.) The second part involves a discussion of those implementations of laser diagnostics that are most often used in experimental combustion research, as well as a few new techniques that I consider promising or otherwise interesting.

1 Non-resonant light scattering fundamentals

1.1 A coarse-grained classification of light scattering

Light can be described in terms of photons ('light particles') or in terms of waves. The relation between photon energy E and wavelength λ or frequency ν is well known[1]:

$$E = h\nu = hc/\lambda \tag{15.1}$$

(with Planck's constant h and the speed of light c). We will usually describe a light beam in terms of its spectral intensity $I(\nu) = I_0 g(\nu)$, in which I_0 is the overall intensity, and $g(\nu)$ a normalised spectral distribution function, that is,

$$\int_0^\infty g(\nu)\,\mathrm{d}\nu = 1\ , \quad \text{so that} \quad \int_0^\infty I(\nu)\,\mathrm{d}\nu = I_0\ . \tag{15.2}$$

A light beam is called monochromatic if the width of the spectral distribution $g(\nu)$ is small with respect to other spectral features in the experiment (like a molecular transition linewidth, or the resolving power of a spectrograph; this varies with the experiment).

The basis of laser diagnostics has been laid in the previous chapter on molecular physics. Scattering of light can be described in terms of an exchange of energy between the optical (electro-magnetic) field and individual molecules in a medium. Since molecular energy levels are quantised, energy exchange, involving transitions between molecular energy levels, is quantised as well. The net scattered field is, of course, the sum of all contributions by individual molecules.

All irradiated molecules in a probe volume will interact with an incident light beam (that we will assume to be monochromatic in the following, that is, $g(\nu) = \delta(\nu - \nu_{\mathrm{in}})$), and it is good practice to start worrying about the number of different kinds of scattering particles that may contribute to the scattered light. In principle, molecules of a specific chemical species in a specific quantum state each comprise one class of scattering particles.

Example: A light scattering experiment on room air would involve contributions from O_2, N_2 and possibly water vapour and CO_2. Depending on the experimental technique, these contributions can or can not be distinguished.

The density $\rho_\alpha(E_j)$ of molecules of chemical species α (e.g. CO, O_2, H,...) in internal energy state E_j (involving electronic, vibrational and rotational degrees of freedom) depends on the (local) composition of the medium and on the (local) temperature (via the Boltzmann factor, discussed in the previous chapter). Each class of scatterers will interact with the incident light in its own way, and contribute its own components to the scattered light. It is the experimentalists concern to sort out the different components, and this is the discriminating factor between many laser diagnostic techniques, as will be discussed further in the second part of this chapter.

A global classification of the kinds of light scattering that may occur on a single-molecule basis is based on the net energy exchange between scatterer and incident light, and on the degree to which the incident light frequency matches an allowed optical transition in a scatterer. We will call ν_{in} the incident light frequency, ν_{out} the frequency of (a component of) the scattered light, and $E_{i,\,f}$ the energy of the initial/final quantum state of the scattering molecule.

[1] **Units:** Wavelengths are usually expressed in nm or Å (obsolete, but convenient). For frequencies several commonly employed units are Hertz (Hz), wavenumber (the number of waves per cm; cm^{-1}), electronvolt (eV) or even Kelvin (K). They can be related through eq. 15.1: 1 eV $\equiv$ 8065.5 cm^{-1} $\equiv$ 11604 K, and 1 cm^{-1} $\equiv$ 30 GHz (taking $c = 3 \cdot 10^8$ m/s). Besides this, angular frequencies $\omega = 2\pi\nu$ are often used in the literature.

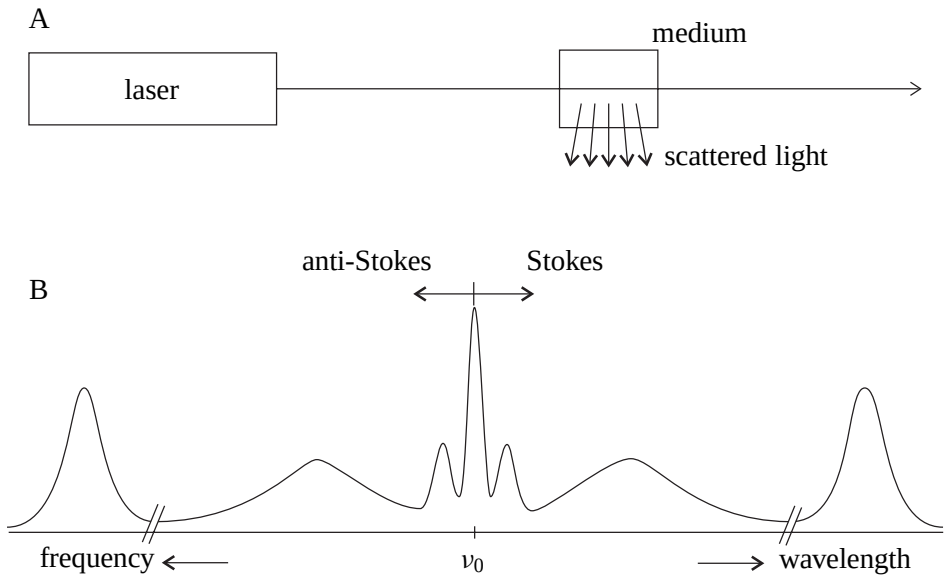

Figure 15.1: A) Typical experimental configuration for a light scattering experiment. B) Schematic spectrum of the scattered light. The intensities of the individual components are not to scale.

elastic scattering: $\nu_{\text{in}} = \nu_{\text{out}}$.
There is no energy exchange with the medium, so that the elastic contribution is not specific to any class of scatterers: they all contribute.

inelastic scattering: $\nu_{\text{in}} \neq \nu_{\text{out}}$.
Energy conservation requires that

$$E_i + h\nu_{\text{in}} = E_f + h\nu_{\text{out}} \quad \Leftrightarrow \quad \nu_{\text{in}} - \nu_{\text{out}} = (E_f - E_i)/h \ .$$

Since the initial state is connected to only a limited number of final states by optically allowed transitions, each class of scatterers contributes a relatively small number of very specific frequency components to the scattered light.

resonant scattering: $\nu_{\text{in}} = |E_f - E_i|/h$.
Can be elastic or inelastic. The final state f must be connected to the initial state by an optically allowed transition. Elastic scattering requires careful tuning of the incident light to a molecular transition of interest.

non-resonant scattering: $\nu_{\text{in}} \neq |E_f - E_i|/h \quad \forall$ allowed f.
Can be elastic or inelastic. The main difference between resonant and non-resonant scattering is to be found in the scattering efficiency, this being much higher in the former case.

Although this classification is not as clear-cut as it may seem, it is useful from a practical point of view, and it will be used as such in the rest of this chapter.

1.2 Molecular light scattering mechanisms

Consider a light beam, incident on a gaseous medium. Even if the wavelength of the light is not resonant with any optically allowed transition of the medium, there will be some interaction between

Table 15.1: Order-of-magnitude values for chraracteristic parameters of the most-used kinds of non-resonant scattering. Shift: Frequency shift of the scattered light relative to the incident light. Width: Typical spectral width of the scattered light, assuming monochromatic incident light. Coherent: Yes or No. (After Boyd (1992).)

Process	Shift [cm^{-1}]	Width [cm^{-1}]	Coherent
Vibrational Raman	1000	5.0	N
Rotational Raman	100	0.5	N
Brillouin	0.1	0.005	Y
Rayleigh	0	0.0005	Y

the two. This interaction is mainly due to the non-resonant response of the electrons to the oscillatory electric field, and results, for instance, in well-known phenomena like the refractive index or the blue sky. The latter is a manifestation of what we will be concerned with here: *non-resonant light scattering*. Resonant light scattering, in the context of optical combustion diagnostics, is more or less synonymous with LIF, and has been dealt with in the previous lecture (Molecular Physics in a Nutshell).

Figure 15.1 shows a typical configuration for any kind of light scattering experiment, together with an observed spectrum that is typical for the case of a non-resonant incident beam. If the incident beam is resonant with an allowed transition in the medium, the non-resonant part of the scattered light is still present, but usually swamped in the much stronger resonant contribution. Some order-of-magnitude values of characteristic parameters of each kind of scattering are listed in table 15.1.

The individual contributions to the non-resonant spectrum are due to different mechanisms:

- *Vibrational Raman scattering* is due to the interaction of the incident light with vibrational modes of the individual molecules (optical phonons, if you wish); *rotational Raman scattering* is analogous due to the interaction with rotational motion.

- *Rayleigh scattering* is due to the scattering off non-propagating density fluctuations (and is therefore really elastic), whereas

- *Brillouin scattering* is due the scattering off propagating density fluctuations (acoustical phonons, or sound waves), and experience a (small) frequency shift.

All kinds of scattering are subject to a *Doppler shift* of the scattered frequency if the scattering agent moves. The Doppler shift $\Delta\nu_D$ can be expressed as

$$\Delta\nu_D = \frac{1}{2\pi}\,\vec{\Delta k}\cdot\vec{v}\ , \tag{15.3}$$

in which $\vec{\Delta k} = \vec{k}_{\text{out}} - \vec{k}_{\text{in}}$ is the so-called *scattering wavevector* and $\vec{v}$ is the velocity of the scattering molecule (lab frame). The Doppler shift therefore depends on the experimental setup, via $\vec{\Delta k}$. Doppler shifts typically vary between 1 MHz and 1 GHz (see also §2.5 on Filtered Rayleigh Scattering), and Doppler-shifted elastic scattering is therefore also referred to as quasi-elastic scattering.

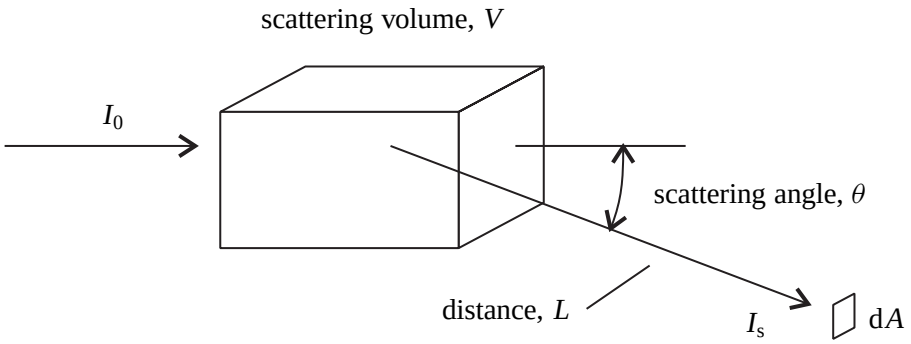

Figure 15.2: Parameters used in the description of scattering efficiency. (After Boyd (1992))

1.3 Polarisability and scattering cross section

Light scattering in terms of macroscopic properties of the medium is described by the Maxwell wave equation,

$$\nabla^2 \vec{E}(\vec{r},t) - \frac{1}{c^2}\frac{\partial^2 \vec{E}(\vec{r},t)}{\partial t^2} = \mu_0 \frac{\partial^2 \vec{P}(\vec{r},t)}{\partial t^2} \ , \tag{15.4}$$

in which $\vec{E}$ denotes the electric field strength and $\vec{P}$ the (induced) polarisation. From this equation it can be seen that $\vec{P}$ acts as a driving force for the field. Since, in the case of light scattering, $\vec{P}$ is also *induced* by the field, the problem becomes recursive, and has to be solved in a self-consistent way. We will only consider the linear regime, in which

$$\vec{P} = \vec{\mu}_p + \alpha \vec{E} = \chi \epsilon \vec{E} \tag{15.5}$$

(μ_p is a possible permanent dipole moment, α is the polarisability, χ the susceptibility, and ϵ the dielectric constant of the medium). We will neglect μ_p, and consider α and χ, which are second rank tensors in the most general case, as scalars in the following. The polarisability contains a static term α_0 that gives rise to elastic Rayleigh scattering, but also contains (usually smaller) dynamical terms related to, for instance, the vibrational motion of the constituent atoms or the molecular rotation:

$$\alpha = \alpha_0 + \frac{\partial \alpha}{\partial q} q + \dots \ , \tag{15.6}$$

in which q denotes some appropriate coordinate (see further discussion in §2.6, on Raman scattering). In all cases the second time derivative in the driving term $\partial^2 \vec{P}/\partial t^2$ gives rise to a scattered electric field strength $E_s \sim \nu_s^2$ and thus to a scattered field intensity $I_s \sim \nu_s^4$, in which ν_s denotes the scattered light frequency. This explains the probably familiar 4$^{\text{th}}$ power dependence of Rayleigh and Raman scattering efficiency on the frequency.

The intensity of the scattered light is usually expressed in terms of a *scattering cross section*, σ (kind of a geometrical surface area for removing light out of an incident plane wave), or, alternatively, a *scattering coefficient*, R. In the linear regime, the intensity I_s of the light scattered into a particular direction θ (see figure 15.2) is linearly proportional to the incident light intensity I_0 and the illuminated volume (or that part of the illuminated volume that is imaged onto the detector), and is inversely proportional to the square of the distance L to the detector:

$$I_s = R \, \frac{I_0 V}{L^2} \ . \tag{15.7}$$

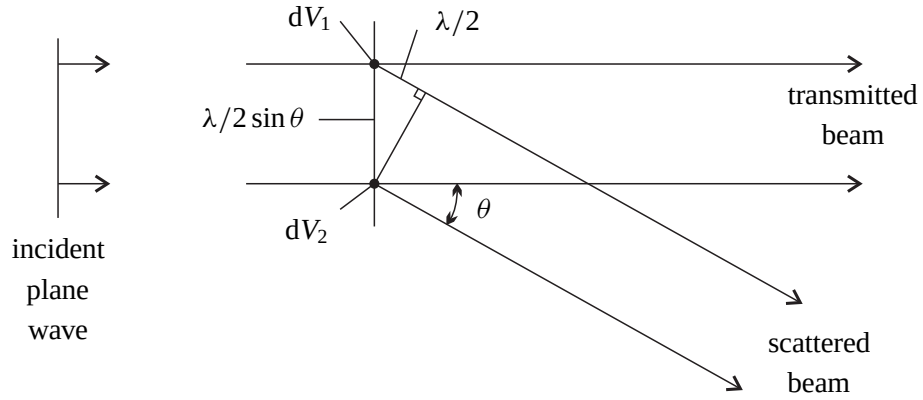

Figure 15.3: Scattering configuration (after Boyd (1992)).

The power incident on a small detector of surface area dA is

$$\mathrm{d}P_{\mathrm{det}} = I_s \mathrm{d}A \tag{15.8}$$

or, in terms of the solid angle $\mathrm{d}\Omega = \mathrm{d}A/L^2$ that it subtends,

$$\frac{\mathrm{d}P_{\mathrm{det}}}{\mathrm{d}\Omega} = I_s L^2 = RVI_0 \ . \tag{15.9}$$

Unlike the scattering coefficient, the scattering cross section is defined on a single molecule basis:

$$P_s = \sigma I_0 \qquad \text{(single molecule)} \ , \tag{15.10}$$

in which P_s denotes the total power scattered out of the incident beam. For a particular scattering direction the definition is

$$\frac{\mathrm{d}P_s}{\mathrm{d}\Omega} = \frac{\mathrm{d}\sigma}{\mathrm{d}\Omega} I_0 \ . \tag{15.11}$$

This last expression defines the so-called *differential scattering cross section* $\mathrm{d}\sigma/\mathrm{d}\Omega$. By comparison of eqs. 15.9 and 15.11 we find a relation between macroscopical and microscopical parameters:

$$R = \frac{N}{V} \frac{\mathrm{d}\sigma}{\mathrm{d}\Omega} = \rho \frac{\mathrm{d}\sigma}{\mathrm{d}\Omega} \ . \tag{15.12}$$

The inclusion of the factor N (the total number of scattering molecules in the scattering volume V) assumes each molecule to scatter light independently of all the others, as will be explained in the next section.

1.4 Fluctuations

Coherent light scattering (like Rayleigh scattering) can only result from non-uniformities in the optical properties of a medium. In a completely homogeneous medium, illuminated by a plane wave (that is, the illumination is also homogeneous; figure 15.3), the scattering by any volume element (*voxel*) dV_1, in any particular direction θ, is nearly always cancelled by destructive interference with scattered light by another voxel, dV_2. There is one exception, viz. the forward direction, for which $\theta = 0$ and the distance between dV_1 and dV_2 goes infinite.

In practice, a medium is never completely homogeneous, nor illuminated by a plane wave. For the specific case of laser diagnostics of combustion phenomena, for instance, the medium is spatially non-uniform in composition, temperature and, consequently, density, and all these parameters also fluctuate in time.

These non-uniformities are crucial to the occurrence of non-resonant, coherent light scattering. To see this, consider a total scattering volume V in a gaseous medium with nominal number density ρ, that is illuminated by a uniform intensity I_0. The volume V can be divided into a large number, $\mathcal{N}$, of identical voxels of volume $\Delta V = V/\mathcal{N}$, each of which is sufficiently small so that all molecules in ΔV essentially radiate in phase. That is, the linear dimensions of ΔV are small with respect to the wavelength of the incident light[2], but large with respect to molecular dimensions. The radiated electric fields of all molecules in ΔV then add up, so that the intensity ($\propto |E|^2$) of the radiation scattered into some direction θ by ΔV is given by

$$I_{\Delta V}(\theta) = N^2 I_{\mathrm{mol}}(\theta) \ , \tag{15.13}$$

in which I_{mol} is the intensity due to scattering by a single molecule, and $N = \rho \Delta V$ is the number of molecules in ΔV. From the discussion accompanying figure 15.3 we concluded that there would be total cancellation of the fields for $\theta \neq 0$ if N were constant. If N fluctuates, this cancellation will not be perfect. What remains is a net intensity

$$I_V(\theta) = \sum_{\Delta V} (N - \langle N \rangle)^2 I_{\mathrm{mol}}(\theta) = \langle \Delta N \rangle^2 \mathcal{N} I_{\mathrm{mol}}(\theta) \ , \tag{15.14}$$

in which $\langle \Delta N \rangle^2 = \langle N^2 \rangle - \langle N \rangle^2$, and the angle brackets denote averages. For a dilute ideal gas, $\langle \Delta N \rangle^2 = \langle N \rangle$, and we have

$$I_V(\theta) = \langle N \rangle \mathcal{N} I_{\mathrm{mol}}(\theta) = \rho V I_{\mathrm{mol}}(\theta) \ . \tag{15.15}$$

A similar argument holds for fluctuations in other parameters that affect the optical properties of a medium.

In short: Coherent light scattering is due to fluctuations in the (optical) properties of a medium, and the proportionality to density is a result of the statistical properties of a dilute gas. Note that incoherent light scattering (like spontaneous Raman scattering) also obeys relation 15.15, but more directly because every single scattering event is uncorrelated with other events.

1.5 Rayleigh scattering

A scattering event is termed *elastic* if the scattered light has the same frequency as the incident light, that is, if there has been no energy transfer to the scattering agent. On close inspection, molecular scattering can hardly ever be elastic in this strict sense, because random motion of the scatterers imposes a Doppler shift on the scattered light. The (angular) frequency of light scattered off a molecule moving with velocity $\vec{v}$ is given by

$$\nu_s = \nu_0 - \frac{1}{2\pi} \vec{k} \cdot \vec{v} \quad \text{or} \quad \omega_s = \omega_0 - \vec{k} \cdot \vec{v} \ , \tag{15.16}$$

[2]This statement is in fact not completely correct. The relevant scale is not so much the wavelength, but rather the inverse of the so-called *scattering wavevector*, $\vec{k} = \vec{k}_{\mathrm{inc}} - \vec{k}_{\mathrm{sc}}$. Under typical experimental conditions (say 90° scattering), $|\vec{k}| \approx |\vec{k}_{\mathrm{inc}}|$, and the argument in the text holds. For nearly-forward scattering, however, $|\vec{k}| \ll |\vec{k}_{\mathrm{inc}}|$, and density fluctuations on a much larger scale become important. This gives rise to effects known as Collective Light Scattering (CLS). These effects will not be considered here; a review can be found in Bonnet *et al*. (1995).

in which $\vec{k}$ is the scattering wave vector and $\omega_0 = 2\pi\nu_0$ is the angular frequency of the incident light. We will enlarge the definition of elastic scattering to include this kind of quasi-elastic scattering, and will reserve the term *inelastic scattering* for events in which energy is transferred to internal degrees of freedom (Raman scattering) or collective motion (Brillouin scattering) of the scatterers. For elastic scattering of monochromatic incident light by a (single component) gas at temperature T, the spectrum of the scattered light will reflect the Maxwell-Boltzmann distribution of the molecular velocities, that is,

$$I_s(\nu) = I_s \frac{1}{\sqrt{2\pi}\,\delta} \exp\left\{-\frac{(\nu-\nu_0)^2}{2\delta^2}\right\} , \tag{15.17}$$

with a rms-width δ given by

$$\delta = \nu_0\sqrt{\frac{k_B T}{mc^2}} \tag{15.18}$$

(k_B is the Boltzmann constant, m is the molecular mass, c is the speed of light). The spectral lineshape[3] thus has a gaussian profile, and is said to be *Doppler broadened*.

Because the mass of the scattering particles figures in the expression for the spectral width of the scattered light, the Doppler broadening for scattering off particulates (like soot or dust particles, or liquid fuel or oil droplets) is usually negligible. This is exploited in the technique of Filtered Rayleigh Scattering (FRS) for temperature field measurements (see below, Individual techniques, §2.5).

The differential cross section for 90° Rayleigh scattering of monochromatic light can be expressed in terms of the refractive index n as

$$\left(\frac{\mathrm{d}\sigma}{\mathrm{d}\Omega}\right)_{\mathrm{Rayl}} = \frac{4\pi^2(n-1)^2}{\rho^2 c^4}\nu^4 , \tag{15.19}$$

and the power radiated into a solid angle $\Omega \ll 4\pi$ is

$$P_{\mathrm{Rayl}} = \eta\rho\left(\frac{\mathrm{d}\sigma}{\mathrm{d}\Omega}\right)_{\mathrm{Rayl}} \Omega V I_0 , \tag{15.20}$$

in which η denotes a collection efficiency. Since the refractive index term $(n-1)$ is itself proportional to the density, the differential scattering cross section is independent of the density, and Rayleigh scattering is therefore a measure for the total density ρ.

For scattering by a mixture of gases, every component (with mole fraction x_i) contributes to the total scattered power according to its own efficiency, and

$$P_{\mathrm{Rayl}} = \eta\rho\sum_i x_i\left(\frac{\mathrm{d}\sigma}{\mathrm{d}\Omega}\right)_i \Omega V I_0 . \tag{15.21}$$

Thus, in order to interpret a measurement of Rayleigh scattered power in terms of a total density, the composition of the medium should be known[4]. Moreover, since the scattering cross sections of particulates are many orders of magnitude larger than those of molecules, the scattering medium must be virtually devoid of particulates for (unfiltered) Rayleigh scattering to be interpretable. This, of course, considerably limits its application to combustion diagnostics.

[3] Note that $I_s(\nu)$ and I_s in eq. 15.17 have different units: I_s is an intensity (*e.g.* W/m^2), whereas $I_s(\nu)$ is a spectral intensity (*e.g.* W/m^{2}cm^{-1}).

[4] Or, at least, the *effective* differential scattering cross section

$$\left(\frac{\mathrm{d}\sigma}{\mathrm{d}\Omega}\right)_{\mathrm{eff}} = \sum_i x_i\left(\frac{\mathrm{d}\sigma}{\mathrm{d}\Omega}\right)_i$$

should be known to within the desired experimental accuracy.

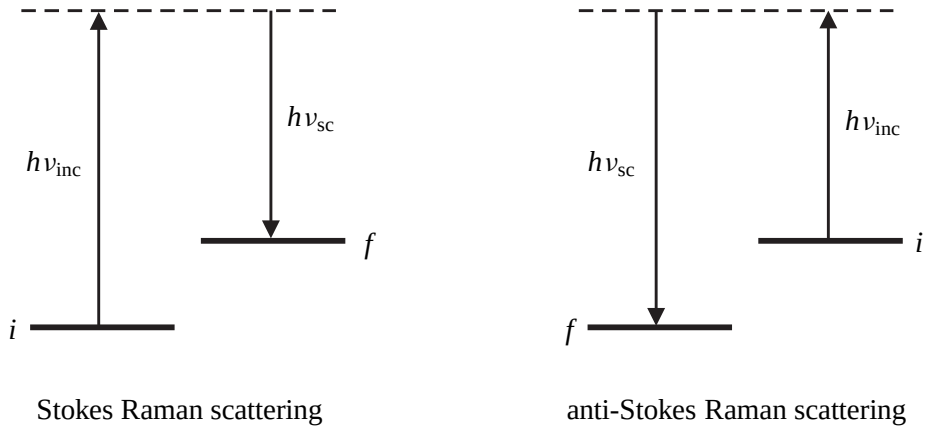

Figure 15.4: Energy level schemes for Stokes (red shifted; left) and anti-Stokes (blue shifted; right) Raman scattering. The initial and final energy levels of the molecular scattering partner are indicated by i and f, respectively.

1.6 Raman scattering

Unlike Rayleigh scattering, Raman scattering comes in a few flavours, like rotational, vibrational and electronic Raman scattering, stimulated Raman scattering (SRS), and CARS. These differ in the molecular energy levels that are involved, and whether they are spontaneous or stimulated processes. Here we will consider only vibrational Raman scattering, which is probably the most widely used form of spontaneous Raman scattering. CARS will be dealt with in a separate lecture.

Raman scattering involves an exchange of energy between the electromagnetic field and the internal degrees of freedom of the scattering molecules. In the case of vibrational Raman scattering this implies a change in the vibrational state (quantum number) of the molecule by the scattering event (figure 15.4). If the molecule takes up energy from the field (the only possibility for a molecule in the vibrational ground state), the scattered light will be red-shifted with respect to the incident light, and the process is called *Stokes Raman scattering*. If a vibrationally excited molecule gives up energy to the field, the scattered light is blue-shifted, and the process is called *anti-Stokes Raman scattering*. Since the vibrational energy of molecules is quantised, energy conservation imposes a discrete frequency spacing between incident and Raman-scattered light. The frequency difference is called *Raman shift*, and is given by

$$\Delta\nu_R = \nu_{\mathrm{inc}} - \nu_{\mathrm{s}} = \frac{E_i - E_f}{h} \,, \tag{15.22}$$

in which $E_{i,\,f}$ denote the inital and final energy levels of the molecule, and h is Planck's constant. Expressions for the vibrational energy levels have been given in the previous lecture on Molecular Physics. Because the vibrational mode frequencies are specific for a specific molecule, a Raman spectrum provides information on the chemical composition of the medium. Raman shifts of a few representative molecules are collected in table 15.2.

Polyatomic molecules (three or more atoms) may contribute more than one band to the Raman spectrum, since they possess more than one internal degree of freedom. An M-atomic molecule has $(3M-6)$ internal degrees of freedom (or $(3M-5)$ if it is a linear molecule), all of which correspond to a vibrational mode (some of which may be degenerate, though). Which of these modes show up in a Raman spectrum is determined by selection rules, and, more generally, by transition strengths. For molecules that possess some degree of structural symmetry (like homonuclear diatomics (H_2, O_2, N_2)

Table 15.2: Raman shifts ($\Delta\nu_R$), differential scattering cross sections ($d\sigma/d\Omega$) and vibration-rotation interaction constant (α_e) for a number of molecules relevant to combustion processes. (After Eckbreth (1996))

			$d\sigma/d\Omega$ (10^{-30} cm^2/sr)			
Molecule	band	$\Delta\nu_R$ [cm^{-1}]	337 nm	532 nm	α_e [cm^{-1}]	Remarks
N_2		2331	2.8	0.37	0.0173	
H_2		4160	8.7	0.943	3.062	
O_2		1556	3.3	0.47	0.0159	
NO		1877	1.5	0.2	0.0171	
NO_2	ν_1	1320	51.0	7.37		
	ν_2	754	24.0	3.63		
CO		2145	3.6	0.48	0.0175	
CO_2	ν_1	1388	4.2	0.6		complex
	$2\nu_2$	1285	3.1	0.45		
H_2O	ν_1	3657	7.8	0.9		
CH_4	ν_1	2915	21.0	2.6		complex
	ν_3	3017	14.0	1.7		
C_2H_4	ν_1	3020	16.0	1.9		
	ν_2	1623	5.4	0.76		
C_6H_6	ν_1	3070	30.0	3.7		
	ν_2	991	44.0	5.6		

or CH_4, CO_2, H_2O, to mention a few examples relevant to combustion), the Raman spectrum tends to be complementary to the linear absorption spectrum, in the sense that any particular vibrational mode tends to be either Raman active or infrared active[5].

As in the case of Rayleigh scattering, the Raman scattered power onto a detector subtending a solid angle $\Omega \ll 4\pi$ can be written as

$$P_{\mathrm{Ram}}(\Delta\nu_R^{(i)}, \theta) = \eta\rho x_i \left(\frac{d\sigma_{\mathrm{Ram}}}{d\Omega}\right)_i \Omega V I_0 \ , \tag{15.23}$$

in which only a single chemical species is assumed to contribute to the band with a Raman shift $\Delta\nu_R^{(i)}$. Note that the detection efficiency, η, now will also contain a term due to the required spectral filtering of the scattered light.

As compared to Rayleigh scattering, Raman scattering is weaker but has the advantage of being inelastic. A Raman spectrum contains information on the composition of the scattering medium (every chemical species gives rise to its own specific Raman bands), and spectral filtering allows to suppress the light elastically scattered off particulates and solid surfaces. Moreover, since Raman scattering (like, by the way, Rayleigh scattering, but unlike Laser-Induced Fluorescence (LIF)) is a second-order process, its scattering cross section is virtually independent of the environmental conditions,

[5] A vibrational mode is called *infrared active* if it can be excited by absorption of single photons, which, in the case of vibrations, are in the infrared spectral range.

notably pressure and temperature (within limits, of course). As a result, Raman scattered intensities are relatively easy to interpret quantitatively.

Obvious applications for Raman spectroscopy in the field of combustion studies are the quantitative determination of molecular densities and of temperature. The latter is probably most conveniently done by comparing the first Stokes and anti-Stokes vibrational Raman bands of one particular molecule, e.g. N_2. (When H_2 is present rotational Raman scattering is an alternative, because of the relatively large frequency spacing between individual lines.) From eq. 15.23 it follows that

$$\frac{P(\Delta\nu_S)}{P(\Delta\nu_{aS})} = \frac{x(v=0)}{x(v=1)} = \exp\left\{+\frac{E_v}{k_B T}\right\} , \tag{15.24}$$

in which E_v denotes the energy of the first vibrationally excited state (see lecture on Molecular Physics). The temperature in eq. 15.24 is actually a *vibrational temperature*, and its interpretation as an overall temperature involves the assumption of thermal equilibrium.

A few spectroscopic details have been left out of the discussion so far, and will be shortly commented upon here. Vibrational Raman scattering not necessarily implies that rotation is conserved. In fact, Raman scattering being a 2-photon process, the rotational selection rules are $\Delta K = 0, \pm 2$. Since, however, the transition strengths for the O-branch ($\Delta K = -2$) and the S-branch ($\Delta K = +2$) are often (diatomics) much smaller than that for the Q-branch ($\Delta K = 0$), vibrational Raman scattering is, for many practical purposes, Q-branch scattering. Still, because the rotational constant B_v weakly depends on the vibrational state (see again the lecture on Molecular Physics), this does imply some extent of inhomogeneous spectral broadening of the Raman scattered light. The distance between adjacent rotational lines in Q-branch Stokes Raman scattering is given by

$$\delta\nu_Q = \nu_{v=1;\,J+1} - \nu_{v=1;\,J} = 2\alpha_e(J+1) , \tag{15.25}$$

which is on the order of 0.5 cm^{-1} for typical values of α_e (see table 15.2, and note the exception H_2). Although this is not particularly large compared with the resolution of typical spectroscopic filters (and thus will not generally be a concern in the interpretation of Raman intensities), it is large compared to typical Doppler shifts. As a result, spontaneous Raman scattering is not very suitable for use in Doppler-based velocimetry or thermometry.

1.7 The relation to fluorescence

Laser Induced Fluorescence (LIF) is a two-step process, photon absorption followed, some time later, by spontaneous photon emission. Both steps are typically single photon events (although various kinds of multiphoton schemes have been reported), and occur between specific energy levels of the molecules involved. Typically, the absorption step promotes a molecule to an electronically excited state (this requires a visible or UV photon), and the radiative decay by spontaneous emission back to the ground state is monitored (see the chapter on Molecular Physics for a more extensive discussion). This implies two main differences with Raman scattering:

- Because both the absorption and the emission step are resonant, the transition strengths in LIF are usually much larger than those involved in Raman scattering. In favourable circumstances (and combustion is <u>not</u> one of those!) LIF allows the detection of single molecules.

- Because the emission step is a spontaneous emission event, the molecule stays a finite time (typically in the order of $1 - 100$ ns) in the excited state. During this time it is subject to interaction with its environment, most notably due to intermolecular collisions. This may result in

premature non-radiative decay, causing a reduced fluorescence yield. This severely complicates a quantitative analysis of LIF intensities.

Fluorescence may interfere with Raman scattering (and, to a lesser extent, Rayleigh scattering) if the incident light has a wavelength close to an optically allowed transition out of a populated state. Exactly how close 'close' means depends on the strengths of the particular transitions involved. Since LIF can easily be several orders of magnitude stronger than Raman scattering, it is generally advisable for Raman experiments to stay several tens of absorption linewidths away from resonance. For the same reason, care should be taken to remove a possible broad-band component from the incident light.

1.8 Some experimental issues

Laser diagnostics of combustion processes nearly always involve shining light on luminous matter. (Emission spectroscopy being the only exception.) The luminous background of the flame itself is generally regarded as a nuisant complication. For this reason, laser diagnostics generally employ pulsed lasers and spectrally selective, gated ('pulsed') detection.

The work horses in pulsed laser spectroscopy are excimer lasers and Nd:YAG (Nd-doped Yttrium-Aluminium Garnet) lasers, either used on their own or as a pump laser for tunable dye lasers. A few parameters of typical laser systems have been collected in table 15.3 (for purposes of illustration only). Under typical experimental conditions of a pulsed laser running at 10 Hz repetition frequency (rep rate; f_r) and gated detection of the scattered light over $\tau_g = 100$ ns after each laser pulse, the luminous background of the flame itself is suppressed by a factor of $(f_r \tau_g)^{-1} = 10^6$. This is usually sufficient to render the background negligible if a narrow wavelength region of interest is singled out by a suitable spectral filter.

The non-resonant light scattering techniques discussed above have the advantage that they can be done with virtually all laser systems, and do not require tunability of the incident light. The ν^4-dependence of the scattering cross section favours the use of UV lasers, but care should be taken to avoid LIF interference. Furthermore, an optimum should be sought between the scattering efficiency and the detection efficiency. Frequently used fixed-frequency[6] lasers that offer a good compromise given the current technology are the tripled Nd:YAG laser ($\lambda \approx 355$ nm) and the KrF excimer laser ($\lambda \approx 248$ nm). These laser systems also offer high-power pulses, which, for the hardly saturable non-resonant techniques, is directly beneficial for the scattered power level. In cases where the incident beam is tightly focussed, care must be taken to stay below the threshold for the onset of the stimulated counterparts of the spontaneous processes discussed above.

On the detection side there is one issue of particular relevance to optical combustion diagnostics, and that is the phenomenon of beam steering. Light generated or scattered in a probe volume located within a flame must travel through (part of) the flame before reaching the detector. Refractive index gradients encountered on the way (caused by temperature or composition gradients), will cause the location of the probe volume to fluctuate in time. Although the problem is well known, it is difficult to perform an *a posteriori* correction for it (see [6] for a recent attempt).

References

[1] Kohse-Höinghaus, K., and Jeffries, J.B. (2002): Applied combustion diagnostics. Taylor and Francis, New York.

[6] In fact, the lasers mentioned can be tuned to some extent.

Table 15.3: Parameters of typical pulsed excimer and Nd:YAG laser systems. Both higher and lower performance systems are commercially available. This compilation gives central wavelength (λ), pulse duration (τ), pulse energy (E), spectral width of broad and narrow-band versions ($\Delta\nu$), and pulse repetition rate.

Laser	λ [nm]	τ [ns]	E [mJ/pulse]	$\Delta\nu$ [cm^{-1}]		Rep rate
Excimer lasers		20		broad	injection seeded	$0-100$
ArF	193		200	150	1.0	
KrF	248		350	50	0.5	
XeCl	308		250	30	0.3	
Nd:YAG system		5				$10-50$
fundamental	1064		1500	1	0.003	
2nd harm.	532		750	2	0.006	
3rd harm.	355		300	3	0.009	

[2] Eckbreth, A.C. (1996): Laser diagnostics for combustion temperature and species, 2nd ed. Gordon & Breach, (UK).

[3] Demtröder, W. (1996): Laser spectroscopy; Basic concepts and instrumentation. Springer Verlag, Berlin etc..

[4] Milonni, P.W., and Eberly, J.H. (1988): Lasers. Wiley, New York.

[5] Boyd, R.W. (1992): Nonlinear optics. Academic press, San Diego etc., chapter 7.

[6] Trollinger, J., Weber, D., Rose, W. (2002): An aero-optical test and diagnostics simulation technique. AIAA paper 2002-0825.

2 Individual techniques

The table below summarizes a few details of more-or-less commonly used (laser) optical diagnostic techniques in combustion studies. Most of the techniques mentioned in the table are concisely discussed on the pages that follow (last column; exclamation marks indicate subjects that are discussed in other chapters of this course). References are given at the end of each section. A dot in one of the following columns indicates the parameter that any particular technique is able to measure:

ρ: overall molecular density
ρ_i: specific molecular density
(* emission spectroscopy is a measure for excited state species density)
T: temperature
$\vec{v}$: velocity
f: soot volume fraction
d: soot particle diameter.

The remaining columns specify experimental parameters:

D: maximum dimensionality in which data can be obtained simultaneously
($\int$: Line-of-sight technique)
e/i: elastic or inelastic light scattering
m/p: molecular or particulate light scattering
n: power dependence, I^n, with I the intensity

Blank entries: not applicable

Technique	ρ	ρ_i	T	$\vec{v}$	f	d	D	e/i	m/p	n	§
Absorption		•	•		•		$\int$	e	m	0	2.2,2.3
CRDS		•	•		•		$\int$	e	m	0	2.4
Emission		$*$					$\int$		m		2.1
Raman (spont)		•	○				2	i	m	1	2.6
CARS		•	•				0 (1)	i	m	$2+1$	!
LIF		•	•				2	i	m	$0-1$	2.7
Rayleigh	•						2	e	m	1	2.5
FRS	•		•	•			2	(i)	m	1	2.5
PIV, PTV				•			2	e	p		!
LDA				•			0	e	p		!
DGV				•			2	(i)	p		(2.5)
MTV				•			2	i	m		2.8
(D)FWM		?	•	•			0	(e)	m		
LII					•	•	2	i	p	?	2.9
Mie						•	2	e	p	1	

Table 15.4: Overview of a number of laser diagnostic techniques that have been used for combustion characterisation.

2.1 Spontaneous Emission Spectroscopy

Spontaneous emission spectroscopy (or chemiluminescence spectroscopy) is the most straightforward optical technique for combustion diagnostics. The generic setup is sketched in figure 15.5. Some light collection optics ('lens') images light emitted by (part of) the flame onto the entrance slit of a monochromator or spectrograph. The latter spectrally disperses the incident light, and the individual components are detected by a photomultiplier tube (PMT) or, more efficiently, a CCD array. A typical spectrum, obtained from a partially premixed CH_4/air Bunsen burner, is shown in figure 15.6.

By its nature, emission spectroscopy is sensitive only to chemical species that are present in (electronically) excited states. Moreover, these excited states must have an efficient radiative decay channel, and the excited molecules must be present in sufficient amounts for their fluorescence to exceed the background luminosity (due, for instance, to glowing soot or furnace walls). The collected power in a specific emission band (that is, spectrally integrated over the band of interest) can be written as

$$P_s = C\wp\rho_\alpha^* \,, \tag{15.26}$$

in which C is a detection efficiency, $\wp = k_r/(k_r + k_{nr})$ a Stern-Volmer factor (the ratio of the radiative decay rate k_r to the total (radiative plus non-radiative) decay rate) and ρ_α^* the density of the excited state species (irrespective of quantum state; we look at the spectrally integrated power). Of course, there is no obvious relation between ρ_α^* and ρ_α, the density of the same chemical species in the ground electronic state. Even though the measured emitted power is directly proportional to the density ρ_α^*, the technique is hard to calibrate because of the difficulty to create a well-known density of excited state species in the probe volume. Moreover, there is a risk of spectral interference, the spectral resolution typically being limited by the resolving power of the spectrometer. Therefore, emission spectroscopy is usually used for qualitative purposes.

The spatial resolution of emission spectroscopy is determined by the collection optics. In general, the (effective) detector size determines the area of the probe volume perpendicular to the line of sight, whereas the depth of field determines the length of the probe volume along the line of sight. Probe volume sizes down to 0.1×0.8 mm^2 (diameter $\times$ length) have been achieved using a Cassegrain telescope [2]. In cases where optical access is limited (high-pressure combustion, for instance) optical fibers can be used as collection optics, at the expense of sacrificed spatial resolution. The latter, however, can be recaptured to some extent by use of tomographic techniques (see e.g. [3]).

In summary, emission spectroscopy is easy to implement, relatively inexpensive and it requires minimal optical access. It does, however, provide only limited information.

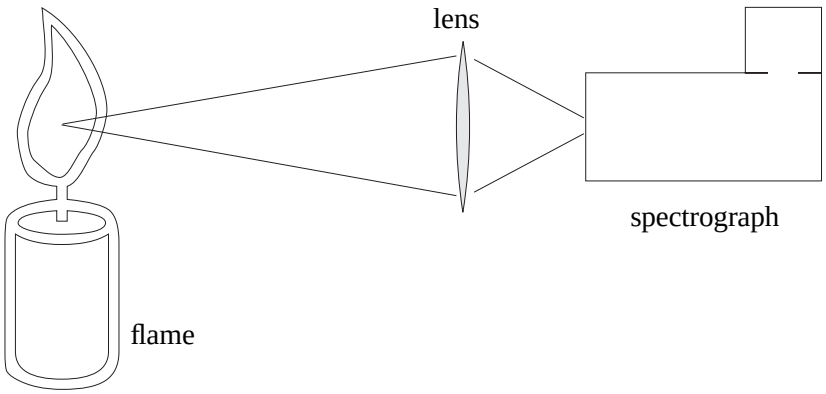

Figure 15.5: Generic experimental setup for (spontaneous) emission spectroscopy.

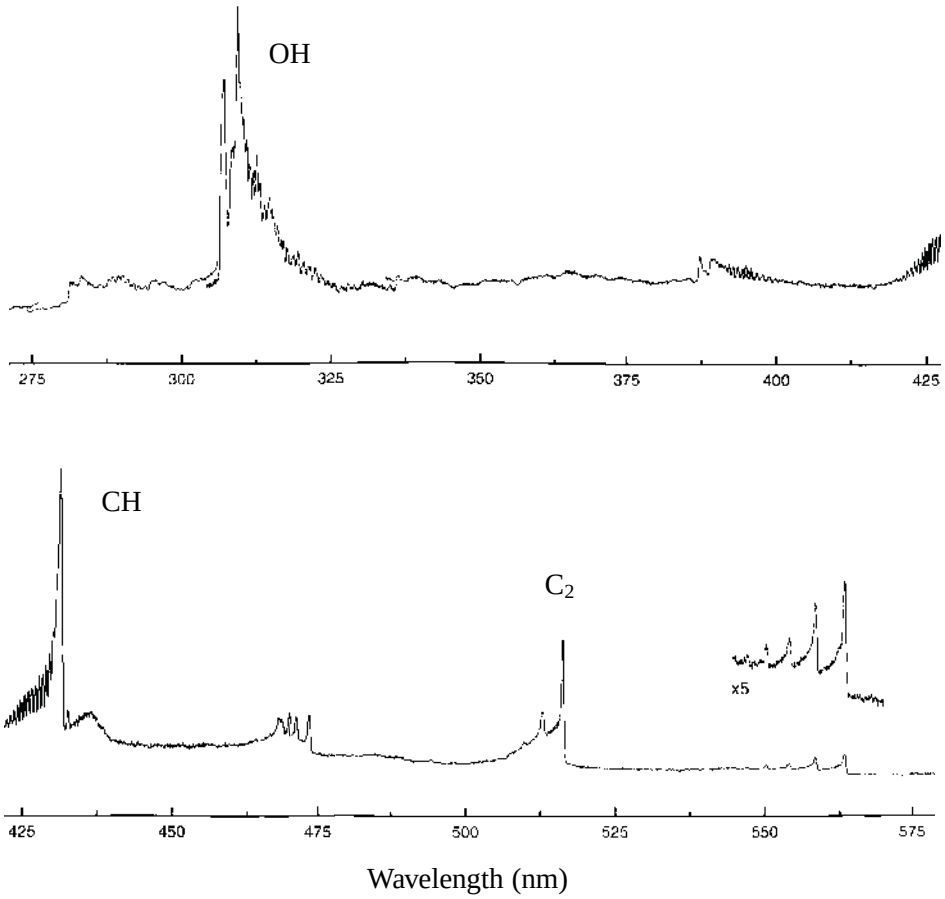

Figure 15.6: Emission spectrum of a partially premixed Bunsen flame. The main features are due to the 3064 Å system of OH* ($A^2\Sigma^+ \rightarrow X^2\Pi$ at 308 nm), the 4300 Å system of CH* ($A^2\Delta \rightarrow X^2\Pi$ at 430 nm) and the Swan bands of C_2^* ($A^3\Pi_g \rightarrow X'^3\Pi_u$ at 516 nm).

References

[1] Pearse, R.W.B., Gaydon, A.G. (1976): The identification of molecular spectra. Chapman and Hall, London.

[2] Ikeda, Y., Kojima, J., Hashimoto, H., Nakajima, T. (2002): Detailed local spectra measurement in high-pressure premixed laminar flame. AIAA paper 2002-0191.

[3] Hentschel, W. (2002): Optical diagnostics in DI gasoline engines. In Kohse-Höinghaus, K. and Jeffries, J.B.: Applied Combustion Diagnostics. Taylor and Francis, New York. Chapter 17.7.

2.2 Absorption Spectroscopy: Linear absorption

Linear absorption spectroscopy is a very straightforward optical diagnostic technique, in which a light beam is sent through the medium of interest, and the transmitted power is recorded as a function of wavelength. Spectral selectivity can be achieved either at the source (scanning configuration; tunable, narrow-bandwidth light source (typically a diode laser or dye laser) and broad-band detector) or at the

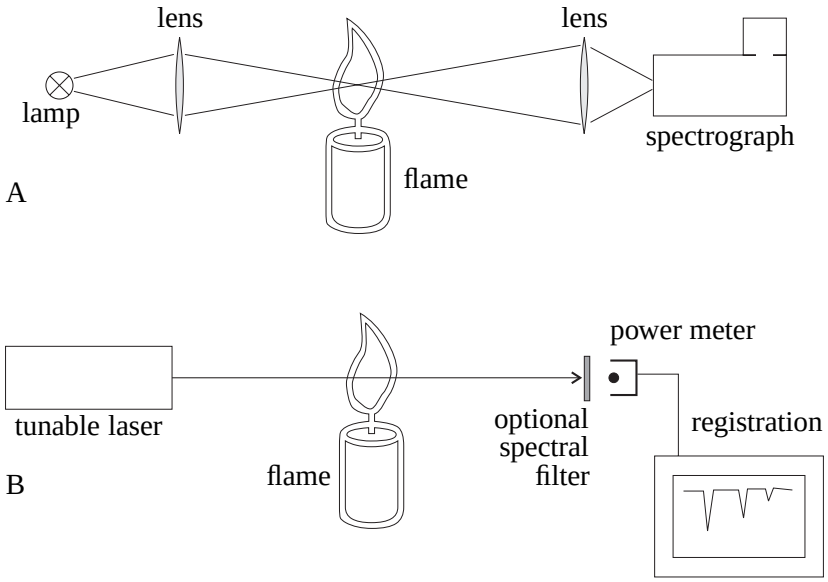

Figure 15.7: Generic experimental setup for linear absorption measurements. A) Multiplexed configuration (spectral resolution at the detector); B) Scanning configuration (spectral resolution at the source).

detector (multiplexed configuration; broad-band source (like a high-pressure Xe lamp), spectrograph in front of the detector). Generic experimental setups for both configurations are shown in figure 15.7. In order to discriminate the external light against the flame luminosity, a light source with high spectral power is advantageous. This is most easily achieved using a laser source in the scanning configuration, and I have focussed the following discussion on that scheme. An example of an absorption spectrum (low-pressure C_2H_4 in the infrared spectral range) is shown in figure 15.8.

The relation between transmitted laser intensity (or power) and the molecular density is rather complicated in the most general case, mainly because the finite bandwidths of both the laser and the molecular transitions have to be taken into account. Below I will derive the general case first[7], and then discuss a few simplifications.

Assume a light source with spectral intensity distribution described by

$$I_L(\nu)\,\mathrm{d}\nu = I_0(\nu_L)\,g(\nu-\nu_L)\,\mathrm{d}\nu\ , \tag{15.27}$$

in which $I_L(\nu)$ is a spectral intensity (units J/m^{2}cm^{-1}), I_0 is the spectrally integrated laser intensity (J/m^2), ν is the frequency, ν_L the central laser frequency, and g a spectral distribution function (cm = (cm^{-1})$^{-1}$). We will take g normalised, so that

$$\int g(\nu-\nu_L)\,\mathrm{d}\nu = 1 \quad \text{and} \quad \int I_L(\nu)\,\mathrm{d}\nu = I_0(\nu_L)\ . \tag{15.28}$$

Lambert-Beer's law for absorption of narrow-band light by a thin slice of the medium (figure 15.9) reads

$$\mathrm{d}\left[I_L(\nu)\,\mathrm{d}\nu\right] = -\left[I_L(\nu)\,\mathrm{d}\nu\right]\cdot\alpha(\nu)\,\mathrm{d}z\ . \tag{15.29}$$

The absorption coefficient $\alpha(\nu)$ can be written as

$$\alpha(\nu) = \sum_i \sigma_i\,(\rho_i - \rho_i^*)\ f_i(\nu-\nu_i)\ , \tag{15.30}$$

[7]Absorption is discussed in the frequency domain, using wavenumbers (cm^{-1}) as a unit. (1 cm^{-1} $\equiv$ 30 GHz)

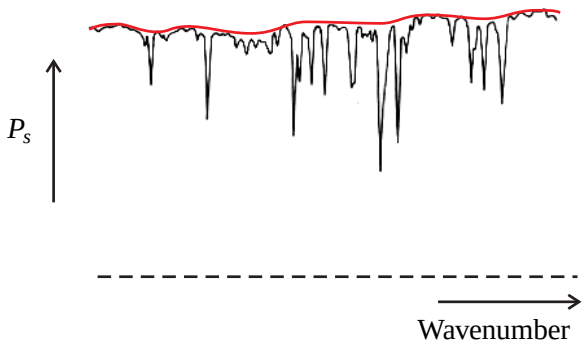

Figure 15.8: Part of the infrared absorption spectrum ($\lambda \approx 3.2\ \mu$m) of ethene, C_2H_4, under low pressure (ca. 130 Pa), recorded with a tunable Color Center Laser (frequency bandwidth $\approx$ 5 MHz) as light source and a pyro-electric detector to measure transmitted laser power. The dashed line indicates the zero power level. Dips in the transmitted power all correspond to specific transitions between rovibrational energy levels of C_2H_4. Note that the power level of the laser is not constant during the scan (red wavy line).

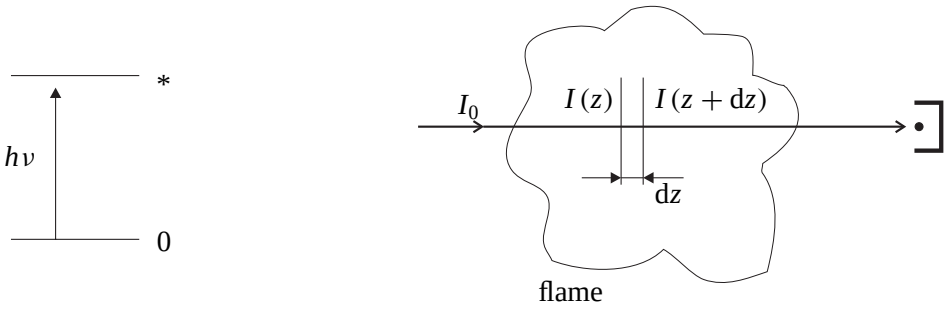

Figure 15.9: Configuration for linear absorption measurements. A laser beam travels along the z-direction through a non-uniform medium. Its wavelength is close to a transition in a particular chemical species (lower state 0, upper state $*$).

in which the summation runs over all transitions in all chemical species in the illuminated volume, σ is the absorption cross section (m^2), ρ_i and ρ_i^* are the number densities of molecules in the lower and upper level of a transition, respectively (m^{-3}) and f is the (dimensionless) absorption line shape function. For non-monochromatic light, eq. 15.30 can be integrated to yield

$$\begin{aligned} \mathrm{d}I_L &= \int_\nu \mathrm{d}\left[I_L(\nu)\,\mathrm{d}\nu\right] \\ &= -\sum_i \sigma_i\,(\rho_i - \rho_i^*) I_0(\nu_L) \int_\nu g(\nu-\nu_L)\, f_i(\nu-\nu_i)\,\mathrm{d}\nu\,\mathrm{d}z\ . \end{aligned} \tag{15.31}$$

In this equation the spectral integrals $\int g(\nu-\nu_L)\, f_i(\nu-\nu_i)\,\mathrm{d}\nu$ are called *overlap integrals*, because they describe the overlap of the incident laser spectrum with the absorption spectrum of a particular molecule. Finally, the expression for the transmitted intensity becomes

$$I_L(z) = I_L(0) \exp\left\{ -\int_0^z \sum_i \sigma_i\,(\rho_i - \rho_i^*)\, g f(\nu_L, \nu_i)\,\mathrm{d}z \right\}\ , \tag{15.32}$$

in which we have written gf for the overlap integrals.

Clearly, since absorption spectroscopy is a line-of-sight technique, there is no spatial resolution along the propagation direction of the laser beam. (See section 2.3 for a variant that *does* provide this.) Equation 15.32 is complicated, and not easily inverted to yield (even average) molecular densities. In the general case, several different chemical species (and particulates) may contribute to the absorption, and in non-uniform flames not only the densities ρ_i and ρ_i^* will vary with position, but also the overlap integrals, because of the composition- and temperature-dependence of the absorption line shape function f_i.

Often, absorption spectroscopy is used under conditions that allow considerable simplification of eq. 15.32. When visible or UV light is used in the measurement (this usually corresponds to electronic transitions), the upper levels of the transitions involved are insignificantly populated, even at temperatures relevant to combustion. In these cases ρ_i^* can be neglected.

Example: Absorption of 500 nm light (photon energy $\approx$ 2.5 eV) implies that the upper level of a transition is 2.5 eV above the lower level. At 2500 K ($kT \approx 0.22$ eV) the relative thermal population of these levels is $\rho^*/\rho \approx \exp\{-\Delta E/kT\} \approx 10^{-5}$.

If the incident frequency can be choosen such that only a single transition contributes to the absorption, the summation can be left out, resulting in

$$I_L(z) = I_L(0) \exp\left\{ -\int_0^z \sigma\rho(z) g f(\nu_L, z)\, \mathrm{d}z \right\} , \tag{15.33}$$

which is the least complicated expression that is still of fairly general use. Note, however, that also in this case it is not the average density ($\bar{\rho} = \int \rho(z)\, \mathrm{d}z$) that occurs in the exponent, but that the density is still 'weighted' by the possibly position-dependent overlap integral. A further simplification would be possible if the laser bandwidth were much smaller than the absorption linewidth (then $\int g(\nu - \nu_L) f_i(\nu - \nu_i)\, \mathrm{d}\nu \approx f_i(\nu_L - \nu_i)$), but that is not generally the case.

The sensitivity of linear absorption spectroscopy is determined by the minimum intensity decrease, $\Delta I = I_L(0) - I_L(z)$, that can be detected. This is determined to a large extent by the stability of the incident intensity (both in time and in frequency). With pulsed laser systems (notorious for their pulse-to-pulse fluctuations), typical values are $\Delta I / I_L(0)\ 10^{-2}$; with stable cw systems (notably diode lasers) and suitable detection techniques (lock-in detection and/or frequency modulation; see DLS) 10^{-5} can be achieved in quiescent media. Higher sensitivity requires a different approach, like Cavity Ring-Down Spectroscopy (CRDS, §2.4) or Laser-Induced Fluorescence (LIF; §2.7). Examples of applications of diode-laser-based absorption spectroscopy to combustion can be found in ACD [1, 2].

References

[1] Allen, M.G., Furlong, E.R., Hanson, R.K. (2002): Tunable diode laser sensing and combustion control. In Kohse-Höinghaus, K. and Jeffries,J.B.: Applied Combustion Diagnostics. Taylor and Francis, New York. Chapter 18.

[2] Zahniser, M.S., Nelson, D.D., Kolb, C.E. (2002): Tunable infrared laser differential absorption spectroscopy (TILDAS) sensors for combustion exhaust pollutant quantification. In Kohse-Höinghaus, K. and Jeffries, J.B.: Applied Combustion Diagnostics. Taylor and Francis, New York. Chapter 26.

2.3 Absorption Spectroscopy: Bidirectional illumination

An interesting recent development in absorption spectroscopy makes use of light scattering (either Mie scattering off particulates, or LIF) induced by two counterpropagating laser beams to measure the local extinction coefficient with spatial resolution along the propagation direction of the laser beams as well. The method is still under development, but (in my opinion) elegant and promising.

First a qualitative description. Consider a thin, monochromatic laser beam traversing a medium (along the $+\hat{x}$-direction, say). The medium absorbs and scatters part of the light. An imaging detector (CCD camera, in practice) records the scattered light intensity, $S(x)$, with spatial resolution along (part of) the beam path. Clearly, $S(x)$ is proportional to the local scattering coefficient and the local laser intensity, that is, at each position x you record one datum ($S(x)$) which is a function of two unknowns. This is insufficient to solve for the parameter of interest, which is the local laser intensity. (Of course, knowing the laser intensity distribution along the beam path is equivalent to knowing the distribution of the extinction coefficient, see eq. 15.33.) Therefore, another measurement on the same medium is made, using an exactly counterpropagating laser beam. At any position, the signal $S'(x)$ is proportional to the same scattering coefficient, but to a different laser intensity, since the beam has arrived there after traversing a different part of the medium. Of course, the total attenuation of both beams will be the same. Thus, $S(x)$ and $S'(x)$ constitute two independent measurements based on two unknowns, so the latter can (at least in principle) be retrieved.

In more rigorous terms, the algorithm (for the slightly more general case of light sheet illumination) runs as follows (copied *in toto* from Stoffels *et al*. [1]). In general, images recorded by a CCD camera represent a spatially resolved light scattering efficiency. Assuming that only a thin plane perpendicular to the line of sight of the camera is illuminated, the signal $S(x, y)$ recorded by any pixel can be written as

$$S(x, y) = C A(x, y)\, n(x, y)\, \sigma(x, y)\, I_L(x, y), \tag{15.34}$$

in which (x, y) represent co-ordinates in the illuminated plane, $I_L(x, y)$ denotes the local illumination intensity, $\sigma(x, y)$ is a light scattering cross section, $n(x, y)$ the density of scattering particles and $A(x, y)$ a collection efficiency. The detailed forms of $n(x, y)$ and $\sigma(x, y)$ depend on the actual light scattering mechanism (like *e.g*. LIF, Rayleigh/Mie, Raman), whereas $A(x, y)$ is determined mainly by the experimental setup.

Equation 15.34 generally contains several unknowns, so that additional information is needed to extract any of these. Often, the density $n(x, y)$ is the parameter of interest, and then the distribution of the illumination intensity $I_L(x, y)$ should be known. This is a notoriously difficult problem in absorptive media, in which the intensity changes along the propagation direction in a way that depends on the characteristics of the medium at hand. As a rule, $I_L(x, y)$ is not amenable to direct and non-intrusive measurement.

In this paper the determination of $I_L(x, y)$ in an absorbing medium will be considered, using two distributions of elastically scattered light $S(x, y)$ recorded from the same probe volume but using laser

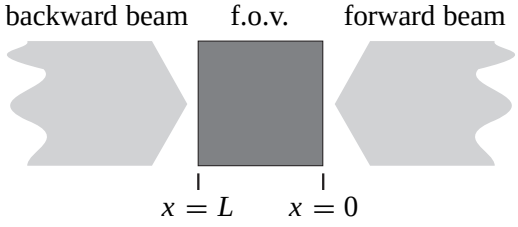

Figure 15.10: Configuration for bidirectional scattering.

illumination from opposite directions (see figure 15.10). If the images are recorded simultaneously (or in any case on a time scale that is much shorter than the time scale on which macroscopical fluctuations in the probe volume occur), the only difference between the images will be due to the different laser intensity distributions. Since, however, the attenuation of the laser beams is due to the same medium, the distribution of the attenuation coefficient can be reconstructed, as will be shown below.

The local intensity of a laser beam traveling along the positive x-direction (henceforth called 'forward direction') $I_{\text{for}}(x, y)$, is given by Lambert-Beer's law as

$$I_{\text{for}}(x, y) = I_{\text{for}}(0, y) \exp\left(-\int_0^x [n\sigma]_{\text{ext}}(x', y)\, \mathrm{d}x' \right), \tag{15.35}$$

in which $I_{\text{for}}(0, y)$ is the initial laser intensity at $(x = 0, y)$. This initial distribution need not be uniform along the y-direction. The factor $[n\sigma]_{\text{ext}}(x, y)$ is an effective attenuation coefficient for the laser radiation given by

$$[n\sigma]_{\text{ext}}(x, y) = [n\sigma]_{\text{sca}}(x, y) + [n\sigma]_{\text{abs}}(x, y), \tag{15.36}$$

where $[n\sigma]_{\text{abs}}(x, y)$ and $[n\sigma]_{\text{sca}}(x, y)$ are the effective contributions of absorption and scattering to the laser extinction. It will be assumed in the following that $[n\sigma]_{\text{abs}}(x, y) \gg [n\sigma]_{\text{sca}}(x, y)$.

If the laser sheet traverses the medium along exactly the same path but in opposite direction (called the backward direction), a similar equation can be used. The intensity of the backward travelling light sheet, $I_{\text{back}}(x, y)$, with an initial intensity $I_{\text{back}}(L, y)$ at $(x = L, y)$, is given by

$$I_{\text{back}}(x, y) = I_{\text{back}}(L, y) \exp\left(-\int_L^x [n\sigma]_{\text{ext}}(x', y)\, (-\mathrm{d}x') \right), \tag{15.37}$$

in which the reverse direction of integration is indicated explicitly.

If the forward and backward scattering signals are recorded simultaneously from the same area, both the loss factors $A(x, y)$ as well as the absorption cross section and density of the scattering particles (equation 15.34) are the same, and cancel if both scattering signals are divided. The sensitivity factor C may be different for the two cases (say C and C' for the forward and backward going beams, respectively), for instance because different detectors may be used. Using equations 15.34 to 15.37, the ratio $R(x, y)$ between both scattering signals can be written as

$$\begin{aligned} R(x, y) &\overset{\text{def}}{=} \frac{S_{\text{back}}(x, y)}{S_{\text{for}}(x, y)} \qquad (15.38) \\ &= \left(\frac{C'}{C} \frac{I_{\text{back}}(L, y)}{I_{\text{for}}(0, y)} \right) \exp\left(-\int_L^x [n\sigma]_{\text{ext}}(x', y)\, (-\mathrm{d}x') + \int_0^x [n\sigma]_{\text{ext}}(x', y)\, \mathrm{d}x' \right) \\ &= \left(\frac{C'}{C} \frac{I_{\text{back}}(L, y)}{I_{\text{for}}(0, y)} \right) \exp\left(2\int_0^x [n\sigma]_{\text{ext}}(x', y)\, \mathrm{d}x' - \int_0^L [n\sigma]_{\text{ext}}(x', y)\, \mathrm{d}x' \right). \end{aligned}$$

Note that after the division of the signals only the part concerning the extinction of the laser radiation is left and the experiment actually is reduced to measuring extinction. Taking the natural logarithm of

the ratio of the scattered signals results in

$$\ln R(x, y) = \ln\left(\frac{C'}{C}\frac{I_{\text{back}}(L, y)}{I_{\text{for}}(0, y)}\right) + 2\int_0^x [n\sigma]_{\text{ext}}(x', y)\,\mathrm{d}x' - \int_0^L [n\sigma]_{\text{ext}}(x', y)\,\mathrm{d}x'. \tag{15.39}$$

If the derivative of $\ln R(x, y)$ with respect to x is taken, only the second term on the right-hand side of equation 15.39 contributes, since the other terms are independent of the variable x. Using the Leibnitz theorem for differentiation of an integral this gives

$$\frac{\mathrm{d}}{\mathrm{d}x}\ln R(x, y) = 2\,[n\sigma]_{\text{ext}}(x, y), \tag{15.40}$$

which can be rewritten as

$$[n\sigma]_{\text{ext}}(x, y) = \frac{1}{2}\frac{\mathrm{d}}{\mathrm{d}x}\ln\left(\frac{S_{\text{back}}(x, y)}{S_{\text{for}}(x, y)}\right). \tag{15.41}$$

Thus, an effective attenuation coefficient $[n\sigma]_{\text{ext}}$ at any position (x, y) can be determined from two simultaneously recorded elastic scattering images. This result is independent of the initial intensity distribution of the two beams along the y-direction, and also does not depend on losses in the optical detection pathway. A distribution of the local laser intensity decrease inside the observation volume can be calculated by integrating $[n\sigma]_{\text{ext}}(x, y)$ over the path in the observation volume, for both the forward and backward directed laser beams (using equation 15.35 or 15.37, respectively).

Following the above recipe, this method, combined with light sheet illumination, in principle allows to determine the 2-D distribution of the extinction coefficient (each image line is treated separately). Up to now, the method has been used in Diesel engines to reconstruct the local laser intensity, required for processing independent LIF images [1]. In a non-sooting flame, the bidirectional illumination method has been used as an alternative to LIF, for the quantitative determination of OH-densities [2].

Sensitivity, as so often, is the main limitation of the method. Even though it is based on a scattered light measurement, the bidirectional illumination method is essentially an absorption measurement. Moreover, the measured signal is interpreted as reliable data, which is supposed to be free of noise. Noise, however, cannot be avoided. The reconstruction recipe, involving logarithms and a derivative, is very sensitive to noise. Additive noise, as illustrated in figure 15.11, is considerably worse than multiplicative noise. The development of robust statistical methods to evaluate the signals in the presence of noise is a still untackled challenge.

References

[1] Stoffels, G.G.M., Stoks, S., Dam, N., ter Meulen, J.J. (2000): Methods to correct planar laser-induced fluorescence distributions for local non-uniform laser attenuation. Appl. Opt. 39: 5547–5559.

[2] Versluis, M., Georgiev, N., Martinsson, L., Aldén, M., Kröll, S. (1997): 2-D absolute concentration profiles in atmospheric flames using planar LIF in a bi-directional laser beam configuration. Appl. Phys. B **65**, 411–417.

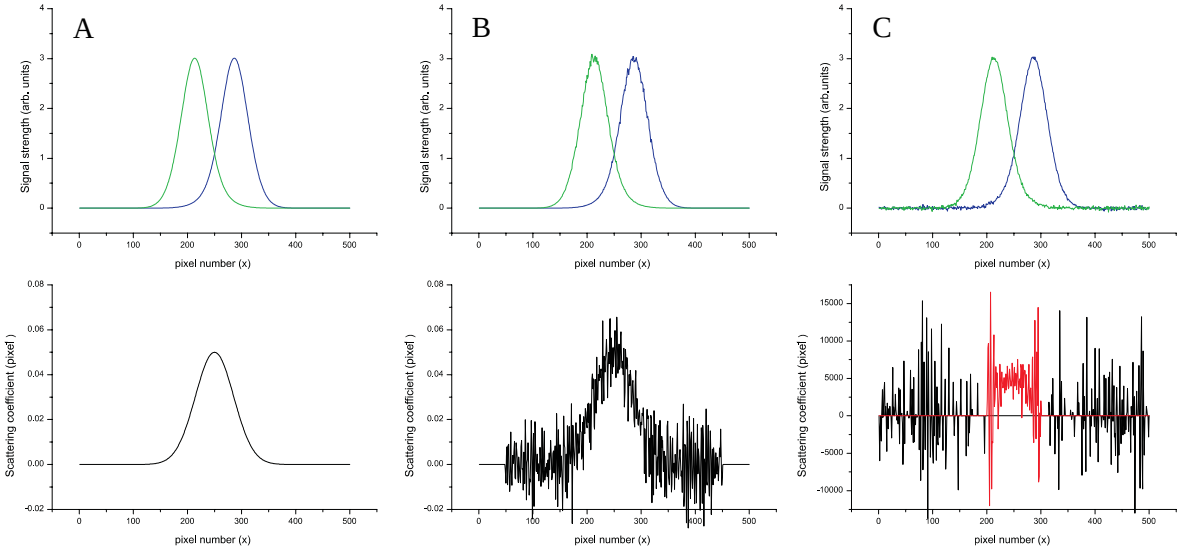

Figure 15.11: Effect of noise on the reconstruction of a linear extinction coefficient distribution (one image line of a CCD image, if you want). The columns correspond to different noise contributions, the upper row shows the simulated signals generated by forward (green) and backward (blue) travelling laser beams on a gaussian scatterer distribution; the lower row shows the reconstructed distribution of the scattering coefficient. Column a: no noise; the input distribution is faithfully reproduced. Column b: 2% multiplicative noise (noise level proportional to signal strength); this reduces the S/N ratio to about 6, with considerable noise levels in the wings. Column c: 2% additive noise (noise level independent of signal strength); reconstruction dominated by noise in the wings. In red: magnified central part ($\times 10^5$).

2.4 Cavity Ring-Down Spectroscopy

Like the bidirectional illumination method (§2.3), cavity ring-down spectroscopy (CRDS) is also an alternative approach to measuring absorption coefficients. It is based on the following principle. A short light pulse (of, say, a few ns duration) is locked inside a high-finesse optical cavity. Here it will bounce back and forth between the mirrors, loosing energy in each round trip because of mirror

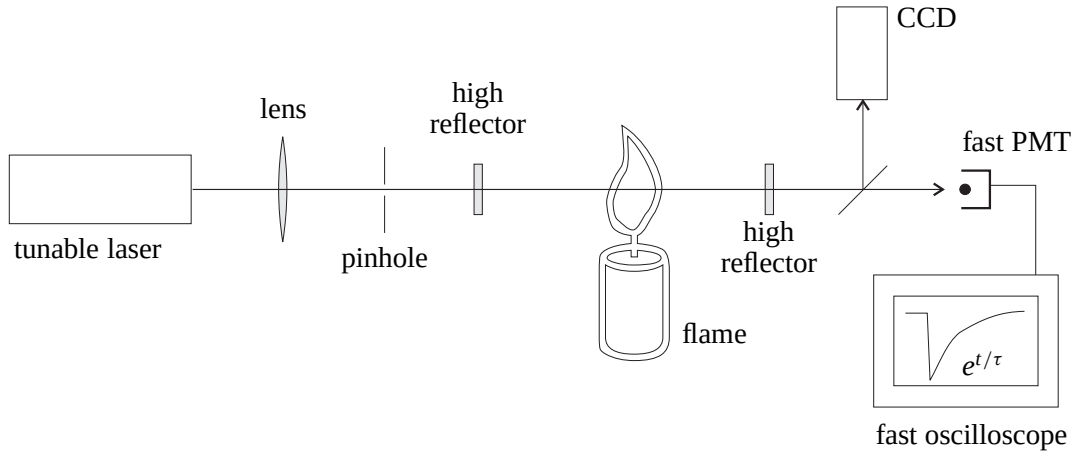

Figure 15.12: Experimental setup for Cavity Ring-down Spectroscopy.

imperfections and by absorption and/or scattering by the medium between the mirrors. The decay time of the intensity of the light pulse in the cavity (also called the *ring-down time* of the cavity) is a measure for the extinction losses induced by the medium. In CRDS this ring-down time is measured as a function of incident light frequency (or wavelength). The subject has recently been reviewed by Berden *et al*. [1], and applications to CRDS to combustion environments have been treated in detail by e.g. Evertsen [2] and by McIlroy & Jeffries [3]. Only a concise description of the essentials will be given below.

A setup for the practical implementation of CRDS is shown in figure 15.12. The tunable laser is typically a pulsed dye laser (pulse duration ca. 5 ns), which is followed by a lens/pinhole combination to clean up its spatial intensity profile. This beam is sent into a stable optical cavity[8], formed by two (usually identical) concave mirrors, a distance d apart. The light that leaks out of the cavity through one of the mirrors is detected by a fast photomultiplier tube (PMT; rise time typically in the order of the laser pulse duration), the transient output of which is recorded, for instance by a fast digital oscilloscope. It is good practice to split off part of the output and record it on a CCD camera, in order to monitor the mode structure of the cavity (see figure 15.13 [2]). Assuming a properly aligned cavity, each laser pulse gives rise to the PMT detecting a light pulse with a steep rising edge (determined by the temporal profile of the laser pulse and the detection system), and a much slower exponentially decaying trailing edge, the decay (ring-down) time τ of which is given by [1]

$$\begin{aligned} \tau(\nu) &= \frac{d}{c\left(|\ln R(\nu)| + \sum_i \sigma_i(\nu) \int_0^l \rho_i(x)\,\mathrm{d}x\right)} \\ &\approx \frac{d}{c((1-R)+\kappa(\nu)l)} \end{aligned} \tag{15.42}$$

in which c is the speed of light (30 cm/ns is a practical unit, in this case), R the mirror reflectivity, σ_i the absorption cross section of chemical species i with number density ρ_i, and the integration runs over the extent $l \leq d$ of the absorbing medium within the cavity. The lower line of eq. 15.42 shows a simplified form, in terms of the decay time τ_0 of the empty cavity ($\tau_0 = \frac{d}{c(1-R)}$, in which $1 - R \ll 1$ has been assumed) and the effective absorption coefficient $\kappa(\nu)$.

Evidently, CRDS derives its sensitivity from two features. One of them is the fact that high mirror reflectivities cause the light pulse to traverse the medium many times.

Example: Using mirrors with $R = 99.95\%$, each pulse traverses the cavity about 2000 times. A $d = 0.5$ m cavity would then result in an effective absorption pathlength of 1 km.

The second feature concerns the fact that a *decay time* is measured, rather than the absolute value of the transmitted power. This renders the method insensitive to the incident laser power, as long as it is sufficient, of course, to yield a good PMT output. Thus, CRDS can be performed with the ubiquitous pulsed laser systems, that are notorious for their pulse-to-pulse intensity fluctuations (10% being no exception). Nevertheless, CRDS is not a true zero-background technique, because the experimental parameter of interest is the decrease of the ring-down time of the empty cavity.

There are some practical issues that should be considered:

- The cavity length should be (much) shorter than the laser pulse length, so that the light pulse is 'folded' inside the cavity, and the output has a smooth time profile rather than consisting of individual spikes. Typically, $d \approx 0.3 - 0.5$ m and the light pulse is about 1.5 m long.

[8] An optical cavity of two mirrors with radius of curvature r and distance d is stable if $(1 - d/r)^2 < 1$.

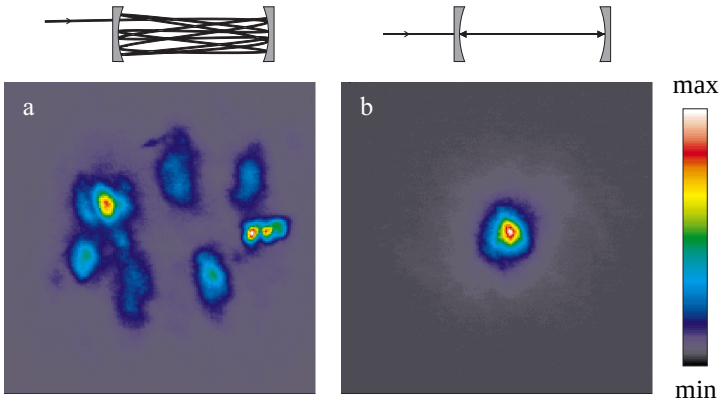

Figure 15.13: Output of the cavity in case of bad alignment (a) and good alignment (b). (False colour images recorded with a CCD camera that looks into the cavity along its axis.) Artist impressions of the beam path within the cavity are shown above each image.

- Best sensitivity is obtained if $\kappa(\nu) \gg c(1-R)$, that is if $R \to 1$. Typically, R 99.8%, and mirrors with R 99.99% can be bought for specific wavelengths. Such specifications, however, only hold for very narrow wavelength ranges, and often each chemical species of interest requires its own dedicated set of mirrors.
- If averaging is required to increase signal-to-noise ratio, one should average the decay times of individual transients, not the transients themselves.

Recently, there have been a few derivative implementations of CRD that, for instance, allow its use with cw lasers. This is discussed in Berden's review [1].

References

[1] Berden, G., Peeters, R., Meijer, G. (2000): Cavity ring-down spectroscopy: Experimental schemes and applications. Int. Rev. Phys. Chem. **19**, 565-607.

[2] Evertsen, R. (2002): Cavity ring-down spectroscopy in combustion environments. PhD thesis, University of Nijmegen, NL.

[3] McIlroy, A., Jeffries, J.B. (2002): Cavity ringdown spectroscopy for concentration measurements. In ACD (see §1), ch. 4.

2.5 Rayleigh scattering

Rayleigh scattering is undoubtedly the most straightforward non-resonant light scattering mechanism. Its physical basis was discussed in section 1.2, which resulted in the following expression for the Rayleigh-scattered power into the (small) solid angle Ω:

$$P_{\text{Rayl}} = \eta\rho \sum_i x_i \left(\frac{\mathrm{d}\sigma_{\text{Rayl}}}{\mathrm{d}\Omega}\right)_i \Omega V I_0 \ . \tag{15.43}$$

Here, η is a detection efficiency, ρ the total number density, x_i the mole fraction of chemical species i with differential Rayleigh scattering cross section $\left(\frac{\mathrm{d}\sigma_{\text{Rayl}}}{\mathrm{d}\Omega}\right)_i$, V is the irradiated volume and I_0 the incident laser intensity. Rayleigh scattering is elastic (or quasi-elastic, *vide infra*), and therefore does not

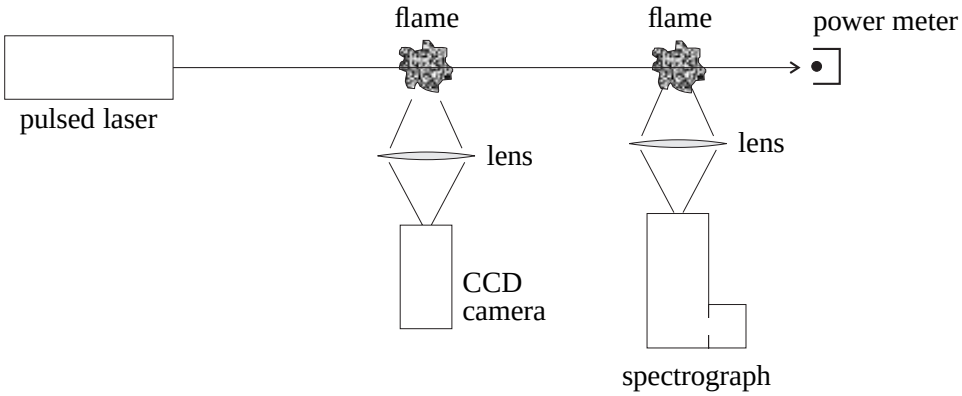

Figure 15.14: Generic setup for (planar) Rayleigh scattering measurements, with two alternatives for detection.

provide information on individual chemical species. Thus, in order to extract ρ from the measurement of P_{Rayl}, the composition of the medium (the mole fractions x_i) must be known.

A typical experimental setup is shown in figure 15.14, which includes two alternatives on the detector side. In the simplest setup (left) all scattered light is detected without spectral filtering. This, evidently, is prone to errors due to spurious sources, notably Mie scattering (off dust or soot particles, for example) and reflections off solid objects, even if these are far outside the depth of field. Inelastically scattered light, due to Raman scattering or LIF, is also detected by this setup. Raman scattering cross sections tend to be several orders of magnitude lower than those for Rayleigh scattering, and can generally be neglected, but LIF should be avoided by proper choice of the incident laser wavelength. A slightly more involved setup (figure 15.14, right) includes a spectral filter in front of the detector to suppress the inelastic contributions. Also in this case, however, a main source of error is elastic scattering off solid or liquid objects. For this reason, it is advisable to use CCD cameras as detector, even if only point measurements are taken, because a camera allows to recognize and interpret the scattering sources. As an example, figure 15.15 shows an image of a thin light sheet passing through still, ambient air, recorded without spectral filtering. The bright dots represent dust particles, some of them hit directly by the laser beam, some others just illuminated by stray light.

Rayleigh imaging has been used mainly for qualitative flow imaging. Also, it has been used for thermometry in incompressible flows, relating density to temperature through the ideal gas law. For temperature imaging, however, the method of Filtered Rayleigh scattering, briefly discussed below, is probably better suited.

Filtered Rayleigh scattering

Rayleigh scattered light is, in practice, not really elastically scattered. Instead, individual molecules impose a (small) Doppler shift onto the scattered light, due to their random thermal motion. Thus, one often refers to Rayleigh scattering as quasi-elastic scattering, or Rayleigh-Brillouin scattering. Narrow-band light incident on a gas phase sample will therefore give rise to scattered light with a gaussian, Doppler-broadened spectral profile. For scattering of monochromatic light (frequency ν_{in})

by a single-component gas (molecular mass m) at temperature T, one has[9]

$$P(\nu)\,\mathrm{d}\nu \propto \exp\left\{-\frac{(\nu-\nu_{\mathrm{in}})^2}{2\,\delta\nu^2}\right\} \quad \text{with } \delta\nu = \nu_{\mathrm{in}}\sqrt{\frac{kT}{mc^2}}\,. \tag{15.44}$$

Thus, the spectral width of the scattered light is related, via the average thermal velocity, to the temperature.

Example: N_2 at room temperature results in $\delta\nu = 550$ MHz for illumination with 532 nm light. The Doppler linewidth of the much heavier I_2 at about 60 °C, often used in Filtered Rayleigh Scattering, amounts to about 200 MHz.

In Filtered Rayleigh Scattering (FRS), Rayleigh-scattered light is detected through a spectrally narrow molecular absorption filter, using a laser frequency that is tuned to be blocked by this filter. Thus, the filter only transmits the wings of the Doppler-broadened scattered light, which results in a measured power that is related to the temperature of the scattering medium. This principle is outlined in figure 15.16. If the laser frequency is tuned to the center of the molecular absorption filter, truly elastically scattered light (like that off solid objects, or dust particles; the latter move so slowly that the Doppler shift is negligible) is absorbed completely.

The setup required for FRS (figure 15.17) is much more complicated than that for unfiltered Rayleigh scattering. More details can be found in Elliott's review [2]. Because of the small Doppler shifts (a few GHz, when visible light is used; the frequency of the incident light itself amounts to about $6 \cdot 10^5$ GHz), both the laser and the absorption filter must have a bandwidth of at most a few hundred MHz. In practice, an injection-seeded frequency doubled Nd:YAG laser is used, in combination with gently heated cells containing molecular I_2. A separate I_2 filter is used to monitor the laser frequency. Since injection-seeded Nd:YAG lasers can be tuned over a few GHz, two modes of operation are possible:

Fixed mode: In fixed mode the Nd:YAG laser frequency is fixed, either at the center of a strong I_2 absorption line (for T measurements) or halfway the flank of an absorption line (for $|\vec{v}|$ measurements). The amount of light transmitted by the filter is a measure for either the thermal Doppler broadening and/or the Doppler shift, respectively.

[9] The line shape is actually more complicated, because of the contribution of acoustical modes. This will not be considered here; see Forkey's thesis [1] for details.

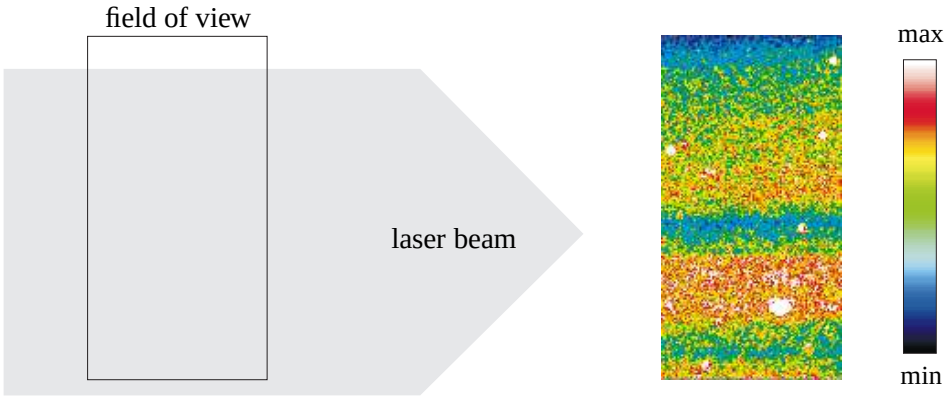

Figure 15.15: Elastic scattering image of a thin light sheet, derived from a single pulse of a KrF excimer laser ($\lambda \approx 248$ nm), in ambient air. These are raw data, represented in false colour. Vertical structure is due to the inhomogeneous laser intensity profile; the bright (white) blobs are due to dust particles.

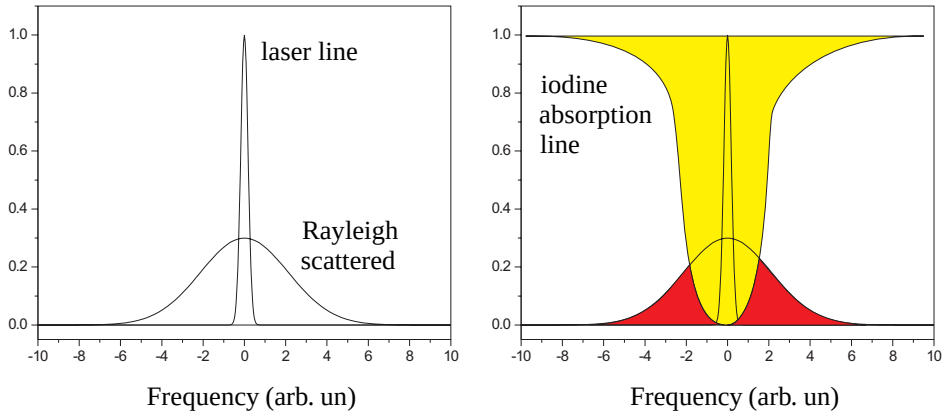

Figure 15.16: Principle of Filtered Rayleigh Scattering. Left: Spectral profiles of the incident laser light and the scattered light. Right: Idem, plus the absorption line shape of a molecular absorption filter (in practice: a gas cell with low-pressure I_2 vapour). The laser line is completely absorbed, whereas the wings of the scattered light are partly transmitted (red).

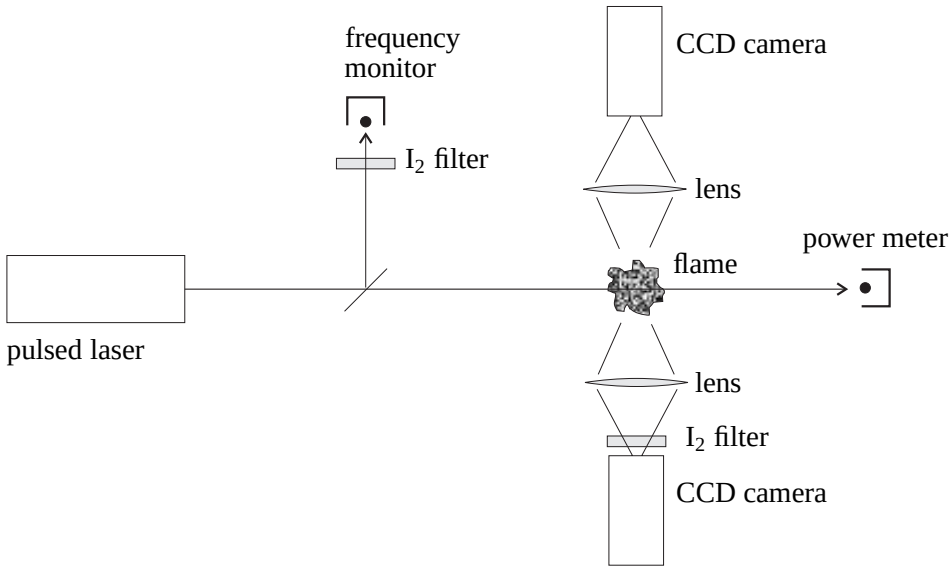

Figure 15.17: Typical setup for Filtered Rayleigh Scattering.

Scanning mode: By scanning the Nd:YAG laser frequency over an I_2 absorption line and recording the scattered light through the filter, the spectral profile of the scattered light can be reconstructed. This profile has a non-trivial shape, that allows to retrieve Doppler shift (i.e. velocity), temperature and density [1].

Finally, FRS is applied in particulate-seeded flows in the techique known as Doppler Global Velocimetry (DGV). Since it here concerns a particulate-seeded technique, it falls outside the scope of this chapter, and will be considered here only very briefly. Thermal motion plays no role for the particles, so that the Doppler shift imposed on light scattered off seed particles is due only to the gross velocity of the flow. Thus, the measured transmission is actually a measure for the translation (in frequency space) of the spectral profile of the scattered light, that is, to the Doppler shift. Since the scattering vector $\vec{k} = \vec{k}_L - \vec{k}_s$ (subscript L for laser, s for scattered) not only depends on the viewing

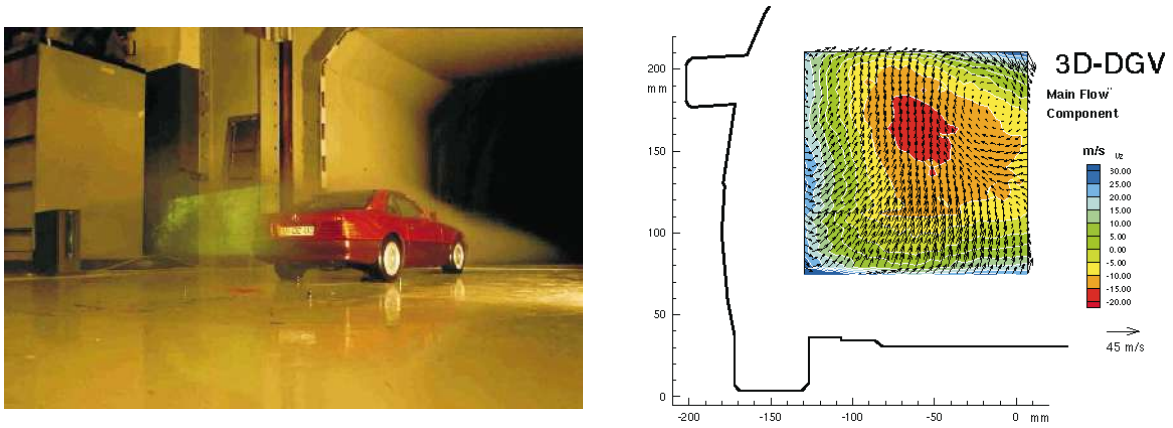

Figure 15.18: Left: Car in the large wind tunnel at DLR-Cologne, with a light sheet passing at the back. Right: 3-component 2-D DGV data.

direction but also on the incident light propagation direction, illumination of the same volume with three different light sheets results in three different scattering vectors, and three different velocity components. (The same can be achieved through a combination of PIV with single-component DGV.) An example is given in figure 15.18, taken from the DLR-Cologne (D) website, where the technique is used in large scale wind tunnel applications (R. Schodl's Institute of Propulsion Technology; see e.g. Roehle *et al*. [3] for a description of the equipment).

References

[1] J.N. Forkey (1996): Development and demonstration of Filtered Rayleigh Scattering – A laser-based flow diagnostic for planar measurement of velocity, temperature and pressure. PhD thesis, Princeton University.

[2] G.S. Elliott, M. Boguszko, C.D. Carter (2001): Filtered Rayleigh scattering; towards multiple property measurements. AIAA paper 2001-0301.

[3] Roehle, I., Schodl, R., Voigt, P., Willert, C., 2000: Recent developments and applications of quantitative laser light sheet measuring techniques in turbomachinery components. Meas. Sci. Technol. **11**, 1023-1035.

2.6 Raman scattering

Spontaneous Raman scattering is arguably the single most powerful laser diagnostic technique, limited, however, by its low sensitivity. It is based on the non-resonant response of molecules to incident radiation, which not only involves an elastic component (Rayleigh scattering), but also inelastic components as a result of energy exchange between the molecules and the electro-magnetic field. For diagnostic purposes, vibrational Raman scattering is used most frequently (as compared to rotational and electronic Raman scattering), and this will be the only variant discussed here. Schematically, Raman scattering is often discussed in terms of a so-called *virtual level* as intermediate state (see figure 15.4 in the introduction). This virtual level, indicated by a dashed line in figure 15.4, does not correspond to a real (stationary) energy state of the molecule, but rather serves as a mnemonic for the

net non-resonant interaction of the field with all energy states of a molecule. In fact, therefore, Raman scattering (like Rayleigh scattering, by the way) is a *two-photon process*: the interaction between molecule and field involves two photons (the incident and the scattered ones) simultaneously.

The fact that there is no real intermediate state involved has two important consequences:

1. Scattering cross sections are small (in the order of 10^{-10} Å^2/molecule; see table 15.2 in the introduction). Typically, Raman scattering is two to three orders of magnitude less efficient than Rayleigh scattering, and up to ten orders of magnitude less than Laser-Induced Fluorescence (LIF; see section 2.7). This is a main limitation of the technique, especially in non-stationary situations.

2. Collisional quenching, a main bottleneck in the quantitative interpretation of LIF signals (§2.7), is irrelevant, there being no excited intermediate state that is populated. This facilitates straightforward interpretation of Raman scattering signals.

It should be stressed, by the way, that Raman scattering and LIF, although superficially similar, are two very different processes. LIF is a sequence of two single-photon events (absorption followed, some finite time later, by emission), whereas Raman scattering is one single event involving two photons simultaneously.

The general experimental setup for Raman scattering experiments is shown in figure 15.19. A crucial role is reserved for the spectral filter, for two reasons:

1. Because Raman scattering cross sections are so small, the technique is sensitive to stray light.

2. Raman shifts typically range from 500–3500 cm^{-1} (see table 15.2 in the introduction; remember that we discuss vibrational Raman scattering only). As a result, contributions by different chemical species tend to be spectrally close, both to each other and to the incident light.

Example: For O_2 and N_2 the Raman shifts $\Delta\nu_R$ are 1556 cm^{-1} and 2331 cm^{-1}, respectively. Using 355 nm incident light (frequency-tripled Nd:YAG laser) yields the O_2 Raman band at 376 nm and the N_2 band at 387 nm. These cannot be satisfactorily separated by off-the-shelf optical band-pass filters of 10 nm fwhm.

Experimentally, spectral filtering is most easily accomplished by interference band-pass filters. These are easy to handle, can be purchased for a variety of central transmission wavelengths, but are not

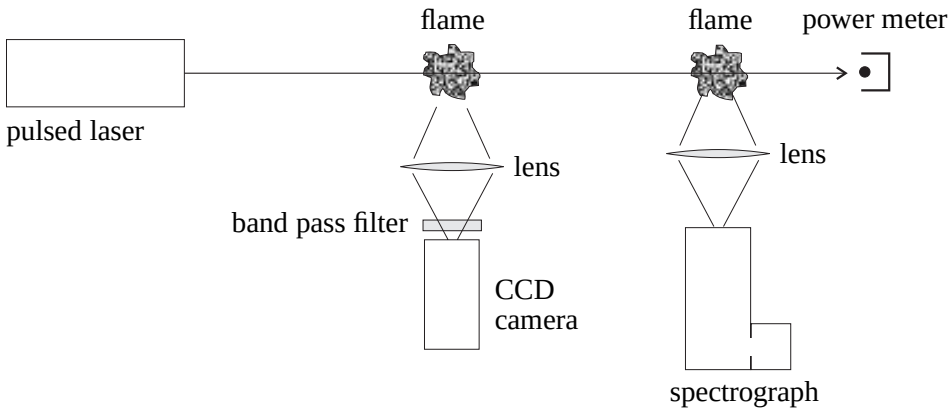

Figure 15.19: Generic setup for (planar) Raman scattering measurements, with two alternatives for the detection.

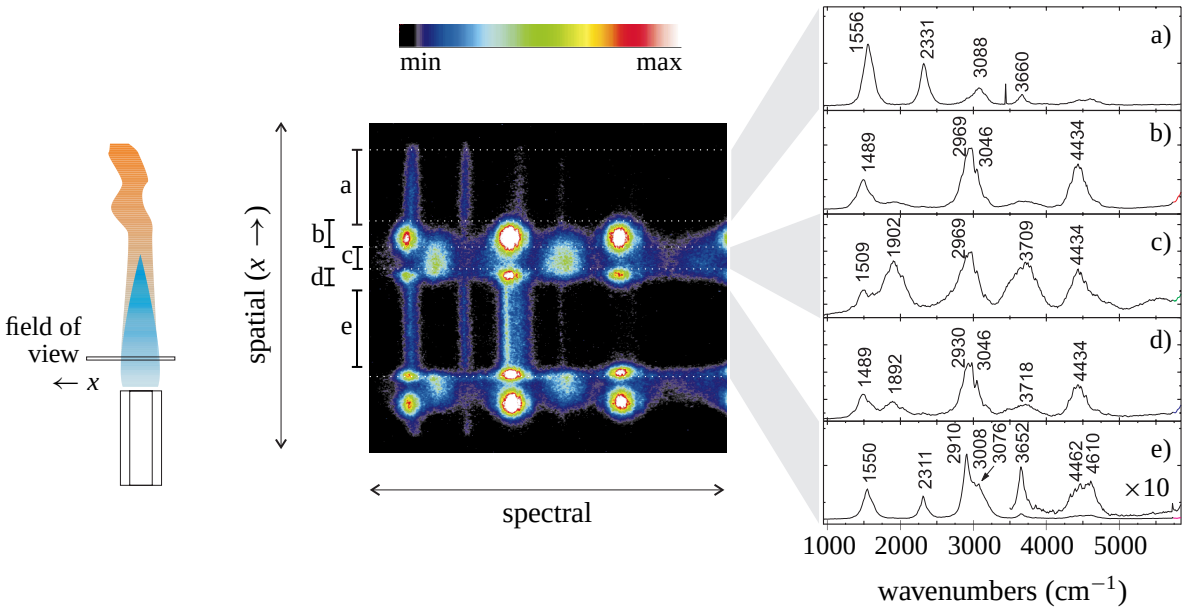

Figure 15.20: Raman spectrum of a lean methane/air Bunsen-type flame, with 1-D spatial resolution. Left: Setup. The incident laser beam propagates along the x-direction. Middle: Spectrum. False colours correspond to intensity; image lines correspond to parts of the spectrum at a particular position along x; columns correspond to scattered light wavelengths. Right: Average spectra over regions indicated; see text for details.

usually selective enough to single out individual contributions to the Raman spectrum of a sample. (Selectivity and transmission efficiency are mutually exclusive; increasing one decreases the other.) Moreover, such filters have the disadvantage that spectral interferences, if they occur, cannot be detected. For this reason it is recommendable to incorporate a spectrograph in Raman diagnostics, in parallel with, or even instead of, a band-pass filter. When combined with a detector array (linear or 2-D CCD device), a spectrograph with a suitably chosen grating allows constant monitoring of the whole spectral range of interest.

As an example, figure 15.20 shows the spectrograph output recorded by an intensified CCD camera. The object is a partially premixed CH_4/air Bunsen flame, intersected by an ArF excimer laser beam ($\lambda_{in} \approx 193$ nm). The field of view of the detection system is indicated by the narrow rectangle on the left. The image in the center is a false colour representation of the spectrum, with a spectral axis along the horizontal direction, and a spatial one along the ordinate. The spatial axis corresponds to the long side of the field of view. Graphs of the average spectra over the individual regions in the flame are shown at the right. They correspond to the following regions:

a) Ambient air, outside the flame. Spectral features are due to O_2 (1556 and 3088 cm^{-1} Raman shift), N_2 (2331 cm^{-1}) and H_2O (3660 cm^{-1}). The O_2 bands are relatively strong because of near-resonance effects.

b) Flame boundary. Spectral features are due to hot O_2.

c) Coflow region. Spectral features mainly due to NO (1902 and 3709 cm^{-1}).

d) As in b) (boundary between coflow and central flow).

e) Central flow, with bands due to O_2, N_2 and CH_4 (the complex structure around 3000 cm^{-1}).

Clearly, a lot of information can be obtained simultaneously from a single spectrum, but it is also clear that good spectral filtering is required to isolate individual spectral components out of such complex spectra. In fact, quite a few spectral features in figure 15.20 are due to LIF rather than to Raman scattering[10]; this is the case for the NO-bands and to some extent the O_2-bands. Only the N_2 bands and the CH_4 band structure are due solely to Raman scattering.

Intermezzo: For quantitative Raman experiments on combustion phenomena, the ArF excimer laser is probably not a very good choice, in spite of the ν^4-scaling of the scattering cross section (see the introduction). Main reasons for this are the unavoidable resonance enhancement of the O_2 bands, and the relatively low sensitivity and selectivity of detection equipment at this wavelength. In practice, the use of frequency-tripled ($\lambda \approx 355$ nm) or -doubled ($\lambda \approx 532$ nm) Nd:YAG lasers is recommended.

Under favourable circumstances an imaging spectrograph in combination with a CCD camera can also be used to record full 2-D images by Raman scattering. The principle is as follows. An imaging spectrograph is designed to project an image of the entrance slit onto the exit plane. Every wavelength component in the incident light produces its own image on the exit plane, and the position of that image depends on the wavelength: A spectrograph is essentially a λ-to-x encoder. All this holds irrespective of the width of the entrance slit; a wider entrance slit just means a wider image on the exit plane, and this is the key to imaging through a spectrograph. Of course, this works well only for monochromatic light. For polychromatic incident light (as is typically the case if one considers Raman-scattered light), the overlap between images produced by different λ-components increases if the entrance slit is opened up. (This is generally referred to as 'loss of spectral resolution', but that is a result, rather than a cause.) Complications arise because of this intermingling of spectral and spatial information[11]. It can be shown that this mix of spatial and spectral information takes the form of a convolution. Thus, when the spectral structure is known (from a reference measurement on the pure compound, for instance), the hidden spatial information can be retrieved by a deconvolution procedure. In practice, this is not at all straightforward (deconvolution tends to enhance noise), but statistical methods of data analysis exist that can do the job [1].

As an example, figure 15.21 shows the steps in the determination of the spatially resolved stoichiometry distribution in a non-burning premixed methane/air flow. The flow issues from a flat-flame burner (25 mm diameter) and hits a fine metal mesh about 12 mm downstream of the burner deck. A light sheet derived from a tripled Nd:YAG laser passes between the burner deck and the metal mesh. Raman scattered light is collected in a direction perpendicular to the plane of the light sheet by a spectrograph equipped with an intensified CCD camera in the exit plane. The field of view is such that part of the methane/air flow and part of the adjacent ambient air are imaged along the height of the entrance slit, whereas the gap between burner deck and metal mesh just fills the width of the spectrograph entrance slit. The raw data (average of 625 laser pulses of 320 mJ each) are presented as a false colour image on the left. The uppermost structure is due to N_2 (present in the flow as well as in ambient air; truncated at left and right by the spectrograph entrance slit height), the lower structure is due to CH_4. In this image, the horizontal axis (parallel to the entrance slit height) is a purely spatial axis, whereas along the vertical axis (perpendicular to the entrance slit height) spatial and spectral information are convolved. The Raman spectra of both compounds are indicated in the middle. This is used to deconvolve the raw data, yielding the spatial distributions shown at the right. Qualitatively,

[10] In cases of doubt, scanning the excitation laser allows to distinguish between Raman and LIF. Raman bands shift together with the excitation wavelength (constant Raman shift), whereas fluorescence bands appear and disappear if the excitation laser is scanned over a resonance.

[11] Along one axis of the image only; a good imaging spectrograph spectrally disperses the incident light along one axis (perpendicular to the entrance slit height), and produces a faithfull image along the other axis (parallel to the entrance slit).

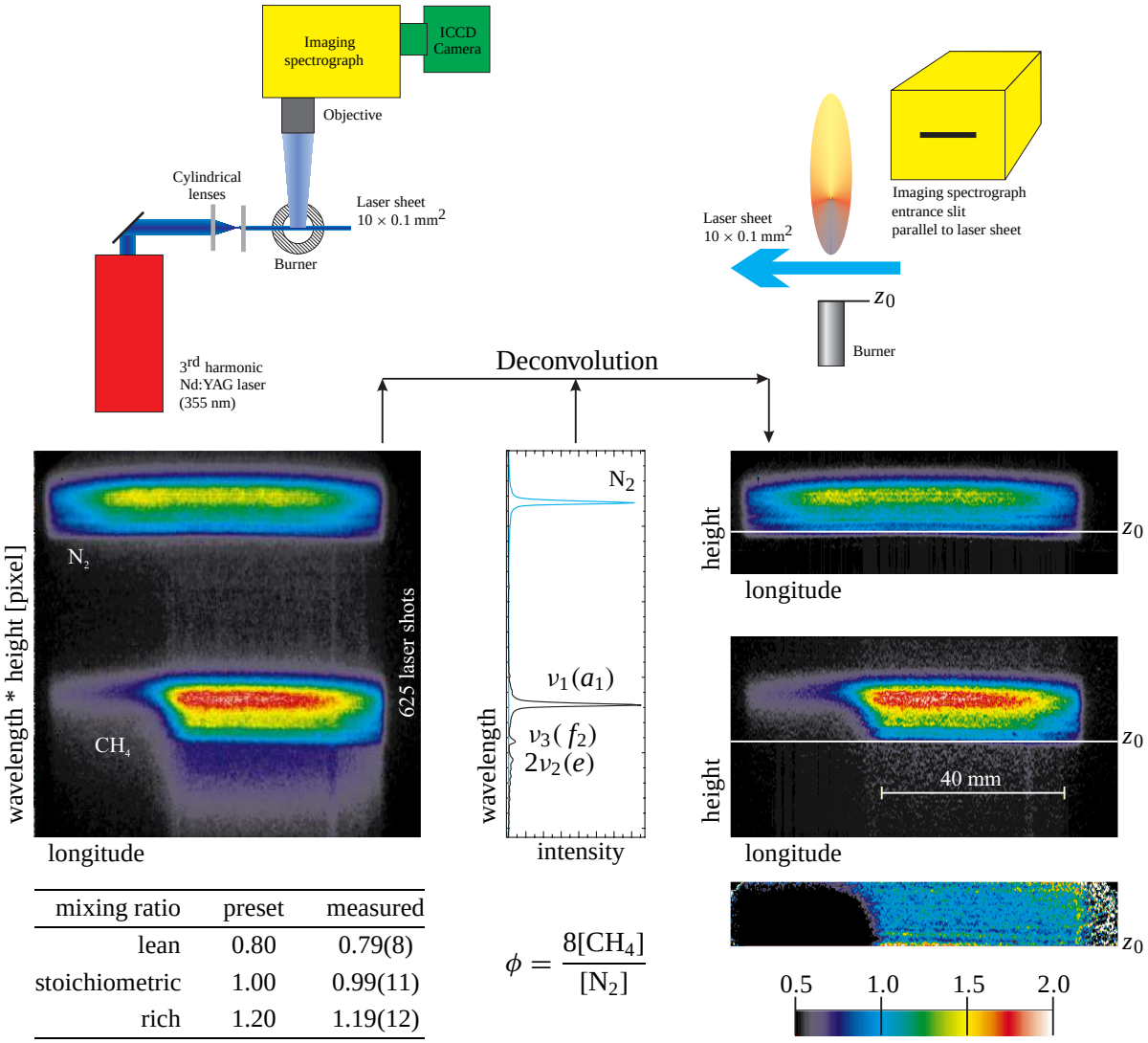

mixing ratio	preset	measured
lean	0.80	0.79(8)
stoichiometric	1.00	0.99(11)
rich	1.20	1.19(12)

$$\phi = \frac{8[CH_4]}{[N_2]}$$

Figure 15.21: Raman imaging through a spectrograph of N_2 and CH_4 in a premixed methane/air flow issueing from a flat-flame burner. The experimental setup (side and top views) is shown at the top. The left panel shows the raw data in false colours, the right panel shows the same data, after deconvolution using the spectrum indicated in the middle. Note that especially the tail at the bottom of the methane band has disappeared. The stoichiometry distribution in this flow field, as derived from the N_2 and CH_4 data, as shown in the bottom-right. (Figure taken from a poster by René Tolboom (KUN), presented at the meeting of the FOM section Stroming & Warmte, fall 2001.)

the disappearance of the diffuse tail below the methane structure is most apparent. The stoichiometry distribution of this (non-burning) mixture can now simply be derived by a pixel-by-pixel division of the two spatial distributions. This results in the false colour image (colour scale indicated) shown in the bottom-right. The fanning out of the boundary of CH_4 flow where it hits the metal mesh is clearly visible. Also, there is a weak horizontal ripple-structure in the stoichiometry image, which is a residual artefact of the deconvolution procedure. Quantitatively, the results agree very well with the preset conditions of the flow (using calibrated mass flow controllers for methane and air), with a standard deviation of typically 10% (table at bottom-left).

References

[1] Tolboom, R.A.L., 2002: Expanding laser diagnostics in non-seeded compressible flow research. PhD thesis, University of Nijmegen.

2.7 Laser Induced Fluorescence Spectroscopy

Laser Induced Fluorescence spectroscopy is probably the most widely used optical diagnostic technique for at least qualitative assessment of chemical species distributions. Many molecules will fluoresce when promoted to a suitable excited state, and this is the key to the wide applicability of LIF. Because LIF is a resonant process, the excitation and fluorescence efficiencies are generally large, resulting in strong signals. Thus, LIF is often very suitable for 2-D imaging studies, also on minority species. Because of the same reason, however, most laser-excited molecules dwell some finite time in the excited state before radiative decay takes place. During this time, there are other processes that may cause non-radiative decay. In practical cases, these processes are collisional energy transfer and/or intersystem crossing. The parameters governing these non-radiative decay processes are often not or incompletely known, and that is the main problem in the quantification of LIF data.

There is an enormous body of literature on both the principles of LIF and its application to the study of combustion phenomena. An overview of minority species that have been detected by laser techniques (often LIF) is given by Smyth & Jeffries [1]. A useful simulation program for the calculation of spectra of diatomics like OH, NO and CH is provided (free) by Luque [2]. Below, I will

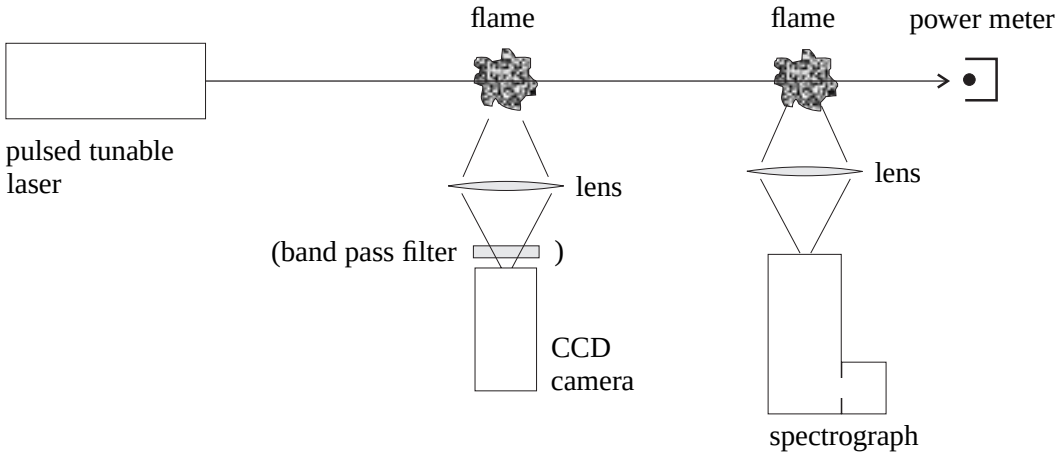

Figure 15.22: Generic experimental setup for Laser-Induced Fluorescence (LIF) spectroscopy, with two alternatives for detection.

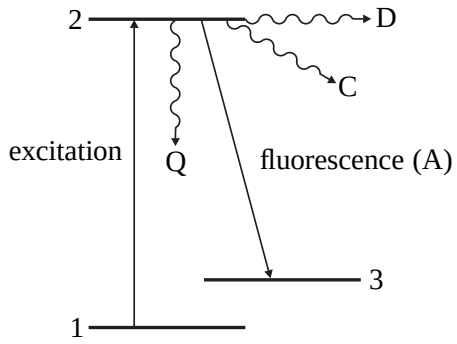

Figure 15.23: Simplified and schematic energy level scheme relevant to LIF experiments. Incident (laser) light is resonant with the transition between levels 1 and 2; absorption of each photon results in exciting one molecule out of level 1 into level 2. Stimulated emission back to level 1 is neglected. Excited molecules may loose energy by radiation (A; only one lower state 3 is indicated, but in general there are several possibilities), by non-radiative, collision-induced decay (so-called quenching; Q), by dissociation (D) or by chemical reactions (C; can also be included in Q).

not attempt anything like a review, but just discuss the general principles. Usually, every particular molecule has its own special peculiarities that have to be taken into account.

The experimental setup for LIF (figure 15.22) is not much different from that used for Rayleigh or Raman scattering, except that a tunable laser is required for resonant excitation. Absorption of this radiation produces molecules in an excited state, that is, molecules with a lot of internal energy. Usually, it concerns electronically excited states, but there is some progress in LIF imaging by vibrational excitation [3]. These excited molecules will loose energy, but there is a variety of competing mechanisms by which this can occur. The main pathways are illustrated in figure 15.23, in which radiative transitions (either induced or spontaneous) between energy levels (horizontal lines) are indicated by straight arrows, and all other processes that affect the level populations by wavy arrows. Important mechanisms by which excited molecules may loose energy include

- Radiative decay, that is, fluorescence (A). The associated time scale strongly depends on the molecule and on the excited state that is produced; typical values range from $1 - 100$ ns.

- Non-radiative decay (Q), caused by intermolecular collisions. At atmospheric pressure, typical time scales are $1 - 10$ ns, but this, again, depends strongly on the particular system at hand.

- Dissociation (D), that may occur if a molecule is excited above its lowest dissociation limit. A well-known case is O_2, that can be excited in the so-called Schumann-Runge bands by 193 nm radiation from an ArF excimer laser. The upper state involved ($B^3\Sigma_u^-(v' = 4)$; see the previous lecture by ter Meulen for notation) is strongly predissociated. This means that, although it is in principle a bound state, there is an internal mechanism that efficiently leads to dissociation. The dissociation process, that produces two ground state O-atoms, takes place on a ps time scale.

- Chemical reactions (C), that may be expected to be of special importance in combustion environments, which already contain a lot of reactive species. This, however, is a subject of which little is known.

The population transfer (that is, the number of molecules that, on average, make transitions between energy levels) in systems like those of figure 15.23 can conveniently be described in terms of rate

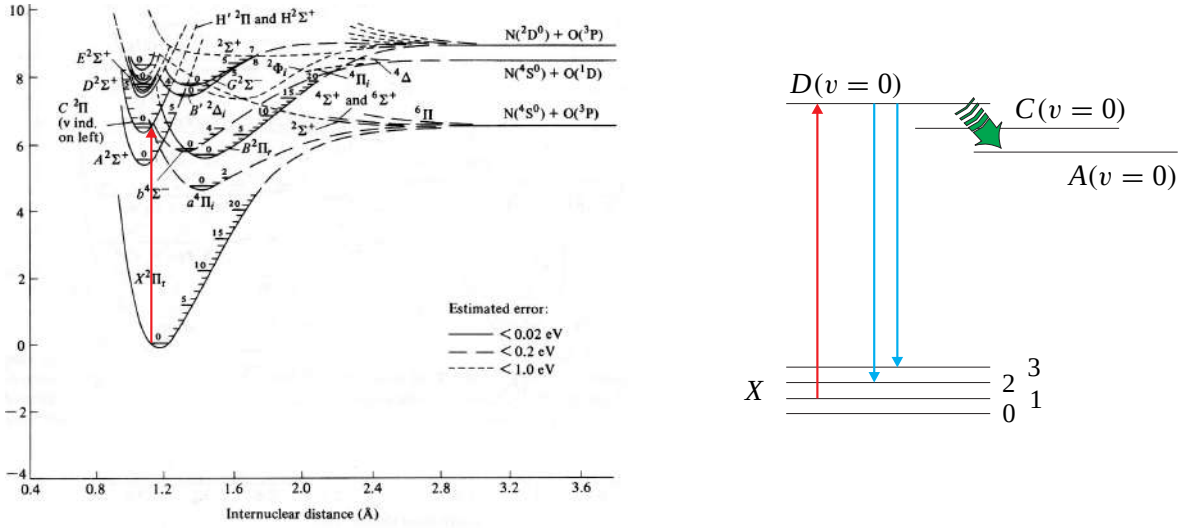

Figure 15.24: Left: Potential energy curves for the NO molecule. The ArF excimer laser can induce transitions between rotational levels of the ground state ($X(v'' = 1)$) and the electronically excited $D(v' = 0)$-state (arrow). Right: Energy levels relevant for ArF laser-induced fluorescence of NO. Horizontal lines represent energy levels, the energy increases vertically upwards (not to scale). Red: excitation; blue: fluorescence; green: collisional decay routes.

equations. Denoting level populations by N, the excitation rate by k_I and decay rates by k (all rates in s^{-1}) we have, for the (simplified) case of figure 15.23,

$$\frac{dN_1}{dt} = -k_I(t)N_1 \tag{15.45}$$

$$\frac{dN_2}{dt} = +k_I(t)N_1 - (k_Q + k_D + k_C + k_A)N_2 \tag{15.46}$$

$$\frac{dN_3}{dt} = +k_A N_2 \tag{15.47}$$

Note that the excitation rate $k_I(t)$ has been written with explicit time dependence, because it is proportional to the incident laser intensity. LIF experiments are often performed using pulsed lasers, and $k_I(t)$ is often approximated by a block function. The other rate constants are either intrinsic molecular properties (k_A and k_D) or depend in part on the environment (k_C and k_Q). Since all molecules that end up in level 3 must have gotten there by fluorescence, $N_3(t \to \infty)$ equals the number of emitted fluorescence photons. Evidently, this is only a fraction $k_A/(k_A + k_Q + k_D + k_C)$ of the total number of molecules that ever were excited. This factor, $k_A/\sum k_i$, is a quantum efficiency for fluorescence, known as Stern-Volmer factor.

For the sake of definiteness, let us consider the case of LIF of nitric oxide, NO, induced by a pulsed, tunable ArF excimer laser ($\lambda \approx 193$ nm). A compilation of potential energy curves of NO is shown in figure 15.24, together with a schematical representation of the relevant energy levels. The ArF laser can be tuned to some extent, between 192.8 and 193.8 nm. Within this range a number of rovibronic transitions in the so-called ϵ-system of NO, $D^2\Sigma^+(v' = 0, J') \leftarrow X^2\Pi(v'' = 1, J'')$, can be resonantly excited. Note that the lower state of this transition is a vibrationally excited state ($\omega_e = 1904$ cm$^{-1} \equiv 2726$ K; see table 2 of the previous lecture by ter Meulen), the population of which is strongly temperature-dependent: this transition is good for probing hot NO. Assume the laser to be tuned to one particular rovibronic transition. During the laser pulse, the lower level is depleted,

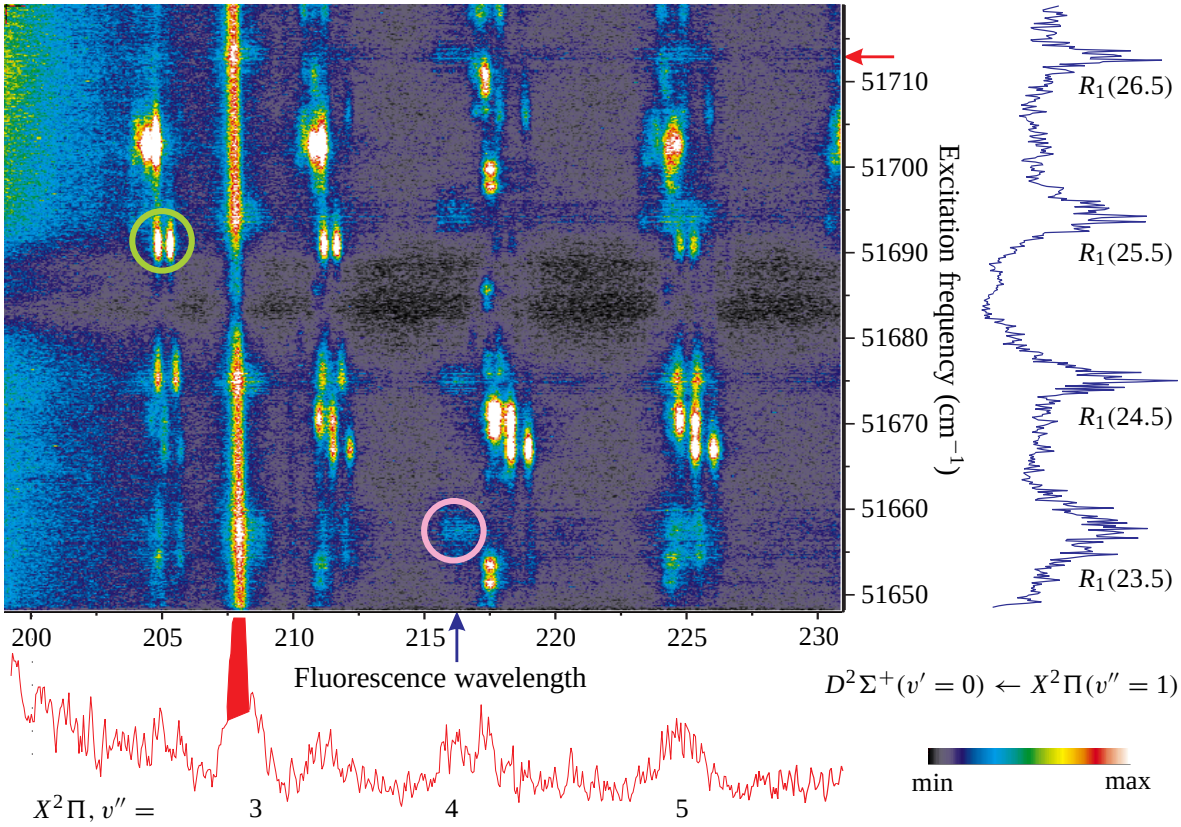

Figure 15.25: Excitation emission spectrum recorded in the combustion chamber of a running Diesel engine, at 42 °aTDC. See text for a aTDC: Undefined variable. description.

and the upper level is populated. This creates strongly non-thermal population distributions in both the ground electronic state (thermal, except for a 'hole' in the depleted J'' level) and the upper electronic state (only one J' populated). Intermolecular collisions will tend to restore thermal equilibrium by (mainly) rotational energy transfer (RET), a very efficient process that operates on the time scale of typical laser pulse durations.

Example: Intermolecular collision rates can be approximated by considering the molecules as hard spheres, with a geometrical cross-sectional area σ_{gk} that is in the order of several tens of Å^2. The hard-sphere collision rate, or *gas kinetic collision rate* is then given by $k_{gk} \approx \rho\sigma_{gk}\bar{v}_{\text{rel}}$, in which ρ is the total number density and $\bar{v}_{\text{rel}}$ the average relative velocity of two molecules. For flames at atmospheric pressure, $k_{gk} \approx 10^9$ s^{-1}, or one collision per nanosecond. Since about every collision is effective for rotational energy transfer [4], the timescale for rotational equilibration is in the order of nanoseconds.

For the purpose of laser diagnostics, the occurrence of fast RET is beneficial, because it delays the onset of saturation (which occurs as soon as the lower level is considerably depleted; not discussed further here).

In the case of NO, predissociation does not occur, and on eventual reaction rates there are no data (which I take as good justification for neglecting them). Fluorescence is observed not only out of rotational levels in the $D(v'=0)$-state, but also out of the vibrational ground states of the nearby $C^2\Pi$ and $A^2\Sigma^+$ electronic states. Apparently, there is efficient collisional energy transfer from the D-state into the C- and A-states. An example of the rich spectral structure usually present in LIF measurements is shown in figure 15.25. This is a so-called *excitation-emission spectrum*, in which

the measured fluorescence intensity is represented in false colours as a function of both the excitation wavelength (or wavenumber, in this case; along the ordinate) and of fluorescence wavelength (along the abscissa). Horizontal cross sections through such a spectrum provide fluorescence spectra (bottom) induced by a particular excitation wavelength (red arrow at $\approx$ 51713 cm^{-1}), and vertical cross sections provide excitation spectra (right) at one particular fluorescence wavelength (purple arrow at $\approx$ 216 nm). Clearly, there is a lot of information in such an excitation-emission spectrum. Some specific features of the spectrum of fig. 15.25:

- Bright fluorescence spots often occur in pairs (one of them is green encircled at $(x, y) = (205, 51690)$). These can all be attributed to hot O_2, not to NO.
- The relatively dark horizontal band through the middle of the spectrum ($y \approx 51685$) is due to absorption of the excitation laser by cold O_2 on its way through ambient air towards the engine.
- Fluorescence bands of NO are diffuse blobs (one of them encircled at $(215, 51655)$) and relatively weak (compared to the O_2 features).
- The fluorescence spectrum at the bottom shows several vibrational bands of the $D(v' = 0) \rightarrow X(v'')$ progression (v'' is indicated in the graph). The band at 225 nm in fact overlaps with another band, that belongs to a different electronic transition, viz. the $A(v' = 0) \rightarrow X(v'' = 0)$ band (with a progression that extends further to the red; not shown).
- Fluorescence bands are typically 1–2 nm broad ($\approx$ 200–400 cm^{-1} in this wavelength range), that is, much broader than you would expect from fluorescence out of a single rotational state. This is due to the fact that the upper state (mainly $D(v' = 0)$) is rotationally thermalized by RET, so that there is fluorescence out of many different J'-levels. Detection equipment generally does not resolve individual rotational transitions.
- The intense vertical line at $x \approx 208$ nm is due to fluorescence of the entrance window for the excitation laser beam.

The main conclusion to be drawn out of this example is that LIF is a very selective technique. In order to fully exploit this selectivity (and to fully avoid unexpected spectral interferences), it is good practice to start experiments with a spectroscopic survey.

From an excitation-emission spectrum, a combination of excitation and detection wavelengths can be selected for quantitative measurements on a particular chemical species. One of the large advantages of LIF is that scattering efficiencies tend to be high, and once a suitable combination of excitation and detection wavelengths has been choosen, it is often possible te record two-dimensional fluorescence images, even with relatively low-power lasers (usually Nd:YAG-pumped pulsed dye lasers, with $1-10$ mJ/pulse). To this end, the laser output is shaped into a thin light ribbon by means of cylindrical lenses. This light sheet cuts through the medium of interest, and fluorescence (which now originates from the illuminated plane only; this provides spatial resolution along the line of sight) is collected in a direction perpendicular to the plane of the light sheet by a (usually intensified) CCD camera. This scheme is known as planar LIF, or PLIF. An example is reproduced in figure 15.26, showing a false colour map of OH fluorescence in the flame of an oxy-acetylene welding torch. Excitation was in the $A^2\Sigma^+(v' = 0) \leftarrow X^2\Pi(v'' = 0)$ band near 308 nm, using a frequency-doubled pulsed dye laser; fluorescence in the $A(0) \rightarrow X(1)$ band at 343 nm was recorded by an intensified CCD camera (384×256 pixels) through a Schott WG305 cut-off filter, the latter to block reflections of laser light off the burner and substrate surfaces [5]. Residual reflections of stray laser light are still visible, but they

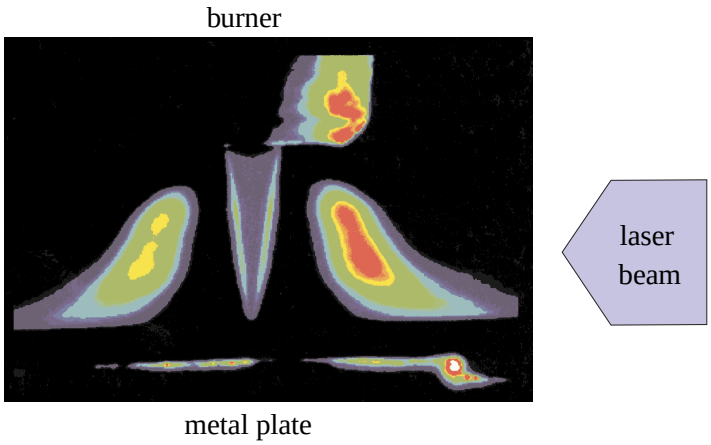

Figure 15.26: False colour image of laser-induced OH fluorescence, recorded in an oxyacetylene flame produced by a welding torch. The flame burns downwards onto a metal plate. See text for discussion.

are localised and not interfering. The sharp "V" in the center is due to OH present in the flame front, but the main OH fluorescence lobes are located at the boundary between the flame and the ambient air.

In order to evaluate fluorescence intensities quantitatively, the recorded pixel values S_{LIF} can be expressed as

$$S_{\mathrm{LIF}} = \eta \wp(T, P) g(\nu_a, \nu_L) f_{v,J}(T) I_L \rho_i \ , \tag{15.48}$$

that is, the pixel values are proportional (factor η) to the number density ρ of the molecule that is probed (OH in this case), and to the local laser intensity, I_L. The latter decreases along the path of the laser beam through the medium, and this explains why the left-side fluorescence lobe is less intense than the right-side one in figure 15.26. Because only a single rotational transition is excited, the total number density has to be multiplied by a (temperature-dependent) Boltzmann-factor $f_{v,J}(T)$ to yield the number density of the probed state. Finally, there is a Stern-Vollmer factor $\wp(T, P)$, discussed above (depends on temperature, pressure and local composition of the medium) and an overlap integral (discussed in section 2.2) to account for the excitation efficiency. In many cases, the total density ρ of the species of interest is the desired quantity, and it is clear that there are quite a lot of other parameters that need to be known in order to extract this ρ out of the measured pixel values S_{LIF}. In favourable cases, this can be achieved by a simple calibration on a known density of the species of interest. In combustion environments, however, there tend to be large spatial variations of at least temperature and composition, which give rise to more or less strong position dependence in all factors appearing in eq. 15.48. Much research is directed to finding appropriate ways to achieve calibration also in such circumstances, and the reader is urged to consult the relevant literature (ADC is a good start, in particular the compilation by Smyth & Jeffries [1]) before setting up an LIF experiment.

References

[1] Smyth, K.C., Crosley, D.R. (2002): Detection of minor species with laser techniques. In ACD (see §1), ch. 2.

[2] Luque, J., Crosley, D.R.: LIFBASE, database and spectral simulation program, version 1.9.103. SRI internal report. (http://www.sri.com/psd/lifbase)

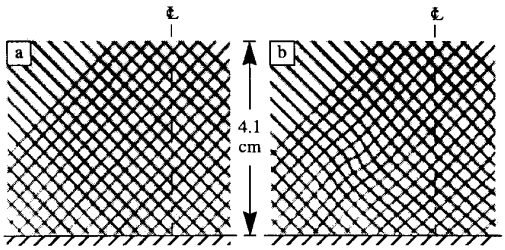

Figure 15.27: Principle of Molecular Tagging Velocimetry (from Gendrich *et al.* (1997)). (a) Initial distribution of tagged molecules, created by two 'combs' of thin laser beams (grey scale; white = 0%, black = 100%). (b) 8 ms later, the distribution is modified by the flow.

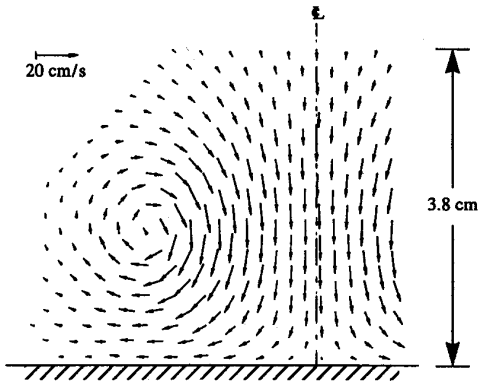

Figure 15.28: Principle of Molecular Tagging Velocimetry (from Gendrich *et al.* (1997)). Velocity field derived from figure 15.27. This experiment was done in water, using phosphorescent molecules.

[3] Kirby, B.J., Hanson, R.K., 1999: Planar laser-induced fluorescence imaging of carbon monoxide using vibrational (infrared) transitions. Appl. Phys. B **69**, 505-507 (1999).

[4] Lambert, J.D., 1977: Vibrational and rotational relaxation in gases. Clarendon press, Oxford, UK.

[5] Klein-Douwel, R.J.H., Spaanjaars, J.J.L., ter Meulen, J.J., 1995: Two-dimensional distributions of C_2, CH and OH in a diamond-depositing oxyacetylene flame measured by laser-induced fluorescence. J. Appl. Phys. **78**, 2086-2096.

2.8 Molecular Tagging Velocimetry

Velocity is defined as the rate of change of position with time (all relative to one specific frame of reference),

$$\vec{u} = \frac{\mathrm{d}\vec{r}}{\mathrm{d}t} \; . \tag{15.49}$$

Velocity (field) measurement techniques can accordingly be categorized in two classes, as follows:

Indirect methods: These do not measure velocity itself, but a related quantity, like heat flux (hot wire anemometry) or total pressure (pitot tube).

Direct methods: These measure the displacement of tracer particles over a well-defined time span, that is, the r.h.s. of eq. 15.49.

The indirect techniques will not be considered here. All optical techniques belong to the second class[12], the direct velocimetry methods. Some of them are based on light scattering off small solid or liquid particles that are 'seeded' into the flow of interest (LDA, PIV, PTV; see the lecture by Koen Schreel). Others avoid particulate seeding, since they are based on optical labelling of specific

[12]Whether LDA is a direct or an indirect method is open to discussion, but to some extent semantic. It depends on the point of view you adopt: Doppler or fringe traversal.

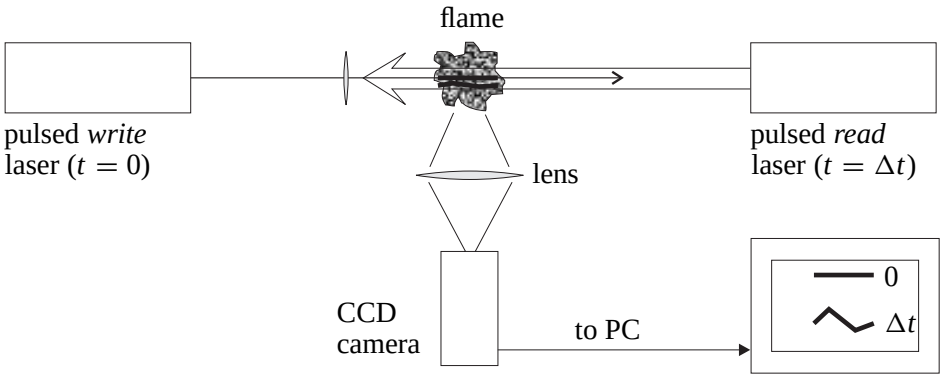

Figure 15.29: Experimental setup for APART. Other implementations may require a different write-laser (read-laser is more flexible). In the case of tagging with phosphorescent molecules (like in the example of figure 15.27), no read-laser is required.

molecules in the flow. The latter techniques are collectively known as Molecular Tagging Velocimetry (MTV), and they are the subject of this section.

Molecular tagging velocimetry is typically a two-step process (illustrated in figure 15.27). In the first, so-called *write*-step, a well defined spatial pattern of molecules in the flow is labelled (*tagged*). The labelling process (discussed below) makes these molecules in some way or another distinguishable from their surroundings (figure 15.27-a). In the second step (the *read*-step), taken a well-defined time interval Δt after the write-step, the distribution of tagged molecules, now modified by the flow in which they are embedded, is read out (figure 15.27-b), often by means of LIF (section 2.7). The velocity field is then derived from the displacement and/or deformation of the pattern (figure 15.28). Thus, the evaluation of the velocity field proceeds similarly to that of PIV, but the markers are molecular, rather than particulate.

Over the last 15 years or so a variety of MTV implementations have been developed, that differ from each other in the way by which tagged molecules are created, and how they are read out. Some of them have been designed for liquid velocimetry (like figure 15.27), some others are suitable for the gas phase. As in other sections of this lecture, I will not attempt a review[13], but rather restrict myself to one particular scheme (dubbed APART), that has been shown to be applicable not only to non-reactive flows but in combustion environments as well [4].

Air photolysis and recombination tracking

Air Photolysis And Recombination Tracking (APART) is an implementation of MTV that uses newly created NO molecules as flow label [3]. The experimental setup (in principle similar to most other MTV schemes) is shown schematically in figure 15.29. At $t = 0$ a pulse from the ArF excimer laser, weakly focussed into the flow field, 'writes' a thin line of NO molecules in its waist region. For a single beam, this results in a thin line of NO molecules, typically about 100 μm diameter and 10 mm long. Read-out is performed by planar LIF in the γ-system ($A^2\Sigma^+ - X^2\Pi$) of NO, using a pulsed, frequency-doubled dye laser ($\lambda \approx 226$ nm) that is fired at an adjustable time delay Δt after the write-laser.

Chemistry: The chemical pathway along which the NO formation proceeds is not known exactly. In plain

[13] See Koochesfahani [2] for the most recent one. Since then, a few interesting new schemes have been reported; these are cited in ref. [3].

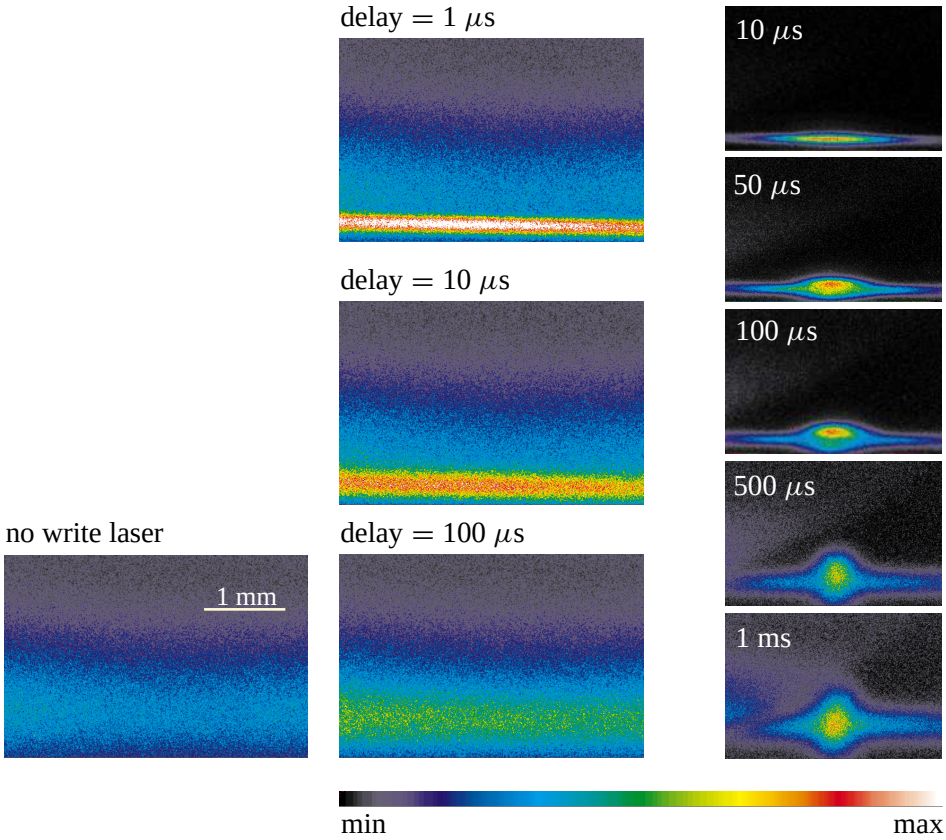

Figure 15.30: APART velocimetry in a CH_4/air flame. See text for details.

air, it is very likely that O-atoms and N_2^+-ions play a role. Both are present in the waist region of the excimer laser beam. In practice, the NO production can conveniently be optimized by optimizing the fluorescence in the first negative system ($B^2\Sigma_u^+ - X^2\Sigma_g^+$) of N_2^+ at about 392 nm. When applied to a flame, the mechanism is probably different from that in air, perhaps involving H_2O photolysis (very speculative).

Two examples[14] of the application of APART to a methane/air flame are given in figure 15.30. All panels show an image recorded by the CCD camera, with the timing chosen such that all NO fluorescence induced by the read laser would be captured; the time delay between read and write lasers is indicated. In the images of the middle column, the write-laser wrote a line of NO downstream of the flame front of a flat, laminar flame. Because the flame itself produces NO as well, the images contain a broad background (image in the left column; the height is limited by the width of the read laser light sheet) onto which a well-defined more intense line (obviously due to the 'written' NO) is superposed. This line is advected by the flow (upwards in the images) at a speed of 2.3(3) m/s, as derived from the images. Also, the written line is seen to broaden considerably with increasing time delay. This is due to molecular diffusion. In the end, it will be a limiting factor for the velocity resolution that can be achieved. An important conclusion that can be drawn from these images is that, on the spatial scale that is resolved by this setup, there is no evidence for a perturbation of the flame, that is, under the conditions of this experiment the APART method is non-intrusive indeed.

The column at the right in figure 15.30 shows an example in which APART is not non-intrusive

[14] Including a bad one; this is an honest course.

Figure 15.31: Denver airport (from `http://www.ala.org/acrl/bigdia.html`).

any more. This experiment was performed on the same burner, but the gas flow speed was increased to such an extent that the flame front became wrinkled, with upward cusps and local points of attachment to the burner surface (looking more-or-less like the roof of Denver airport, see figure 15.31). The write-laser beam passed through one of these cusps, crossing the flame front on two points in the field of view. In the center of the field of view, a bright blob is seen to grow, undoubtedly due to local ignition of the flame by the write laser. This, of course, is an expression of the fact that, when all is said and done, MTV is not *really* non-intrusive. Energy is put into the flow by the write-laser (and this holds for all MTV schemes published thus far), and this energy may (or, in some cases, must) trigger chemistry. Especially in combustible mixtures, which are already chemically unstable by themselves, this may lead to undesired side-effects. However this may be, I would assert that MTV in principle allows velocimetry in the least intrusive way.

References

[1] Gendrich, C.P., Koochesfahani, M.M., Nocera, D.G., 1997: Molecular tagging velocimetry and other novel applications of a new phosphorescent supramolecule. Exp. Fluids **23**, 361-372.

[2] Koochesfahani, M.M., 1999: Molecular tagging velocimetry (MTV): Progress and applications. AIAA paper no. AIAA-99-3786.

[3] Dam, N., Klein-Douwel, R.J.H., Sijtsema, N.M., ter Meulen, J.J., 2001: Nitric oxide flow tagging in unseeded air. Opt. Lett. **26**, 36-38.

[4] Sijtsema, N.M., Dam, N.J., Klein-Douwel, R.J.H., ter Meulen, J.J., 2001: Molecular tagging velocimetry in unseeded air flows. AIAA paper no. AIAA-2001-0851.

2.9 Laser-Induced Incandescence

Laser Induced Incandescence is about the only technique that provides global information on soot properties. It is *not* non-intrusive, being based on brute force overheating of the soot particles, and this is part of the reason why there is still some controversy on the interpretation of the data. The treatment given below is based mainly on ACD [1].

Soot is not a well-defined notion. What it generally refers to is a broad class of particulate matter, to a larger or lesser extent based on carbon, but possibly containing all kinds of chemical compounds,

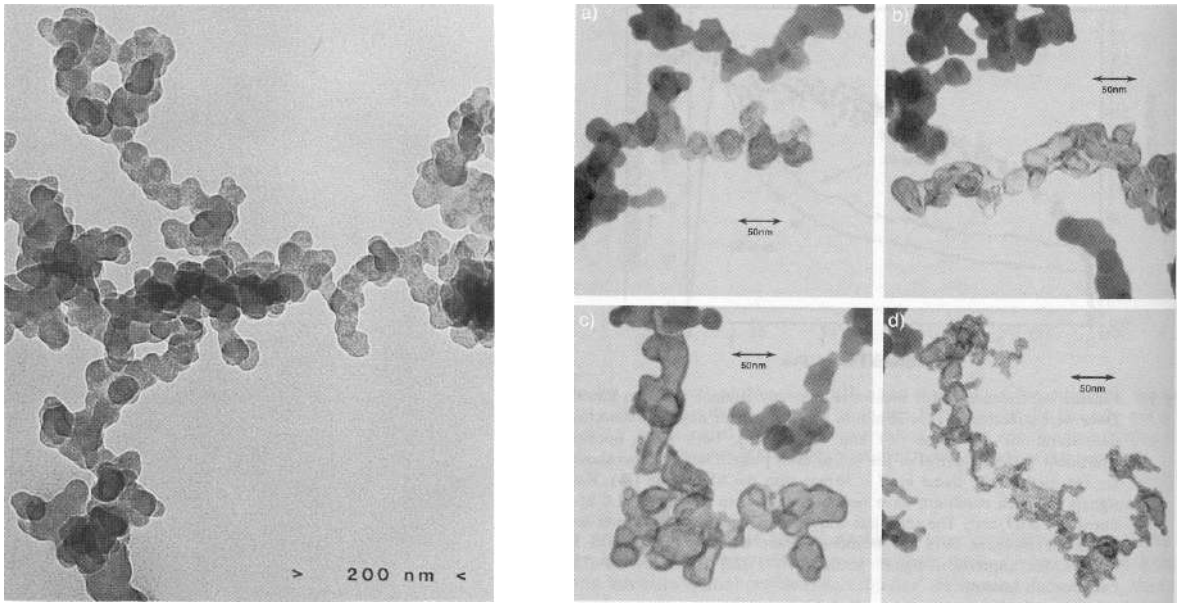

Figure 15.32: Soot morphology in an ethene flame. Left: sampled from the upper buoyancy region, without laser irradiation [2]. Right: Sampled after heating by Nd:YAG laser pulses ($\lambda = 1064$ nm) of different energy content (a–d: 0.15, 0.3, 0.6 and 0.9 J/cm^2) [3].

including aromatics and traces of metallic elements. Moreover, the morphology is generally erratic, and the size distribution may span the range from several tens of nanometers to several hundred micrometer. A diagnostic method to nevertheless characterize the soot distribution in a combustion process would have to deal with all this variation. The philosophy behind Laser-Induced Incandescence (LII) is that the variation is removed when the soot particles are heated up to their evaporation limit ($\approx$ 4000 K). At this temperature the soot, irrespective of its initial constitution, has metamorphosed into rather loose agglomerations of $\pm$spherical carbonaceous particles, the so-called *primary particles* (figure 15.32). These particles (typically 10–60 nm diameter) emit black- (or grey-)body radiation, and this is the incandescence detected experimentally. The amount of light that is emitted by a single soot particle is a measure for the particle volume, whereas the time during which it emits light, which is finite because the particle cools down, is a measure for the size of the particle.

There are two main implementations of the technique:

- Time resolved LII (Tire-LII). The time-resolved radiative output is monitored immediately following the heating laser pulse. Basic idea is that small particles cool down faster than larger ones, and Tire-LII is often used for primary particle size measurement.

- Planar LII. The total radiative output after a heating laser pulse is monitored by a CCD camera (see setup in figure 15.33). This is a measure for the soot volume fraction within the field of view.

Analysis of the LII signal proceeds through an energy balance equation, that can be written as

$$m_s \frac{\mathrm{d}c_s T_s}{\mathrm{d}t} - \frac{H_v}{M_v}\frac{\mathrm{d}m_s}{\mathrm{d}t} = I_L C_{abs} - hA_s(T_s - T_\infty) - \int_0^\infty 4C_{abs}E_{b,\lambda}(T_s)\,\mathrm{d}\lambda + \int_0^\infty 4C_{abs}E_{b,\lambda}(T_w)\,\mathrm{d}\lambda\ , \quad (15.50)$$

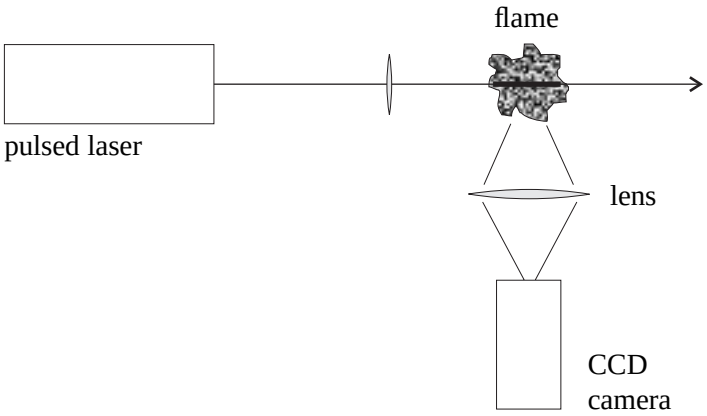

Figure 15.33: Experimental setup for planar LII measurements. For time-resolved measurements, the CCD camera must be supplemented with a fast detector.

in which the symbols have the following meaning: m_s: mass of the (primary) soot particle with surface area A_s, specific heat c_s, and temperature T_s; T_∞: surrounding gas temperature; T_w: temperature of radiant surroundings; H_v: vaporization enthalpy; M_v: vapour molecular weight; I_L: incident laser intensity; C_{abs}: absorption cross section of the particle; h: convective coefficient; $E_{b,\lambda}$: black body spectral irradiance. The individual terms in eq. 15.50 can be identified as follows. Left hand side: (1) rate of increase of the particle internal energy; (2) loss rate of internal energy due to vaporization. Right hand side: (1) rate of energy absorption from the incident light; (2) collisional cooling rate (this is a tricky term); (3) radiative emission rate; (4) radiative absorption rate (of radiation emitted by the surroundings). The total radiative output power can be shown to be approximately proportional to the soot volume fraction f_v, and this has also been confirmed experimentally (see e.g. [4]). Calibration can be performed by extinction measurements, or, in the case of only weakly sooting flames, by CRDS (see section 2.4).

A typical setup for planar LII is shown in figure 15.33. Excitation is usually performed by the fundamental (1064 nm) or second harmonic (532 nm) of a Nd:YAG laser; the former has the advantage that C_2 fluorescence in the Swan bands (ca. 515 nm) is avoided. Besides the CCD camera, it is advisable to have a spectrograph available, to have at least some clue as to the structure of the emitted spectrum. Possible pitfalls include the aforementioned Swan bands as well as grey body effects.

References

[1] Santoro, R.J., Shaddix, C.R., 2002: Laser-Induced Incandescence. In ADC, chapter 9.

[2] Dobbins, R.A., Subramaniasivam, H., 1994: Soot precursor particles in flames. In: Bockhorn, H. (ed.): Soot formation in combustion. Springer Series in Chemical Physics, vol. 59, pp. 290-301.

[3] Vander Wal, R.L., Ticich, T.M., Stephens, A.B., 1998: Optical and microscopical investigations of soot structure alteration by laser-induced incandescence. Appl. Phys. B **67**, 115-123.

[4] VanderWal, R.L., Weiland, K.J., 1994: Laser-induced incandescence: Development and characterization towards a measurement of soot volume fraction. Appl. Phys. B **59**, 445-452.

Chapter 16

Coherent Anti-Stokes Raman Spectroscopy (CARS)

Th. H. van der Meer and H. B. Levinsky

1 Introduction

In combustion, next to fluid velocities, temperature is an important variable to be measured. Thermocouples have been used quite successfully in the past, but they have the drawback, that their accuracy for very high temperatures is rather low. Radiation losses, conduction losses and catalytic properties of the thermocouple material are error sources. Besides it is impossible to measure temperature fluctuations in turbulent flames. Several laser techniques can be used for temperature measurements. One of the most powerful techniques is Coherent anti-Stokes Raman Spectroscopy.

CARS has been a very attractive diagnostic technique for various combustion processes for over 20 years [1]–[6]. It allows non-intrusive, temporally and spatially resolved measurements of temperature and major species concentrations. The large increase in S/N afforded by CARS relative to spontaneous Raman scattering makes it possible to probe the highly luminous, particle laden flames as used in many practical combustion systems. In air-fed turbulent flames, broadband CARS thermometry of nitrogen is most commonly applied to measure instantaneous and mean temperatures, temperature fluctuations and PDFs (probability density functions) [6]–[10].

CARS is a non-linear Raman technique. With the linear Raman technique photons at frequency ω_1 induce a linear polarisation in a medium (see figure 16.1). During this interaction process energy is exchanged. If the photon loses energy, the scattered photon is Stokes shifted, if the photon gains

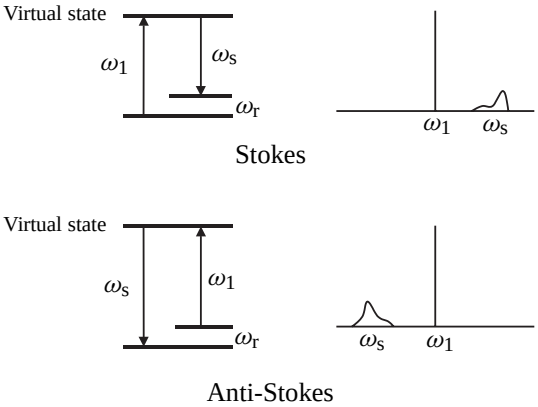

Figure 16.1: Raman scattering.

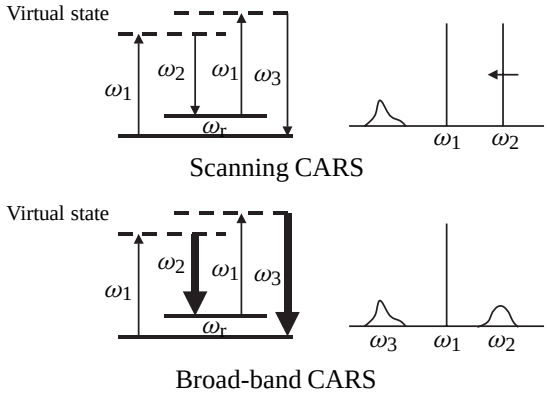

Figure 16.2: CARS.

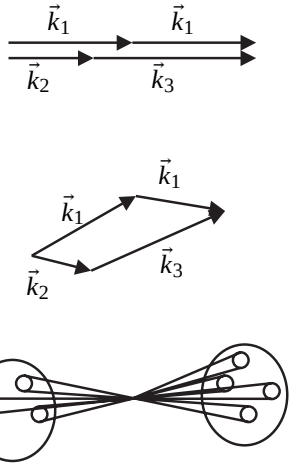

Figure 16.3: Phase mathching schemes.

energy, it is anti-Stokes shifted. From the amount of energy transferred during this interaction process, medium properties can be obtained. Raman scattering occurs in all directions and it is a very weak signal. One of every 10 million photons is inelastically scattered. Very powerful lasers have to be used and only very clean flames can be probed with this technique. CARS is a non-linear four-wave mixing process (see figure 16.2). Two laser beams of frequency ω_1, the pump beam, and ω_2 , the Stokes beam, interact with the medium via the third order susceptibility. This interaction induces a third coherent beam at frequency $\omega_3 = (2\omega_1 - \omega_2)$. If $\omega_1 - \omega_2$ is tuned to a Raman transition of molecules present in the measuring volume, the CARS signal is resonant and species can be detected. The CARS beam is laser-like and thus the collection efficiency can be much higher than for Raman. Also the conversion efficiency is a factor of 1000 higher. So CARS is much stronger. The Stokes laser beam can be narrow band for scanning CARS or broadband for single-shot CARS. In this broadband configuration an entire *Q*-branch signature of a molecule can be recorded in one single laser shot. This allows single shot temperature measurements in turbulent flames. The CARS process is most effective if conservation of momentum is maintained. The incident beams must be aligned such that the mixing process is properly phased. This ensures that the CARS signal generated at a certain point will be in phase with the CARS generated at all points in the measuring volume are in phase, leading to a constructive build-up of the signal. In figure 16.3 two phase matching schemes are illustrated. In the first scheme all CARS beams are aligned with each other. This is the simplest arrangement, but the overlapping region where the CARS signal is generated, is very wide. A better spectral resolution can be obtained with the BOXCARS arrangement. Here the three beams cross each other in a measuring volume, which may have similar sizes as a measuring volume of LDA optics.

2 Thermometry

The intensity of the CARS signal is dependent in a non-linear way on parameters such as temperature, species concentrations Raman line width and pressure. A computer model of the spectrum of the probed species must be used for the quantification of the intensity of the CARS signal. For the CARS theory is refered to [1]. The temperature sensitivity of the CARS technique results from the variation in rotational-vibrational populations of the Raman transitions of the species probes, which is N_2 for thermometry. Thus a spectroscopic, rather than a translational temperature is measured with this technique. In most combustion sytems these temperatures are equal. An example of a CARS spectrum of N_2 at 2000 K is given in figure 16.4. This spectrum would be measured if the resolution

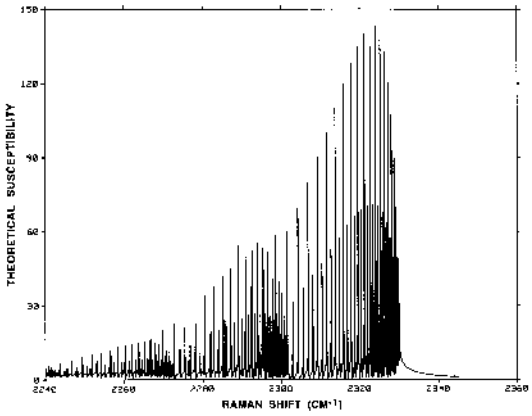

Figure 16.4: CARS spectrum of N_2

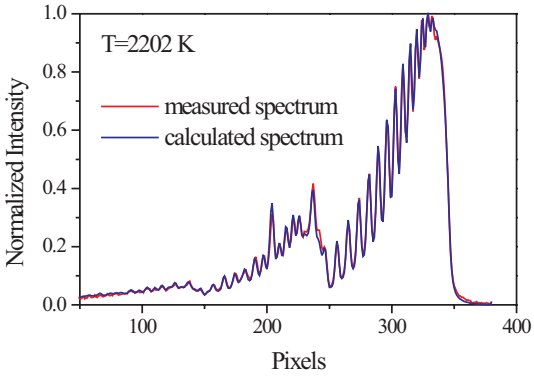

Figure 16.5: Measured and fitted spectrum.

of the laser and the detector system would be perfect. The spectrum however is broadened by the laser system, the grating of the spectrometer and the detector used. A typical spectrum that was measured in a real laminar flame up is given in figure 16.5, together with a calculated spectrum, which is corrected for the broadening of the laser and detection system. The comparison of the calculated spectrum with the measured spectrum gives us an accurate measure of the temperature.

The CARS intensity is very dependent on temperature: the intensity at 300 K is more than 1000 times the intensity at 2000 K. The reason for this is twofold. In the first place the densities differ by a factor of 6 to 7. In the second place the width of the spectrum is much smaller at low temperatures. In turbulent diffusion flames with large temperature gradients this is a cause of high inaccuracy. With only a small portion of the measuring volume in a cold region the spectrum is so much influenced by the signal from this region that an accurate measuring volume averaged temperature is impossible to determine. This leads to inaccuracies of over 150 K in temperature measurements near flame zones, even with a very small length of the measuring volume less than 1 mm [10].

3 Experimental arrangement

A typical CARS experimental set-up is shown in figure 16.6 [10]. It consists of a frequency-doubled Nd:YAG laser (Continuum YA-680) which yields 400 mJ per pulse at $\lambda_p = 532$ nm, with a typical pulse duration of 6 ns at a repetition rate 10 Hz. The laser is multimode pumped, resulting in a ω_p linewidth of 1 cm^{-1}. Eighty percent of the ω_p beam is split off to pump a broadband oscillator amplifier dye laser (Continuum TDL-60). Rhodamine 101 in methanol is used in the dye laser to generate a broadband Stokes beam ω_s with a bandwidth of 150 cm^{-1} FWHM centered at 607 nm. The remaining 20% of the pump radiation is split off to form two equal intensity pump beams. The Stokes and the two pump beams are focused inside the flame by a 350 mm focal length lens. A folded BOXCARS phase-matching scheme is used for good spatial resolution and ease of CARS signal separation. The resulting CARS beam ($\omega_{as} = 2\omega_p - \omega_s$) is recollimated, spectrally dispersed in a SPEX-1404 0.85 m double spectrometer and recorded on a CCD camera (Princeton Instruments TE/CCD-1100P) with a 17-bit dynamic range. The camera contains 1100×330 pixels and the vertical direction was accumulated within the laser repetition rate of 10 Hz to obtain an array with 1100 pixel values. The corresponding spectral dispersion is 0.3 cm^{-1} per pixel and the spectral resolution of the recorded CARS spectra is about 1 cm^{-1}. The pixel arrays containing active CARS spectra are digitized and stored in a Pentium-based PC.

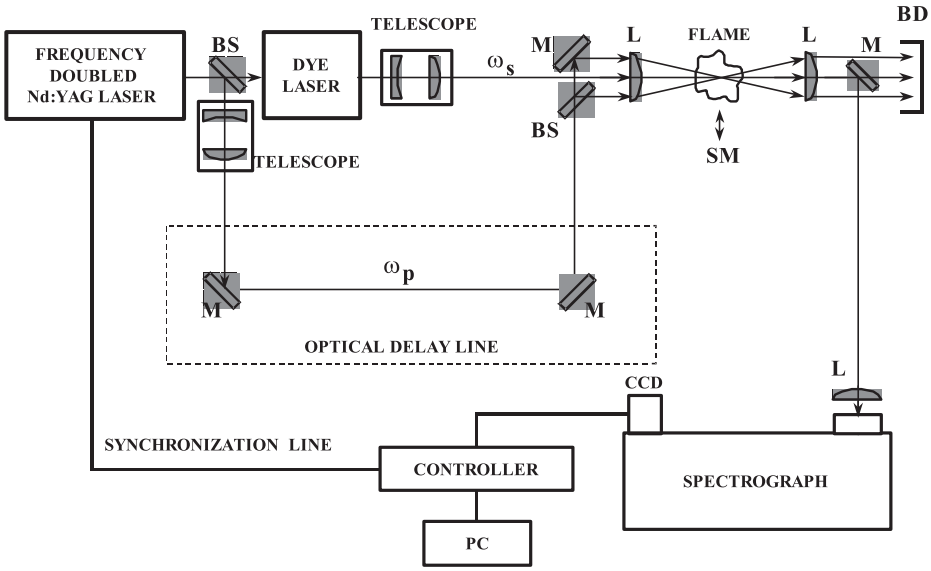

Figure 16.6: Experimental CARS arrangement.

Several computer codes that can be used to fit the experimental spectra with theoretical spectra are available, such as CARP3 [11], CARSFIT [12] and DACAPO [13]. These codes calculate the theoretical CARS spectra, contain a calibration procedure to determine and incorporate instrumental parameters and a least squares fitting program. A library of N_2 CARS theoretical spectra is firstly calculated in the range of 300–2200 K with steps of for example 100 K. Interpolation results in accurate spectra for other temperatures.

In a typical CARS experiment, the background, non-resonant (in a pure methane cell) and resonant room temperature nitrogen CARS spectra are recorded for calibrations purpose. The instrument function for the CARS optical arrangement is determined from the room temperature CARS spectrum. The non-resonant CARS spectrum in a pure methane cell represents the spectral intensity profile of broadband dye laser. In order to eliminate the shot-to-shot fluctuations, a large number of non-resonant spectra are averaged to generate the reference non-resonant spectrum. The resonant N_2 CARS spectra are then measured in the flame. The flame spectra and reference non-resonant spectra are background subtracted. The flame spectra are then fitted with theoretical spectra, which are convoluted with the instrument function and multiplied by the reference non-resonant spectrum. In spectra fitting processes, the temperature and the concentration of nitrogen are the main varying parameters, but frequency shifting and vertical stretching are also fitted.

References

[1] C. Eckbreth, *Laser diagnostics for combustion temperature and species*, OPA Amsterdam B.V., The Netherlands, 1996.

[2] D. A. Greenhalgh, *Quantitative CARS Spectroscopy*, in Advances in Non-linear Spectroscopy, R. J. H. Clark and R. E. Hester, Eds, Wiley and Sons, New York, 1988.

[3] L. P. Goss, D. D. Trump, W. F. Lynn, and T. H. Chen, *Second-generation combined CARS-LDV instrument for simultaneous temperature and velocity measurements in combusting flows*. Rev. Sci. Instrum., 60, 638 (1989)

[4] P.- E. Bengtsson, L. Martinsson, and M. Aldén, *Dual-broadband rotational CARS measurements in an IC engine*, Twenty-fifth symposium on combustion, The Combustion Institute, Pittsburgh, PA, 1735 (1994)

[5] T. Dereier, M. Ridder, and G. Schiff, *Determination of temperature from N2 and O2 CARS spectra at very high pressure*, Twenty-fifth symposium on combustion, The Combustion Institute, Pittsburgh, PA, 1727 (1994)

[6] A.C. Eckbreth, G. M. Dobbs, J. H. Stufflebeam, and P. A. Tellex, *CARS temperature and species measurements in augmented jet engine exhausts*, App. Opt. 23, 1328(1984)

[7] D. A. Greenhalgh and F. M. Porter, *The application of coherent anti-Stokes Raman scattering to turbulent combustion thermometry*, Combust. Flame, 49, 171 (1983)

[8] L. P. Goss, G. L. Switzer, D. D. Trump, and P. W. Schreiber, *Temperature and species-concentration measurements in turbulent diffusion flames by the CARS technique*, AIAA 82-0240, (1982)

[9] D. Klick, K. A. Marko, and L. Rimai, *Optical multichannel analysis with rapid mass storage of spectra: application to CARS measurements of temperature fluctuations*, App. Opt. 23, 1347 (1984)

[10] J. Mantzaras and T. H. Van Der Meer, *Coherent anti-Stokes Raman spectroscopy measurements of temperature fluctuations in turbulent natural gas-fueled piloted jet diffusion flames*, Combust. Flame, 110.

[11] CARP3 is a CARS spectral analysis code developed by AEA Technology, Harwell, Oxon. OX11 0RA, UK. CARP3 is marketed by Epsilon Research Ltd, PO Box 354, High Wycombe, Bucks, HP12 9BZ, UK

[12] CARSFIT is a CARS spectral analysis code developed by CRF, Sandia National Laboratories, Lvermore, CA., USA

[13] D. Bruggemann and S. Heshe, *DACAPO-CARS spectra evaluation code users guide*, ITLR, University of Stuttgart, 1993.

Chapter 17

Laser Velocimetry Techniques: LDV, PTV, PIV

K. R. A. M. Schreel

1 Introduction

The velocity of a flowing medium can be measured in many different ways. One can be interested in purely statistical information, time-resolved information, space resolved information, or combinations of any of these. The ideal method measures the complete three dimensional field with a very high spatial and time resolution, but obviously, such a method does not exist. What do exist, are methods which have both weak and strong properties, and have a limited applicability. The choice of method depends on the problem that is to be solved, and for some problems, no solutions exist as of today.

In this chapter I will focus on three optical methods, one point method (Laser Doppler Velocimetry) and two closely related whole field methods (PIV/PTV). All three methods rely on the use of seeding particles in the flow and are suited for combustion problems. Other promising techniques are Molecular Tagging Velocimetry (treated in section 2.8 on page 274), Filtered Rayleigh Scattering, and Doppler Global Velocimetry (treated in section 2.5 on page 260). A more intrusive (non-optical) technique for point measurements is hot-wire anemometry (HWA). For some problems this technique is better suited than LDV, but not in the case of combustion, and will not be treated here.

Velocimetry techniques can be characterized by the following properties.

- Dimensionality: the number of vector components that can be retrieved in what number of spatial dimensions. Common PIV and PTV are both a two component (2C) and two dimensional (2D) technique. LDV can be characterized as (up to) 3C/0D.

- Data rate: the number of measurements per second. Typical values are 50 kHz for hot-wire anemometry, 1 kHz for LDV, 30 Hz for PTV and 15 Hz for PIV. When one really wants to follow coherent structures in fast gas flows, the possibilities are very limited.

- Dynamic range: the variation in velocities that can be recorded at one instant or during a series of measurements. LDV has a high dynamic range of two or more orders of magnitude. PTV and PIV do not offer more than a factor of 10. For both techniques spatial resolution can be sacrificed in favor of the dynamic range. PIV is better to measure higher velocities (see later).

- Spatial resolution: the ability to measure differences in velocity between neighboring points in space. The resolution of LDV is very high (sub-mm), but measurements at different positions cannot be performed simultaneously otherwise than by duplicating a complete setup for every measurement point. The resolution of PTV is slightly higher than that of PIV, at the sacrifice of a bit of accuracy.

- Accuracy: speaks for itself. Seeding (when needed) is a very important factor in the accuracy. For techniques using cameras, optical distortions (by lenses, at interfaces, due to variations in refractive index) also play an important role.

- Intrusivity: the extent to which a technique disturbs the flow. A hot wire disturbs the flow rather badly in comparison to seeding. Seeding, however, can disturb the flow too. It changes the density and heat capacity of the gas. Especially with PIV, where one needs quite a high seeding density, this can pose problems.

As shall be seen, both PTV and PIV have good properties for various types of meaurements. PIV is at the moment better suited for application in combustion processes, but PTV will be treated in detail too, because interesting hybrid combinations of PTV and PIV have been introduced lately. Furthermore, PTV can be extended to a 3C/3D technique with a simpler set-up than holographic PIV.

Both techniques have a lot in common, but there are some notable differences and they both come in various different variants. The common denominator is the use of tracer particles, and the use of comparable lighting sources and cameras. These aspects will be treated first.

1.1 Seeding

As already stated, seeding is common to both PIV, PTV, and LDV. These particles seeded must be chosen carefully. The following requirements hold for the sake of accuracy and non-intrusivity:

- Ideally the particles have the same density as the flow. This is possible for liquids, but for gases this is very difficult.

- The particles have to be small and monodisperse. Smaller sizes follow the flow better, especially when their density is much larger than the density of the flowing medium. A possible disadvantage of small particles is agglomeration and their (lack of) visibility. The monodisperse criterion is important when imaging particles, since the intensity of the scattered light is (for small particles) proportional to d_p^2, with d_p the diameter of the particle. Since digital cameras typically have a dynamic range of 8 bits, even a rather small variation in size (or agglomeration) can lead to overexposed areas in the image. When using LDV, one can often reject the measurements of too large particles based on scattering intensity.

- The particles should be spherical. This is to achieve uniform light scattering properties. If a particle rotates between two successive images and this results in a change in scattered intensity, this can lead to unwanted noise when analyzing the images.

- The particles should be distributed homogeneously in the flow. A lot depends on the way the seeding is introduced in the flow. But even if this is performed to perfection, most combustion problems feature large density differences due to thermal expansion. These differences are reflected in the seeding density.

For combustion a special requirement holds:

- The particles should not be consumed by the combustion process.

In practice, Al_2O_3 particles of 1 μm diameter are best suited for combustion problems. The melting point of 2300 K is high enough to survive most fuel-air combustion and it can be produced relatively cheap at the required diameter. For a detailed overview see e.g. Hassel and Linow [10] and

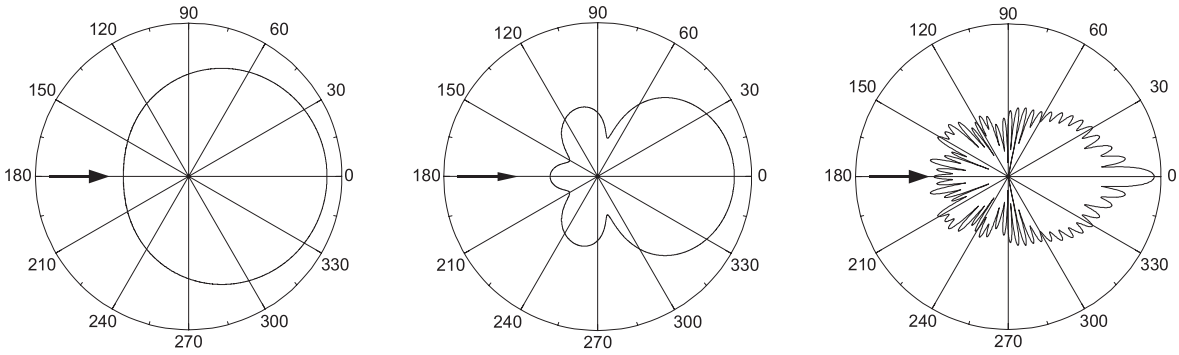

Figure 17.1: Polar representation of the intensity of Mie scattering for particles at several diameters. The incoming radiation comes from the left and the figure is axi-symmetric around this direction. The intensity is scaled logarithmically.

Melling [11]. Other candidates are MgO (higher melting point) and ZrO_2 (high melting point of 2800 K and extremely high evaporation point of > 4000 K, but twice the density of Al_2O_3).

I will highlight four important aspects which are of influence on meaurements: scattering by particles, the motion of particles in a fluid, the imaging of particles, and the seeding density.

Mie scattering

In contrast to Rayleigh scattering, which has a simple angular dependence of the scattered radiation, scattering off particles with a diameter of the order of the wavelength is rather complex. As can be seen in figure 17.1, the angular dependence can show strong fluctuations, and has as a general property that forward scattering is much more effective than backward scattering.

Motion of a particle in a moving fluid

Particles dispersed in a fluid will generally move with a different velocity than the fluid. Due to this velocity difference, $\vec{u}_p - \vec{u}_f$, the particles will experience a drag force. Spherical particles in viscous fluids at very low Reynolds number can be described with

$$\vec{F} = m\vec{a}_p = \rho_p \frac{\pi d_p^3}{6} \frac{d\vec{u}_p}{dt} = (\rho_f - \rho_p)\frac{\pi d_p^3}{6}\vec{g} - k(\vec{u}_p - \vec{u}_f), \tag{17.1}$$

with $k = 3\pi\eta d_p$ the viscous friction coefficient for a sphere with diameter d_p according to Stokes. The difference in density between the particle and the fluid gives rise to the term with the gravitational force $\vec{g}$. Because of temperature gradients an additional thermophoreses force can arise ($\propto -\nabla T/T$), because of which particle velocities will differ even more in areas with strong temperature gradients (e.g. flame fronts). In a quiescent isothermal medium, the fall (or rise) velocity follows from equation (17.1) as

$$\vec{u}_p = (\rho_p - \rho_f)\frac{d_p^2}{18\eta}\vec{g}. \tag{17.2}$$

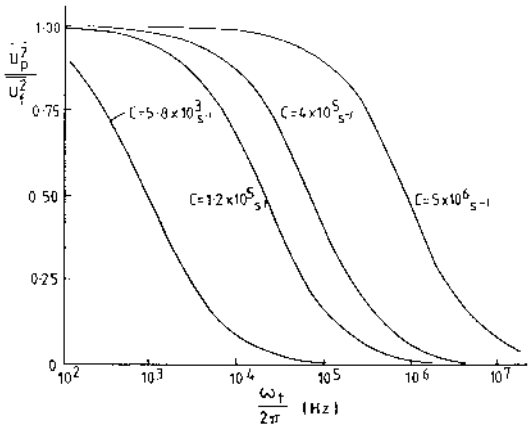

Figure 17.2: The response of a particle in a turbulent flow.

When the fluid has a constant velocity $\vec{v}$, the following expression follows

$$\vec{u}_\mathrm{p} - \vec{u}_\mathrm{f} = (\rho_\mathrm{p} - \rho_\mathrm{f})\frac{d_\mathrm{p}^2}{18\eta}\vec{g}. \tag{17.3}$$

If the flow accelerates, the acceleration $\mathrm{d}\vec{u}_\mathrm{p}/\mathrm{d}t$ will have to be calculated according to equation (17.1). Neglecting gravitation, equation (17.1) can be rewritten as

$$\frac{\mathrm{d}\vec{u}_\mathrm{p}}{\mathrm{d}t} = \frac{18\eta}{d_\mathrm{p}^2\rho_\mathrm{p}}\left(\vec{u}_\mathrm{p} - \vec{u}_\mathrm{f}\right) = C\left(\vec{u}_\mathrm{p} - \vec{u}_\mathrm{f}\right). \tag{17.4}$$

In figure 17.2 the response of the particle velocity to a sinusoidally fluctuating fluid velocity is plotted as a function of frequency and C. For an Al_2O_3 particle with a diamter of 1 μm ($C = 1.2 \cdot 10^5$ s^{-1}), the response is very good up to several kHz. See also Melling [11].

Imaging of particles

In figure 17.3 a schematic drawing of the imaging of particles is presented. The relation between the object distance (Z_0) and the image distance (z_0) is given by the well known equation

$$\frac{1}{f} = \frac{1}{Z_0} + \frac{1}{z_0}, \tag{17.5}$$

with f the focal length of the lens. The magnification factor M is defined as

$$M = \frac{z_0}{Z_0} \tag{17.6}$$

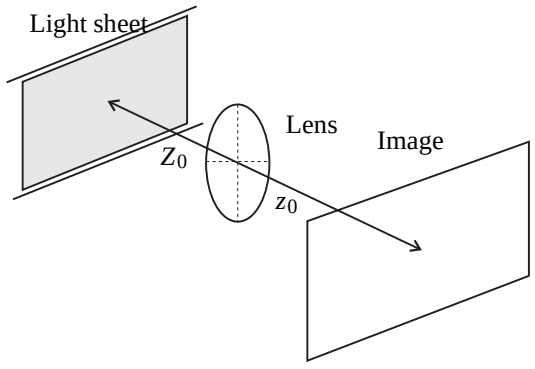

Figure 17.3: Imaging a light sheet on a film or CCD.

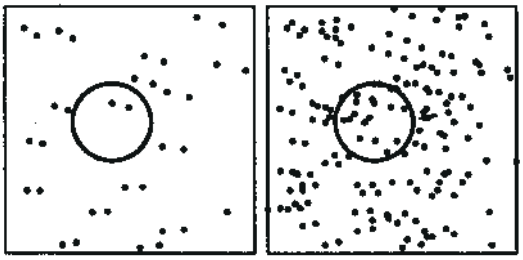

PTV
$N_i \ll 1$, $N_s \ll 1$

PIV
$N_i \gg 1$, $N_s \lesssim 1$

Figure 17.4: The differences in particle images between PTV and PIV

and is equal to the ratio of the size of the image and the size of the object. For small particles, however, diffraction plays a role, which will effectively *increase* the diameter of the particle image. The real diameter (d_r) of the particle image is related to the diameter of the particle (d_p according to

$$d_\mathrm{r}^2 = M^2 d_\mathrm{p}^2 + \left(2.44\frac{\lambda z_0}{\phi}\right), \tag{17.7}$$

with λ the wavelength of the incident light, and ϕ the diameter of the lens.

Marker density

For both PIV and PTV the marker density is a key parameter, determining the feasibility of the technique. If the fluid contains particles with a density C (in units of number per volume), the source density is defined as

$$N_\mathrm{s} = C\delta Z_0 \frac{\pi d_\mathrm{r}^2}{4M^2}, \tag{17.8}$$

with δZ_0 the thickness or depth of the illuminated volume. A source density of $N_\mathrm{s} > 1$ indicates that the particle images start to overlap eachother.

The image density is defined as

$$N_\mathrm{i} = C\delta Z_0 \frac{A}{M^2}, \tag{17.9}$$

with A the surface of the area of interest. For PIV this is the interrogation area and for PTV this is the search area (see later).

2 Laser Doppler Velocimetry

As already mentioned, Laser Doppler Velocimetry is a 3C/0D technique at best, but with a high temporal resolution. Because of this, it can be used for the measurements of turbulent kinetic energy and turbulent length scales. LDA was introduced in 1964 by Yeh and Cummings [1]. In the 1970's the technique matured and in the 80's it was fully commercialised. Now very compact instruments using fibre optics are widely used.

Another (older) technique with characteristics comparable to LDV is Hot Wire Anememometry (HWA). Compared to HWA, LDA has the following advantages

- LDA is non-intrusive apart from the seeding of small particles in the flow.
- LDA measurements can be directionally unambiguous. Especially for low velocities hot wire anemometry is not.

- With hot wire anemometry in both gas and water flows high turbulent frequencies up to 100 kHz can be measured. With LDA this is possible in water flows, but problematic in air flows.
- With LDA very low velocities can be measured. Hot wire anemometry is problematic in the cm/sec range.
- With LDA measurements in high turbulence and recirculations are possible
- LDA can be used in non-isothermal flows such as flames
- LDA does not need calibration
- The spatial resolution of hot wire anemometry is higher

For more detailed information on LDA see references [2] to [4].

2.1 The Doppler effect

When waves are scattered by a moving object, a frequency difference is introduced between the incident and scattered wave. This effect is commonly refered to as the Doppler effect and can, for example, be experienced when listening to the sound of a passing car. The pitch of the sound is high for an approaching car, and low when the car is moving away. As will be shown, the frequency difference between the two signals is proportional to the velocity of the car.

For an observer moving towards a source with velocity v, the measured frequency ω_i is given by

$$\omega_\mathrm{i} = \frac{\omega_0}{1 - \dfrac{v}{c}}, \tag{17.10}$$

with c the group velocity of the wave, and v is taken to be positive when the observer is moving towards the source. This expression holds in principle for all wave-like phenomena like sound, surface waves, electro-magnetic waves etc.[1] For the frequency shift $(\omega_\mathrm{i} - \omega_0)$ the following expression holds

$$\Delta\omega_\mathrm{i} = \omega_\mathrm{i} - \omega_0 = -\frac{\omega_\mathrm{i} v}{c} = -k_\mathrm{i}\, v, \tag{17.11}$$

or, more generally,

$$\Delta\omega_\mathrm{i} = -\vec{k}_\mathrm{i} \cdot \vec{v}. \tag{17.12}$$

When the source is moving, this changes to

$$\Delta\omega_\mathrm{s} = \vec{k}_\mathrm{s} \cdot \vec{v}. \tag{17.13}$$

When light is scattered from a particle, both effects apply at the same time. The frequency shift seen by a motionless observer with respect to a motionless source is then given by (see figure 17.5)

$$\Delta\omega = \Delta\omega_\mathrm{s} + \Delta\omega_\mathrm{i} = (\vec{k}_\mathrm{s} - \vec{k}_\mathrm{i}) \cdot \vec{v}, \tag{17.14}$$

leading to

$$\begin{aligned} \Delta\omega &= 2|\vec{k}_\mathrm{i}||\vec{v}| \sin\theta\, \cos\alpha \quad \text{of} \\ \Delta\nu &= \frac{2|\vec{v}|}{\lambda} \sin\theta\, \cos\alpha \end{aligned} \tag{17.15}$$

[1] For very high velocities (v in the order of the velocity of light), a relativistic expression needs to be used.

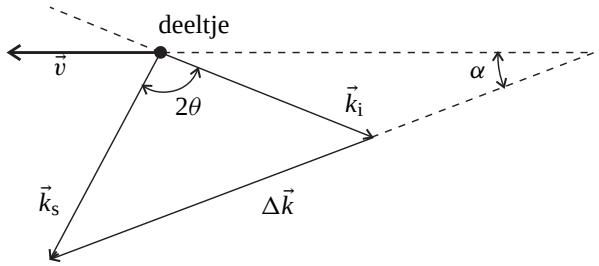

Figure 17.5: Geometry of the scattering of light by a moving particle.

approximating $|\vec{k}_\mathrm{i}| \approx |\vec{k}_\mathrm{s}|$. This approximation is valid for frequency shifts that are small in comparison with the source frequency. The relative shift is given by

$$\frac{\Delta\nu}{\nu} = \frac{2|\vec{v}|}{c} \sin\theta \, \cos\alpha, \tag{17.16}$$

giving an order of magnitude of $v/c = 10^{-8}$ for the scattering of light and a velocity of $v = 1$ m/s. This is of course sufficiently small for using equation 17.15, but poses a problem with regard to detectibility. In order to detect the shift directly, the frequency of the light has to be measured with an accuracy better than 10^{-9}. The answer to this problem is heterodyning the source wave with the scattered wave. This is basically nothing more than using the fundamental trigonometric relation

$$\cos\omega_1 t + \cos\omega_2 t = 2\cos\left(\tfrac{1}{2}(\omega_1+\omega_2)t\right) \cos\left(\tfrac{1}{2}(\omega_1-\omega_2)t\right). \tag{17.17}$$

In our case we can write

$$\begin{aligned} \omega_1 &= \omega \\ \omega_2 &= \omega + \Delta\omega. \end{aligned} \tag{17.18}$$

yielding for equation 17.17

$$\cos\omega + \cos(\omega+\Delta\omega) = 2\cos\left(\left(\omega+\tfrac{1}{2}\Delta\omega\right)t\right) \cos\left(\tfrac{1}{2}\Delta\omega\, t\right). \tag{17.19}$$

The sum of two cosines with a difference in frequency can be written as a product of two cosines, one having the average frequency and the other having half the difference frequency. In the case that $\Delta\omega/\omega \ll 1$ a wave results with frequency $\omega + \frac{1}{2}\Delta\omega \approx \omega$ which is amplitude modulated with frequency $\frac{1}{2}\Delta\omega$. In figure 17.6 the resulting 'beat pattern' is shown.

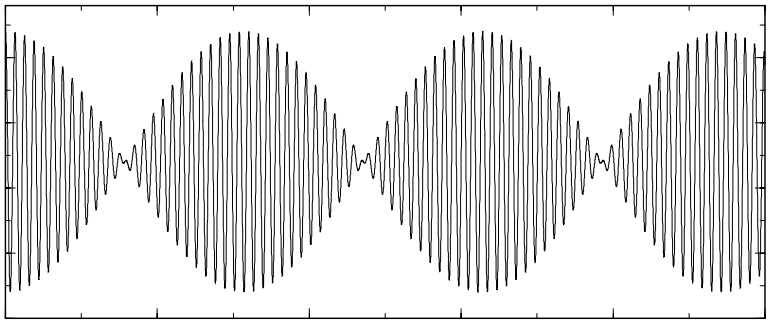

Figure 17.6: Amplitude modulated signal as given by equation (17.19). The number of zero crossings of the envelope is double the modulation frequency, $\Delta\omega$.

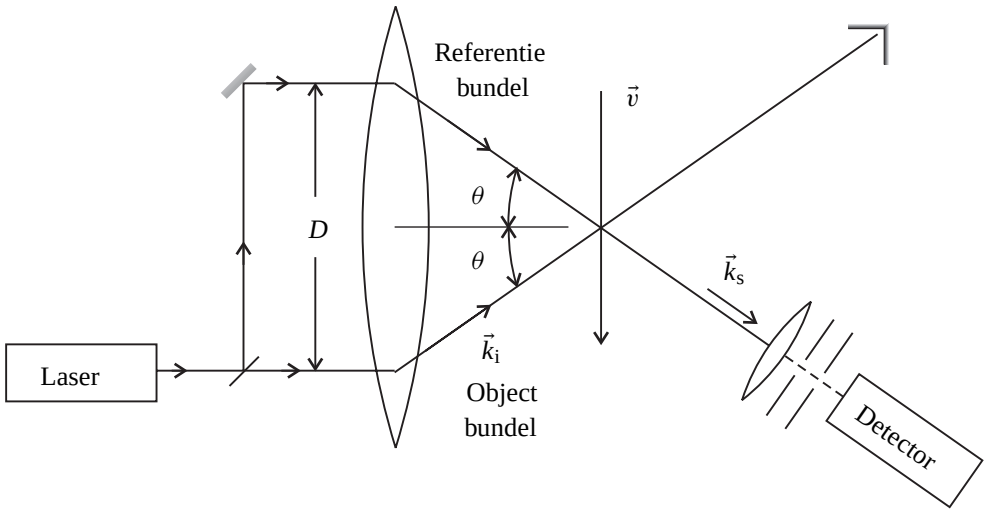

Figure 17.7: An LDV setup using a reference beam. The angle α as defined in figure 17.5 is 0° in this case. Check this for yourself.

In practice, light detectors behave as *power*-detectors, meaning that the signal is proportional to the *square* of the amplitude. Furthermore, they have a limited bandwidth and cannot detect the high frequency part in equation 17.19. The detector signal will be proportional to

$$\begin{aligned} I(t) &\propto \cos^2\left(\tfrac{1}{2}\Delta\omega t\right) \\ &\propto \cos(\Delta\omega t). \end{aligned} \tag{17.20}$$

When the original wave and the scattered wave are combined with approximately equal amplitude onto a power detector (retaining coherence between the two waves), the detector will see a beat signal, of which the frequency is proportional to the velocity of the particle.

2.2 Basic setup

The most straightforward configuration with which one can do LDV measurements is presented in figure 17.7. The beam of a laser is split into two beams: an object beam and a reference beam. Since the intensity of the scattered radiation arriving at the detector needs to be approximately equal to the intensity of the reference beam, the intensity ratio between the object and reference beam needs to be adjustable and quite strongly in favor of the object beam. Both beams are focused and overlaid by the lens, and the detector is placed in the path of the reference beam. The focussing of the beams limits the detection volume and increases the scattering intensity. When the geometry of this set-up is compared to figure 17.5, it can be concluded that $\alpha = 0$ for the reference beam and $\theta = 0$ for the object beam. Hence, the reference beam is not shifted, only the object beam. The frequency shift of the object beam is determined by $|\vec{v}|$, the angle θ and the angle between $\vec{v}$ and $\Delta\vec{k}$ (α, not indicated in figure 17.7), according to

$$\begin{aligned} \Delta\nu &= \frac{2|\vec{v}|\cos\alpha\sin\theta}{\lambda} \\ &= \frac{2v_\perp\sin\theta}{\lambda}. \end{aligned} \tag{17.21}$$

Effectively, in this way the absolute value of the 'vertical' velocity component is detected. A disadvantage of this setup is that your experiment needs to be optically accessible from two fixed directions. A

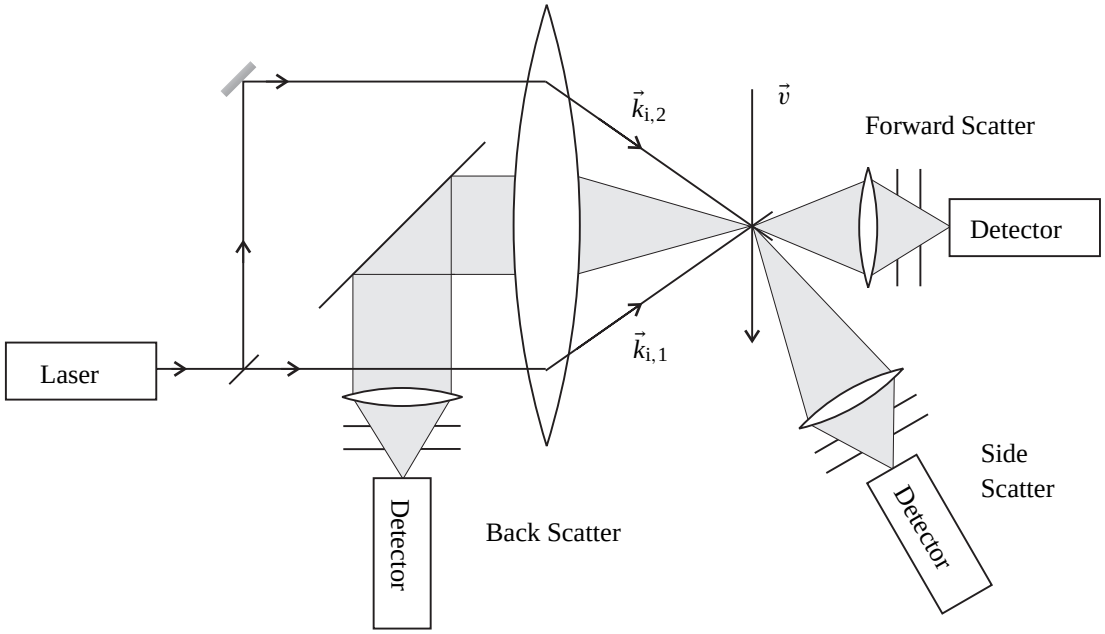

Figure 17.8: An LDV setup in 'dual-beam' or 'fringe' mode. Three different configurations can be distinguished: *back scatter*, *forward scatter* and *side scatter*.

more flexible way of working is by using equal intensity beams and to combine the scattered radiation of both beams (see figure 17.8). The detector signal is then the sum of two Doppler shifted signals. For beam 1

$$\nu_{s,1} = \nu_i \frac{1 - \vec{v} \cdot \vec{k}_{i,1}/c}{1 - \vec{v} \cdot \vec{k}_s/c}, \tag{17.22}$$

and for beam 2

$$\nu_{s,2} = \nu_i \frac{1 - \vec{v} \cdot \vec{k}_{i,2}/c}{1 - \vec{v} \cdot \vec{k}_s/c}. \tag{17.23}$$

The frequency difference at the detector, under the assumption that $1 - \vec{v} \cdot \vec{k}_s/c \approx 1$, is then given by

$$\Delta\nu = \nu_{s,1} - \nu_{s,2} = \nu_i \frac{\vec{v} \cdot (\vec{k}_{i,1} - \vec{k}_{i,2})}{c}. \tag{17.24}$$

When we make use of

$$\nu_i \lambda = c, \tag{17.25}$$

it follows that

$$\begin{aligned} \Delta\nu &= \frac{\vec{v} \cdot (\vec{k}_{i,1} - \vec{k}_{i,2})}{c} \\ &= \frac{2v_\perp \sin\theta}{\lambda}, \end{aligned} \tag{17.26}$$

which is the same result as for the reference beam setup. There is no real influence of the detector's position on the Doppler shift. Generally three configurations are distinguished: forward-, side-, and back-scatter. Currently, back-scatter is the most frequently used. The clear advantage is the easy

optical access, and often commercial systems are built with 'LDV heads' containing all foucusing and detection optics in one package, which is fiber-optically coupled to a laser. The disadvantage of back-scatter is that the intensity of Mie scattering for the backward direction is nearly two orders of magnitude weaker than for the forward direction (see section 1.1). Where you can use a 20 mW HeNe laser for forward scattering, one usually uses a Ar^+-laser of several Watts for a backward scatter system.

Another way of analyzing LDV is not to interpret the signal as being Doppler shifted, but as a fluctuating scattering intensity due to so-called Moiré fringes. When two coherent beam are overlaid, an interference pattern arises, consisting of bands with constructive intereference, alternated with bands of destructive interference. This is sketched in figure 17.9. The intersecting wave fronts cause a fringe pattern parallel with the bisector of the angle between the beams. The vertical distance (δz) between the fringes is given by

$$\delta z = \frac{\lambda}{2\sin\theta}, \tag{17.27}$$

with λ the wavelength. When a particle moves through this interference pattern, the scattered light will vary in intensity with frequency

$$\nu_{\text{det}} = \frac{v_\perp}{\delta z} = \frac{2v_\perp \sin\theta}{\lambda}, \tag{17.28}$$

with $v_\perp$ the velocity perpendicular to the fringes. It won't be a surprise that this result is equal to the result obtained previously with the Doppler analysis. It is, however, in this way easier to understand the time depenendency of the Doppler signal.

A particle can only scatter light when there is incident light. Hence, the oscillating Doppler signal will only be visible during a short time. This is called a *Doppler burst*. In figure 17.10 the idealized shape of such a burst is given. The faster the particle moves, the shorter the burst will be, but the number of oscillations will remain the same. This number can be estimated using the fringe model. The width of the focus of the laser beams (d) can be estimated using the diffraction limit

$$d = 2.44\frac{\lambda f}{\phi}, \tag{17.29}$$

with d as defined in figure 17.9 and ϕ the diameter of the laser beam at the position of the lens. Although the shape of the beam is not really parallel in the focus, we will assume this to be the case over the short length of the overlap region of the two beams. For the largest width of the overlap region (W, see figure 17.9), one can write

$$W = \frac{d}{\cos\theta} = \frac{2.44\lambda f}{\phi\cos\theta}. \tag{17.30}$$

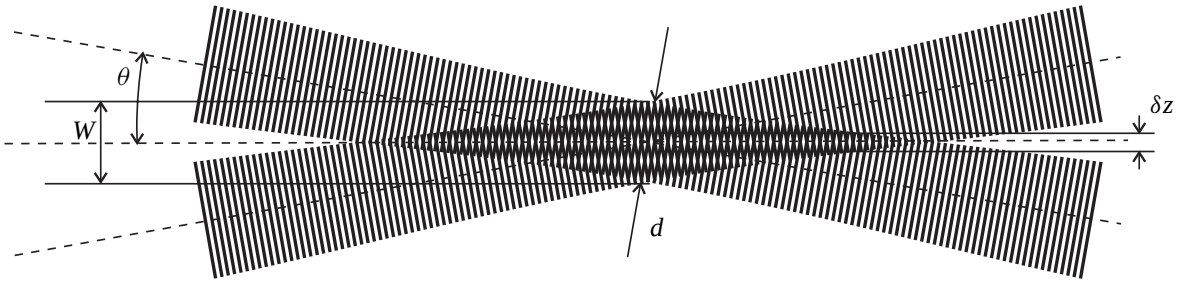

Figure 17.9: The interference pattern resulting from the overlay of two coherent beams.

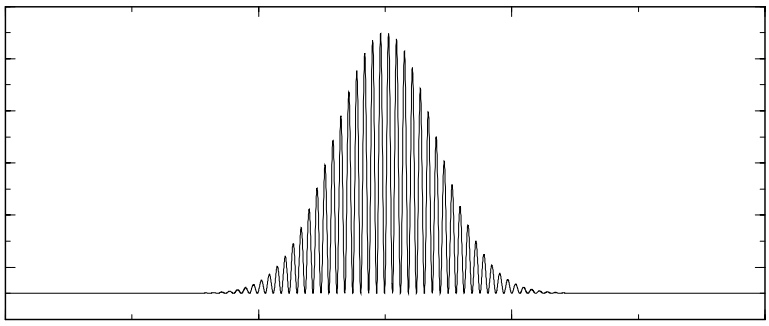

Figure 17.10: Detector signal of the light scattered by a particle moving through the area of intersection, a so-called *Doppler burst*. The envelope of the beat pattern is a result of the variation of incident light intensity (beam profile of the laser).

The maximum number of fringes $n_{\max}$ is then given by

$$\begin{aligned} n_{\max} &= \frac{W}{\delta z} = \frac{2.44\lambda f}{\phi \cos\theta}\frac{2\sin\theta}{\lambda} \\ &= \frac{2 \cdot 2.44 f}{\phi}\tan\theta. \end{aligned} \tag{17.31}$$

Taking into account that $\tan\theta = \frac{1}{2}D/f$ (figure 17.7), it follows that

$$n_{\max} = 2.44\frac{D}{\phi}. \tag{17.32}$$

The average number of fringes can then be estimated with

$$n \approx \frac{D}{\phi}, \tag{17.33}$$

which is, perhaps a bit surprisingly, independent of λ and f. The spatial resolution is, however, determined by W and this is dependent of λ and f.

2.3 Frequency preshifting

An issue not addressed yet, is formed by the directional ambiguity of LDV in its basic form. The frequency shift is in principle sensitive to the direction of the particle moving through the overlap area. If in equation (17.26) $v_\perp$ is exchanged by $-v_\perp$, $\Delta\nu$ will get a minus sign as well. The detector signal, however, will not change. The solution to this is to introduce deliberately a well defined frequency shift into one of the two beams ($\Delta\nu_{\text{shift}}$), which transforms equation (17.20) into

$$I(t) \propto \cos\left((\Delta\nu_{\text{shift}} + \Delta\nu)2\pi\, t\right). \tag{17.34}$$

When $\Delta\nu$ gets a minus sign, the detected frequency will change as well.

In practice, often a frequency shift of 40 or 80 MHz is used, and is introduced via an acousto-optic modulator (or Bragg-cell) into one of the beams. The frequency shift has as an additional advantage that noise filtering becomes easier.

2.4 Signal processing

The signal from the detector needs to be analyzed to derive the Doppler frequency. Several methods exist and are applied to do this. An extensive overview of signal processors is given by Heitor *et. al.* [2].

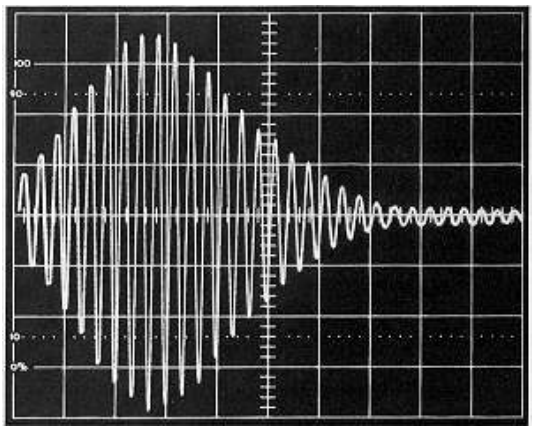

Figure 17.11: A filtered Doppler burst.

Frequency counter

One of the most frequently used processors is the frequency counter. The Doppler signal is passed through a broad band-pass filter. This filter removes the pedestal of the Doppler burst and removes at the same time high frequency noise. The filter has to be broad enough to allow all possible velocities present in the measuring volume. Often criteria for the band-pass filter are used related to the width of the probability density function of the velocity (3σ or 5σ criterium). A filtered Doppler burst is shown in figure 17.11.

After filtering the frequency counter performs a burst detection. When the filtered signal is higher than a certain threshold level a Doppler burst is expected to be passing the measuring volume. With the help of an amplitude discriminator, a Schmidt trigger, the Doppler signal is transformed into a rectangular wave with the same frequency. Then the time required for the signal to pass a certain number of zero crossings is measured with a fast electronic clock (500 MHz). Commonly two numbers of zero crosses (for instance 5 and 8) are counted and if the result of both measurements is in agreement with each other, this is classified as a valid measurement.

Correlator

An autocorrelation of the filtered Doppler signal can also be used to determine the dominant frequency. A fast correlation of the signal serves a burst detector. At the same time the signal is digitised. If the correlation coefficient passes a preset threshold, a more accurate correlation from the digitised signal is made. This results in a frequency measurement. The correlator can handle signals with a lower S/N ration than the signal processing counter.

Burst Spectrum Analyser

For signals with a very low signal-to-noise ratio also the correlator fails to give reliable results. In that case a spectral investigation of the signal might still be an option. With a burst spectrum analyser (BSA) the filtered signal is processed using a fast Fourier Transform Circuit. This is a very good method to find a dominant frequency in a signal with a low signal-to-noise ratio.

2.5 Multicomponent LDV

LDV can quite easily be extended to a two component technique. The straightforward and often applied approach is to use a second pair of beams through the same optics, but placed in a plane

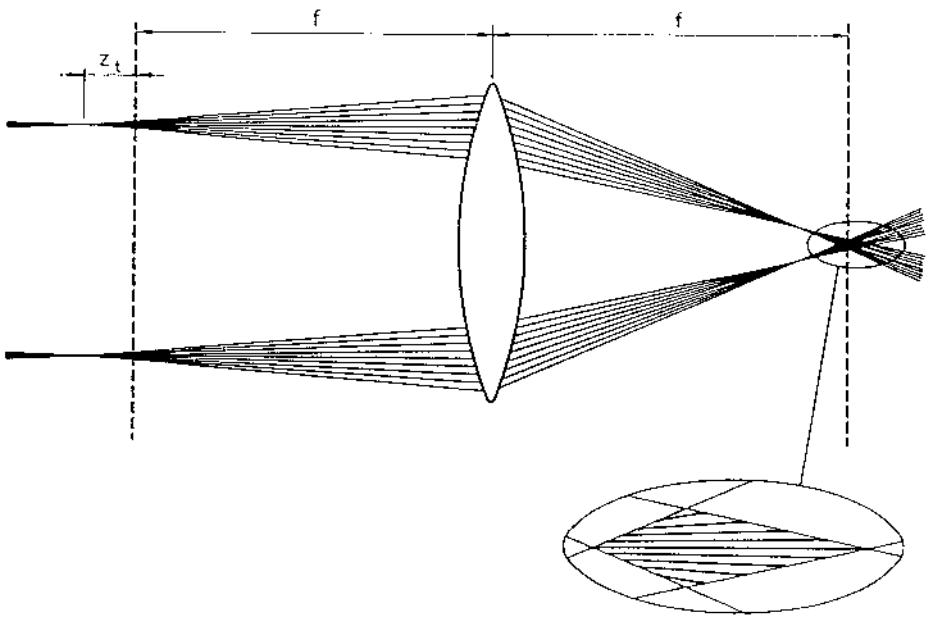

Figure 17.12: Diverging fringes because of misalignment of the focus. [What's wrong in this figure?]

perpendicular to the plane of the other two beams. These beams need to have a different wavelength than the other two beams, otherwise their signals will interfere with eachother. When the detectors are fitted with a spectrally selective filter, each of both detects only scattered radiation from one set of beams. In this case it is very advantageous to use the multiline feature of the Ar^+-laser, utilizing the 488 nm and 514 nm lines at the same time. In this case the alignment is relatively easy.

Special consideration is needed with regard to the timing of the signal processor. To do real two-component measurements, both detectors must see the same particle, and a stringent check on the correlation between the bursts of he two signal analyzers is to be performed. This will lead to a drop in sample rate.

The extension to three components is less straightforward. Of course the same trick can be used with regard to wavelength, but the measurement head needs to be placed perpendicular to the head used for the other two components. This alignment is far from trivial and even if one succeeds to do it properly, the overlap region between the three foci is very small due to their elongated shape. This will drastically reduce the sample rate.

2.6 Practical issues

Optical requirements

Optically the most important consideration is alignment of the foci. This seems trivial, because a geometrical consideration can only lead to the conclusion that two parallel beams are focused in exactly the same spot. This, however, is not true for diverging beams (see figure 17.12). In that case the foci of the beams are positioned slightly further away than the overlap region, and the resulting fringes will not be parallel anymore. The same can happen when the beams travel through thick windows, leading to a displacement of the beams without changing the position of the focus.

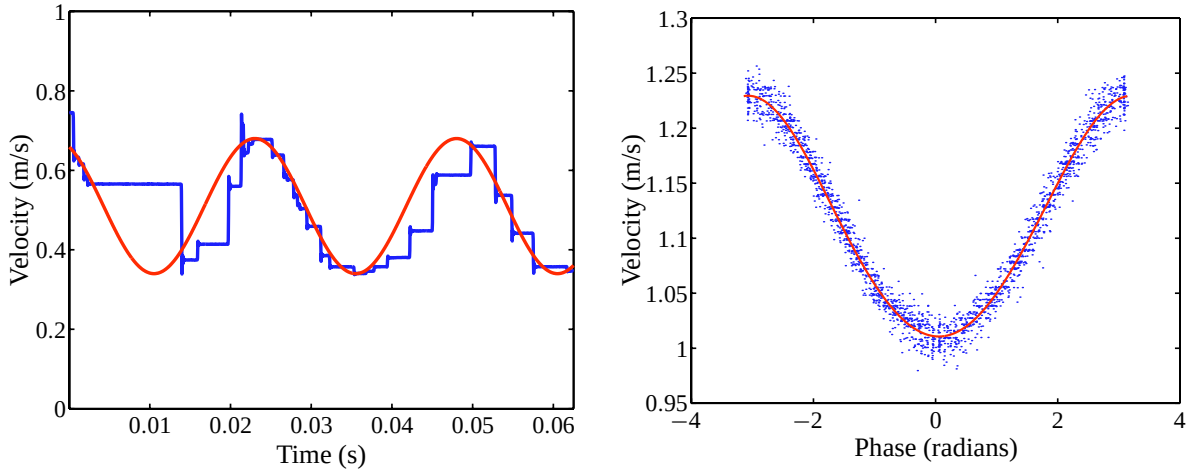

Figure 17.13: LDV measurements of a sound wave. The left graph shows a real-time (sample and hold) signal with a supposed waveform superposed. The right graph shows a phase correlated plot of a large set of velocity meaurements and a sinusoidal fit to the data. Note that Fourier transforming the sample and hold signal would lead to a phase shift and an underestimation of the amplitude.

Random sampling

LDV is a random sampling technique. There is no fixed time between the occurrence of Doppler bursts. This has a significant impact on the analysis of the obtained data. When converting the time dependent information to the frequency domain, a Fourier transform cannot be applied. There are roughly two approaches to solve this problem, which are extensively described and analyzed by Van Maanen [9].

- Velocity signal reconstruction.

  When the data rate is high in comparison to the highest frequency occurring in the flow (preferably one order of magnitude), the velocity data can be resampled (effectively interpolated) on a regular time basis. Subsequently, standard techniques can be used to obtain frequency information and correlation functions.

- Using known properties of the flow.

  When certain statistical properties of the flow are known, they can be combined with the known statistical properties of the LDV measurement technique. For the estimation of the auto correlation function this has lead to the development of the slotting technique. An extreme example of using flow properties is the measurement of sound. When each Doppler burst is correlated to the phase of the driving signal, an accurate reconstruction can be obtained for sampling rates even far lower than the actual frequency, see figure 17.13.

Biasing

Inherently to the LDV technique is the presence of a bias towards higher velocities when statistically interpreting the data. This effect is best explained using a simple example. Suppose that a flow has a velocity v during half a second and velocity $2v$ for another half a second. When in the first half a second 500 particles pass through the measurement volume, 1000 particles will pass through the

measurement volume during the second half a second. When estimating the average velocity based on the sum of all measured velocities divided by the number of samples, the average velocity becomes

$$\bar{u} = \frac{500 \cdot v + 1000 \cdot 2 \cdot v}{1500} = 1\tfrac{2}{3}v,$$

which is clearly wrong, since the actual average is $\bar{u} = 1.5v$.

This effect is closely related to the random sampling property of the LDV technique, and the more advanced techniques of data anlysis deal with both biasing and randomness at the same time.

3 PIV and PTV

3.1 Light sources

Because of the requirement of small seeding particles, often a strong light source is required. Furthermore, the light source should have nice optical properties so it can be shaped in sheets or beams with a uniform intensity. Light sources which are used include Xe-lamps, slide projectors, and flashlamps or strobe lights. The most suited for the purpose of PIV and PTV, however, is a laser. Although it seems relatively expensive to use a laser as an upgraded flashlight or slide projector, lasers have excellent properties which cannot be matched by any other lighting source. Their most outstanding properties are the fact that they are monochromatic, have a high intensity, and that they are stable. Furthermore, pulsed lasers can have a very short pulse duration and can be excellently timed. Monochromaticity is important when dealing with interfaces (glass) or media (water) which are dispersive, and when several techniques are combined (e.g. LIF and PIV) and the laser used for PIV must be blocked for the LIF camera.

Three types of lasers are commonly used, the Ar-ion laser, the Nd:YAG laser, and the copper-vapor laser (although occasionally someone uses a Ruby laser).

The Ar-ion laser can be operated at several different wavelengths (single mode) ranging from the UV to the blue green, but their highest power output is achieved when operated in multimode, i.e. all lines at the same time. In that case it is not a real monochromatic light source anymore. There are both continuous wave (cw) and pulsed types, but the cw variant is the most common. Power output can be as high as 8 W cw (multimode).

The Nd:YAG laser has a fundamental wavelength in the near-infrared of 1.064 μm, but is used most frequently in combination with a frequency doubler (output 532 nm). Also frequency tripling (355 nm) and quadrupling (266 nm) is possible. Both cw and pulsed versions exist. The modern cw versions combine a very small laser head with high output powers (up to 10 W) and are even price competitive with Ar-ion lasers. The pulsed versions can have a pulse duration in the order of 6–8 ns and typical pulse energies are 200 mJ/pulse at 532 nm. Typical repetition frequencies are in the range of 10–50 Hz for flashlamp pumped systems. For PIV, where two images are recorded in short succession, often a double Nd:YAG laser is applied, or a single laser which is doubly pulsed. The latter is less flexible with timing and intensity variations. Diode pumped systems can be operated at several kHz, but with much lower pulse energies, comparable to a copper vapor laser.

Copper vapor lasers typically operate at very high repetion frequencies of 5–20 kHz at 511 or 578 nm. Their pulse energies are low in comparison to a Nd:YAG laser, 10 mJ. They are mainly applied in applications where a strobe illumination is required or in combination with high-speed cameras.

3.2 Photographic/video equipment

There used to be a time when photography on film was the only way to record images of sufficient resolution. This had the disadvantage that the time between setting up the equipment and the final measurements was large due to the processing time of the films. Nowadays, modern (digital) cameras allow for instant access and analysis of the image data. Several different systems can be applied, ranging from (cheap) monochrome video cameras to (expensive) interline frame transfer digital cameras. I will only treat digital systems, because the modern camera systems almost outperform classical photography.

Overview

ANALOG (VIDEO) CAMERAS Since this type of camera is frequently used in surveillance and inspection systems, it is relatively cheap and easy to interface. They have a resolution of 767×582 (PAL) or 647×484 (NTSC) pixels. Their most important drawback is the fact that they are *interlaced*. This means that the camera operates at 50 Hz, but at every clock tick only the even or the odd lines are recorded. When imaging moving objects (and that's what we do), the even lines will show the image at a different position than the odd lines. When dealing with particle images measuring only a few pixels, this can distort the images severely even for moderate displacements. Only to be applied for PTV at very small displacements between time steps.

Digital recording systems consist of a camera, frame-grabber, and a computer. When the recording capacity of the computer is not large enough, images can be temporarily stored on a VCR, and later on digitized. The dynamic ratio is often not too good. Although the frame grabbers usually work with 8 bit digitization, only 6 bits are usable.

PROGRESSIVE SCAN CAMERAS They use the same protocol as ordinary video cameras, but the image is recorded non-interlaced. The image is transferred to the frame grabber as an interlaced signal, so the same frame grabber hardware can be used as for normal video cameras. They are available at resolutions up to 1000×1000 pixels and much more suited for flow visualization than ordinary cameras.

DIGITAL CAMERAS There used to be a time when this type of camera was called 'slow scan'. The principle is that the content of a pixel of the CCD (several thousand electrons) is not converted into an analog signal, but digitized in the camera itself into a digital value. These digital values are then transferred to a computer via a special interface (often also called frame grabber). The term 'slow scan' is a remainder of the time when pixel rates were limited to 100 kHz. For average resolutions this means that only a few images/second can be recorded. Today, pixel rates up to 30 MHz or more can be achieved, allowing 30 frames/s for 1000×1000 pixel images. Digitization often occurs at 8 bits. Increased digitization accuracy often has the penalty of (much) slower readout rates.

Another advantage of this type of camera is the timing flexibility. Since there is no analog protocol to which must be adhered, images can be taken randomly or externally triggered (e.g. by a laser).

INTERLINE FRAME-TRANSFER CAMERAS This special type of digital camera uses a special CCD sensor of which half the amount of pixels is masked (the even or the odd lines). The charge content of a pixel can be moved very quickly to a neighboring pixel (down to 1 μs). These cameras can be operated at two modes. The first mode (and that is what they were designed for initially) is that as soon as an image has been recorded, the image is moved under the mask. Then readout of the masked

pixels can proceed concurrently with the recording of the next image by the unmasked pixels. This means that exposure times of 1/30 s are possible with a readout rate of 30 frames/s.

The other mode of operation is the so called 'double frame mode'. As soon as the first image has been recorded, this image is moved and the second image is recorded. After this, the CCD is completely filled, and readout can start of all pixels. In this way, for a 30 frames/s camera, 15 image pairs per second can be recorded with a time delay between the images of each pair down to 1 μs. This type of camera is often sold as 'PIV' camera. The best known commercial model is the Kodak/Roper Scientific ES1.0.

HIGH SPEED DIGITAL CAMERAS This type of camera can acquire a short succession of images in a very short time. This is due to the storage of the image data *in* the camera itself. Although a lot of useful applications exist, their use in flow visualization is limited to the tracking of a low number of particles because of their limited resolution. Frame rates of up to 10 kHz can be achieved at a resolution of 64×64 pixels. Higher resolutions can be obtained at a reduced frame rate.

3.3 Storing image data

The storage of digital image data is an art on its own. The modern Megapixel cameras operating at 30 frames/s and digitized at 8 bits result in a data stream of 30 MB/s. The easiest way to record this stream is to fill the main memory of the computer. This RAM, however, is usually limited to 512 or 1024 MB. For PIV this can be sufficient, but for PTV this is quite limited. The only solution is to use hard disk recording on high speed devices. With the right hardware, storage speeds limited by the PCI bus bandwidth (133 MB/s) can be achieved.

4 Particle Tracking Velocimetry

The name particle tracking velocimetry is used for a broad class of methods. Some people use the name to denote a technique where one (or a small set of) particles is illuminated by a stroboscopic light source. The particle is then photographed by exposing one image for some time resulting in a trace of particle images in one photograph. Analysis of this trace is relatively straightforward, and yields positions and velocity information of the particle. Another technique carrying the same name is formed by illuminating a set of particles for a long time compared to their velocity. The particle images will then appear as a line on the photograph. The length of the line is a measure of the speed.

PTV as we use it, applies to a technique in which a large set of particles is followed ('tracked') in time. This number can be quite large, up to several thousands. PTV is a technique in which every image is illuminated only once. After identification of all the particles in one frame, their positions are matched (correlated) with the positions of particles in the next frame. This results in a trace of every imaged particle, yielding the velocity (and shear!) information. It is in its basic form a 2C/2D technique.

4.1 Analysis

In more detail, the following steps are taken in the analysis algorithm (see figure 17.14):

1. **Particle localization.** After preprocessing of the images (usually some background filtering is applied), the positions of all particle images is calculated. Several algorithms can be used, but most often used are

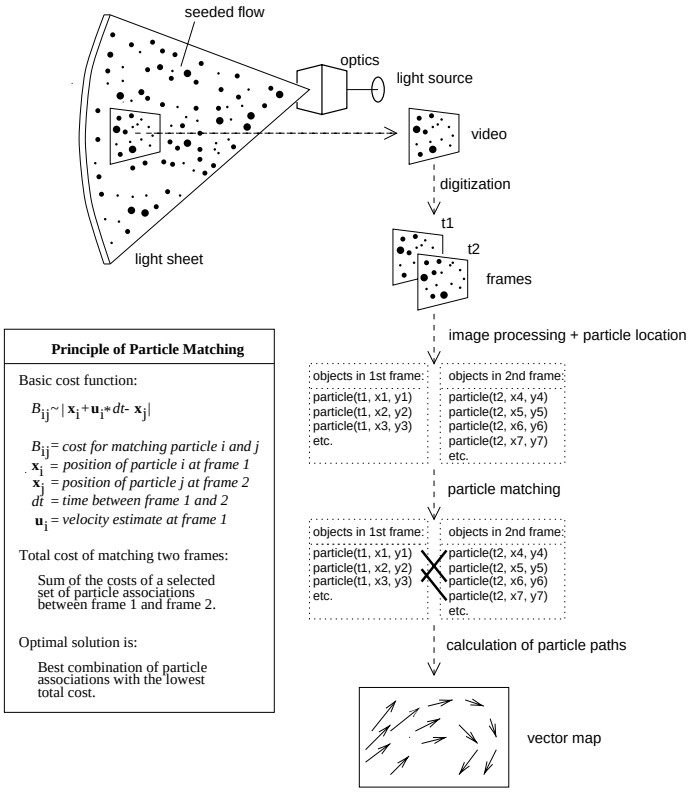

Figure 17.14: Schematical illustration of a 2D PTV algorithm.

(a) an intensity weighted average of a group of pixels above a certain threshold, or

(b) the center position as obtained by fitting a two-dimensional Gaussian function through the group of pixels.

Both methods yield good results with differences in the order of 0.1 pixel. The general accuracy of the position estimation is 0.1 pixel for particle images with an area of 6 pixels. Smaller images result in a worse accuracy, and larger images result in a lower maximum image density.

2. **Transformation.** When the camera image coordinates (x, y) are calibrated with respect to the world coordinates (X, Y), a transformation can be applied $(x, y) \rightarrow (X, Y)$. This transformation can be quite complex, depending on the distortions by lenses and interfaces.

3. **Matching.** This is the crucial step in which a particle at time t_1 is correlated with a particle at time t_2. The most straightforward approach is to just select the particle in the next frame located most closely to the particle under consideration at t_1. This results in the following restrictions on the images:

   (a) Within a certain area of interest, only one particle can be present. This means that the image density N_i must be smaller than 1 and consequently the diameter of the area of interest can be at most the average distance between two neighboring particles.

   (b) Between two timesteps, the maximum displacement is the (equivalent of the) diameter of the area of interest.

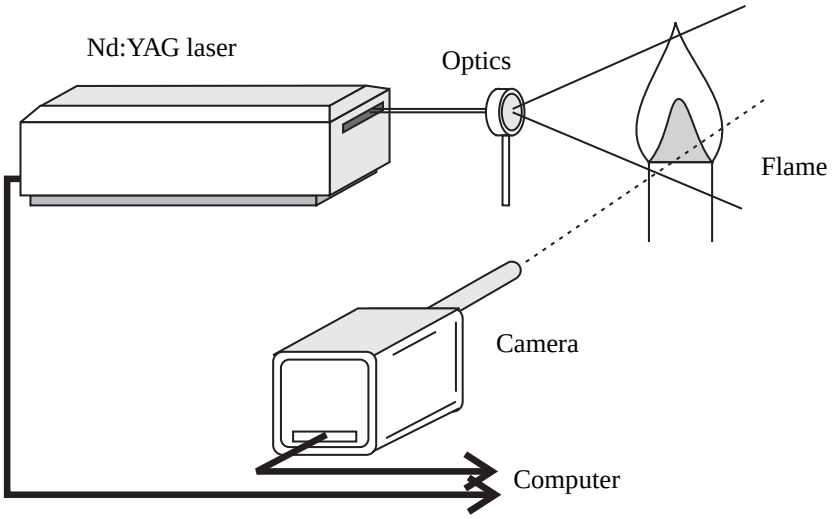

Figure 17.15: General PIV/PTV setup consisting of a light source (laser), sheet forming optics, and a camera.

The last requirement puts an upper bound on the (image) velocity of the particles of about 3 pixels/timestep. For 30 frames/s cameras, this renders the method practically useless for combustion problems.

4. **Iteration.** The above steps are iterated for every following timestep. The resulting traces can be analyzed for velocity information and more (e.g. shear). Normally only traces with a length of at least five consecutive timesteps are taken into consideration. Shorter track lengths have a too high risk of containing mismatches.

4.2 Experimental setup

A typical experimental setup is presented in figure 17.15. The output of a laser is formed with optics into a thin lightsheet, which illuminates the volume of particles. A camera is positioned at a square angle to avoid a large perspective error.

4.3 Sources of errors

Mismatches

The largest source of errors is formed by mismatches. If there are areas in the image where the velocity exceeds the maximum allowable, these regions will generate only nonsense after analysis. The best remedy is to avoid large particle displacements and to use a long minimum track length. An alternative is to use High Resolution PV (see section 6.1).

Perspective error

Another source of errors which is often overlooked and for which no remedy exists, is the presence of an out-of-plane velocity component. If this component of the velocity is significant this will at first lead to the loss of particles. As soon as a particle leaves the illuminated sheet, the trace is ended. In the same way, a particle which enters the lightsheet can give rise to mismatches. This ‘problem’ can be softened by using a thicker lightsheet, but then a subtle error comes into play, the perspective error.

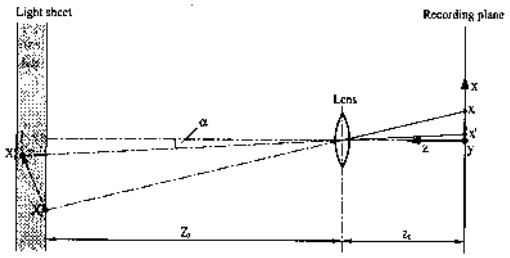

Figure 17.16: Illustration of the perspective error.

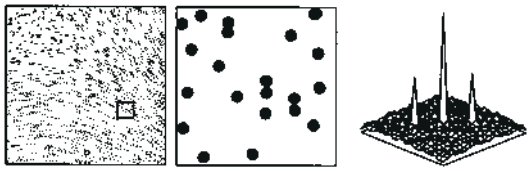

Figure 17.17: Illustration of the digital autocorrelation function.

In figure 17.16 a sketch of this situation is drawn. As can bee seen, a particle with an out-of-plane component of the velocity will have a different displacement on the image than a particle without the out-of-plane component, but otherwise the same velocity. This effect is the strongest towards the edges of the image.

5 Particle Image Velocimetry

Where PTV uses a trace of particles to obtain velocity information, PTV uses groups of particles which are correlated between two (or more) timesteps. Only two frame single exposure and one frame double exposure digital PIV will be treated here. For an overview of the other techniques the reader is referred to the books by Raffel *et al.* [12] and Westerweel [13]. Standard PIV is a 2C/2D technique.

With PIV, the image density is strongly increased in comparison to PTV, see figure 17.4. This means that no single particles can be tracked in time. A pattern of particles, however, still can be tracked, provided that the velocity gradients are not too high. The images are then analyzed by digital correlation techniques. Suppose that $I = I(\vec{x}, t)$ and $I' = I(\vec{x}, t + \delta t)$ are two consecutive intensity patterns. In the case of two frame PIV I and I' are recorded in two different images. In the case of one frame PIV both I and I' are recorded in the same image yielding an intensity distribution $G = I + I'$.

5.1 Cross correlation

In the case of two frame PIV, the cross correlation function yields the average displacement within a certain interrogation area:

$$\begin{aligned} R_{II'}(\vec{x} - vecx', t, t + \delta t) &= \iint_{A_i} I(\vec{x}, t) I(\vec{x}', t + \delta t)\, \mathrm{d}\vec{x} \\ &= \iint_{A_i} I(\vec{x}, t) I(\vec{x} + (\vec{x}' - \vec{x}), t + \delta t)\, \mathrm{d}\vec{x}, \end{aligned} \tag{17.35}$$

in which A_i is the interrogation area. The cross correlation only depends in de difference vector $(\vec{x} - \vec{x}')$. The function $R_{II'}$ will contain a peak at $\vec{x} - \vec{x}' = \vec{D}_i$, where $\vec{D}_i = \vec{D}_i(\vec{x}, t, t + \delta t)$ denotes the average displacement of the particles in interrogation area i. The velocity is found by calculating $\vec{v}_i = \vec{D}_i / \delta t$.

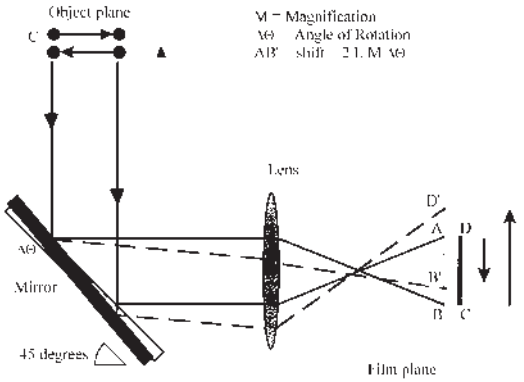

Figure 17.18: An example of image shifting by rotating a mirror.

5.2 Auto correlation

In the case of doubly exposed single frame PIV, the autocorrelation is calculated:

$$R_{GG}(\vec{x}-\vec{x}') = \iint_{V_i} G(\vec{x})G(\vec{x}')\,\mathrm{d}\vec{x} = \iint_{V_i} G(\vec{x})G(\vec{x}+(\vec{x}'-\vec{x}))\,\mathrm{d}\vec{x}. \tag{17.36}$$

The function R_{GG} will now show three peaks, one peak at position $\vec{x}-\vec{x}' = \vec{D}_i$, but because the information about which frame was recorde first, also a peak at position $\vec{x}-\vec{x}' = -\vec{D}_i$ will show up. The third peak is formed by the correlation of all particle images with themselves, at $\vec{D}_i = 0$, see figure 17.17.

This ambiguity is not always a problem, because in some cases the global direction of the flow is known. If it is a problem, however, and two frame PIV cannot be applied, a solution might be to use image shifting between the two exposures. This is somewhat similar to frequency shifting with LDA. In figure 17.18 this is illustrated

5.3 Calculation of the correlation function

The direct calculation of the correlation function is, even with today's computers, not something one wants to wait for too long. It can be shown [12, 13] that the correlation function can be calculated quite efficiently by using fast Fourier transforms. This limits the size of the interrogation areas to powers of two. Common sizes found in the literature are 32×32 or 64×64 pixels.

5.4 Experimental requirements

1. **Size of the interrogation area.** De velocity gradient in one area should not exceed a certain value. Either choose a smaller interrogation area, or zoom in. A good value is to choose the length of a side a such that $ga/v_i \ll 0.05$, with g the local velocity gradient end v_i the local velocity.

2. **Minimum number of particles.** The minimum number of particle image pairs should be larger than 10, otherwise the signal to noise ratio of the correlation function is too large and the chances on lost pairs are too large.

3. **Maximum in-plane displacement.** Both in the x and y-direction in the interrogation area the displacement should not be too large: $\delta s_x/a < \frac{1}{4}$ and $\delta s_y/a < \frac{1}{4}$. When $\delta s/a > \frac{1}{2}$ the correlation peak disappears.

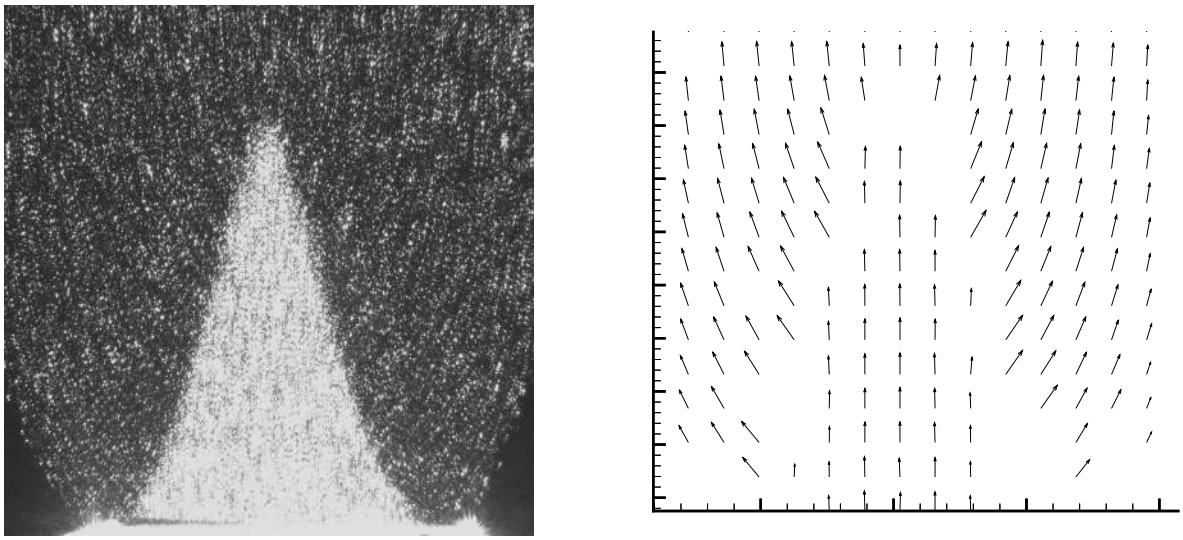

Figure 17.19: Image and vector map of a Bunsen flame. This is a doubly exposed image which has been analyzed by autocorrelation.

4. **Maximum out-of-plane displacement.** In the direction perpendicular to the plane of illumination the velocity should be small. An optimal value is $\delta s_z / \delta Z_0 < \frac{1}{4}$. Note, however, that the perspective error as described with PTV (section 4.3) also applies for PIV, so there is a limit to the thickness of the sheet.

5. **Minimum displacement.** The minimum displacement should be 2 pixels for autocorrelation and 1 pixel for cross correlation PIV.

5.5 Sources of errors

Apart from the perspective error and mismatches due to a bad S/N ratio, the main error is formed by the accuracy with which the correlation peak can be detected. Several methods exist, similar to the particle image detection techniques used with PTV. A subtle error comes into play when the particle images are too small. Just like PTV, the accuracy then drops from 0.1 pixel to 1 pixel, because most intensity information is lost. In PIV this effect is called ‘peak locking’.

Furthermore, when using the standard FFT analysis technique, a certain bias is introduced in the displacement detection for large displacements, because the correlation function automatically get a lower value due to the smaller overlap.

5.6 PIV in combustion

PIV is a well known technique in the combustion society, and has been applied successfully in many applications ranging from Bunsen flames [14] to turbomachinery [15]. Especially the combination of PIV with other whole field techniques like planar LIF gives good insight in combustion phenomena [16, 17, 18, 19].

In figure 17.19 an example of autocorrelation PIV is shown on a Bunsen flame. Note especially the drop in density after the flame front and the problems arising from the large gradient at the flame front.

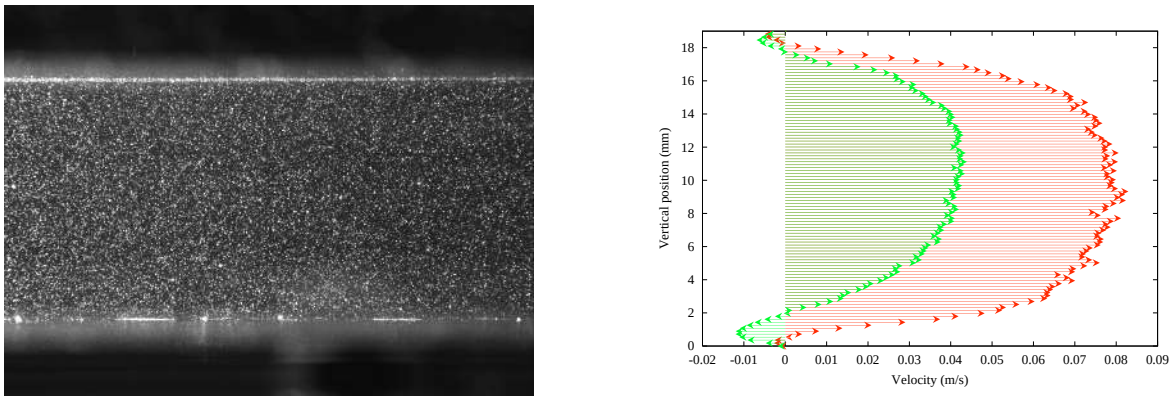

Figure 17.20: Image en velocity map of a rectangular water channel. As can be seen from the image the seeding is very homogeneously dispersed. This image was analyzed with an interrogation area size of 4×128 pixel leading to a very high vertical resolution. The vertical velocity denpendence is plotted in the graph for two different phases of the oscillating flow (measurement by C. Meuleman).

6 Advanced techniques

The limitations of standard PIV and PTV give rise to numerous enhancements and special techniques. I will address some of them. The first interesting technique is called 2 color PIV. In this technique a color camera is used to record both exposures on the same image, but now both exposures are made with a different color of laser. This combines the advantage of one frame frame PIV (cheaper camera) with the advantage of two frame PIV (cross correlation). This technique has been demonstrated by Watson *et al.* [16] in combination with CH imaging via LIF.

Another collection of enhancements is formed by interrogation area tricks. Examples include multipass analysis in which the interrogation area is reduced in every pass, but the velocity result of the former pass is used to select another area to correlate with. Effectively the reolution is enhanced because very small ineterrogation areas can be used in the final step. Another example is shown in figure 17.20 where the flow is essentially 1D. This allows for the application of an odd interrogation window size of 4×128 pixels, yielding a loss of resolution in te horizontal direction, but a strong enhancement in the vertical direction.

Two techniques will be treated in more detail now: HiResPV, stereo PIV, and 3D-PTV.

6.1 High resolution PV

Hig Resolution Particle Velocimetry [20] and Super-Resolution PIV [21] apply to principally the same technique: a hybridization of PIV and PTV. That is, first a standard PIV analysis of an image is performed, and subsequently a PTV analysis, using the information obtained with the PIV analysis. This works only when cross correlating two separate images. This technique combines the advantages of both PIV and PTV. It offers the resolution of PTV, but without the requirement of needing a trace length of 5 timesteps. Furthermore the particle density can be increased with regard to standard PTV, because the area of interest can be made very small, since an average velocity is known.

The particle density must be high enough for PIV, but single particles still must be detectable, otherwise the PTV step will fail. An example of a measurement in water is shown in figure 17.21, where a Von Kármán vortex street is measured with approximately 10,000 independent vectors.

This technique holds the promise that the advantages of PTV can be made accessible to combus-

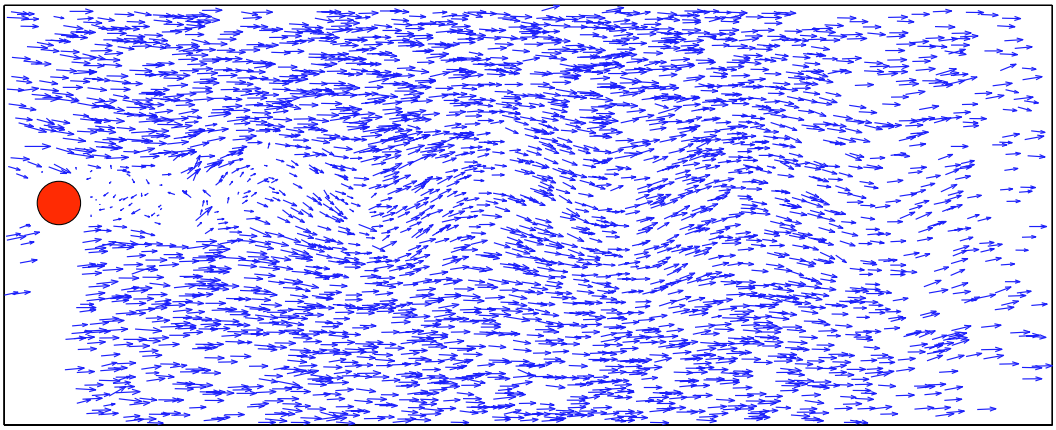

Figure 17.21: Image obtained with Hi-Res PV containing 10000 vectors. The object is a cylinder dragged through water at moderate Reynolds number showing a Von Kármán vortex street.

tion research.

6.2 Stereo-PIV

Stereo PIV is a technique in which two cameras are used to record the same area, but with a different angle. What first was presented as the perspective error, now is pursued actively: the lightsheet is made much thicker, introducing a strong perspective effect for each camera. But since the perspective of each camera is different, the third velocity component can be resolved. This is a 3C/2D technique with the possibility of application to combustion.

6.3 3D-PTV

3D-PTV is PTV, but now for three (or more) cameras at the same time [22]. The difference with standard PTV is that in the transformation step, images of three cameras are used to reconstruct 3D positions of the particles. This is a full 3C/3D technique.

The key is formed by the 3D localization. For a camera setup as shown in figure 17.22 first a grid with known dot positions is photographed. This grid is recorded at several different positions, resulting in a rectangular volume of points of which for every point the particle image location on each of the cameras is known. Now the inverse transformation is calculated: for every particle image position (x, y) on each of the camera images, a line in world coordinates (X, Y, Z) can be assigned on which the particle should be positioned. When combining all lines from all cameras (see figure 17.23), all points where three lines cross is a particle position.

In figure 17.24 the same Von Kármán vortex street as in figure 17.21 has been recorded. This was done with a rather low quality video camera setup (3 512^2 pixel interlaced video cameras) but it still yielded several hundred particle traces. With a new setup, we expect to be able to track 2000 particles.

This technique is not directly applicable to combustion, but one never knows what the future holds...

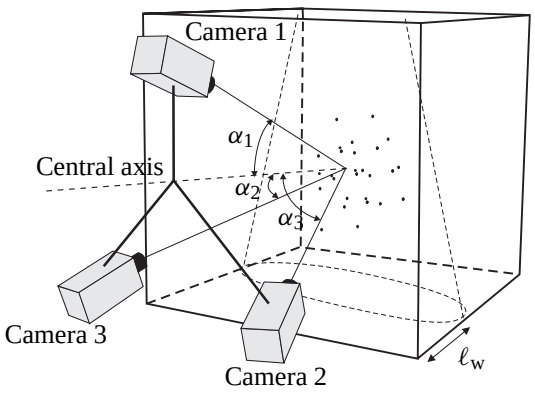

Figure 17.22: Camera setup for 3D-PTV

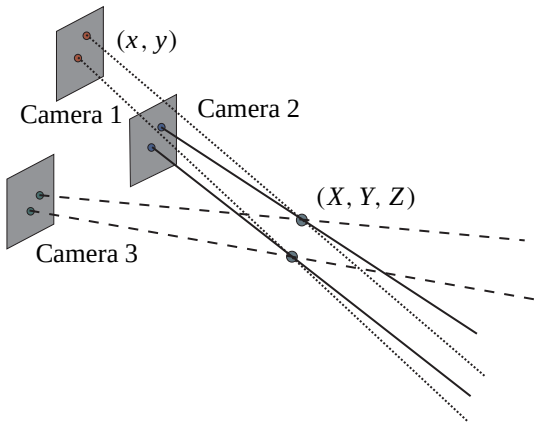

Figure 17.23: The localization of particles in 3D space.

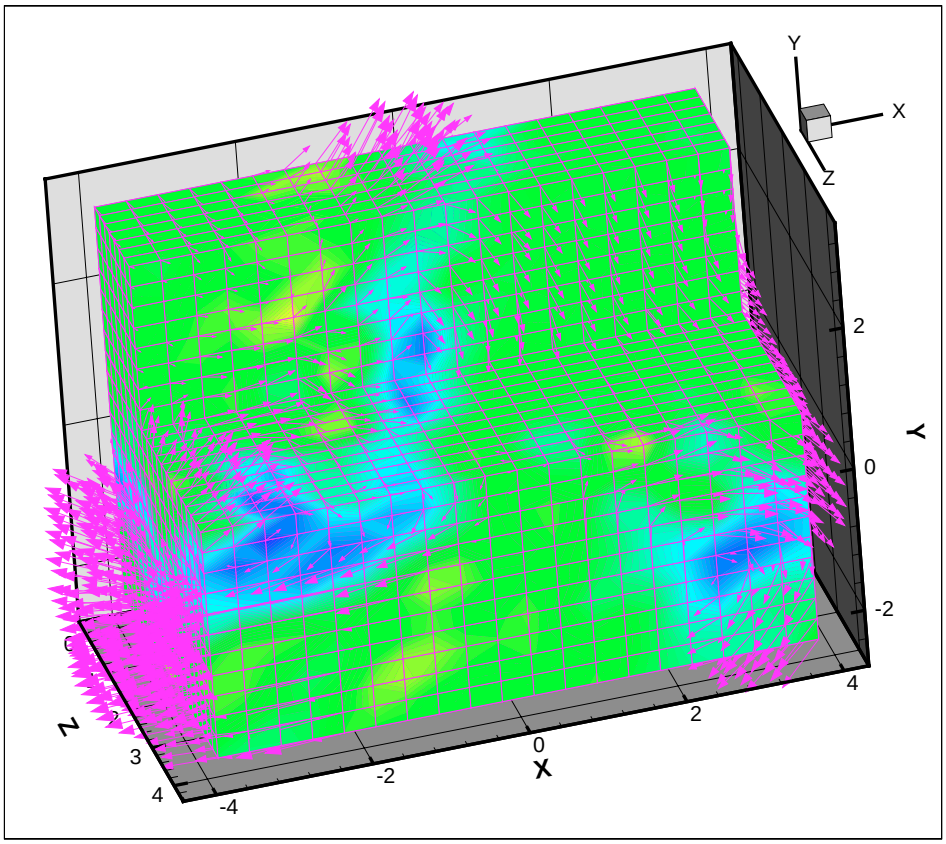

Figure 17.24: Interpolated 3D-PTV result showing the velocity and z-component of the vorticity of a Von Kármán vortex street behind a heated cylinder. An escaping thermal plume can be identified.

References

[1] Y. Yeh and H. Z. Cummings, *Localized flow measurements with an He-Ne laser spectrometer*, Applied Physics Letters, 4, 176 (1964)

[2] M. Heitor, S. H. Starner, A. M. K. P. Taylor and J.H. Whitelaw, *Velocity, Size and Turbulent Flux Measurements by Laser Doppler Velocimetry,* in Instrumentation for Flows with Combustion (Ed. A. M. K. P. Taylor) Academic Press (1993)

[3] L. E. Drain, *The Laser Doppler Technique*. Wiley, Chichestrer (1980)

[4] F. Durst, A. Melling and J. H. Whitelaw, Principles and Practice of Laser Doppler Anemometry, Academic Press. London (1981)

[5] I. G. Shepherd and J. B. Moss, *Measurements on conditioned velocities in a turbulent premixed flame*, AIAA Journal, 20, 566–569, 1982.

[6] M. Glass and I.M. Kennedy, *An improved seeding method for high temperature laser Doppler velocimetry*, Combustion and Flame, 29, 333-335, (1977)

[7] A. Melling, *Seeding Gas Flows for Laser Anemometry*, AGARD-CP-399, paper 8 (1986).

[8] M. J. Tummers, *Investigation of a turbulent wake in an adverse pressure gradient using laser Doppler anemometry*, PhD thesis, TU Delft, 1999.

[9] H. R. E. van Maanen, *Retrieval of turbulence and turbulence properties from randomly sampled laser-Doppler anemometry data with noise*, PhD thesis, TU Delft, 1999.

[10] E. P. Hassel, S. Linow, *Laser Diagnostics for studies of turbulent combustion,* Meas. Sci. Technol. **11** R35–R57 (2000).

[11] A. Melling, *Tracer particles and seeding for particle image velocimetry,* Meas. Sci. Technol. **8** 1406–1416 (1997).

[12] M. Raffel, C. Willert, J. Kompenhans, *Particle Image Velocimetry, A Practical Guide*, Springer Verlag (1998).

[13] J. Westerweel, *Digital Particle Image Velocimetry, Theory and Applications*, Delft University Press (1993).

[14] M. G. Mungal, L. M. Lourenco, and A. Krothapalli, *Instantaneous Velocity Measurements in Laminar and Turbulent Premixed Flames Using on-line PIV*, Combust. Sci. and Tech. **106** (1995) 239–265.

[15] M. P. Wernet, *Development of digital particle imaging velocimetry for use in turbomachinery*, Exp. in Fluids **28** (2000), 97–115.

[16] K. A. Watson, K. M. Lyons, J. M. Donbar, and C. D. Carter, *Scalar and Velocity Field Measurements in a Lifted CH_4-Air Diffusion Flame*, Combustion and Flame **117** (1999) 257–271.

[17] J. H. Frank, P. A. M. Kalt, and R. W. Bilger, *Measurements of Conditional Velocities in Turbulent Premixed Flames by Simultaneous OH PLIF and PIV*, Combustion and Flame **116** (1999) 220–232.

[18] T. Plessing, P. Terhoeven, N. Peters, and M. S. Mansour *An experimental and numerical study of a laminar triple flame*, Combustion and Flame **115** (1998) 335–353.

[19] T. Plessing, *Laseroptische Untersuchunen turbulenter Transport- und Reaktionsvorgänge in Vormischflammen*. Ph.D. Thesis RWTH Aachen (2000).

[20] G. A. J. van der Plas and R. J. M. Bastiaans, *Accuracy and resolution of a fast PTV algorithm suitable for HiRes-PV*, proceedings of the 8th int. conf. on flow vis., paper 87 (1998).

[21] R. D. Keane, R. J. Adrian, and Y. Zhang, *Super-resolution particle imaging velocimetry*, Meas. Sci. Technol. **6** (1995) 754–768.

[22] K. R. A. M. Schreel, G. A. J. van der Plas, and R. N. Kieft, *Accuracy of a 3D Particle Tracking Velocimetry Method*, proceedings of the 9th int. conf. on flow vis. (2000).

[23] R. J. Adrian, *Particle Imaging Techniques for Experimental Fluid Mechanics*, Ann. Rev. Fluid Mech. **23** (1991) 361–304.

Chapter 18

Application of Laser Diagnostics in Turbulent Flame analysis

Th. H. van der Meer

1 Introduction

One of the biggest challenges in turbulent combustion is its accurate modeling. The modeling should help to organize a combustion system in such a way that the combustion process is most efficient, the heat transfer is optimal, emission of pollutants are minimal, and that product quality is maximal. Since this is not an easy task in which many model assumptions have to be made there is a need for comparisons of model predictions with experimental data. These experiments should be done under well defined conditions, leaving as little room as possible for the modeler to tune the models into the direction of the experimental data. Experiments on an industrial scale for this reason are not very suitable for detailed model validations. Over the years experimental databases have been gathered from experiments on laboratory flames using different gaseous fuels in different burner configurations. These flames have been discussed in an international forum and are now well accepted as standard flames for model comparisons. One of these flames is the Delft piloted diffusion flame, which is the topic of this contribution. Here results from various experimental studies are gathered (see references[1]–[7]).

2 The Delft piloted diffusion flame burner

The Delft piloted diffusion flame burner was used to produce a laboratory-scale axisymmetric turbulent diffusion flame. The burner is described by Peeters et al. [1] and in full detail in the theses of Stroomer [3] and de Vries [2]. The burner consists of a central fuel jet, surrounded by two concentric co-flows of air. Figure 18.1 shows the burner head.

The fuel jet nozzle is 6 mm in diameter. It is separated from the primary air stream by a 4.5 mm wide rim. Twelve small pilot flames, necessary for the stabilization of the flame on the burner, are issued from holes located on this rim. The outer diameter of the primary air annulus is 45 mm. The length of the burner is 100 cm. In the first 94 cm, the inner diameter of the primary air annulus is 30 mm, decreasing to 15 mm in the final 6 cm. This gives rise to a small negative radial velocity component of the primary air in the exit plane of the annulus. The initial diameter of the central fuel pipe is 8 mm. A pilot flame insert placed in the exit of the fuel pipe causes a decrease in diameter to 6 mm starting at a position 16 mm upstream of the nozzle exit. Although the decrease in diameter is gradual, with a 7° angle, the flow leaving the fuel pipe cannot be considered to be fully developed.

Experiments were performed for different sets of inlet boundary conditions. In this contribution we will restrict ourselves to two flames, denoted Flame III and IV. Figure 18.1 shows photographs of

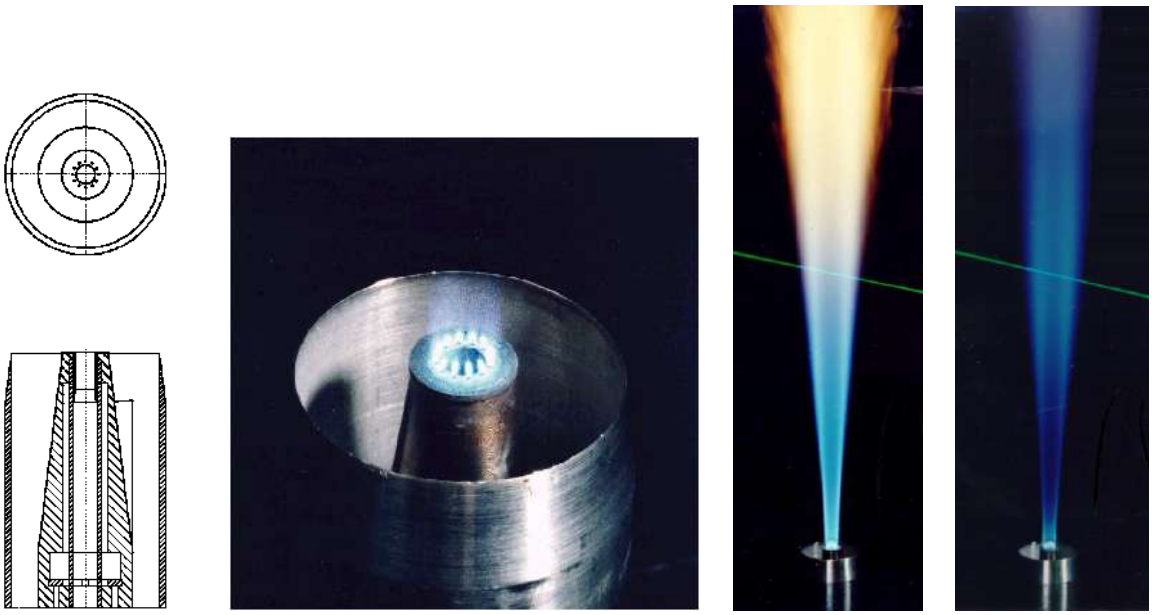

Figure 18.1: Top and side view and photograph of the burner head, dimensions are in mm. At the right photographs of Flame II and Flame IV.

these flames. Flame III is considered as a reference flame or 'base case'. The fuel jet velocity was 21.9 m/s and at room temperature ($Re = 9700$). The primary air flow velocity was 4.4 m/s, also at room temperature ($Re = 8800$). In Flame IV the flow rate of the primary air stream was doubled ($U_{\text{annulus}} = 8.0$ m/s, $Re = 16000$) to study the effect of different turbulent mixing rates. For both flames, the secondary air stream was kept at a velocity of 0.3 m/s. The air flow was produced by positioning the burner in a wind tunnel with an exit cross-section of 254 $\times$ 254 mm.

The pilot flames were fed with a premixed acetylene/hydrogen/air mixture with an equivalence ratio φ of 1.4. The C/H ratio was the same as that of the natural gas. The heat release in the pilot flames was about 1% of the total thermal power of Flame III. A small recirculation zone located directly above the narrow rim provided a second mechanism for flame stabilization.

A large number of measurements using different techniques have been performed in the flames from this burner. The techniques that have been used are Laser Doppler velocimetry (LDA) for velocity measurements, Laser Induced Fluorescence (LIF) for the measurements of radical species concentrations, Coherent anti-Stokes Raman spectroscopy (CARS) for temperature measurements. These experiments were performed in the Thermofluids group of Delft University of Technology. Next in cooperation with Sandia National Laboratories combined Rayleigh-Raman-LIF for simulataneous measurements of species concentrations and temperature were done. Finally time resolved PLIF measurements of OH were done in cooperation with the Division of Combustion Physics of Lund Institute of Technology. In the following measurements from these studies will be discussed.

3 Experimental results

3.1 LDA experiments

Measurements of the fluctuating velocity component at a position of 50 mm. above the burner exit at two positions in Flame IV are given in figure 18.2 together with results from temperature measure-

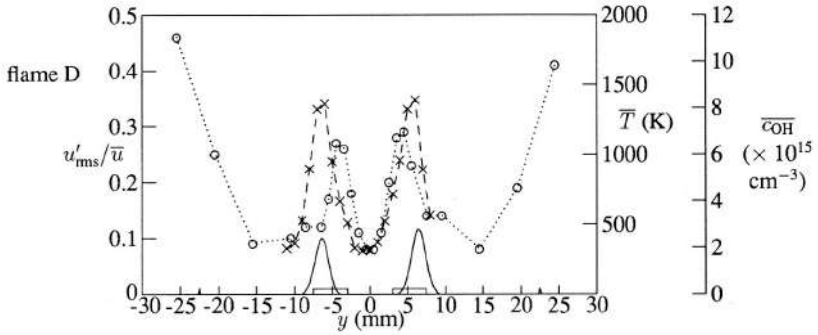

Figure 18.2: Radial profiles of velocity fluctuation, OH-concentration and temperature at axial location of 50 mm

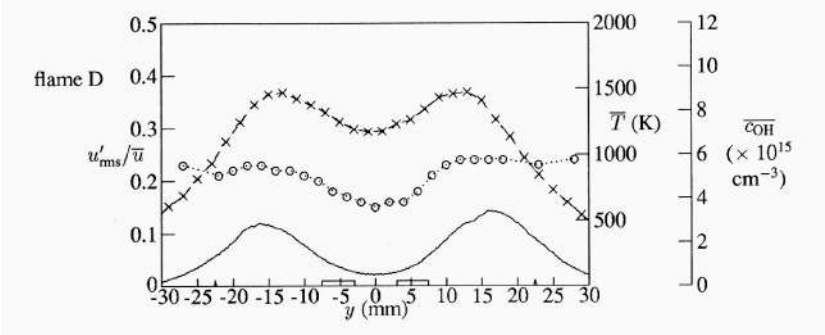

Figure 18.3: Radial profiles of velocity fluctuations, OH-concentration and temperature at axial location of 250 mm.

ments and measurements from OH-concentrations. Figure 18.3 shows the same variables at a position of 250 mm. above the burner exit.

Figure 18.2 shows symmetric profiles of u'_{rms} , c_{OH} and T with peaks is the region where the natural gas from the inner tube mixes with the air from the annulus. The position of the flame front can be expected at the stoichiometric value of the mixture fraction, being 0.06. From figure 18.2 it is clear that the position where the OH-concentration and the temperature have their maximum, does not coincide with the position where the fluctuating velocity is maximal. This position of max. c_{OH} and T is on the air side of the shear layer between natural gas and air from the annulus. This is in agreement with the position where the mixture fraction has a the stoichiometric value. From figure 18.3 this difference in position of the maxima is not present anymore. The turbulent mixing process now has caused much broader peaks at this location.

From autocorrelation functions of axial velocity fluctuations at several locations turbulent integral time scales were found in the flames. Taylors hypothesis was used to find estimates of turbulent integral length scales from these time scales. In such a way at the centerline of flame IV at axial distance of 250 mm. an integral length scale of 7.5 mm. was found. Also from 1D LIF measurements of OH-concentrations and NO-concentrations turbulent length scales of OH-structures and NO-structures could be derived. This led to an integral scale for NO of 3.1 mm. and an integral scale of OH equal to 1.9 mm. At the radial location where the turbulence intensity has its maximum also estimates of these scales were found: a velocity scale of 8.5 mm., from NO measurements also 8.5 mm, from OH-measurements 1.5 mm. The integral OH scales are much smaller than the velocity and NO scales.

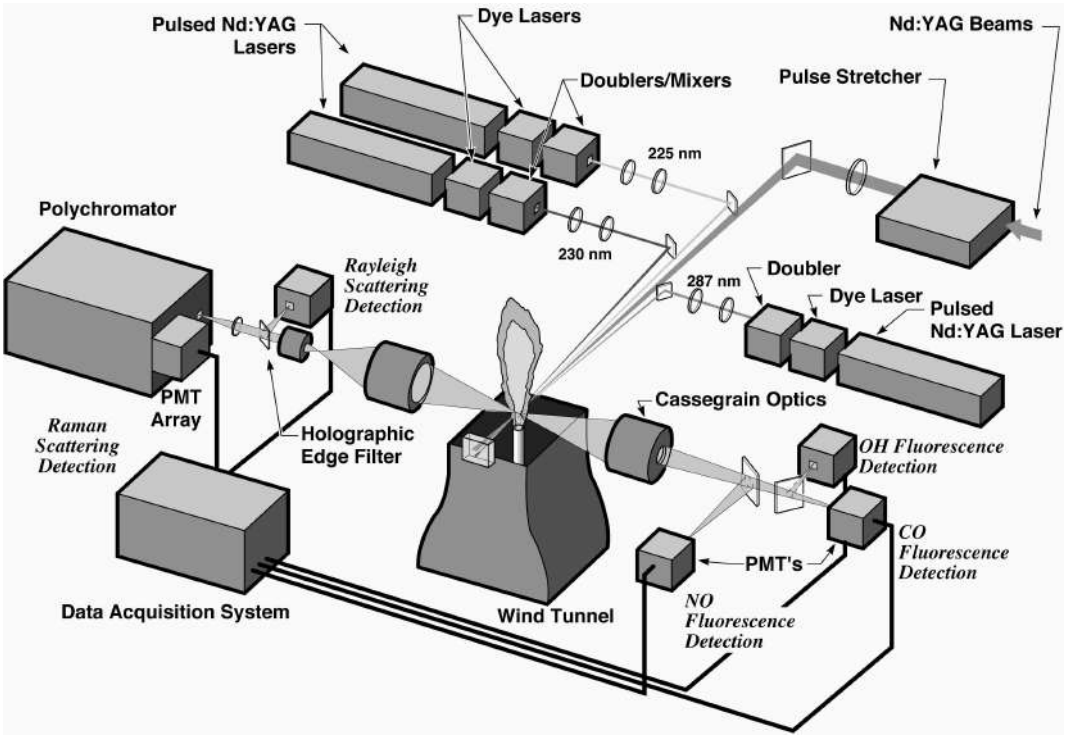

Figure 18.4: The Raman-Rayleigh-LIF system

This is because OH is strongly influenced by chemical reactions. OH exists in very narrow regions and the chemical time scale of the reactions in which OH takes part must be smaller than the integral velocity scale. This may lead to the smaller integral OH-scales, which will be confirmed later by time resolved OH measurements.

3.2 Rayleigh-Raman-LIF measurements

The experimental set up for simultaneous temperature and species concentration measurements is shown in figure 18.4. This set-up is described in detail elsewhere [8]–[12]. The set up consisted of four separate laser systems. One Nd:YAG laser for the Raman-Rayleigh measurements and three separate Nd:YAG/dye laser systems for the LIF measurements of OH, CO and NO. Because all lasers were fired almost simultaneous quantitative corrections were possible for collisional quenching of the LIF signals. Interferences between the different systems were avoided by the application of a timing delay of 100 ns, small compared to typical chemical and turbulent length scales. The vibrational Raman signals of CO_2, O_2, CO, N_2, CH_4, H_2O and H_2 were recorded using PMT tubes aligned along the exit plane of a polychrometer. Three additional PMTs were positioned in between the Raman channels to mionitor the fluorescence background. The probe volume length was estimated to be 0.75 mm.

3.3 N_2, CO_2 and O_2

The interpretation of the Raman signals was complicated by interferences with Raman scattering from other species and with non-resonnant fluorescence from heavy hydro-carbons such as PAHs and other soot precursors. The cross-talk with other species was taken into account by a calibration procedure

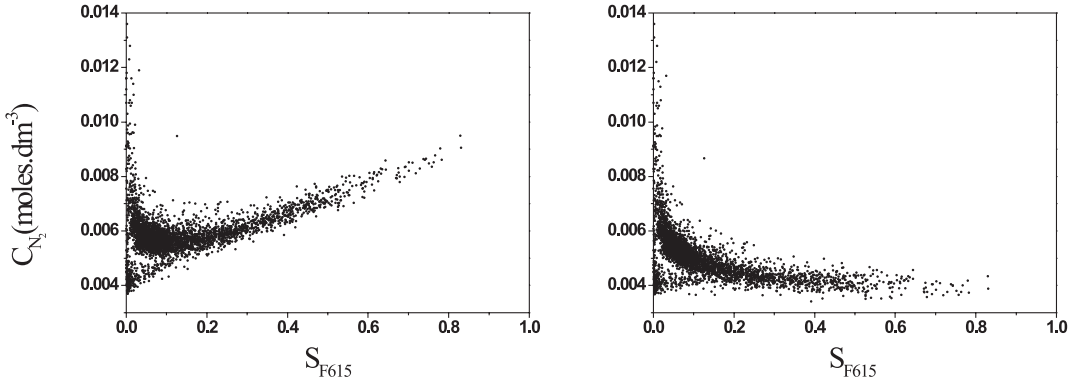

Figure 18.5: Scatterplot of the N_2 Raman signal versus the fluorescence interference signal without (left) en with (right) interference correction (Flame III, $x = 150$ mm, $r = 8$ mm).

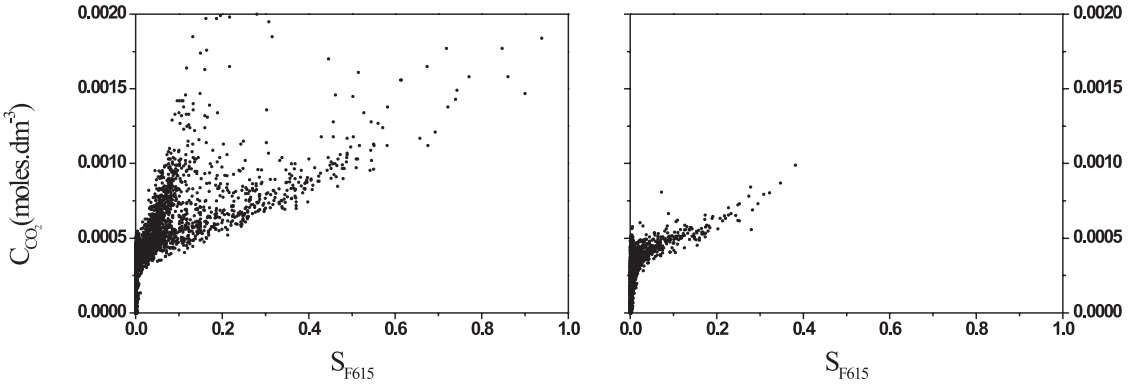

Figure 18.6: Scatterplot of the CO_2 Raman signal versus the fluorescence interference signal without interference correction at $x = 150$ mm. Flame III (left), Flame IV (right).

involving the recording of Raman signals over a wide range of temperatures, gas compositions and concentrations. The broadband fluorescence interferences from the heavy hydrocarbons were monitored by PMTs positioned at spectral locations in between the Raman channels. The PMT at the 615 nm channel provided the best signal-to-noise ratio and was used in the correction procedure. The correction procedure for fluorescence intereferences is illustrated in the scatter plots in Figure 18.5. The uncorrected N_2 Raman signal in the left graph shows a positive correlation with the interference channel. To the right, the fluorescence contributions to the single-shot N_2 concentration have been corrected and the resulting N_2 concentration shows no correlation with the fluorescence signal.

For the species O_2 and CO_2 the interference correction cannot be performed in the above manner as for N_2. Figure 18.6 shows the scatterplots of CO_2 versus fluorescence interference signal at a typical position in Flames II and IV. The scatter plot for flame III shows two distinct branches, apparently corresponding to two different fluorescence interference modes. In flame IV, the interferences are weaker and, more importantly, only the lower branch is observed. Clearly, the structure of the fluorescence interferences in flame III is such that it is not possible to correct for it using a single linear correlation with the monitor channel. It was found that the upper branch corresponds to fluorescence from richer mixtures at lower temperatures. However, no useful correlation between this additional fluorescence and the interference contribution to the CO_2 Raman signal could be identified. In the processing of

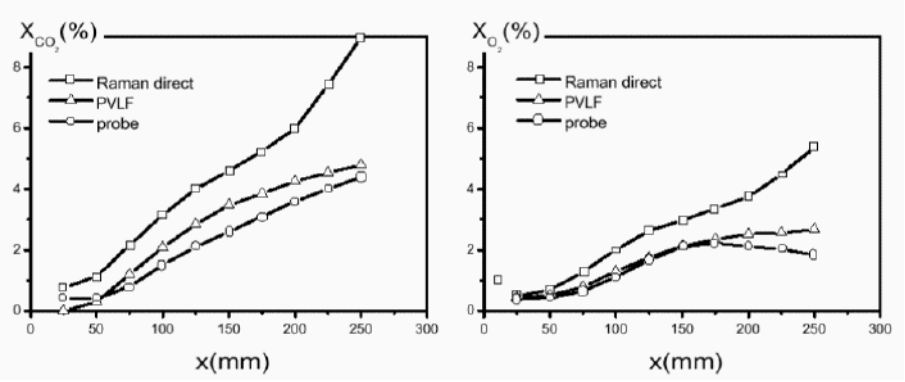

Figure 18.7: Comparison of centerline dry CO_2 (left) and O_2 (right) mole fractionprofiles for flame III.

the data collected in flame III, it is therefore preferred not to use the CO_2 Raman signals from points with instantaneous signals on the 615 nm fluorescence monitor channel above a certain threshold. For these points, the CO_2 concentration is obtained from an indirect procedure using the measured Rayleigh temperature and data from a laminar flamelet calculation instead. In this procedure, it is assumed that the thermochemical composition in the flame is close to that in a laminar flamelet with strain rate $a = 100$ s^{-1}. A progress variable based on the Rayleigh temperature, introduced below, is used to describe small deviations from this composition. Simulations show that flame III exhibits a wide range of strain rates. However, realistic CO_2 concentrations can be obtained with a procedure based on a single representative strain rate. The same procedure was used for the determination of O_2 concentrations. Obviously, the resulting CO_2 and O_2 concentrations are strongly correlated with temperature. As such, they do not provide independent information on the interaction between the turbulent flow field and the chemistry. The main purpose of the procedure is to obtain CO_2 and O_2 concentrations that are adequate for the evaluation of the mixture fraction and the effective Rayleigh cross- section. For further analysis of the limitations of the above method for determining CO_2 and O_2 concentrations the mean values were compared to probe measurements. For Flame III on the centerline at $x = 150$ mm. this comparison is shown in Figure 18.7.

On the centerline, the CO_2 and O_2 Raman signals suffer from substantial contributions of fluorescence interferences. Consequently, the CO_2 and $O-2$ concentrations are overestimated if calculated directly from the Raman signals. The values from the laminar flamelet procedure show a reasonable agreement with the probe data. For the radial traverse at $x = 150$ mm, similar results are obtained. These results indicate that the CO_2 and O_2 concentrations from the laminar flamelet procedure are more reliable than those derived directly from the Raman signals.

3.4 OH, NO and CO

Here some results of the OH, NO and CO measurements are presented. The OH and NO LIF signals are calibrated by comparing them to signals from flames with well-known concentrations. For OH, a premixed CH_4air flame from a Hencken burner with an equivalence ratio of 0.95 is used. The nominal OH concentration in this flame is 1.44×10^{-5} moles.dm^{-3}, determined by a laser absorption measurement. This concentration is close to the non-adiabatic equilibrium concentration at the reference flame equivalence ratio and at a temperature 50 K below the equilibrium temperature. The NO system is calibrated using a premixed CH_4-N_2-O_2 flame ($\varphi = 0.72$), stabilized on a McKenna burner. By replacing part of the N_2 by NO, flames with different concentrations of NO can be produced. Laminar

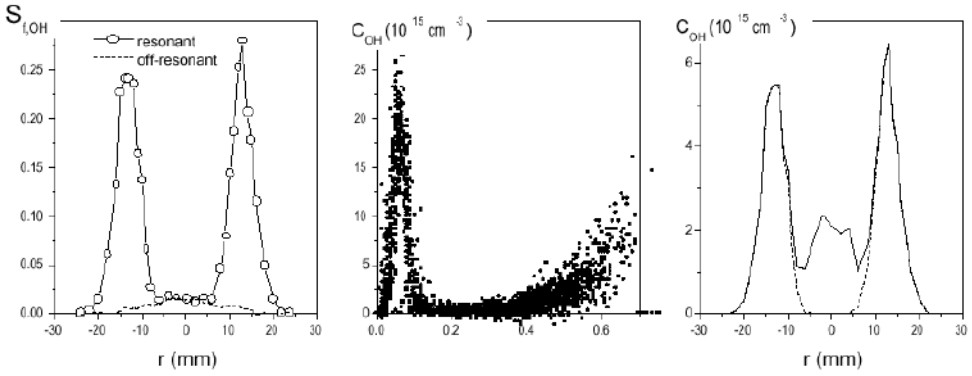

Figure 18.8: Mean resonant and non-resonant OH fluorescence signals (left) and scatterplot of uncorrected OH concentration (molecules cm^{-3}) versus mixture fraction (middle) at $x = 150$ mm in flame III. To the right, the effect of interference correction on the mean OH concentration (molecules cm^{-3}) at $x = 150$ mm in flame III.

flame calculations show that the doped NO is conserved through the flame front. Thus, the signals recorded from flames with different known doped NO levels can be used to construct a calibration. The single shot temperature and composition measurements are used to correct for:

- the difference between the population fractions at the reference temperature in the calibration flame and the temperature in the probe volume,
- the collisional quenching rate in the calibration flame relative to the collisional quenching rate in the probe volume,
- the different spectral overlaps between the laser and the selected transition at the reference temperature in the calibration flame and at the probe volume.

Although the LIF signals are stronger than the Raman signals, they still are affected by interferences from heavy hydrocarbons. This is mainly because of the wider spectral intervals over which the signals were collected. The interference contribution to a LIF signal was estimated from the off-resonance signal, where the dye laser system was tuned to a wavelength where none of the probed molecules were excited. As the fluorescence interferences from heavy hydrocarbon species are generally broad-band, the off-resonance signal is considered to be a reliable estimate for the interference contribution to the LIF signal. The off-resonant signals cannot be measured simultaneously with the resonant signals. Consequently, they cannot be used to subtract the interference contributions from the LIF signals on a single-shot basis. However, the off-resonant measurements provide valuable insights into the distribution of the interferences in both physical and composition space.

The left graph in figure 18.8 presents the mean resonant and non-resonant OH signals measured at $x = 150$ mm in flame III. It is seen that near the centerline, for $r < 5$ mm and where $\xi > 0.4$, nearly the entire recorded LIF signal originates from interferences. At the positions where the maximal resonant OH signals are measured, the non-resonant contribution is only about 2%. The middle graph shows the distribution in mixture fraction space of the OH concentration calculated from the uncorrected resonant signal. Clearly, the non-zero OH concentrations for $\xi > 0.4$ stem from interferences: the OH is expected to be confined to a narrow zone located around stoichiometric mixture fraction. The non-resonant contributions to the measured OH concentrations can therefore be removed by setting the OH concentrations to zero for mixture fraction values above a certain threshold. The threshold value employed in this work is 0.20. This value is not critical: threshold values of 0.10

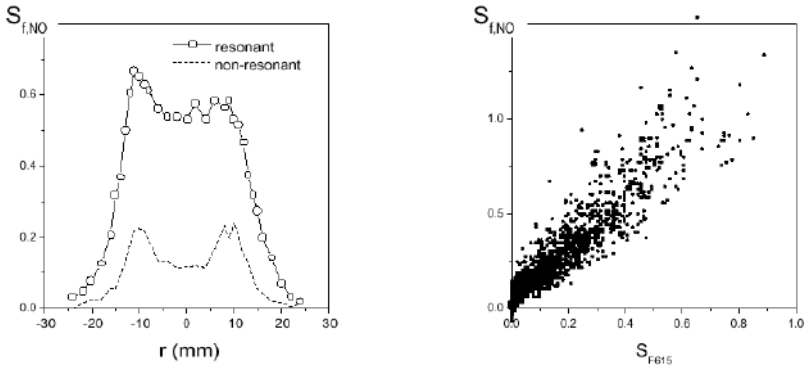

Figure 18.9: Mean resonant and non-resonant NO fluorescence signals (left) and scatterplot of non-resonant NO signal versus the fluorescence interference channel (right) at $x = 150$ mm in flame III.

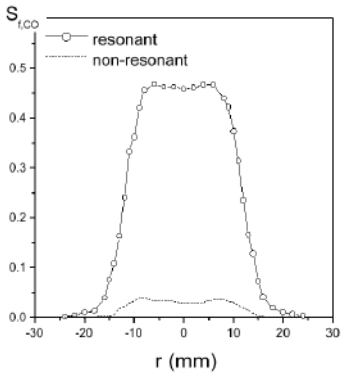

Figure 18.10: Mean resonant and non-resonant CO fluorescence signals at $x = 150$ mm in flame III

and 0.30 give nearly identical results for the mean OH concentration. The unphysical non-zero OH levels found near the centerline position in the uncorrected profile are hereby eliminated. In the zones with high OH concentrations around $r = 14$ mm, the non-resonant contributions are negligible and the corrected and uncorrected profiles coincide.

For the case of NO, a different approach was employed to suppress non-resonant interferences. The left graph in figure 18.9 shows the mean resonant and non-resonant signals at $x = 150$ mm in flame III. The ratio of the non-resonant and resonant signals is found to be approximately constant across the profile. Scatter plots show that the structure of the NO off-resonance signal in mixture fraction space does not allow for a correction analogous to that used for OH. However, the off-resonant signal exhibits a strong correlation with the fluorescence interference channel monitored at 615 nm (figure 18.9 to the right). This correlation is used to subtract the interference contributions from the resonant signal before the NO concentration is calculated.

Figure 18.10 presents the mean resonant and non-resonant CO signals at $x = 150$ mm in flame III. The non-resonant contribution is some 8% of the total signal. The CO non-resonant signal is found to exhibit a correlation with the interference channel, although not as strong as in the case of NO. This correlation is incorporated in the response matrix used in the inverse Raman signal problem. Using this approach, the non-resonant contributions are reduced to about 5%. In flame IV, the absolute non-resonant OH signals at $x = 150$ mm are found to be typically four times smaller than those in flame III. The absolute OH concentrations are somewhat smaller as well. The non-resonant contribution near the centerline is about 50%. The non-resonant NO and CO signals at $x = 150$ mm in flame IV are

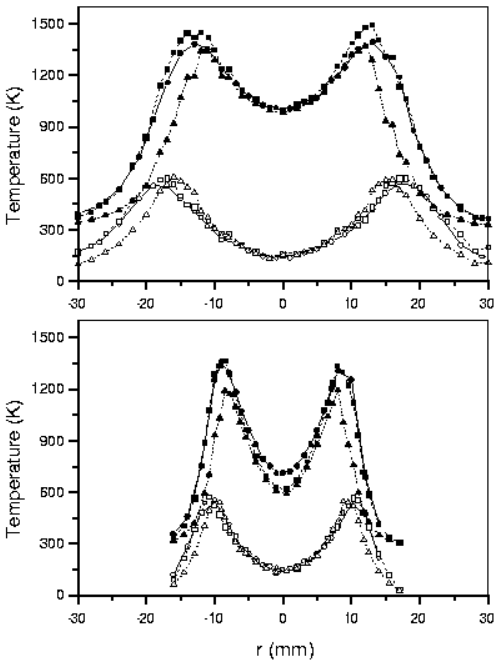

Figure 18.11: Comparison of measured mean and RMS of temperature at $x = 100$ mm (bottom) and 200 mm (top) in flame III. Mean temperatures of CARS (red), Reynolds-averaged Raman-Rayleigh (blue) and Favre-averaged Raman-Rayleigh (green) measurements are indicated with solid symbols. Open symbols give temperature standard deviations.

typically six and three times smaller, respectively, than those at the same position in flame III.

3.5 Temperature

Figure 18.11 presents profiles of the mean and standard deviation of temperature from the Raman-Rayleigh measurements together with the CARS data for two axial locations in flame III ($x = 100$ mm and $x = 200$ mm). As the instantaneous density is available in the Raman- Rayleigh measurements, it is straightforward to compute both the Favre- and Reynolds-averaged temperature for these data. The density weighting in the Favre averaging procedure gives rise to lower mean temperatures. The difference between the Reynolds and Favre mean temperature varies from about 15 K at positions near the centerline to some 350 K in the outer flanks of the profiles. The Favre peak mean temperatures are typically 120 K lower than the Reynolds values. The maximum and centerline values of the temperature standard deviations are similar. The Favre-averaged profiles show a faster decay in the flank region, consistent with the shape of the mean temperature profile. It is unclear whether the CARS measurements yield conventional (Reynolds) or density-weighted (Favre) averages. The CARS mean temperatures in figure 18.11 are nearly identical to the Reynolds-averaged Raman-Rayleigh results, especially in the flank regions of the flame. At the centerline, where the differences between Reynolds- and Favre-averaged temperatures are relatively small, the CARS and Raman-Rayleigh means agree well and are within the experimental uncertainty. The CARS temperature standard deviations are closer to the Reynolds-averaged Raman-Rayleigh values as well. Comparison of the different datasets at other axial locations yields similar results.

Figure 18.12 shows temperature PDFs measured at four radial positions at $x = 150$ mm in flame III. The graphs compare the CARS PDFs with the Reynolds and Favre PDFs obtained from the Raman-Rayleigh measurements. The CARS and Raman-Rayleigh PDFs are constructed from 5000 and 4000 points, respectively. For the relatively narrow, monomodal PDF found at the centerline, the Reynolds and Favre PDFs are very similar (figure a). Except for a small difference in standard deviation, they agree well with the CARS result. At $r = 7.5$ mm (figure b), the PDFs are somewhat

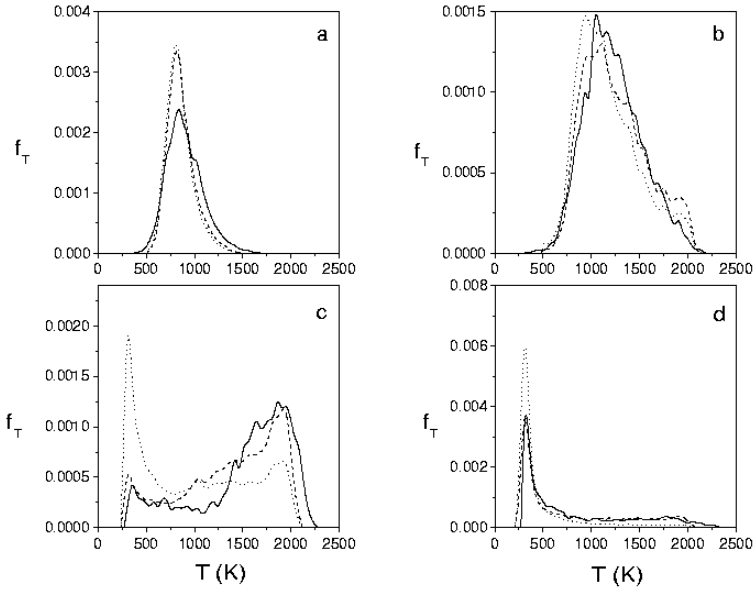

Figure 18.12: Comparison of measured temperature PDFs for different radial positions at $x = 150$ mm in flame III. Favre-averaged (green) and Reynolds-averaged (blue) PDF'ss constructed from the Raman-Rayleigh measurements. CARS results from Zong *et al*. Positions: $r = 0.0$ mm (a), $r = 7.5$ mm (b), $r = 11.5$ mm (c) and $r = 15.5$ mm (d).

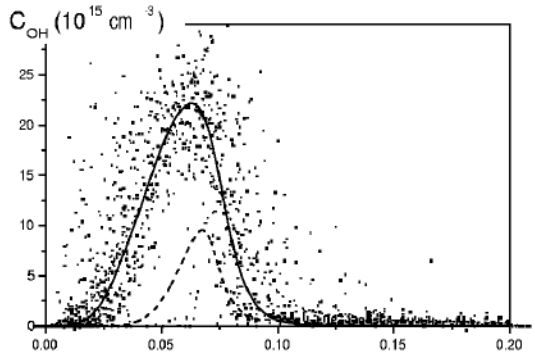

Figure 18.13: Scatterplot of the measured OH concentration (molecules.cm$^{-3)}$ at $x = 150$ mm. The lines represent the Favre conditional average (red), a laminar flamelet calculation with $a = 100$ s^{-1} (magenta) and and chemical-equilibrium calculation (blue).

wider. For the bimodal PDF at $r = 11.5$ mm, figure c, the Favre and Reynolds PDF shapes differ substantially. The density weighting in the Favre PDF produces a larger probability at lower temperatures. At this position, the CARS PDF is closer to the Reynolds than to the Favre result. Figure d shows the PDFs measured in the outer flank of the temperature profile ($r = 15.5$ mm). Although the three results are qualitatively similar, the relative weights of the room temperature peak and the high-temperature tail are different for the Favre PDF on one side and the Reynolds and CARS PDFs on the other side.

Figure 18.16 shows typical C_{OH}-ξ scatterplot data obtained from the Raman-Rayleigh-LIF experiments in flame III, together with the profiles from a 100 s^{-1} flamelet and a chemical-equilibrium calculation. Comparison of the scatterplot data to the equilibrium profile clearly shows that OH is present in super-equilibrium concentrations in the upstream part of the flame. The OH levels predicted by the equilibrium model are some 3 to 5 times lower than the measured values. The occurrence of super-equilibrium OH concentrations is a well-known phenomenon in the type of jet flame considered

here. Figure 18.16 shows that super-equilibrium OH levels are similar to those observed in moderately strained flamelets.

3.6 Time resolved PLIF of OH

Although much insight into the natural gas flames has been gained from the measurements discussed above, time resolved measurements are needed to visualize the evolution of turbulent reactive structures. With these measurements a better understanding of turbulence chemistry interactions can be obtained. Time resolved measurements also add to a more complete database.

In this paragraph, we present time-resolved OH PLIF measurements, at repetition rates of the same order as the characteristic frequencies of the flow, in turbulent diffusion flames from the Delft burner with Re number in the range of 7000 to 16000. We show how turbulent structures interact with the reaction zone in the turbulent diffusion flames and track their development in a film like manner.

For details on the laser system the reader is referred to [13]. Briefly, the laser consists of 4 individual Nd:YAG oscillator/amplifier units (B.M. Industries, France). The individual channels are each equipped with a double pulse option (DPO) where the Pockels cell is switched twice during the duration of the flashlamp pulses. In this way two pulses can be extracted per cavity with selectable delays ranging from $\approx$ 25 to 145 μs. Thus a total of 8 pulses can be obtained from the system propagating as a single beam. Pulse energies at 532 nm are around 600 mJ per pulse in single pulse mode (total of four pulses) or around 270 mJ per pulse in DPO mode. For the experiments presented here, the laser was mostly run with a total of four pulses per sequence thus affording higher pulse energies and better signal to noise ratios.

A single, frequency doubled, dye laser system (Continuum) operating with Rhodamine 590 dye containing methanol solutions was pumped with this laser pulse train. Due to thermal loading effects and dye degradation in the dye laser the resulting beam profile and intensity was degraded from one pulse to the next within a sequence. This dye memory effect made shot-to-shot referencing of the beam profile essential (see subsequent paragraphs for details).

Typically around 8–10 mJ per pulse around 283 nm were obtained with a linewidth of 0.3 cm^{-1}. The wavelength was tuned to the $Q_1(8)$ transition in the $v' = 1 \leftarrow v'' = 0$ band of the $A^2\Sigma^+ \leftarrow X^2\Pi$ system of OH. For all experiments OH fluorescence in the $1 \rightarrow 1$ and $1 \rightarrow 0$ bands near 310 nm were detected by passage through bandpass interference filters. The light was spatially filtered and focused into a sheet whose dimensions in the interaction region were approximately 50 mm in height and 0.25 mm in thickness.

For the concentration measurements described, laser sheet profiles were recorded online which could be used to normalize PLIF data on a shot by shot basis. For this purpose, a reflection of the laser sheet was directed into a cell containing fluorescing dye. The resulting LIF signals were imaged onto the detector concurrently with the OH PLIF images which were subsequently divided by this profile. The procedure is described in detail in [12].

A custom modified Imacon 468 framing camera (Hadland Photonics, UK, see [12] for details) was used as a detector for the PLIF signals. The system features 8 independent intensified CCD detectors (ICCD) with 384 $\times$ 576 pixel arrays and 8 bit dynamic resolution. To increase the overall gain of the system and to make it UV sensitive an additional three-stage intensifier module was attached to the optical input of the camera prior to the prism beam- splitter.

Measurements were performed at eight heights from 0 to 395 mm above the nozzle for each flame. Different time separation between events in a recorded sequence at 125 μs, 250 μs, 500 μs, 1 ms and 2 ms were varied to track the different temporal scales of the turbulent eddies. Several representative images showing the time development of the turbulence-flame interaction are presented

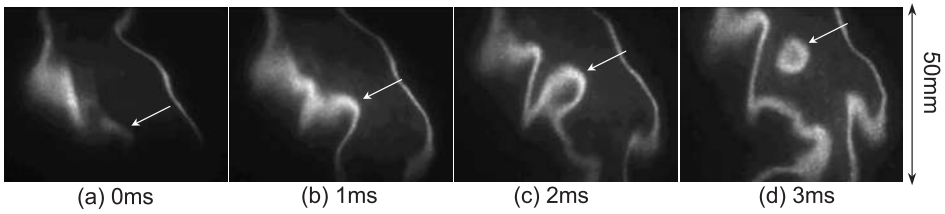

Figure 18.14: OH island formation: Time sequence OH PLIF images of Flame III show the formation of an OH island indicated by the arrow. Image center height is 370 mm from nozzle.

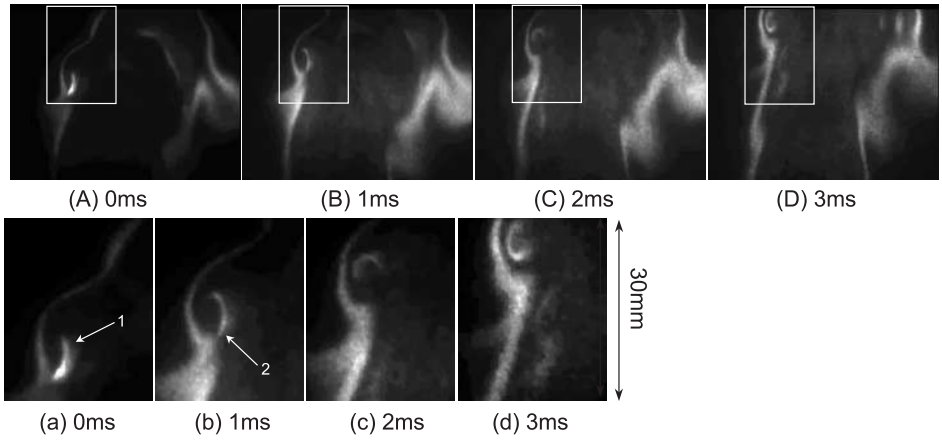

Figure 18.15: Flame vortices movement: Time sequence of OH PLIF images shows a flame vortices movement. Images are of flame III, center height of upper images is 370 mm from nozzle. Lower images correspond to the indicated box in the upper images.

in figures 18.14–18.17.

Figure 18.14 shows OH island formation in flame III at the height of 345 to 395 mm downstream from the nozzle. In the remainder of this discussion we will refer to center heights only, which is for this case 370 mm. In image (a) (t=0 ms), a very low intensity OH layer (indicated by the arrow) is wrinkled, most probably because of an air-sided anticlockwise turbulent eddy near the air/fuel shear layer. The wrinkle develops into a flame tongue wrapped around the eddy and the tip of the tongue connects with the upper thick OH area in the next 1ms. The tip of the flame tongue becomes thick and strong due to both the strains of the eddy and the connection with the upper thick flame area. At $t = 2$ ms, the flame tongue highly curves and almost touches itself. It stretches the upper thick flame area and makes it thin and weak. Finally, at $t = 3$ ms in image (d), the flame tongue touches itself, resulting in a flame island separating from the main body. The flame island becomes smaller by consuming the oxidizer inside the island, while it continues moving upwards and rotating. The time scale of the formation of an OH island is of the order of several ms. The length scale of the turbulent eddy, which causes the formation of the flame island, is about 10 mm.

At the same axial position in the same flame another interesting event is illustrated in Figure 18.15. Further details are presented in the lower enlarged images (a) to (d). At $t = 0$ ms, an upstream flame tail caused by turbulent movement is seen in image (a) (indicated by arrow 1). After 1 ms it has become thinner, especially in the base position (indicated by arrow 2). It could be caused by a significant strain due to an anticlockwise vortex-induced rotational motion. Then, at $t = 2$ ms, the

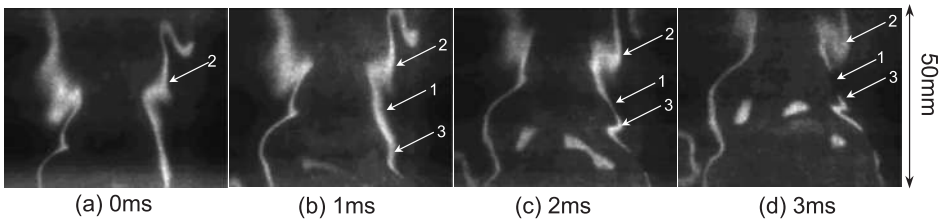

Figure 18.16: Flame extinction: Time sequence OH PLIF images shows occurrence of a local extinction (indicated by arrow 1). Images are of flame III, at the image center height of 270 mm from nozzle.

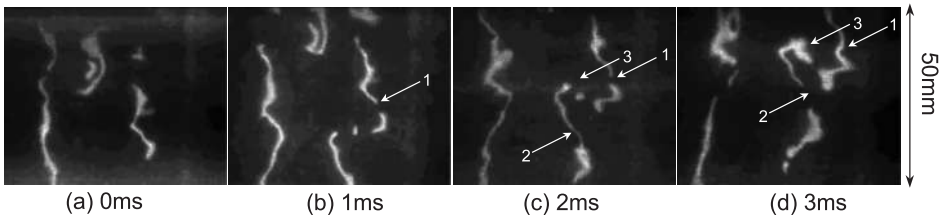

Figure 18.17: Extinction and re-ignition: Time sequence OH PLIF images from flame IV at a center height of 170 mm from nozzle. A local extinction is indicated by arrow 2. Arrow 1 and 3 indicate flame re- ignition.

flame tail separates from the main flame layer. It follows the anticlockwise rotational movement while moving up and consuming itself. In the last image at 3 ms. we see OH in the complete structure, which means that gas and air were trapped inside the structure and reactions have taken place. Meanwhile the main flame zone becomes thick too. It could be predicted that at the next moment the separated flame tail would connect with the main flame and the topology changes into one thick flame zone. The scale of the flame vortices, estimated from the images, is 5mm in diameter.

An occurrence of local extinction indicated by arrow 1 can be seen clearly in Figure 18.16. This is caused by two turbulent eddies. A thick curved OH layer (indicated by arrow 2) curves and rotates with time. Following this structure 2 in time shows that it rotates clockwise. The compressive strain induced by the eddy thickens the flame layer and the extensive strain thins it. Such a mechanism has been previously postulated to explain the oscillating flame layer thickness in jet flames . Another wrinkle occurs in the lower OH layer indicated by arrow 3 in figure 18.16. It could be caused by the same reason as the upper structure (indicated by arrow 2). The OH layer between these two curved flame layers (indicated by arrow 1) undergoes significant extensive strain caused by both eddies. The result is that here the flame zone becomes thinner, and, finally, extinguishes due to the high strain (see image (d)). The whole local extinction procedure occurs within several ms.

Figure 18.17 shows a time sequence of OH PLIF images in flame IV at a height of 170 mm downstream. Very curved flame structures can be seen all over the image region. These flame structures show more and smaller wrinkling than those from flame III in figure 18.16. This is because the Reynolds number of the air flow for flame IV is twice as high as that of flame III. A local extinction is indicated by arrow 2. It is most possibly caused by either a high strain from the flame layer above it or by strain coming from a turbulent eddy beside it. Arrow 1 and 3 highlight regions where a broken flame re-ignites. These re-ignited structures are thick pointing at a certain degree of premixing during the period that the flame was locally extinguished. These results show the interaction between combustion and small turbulent structures.

4 Conclusions

The application of the Raman technique in the undiluted natural-gas flames considered here proves to be very challenging because of the high fluorescence interference levels. The interference contributions to the recorded Raman signals are identified and subtracted using empirical correlations between the Raman signals and the signals on the interference monitor channels. This procedure proves to be adequate for most species. However, it is found that the empirical approach cannot be used to remove the interference contributions to the CO Raman signal. This also holds for the CO_2 and O_2 signals in Flame III, the flame with the highest interference levels. The concentrations of these species are determined using alternative approaches. Because of the fluorescence interferences, the acquired Raman-Rayleigh-LIF dataset has certain limitations, the most important of which is the absence of independent CO_2 and O_2 measurements in Flame III. The obtained profiles of mean temperature and temperature fluctuations agree very well with CARS temperature measurements obtained in Flame III. In Flame IV, which shows substantial local extinction, small differences in the boundary conditions are expected to be important. The Raman-Rayleigh-LIF measurements of the OH concentration compare well with the existing semi-quantitative one-dimensional LIF data. The Raman-Rayleigh-LIF experiments provide nearly all of the desired simultaneous measurements of temperature and major species concentrations. The Raman-Rayleigh-LIF data therefore form a valuable and useful extension of the existing database for the Delft piloted jet diffusion flame burner. The film-like results presented here give a detailed view of the evolution of the flame front following turbulent eddies and vortex motion. Several phenomena, which are characteristic for turbulent flames, were visualized in time and analyzed qualitatively in this paper. A turbulent eddy causing the formation of a flame island was clearly observed. The pattern of a flame vortex movement—rotating, departing and attaching—was catched in time. The secret of single flame extinction caused by turbulence was revealed from the time sequent images. The extinction occurred when the flame zone was stretched too much by the turbulent eddies. Flame re-ignition was also visualized. In contrast with previous structural investigations based on planar LIF measurements, time- resolved PLIF measurement results allow direct observation of both the spatial and the temporal effects of flame turbulence interaction. However, some of the results are ambiguous to interpret due to the general limitation of 2D imaging techniques for the study of essentially 3D phenomena. A 3D volumetric rendering technique is being developed in Lund Laser Center to perform 3D OH concentration measurements.

References

[1] Peeters, T. W. J., Stroomer, P. P. J., De Vries, J. E., Roekaerts, D. J. E. M., and Hoogendoorn, C. J. (1994) *Comparative experimental and numerical investigation of a piloted turbulent natural-gas diffusion flame*, Twenty-Fifth Symposium (International) on Combustion/The Combustion Institute, pp. 1241–1248.

[2] Vries, J. E. de (1994) *Study on turbulent fluctuations in diffusion flames using laser induced fluorescence*, Ph.D. thesis, Delft University of Technology.

[3] Stroomer, P. P. J., De Vries, J. E., Van Der Meer, Th. H. (1999), *Effects of Small- and Large-scale Structures in a Piloted Jet Diffusion Flame*, Flow, Turbulence and Combustion **62**, pp. 53–68 (1999).

[4] Mantzaras, J., and Van Der Meer, Th. H. (1997) *Coherent AntiStokes Raman Spectroscopy measurements of temperature fluctuations in turbulent natural gasfueled piloted jet diffusion flames*, Combustion and Flame **110**, pp. 39–53

[5] Nooren, P. A., Wouters, H. A., Peeters, T. W. J., Roekaerts, D., Maas, U. and Schmidt, D. *Monte Carlo PDF modeling of a turbulent natural-gas diffusion flame*, Combustion, Theory and Modeling **1**, pp. 79–96 (1997).

[6] Nooren, P. A., Versluis, M., Van Der Meer, Th. H., Barlow, R. S., and Frank, J. *Raman-Rayleigh and LIF measurements of temperature and species concentrations in the Delft piloted turbulent jet diffusion flame*. Appl. Phys. B **71**, pp. 95–111 (2000).

[7] Ding, T. J., Van Der Meer, Th. H., Versluis, M., Golombok, M., Hult, J., Aaldén, M., Kmaminski, C., *Time-resolved PLIF measurement in turbulent diffusion flames*, Proc. Of the third Int. Symposium on Turbulence, Heat and Mass Transfer, Nagoya, Japan, April 2–6, 2000, pp. 857–864.

[8] Nguyen, Q. V., Dibble, R. W., Carter, C. D., Fiechtner, G. J., and Barlow, R. S., *RamanLIF measurements of temperature, major species, OH, and NO in a methaneair Bunsen flame*, Combustion and Flame **105**, pp. 499–510 (1996).

[9] Barlow, R. S. and Carter, C. D., *Raman/Rayleigh/LIF measurements of nitric oxide formation in turbulent hydrogen jet flames*, Combustion and Flame, **97**, pp. 261–280 (1994).

[10] Carter, C. D. and Barlow, R. S., *Simultaneous measurements of NO, OH, and the major species in turbulent flames*, Optics letters, **19**(4), pp. 299–301 (1994).

[11] Dally, B. B., Masri, A. R., Barlow, R. S., Fiechtner, G. J., and Fletcher, D. F., *Measurements of NO in turbulent nonpremixed flames stabilized on a bluff body*, in: TwentySixth Symposium (International) on Combustion/The Combustion Institute, pp. 2191–2197 (1996) .

[12] Barlow, R. S., Dibble, R. W., Chen, J. Y. and Lucht, R. P., *Effect of Damköhler number on superequilibrium OH concentration in turbulent non-premixed jet flames*, Combustion and Flame **82**, pp. 235–251 (1990).

[13] Kaminski, C. F., Hult, J., and Aldén, M., *High repetition rate planar laser induced fluorescence of OH in a turbulent non-premixed flame*, Applied Physics B **68**, pp. 757–760 (1999).

Part 6

Applications

Chapter 19

Combustion applications: furnaces

D. Roekaerts, Th. H. van der Meer

1 Introduction

Combustion is used in many practical devices and industrial systems such as gas turbines (in aircraft engines, or for stationary power production), internal combustion engines (Diesel or spark ignited engines), industrial processes (manufacturing of steel, cement, glass or chemicals, waste incinerators). Combustion has also a strong impact on the environment as it produces pollutants contributing to acid rain. This has led to more tight environmental legislation, specifying the maximally allowed emissions in many countries. Furthermore the contribution of the main combustion product CO_2 to the greenhouse effect and global warming has intensified the search for more efficient ways of combustion. For these reasons progress in the area of clean and efficient combustion science and technology is of great interest.

Figure 19.1 gives and overview of both the application areas and the research areas, focused on the topic *combustion dynamics*. The figure expresses that to come to applications of combustion research integration of contributions from experimental work, theoretical analysis and numerical simulations is needed. The view expressed by figure 19.1 is in fact somewhat futuristic. The amount of fundamental science that was used in the development of many of the current combustion systems is much less than what the picture suggests. Straightforward engineering tools and trial and error always have played an important role and still do. Nevertheless, the trend towards the use of more sophisticated experimental and computational tools is real.

The rest of this chapter is restricted to gas-fired furnaces. The description should give some hints on the gaps between fundamental combustion research and needs of practical industrial combustion. A good insight on what is important in practical combustion in process furnaces is given in Refs. [1, 2], which has been used as reference material. On the other hand, in addition to the material presented in these lecture notes, a detailed presentation of theoretical and numerical modeling of combustion is given in Ref. [3].

2 Industrial furnaces

Major refinary processes requiring a combustion chamber are: distillation, thermal cracking, catalytic cracking, hydroprocessing, hydroconversion. They are used for preheating, direct firing and reboiling. The application in the petrochemical plants can be broadly classified in two categories depending on the temperature. Low and medium firebox temperatures are needed for preheaters, reboilers and steam superheaters. High firebox temperatures are needed in pyrolysis furnaces and steam-hydrocarbon reformers. The latter category represent about 80% of the chemical industry heater requirements and

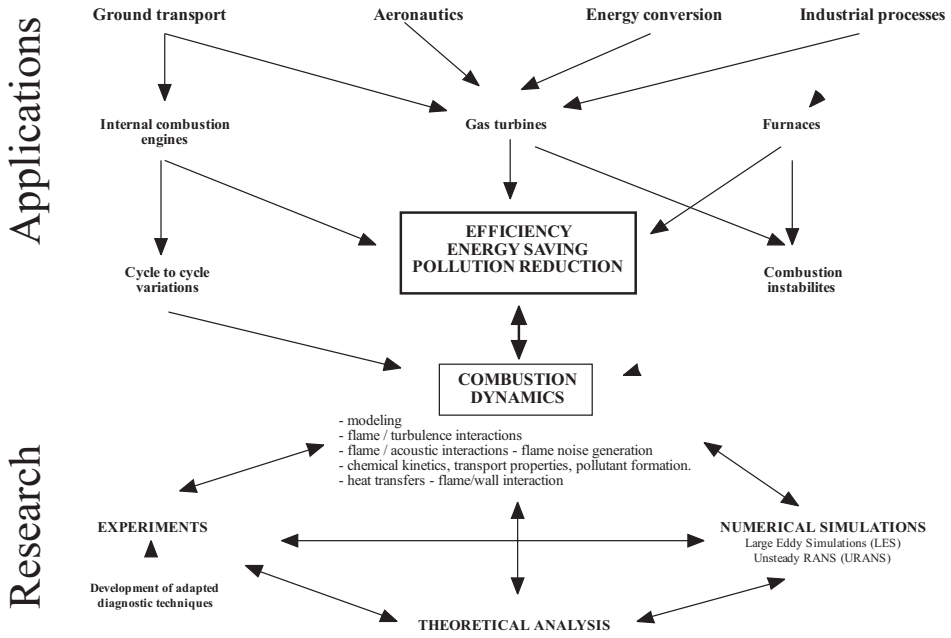

Figure 19.1: Objective and organization of a combustion research network in the area of combustion dynamics (from an expression of interest prepared by D. Veynante and S. Candel, Ecole Centrale Paris, and with participation of several research groups in the Netherlands.)

are unique to the chemical industry.

Typical petrochemical process heaters consist of a radiant section and a convection section. These regions are named after the dominant mode of heat transfer. In the radiant section, refractory wall surface temperatures can be higher than 1200 °C. Radiant heat is incident on the process tubes carrying the fluid to be heated, both from the high-temperature surfaces and directly from the flame. In the convection section convective tubes receive heat from the direct contact with the flowing combustion gases. The transition from the radiant to convective sections is knows as the bridgewall. Typical fluids to be heated include gasoline, naphta, kerosine, gas oil. Using tubes to contain the load (the object to be heated) is somewhat special compared to other types of industrial furnaces found in the steel industry or glass manufacturing industry. Advantages include suitability for continuous operation, good controllability, high heating rates, more compact equipment

In general well-controlled profiles of heat flux are needed to guarantee process stability and product quality. When the heat flux exceeds certain peak values the formation of deposits at the inside of the process tubes will rapidly lead to coking, increase of pressure drop and the need to stop and clean the furnace tubes. Since this leads to production loss a lot of effort has been made to avoid this scenario by careful design.

Reactors such as cracking furnaces and reforming furnaces are more extreme versions of process heaters. Here, the process fluid undergoes chemical transformations. For example, in an ethylene cracking furnace, liquid or gas feedstock transforms to ethylene (C_2H_4), an intermediate in the production of polyethylene and other plastics. A hydrogen reformer takes natural gas and reformulates it into hydrogen in a catalytic chemical process that involves a significant amount of heat. The reformer is a direct-fired combustor containing numerous tubes, filled with catalyst, inside the combustor. The raw feed material flows through the catalyst in the tubes which, under the proper conditions converts that material to the desired end products. The burners provide the heat needed for the highly

endothermic chemical reactions.

3 Emissions

The major pollutant species arising in combustion of hydrocarbon fuels are CO, nitrogen oxides (NO_x), sulfur oxides (SO_x), volatile organic compounds and particulates (e.g. soot). (NO_x stands for either nitric oxide NO, nitrogen dioxide NO_2 or nitrous oxide N_2O, SO_x for a whole set of sulphur oxides.) For high temperature natural gas combustion the formation of NO is the prime NO_x source. (Once in the atmosphere NO rapidly combines with O_2 in the atmosphere to form NO_2.) The formation of NO can be split into three routes: 'thermal' NO, 'prompt' NO and 'fuel' NO. The last depends on the presence of fuel-bound nitrogen and is not active in natural gas combustion. The prompt NO formation mainly occurs in fuel rich regions of the flames. The thermal NO formation mechanism (or Zel'dovich mechanism) is the major NO formation pathway in high-temperature furnaces. The emissions of CO, partially burned or unburned hydrocarbons and soot can be suppressed by tuning the combustion equipment such that sufficiently long residence times and high temperature are achieved, allowing a complete oxidation process. However, in general this conflicts with the optimal conditions for low NO_x formation.

4 Burners

The burners can be located in the furnace at various locations: for example in the floor, firing vertically upward, or in the wall firing parallel to the floor or firing radially along the wall (radiant wall burners). A unique aspect of process heaters is that they often used natural-draft burners. This means that no combustion air blower is used. The air is inspirated into the furnace by the suction created by the hot gases through the combustion chamber and exhausting to the atmosphere. On the other hand, the radiant wall burners use high pressure fuel to educt combustion air from the ambient environment. The fuel and combustion air are then mixed in a tube prior to the combustion zone.

Another unique aspect of those heaters is the wide range of fuels used, which are often byproducts of the petroleum refining process. These fuels can contain a large amount of hydrogen which has a large impact on the burner design. It is also fairly common for multiple fuel compositions to be used, depending on the conditions at a given time. Adding this to the requirements for turndown, it becomes clear that it is quite a challenge to design burners that will maintain stability, low emissions and the desired heat flux distribution over the range of possible conditions.

The interest in reducing pollutant emissions has had a large impact on burner design. For example, a well accepted technique for reducing NO_x emissions is known as staging, where the primary flame zone is deficient in either fuel or air. The balance of the fuel or air is injected further downstream. Staging reduces the peak temperatures in the primary flame and influences the chemical conditions, leading to lower NO_x emissions. Lower flame temperatures due to staging may adversily affect the radiative heat transfer (proportional to T^4). But on the other hand staged combustion may produce more soot which can increase flame radiation. The actual impact of staging on the heat transfer from the flame is highly dependent on the actual burner design.

Many types of burner designs exist due to the wide variety of fuels and oxidizer composition, combustion chamber geometry, environmental regulations, thermal input size and heat transfer requirements. There are many potential problems that could affect the performance of burners and therefore the performance of the heaters, boilers and furnaces. Flame impingement on the tubes can cause premature coking and significantly reduce the operational run time. Flames leaning away from

the tubes may reduce performance. Ref. [1] contains chapters on burner testing, installation and maintenance, burner/heater operations and troubleshooting and several chapters on specific types of burners (duct burners, boiler burners, flares).

5 CFD of industrial furnaces

As should be clear from the other lectures in this course, numerical solution of combustion models is intrinsically difficult because they combine the difficulties of fluid mechanics equations and kinetic equations. In general, solving for combustion means solving for the flow and for the chemical species. Since flow and species distributions are strongly coupled the solutions must be simultaneous. Combusting flows require new numerical schemes compared to inert flows because heat release induces changes in density, viscosity and diffusion coefficients. The stiffness of the chemical source terms is an additional crucial problem. In addition, in the case of furnaces the radiative transfer equation, also has to be solved simultaneously using specific solutions methods.

In industry, most CFD simulations of furnaces are made using one of the large commercial CFD packages. In these codes not all models for turbulent combustion discussed in other lectures of this course are available. It would in fact not be possible to use them, because of the size of the problem, which appears in:

- The need to consider a three-dimensional computational domain
- The large size of the computational domain in combination with the need to focus on details.
- The need to include radiative heat transer
- The complexity of the turbulent flow
- The complexity of the combustion chemistry
- The limited amount of information available on boundary conditions (turbulence profiles at inlets, wall radiative properties)

There is a long tradition of drastic model simplifications most notably the use of simplified chemistry and of turbulence modelling. In general simplification cannot be avoided but the challenge is to use the available numerical techniques and computational power in the optimal way, making only simplifications not destroying the (limited) predictive capability. To judge the role of various model assumptions and the lack of information on boundary conditions often a number of simulations have to be done in order to show the sensitivity of the predictions to the assumptions.

Past research has identified a suitable set of submodels for predicting overall properties of heat transfer quite well. The next section reports on the application of such a set of submodels.

6 CFD simulation of a semi-industrial furnace

6.1 Introduction

At TU Delft, simulations have been performed of the NG7 trials carried out by the International Flame Research Foundation (IFRF) at IJmuiden. The calculations reported here were done using the CFD code FURNACE. A complete description of the code and the simulation results can be found in [9] and [10]. The experiments are described in full detail by Nakamura [7, 8]. A schematic drawing of this furnace is given in figure 19.2.

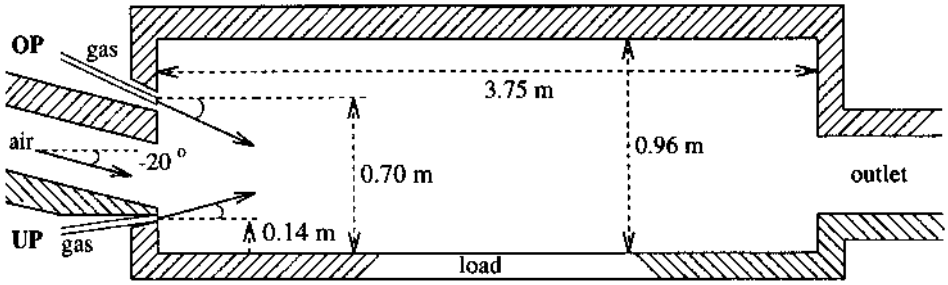

Figure 19.2: Schematic drawing of the IFRF furnace.

In these experiments the load was located on the floor, an arrangement representative for furnaces used in glass manufacturing and in the steel industry. The burner has a simple design. It consists of separate air and fuel injection ports (non-premixed combustion). Several firing modes were used: natural gas injection above the air injection port (overport firing) and injection of fuel under the air injection port (underport firing). It can be expected that the heat transfer and the emissions depend on the location and angle of the fuel jet and this has been studied in the experiments and the modeling. The firing characteristics were:

Thermal input	500 kW
Combustion air temperature	1373 K
Mean load temperature	1400-1470 K
Excess air level	10%

The high air preheat temperature is characteristic for the use of regenerative burners (see below) and can lead to high NO_x emissions.

6.2 Description of the computational model

Turbulence model

The standard k-ϵ turbulence model, including wall functions to treat the near wall zone, was used. The solution of the k-ϵ model uses the mean density provided by the combustion model. The Reynolds flux in the scalar transport equations (enthalpy, mean mixture fraction, mixture fraction variance, NO_x mass fraction and soot variables (see below)) is modeled using the gradient diffusion assumption using the turbulent diffusivity provided by the k-ϵ model.

Combustion model

The conserved scalar approach to non-premixed combustion (See chapter 8) is used. The temperatures in flames in furnaces generally are high enough to lead to high Damköhler numbers necessary to use the conserved scalar approach. Since flames in furnaces are generally non-adiabatic, because of the large amount of radiative heat transfer, the enthalpy is not a conserved scalar, and has to be kept as an independent scalar variable, besides mixture fraction. Furthermore soot and NO_x are added as reacting scalars, independent of mixture fraction. In the subdivision of models presented in chapter 8 the present model combines points 4 and 5 of paragraph 5.2 ‘flamelet models, including mixture fraction PDF models’ on page 125. Several fast chemistry models have been used in this study:

1. An extension of the *mixed-is-burnt* model. Rather than the standard one-step irreversible infinitely fast reaction, a two step model is used. The first step forms intermediate species CO

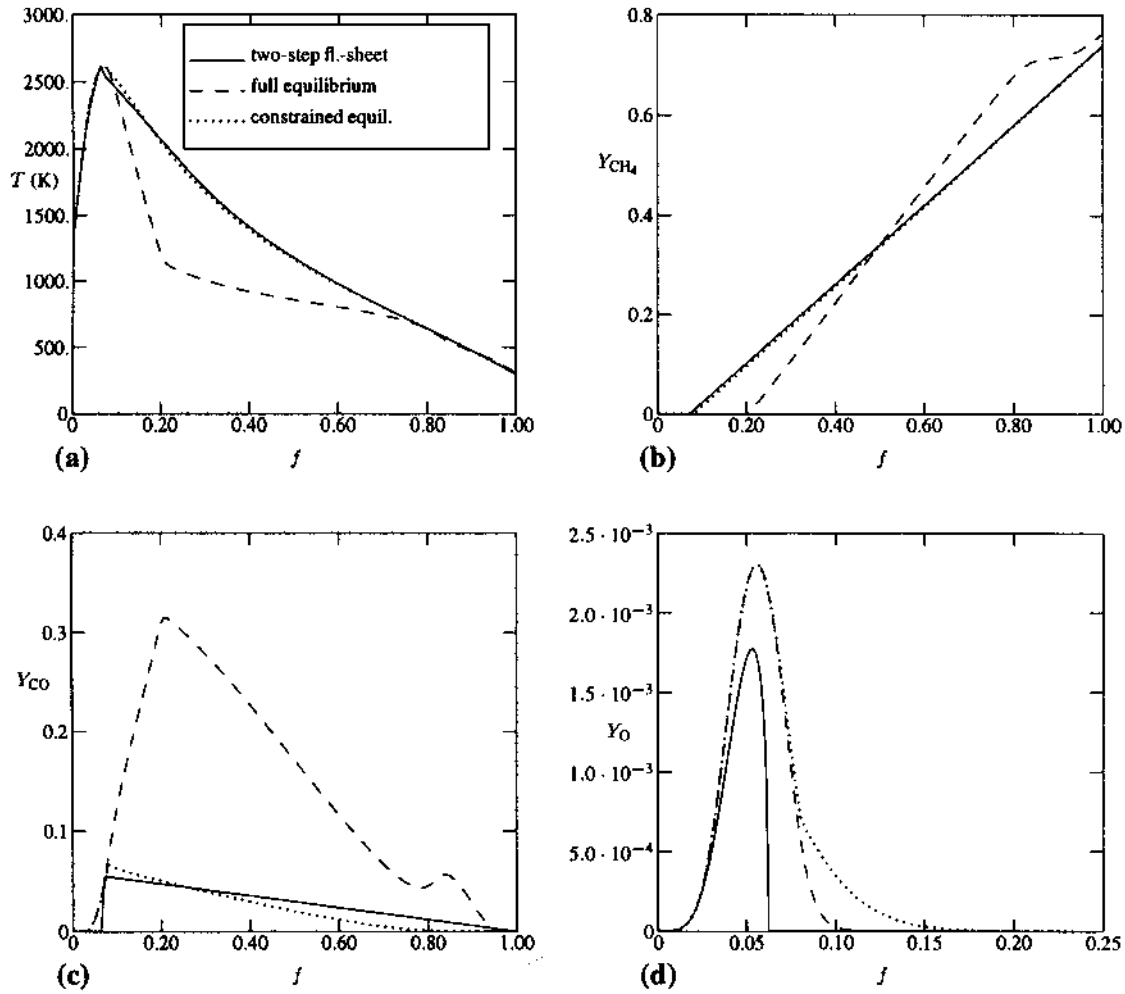

Figure 19.3: Comparison of three conserved scalar chemistry models. Adiabatic case.

and H_2, the second step forms the final products of combustion. To allow NO_x predictions, the model is combined with the assumption that the O-radicals are in chemical equilibrium with the O_2 molecules.

2. The full chemical equilibrium model.

3. The constrained chemical equilibrium model. In this model the mass fraction of fuel hydrocarbons are prescribed as piecewise linear functions of the mixture fraction. (See also chapter 8)

Figure 19.3 shows the adiabatic flame temperature and mass fractions of CH_4, CO and O as a function of the mixture fraction for these three models. In the fuel rich zone CO is strongly over predicted by the full equilibrium model resulting in under predicted temperatures. The two-step model predicts presence of O-radicals at the lean side of the stoichiometric mixture fraction (0.06) only.

Fuel rich mixture, for which the predictions of the different conserved scalar models deviate from each other, is present in only a small part of the furnace. In fact, when the models are applied in a full furnace simulation, the difference in predicted mean furnace temperature, flue gas temperatures

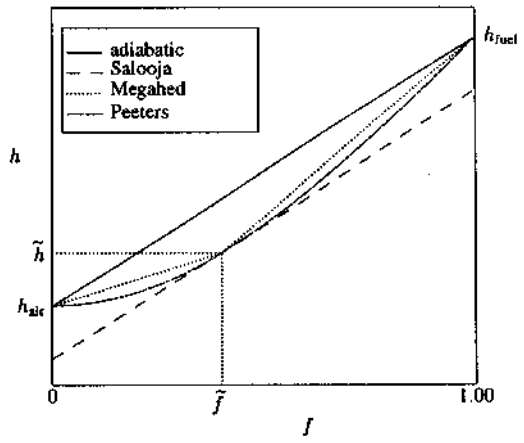

Figure 19.4: Enthalpy loss models.

and furnace roof temperatures are only in the order of 1% . More important differences occur in CO and NO_x concentrations. The equilibrium models predicted 40% higher NO-values and 50% lower CO-values than the two-step flame-sheet model.

Enthalpy loss model and PDF shape

Because of substantial radiative heat transfer the enthalpy may not be treated as a conserved scalar in furnace calculations. This means that the dependent thermo-chemical quantities are not only a function of the mixture fraction, but also a function of enthalpy. The two dimensional joint PDF of both mixture fraction and enthalpy is required to determine averaged quantities. This would require the solution of transport equations for both mean mixture fraction and mean enthalpy as well as for their variances and covariance. To avoid this complexity a simplification is adopted. It is assumed that the fluctuations in mixture fraction and enthalpy are coupled. It is assumed that in each region with a certain mean value of mixture fraction $\tilde{Z}$ and a mean value of enthalpy $\tilde{h}$, the coupled fluctuations in mixture fraction and enthalpy are described by a curve $h = h(Z; \tilde{Z}, \tilde{h})$, passing through ($\tilde{Z}$,$\tilde{h}$). Several approximations for this function have been suggested in the literature.

Figure 19.4 shows three models together with the adiabatic case. The first model, proposed by Salooja [11], assumes that the enthalpy loss is independent of the fluctuation in the mixture fraction (and equal to the mean enthalpy loss). However this implies high losses from initially cold regions (air or fuel), which is physically unrealistic. Therefore Megahed [12] proposed a piecewise linear profile. Peeters [10] proposed a parabolic function. For small fluctuations it resembles Salooja's model, for large fluctuations it resembles Megahed's model.

Applying any of these enthalpy fluctuation models we can evaluate the influence of turbulent fluctuations on mean thermo-chemical variables if we know the fluctuations of the mixture fraction, as expressed by the PDF. In the frame of the assumed PDF approach, the simulation results then in principle depend on the assumptions made on the shape of PDF. The sensitivity of some key variables to the chosen shape have been studied. The following shapes were considered: a single Dirac delta function (this means neglect of turbulent fluctuations), a double Dirac delta function, a top-hat distribution, a β-function and a clipped Gaussian distribution. When using a single δ-function, the maximum temperature in the furnace is much higher and consequently the NO_x concentration is much higher than when using any of the other PDF's.

For a given choice of assumed PDF one can also look in more detail at the influence of the chosen

enthalpy loss model. Table 19.1 shows the results of such comparison for the case of β-function PDF and double delta PDF. The results for the predicted mean furnace temperature, maximal furnace temperature, flue gas temperature, NO_x and CO concentration in the flue gas and the heat flux to the furnace load are shown.

The Megahed model predicts higher averaged temperatures and consequently the NO_x emissions and bath load are also higher. This is related to the fact that, taken local fluctuations into account, the parabolic fit model always predicts higher local heat losses; hence lower temperatures, than the Megahed model. The choice of the PDF shape also has a clear effect on the results, especially on the flue gas temperature and the bath load. Using the β-function PDF the averaged emissive power, which is proportional to T^4, is higher in regions just above the load. Hence the gas loses more energy to the load and the flue gas temperature is lower.

Thermal NO_x model

Simplified kinetics of thermal NO formation

Many high temperature industrial furnaces, *e.g.* glass melting furnaces, are operated at fuel-lean or near-stoichiometric conditions. In that case, the NO formation kinetics are described by the Zel'dovich mechanism:

$$N_2 + O \rightleftharpoons NO + N \tag{19.1}$$

$$N + O_2 \rightleftharpoons NO + O \tag{19.2}$$

$$N + OH \rightleftharpoons NO + H \tag{19.3}$$

The forward and reverse reaction rate constants of these three reactions (k_{1f}, k_{1b}, k_{2f}, k_{2b}, k_{3f} and k_{3b}) have been determined experimentally with reasonable accuracy (values are given in [10]).

The rate limiting step is the reaction $N_2 + O \rightarrow NO + N$ which has the highest activation energy. High temperatures will promote the formation of 'thermal' NO, as will the presence of sufficient oxygen and nitrogen atoms and molecules.

The Zel'dovich reactions are relatively slow; in the flame zone the NO concentrations will often lie below their equilibrium values at the local conditions. Beyond the flame zone the concentrations may exceed their local equilibrium values, because the destruction of NO is slow as well. Since the Damköhler number for NO formation is small, no direct conserved-scalar analogy can be made. It is not a good assumption to relate NO_x directly to mixture fraction. Instead, the evolution of NO_x has to be described as a finite rate process and in the case of a turbulent flame the closure of the mean reaction rate has to be addressed.

Enthalpy loss model	PDF type	T_{mean} (K)	T_{flue} (K)	$NO_{x,flue}$ (ppm)	CO_{flue} (%)	$\underline{q}_{load,av}$
Megahed	β-function	1696	1748	1378	0.481	71.18
parabolic fit	β-function	1684	1730	1122	0.475	67.87
Megahed	$\delta\delta$-function	1694	1777	1421[1]	0.592	68.52
parabolic fit	$\delta\delta$-function	1682	1756	1202[1]	1.553	64.15

[1] A top-hat PDF has been used for the closure of the NO source term.

Table 19.1: Results from different choices of enthalpy-loss model and PDF-model

In this lecture we restrict to the standard 'short' Zel'dovich mechanism, by assuming that the third reaction (19.3) has a negligible contribution. For a similar treatment of the complete mechanism, see [10].

¿From the known forward and reverse reaction rates, we have:

$$\frac{\mathrm{d}C_{\mathrm{NO}}}{\mathrm{d}t} = k_{1\mathrm{f}} C_{\mathrm{N}_2} C_{\mathrm{O}} + k_{2\mathrm{f}} C_{\mathrm{N}} C_{\mathrm{O}_2} - k_{1\mathrm{b}} C_{\mathrm{NO}} C_{\mathrm{N}} - k_{2\mathrm{b}} C_{\mathrm{NO}} C_{\mathrm{O}} \tag{19.4}$$

or:

$$\rho S_{\mathrm{NO}} = M_{\mathrm{NO}} \frac{\mathrm{d}C_{\mathrm{NO}}}{\mathrm{d}t} \tag{19.5}$$

where in general:

$$S_{\mathrm{NO}} = S_{\mathrm{NO}}(\rho, T, Y_{\mathrm{NO}}, Y_{\mathrm{N}_2}, Y_{\mathrm{O}_2}, Y_{\mathrm{O}}, Y_{\mathrm{N}}) \tag{19.6}$$

The quantity S_{NO} is a scaled formation rate with dimension s^{-1}, and may be viewed as the reciprocal characteristic chemical time scale of net production or destruction of NO. The quantity ρS_{NO} is the net source term in the transport equation for Y_{NO}. ¿From (19.6) it is seen that not only the mass fractions of the main species O_2 and N_2, but also of the radicals O and N are required in order to determine the instantaneous formation rate of NO, assuming that the NO concentration is known. In the simple one-step or two-step *mixed-is-burnt* model no direct information on radical concentrations is included. To allow for reasonable predictions, a reduction of the chemistry description is pursued, as described by Peters [13]. The procedure described here provides examples of more generally used chemistry reduction methods.

Firstly, it is assumed that the N-radicals are in steady state:

$$\frac{\mathrm{d}C_{\mathrm{N}}}{\mathrm{d}t} = k_{1\mathrm{f}} C_{\mathrm{O}} C_{\mathrm{N}_2} + k_{2\mathrm{b}} C_{\mathrm{O}} C_{\mathrm{NO}} - k_{1\mathrm{b}} C_{\mathrm{N}} C_{\mathrm{NO}} - k_{2\mathrm{f}} C_{\mathrm{N}} C_{\mathrm{O}_2} = 0 \tag{19.7}$$

This yields the N-radical concentration as a function of the other species concentrations:

$$C_{\mathrm{N}} = C_{\mathrm{O}} \frac{k_{1\mathrm{f}} C_{\mathrm{N}_2} + k_{2\mathrm{b}} C_{\mathrm{NO}}}{k_{1\mathrm{b}} C_{\mathrm{NO}} + k_{2\mathrm{f}} C_{\mathrm{O}_2}} \tag{19.8}$$

Secondly, it is assumed that O-atoms are in equilibrium with O_2 molecules through the dissociation/recombination reaction:

$$\mathrm{O}_2 + M \rightleftharpoons \mathrm{O} + \mathrm{O} + M \tag{19.9}$$

In low-temperature flames the O-atom concentration is known to exceed its equilibrium value considerably, but for higher temperatures and increasing Damköhler numbers, the equilibrium assumption will become valid more and more. Since the Zel'dovich mechanism itself is a valid simplification only at high temperatures the approximations made are justified. This produces:

$$C_{\mathrm{O}} = K_{\mathrm{O}} C_{\mathrm{O}_2}^{\frac{1}{2}} \tag{19.10}$$

where K_{O} is the square root of the equilibrium constant for the dissociation/recombination reaction. Thus, the O-radical concentration is directly coupled to the O_2 concentration.

With the aid of the expression (19.8) for C_{N} we can derive the modeled chemical source term for NO formation:

$$\frac{\mathrm{d}C_{\mathrm{NO}}}{\mathrm{d}t} = 2\, C_{\mathrm{O}} \frac{k_{1\mathrm{f}} k_{2\mathrm{f}} C_{\mathrm{N}_2} C_{\mathrm{O}_2} - k_{1\mathrm{b}} k_{2\mathrm{b}} C_{\mathrm{NO}}^2}{k_{1\mathrm{b}} C_{\mathrm{NO}} + k_{2\mathrm{f}} C_{\mathrm{O}_2}} \tag{19.11}$$

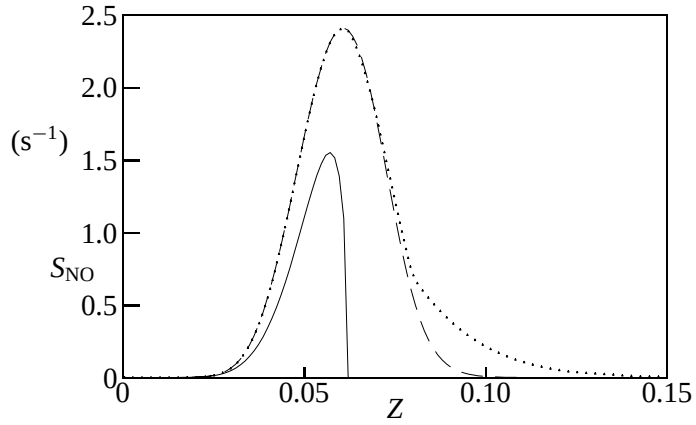

Figure 19.5: Thermal NO formation rate at $Y_{NO} = 0$ for various chemistry models, using air at 1400 K and natural gas at 300 K. Symbols: —- one-step flame sheet, – – full equilibrium, $\cdots$ constrained equilibrium.

This expression can be rewritten if we employ the relationship for the equilibrium concentration $C^2_{NO,eq} \equiv K_{eq} C_{N_2} C_{O_2}$:

$$\frac{dC_{NO}}{dt} = 2\, C_O \frac{k_{1f} k_{2f} C_{N_2} C_{O_2}}{k_{1b} C_{NO} + k_{2f} C_{O_2}} \left(1 - \frac{C^2_{NO}}{C^2_{NO,eq}} \right) \tag{19.12}$$

In the limit of very low NO concentrations the NO formation rate can be approximated by:

$$\frac{dC_{NO}}{dt} \approx 2 k_{1f} C_O C_{N_2} \approx 2 k_{1f} K_O C^{\frac{1}{2}}_{O_2} C_{N_2} \tag{19.13}$$

In the presence of significant amounts of NO_x, this approximation is no longer justified, and the complete formula (19.11) should be used.

Combining NO source term with fast chemistry model

Within the framework of the conserved scalar models, all thermochemical quantities are directly related to the mixture fraction Z. Non-adiabaticity effects are included by means of an empirical local relationship $h = h(Z; \widetilde{Z}, \widetilde{h})$, as explained above. As a result, all concentrations and the temperature appearing in (19.11) are functions of Z:

$$S_{NO} = S_{NO}(Z, Y_{NO}) \tag{19.14}$$

This serves as a starting point for the closure of the average reaction rate.

In figure 19.5 a comparison of the formation rate as a function of mixture fraction is given for three different chemistry models. The NO mass fraction is taken to be zero. Calculations have been performed for the combustion of natural gas at 300 K with preheated air at 1400 K, closely resembling the fuel and air streams in high-temperature glass melting furnaces. The stoichiometric mixture fraction for the natural gas fuel under consideration is 0.062. The O-atom concentration in the one-step infinitely fast chemistry model is inferred from (19.10), and is compared with the mass fraction profiles for the two equilibrium models in figure 19.6. Since in the flame sheet model $Y_{O_2} = 0$ for

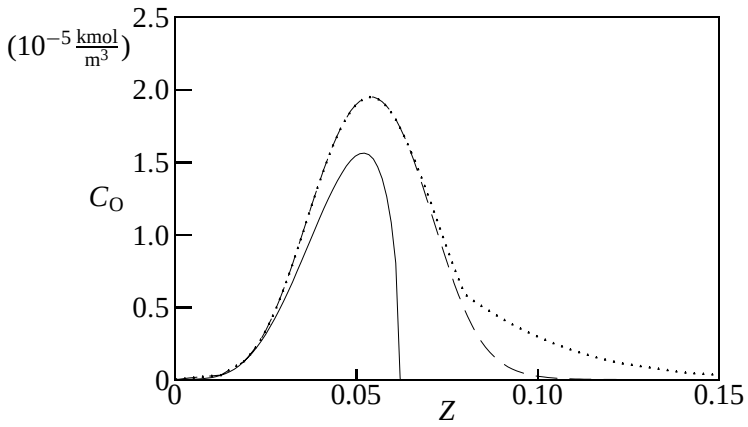

Figure 19.6: Concentration of O-atoms for various chemistry models. For symbols see figure 19.5.

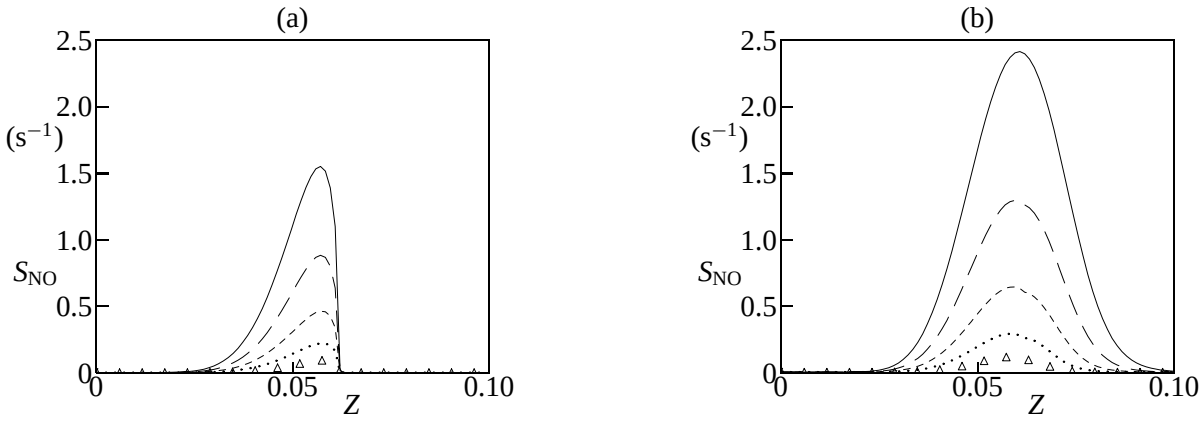

Figure 19.7: Influence of non-adiabaticity on thermal NO formation. (a) One step mixed-is-burnt model (b) Full equilibrium model. Symbols: —- adiabatic case; — — 5% heat loss, - - - 10% heat loss, ··· 15% heat loss, △ 20% heat loss.

$Z > Z_{st}$, the largest differences in figure 19.5 occur for fuel rich conditions, and there is a similarity between the dependence on mixture fraction of the O-atom concentration and the NO formation rate.

The influence of non-adiabaticity is investigated in figure 19.7. For lower enthalpy (representing radiative heat loss) the instantaneous NO formation rate drops quickly, as a consequence of the large activation energy of reaction 1f.

As the NO mass fractions increases, the net formation rate will decrease and become zero for chemical equilibrium. The equilibrium concentration as a function of mixture fraction is plotted in figure 19.8. In figure 19.9 the net formation rate of NO is depicted for increasing concentration levels. In large scale furnaces the concentration may exceed 1000 ppm, showing that the reverse reaction rates become non-negligible.

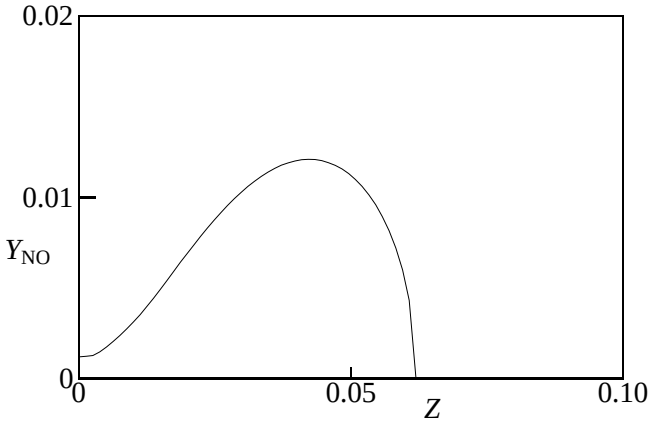

Figure 19.8: Equilibrium NO mass fraction as a function of mixture fraction, for natural gas combustion using air at 1400 K and fuel at 300 K, calculated by the one-step mixed-is-burnt model.

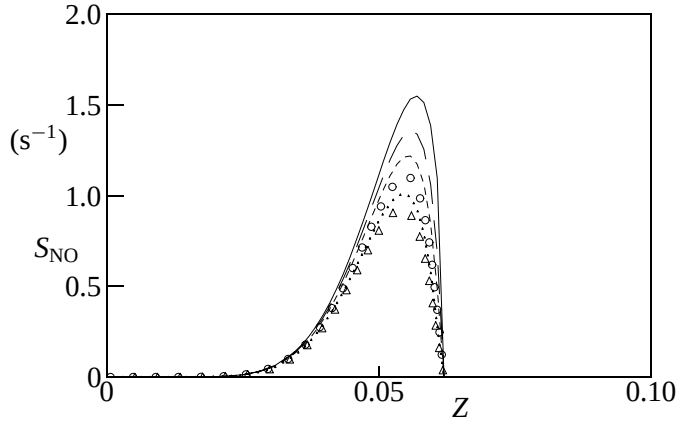

Figure 19.9: Thermal NO formation rate for increasing values of Y_{NO}, using the one-step mixed-is-burnt model for combustion of air at 1400 K and natural gas at 300 K. Symbols: —- 0 ppm, — — 400 ppm, - - - 800 ppm, ∘ 1200 ppm, · · · 1600 ppm, △ 2000 ppm.

6.3 PDF closure for mean NO formation rate

As shown in the previous section, the modeled NO formation rate only depends on the mixture fraction Z and the NO mass fraction. This offers the possibility to calculate the mean source term $\widetilde{S}_{\mathrm{NO}}$ by means of a two-dimensional joint Favre p.d.f. of Z and Y_{NO}.

$$\widetilde{S}_{\mathrm{NO}} = \int_0^1 \int_0^1 S_{\mathrm{NO}}(z, y)\ \widetilde{f}_{ZY_{\mathrm{NO}}}(z, y)\,\mathrm{d}y\,\mathrm{d}z \tag{19.15}$$

This presents a difficulty, since the joint p.d.f. $\widetilde{f}_{ZY_{\mathrm{NO}}}$ is an unknown function in our model so far. As a first important approximation, it is assumed that fluctuations of Z and Y_{NO} are independent. In that case, the joint p.d.f. can be written as the product of the two marginal p.d.f.'s of Z and Y_{NO}:

$$\widetilde{f}_{ZY_{\mathrm{NO}}}(z, y) = \widetilde{f}_Z(z)\,\widetilde{f}_{Y_{\mathrm{NO}}}(y) \tag{19.16}$$

For convenience, we will drop the index $_{\mathrm{NO}}$ in the sequel, taking $Y \equiv Y_{\mathrm{NO}}$. $\widetilde{f}_Z$ is already known from the model for the main combustion process. The p.d.f. for the NO mass fraction $\widetilde{f}_Y$ can be modeled analogously to $\widetilde{f}_Z$. In other words, $\widetilde{f}_Y$ is characterized by its first and second moment. Generally speaking, we have to solve the transport equation for $\widetilde{Y''^2}$ which closely resembles the transport equation for the mixture fraction variance $\widetilde{Z''^2}$, with the exception that an additional correlation term $\widetilde{Y''S}$ enters the equation.

With the present model assumptions (mixture fraction, reduced NO kinetics), the correlation term $\widetilde{Y''S}$ is closed through the p.d.f. integration:

$$\widetilde{Y''S} = \int_0^1 \int_0^1 (y - \widetilde{Y})\, S(\zeta, y)\ \widetilde{f}_Z(\zeta)\ \widetilde{f}_Y(y)\, d\zeta\, \mathrm{d}y \tag{19.17}$$

As a first approximation, one can consider the marginal p.d.f. of Y_{NO} to be represented by a single δ-function p.d.f., thus neglecting fluctuations in Y_{NO}: $\widetilde{f}_Y = \delta(y - \widetilde{Y})$. The final simplified model for the joint p.d.f. then reads:

$$\widetilde{f}_{ZY} = \widetilde{f}_Z\, \delta(y - \widetilde{Y}) \tag{19.18}$$

The mean NO_x source term then becomes simply:

$$\widetilde{S}_{\mathrm{NO}} = \int_0^1 \widetilde{f}_Z(z) S_{\mathrm{NO}}(z, \widetilde{Y}_{\mathrm{NO}})\,\mathrm{d}z \tag{19.19}$$

Radiation model

Accurate prediction of heat transfer in furnaces requires accurate prediction of the radiative heat transfer. For NO_x-emission predictions the accurate prediction of temperature is necessary and this also requires accurate treatment of radiative transfer.

The radiation transport in absorbing, emitting and scattering media is described by the radiation transport equation (RTE), which is an equation for the radiant intensity. Radiant intensity is an amount of radiative energy per unit surface orthogonal to the direction of propagation, per unit spherical angle, per unit wavelenght interval. It is a function of position in space (three coordinates), direction (two angular coordinates) and wavelength. In the absence of scattering, the radiative transfer equation,

describing the transport of radiating heat through a participating medium at local thermodynamic equilibrium along a line-of-sight, is given by:

$$\frac{\partial i'_\lambda(s)}{\partial s} = -\kappa_\lambda i'_\lambda(s) + \kappa_\lambda i'_{b,\lambda}(s) \tag{19.20}$$

where s is the distance through the medium, i_λ the spectral intensity in an interval $d\lambda$ around λ and $i'_{b,\lambda}$ the spectral black body intensity. Here κ_λ is the spectral absorption-emission coefficient.

To obtain the net energy crossing an infinitesimal area requires integration over a solid angle to include the contributions from all directions. Because we are dealing with integral equations, as opposed to partial differential equations arising from the flow field modelling, specific techniques are used for solving the radiative transfer equation. Two of the most often used models are the Hottel Zone Method (HZM) [15] and the Discrete Transfer Method (DTM) [16]. Alternatively, the angular dependence can be treated using either an expansion in spherical harmonic functions (P_n approximation) or by discretizing the range of the spherical coordinate (discrete ordinates method). Also a Monte Carlo method can be used . In the latter method, individual 'photons' of radiant energy are emitted, reflected and absorbed by opaque surfaces and participating media using ray tracing algorithms. For more information on solution methods of the radiative transfer equation, see the books by Modest [4], by Siegel and Howell [5] and by Mbiock and Weber [6].

Molecular gas radiation from nonluminous (blue) hydrocarbon flames is mostly due to CO_2 and H_2O, and in most cases it is sufficient to consider only these molecules. Their radiative properties are well understood, but have to be represented in a simplified way to keep the computational cost of the CFD simulation within acceptable limits. The presence of soot in a flame can significantly increase the flame emissivity. Soot consists of particles formed in the fuel rich zone of the flame. The radiation of soot is smoothly depending on wavelength and its contribution can be computed and added to the absorption and emission by the combustion gases.

A complete simulation would account for each individual line in the spectra of the absorbing species. This involves considerable computing times [14]. For engineering applications often the wavelength dependency is neglected, and the medium is treated as a grey gas. Both absorption and emission can then be characterised by a single, uniform absorption-emission coefficient. Boerstoel [9] compared several radiative gas property models with various degrees of complexity, which yield total emissivities and absorptivities. From this study he concludes that for engineering calculations, where one is merely interested in predicting trends qualitatively, it seems sufficient to use a constant absorption-emission coefficient. However, when NO_x-emissions has to be known quantitatively as well, this is not accurate enough, and it is necessary to use a more accurate model (E.g. statistical narrow band model).

The HZM is based on a discretization of the boundary surface and gas volume into a number of elements, which are assumed to be uniform of temperature, emissivity and absorption coefficient. A set of geometrical factors, usually called direct exchange areas, is defined, which are used to express the heat exchange from one surface or gas element to another. The integral form of the radiative transfer equation can then be described by a set of algebraic equations, which are solved by matrix calculations. With a constant absorption-emission coefficient the direct exchange areas can be calculated in advance. Then this method is very economic. However when the absorption-emission coefficient has to be varied, for instance when soot radiation is being accounted for, the direct exchange coefficients will have to be recalculated many times, and computer times increase dramatically.

Also the DTM starts by dividing the geometry into a number of surface and volume elements with uniform properties. In each surface element the hemisphere is divided into a number of solid angle elements for each of which beam direction has been defined. Given this direction the beam is traced

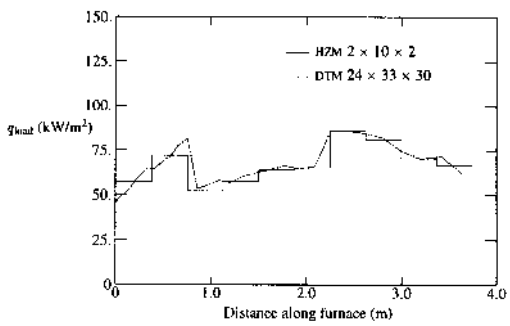

Figure 19.10: Distribution of the heat flux to the load computed with the HZM and the DTM.

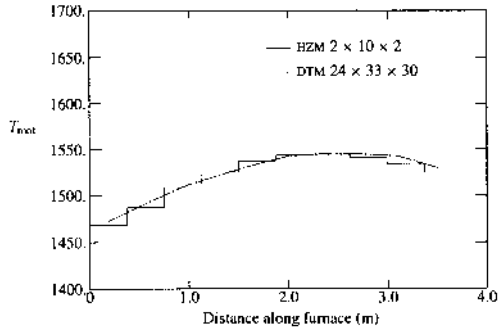

Figure 19.11: Roof temperature computed with the HZM and the DTM.

towards the other side of the enclosure. From there the beam is thought to emerge with an energy depending on the boundary conditions. Then, the beam is followed backwards and the intensity is determined in each volume it crosses, until the beam has reached the first surface element where now the incoming intensity from this direction is known. The absorption-emission coefficient can be non-constant and position dependent with this method. Also non-grey gases can be described more economically with DTM then with HZM.

A comparison between HZM and DTM is shown in figures 19.10 and 19.11. These are results form a complete furnace calculation done by Boerstoel [9] with the constrained equilibrium model, parabolic enthalpy loss model, β-function PDF closure, constant and uniform absorption-emission coefficient, without soot. Both heat flux distribution to the load and roof temperature of the furnace agree very well in both solutions. Also the mean, maximum and flue gas temperatures between both simulations are very similar, while the NO_x-concentration only deviated 4% .

When using the DTM in combination with very fine grids for the flow field, the number of beams will increase dramatically in order to have enough beams crossing each individual volume. In the present furnace calculation an accurate solution of the radiation can be obtained on a relatively coarse and uniform grid.

Soot model

For the simulation of sooting flames it is important to include a model predicting soot, because soot has a clear effect on flame temperature and thus on the NO_x production.

Soot generated in natural gas combustion consists of mainly carbon with a quite different structure than graphite. Soot particles are aggregates of a diameter up to about 200 nm. Despite essential progress in understanding the highly complex nature of the chemistry of soot formation and oxidation in flames, no comprehensive theory or models are currently available. The available models are based upon general principles, like nucleation, coagulation, surface growth and oxidation. These models consist of transport equations for soot particle number density and soot mass fraction, with appropriate source terms, which are solved in addition to the transport equations describing the main combustion process (mixture fraction, enthalpy). The effect of the soot evolution on the main combustion process is essentially only via the enhancement of the radiative heat loss term via the soot emissivity. The source terms depend on mixture fraction and enthalpy (temperature) and on the soot properties. They contain terms describing soot formation and terms describing soot destruction (oxi-

dation). The influence of turbulent fluctuations is taken into account by averaging the soot source term with the PDF of mixture fraction. In the following we give two examples of soot formation models and a soot oxidation model.

KHAN AND GREEVES FORMATION MODEL This is a one-equation model for the soot mass fraction Y_s, similar to that developed by Khan and Greeves [17] for the simulation of soot in diesel engines. The source term for the soot mass fraction takes the form:

$$S_f(Y_\mathrm{s}) = C_\mathrm{f} p_\mathrm{fu} \varphi^n \exp\left(\frac{-T_f}{T}\right) \tag{19.21}$$

Here p_{fu} is the partial pressure of the fuel, T is the temperature and φ is the local equivalence ration defined by

$$\varphi = \left(\frac{f}{1-f}\right)\left(\frac{1-f_\mathrm{st}}{f_\mathrm{st}}\right)$$

with f_st the stoichiometric mixture fraction. C_f, n and T_f are model parameters.

MOSS, STEWART AND SYED FORMATION MODEL This is a two-equation model for the evolution of soot mass fraction Y_s, and the particle number density n_p, developed by Moss et al. [18] for a laminar acetylene diffusion flame. Two convection-diffusion equations have to be solved for which the following source terms were formulated:

$$\begin{aligned} S_f\left(\frac{n_\mathrm{p}}{\rho N_0}\right) &= \alpha(f) - \beta(f)\rho^2\left(\frac{n_\mathrm{p}}{\rho N}\right)^2 \\ S_f(Y_\mathrm{s}) &= \gamma n_\mathrm{p} + C_\delta \alpha(f) \end{aligned} \tag{19.22}$$

Here N_0 is Avogadro's number and α, β and γ are functions of the mixture fraction f. They are given by:

$$\begin{aligned} \alpha &= C_\alpha \rho^2 T^{\frac{1}{2}} X_\mathrm{fu} \exp\left(\frac{-T_\alpha}{T}\right) \\ \beta &= C_\beta T^{\frac{1}{2}} \\ \gamma &= C_\gamma \rho T^{\frac{1}{2}} X_\mathrm{fu} \exp\left(\frac{-T_\gamma}{T}\right) \end{aligned} \tag{19.23}$$

and represent the processes of nucleation, coagulation and surface growth, respectively. C_i and T_i are model parameters.

MAGNUSSEN AND HJERTAGER OXIDATION MODEL This oxidation model is an eddy-beak up model [19] assuming that turbulence decay controls the rate of oxidation. The source term is computed as the minimum of two expressions, one for the regions where the local mean soot concentration is low compared to the oxygen concentration, and the other applicable to regions where oxygen concentration is low and limits the rate of soot combustion. For the soot mass fraction the oxidation rate is given by:

$$S_\mathrm{o}(Y_\mathrm{s}) = A\rho Y_\mathrm{s}\frac{\epsilon}{k}\min\left(1, \frac{Y_{\mathrm{O}_2}}{Y_\mathrm{s} s_\mathrm{s} + Y_\mathrm{fu} s_\mathrm{fu}}\right) \tag{19.24}$$

Where Y_fu and Y_{O_2} are fuel and oxygen mass fractions s_s and s_fu are stoichiometric oxygen requirements for the soot and fuel. A is a model parameter with a value of 4.

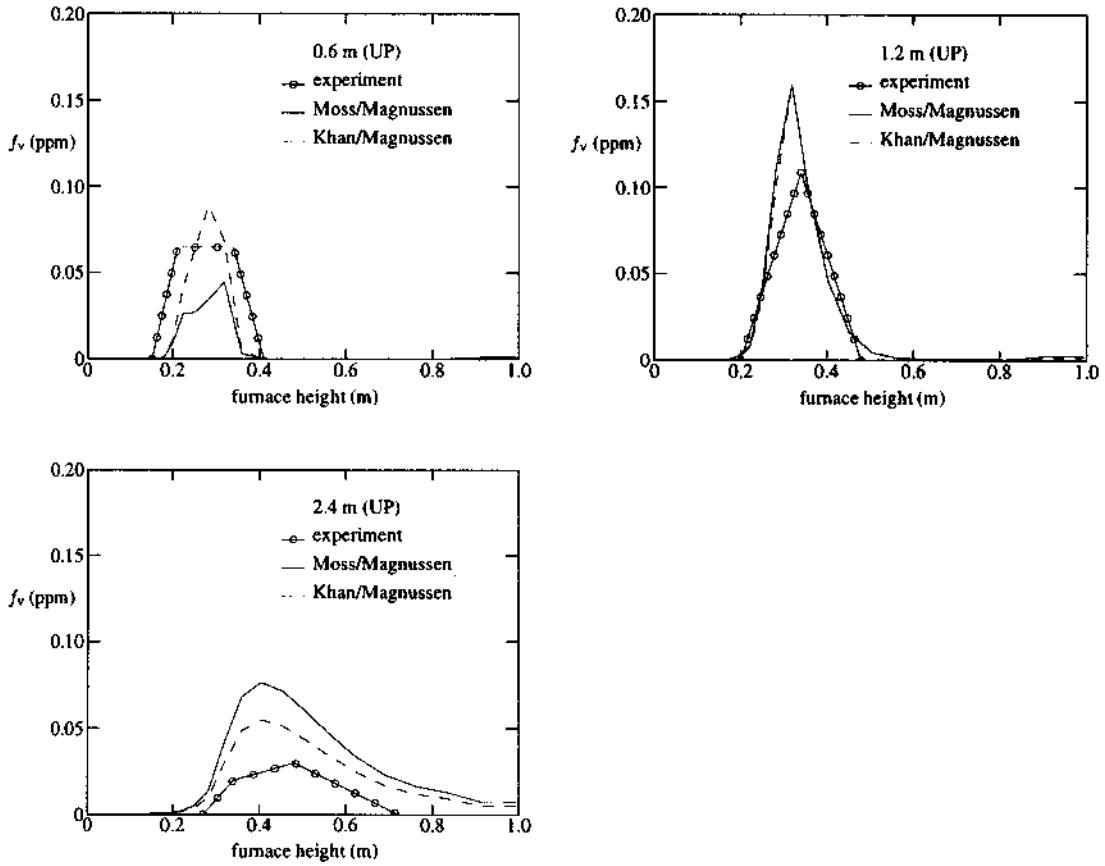

Figure 19.12: Soot volume fraction profiles of the UP flame at three distances from the furnace inlet.

The above-mentioned models have been validated for high temperature furnaces by Boerstoel [9]. Soot volume fraction measurements reported by Wieringa [20] for an underport fired case and an overport fired case were used. With the original model constants from both oxidation models the simulation results were far off. It appeared not to be possible to simulate both cases UP an OP firing with the same set of model constants. Figure 19.12 shows the fit of the Khan model and the Moss model to the experimental results for the UP flame. The fit for the OP flame is shown in figure 19.13. In the Magnussen oxidation model for both cases the original model constant of 4 was used. The profiles at 1.2 meter were used to fit the constants. For the UP flame the Khan model predicts the right volume fraction close to the inlet, where the Moss model under predicts the level of soot here. At 2.4 meter in the furnace both models over predict the volume fraction largely. This indicates a too slow oxidation of soot. For the OP case the Khan model over predicts at 0.6 meter, while the Moss model fits reasonably well. At 2.4 m both models under predict soot levels pointing at a too fast burnout of soot. The results show that there is a lack of generality of these soot models. The influence of soot on the model predictions of some characteristic variables is shown in Table 19.2. With the fitted models the influence on the NO_x concentration is large: for the low sooting UP flame the NO_x concentration is 10% less, for the highly sooting OP flame the NO_x concentration is predicted to be 30% less. This clearly shows the importance of including the effects of soot.

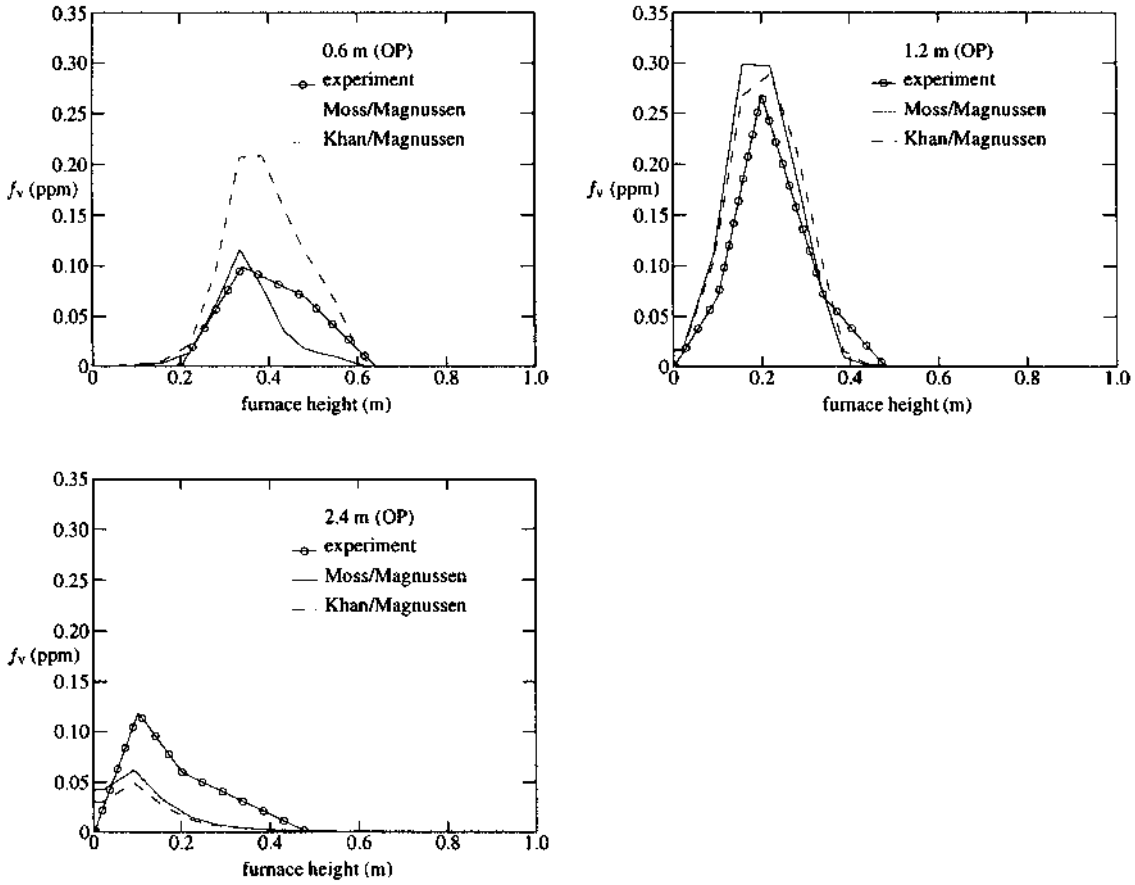

Figure 19.13: Soot volume fraction profiles of the OP flame at three distances from the furnace inlet.

	Underport			Overport		
	T_{flue}	NO_{flue}	$q_{\text{load,av}}$	T_{flue}	NO_{flue}	$q_{\text{load,av}}$
Soot model	K	ppm	kW/m^2	K	ppm	kW/m^2
No soot	1724	1167	64.3	1724	893	75.9
Khan-Magnussen	1703	1025	66.7	1687	607	80.6
Moss-Magnussen	1700	1042	67.0	1686	652	80.7

Table 19.2: Influence of soot on model predictions and measured values: flue gas temperature, NO emission and average heat flux to the load.

6.4 Full furnace predictions

As an example of the capabilities of the full model two examples are shown of predictions of the UP and OP flame in the IFRF furnace. The model consists of the constrained chemical equilibrium model, β-function PDF closure for both the combustion reactions as for the NO_x post processor, the parabolic heat loss model, the DTM radiation model, the Khan soot formation model, the Magnussen soot oxidation model, and $32 \times 48 \times 40$ grid points.

Simulated and measured temperature profiles at five downstream distances ($y = 0.6$ m, $y = 0.9$ m, $y = 1.2$ m, $y = 1.8$ m, $y = 2.4$ m) in the symmetry plane ($x = 0.0$ m) of the furnace are shown in figure 19.14, as well as at three downstream distances ($y = 0.6$ m, $y = 1.3$ m, $y = 1.8$ m) in the parallel plane 0.1 m from the symmetry plane. At $x = 0$ m, $y = 0.6$ m the two peaks at either side of the gas jet are clearly visible. These peaks are not captured by the measurements. In the recirculation zone, i.e. for heights > 0.5 m, the temperature profile is nearly uniform and the simulations agree very well with the experiments. Further downstream, $y > 1.8$ m, measurements show a lifted flame with a more smeared out temperature profile than the simulation, and the temperatures in the recirculation zone are under predicted. This is probably due to buoyancy effects, which are not properly predicted by the simulations. At $x = 0.1$ m, parallel to the symmetry plane, the temperature distribution is much more even. Here, the agreement between simulation and experiment is very good. figure 19.15, shows the comparison between simulated and measured NO concentration profiles. The very high peaks at $y = 0.6, 0.9$ and 1.2 m in the symmetry plane, that are found in the simulations were not found experimentally. It is possible that the peaks are narrower than the simulations indicate and that they are missed by the experiments. However, in the recirculation zone and at the plane parallel to the symmetry plane, the agreement is very good. Also the simulated NO flue gas concentration agrees very well with the measurements: 1271 ppm and 1214 ppm, respectively.

In the OP flame the fuel and air injections are parallel. For that reason the mixing between fuel and air is much slower than in the UP flame where the fuel is injected upwards and air is injected downwards. The simulations clearly show a temperature peak between the fuel and air streams. This is not so pronounced in the experiments as can be seen from figure 19.16. At $x = 0, y = 0.6$ m a minimum at a height of 0.45 m. is found, representing the gas jet. At either side peaks are observed, with the one above the gas jet being the lower one, because here gas mixes with oxygen lean recirculation gases. This peak is simulated accurately. Below the jet the peak flame temperature is higher because of the higher oxygen availability. In the simulations this peak is largely over predicted. Also next to the gas jet, at $x = 0.1, y = 1.2$ m, peak temperatures are over predicted. Apparently the combustion rate is over predicted, probably due to errors made by the turbulence model, leading to an over prediction of the peak flame temperatures. In the second half of the furnace the agreement between simulations and experiment is better.

The over prediction of peak flame temperatures leads to an over prediction of NO concentrations, as can be seen from figure 19.17. The simulated NO concentrations are almost twice as high as the measurements, and, therefore, NO concentration in the flue gases is over predicted by a factor of two.

7 A new development: flameless combustion

Simply using the heat of the flue gases to preheat the air increases furnace efficiency but in general leads to higher NO_x emissions because of the increased temperature of the flame zone. Therefore additional techniques to reduce peak temperatures have been introduced in burner and furnace design, mostly based on dilution techniques. It turns out that the combination of sufficiently high temperature and strong dilution leads to stable combustion with low NO_x formation. This is such a remarkable

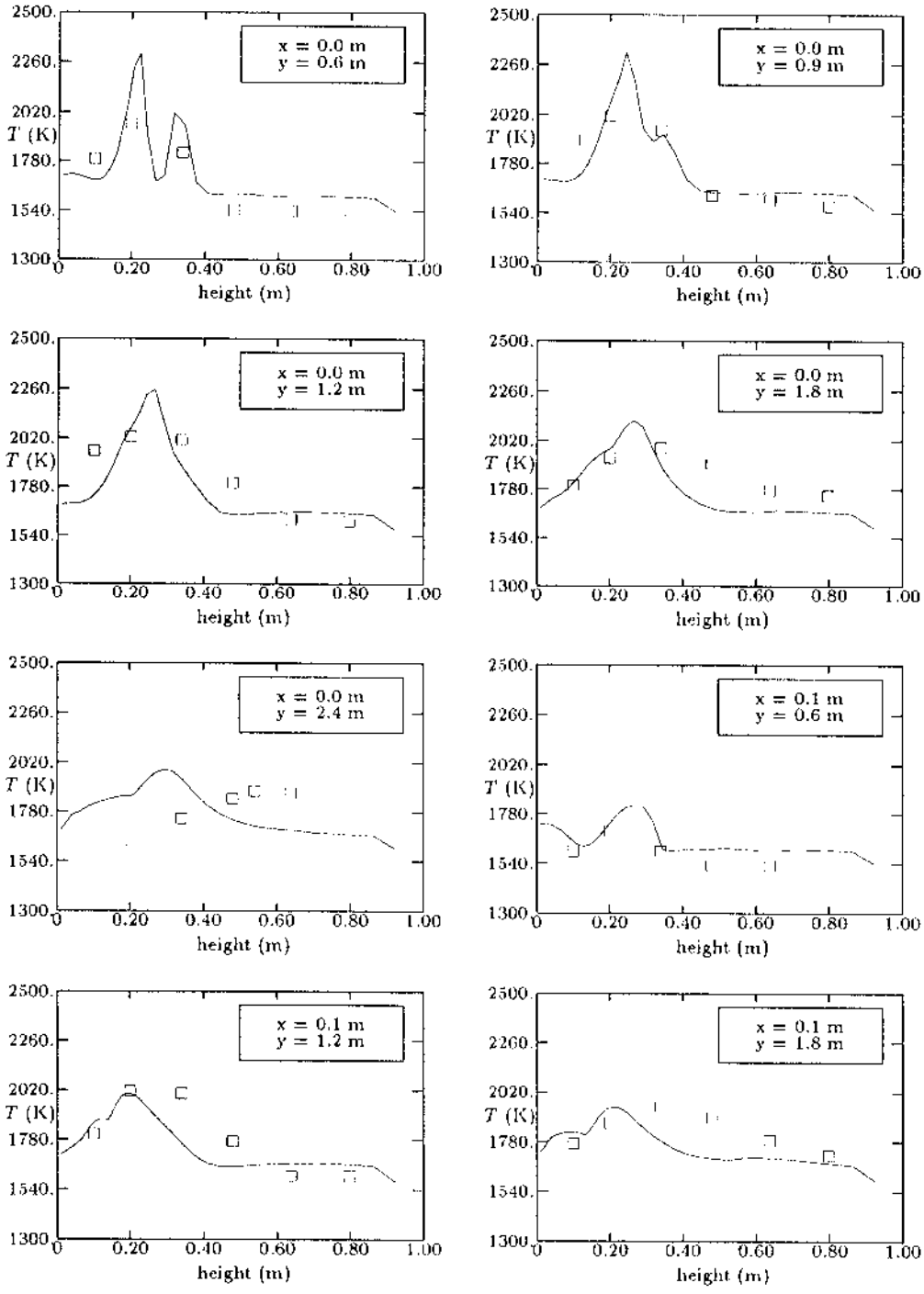

Figure 19.14: Comparison between simulations and in-flame measurements of temperature for the NG7 UP flame, y is the distance along the furnace from the inlet, x is the distance from the symmetry plane of the furnace.

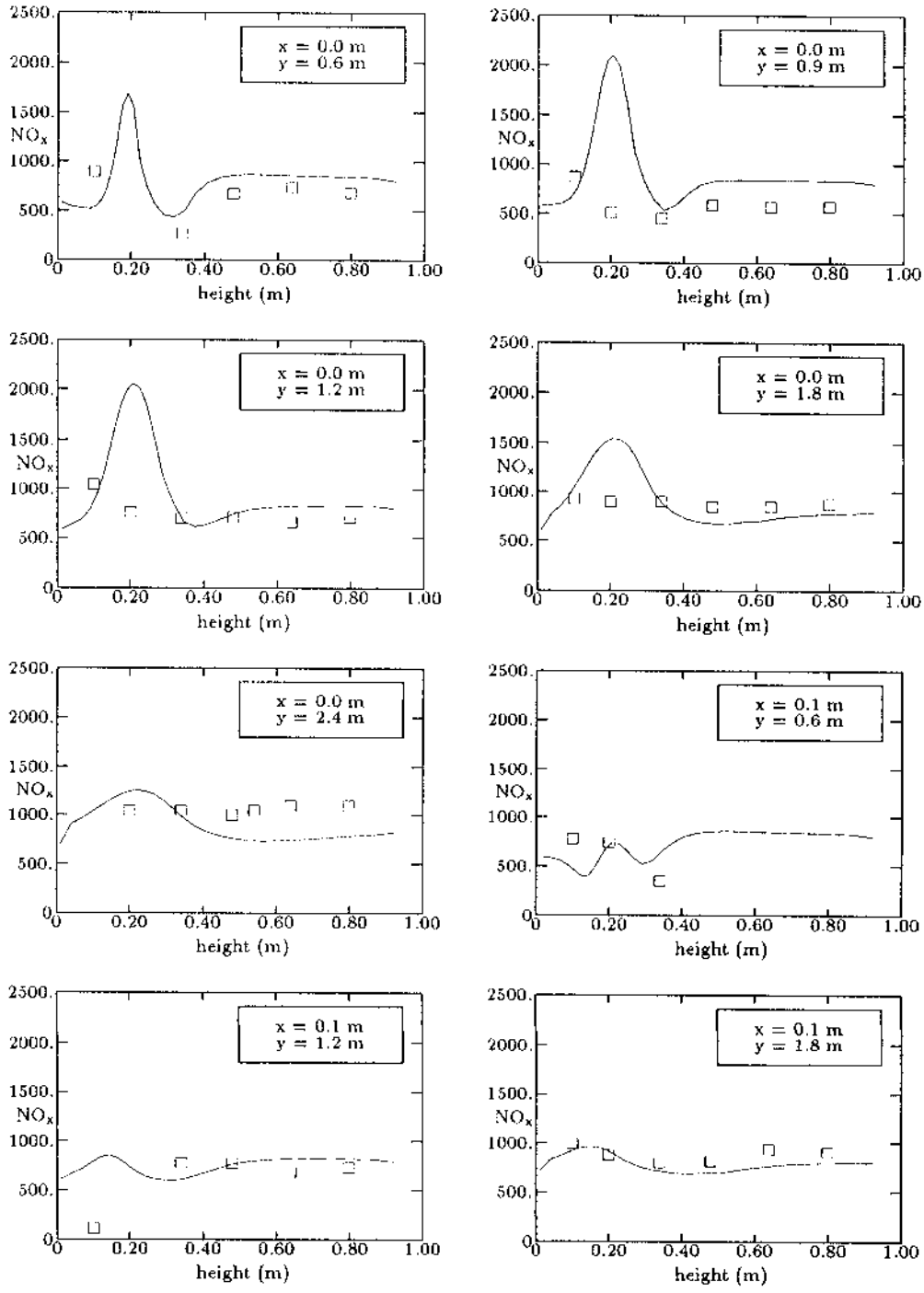

Figure 19.15: Comparison between simulations and in-flame measurements of NO concentration for the NG7 UP flame, y is the distance along the furnace from the inlet, x is the distance from the symmetry plane of the furnace.

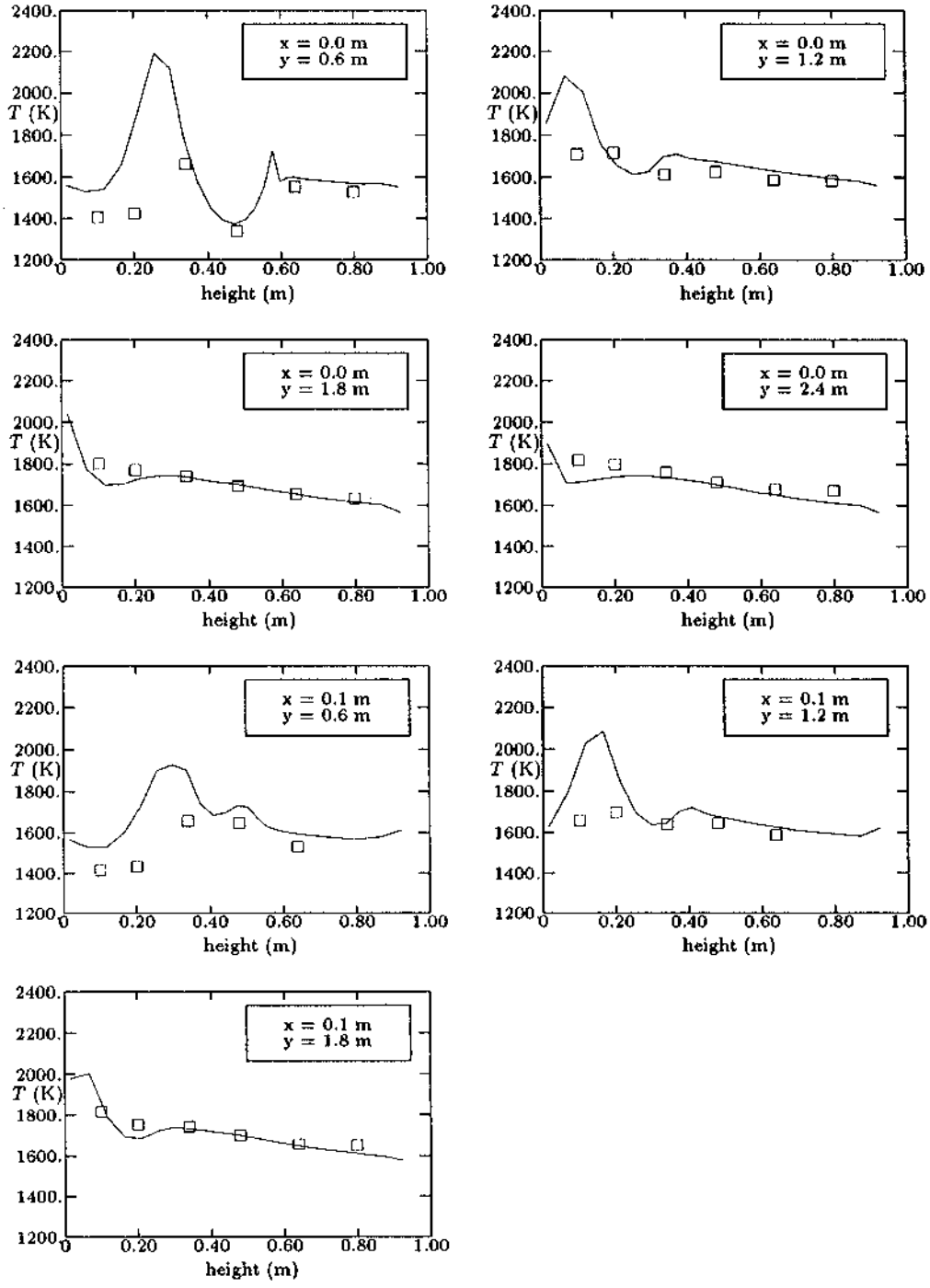

Figure 19.16: Comparison between simulations and in-flame measurements of temperature for the NG7 OP flame, y is the distance along the furnace from the inlet; x is the distance from the symmetry plane of th e furnace.

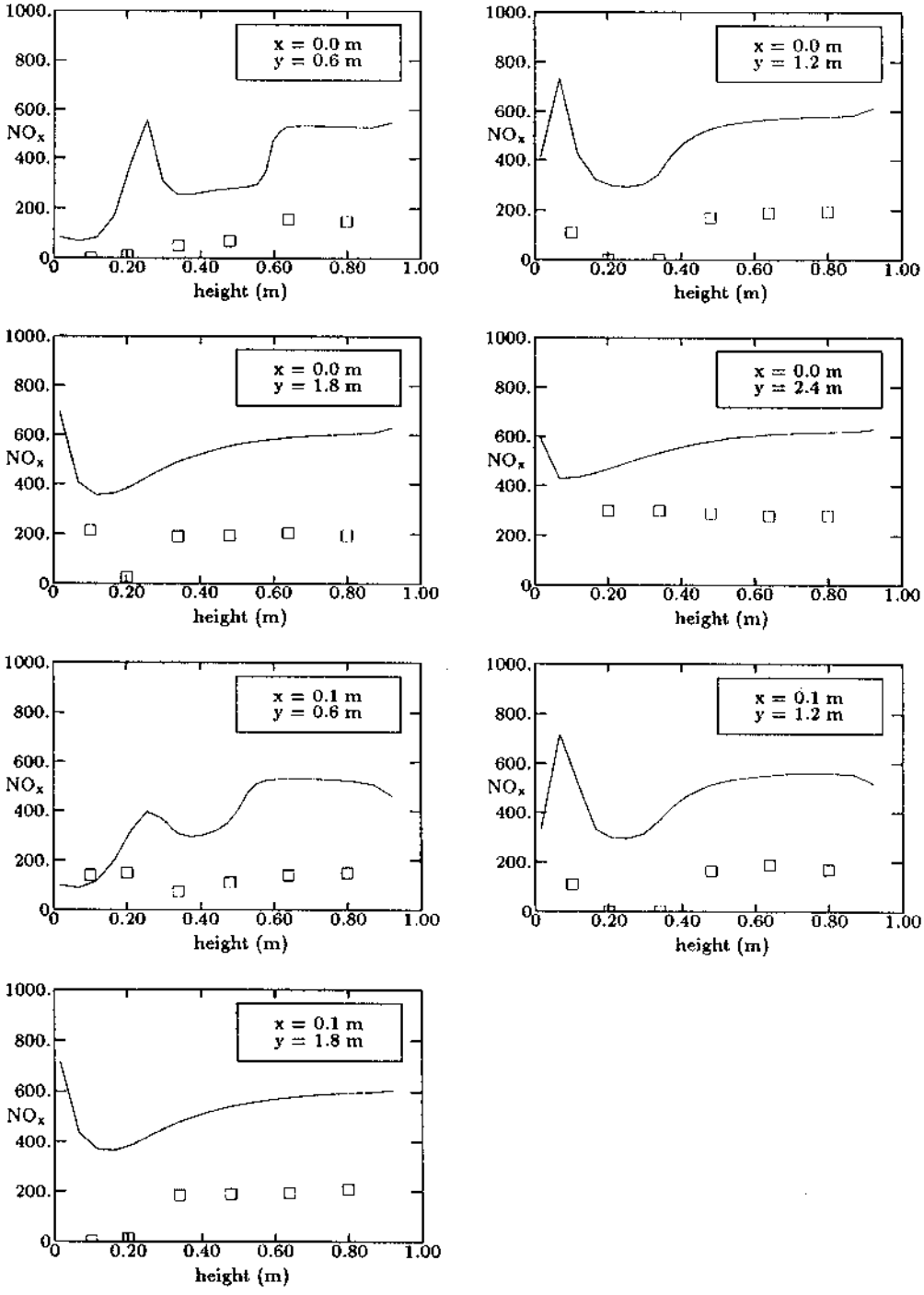

Figure 19.17: Comparison between simulations and in-flame measurements of NO concentration for the NG7 OP flame, y is the distance along the furnace from the inlet; x is the distance from the symmetry plane of the furnace.

achievement that it has lead to research and development programs specifically devoted to the advancement of these new techniques. The dilution is so high that the oxygen concentration in the reactive mixture is substantially reduced with respect to the standard 21%. This has strong effects on the properties of the reaction zone. This regime is characterized by the absence of a steady flame front (with its strong gradients in temperature and species concentration) where temperature and species are distributed over a larger volume within the combustion chamber. One can speak of a volumetric combustion regime instead of a flame front regime. A stabilized flame front is already missing with a modest depletion of oxygen to 17% (corresponding to 20 to 30% of flue gas recirculation) under the conditions that gas temperatures are sufficiently high to prevent flame extinction. Different names have been introduced in the literature to denote more or less the same development: *High temperature air combustion* [21], Excess Enthalpy Combustion (EEC), flameless oxydation (FLOX), MILD combustion, Fuel Direct Injection (FDI).

A very interesting aspect of flameless oxydation is that the heat flux to the wall or the process tubes tends to be more uniform than in standard flame-mode combustion.

In EEC, part of the heat of the flue gas is used to preheat the air. The air preheating is done locally in a burner, in contrast with conventional air preheating methods which use an external heat exchanger. To preheat the air the burner contains a heated ceramic block. This system is dynamic because the ceramic cools down in time. After a certain time the air inlet temperature would decrease to a value where the required oven temperature would not be maintained. Before this limit is reached, the burner switches from combustion mode to regeneration mode. In some cases the burners operate in pairs, with always one burner in combustion mode and the other in regeneration mode, in other cases, the burner is auto-regenerative and the switching between combustion mode and regeneration mode applies to different channels in a the burner. (In the start-up phase hot flue gas is not yet present and the burners operate in a standard combustion mode, possibly with externally preheated air.)

The basic chemical-physical phenomena are still far from fully understood but this (of course) does not prevents pilot and larger scale demonstration projects to be started and show very attractive breakthrough performance in new, clean and energy effective processes. The book by Tsuji *et al.* [21] describes a set of computational models used in the prediction of high temperature air combustion. Partial success and limitations of the models are described.

8 Conclusion

The presentation given in this lecture was restricted to a general description of the design of some industrial furnaces, a detailed description of a specific computational study and an outlook towards future developments. As such it is far from complete. However, it should have made clear that it is difficult to directly apply the precise models described in the other lectures.

Radiative heat transfer, which most often is not included in studies of laboratory scale flames plays a dominant role in furnaces and should be included from the start. The geometry of a furnace with many burners and process tubes is complex and to obtain a solution of the computational model within acceptable time one has to restrict to simple models. It is a remarkable achievement that using these models often very reasonable predictions of flow patterns, and profiles of heat flux profiles and temperature in industrial furnaces can be obtained.

The complexity of the flow in the near burner zone of low NO_x burners however is too high to capture it with simple fast-chemistry combustion models and simple turbulence models. The need to reduce emissions has led to flames with regions of local extinction, caused by the combination of high turbulence levels and dilution effects. Accurate NO_x predictions continue to be a challenge.

Quantitatve prediction of thermal NO_x in turbulent flames remains a problem because it requires accurate prediction of temperature fluctuations. Predicting other pathways to NO_x formation is difficult because it involves more extended chemical reaction mechanisms. It is a challenge to use and extend the models described in some of the other lectures of this course. Carefully combining improvements in turbulence modeling, with efficient but still accurate models for radiative heat transfer and chemical transformation processes, better accuracy and good prediction of a wider range of quantities is possible.

9 Exercise

The Reynolds number of the flow in furnaces are generally much larger than in labscale experiments. This has impact on the characteristics of the turbulence-chemistry interaction. Consider a burner in a furnace. Premixed reactants (fuel and air) are injected via an inlet with diameter L. The speed of injection is U, the throughput M then is proportional to UL^2. Burners of different throughput can differ in L and in U, and there are several possibilities for 'scale up', to a larger throughput. The rule determining the relation between the size and injection speed at different throughputs is called scaling rule. When scaling a reacting system it is important to take into account the relations between the scales of turbulence and the scales of flame structures.

Consider a scale up problem with an increase by a factor 1000 between labscale and industrial scale for a system with chemical time scale 0.01 ms. Construct a diagram with on the horizontal axis the Damköhler number and on the vertical axis the throughput (logarithmic scale). How do appear lines of constant Reynolds number in this diagram? And lines of constant Karlovitz number? And lines of constant Damköhler number? How does appear the line corresponding to the scaling rule 'Keeping U constant'? How different is the turbulence-chemistry interaction at the labscale and at the industrial scale?

References

[1] *The John Zink Combustion Handbook*, Charles E. Baukal Jr. (editor), CRC Press, 2000

[2] Charles E. Baukal Jr. , *Heat Transfer in Industrial Combustion*, CRC Press, 2001

[3] T. Poinsot and D. Veynante, *Theoretical and Numerical Combustion*, Edwards, 2001

[4] M.F. Modest, *Radiative Heat Transfer*, Mc Graw-Hill, New York, 1993.

[5] R. Siegel and J.R.Howell, *Thermal Radiation Heat Transfer*, Hemisphere, Washington DC, 1992.

[6] Aristide Mbiock and Roman Weber, *Radiation in enclosures. Elliptic Boundary Value Problem*, Springer-Verlag, Berlin etc., 2000.

[7] T. Nakamura, W.L. van de Kamp and J.P. Smart, *Further studies on high temperature natural gas combustion in glass furnaces*. Technical Report Doc. No. f90/y/7, IFRF, IJmuiden, 1991

[8] T. Nakamura, W.L. van de Kamp and J.P. Smart, *The effects of fuel air mixing on* NO_x *reduction and heat transfer in high-temperature gas-fired glass melting furnaces*. In First International Conference on Combustion & Emission Control, 1993

[9] P.G. Boerstoel, *Modelling of gas-fired furnaces*, PhD thesis, TUDelft, 1997.

[10] T.W.J. Peeters, *Numerical modelling of turbulent natural-gas diffusion flames*, PhD thesis, 1995

[11] A.P. Salooja, *Mathematical modelling of and experimental studies in axisymmetrical combustion*. PhD thesis, London University, 1968

[12] I.E.A. Megahed, *The prediction of three dimensional gas fired combustion chamber flows*, PhD thesis, Imperial College, London, 1979.

[13] N. Peters, Reducing mechanisms, in *Reduced kinetic mechanisms and asymptotic approximations for methane-air flames*, Vol. 384 of *Lecture Notes In Physics*, pp. 48-67, Springer-Verlag, 1991.

[14] J. Taine, *A line-by-line calculation of low-resolution radiative properties of CO_2-CO transparent nonisothermal gases mixtures up to 3000 K*. J. Quant. Spectrosc. Radiat. Transfer, 30 (40), 371–379, 1983.

[15] H.C. Hottel and A.F. Sarofin, *Radiative Transfer*, McGraw-Hill, 1967

[16] F.C. Lockwood and N.G. Shah, *A new radiation solution method for incorporation in general combustion prediction procedures*. In Eighteenth Symposium (International) on Combustion, 1405–1414, 1981.

[17] I.M. Khan and G. Greeves, *A method for calculating the formation and combustion of soot in diesel engines*, In: Afgan and Beer (eds.), Heat transfer in flames, 391–404, 1974.

[18] J.B. Moss, C.D. Stetart and K.J. Syed, *Flowfield modelling of soot formation at elevated pressure*, In Twenty-second symposium (International) on Combustion, 413–423, The Combustion Institute, 1988.

[19] B.F. Magnussen and B.H. Hjertager, *On mathematical modelling of turbulent combustion with special emphasis on soot formation and combustion*, In: Sixteenth Symposium (International) on Combustion, 719–729, The Combustion Institute, 1976.

[20] J. A. Wieringa, *Spectral radiative heat transfer in gas-fired furnaces*, PhD Thesis, TU Delft, 1992.

[21] Hiroshi Tsuji, Ashwani K. Gupta, Toshiaki Hasegawa, Masashi Katsuki, Ken Kishimoto and Mitsunobu Morita, *High Temperature Air Combustion. From Energy Conservation to Pollution Reduction*, CRC Press, 2003

Chapter 20

Combustion Systems for Solid Fossil Fuels

H. Spliethoff

1 Introduction

Solid fuels are responsible for approximately 25% of the world primary energy production. When only electrical power generation is considered, this fraction increases to almost 50% (figure 20.1). It may be evident that the combustion of solid fuels is economically very important. Scientific understanding, however, is limited, mainly due to the complex nature of the process.

This chapter can serve as an introduction to the combustion of solid fuels, and solid fossil fuels in particular. First the different solid fuels are classified, after which some fundamentals of solid particle combustion are treated. The chapter is concluded with an overview of some techniques for large scale solid fuel combustion.

2 Classification of fuels

Solid fuels comprise a large category of different materials with varying properties. Two large groups can be distinguished: the coal like fuels and biomass. Examples of the latter are wood, straw, and waste. Coal comes in a large number of varieties like brown coal, bituminous coals, or anthracite.

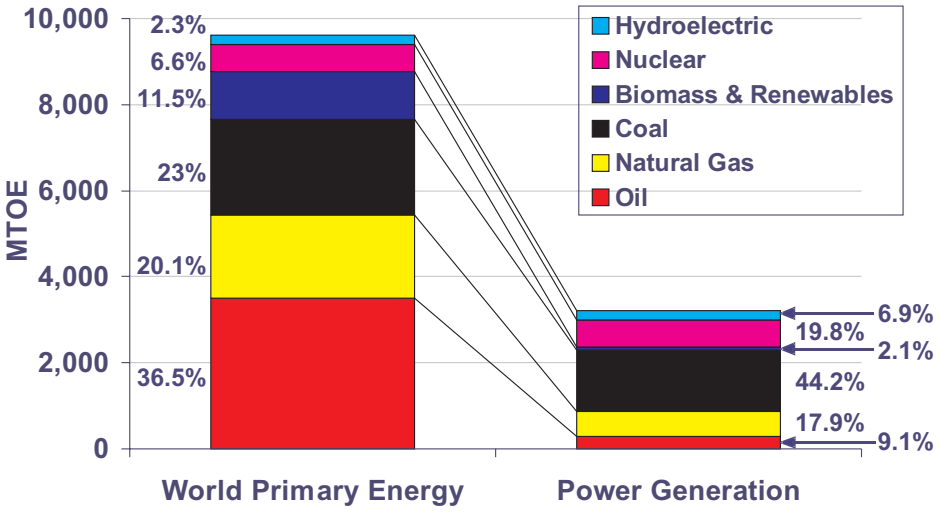

Figure 20.1: Total world energy production (source: IEA, data from 1998).

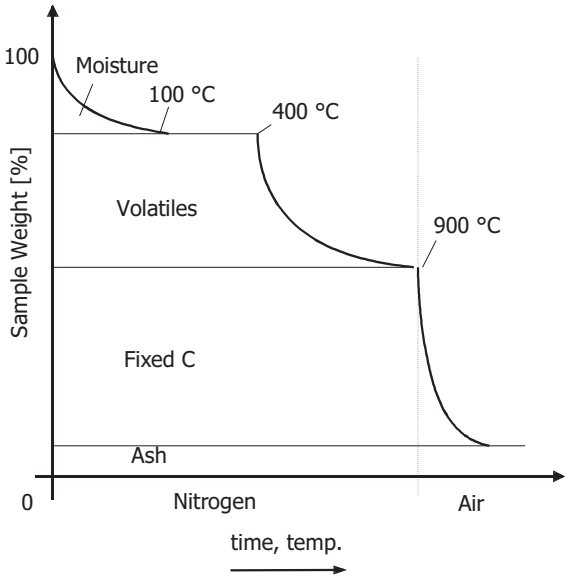

Figure 20.2: A proximate analysis of a solid fuel.

Solid fuels contain both combustible and inert material. Their thermal behavior is complex, and includes thermal decomposition (evaporation, pyrolysis) and even melting or softening of the inert material (ash). All fuels can be characterized by their composition. This can be done either by an ultimate analysis in terms of the mass fractions of the different atoms (C, H, N, S, O, ...), or by a proximate analysis in terms of:

- moisture,
- volatiles,
- fixed C,
- ash.

An example of a proximate analysis is given in figure 20.2. Some fuel is placed on a balance in a nitrogen athmosphere. With an increasing temperature, first the moisture is released from a temperature higher than 100 °C. This mass loss can accurately be registered by the balance. This process stops at a certain temperature, but at a temperature around 400 °C, the volatiles are being released. This process stops at 900 °C, and is followed by a replacement of the athmosphere by air, in order to burn the fixed carbon. When this process is finished, the ash remains.

3 Combustion Fundamentals

The purpose of the combustion process is to release by oxidation the energy which is chemically bound in the fuel and to convert it into sensible heat. The heterogeneous combustion process of solid fuels is more complex than the homogeneous combustion of gaseous fuels. Solid fuels such as coal are built of different fractions of organic matter and minerals. As the fuel heats up in the firing, the pyrolysis of the organic matter starts. In this process, volatile intermediate products are generated such as hydrocarbons, carbon oxides, hydrogen, sulphur and nitrogen compounds and also residual coke as a solid intermediate product of combustion. The ignition starts the combustion. Prerequisite for the ignition besides a sufficiently high temperature is the forming of an explosive mixture. Subsequently,

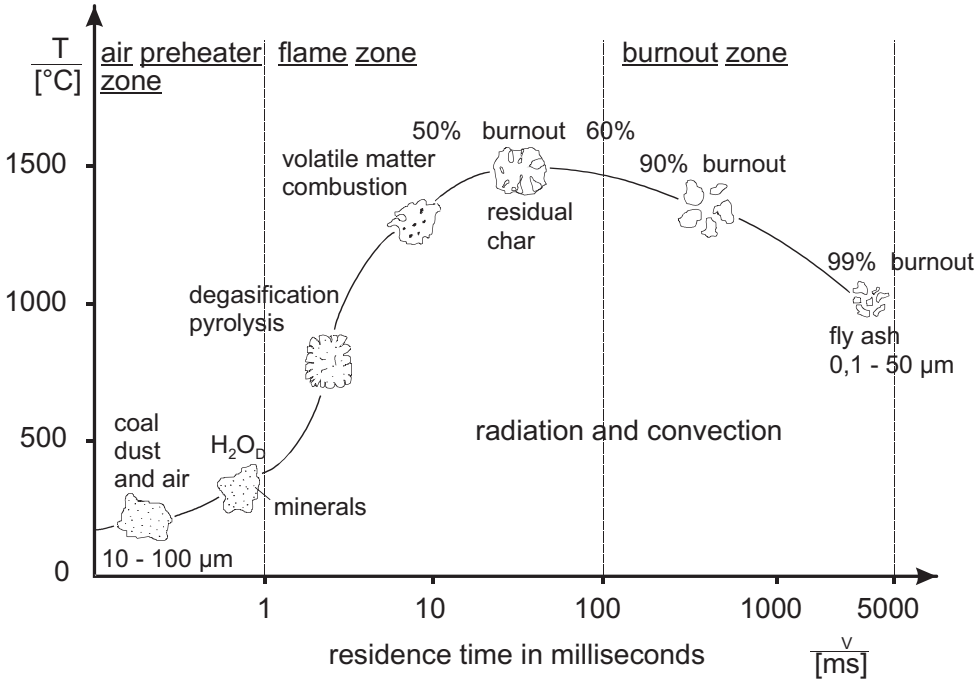

Figure 20.3: Schematic drawing of the combustion process in a pulverised fuel firing.

the volatile matter and the residual coke combust together with the oxygen of the combustion air. Figure 20.3 schematically presents the combustion process of coal in pulverised fuel firing. The combustion of solid fuels evolves in partial processes:

- drying,
- pyrolysis,
- ignition,
- combustion of volatile matter, and
- combustion of the residual coke.

The first two partial processes are a thermal decomposition as a consequence of the heating up of the fuel. The quantity of heat necessary to heat up the fuel to ignition temperature is mostly transferred by convection. In pulverised fuel firing, for example, hot flue gas is admixed in the near-burner zone, and in a fluidised bed, the heat is transferred by particles of solid matter. In grate firing systems, heating up is also carried out by means of refractory-lined hot walls transferring the heat to the fuel by radiation. In the last two partial processes — combustion of volatile matter and combustion of residual coke — the organic matter is converted chemically. Conversion is divided into homogeneous and heterogeneous reactions. The partial processes do not necessarily run one after the other but, depending on the firing type, may overlap. Table 20.1 gives guidelines for the time necessary for each of the partial processes. The table makes clear that the total combustion time of all firing systems is determined by the combustion of the residual coke.

In the following, the partial processes of solid fuel combustion are discussed in more detail.

Table 20.1: Partial processes of coal combustion in firing systems.

Firing System	Particle Diameter [mm]	Heating Rate [K/s]	Drying and Pyrolysis Period [s]	Time of Volatile Matter Combustion [s]	Time of Residual Coke Combustion [s]
fixed-bed firing	< 100	< 1	ca. 100	determined by release and	ca. 1000
fluidised bed firing	< 10	10^3–10^4	10–50	mixing with combustion air	100–500
pulverised fuel firing	< 0.1	10^3–10^6	< 0.1		< 1

3.1 Drying

Water can adhere both to the particle surface and inside the particle pores of the coal. In the furnace, the fuel is heated and the water vaporised at temperatures above 100 °C. At temperatures up to 300 °C, the water vaporised in the pores becomes desorbed or outgases. Besides water vapour, other gases such as methane, carbon dioxide, and nitrogen, which have formed during the coalification process, outgas as well.

Depending on the combustion system, the firing is capable of drying fuels with different moisture contents. Whereas grate or fluidised bed firing systems can be fed with moisture-containing fuels without further treatment, the fuel in the case of a pulverised fuel firing is predried in mills in order to ensure a fast combustion process within the available residence time.

3.2 Pyrolysis

The decomposition of the organic coal substance and the formation of gaseous products during the heating of the coal is termed devolatilisation or pyrolysis.

The devolatilisation process is schematically shown in figure 20.4. Devolatilisation of volatile matter by cracking of compounds of organic coal structures starts at temperatures above 300 °C. In a temperature range up to about 600 °C, tars, liquid at normal temperature, and gaseous products are formed. The gases consist of carbon dioxide (CO_2), methane (CH_4) and other light hydrocarbons such as C_2H_6, C_2H_4 and C_2H_2. Tars are complex hydrocarbon compounds, in their organic structure similar to the base fuel, which evaporate from the coal substance at temperatures between about 500 and 600 °C . The particle form remains almost unchanged up to temperatures of about 400 °C. Above this temperature, the coal particle begins to soften. The tars and gases formed inside the coal can intumesce the particle at temperatures reaching slightly above 550 °C. The particle solidifies into the so-called semi-coke which has a cavity structure with a distinct pore system and an enlarged surface.

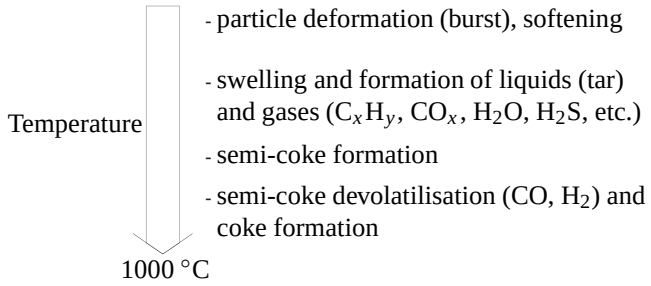

Figure 20.4: Processes during pyrolysis.

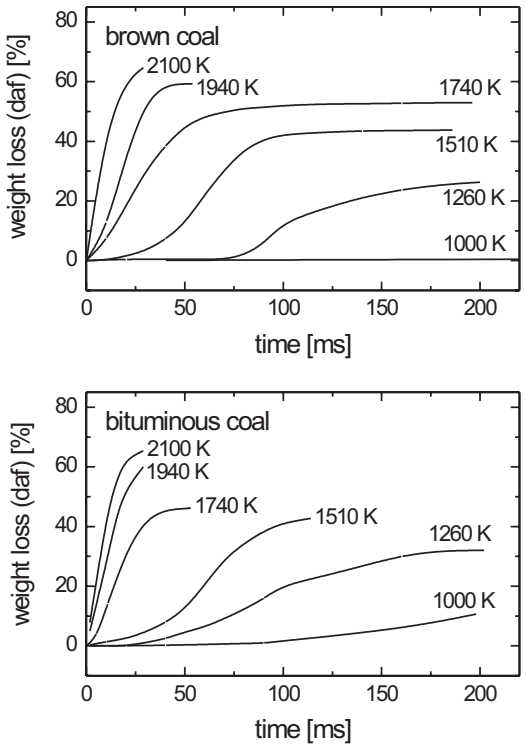

Figure 20.5: Impact of temperature and residence time on weight loss during pyrolysis.

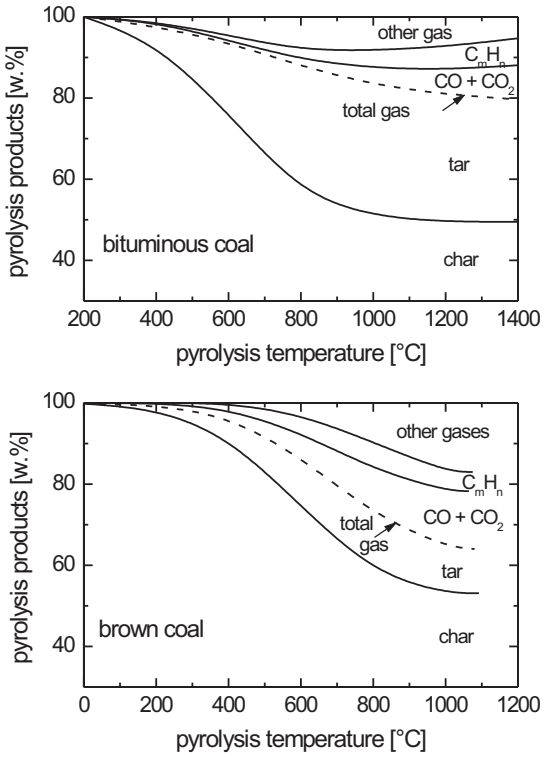

Figure 20.6: Composition of the volatile matter as a function of the temperature during pyrolysis.

Further heating up above more than about 600 °C converts the semi-coke into coke separating mainly carbon monoxide and hydrogen. With rising temperatures, light gas components such as hydrogen and carbon monoxide and also soot form from the tar compounds. The fraction and the composition of the volatile components and the history of their release depend on the coal type, the grain size, the heating rate and the final temperature of the heating. With increasing heating rate and coalification degree, the devolatilisation maxima of the components shift towards higher temperatures.

The yield of volatile matter increases with rising end temperatures. Figure 20.5 shows the weight losses of a hard and a brown coal determined during pyrolysis at short residence times and high heating rates. The volatile matter content determined at high temperatures and heating rates of the entrained-flow reactor may amount to 1.1–1.8 times the content detected in proximate analysis. For coals with a strong tar release in particular, the yields of volatile matter are clearly higher because the conditions of the entrained-flow reactor impede the decomposition of the tar into coke and gas.

Figure 20.6 shows the composition of the volatile matter as a function of the temperature during the pyrolysis of a hard and a brown coal. In the pyrolysis of the hard coal, the tar products predominate whereas CO and water comprise the larger fraction of the volatile matter in the case of the brown coal. At higher temperatures, stable compounds form increasingly, while the tar fraction decreases.

3.3 Ignition

The ignition starts the combustion. The ignition temperature is defined as the temperature above which combustion evolves independently. At temperatures below ignition temperature, the heat released during fuel oxidation is dissipated to the environment, so the temperature does not rise notably. Only

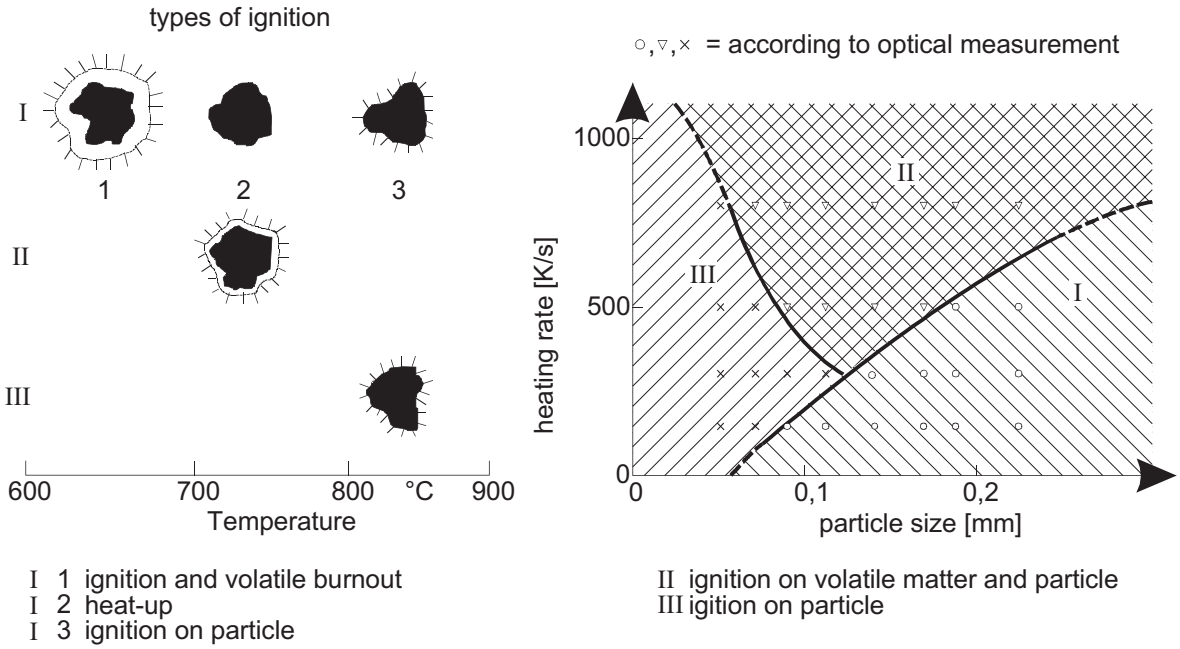

Figure 20.7: Ignition mechanism as a function of the heating rate and the particle size, for a high volatile bituminous coal (hvb).

at or above the ignition temperature does the reaction velocity reach a rate where the amount of heat released exceeds the amount dissipated. Thus the reaction is accelerated so a stable combustion can be maintained.

In the combustion of solid fuels, both the volatile components and the residual coke have to be ignited. The volatile components ignite as soon as they form a combustible mixture with the combustion air and the ignition temperature of the mixture is either reached or exceeded. The residual coke particle, in order to ignite, has to reach or surpass its ignition temperature and receive sufficient oxygen at its surface. The ignition temperatures of the combustible mixture of volatile matter and combustion air range between 500 and 700 °C, the ignition temperatures of the residual coke particle lie above 800 °C.

In coal combustion, history and sequence of ignition processes above all depend on the heating rate and the particle size. The impact of these two parameters on the ignition mechanisms in the combustion of a high volatile bituminous coal, determined at a laboratory-scale plant, is described in figure 20.7. During slow heating and with coarse particles, first the volatile components outgas, ignite in the near-particle zone and burn out. Devolatilisation and volatile matter combustion result in a gas atmosphere that envelops large particles thus impeding the diffusion of oxygen to the particle which can ignite only after the volatile matter has burned up (ignition mechanism I). Coarse particles and high heating rates favour the simultaneous ignition of volatile matter and residual coke (ignition mechanism II). Pyrolysis reactions shift towards higher temperatures, with the ignition temperature of the particle changing to less extent. This way, the ignition on the particle is possible already before all gases are burned completely.

With very small particles, ignition happens directly on the particle surface. Given the great surface-to-volume ratio, these particles are rapidly heated also from the inside so the ignition temperature of the particle is already reached before an ignitable mixture has formed around the particle

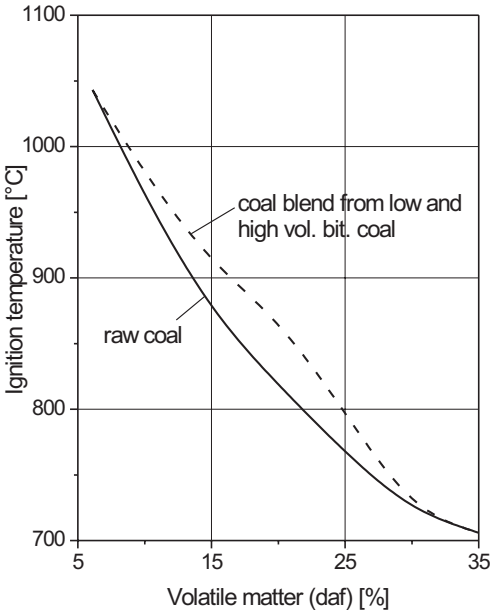

Figure 20.8: Ignition temperature as a function of the volatile matter.

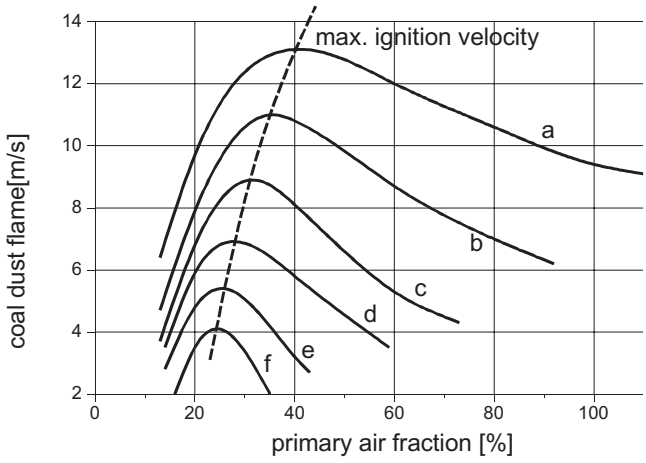

	a	b	c	d	e	f
volatiles %	30	30	30	20	30	15
ash %	5	15	30	5	40	5

Figure 20.9: Ignition rate as a function of the primary air fraction.

(ignition mechanism III).

Besides the gas, coal analysed in figure 20.7, a low-volatile anthracite coal was investigated as well. At the same parameter range, ignition, with this coal, takes place on the particle.

In the case of a coarse-grained coal in a grate firing, the volatile matter ignites first, whereas medium-sized coal particles and higher heating rates in the fluidised bed firing promotes the simultaneous ignition of volatile matter and particle. High heating rates and small particle sizes in a pulverised fuel firing make low-volatile bituminous (lvb) coal ignite on the particle, whereas high-volatile bituminous (hvb) coals ignite both on the volatile matter and on the particle.

The ignition temperature, in solid fuel combustion, not only depends on the properties of the substance characteristics such as volatile matter, moisture and ash contents and on the physical structure, such as particle size and inner surface of the coal but also on the combustion conditions of the firing system (heating rate, dust and gas concentrations etc.). Depending on the fraction of volatile components, the ignition temperature is high with lean fuels and coke and low with higher-volatile fuels. The temperature decreases with increasing fineness of the fuel. Figure 20.8 gives reference values as a function of the volatile matter content for the design of pulverised-coal firing systems. These values were determined at heating rates comparable to those in a pulverised fuel firing.

The ignition velocity — which has to be understood as the rate of flame propagation in the mixture — has a clear dependence on the volatile components, the ash content and the primary air mixture in the case of a hard coal flame, as figure 20.9 shows. The ignition velocity always reaches a maximum depending on the primary air fraction. At low air ratios, the oxygen in the primary air is not sufficient anymore to combust the volatile matter in the near-burner zone. With a stronger primary air flow, the primary air fraction which is not needed for the combustion of the volatile matter decreases the flame temperature. In both cases, the ignition velocity decreases. A higher ash content also has a delaying effect on ignition. The ignition velocity is a crucial parameter for the burner design for two reasons. On the one hand, the burner throat velocity has to be notably higher than the ignition velocity in order

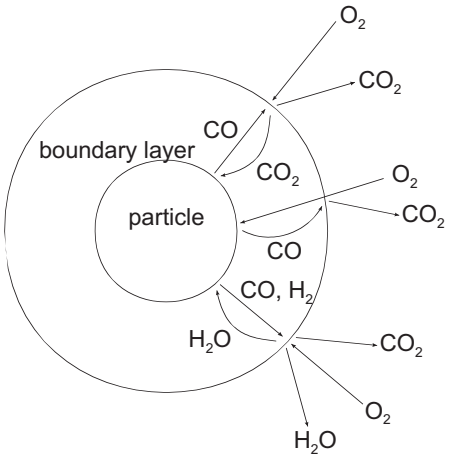

Figure 20.10: Combustion process on a char particle.

to surely prevent the flame from flashing back. On the other hand, to have a stable flame front, it has to be possible that zones form where the flow velocity is equal to the ignition velocity.

In pulverised fuel firing, along with the coal also the carrier gas flow, consisting of primary air fraction and vapours, has to be preheated — starting from classifier temperature — to values equal to or higher than the ignition temperature. For this reason, only that amount of primary air should be fed as is necessary for the combustion of the volatile matter.

3.4 Combustion of Volatile Matter

The homogeneous combustion of the volatile components is characterised by a very high reaction velocity. The burning time of volatile matter is essentially determined by its release and mixing with air.

The relatively highest concentrations of volatile components develop on the particle surface, diminishing again with increasing distance from the particle. Temperature and oxygen concentration of the particle environment show the reverse behaviour. Their diminishing goes along with a decreasing distance from the particle. The volatile matter combustion stabilises as diffusion flame in the area of a stoichiometric concentration of volatile matter and oxygen. The diameter of a flame enveloping a particle is about three to five times the diameter of a particle. In pulverised coal combustion, the volatile matter combustion processes of the individual particles combine so they can be considered a coherent gas flame.

3.5 Combustion of the Residual Char

The volatile matter being released from the particle, it remains a porous structure consisting almost only of carbon and ash. The carbon, at a sufficiently high particle surface temperature, is oxidised with oxygen, carbon monoxide, carbon dioxide and water vapour.

At the same temperature, the reaction velocity of the heterogeneous combustion of solid residual coke with oxygen is orders of magnitude lower than the homogeneous volatile matter combustion. Residual coke combustion therefore determines the total combustion time and is decisive for the design of firing systems.

Figure 20.10 schematically shows the course of residual coke combustion on a single particle. On the surface or inside the particle, the heterogeneous oxidation of the carbon takes place with oxygen,

carbon dioxide and water vapour as oxidants.

$$C + \tfrac{1}{2}O_2 \rightleftharpoons 2\,CO \tag{20.1}$$

$$C + CO_2 \rightleftharpoons 2\,CO \quad \text{(Bouduard reaction)} \tag{20.2}$$

$$C + H_2O \rightleftharpoons CO + H_2 \quad \text{(heterogeneous water-gas reaction)} \tag{20.3}$$

Today it is considered proven that directly on the particle, first only a conversion to carbon monoxide takes place, either by combustion (20.1) or by gasification (20.2 and 20.3). Around the coal particle, a gaseous atmosphere forms consisting of the combustion products CO and H_2 and the oxidants O_2, CO_2 and H_2O. The oxidants have to diffuse to the particle surface through this laminar boundary layer and, vice versa, the combustion products from the particle to the environment.

The following homogeneous oxidation

$$CO + \tfrac{1}{2}O_2 \rightleftharpoons CO_2 \tag{20.4}$$

$$H_2 + \tfrac{1}{2}O_2 \rightleftharpoons H_2O \tag{20.5}$$

takes place in the surrounding boundary layer.

In heterogeneous reactions, the conversion velocity $\mathrm{d}m_C/\mathrm{d}t$ of the carbon mass m_C of a coal particle is proportional to the reacting surface A, to the reaction velocity k_{tot} and to the oxygen partial pressure p_{O_2} in the environment of the particle.

$$\frac{\mathrm{d}m_C}{\mathrm{d}t} = A k_{tot}\, p_{O_2} \tag{20.6}$$

Given that besides the chemical kinetics also the mass transport processes exert an influence on the burning process, the conversion velocity of the residual coke combustion is limited by the slowest one of the participating processes. Which of the partial processes determines the conversion velocity in the end, depends essentially on the reaction temperature.

As a function of the temperature, a distinction is made between three areas. In each, either

- the chemical reaction, or
- the pore diffusion, or
- the boundary layer diffusion

works as velocity determiner. The three areas are shown in an Arrhenius diagram in figure 20.11. In this diagram, the natural logarithm of the reaction velocity is plotted over the reciprocal of the absolute temperature.

In the chemical reaction (area I), the oxygen can sufficiently fast reach the inside of the coke residue via the finely branched pore system at low temperatures without undergoing notable conversions at first. Thus the concentration is equal to the concentration in the free gas atmosphere, see figure 20.12. Only the chemical reaction of the oxygen with the carbon surface of the pores is decisive for the combustion velocity.

In pore diffusion, the velocity of the chemical reaction increases with rising temperatures. In the inside of the coke residue, the oxygen molecules get depleted so that a concentration drop from the fringe to the centre of the particle develops. The burn velocity in this area depends on how fast oxygen can be supplied by pore diffusion.

In boundary film diffusion (area III), at still higher temperatures, oxygen is not able anymore to penetrate to reach the pore inside. The gradient of the oxygen partial pressure shows that the

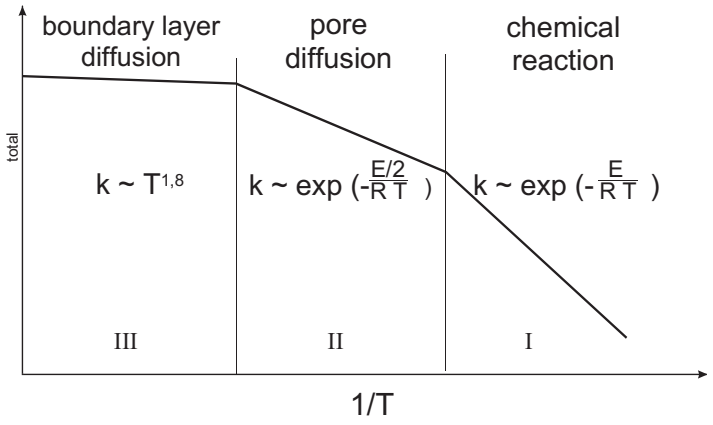

Figure 20.11: Arrhenius diagram of coke combustion.

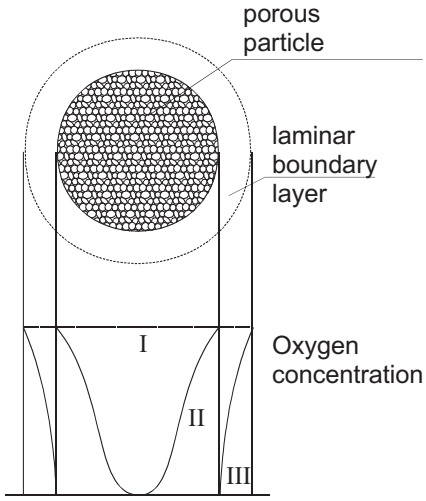

Figure 20.12: Oxygen concentration profile around a char particle.

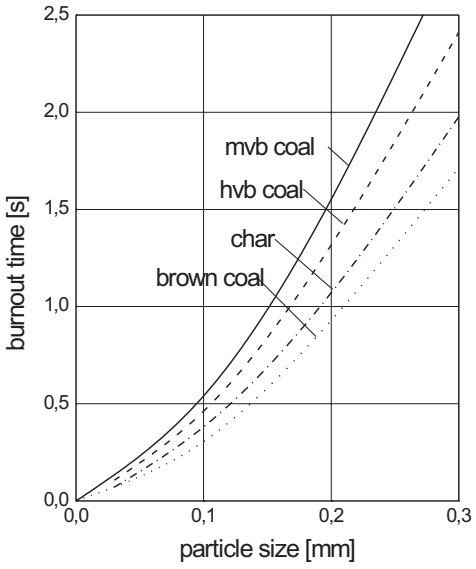

Figure 20.13: Burn times for pulverised coal as a function of particle size ($T = 1300\,°\mathrm{C}$, $\lambda = 1.2$; hvb: high-volatile-, mvb: medium-volatile-, lvb: low-volatile bituminous).

combustion process takes place only on the outer surface of the particle. The particle is enveloped by a laminar boundary layer. The conversion velocity is determined by the diffusion of the oxygen through the boundary layer.

The total velocity is the result of the single reaction velocity constants:

$$k_{\mathrm{tot}} = \left(\frac{1}{k_{\mathrm{diff,b}}} + \frac{1}{k_{\mathrm{diff,p}}} + \frac{1}{k_{\mathrm{chem}}} \right)^{-1} \tag{20.7}$$

The temperature zones shift depending on the particle size and the coal type. Whereas pore and boundary layer diffusion determine the reaction velocity at temperatures above a level of 1450 °C or so in the case of coal particles of 20 μm, this holds true already at 1150 °C in the case of larger particles of 200 μm.

During the combustion process, the relative ash fraction in the coal particle increases. An ash

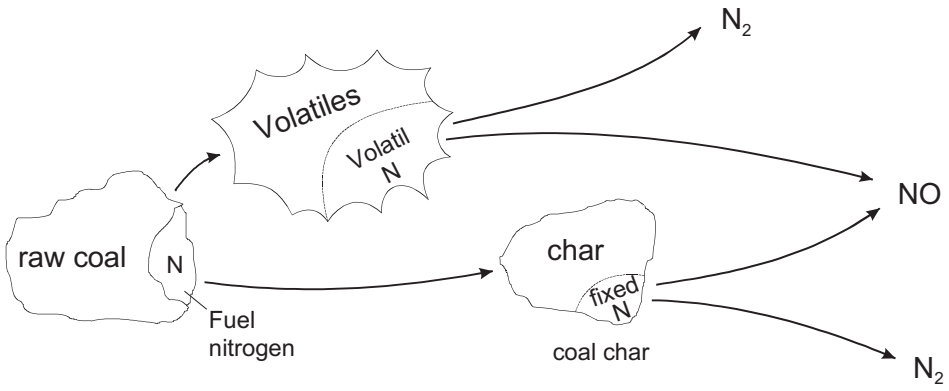

Figure 20.14: Schematic representation of the the different sources and routes of NO_x formation.

layer enveloping the remaining combustible matter develops so the oxygen has to penetrate this ash cover. Given that, as the burn process proceeds, the ash cover grows thicker, the combustion velocity gradually decreases. The combustion is the more retarded, the more ash and the less pores the fuel contains. The pyrolysis process preceding the coke combustion has a positive effect on the burn-up. Depending on the volatile matter content, a more or less marked cavity structure is formed in the coke during pyrolysis. This structure considerably enlarges the surface available for the chemical reaction in the raw coal particle. Coals with higher volatile matter content burn faster because the respective residual coke gets a much larger surface by pyrolysis than the residual coke of a low-volatile bituminous (lcv) coal. Figure 20.13 shows the combustion time of different coals at a temperature of 1300 °C.

3.6 NO_x emissions

Thermal NO_x is generated from the oxidation of N_2 at temperatures exceeding 1500 °C (see figure 20.14). Furthermore, NO_x can be generated from nitrogen present in the fuel (either as part of the volatile compounds, or as part of the coke). The last mechanism is the prompt NO formation via CH radicals.

For gaseous combustion only thermal NO_x formation plays a role. When the temperature of the combustion is limited, NO_x emissions below 100 mg/Nm^3 are possible. For coal combustion, the nitrogen present in the fuel is the main source of NO_x (with a typical content of 1–1.5%). For older burners this leads to NO_x emissions ranging from 800–1500 mg/Nm^3. Modern low-NO_x systems can reduce this to 300–400 mg/Nm^3.

4 Combustion systems

Coal-firing systems comprise fuel supply and preparation, fuel and combustion air transport and distribution, the combustion system for releasing the heat from the fuel in the furnace and the flue gas cleaning. The systems utilised for solid fossil fuels are:

- grate firing,
- fluidised bed firing, and
- pulverised fuel firing.

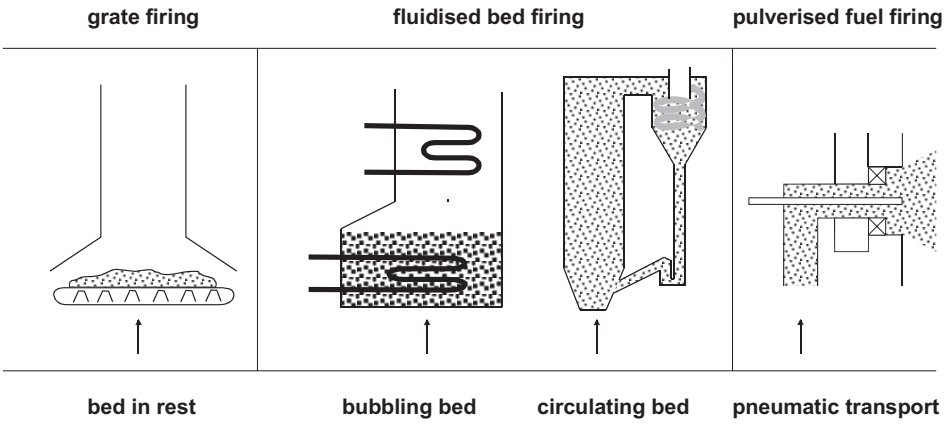

Figure 20.15: Schematic representation of the main types of firing systems.

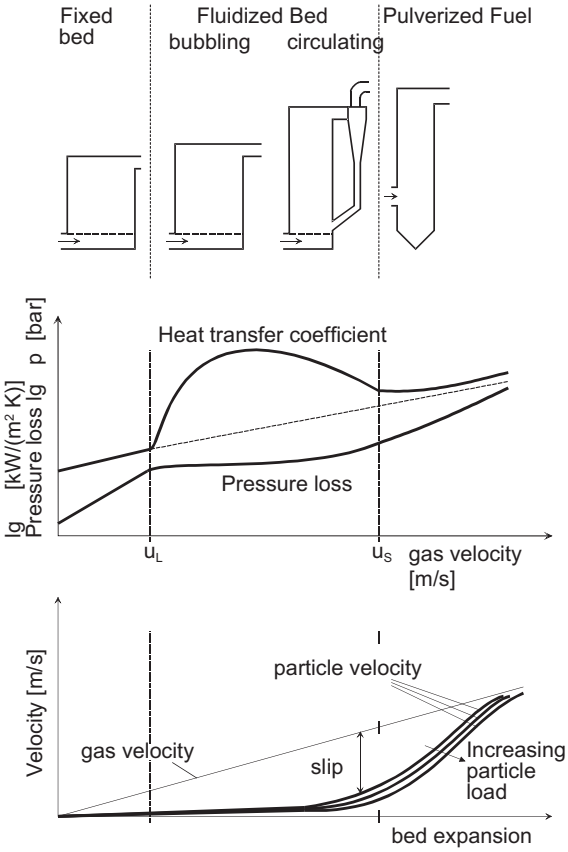

Figure 20.16: Distinctive features of firing systems

Figure 20.15 gives a schematic overview of the different firing systems. Figure 20.16, besides presenting the schematic drawings, gives the characteristic gas and solid fuel flow velocities, pressure losses and heat transfer coefficients of each of the combustion systems.

4.1 Grate firing

In a grate firing system, the solid fuel lies in a bulk bed on a moving grate (figure 20.17). The fuel burns with the combustion air which is blown through the grate bars and the bulk. At low flow velocities,

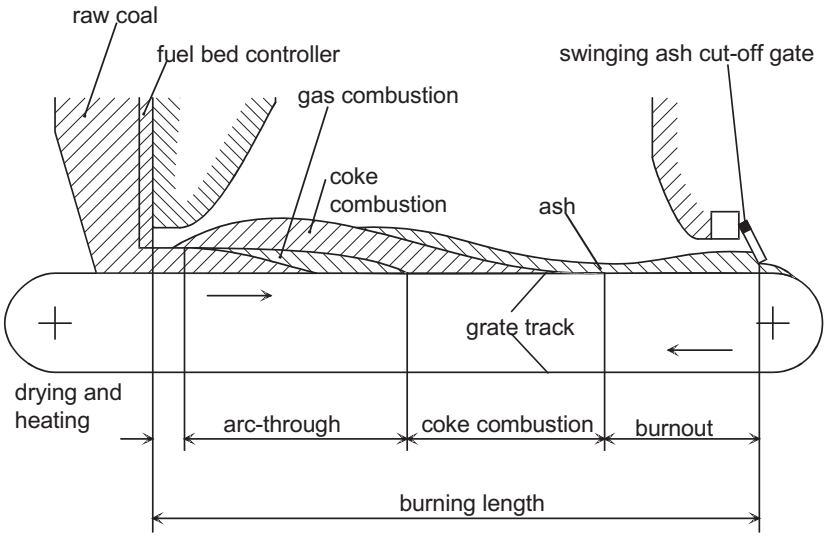

Figure 20.17: The combustion process on a traveling-grate stoker.

the single coarse coal particle with a size up to 30 mm, the size of a nut approximately, remains in the coal layer on the grate. Notable quantities of solids are not ejected from the bulk. Because of the limited size, coal fired grates are only used for industrial and thermal power plants of small capacity. Grate firing is the preferred system for ballast-containing fuels such as waste, or for solid industrial wastes, or biomass.

4.2 Fluidized bed firing

In a fluidised bed firing, the solid fuel whirls and burns staying in a fluidised gas-solids suspension. The fluidising medium also provides the oxygen for the oxidation of the fuel. With the lower flow velocities in the bubbling fluidised bed (BFB), only the fine-grained ash is ejected from the fluidised bed after burnout and abrasion of the coal. Coarse-grained ash accumulates in the fluidised bed, from where it is removed. Given the higher flow velocities of combustion air and combustion gases in the circulating fluidised bed (CFB), the entire solids flow in the furnace is entrained and circulated. The circulating fluidised bed takes the total space of the furnace. In both systems, the solids stay in the furnace clearly longer than the gas flow. In figure 20.18 an example of a circulating fluidized bed combustor is presented.

4.3 Pulverised fuel firing

In pulverised fuel firing systems, the particle is carried along with the air and combustion gas flow. Pulverised fuel and combustion air are injected into the firing and mixed in the furnace. With a fine milling degree of the raw coal and high flow velocities of the combustion gases, particle and gas residence times are almost equal. The combustion of the pulverised-coal/air mixture being a rapid process distributed over the entire furnace makes it possible to utilise relatively higher capacities than in the case of grate or fluidised bed firing systems.

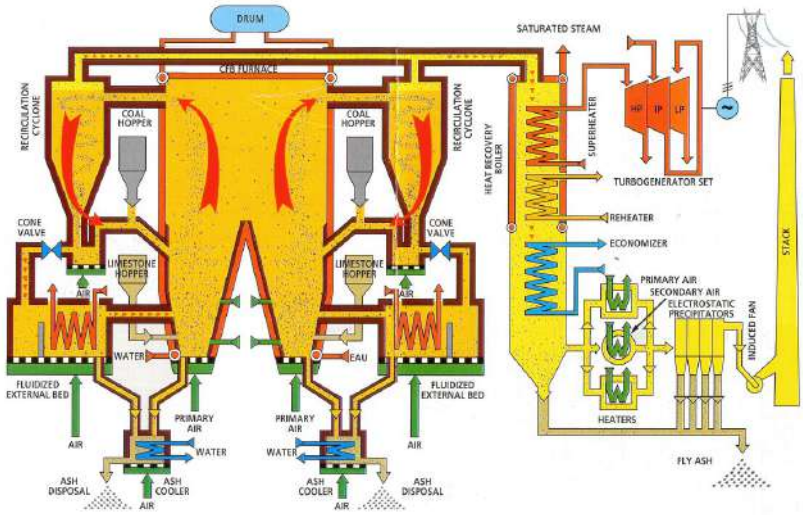

Figure 20.18: Example of a 250 MWe circualting fluidized bed combustor with external bed cooler.

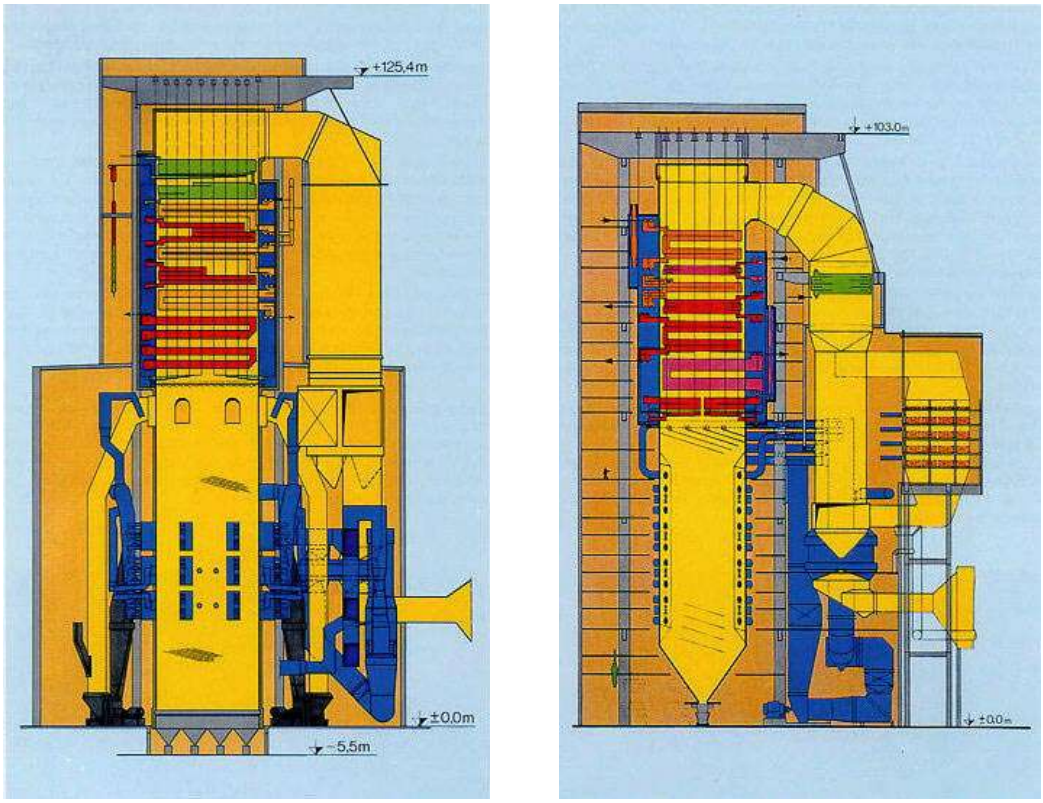

Figure 20.19: Two examples of pulverised fuel combustors. The left side is a sketch of a 600 MW EVT-once through steam generator with EVT-brown coal firing. The right side is a once-through steam generator with EVT-bituminous coal firing, flue gas decentrification and desulphurization for a 475 MW unit.

Table 20.2: Comparison of grate, fluidised bed, and pulverised fuel firing systems.

Grate Firing Systems	Fluidised Bed Firing Systems	Pulverised Fuel Firing Systems
Advantages of grate firing systems: • little fuel preparation expenditure • clear design • high degree of availability • simple operation • little auxiliary power requirements • low NO_x emissions (e.g. bituminous coals < 400 mg/m^3) • partial desulphurisation by limestone addition Disadvantages: • high combustion losses of 2–4% by unburnt carbon • high flue gas temperatures due to limited air preheating • unsuited for fine-grained fuels	Advantages of bubbling and circulating fluidised bed firing systems (BFB and CFB): • little fuel preparation expenditure • flue gas cleaning consists only of flue-gas particulate collection Disadvantages of BFB and CFB: • high limestone demand for sulphur capture at excess air • ash not utilisable without further preparation Advantages of BFB against SFB: • better burnout • lower limestone demand for sulphur capture • better emission values • no in-bed heating surfaces at risk of erosion • better power control	Advantages of pulverised fuel firing systems: • high degree of availability • large capacities • high power density • good burnout • utilisable ash Disadvantages: • high fuel preparation expenditures • flue gas cleaning needed for particulates, SO_2, and NO_x

Table 20.3: Output ranges of firing systems.

Firing System	Output Range [MWth]
pulverised fuel firing	40 up to 2500
stationary fluidised bed firing	up to 80
circulating fluidised bed firing	40 up to 750
grate firing	2.5 up to 175

4.4 Comparison of the different firing systems

Table 20.2 confronts the advantages and disadvantages of different combustion systems. The choice of the firing system depends on the properties of the fuel and on the steam generating capacity. Combustion systems for solid fuels are offered on the market with the capacities shown in table 20.3.